

**FACULTY
OF MATHEMATICS
AND PHYSICS**
Charles University

HABILITATION THESIS

Michal Belda

**Modeling the Climate System Across
Scales**

Department of Atmospheric Physics

Prague 2022

Contents

Abstract	2
Introduction	3
1 Global Models	5
2 Regional Models	7
3 Local Models	8
Conclusions	10
List of Abbreviations	13
List of Publications	14
A Attachments	16

Abstract

Climate system is one of the most complex problems of contemporary physics with components and processes spanning multiple spatial and temporal scales. Throughout the history of climate research many different types of models have been employed ranging from simple conceptual models or statistical models based on observations of historical patterns to fully physically-based models. The state-of-the-art weather and climate models are derived from the basic principles of physics such as the description of motion in the form of the Navier-Stokes equations. However, due to our limited knowledge, these equations need to be solved only by using some form of numerical approximation. Successful application of these techniques was made possible with the advent of electronic computers in the late 1940s and thanks to the advances in computer science and information technology, modern models are able to represent most of the complexity of the climate system components and processes. On the other hand, even with the fastest supercomputers, the full range of scales cannot be covered in sufficient details. Models covering the entire globe are limited in their spatial resolution to typically a hundred kilometers or more and, on the other side of the spectrum, turbulence-resolving models can only be integrated on a limited area, e.g. covering a city quarter. This thesis presents studies based on various numerical modeling systems covering the global, regional and local scales showing examples of results and challenges numerical modeling offers in the applications ranging from global and regional climate scenarios to urban micro-climate. Included are 9 research articles on the assessment of global climate model simulations using the conceptual Köppen-Trewartha climate classification, evaluation of regional climate models in Europe and evaluation of LES model PALM in urban context in three case studies of urban heat island and air quality for Prague.

Introduction

Climate system behavior is one of the most complex problems of contemporary physics. Climate, as one of the main determinants of the biophysical environment on Earth, has in some way been studied throughout most of modern human history, creating more or less sophisticated models based mostly on observations of existing patterns. The idea of applying general principles of physics on atmospheric motions had been floating around since early 20th century starting with the groundbreaking works of Cleveland Abbe, Vilhelm Bjerknes or Lewis Fry Richardson (for a historical review see e.g., Lynch, 2007). However, only in the last couple of decades, with the advent of digital electronic computers, these techniques have been made into full-fledged modeling tools that are being used every day for weather forecasting and in extension for climate projections. In a broad sense, these models belong to the computational fluid dynamics family of models (CFD).

Although most of the rules governing the climate system's various components and processes can be described by known principles and equations of dynamics, thermodynamics or radiative transfer, there are still unknowns. Prime examples are the Navier-Stokes equations, governing climate system dynamics, for which an analytical solution is not known and approximate numerical methods must be used. However, as we know from the seminal work of Edward Lorenz, these methods brought about new challenges due to their inherently chaotic behavior.

All current methods of predicting the state of the climate system still contain considerable uncertainty. In the field of climate projections, this uncertainty stems from the unknown chemical composition of the atmosphere (specifically concentrations of greenhouse gases), internal variability of the system and the models describing it, but also from incomplete knowledge of all relevant processes. A part of the uncertainty cannot be avoided, typically the part coming from the boundary conditions. Some parts, however, can be reduced to a certain degree, for example, in individual models, by making improvements to the representation of relevant processes or increasing resolution. The internal variability of the models can be estimated by constructing ensembles of simulations produced by different models, models with different configurations, initial conditions, etc. The community efforts of the initiatives like the Coupled Model Intercomparison Project (CMIP) and the Coordinated Regional Climate Downscaling Experiment (CORDEX) help immensely in this regard.

In this work, 9 research articles published between years 2014 and 2022 are presented, showing examples of climate system modeling techniques on three separate scales going from global, through regional to the street-scale local modeling for urban applications. In these publications, I was a principal author of the

articles on which chapter 1 is based, contributing to data processing, analysis of the results and formulating conclusions. In the articles of chapters 2 and 3, I was involved in all stages of the research, beginning with experiment design, running regional climate simulations with the RegCM model, development of the LES model PALM and post-processing tools for RegCM and PALM, data processing, analysis and preparation of the manuscript text.

1. Global Models

At the top of the hierarchy of the model family are models that in one way or another see the entire globe, i.e., global models. Loosely speaking, these can range from simple conceptual (e.g., climate zones), statistical, or lower-dimension physics-based models (e.g., Maher et al., 2019). However, in a strict sense, the climate community reserves the label global climate models (GCM; also general circulation models) for a set of models based on the general principles of fluid dynamics and thermodynamics (Stute et al., 2001). GCMs are a direct counterpart to the global numerical weather prediction models (NWP), sharing the basic principle of predicting the behavior of the climate system by solving the fundamental physical equations, providing the most detailed model view of the climate on the global scale.

The global view of the climate in these models brings about their most important drawback which is the insufficient level of detail a GCM can provide in terms of horizontal resolution. Operating these models meaningfully is only possible in the form of numerical integration on powerful supercomputers. The performance of such computers is inherently limited by hardware capabilities, thus setting a limit on the resolution of the climate models. Even though kilometer-scale global simulations exist, the bulk of state-of-the-art GCM scenario simulations in 2020s are produced on grids with horizontal resolution as low as 100 km or coarser. Processes whose typical scale is finer than that (e.g., convection, turbulence, etc.) need to be represented as parameterizations that are not always based on general principles but in many instances derived from observed statistical relations between large and fine scale.

Given all the limitations of the global models, it is only natural that before using these as tools for producing climate projections, one must test their performance on known climate conditions to prove model suitability. Tests like these are usually performed by comparing model simulations with observations of variables such as air temperature, precipitation, wind speed, etc., providing not only information about potential model deficiencies, but also giving the user a set of data that can be used for adjusting the raw future scenario simulations by the means of various statistical methods usually referred to as “bias-correction” (technical term encompassing many techniques of adjusting bias but also other statistical properties).

This chapter is composed of a series of three research articles we published between 2014 and 2016 on the evaluation of GCM simulations from the CMIP5 project (Coupled Model Intercomparison Project Phase 5, simulations that served as the main input for the Intergovernmental Panel on Climate Change Assessment Report 5). In these articles, we provided a validation of the CMIP5 ensemble

with respect to the observed data (Belda et al., 2015a) and a summary of future climate projections based on the CMIP5 ensemble (Belda et al., 2016). The underlining theme of the series was using a conceptual model of climate devised by Wladimir Köppen in the early 1900s (e.g., Köppen, 1923, 1936). The main idea behind this method is an observation of an existing link between the physical and biophysical realm, specifically the fact that the typical vegetation of an area is determined by the climatic conditions in that area. This conceptual model, although extremely simplistic compared to modern numerical models, proves to be useful in this task thanks to its comprehensive look at the climate. One of the challenges of numerical model evaluation is the observation that model performance is usually not uniform across either the physical or variable space. In simple terms, one model can be highly successful in representing e.g., mean temperature, yet fail in simulating correct precipitation patterns or vice versa. With the help of an aggregated metric such as the Köppen climate zone system, one can view the model outputs indeed as an interconnected system instead of a set of independent variables.

In our work, we used a revised version of the original Köppen scheme proposed by Glenn T. Trewartha hereafter named Köppen-Trewartha Climate Classification (KTC; Trewartha et al., 1980). This revised scheme introduced several adjustments for improvement of the correspondence with the observed boundaries, mainly in the North American context. Also, some vague formulations of the original Köppen scheme were improved upon, making this modification more suitable for model evaluation.

Even though the Köppen scheme and its various descendants have for many decades been a go-to tool in climatology taught in many a university course, while preparing the evaluation of CMIP5 ensemble, we found out that quite a large number of discrepancies appear in the existing literature concerning nomenclature but also climate zone definitions and numerical thresholds used in these definitions. This observation resulted in a review article that laid the foundation for the following two papers and was published as Belda et al. (2014).

2. Regional Models

The ultimate goal of climate modeling in terms of applications is to provide regional projections of potential climate system behavior in the future. Global climate models, however advanced, still lack the spatial detail that would allow to take the GCM outputs directly for producing such detailed regional climate scenarios, mainly due to computational costs associated with the numerical method employed. However, several techniques were developed to help with this problem that are usually referred to as regional climate downscaling (RCD). One of these methods is statistical downscaling (SD) which uses the approach of applying known statistical relationships between large-scale patterns and regional-to-local climate to the GCM outputs.

Contrary to the statistical methods, dynamical downscaling methods use the physically consistent approach of numerical integration of fundamental equations in higher resolution. In simple terms, regional climate models (RCM) are the same category of models as GCMs only integrated on a selected region. The technique, analogous to the use of limited-area numerical weather prediction models, was first explored in the seminal works of Dickinson et al. (1989) and Giorgi (1990) and has since evolved into a separate field with its own set of advantages and drawbacks.

In our work, we use the latter approach of limited-area nested regional climate models. The first two studies in this chapter present a validation and inter-comparison of a small ensemble of regional climate models used in a CECILIA project that ran from 2006 to 2009 (<http://www.cecilia-eu.org/>). As with GCMs, their regional counterparts need to have a performance evaluation on known climate conditions before their simulations can be used for construction of future climate projections, which was performed in the Skalák et al. (2014) article. The analysis of the climate change signal in the scenario simulations of the CECILIA model ensemble was then presented in Belda et al. (2015b).

The multi-model ensemble approach that had long been represented by the CMIP project in the global modeling community was also adopted by the RCM world in a number of local projects. Starting in 2009, however, the CORDEX initiative was born with the goal to connect the fragmented RCM communities, devise a common protocol for a coordinated effort in model development, and ultimately produce regional climate scenarios for all continents. Our involvement in this initiative, specifically in the European branch (EURO-CORDEX) was a natural step from the regional projects such as ENSEMBLES or CECILIA. A review of the ten-year experience in this effort was presented in Jacob et al. (2020).

3. Local Models

As discussed in previous chapters, the CFD modeling method based on approximate numerical integration of the fundamental physical equations poses a limit on the resolution of the models. Even when run on the most advanced supercomputers of the 2020s, global and regional models are only able to reach a kilometer-scale resolution for shorter time periods (e.g., individual decades) and long-term simulations are usually only available in resolutions of tens to hundreds of kilometers. Smaller-scale processes that cannot be neglected must be parameterized in these models and, by definition, these models are not able to discern specific micro-climatic features.

In certain practical applications, it is necessary to have a model able to resolve features that are beyond what both global and regional models are capable of. Urban areas are one example of such environments that are at the forefront of interest in connection with climate studies for the changes these areas introduce to the micro-climate. The urban heat island phenomenon (UHI) or deterioration of air quality are among the most studied effects due to their direct influence on thermal comfort and health. The specific behavior of artificial surfaces comprising towns and cities pushes the limits of both global and regional climate simulations. The radiation balance and turbulent processes within the urban canopy can at best be represented by some form of a generalized urban scheme in mesoscale models.

On the other side of the model spectrum are models designed to resolve the microscale. To do that, the models must inevitably use a much finer computational mesh. The limited computer power obstacle standing before the lower-resolution models is multiplied here by the fact that the convergence of the numerical solution is conditioned by a certain ratio between the time step and model grid spacing known as Courant-Friedrichs-Lewy or CFL condition (Courant et al., 1928). The CFL criterion means that increasing model horizontal resolution necessitates choosing a shorter time step for the model to be stable. For example, doubling the model horizontal resolution, i.e., halving the model grid point distance, while keeping the same overall domain size, results in roughly eight times higher number of computational operations.

When attempting to explicitly resolve micro-climatic features such as those of city components (buildings, streets, pavements, etc.), the models must reach spatial resolution of less than tens of meters. In effect, the time step of such models can be as short as a fraction of a second. Reaching a sufficient model resolution for these applications then usually means that only very short case studies can be performed. However, even with such limits, meaningful experiments can be performed in this regard.

The articles selected for this chapter are based on simulations using the large-eddy simulation method (LES) in urban areas. The LES technique allows for explicit representation of large turbulent eddies by scale separation, parameterizing only the smallest eddies by subgrid-scale models. In our studies, we used the PALM model utilizing the computational power of massively parallel computer architectures (Maronga et al., 2015). The open architecture of the PALM model allowed for an implementation of complex urban surface treatment. The then-called Urban Surface Model (USM) was introduced in 2017 and an evaluation of a case-study simulation suite in a typical urban quarter Prague-Holešovice was presented in the first of the included articles (Resler et al., 2017). The improvements also included a newly developed radiative transfer model (RTM) within the urban canopy. Model performance was tested against infrared camera observations. The analysis also included a test of the sensitivity of the model simulation results with respect to domain size and the uncertainty in material parameters.

The results of the Resler et al. (2017) analysis served as a basis for further improvements of the urban surface model (later renamed to Building Surface Model – BSM) and also as a starting point for more comprehensive validation against observations obtained in an extensive observation campaign specifically designed for this purpose. The model performance was evaluated on a larger domain in the densely built-up part of the Prague-Dejvice quarter in several places covering most of the typical urban surface configurations and materials. The details of the observation campaign and model validation were published in Resler et al. (2021).

As a companion paper, an extensive sensitivity study was performed building upon the previous rudimentary evaluation of Resler et al. (2017). High-resolution modeling is not only dependent on the model’s ability to be run on a finer grid, but also on providing input data of sufficient resolution and quality. In urban modeling, this means that detailed information about the physical properties of natural and artificial materials in the cities is required. Belda et al. (2021) analyzed a comprehensive set of simulations studying the model response to artificially introduced changes in physical parameters of surface materials (albedo, emissivity, etc.) to assess the model sensitivity to potentially erroneous setting of these parameters that are hard to obtain in adequate quality. The second set of experiments then analyzed model response to typically considered counter-UHI measures like introduction of urban greenery or changing urban surface configuration.

Topics introduced in this chapter have been the subject of a number of studies and are currently analyzed in more detail within the TURBAN project framework.

Conclusions

Numerical models are an indispensable tool in the modern-era climate research. Their uses range from pure research to applications in decision-making processes and as such, the models need to be properly evaluated. In this thesis, a compilation of 9 studies was presented spanning a large range of spatial and temporal scales.

First three articles explored the application of a “classical” conceptual model of bioclimatic zones for evaluation of GCM ensemble performance in historical and future climate scenarios. The important advantage of this technique is in the aggregation of several climatological variables and their statistics into one metric showing the overall model performance. Combined with the link the classification makes between the climate and biosphere, this method also proves useful as a simple impact model.

The second set of articles showed three studies based on the dynamical down-scaling method by which the outputs of global models can be focused on a specific area in much higher resolution. The regional climate modeling, which has been explored for more than three decades now, brings new possibilities and new challenges. The added value of using meso-scale models by including processes that are beyond the resolution of the global models is an important aspect. Regional climate models are making their way into the forefront and with the growing community centered around the CORDEX initiative are subject to an extensive research.

Urban microclimate and the specific challenges in its modeling were explored in the last chapter consisting of three analyses based on the LES modeling technique. The model studies included here show an application of this method in two typical urban areas in Prague, showing both an validation of newly developed model components as well as scenarios of potential urbanistic changes and their effects on thermal comfort and air quality in the streets.

Altogether, all CFD model applications are conditioned by the availability of computational resources. Fortunately, the advances in the information technology over time have made it possible not only to use the models at all, but with the ever increasing computer performance also to make steady advances in the model resolution and complexity. How long this trend will continue remains to be seen.

Bibliography

- Belda, M., E. Holtanová, T. Halenka, and J. Kalvová (2014). “Climate classification revisited: From Köppen to Trewartha”. In: *Climate Research* 59(1), pp. 1–13. DOI: 10.3354/cr01204.
- Belda, M., E. Holtanová, T. Halenka, J. Kalvová, and Z. Hlávka (2015a). “Evaluation of CMIP5 present climate simulations using the Köppen-Trewartha climate classification”. In: *Climate Research* 64(3), pp. 201–212. DOI: 10.3354/cr01316.
- Belda, M., E. Holtanová, J. Kalvová, and T. Halenka (2016). “Global warming-induced changes in climate zones based on CMIP5 projections”. In: *Climate Research* 71(1), pp. 17–31. DOI: 10.3354/cr01418.
- Belda, M., J. Resler, J. Geletič, P. Krč, B. Maronga, M. Sühling, M. Kurppa, F. Kanani-Sühling, V. Fuka, K. Eben, N. Benešová, and M. Auvinen (2021). “Sensitivity analysis of the PALM model system 6.0 in the urban environment”. In: *Geoscientific Model Development* 14, pp. 4443–4464. DOI: 10.5194/gmd-14-4443-2021.
- Belda, M., P. Skalák, A. Farda, T. Halenka, M. Déqué, G. Csima, J. Bartholy, C. Torma, Boroneant C., M. Caian, and V. Spiridonov (2015b). “CECILIA Regional Climate Simulations for Future Climate: Analysis of Climate Change Signal”. In: *Advances in Meteorology* 2015. DOI: 10.1155/2015/354727.
- Courant, R., K. Friedrichs, and H. Lewy (1928). “Über die partiellen Differenzgleichungen der mathematischen Physik”. In: *Mathematische Annalen (in German)* 100 (1), pp. 32–74. DOI: 10.1007/BF01448839.
- Dickinson, R. E., R. M. Errico, F. Giorgi, and G. T. Bates (1989). “A regional climate model for the western United States”. In: *Climatic Change* 15, pp. 383–422.
- Giorgi, F. (1990). “Simulation of regional climate using a limited area model nested in a general circulation model”. In: *Journal of Climate* 3, pp. 941–963.
- Jacob, Daniela, Claas Teichmann, Stefan Sobolowski, Eleni Katragkou, Ivonne Anders, Michal Belda, Rasmus Benestad, Fredrik Boberg, Erasmo Buonomo, Rita M. Cardoso, et al. (Apr. 2020). “Regional climate downscaling over Europe: perspectives from the EURO-CORDEX community”. In: *Regional Environmental Change* 20.2, p. 51. ISSN: 1436-378X. DOI: 10.1007/s10113-020-01606-9. URL: <https://doi.org/10.1007/s10113-020-01606-9>.
- Köppen, W. (1923). *Die Klimate der Erde. Grundriss der Klimakunde*. Berlin, Leipzig: Walter de Gruyter & Co.
- (1936). “Das geographische System der Klimate”. In: *Handbuch der Klimatologie*. Ed. by Geiger R. Köppen W. Berlin: Gebrüder Borntraeger, pp. C1–C44.

- Lynch, P. (2007). “The origins of computer weather prediction and climate modeling”. In: *Journal of Computational Physics* 227 (2008), pp. 3431–3444. DOI: 10.1016/j.jcp.2007.02.034.
- Maher, P. and E. P. Gerber (2019). “Atmospheric model hierarchies: Connecting theory and models”. In: *Eos* 100. DOI: 10.1029/2019E0133929.
- Maronga, B., M. Gryscha, R. Heinze, F. Hoffmann, F. Kanani-Sühring, M. Keck, K. Ketelsen, M. O. Letzel, M. Sühring, and S. Raasch (2015). “The Parallelized Large-Eddy Simulation Model (PALM) version 4.0 for atmospheric and oceanic flows: model formulation, recent developments, and future perspectives”. In: *Geoscientific Model Development* 8, pp. 2515–2551. DOI: 10.5194/gmd-8-2515-2015.
- Resler, J., K. Eben, J. Geletič, P. Krč, M. Rosecký, M. Sühring, M. Belda, V. Fuka, T. Halenka, P. Huszár, J. Karlický, N. Benešová, J. Ďoubalová, K. Honzáková, J. Keder, Š. Nápravníková, and O. Vlček (2021). “Validation of the PALM model system 6.0 in real urban environment; case study of Prague-Dejvice, Czech Republic”. In: *Geoscientific Model Development* 14, pp. 4797–4842. DOI: 10.5194/gmd-14-4797-2021.
- Resler, J., P. Krč, M. Belda, P. Juruš, N. Benešová, J. Lopata, O. Vlček, D. Damašková, K. Eben, P. Derbek, B. Maronga, and F. Kanani-Sühring (2017). “PALM-USM v1.0: A new urban surface model integrated into the PALM large-eddy simulation model”. In: *Geoscientific Model Development* 10, pp. 3635–3659. DOI: 10.5194/gmd-10-3635-2017.
- Skalák, P., M. Déqué, M. Belda, A. Farda, T. Halenka, G. Csima, J. Bartholy, M. Caian, and V. Spiridonov (2014). “CECILIA regional climate simulations for the present climate: validation and inter-comparison”. In: *Climate Research* 60(1), pp. 1–12. DOI: 10.3354/cr0120.
- Stute, M., A. Clement, and G. Lohmann (2001). “Global climate models: Past, present, and future”. In: *Proceedings of the National Academy of Sciences* 98 (19), pp. 10529–10530. DOI: 10.1073/pnas.191366098.
- Trewartha, G. T. and L. H. Horn (1980). “Introduction to climate”. In: 5th edition. McGraw Hill, p. 416.

List of Abbreviations

BSM	Building Surface Model
CFD	Computational Fluid Dynamics
CFL	Courant-Friedrichs-Lewy condition
CMIP	Coupled Model Intercomparison Project
CORDEX	Coordinated Regional Climate Downscaling Experiment
GCM	General Circulation Model; Global Climate Model
LES	Large Eddy Simulation
KTC	Köppen-Trewartha Climate Classification
NWP	Numerical Weather Prediction
PALM	Parallelized Large-Eddy Simulation Model
RCD	Regional Climate Downscaling
RCM	Regional Climate Model
RTM	Radiative Transfer Model
SD	Statistical Downscaling
UHI	Urban Heat Island
USM	Urban Surface Model

List of Publications

The presented thesis has been compiled from the following peer-reviewed publications:

- Belda, M., E. Holtanová, T. Halenka, and J. Kalvová (2014). “Climate classification revisited: From Köppen to Trewartha”. In: *Climate Research* 59(1), pp. 1–13. DOI: 10.3354/cr01204.
- Belda, M., E. Holtanová, T. Halenka, J. Kalvová, and Z. Hlávka (2015a). “Evaluation of CMIP5 present climate simulations using the Köppen-Trewartha climate classification”. In: *Climate Research* 64(3), pp. 201–212. DOI: 10.3354/cr01316.
- Belda, M., E. Holtanová, J. Kalvová, and T. Halenka (2016). “Global warming-induced changes in climate zones based on CMIP5 projections”. In: *Climate Research* 71(1), pp. 17–31. DOI: 10.3354/cr01418.
- Belda, M., J. Resler, J. Geletič, P. Krč, B. Maronga, M. Sühling, M. Kurppa, F. Kanani-Sühling, V. Fuka, K. Eben, N. Benešová, and M. Auvinen (2021). “Sensitivity analysis of the PALM model system 6.0 in the urban environment”. In: *Geoscientific Model Development* 14, pp. 4443–4464. DOI: 10.5194/gmd-14-4443-2021.
- Belda, M., P. Skalák, A. Farda, T. Halenka, M. Déqué, G. Csima, J. Bartholy, C. Torma, Boroneant C., M. Caian, and V. Spiridonov (2015b). “CECILIA Regional Climate Simulations for Future Climate: Analysis of Climate Change Signal”. In: *Advances in Meteorology* 2015. DOI: 10.1155/2015/354727.
- Jacob, Daniela, Claas Teichmann, Stefan Sobolowski, Eleni Katragkou, Ivonne Anders, Michal Belda, Rasmus Benestad, Fredrik Boberg, Erasmo Buonomo, Rita M. Cardoso, et al. (Apr. 2020). “Regional climate downscaling over Europe: perspectives from the EURO-CORDEX community”. In: *Regional Environmental Change* 20.2, p. 51. ISSN: 1436-378X. DOI: 10.1007/s10113-020-01606-9. URL: <https://doi.org/10.1007/s10113-020-01606-9>.
- Resler, J., K. Eben, J. Geletič, P. Krč, M. Rosecký, M. Sühling, M. Belda, V. Fuka, T. Halenka, P. Huszár, J. Karlický, N. Benešová, J. Ďoubalová, K. Honzáková, J. Keder, Š. Nápravníková, and O. Vlček (2021). “Validation of the PALM model system 6.0 in real urban environment; case study of Prague-Dejvice, Czech Republic”. In: *Geoscientific Model Development* 14, pp. 4797–4842. DOI: 10.5194/gmd-14-4797-2021.
- Resler, J., P. Krč, M. Belda, P. Juruš, N. Benešová, J. Lopata, O. Vlček, D. Damašková, K. Eben, P. Derbek, B. Maronga, and F. Kanani-Sühling (2017). “PALM-USM v1.0: A new urban surface model integrated into the PALM

large-eddy simulation model”. In: *Geoscientific Model Development* 10, pp. 3635–3659. DOI: 10.5194/gmd-10-3635-2017.

Skalák, P., M. Déqué, M. Belda, A. Farda, T. Halenka, G. Csimá, J. Bartholy, M. Caian, and V. Spiridonov (2014). “CECILIA regional climate simulations for the present climate: validation and inter-comparison”. In: *Climate Research* 60(1), pp. 1–12. DOI: 10.3354/cr0120.

A. Attachments

Following are the full prints of the articles used in this thesis. All articles are subject to copyright of their respective copyright holders.



Climate classification revisited: from Köppen to Trewartha

Michal Belda*, Eva Holtanová, Tomáš Halenka, Jaroslava Kalvová

Charles University in Prague, Dept. of Meteorology and Environment Protection, 18200 Prague, Czech Republic

ABSTRACT: The analysis of climate patterns can be performed separately for each climatic variable or the data can be aggregated, for example, by using a climate classification. These classifications usually correspond to vegetation distribution, in the sense that each climate type is dominated by one vegetation zone or eco-region. Thus, climatic classifications also represent a convenient tool for the validation of climate models and for the analysis of simulated future climate changes. Basic concepts are presented by applying climate classification to the global Climate Research Unit (CRU) TS 3.1 global dataset. We focus on definitions of climate types according to the Köppen-Trewartha climate classification (KTC) with special attention given to the distinction between wet and dry climates. The distribution of KTC types is compared with the original Köppen classification (KCC) for the period 1961–1990. In addition, we provide an analysis of the time development of the distribution of KTC types throughout the 20th century. There are observable changes identified in some subtypes, especially semi-arid, savanna and tundra.

KEY WORDS: Köppen-Trewartha · Köppen · Climate classification · Observed climate change · CRU TS 3.10.01 dataset · Patton's dryness criteria

Resale or republication not permitted without written consent of the publisher

1. INTRODUCTION

Climate monitoring is mostly based either directly on station measurements of climate characteristics (surface air temperature, precipitation, cloud cover, etc.), or on some post-processed form of those measurements, such as gridded datasets. The analysis of climate patterns can be performed for each individual climate variable separately, or the data can be aggregated, for example, by using some kind of climate classification that integrates several climate characteristics. These classifications usually correspond to vegetation distribution in the sense that each climate type is dominated by one vegetation zone or eco-region (Köppen, 1936, Trewartha & Horn 1980, Bailey 2009, Baker et al. 2010). Thus, climate classifications can also represent a convenient, i.e. integrated, but still quite simple tool for the validation of climate models and for the analysis of simulated future climate changes.

The first quantitative classification of Earth's climate was developed by Wladimir Köppen in 1900 (Kottek et al. 2006). Even though various different classifications have been developed since then, those based on Köppen's original approach (Köppen 1923, 1931, 1936) and its modifications are still among the most frequently used systems. For application to climate model outputs the Köppen-Geiger system (Köppen 1936, Geiger 1954) or Köppen-Trewartha modification (e.g. Trewartha & Horn 1980) are usually utilized.

The first digital Köppen-Geiger world map for the second half of 20th century was published by Kottek et al. (2006). This study used the Climatic Research Unit (CRU) TS2.1 dataset (Mitchell & Jones 2005) and the VASClm0v1.1 precipitation data (gpcc.dwd.de) for the period of 1951–2000. Prior to this, many textbooks reproduced a copy of one of the historical hand-drawn maps from Köppen (1923, 1931 or 1936) or Geiger (1961). Following up on the work of Kottek

*Corresponding author: Michal.Belda@mff.cuni.cz

et al. (2006), Rubel & Kottek (2010) produced a series of digital world maps covering the extended period 1901–2100. These maps are based on CRU TS2.1 and on GPCC Version 4 data, and Global Climate Model (GCM) outputs for the period 2003–2100 were taken from the TYN SC 2.0 dataset (Mitchell et al. 2004). A new high-resolution global map of the Köppen-Geiger classification was produced by Peel et al. (2007). Climatic variables used for the determination of climate types were calculated using data from 4279 stations of the Global Historical Climatology Network (Peterson & Vose 1997) and interpolated onto a $0.1^\circ \times 0.1^\circ$ grid.

One of the first attempts to use the Köppen climate classification (KCC) to validate GCM outputs was presented by Lohmann et al. (1993). The observed climate conditions were represented by temperature data from Jones et al. (1991) and precipitation data from Legates & Willmott (1990). In Kalvová et al. (2003), the KCC was applied to CRU gridded climatology (New et al. 1999) for the periods 1961–1990 and 1901–1921. The latter period was used for comparison with the original results described by Köppen (1931).

The modifications of KCC proposed by G. T. Trewartha (Trewartha 1968, Trewartha & Horn 1980) adjust both the original temperature criteria and the thresholds separating wet and dry climates (for details see Section 3). The resulting classification is usually denoted the Köppen-Trewartha classification (KTC). Fraedrich et al. (2001) applied KTC to CRU data (New & Hulme 1998) with $0.5^\circ \times 0.5^\circ$ resolution (excluding Antarctica). They analyzed the shifts of climate types during the 20th century in relation to changes in circulation indices (Pacific Decadal Oscillation and North Atlantic Oscillation). KTC types were also used by Guetter & Kutzbach (1990), who studied atmospheric general circulation model simulations of the last interglacial and glacial climates (126 and 18 thousand yr before present). Furthermore, Baker et al. (2010) compared KTC types over China for historical (1961–1990) and projected future climates (2041–2070) simulated using the HadCM3 model under the SRES A1F1 scenario (Nakicenovic & Swart 2000). The KTC types were obtained by applying classification criteria for each grid box of the 30 yr PRISM climatology (Daly et al. 2002) and to eco-regions defined through the Multivariate Spatio-Temporal Clustering algorithm. Feng et al. (2012) used the KTC to evaluate climate changes and their impact on vegetation for the area north of 50° N and the period 1900–2099, focusing on the Arctic region. In addition to the observed data, the outputs of 16

AR4 GCMs (Meehl et al. 2007) under SRES scenarios B1, A1B, and A2 were used. De Castro et al. (2007) used the KTC for validation of 9 regional climate models (RCMs) from project PRUDENCE (<http://prudence.dmi.dk>) over Europe for the period 1961–1990 and for the analysis of simulated climate change for 2071–2100 under scenario SRES A2. They used the CRU climatology as the observed dataset (New et al. 1999). Wang & Overland (2004) quantified historical changes in vegetation cover in the Arctic (1900–2000) by applying the KTC to NCEP/NCAR reanalysis (Kalnay et al. 1996) and CRU TS2.0 (New et al. 1999, 2000), and compared the results with satellite NDVI (Normalized Difference Vegetation Index, providing an areal average measure of the amount of vegetation and its photosynthetic activity). Gerstengarbe & Werner (2009) studied how global warming in the period 1901–2003 influenced Europe by using the KTC types. Their results are based on the data with spatial resolution of $0.5^\circ \times 0.5^\circ$ produced at the Potsdam Institute for Climate Impact Research.

The above examples of studies employing climate classifications show how different authors use various datasets with diverse spatial resolution for time periods of different lengths (e.g. 15, 30, or 50 yr) and over various geographical areas and spatial scales. However, it is not always clearly described how the climate types are defined and which modification of the respective climate classification is used. Therefore, it is appropriate to describe KTC in detail, its differences from KCC, and to create new maps of the KTC types based on the latest version of the CRU dataset; these are the goals of the present study. These results will provide background for further validation of the new generation of CMIP5 GCMs (Taylor et al. 2012), analysis of recent climate change, and for the evaluation of simulated future climate change. These topics will be addressed in studies we are currently preparing for publication.

This study includes only a part of the graphical materials used for our analysis. Additional maps and graphs can be found on a supplementary website at <http://kmp.mff.cuni.cz/projects/trewartha>.

2. DATA

As an observational data source we use the CRU TS 3.10.01 dataset (Harris et al. in press). CRU TS3.10 provides a monthly time-series of global gridded data based on observations from more than 4000 stations. Among other variables, it includes the mean surface air temperature and precipitation, on which the cli-

mate classifications used in this work are based. CRU TS3.10 is available over land areas excluding Antarctica at a high spatial resolution of $0.5^\circ \times 0.5^\circ$ and covers the period 1901–2009. We concentrate on the period 1901–2005, which is also used in further studies for the validation of GCMs. The version 3.10.01 was the most recent update of the dataset at the time of undertaking this analysis. This update includes corrections to precipitation data, as well as to the data files of wet days and frost frequency.

3. KOPPEN-TREWARTHA CLIMATE CLASSIFICATION SCHEME

In the present paper, we adopt the KTC defined in Trewartha & Horn (1980) with Patton's boundaries of arid climates (Patton 1962). This scheme builds upon the original Köppen system and introduces various adjustments to make the climate types better correspond with the observed boundaries of natural landscapes (de Castro et al. 2007). Some of the modifications introduced by the KTC also deal with a certain vagueness of the KCC formulations. This section will describe the KTC and compare the definitions with the KCC, as described by Köppen (1936). See Table 1 and Table 3 for respective summaries of the KTC and KCC classifications.

The KTC defines 6 main climatic groups. Five of them (denoted as *A*, *C*, *D*, *E*, and *F*) are basic thermal zones. The sixth group *B* is the dry climatic zone that cuts across the other climate types, except for the polar climate *F*. The main climate types are, similarly to those of the KCC, determined according to the long-term annual and monthly means of surface air temperature and amounts of precipitation. The main modifications in the KTC in comparison with the KCC are the different definitions of groups *C* and *D*, a newly defined *E* type, and different thresholds for distinguishing between wet and dry climates. In the following text, the individual climate types will be discussed in detail.

3.1. Group A: tropical humid climates

Trewartha & Horn (1980) call this type 'killing frost absent'. The mean air temperature of the coldest month must be over 18°C (i.e. all months must be warmer than 18°C). The subtypes of this group are defined according to the annual cycle of precipitation (number of dry months) Table 1. Two main subtypes are *Ar* (tropical wet, sometimes called tropical rain-

forest climate) and *Aw* (tropical wet and dry, called savanna climate). Subtype *As* is quite rare.

Regarding the definition of 'dry month', Trewartha & Horn (1980, p. 235) state the following: 'In equatorial lowlands where the average annual temperature is about 25 to 27°C , to be dry, a month may not have more than about 5.5 cm of average precipitation totals.' Köppen (1931, 1936) and de Castro et al. (2007) use the precipitation limit of 6 cm to distinguish between a dry and a wet month. In the present study, we also use the 6 cm threshold.

3.2. Group C: subtropical climates

In the *C* climate type there must be 8 to 12 months with a monthly mean air temperature of over 10°C and the temperature of the coolest month must be lower than 18°C . The subtypes are again based on the annual cycle of precipitation. Letters *s*, *w* and *f* have similar meaning as they do in the KCC. However, in the KCC, the conditions are not based on precipitation totals during the winter (summer) half-year, but on the amount of precipitation in the wettest (driest) month of the season. Another difference is in the condition for subtype *s*, which is defined by an average annual precipitation of less than 89 cm, in addition to the driest summer month having less than 3 cm precipitation.

The 2 main subtypes of group *C* in the KTC are *Cs* (subtropical dry-summer climate, sometimes also called Mediterranean) and *Cf* (subtropical humid climate). The subtype *Cw* (subtropical dry-winter) is relatively rare (Table 2).

3.3. Group D: temperate climates

The *D* climate type is defined by the condition that 4 to 7 months must have a monthly mean air temperature of over 10°C . The main subtypes are oceanic *Do* and continental *Dc*. Their definitions are based on the mean air temperature of the coldest month. In this study, we use the 0°C threshold to divide these subtypes.

3.4. Group E: boreal climates

For the *E* climate type, it is necessary to have one to 3 months inclusive with a monthly mean air temperature of over 10°C . Originally, there were no subtypes of this group, but some authors differentiate

Table 1. Climate types and subtypes defined by the Köppen-Trewartha climate classification (Trewartha & Horn 1980). T : mean annual temperature ($^{\circ}\text{C}$); T_{mo} : mean monthly temperature ($^{\circ}\text{C}$); P_{mean} : mean annual rainfall (cm); P_{dry} : monthly rainfall of the driest summer month; R : Patton's precipitation threshold, defined as $R = 2.3T - 0.64P_w + 41$, where P_w is the percentage of annual precipitation occurring in winter (Patton 1962); T_{cold} (T_{warm}): monthly mean air temperature of the coldest (warmest) month

Type / subtype	Criteria Rainfall/temperature regime
A	$T_{\text{cold}} > 18^{\circ}\text{C}$; $P_{\text{mean}} \geq R$
<i>Ar</i>	10 to 12 mo wet; 0 to 2 mo dry
<i>Aw</i>	Winter (low-sun period) dry; >2 months dry
<i>As</i>	Summer (high-sun period) dry; rare in type A climates
B	$P_{\text{mean}} < R$
<i>BS</i>	$R/2 < P_{\text{mean}} < R$
<i>BW</i>	$P_{\text{mean}} < R/2$
C	$T_{\text{cold}} < 18^{\circ}\text{C}$; 8 to 12 months with $T_{\text{mo}} > 10^{\circ}\text{C}$
<i>Cs</i>	Summer dry; at least 3 times as much rain in winter half year as in summer half-year; $P_{\text{dry}} < 3$ cm; total annual precipitation < 89 cm
<i>Cw</i>	Winter dry; at least 10 times as much rain in summer half-year as in winter half-year
<i>Cf</i>	No dry season; difference between driest and wettest month less than required for <i>Cs</i> and <i>Cw</i> ; $P_{\text{dry}} > 3$ cm
D	4 to 7 months with $T_{\text{mo}} > 10^{\circ}\text{C}$
<i>Do</i>	$T_{\text{cold}} > 0^{\circ}\text{C}$ (or $> 2^{\circ}\text{C}$ in some locations inland) ^a
<i>Dc</i>	$T_{\text{cold}} < 0^{\circ}\text{C}$ (or $< 2^{\circ}\text{C}$) ^a
E	1 to 3 months with $T_{\text{mo}} > 10^{\circ}\text{C}$
F	$T_{\text{warm}} < 10^{\circ}\text{C}$
<i>Ft</i>	$T_{\text{warm}} > 0^{\circ}\text{C}$
<i>Fi</i>	$T_{\text{warm}} < 0^{\circ}\text{C}$

^aIn the present study the boundary between subtypes *Do* and *Dc* is $T_{\text{cold}} = 0^{\circ}\text{C}$

oceanic and continental subtypes in the same way as in type *D* (e.g. de Castro et al. 2007). This distinction can prove useful especially when dealing with specific regional features. For the purposes of global evaluation we use the original definition that does not divide the *E* type. The KCC does not have an analogous climate group.

3.5. Group F: polar climates

Within the *F* type, all months must have a monthly mean air temperature of below 10°C . The subtypes are *Ft* (tundra) with the warmest month's air temperature above 0°C and *Fi* (ice cap) where the air temperature in all months remains below 0°C .

3.6. Group B: dry climates

One of the main differences between the KCC and the KTC is the definition of dry climates *B*, or more precisely, the formula for the calculation of the dryness threshold used in these definitions. In the KCC, the boundary distinguishing between wet and dry climates is defined according to Eq. (1), which differs according to the annual precipitation pattern:

$$\begin{aligned}
 R &= 2T + 14 && \text{for evenly distributed rainfall} && (1) \\
 R &= 2T && \text{for rainfall concentrated in winter} \\
 R &= 2T + 28 && \text{for rainfall concentrated in summer}
 \end{aligned}$$

where R denotes the mean annual precipitation threshold in centimeters, and T is the annual mean temperature in degrees Celsius. The subtype *BS* (semi-arid or steppe climate) is found where the mean annual precipitation amount is lower than R , but higher than $0.5R$. If it is lower than $0.5R$, the KCC defines it as an arid (also desert) climate *BW*. Even though Köppen (1936) considered these criteria as convenient approximations, Trewartha & Horn (1980, p. 348) highlighted that when they are simply converted to imperial units, they 'tend to give a false impression of the degree of accuracy'. These authors preferred a modification by Patton (1962), who simplified Eq. (1) as follows:

$$\begin{aligned}
 R^* &= 0.5T^* - 12 && \text{for rainfall evenly distributed} && (2) \\
 R^* &= 0.5T^* - 17 && \text{for rainfall concentrated in winter} \\
 R^* &= 0.5T^* - 6 && \text{for rainfall concentrated in summer}
 \end{aligned}$$

where the mean annual precipitation threshold R^* is in inches, and the mean annual air temperature T^* is in degrees Fahrenheit. The differences resulting from Patton's modification are illustrated in Fig. 1. It is obvious that the boundary between wet and dry climates is similar in areas with lower mean air temperature.

In Köppen (1923, 1931, 1936), the meaning of 'rainfall concentrated in summer/winter' is not explained explicitly, but it is clear that there must be a marked seasonal contrast both in rainfall and in air temperature. Some authors have used the condition that 70% of the annual precipitation amount must be con-

Table 2. Percentage of continental area (without Antarctica) covered by climate types according to the Köppen-Trewartha climate classification (KTC) and the Köppen climate classification (KCC, types are described in Table 3), calculated from the Climate Research Unit TS 3.10 dataset for the period 1961–1990

KCC	KTC													Sum
	<i>Ar</i>	<i>Aw</i>	<i>BW</i>	<i>BS</i>	<i>Cs</i>	<i>Cw</i>	<i>Cf</i>	<i>Do</i>	<i>Dc</i>	<i>E</i>	<i>Ft</i>	<i>Fi</i>		
<i>Af</i>	5.10													5.10
<i>Aw</i>	0.38	11.17		2.09										13.63
<i>Am</i>	1.92	1.74												3.66
<i>BW</i>		0.01	16.76	1.08	0.50			0.01			0.11			18.47
<i>BS</i>		0.01	2.52	6.36	0.27		0.23	0.22	0.39	0.02	0.13			10.15
<i>Cs</i>					0.40		0.46	0.76	0.40	0.05				2.07
<i>Cw</i>				1.46		0.77	2.71	0.38	0.26	0.02				5.59
<i>Cf</i>				0.57			4.72	1.74	1.48	0.17				8.69
<i>Ds</i>									0.48	0.14				0.62
<i>Dw</i>			0.03	1.06					1.14	2.16				4.39
<i>Df</i>				0.42					7.51	12.43				20.36
<i>ET</i>											6.10			6.10
<i>EF</i>												1.16		1.16
Sum	7.40	12.93	19.31	13.04	1.17	0.77	8.12	3.11	11.65	14.99	6.34	1.16		

centrated in the 6 high-sun months (April through September in the Northern Hemisphere, and October through March in the Southern) in order for it to be classified as rainfall concentrated in the summer. An analogous condition is then applied for rainfall concentrated in the winter. Others have used the same definition for summer (winter) rainfall as Köppen used in his *C* climate group (Table 3).

A further simplification of the wet/dry climate threshold was proposed by Patton (1962) who suggested replacing the original 3 criteria (Eq. 2) with one equation for the mean annual precipitation threshold R^* (in inches):

$$R^* = 0.5T^* - 0.25P_w \quad (3)$$

where T^* is the annual mean air temperature in °F, and P_w is the percentage of annual precipitation occurring in winter (meaning the 6 coldest months). If we transform Eq. (3) into centimeters and degrees Celsius, we get Eq. 4, as used, for example, in de Castro et al. (2007):

$$R = 2.3T - 0.64P_w + 41 \quad (4)$$

where R denotes the mean annual precipitation threshold in cm, T is the mean annual air temperature in °C, and P_w is the percentage of annual precipitation concentrated in winter. Instead of the 6 coldest months, the 6 low-sun months are used (October to March in the Northern Hemisphere, and April to September in the Southern Hemisphere).

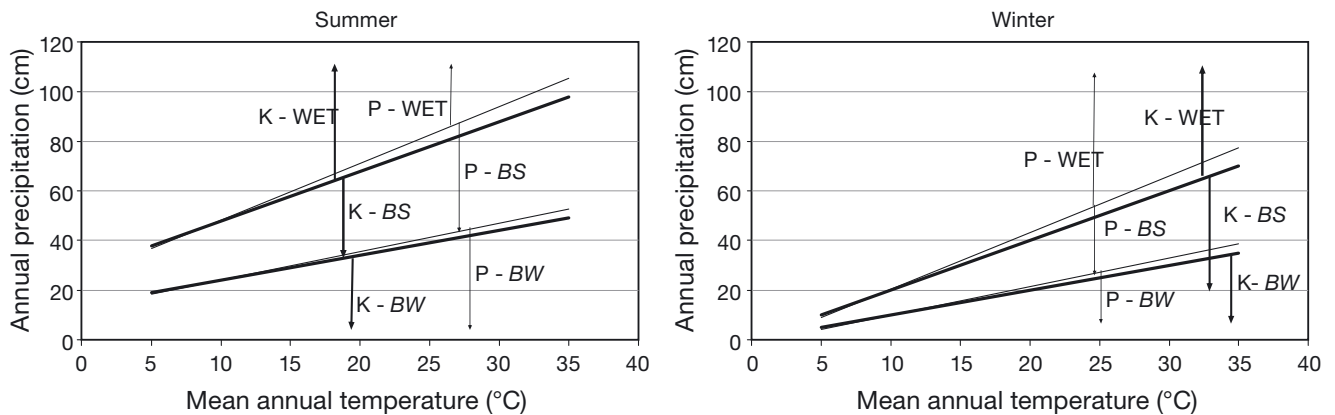


Fig. 1. Boundaries between wet climates and dry climate types *BS* and *BW* (defined in Table 1) based on Eqs. (1) & (2) for areas with rainfall concentrated in summer and winter. **Bold** lines: Köppen's boundary (*K*) based on Eq. (1); thin lines: Patton's modification (*P*) according to Eq. (2). Arrows: areas in graphs corresponding to wet climates and types *BS* and *BW*

Table 3. Climate types and subtypes defined by the Köppen climate classification (KCC) (Köppen 1936). P_{\max} : maximum annual precipitation rainfall; P_{mo} : monthly precipitation; Other abbreviations as in Table 1

Type/Subtype	Criteria Rainfall/temperature regime
A	$T_{\text{cold}} > 18^{\circ}\text{C}$; P_{mean} above value given for <i>B</i>
<i>Af</i>	$P_{\text{mo}} \geq 60$ mm for all months
<i>Aw</i>	$P_{\text{mo}} < 60$ mm for several months; dry season in low-sun period or winter half-year; annual rainfall insufficient to compensate this enough to allow forest
<i>As</i>	$P_{\text{mo}} < 60$ mm for several months; dry season in high-sun period or summer half-year; annual rainfall insufficient to compensate this enough to allow forest (occurs rarely)
<i>Am</i>	$P_{\text{dry}} < 60$ mm, rainfall in the rainy season compensates this enough to allow forest ^a
B	P_{\max} in summer: $P_{\text{mean}} < 2T + 28$; P_{\max} in winter: $P_{\text{mean}} < 2T$; annual rainfall evenly distributed: $P_{\text{mean}} < 2T + 14$
<i>BS</i>	P_{\max} in summer: $(2T + 28)/2 < P_{\text{mean}} < 2T + 28$ P_{\max} in winter: $(2T)/2 < P_{\text{mean}} < 2T$ Annual rainfall evenly distributed: $(2T + 14)/2 < P_{\text{mean}} < 2T + 14$
<i>BW</i>	P_{\max} in summer: $P_{\text{mean}} < (2T + 28)/2$ P_{\max} in winter: $P_{\text{mean}} < (2T)/2$ Annual rainfall evenly distributed: $P_{\text{mean}} < (2T + 14)/2$
C	T_{cold} from 18 to -3°C ; $T_{\text{warm}} > 10^{\circ}\text{C}$; P_{mean} above value given in <i>B</i>
<i>Cs</i>	Summer dry; wettest (winter) month must have more than 3 times the average rainfall of the driest (summer) month; $P_{\text{dry}} < 40$ mm
<i>Cw</i>	Winter dry; wettest (summer) month has ≥ 10 times the rainfall of the driest (winter) month
<i>Cf</i>	No dry season
D	$T_{\text{cold}} < -3^{\circ}\text{C}$; $T_{\text{warm}} > 10^{\circ}\text{C}$; P_{mean} above value given in <i>B</i>
<i>Ds</i>	Summer dry (the same condition as in <i>Cs</i>) (occurs rarely)
<i>Dw</i>	Winter dry (the same condition as in <i>Cw</i>)
<i>Df</i>	No dry season
E	$T_{\text{warm}} < 10^{\circ}\text{C}$
<i>ET</i>	$0^{\circ}\text{C} < T_{\text{warm}} < 10^{\circ}\text{C}$
<i>EF</i>	Mean air temperature of all months $< 0^{\circ}\text{C}$

^aKöppen (1936) describes the relationship between necessary annual rainfall P (cm) and monthly rainfall of the driest month P_{dry} (cm) in the form of graph; it can be expressed as $P_{\text{dry}} = -0.04P + 10$

In the present study, we use Patton's modification as expressed by Eq. (4). The *BS* subtype is defined by a mean annual precipitation amount P_{mean} lower than R and higher than $0.5R$, and the *BW* subtype by a mean annual precipitation lower than $0.5R$. The resulting boundaries between wet and dry *B* climate types are illustrated in Fig. 2. Köppen's original boundaries (Eq. 1), in the case of rainfall concentrated in summer and winter (bold lines 1 and 2, respectively, in Fig. 2), correspond approximately to Patton's thresholds for Pw equal to 30 and 75%, respectively.

4. COMPARISON OF KÖPPEN-TREWARTHA AND KÖPPEN CLIMATE CLASSIFICATIONS IN THE PERIOD 1961–1990

In this section, we apply both the KCC and the KTC to CRU TS3.10 and discuss their differences. The maps for both classifications are presented in Fig. 3. The percentage of continental area (except for Antarctica) classified according to the KCC and the KTC is compared in Table 2. It is important to acknowledge that, even though the designations in both classifications are mostly the same, the definitions of the types might be different in many respects. It is worth noting that in the KTC as described in Trewartha & Horn (1980), the subtype *Cw* is barely mentioned, and similarly, in the KCC (Köppen 1936), the subtypes *As* and *Ds* are considered as rarely occurring. Therefore, we did not incorporate *As* in our analysis. The *Ds* subtype was also considered in this study; however, it was confirmed that, in the CRU data for the period 1961–1990, it is present in only a very small number of grid points (Table 2).

From Fig. 3, the benefit of the KTC in comparison with the KCC is evident. An example is the extent of dry climate types in the interior United States. Trewartha & Horn (1980) discuss that the boundary is placed some 300 to 400 km west according to original Köppen's formulas due to underestimation of the dryness threshold. KTC is much more realistic in placing this boundary. In Europe, we

see a clear division of the western and eastern parts between types *Dc* and *Do* in the KTC. In other words, the KTC provides a more detailed description of climate types than the KCC.

From Table 2, it can be seen that the definition of climate type *A* is practically the same in both the KCC and the KTC. The *Ar* subtype in the KTC is very similar to *Af* in the KCC; therefore, most of the continental area classified as *Ar* corresponds to *Af* in the KCC (69% of continents without Antarctica). The remainder is divided between *Am* (25.9%) and *Aw* (5.1%) in the KCC. Interestingly,

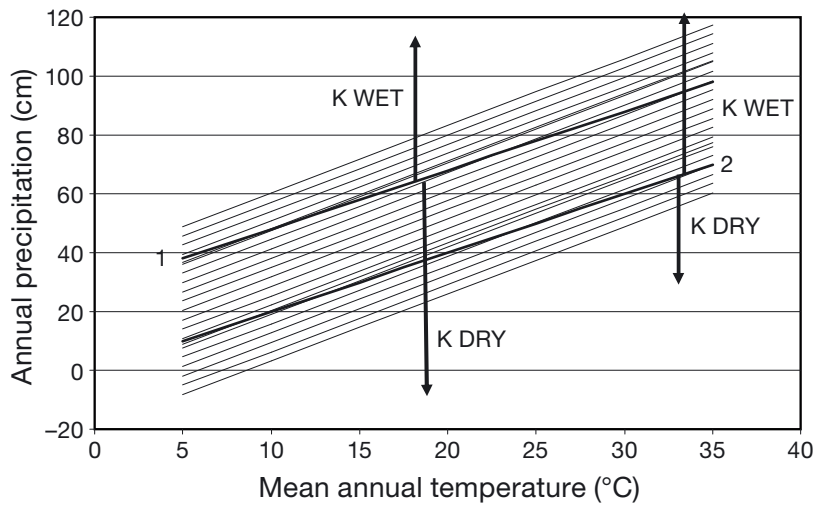


Fig. 2. Boundaries between wet and arid (type *B*) climates. Bold lines conform to Köppen's dryness criteria (Eq. 1) for climates where rainfall is concentrated in (1) summer and (2) winter. Thin lines represent Patton's dryness thresholds (R), based on the percentage of precipitation in the winter half-year (Eq. 4), at 5% intervals from (top line) 5% to (bottom line) 95%. Arrows: areas in graphs corresponding to wet climates and types *BS* and *BW*

all the area falling into *Af* in the KCC is classified as *Ar* in the KTC. In addition, *Aw* in the KTC corresponds well with *Aw* in the KCC. Only 13.5% of area where *Aw* is identified according to the KTC falls into *Am* in the KCC, and only a small part of it is marked as *BS* or *BW*.

Thermal definitions of *C* type in the KTC (Table 1) and in the KCC (Table 3) are different. Additionally, the subtypes *s*, *w* and *f* are defined in slightly different ways (see Section 3.2). *Cs* in the KTC represents only approximately 1% of all continental area (without Antarctica). In the KCC, this area corresponds to *BW* (42.8%), *Cs* (34.4%), and *BS* (23%). *Cw* occurs quite rarely in the KTC, accounting for only 0.8% of continental area without Antarctica; the same areas are also classified as *Cw* in the KCC. *Cf* in the KTC is more widespread than *Cs* and *Cw* (8% of continental area without Antarctica), and in the KCC, it is divided between *Cf* (58.1%), *Cw* (33.4%), *Cs* (5.7%), and *BS* (2.8%).

The definition of type *D* in the KTC with its 2 subtypes *Do* (oceanic) and *Dc* (continental) is again different from the boreal or snow-forest climate group *D* in the KCC. Continental territory with a temperate continental climate, *Dc* in the KTC, is most frequently marked as *Df* in the KCC (64.4%), and occasionally as *Cf* (12.7%), *Dw* (9.8%), and *Ds* (4%). The remainder is divided between *BS* (3.3%), *Cs* (3.5%), and *Cw* (2.2%). Temperate oceanic climate *Do* in the KTC

occurs much less frequently than *Dc*. Most of the *Do* area is classified as group *C* in the KCC (93.5%), with *Cf* defined for 56% of *Do* area, *Cs* for 24.4%, and *Cw* for 12.1%; the remainder (7.5%) falls mostly into dry climates *BS*.

Type *E* in the KTC includes mainly the area that the KCC marks as boreal climate *D*, with 83% of these points falling into *Df* and 14.4% into *Dw*. Only approximately 1.5% of *E* type area in the KTC is classified as *C* in the KCC (mostly *Cf*), and a negligible part falls into *Ds* (0.9%) and dry climates *B* (0.2%).

Thermal definitions of the polar climates *F* are the same in the KTC and the KCC. Because we do not include Antarctica in our analysis, the tundra subtype *Ft* (*ET*) is more widespread (approx. 6.3% of the continental area) than ice cap climate *Fi* (*EF*) (1.2%). All areas classified as *Fi* in the KTC fall into group *EF* in the KCC. *Ft* largely corresponds to *ET* in the KCC (96.2%); approx. 3.7% of *Ft* grid points are

defined as *B* in the KCC. This is because in the KCC, those areas (CRU grid points in our case) satisfying the conditions for *B* climate type are classified in the first step. In contrast, in the KTC, the first step selects the *F* areas, and *B* is evaluated subsequently; i.e. the *B* type cuts across all climate groups except for *F* (Trewartha & Horn 1980). Most of the grid points classified as *Ft* in the KTC, but as *B* in the KCC, occur in high elevations in the Andes in Peru and Chile (Fig. 3). Trewartha & Horn 1980 designate these areas as 'highland' climate type. However, the definition of the highland climate type is not clear enough to be applied unambiguously. Moreover, the orography in CRU data is smoothed and not always realistic. For these reasons the highland climate type was omitted in the present study. Most of the areas designated by Trewartha & Horn (1980) as highland fall into *Fi* or *Ft* according to our results.

As discussed in Section 3.6, the criteria for the determination of wet and dry climates are different in the KCC and the KTC, which results in differences regarding types *BS* and *BW* between the two classifications (Table 2, Fig. 3). *BW* areas in the KTC are mostly divided between *BW* (86.8%) and *BS* (13%) in the KCC. The areas marked as *BS* in the KTC are defined as various climate types in the KCC: most frequently *BS* (48.8%), with the remainder falling into types *Aw*, *Cw*, *Dw*, *BW*, *Cf*, and *Df*. *BS* occurs more often in the KTC than *BS* does in the

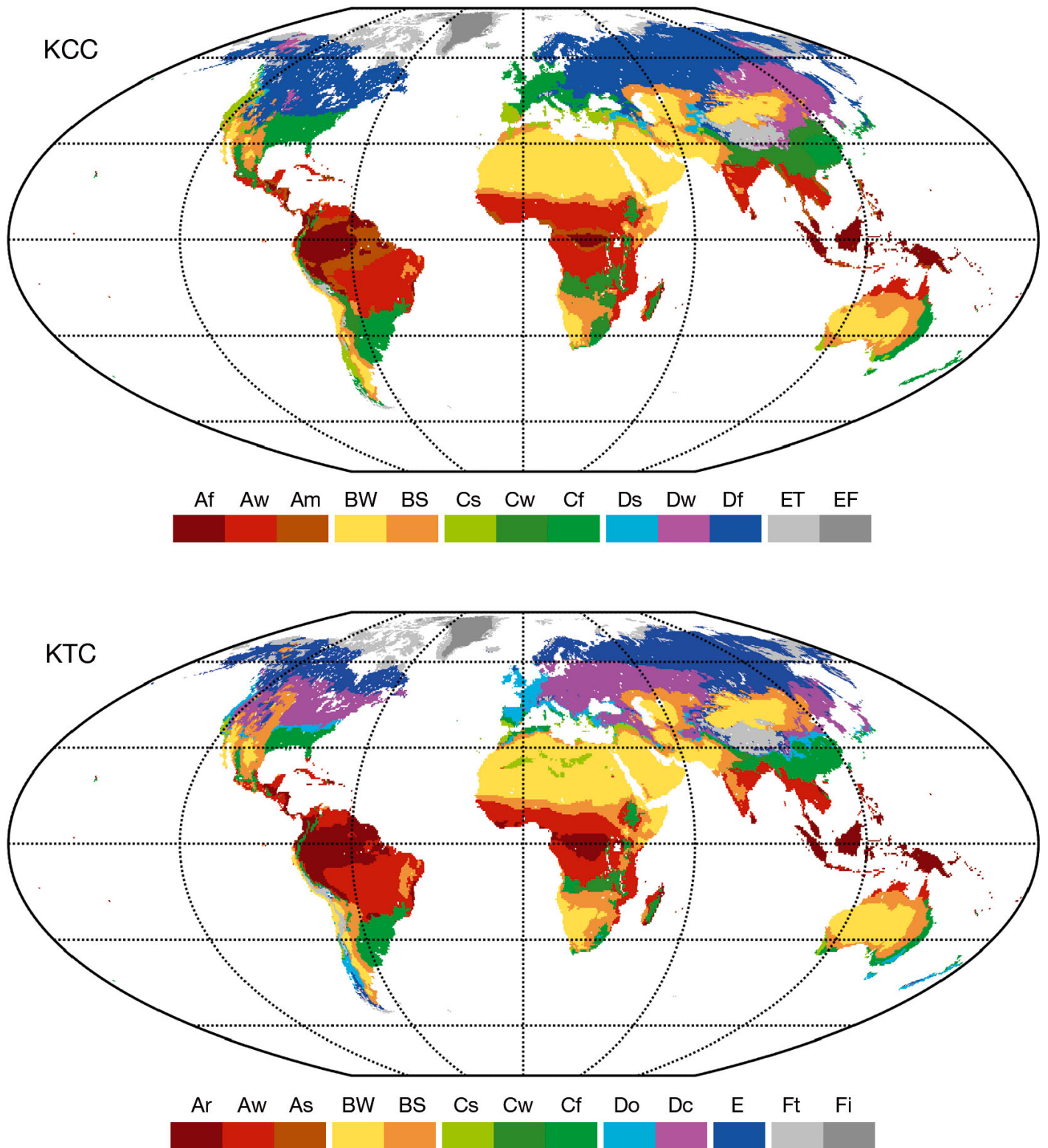


Fig. 3. World maps of Köppen climate classification KCC and Köppen-Trewartha climate classification KTC, based on CRU TS 3.10 data for the period of 1961–1990 on a regular 0.5° latitude/longitude grid

KCC. The percentage of areas classified as *BW* is very similar in both classifications (approx. 19% of continental area).

5. KOPPEN-TREWARTHA CLIMATE TYPES OVER THE PERIOD 1901–2005

We calculated the percentage of continental areas (except Antarctica) occupied by particular KTC types for moving 30-yr averages over the period 1901–2005 for the CRU TS3.10 dataset. The results for the main climate types and selected subtypes are shown in Fig. 4. Transitions of climatic types between 1901–1930 and 1976–2005 are presented in Table 4. Maps showing the KTC distribution for the beginning and the end of 20th century are presented in Fig. 5. The

map for the reference period 1961–1990 is shown in Fig. 3. Maps for other periods based on both the KTC and the KCC can be found on a supplementary website at <http://kmop.mff.cuni.cz/projects/trewartha>.

The area of climate type *A* increased between the periods 1901–1930 and 1935–1964. In the following years, we see either a stagnation or slight decrease; however, since 1965–1994, there has again been an increase in the area of type *A* (Fig. 4). This recent increase is caused mainly by an increase in subtype *Aw*, represented particularly as a shift from types *Cf* and *Cw* (Table 4).

In Fig. 4, we also see an increase of the area occupied by type *B* (approx. 1.2%) in the second half of 20th century. This is mainly because of the extension of semi-arid climates *BS*, chiefly in areas classified as *Aw*, *Dc* and *E* in the beginning of 20th century

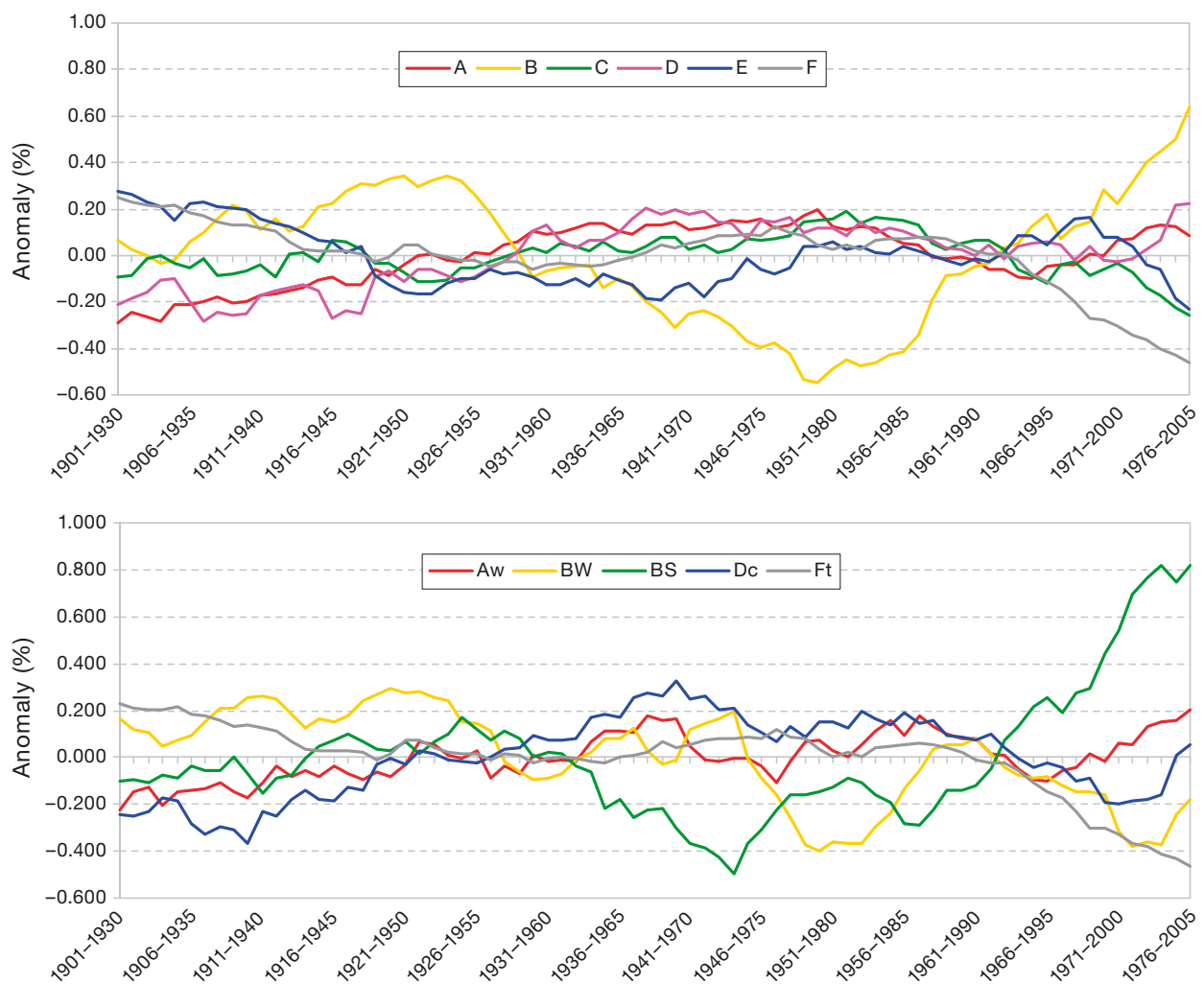


Fig. 4. Anomalies of percentage of continental area (excluding Antarctica) covered by KTC climate types (top) and selected subtypes (bottom) for moving 30 yr means with respect to the mean value for the period 1901–2005, calculated from the CRU TS 3.10 dataset

Table 4. Percentage of continental area (excluding Antarctica) covered by Köppen-Trewartha (KTC) climate types at the beginning and end of the 20th century (1901–1930 and 1976–2005, respectively), calculated from CRU TS 3.10 dataset

		1976–2005											Sum		
		<i>Ar</i>	<i>Aw</i>	<i>BW</i>	<i>BS</i>	<i>Cs</i>	<i>Cw</i>	<i>Cf</i>	<i>Do</i>	<i>Dc</i>	<i>E</i>	<i>Ft</i>		<i>Fi</i>	
1901–1930	<i>Ar</i>	6.93	0.49					0.01							7.43
	<i>Aw</i>	0.41	11.85		0.36		0.00	0.01							12.63
	<i>BW</i>			18.51	0.88							0.00			19.40
	<i>BS</i>		0.29	0.52	11.66	0.01	0.02	0.29	0.10	0.16	0.01				13.06
	<i>Cs</i>		0.00		0.05	1.08		0.05	0.01						1.20
	<i>Cw</i>		0.13		0.05		0.52	0.10							0.79
	<i>Cf</i>	0.04	0.30		0.27	0.06	0.01	7.19	0.04						7.91
	<i>Do</i>				0.03	0.01		0.37	2.73	0.08	0.01				3.22
	<i>Dc</i>				0.52				0.43	10.36	0.03				11.33
	<i>E</i>				0.14				0.04	1.03	14.05	0.02			15.29
	<i>Ft</i>			0.02	0.03						0.68	5.85			6.58
	<i>Fi</i>												0.02	1.14	1.16
	Sum	7.38	13.06	19.06	13.98	1.16	0.56	8.02	3.35	11.63	14.78	5.89	1.14		

(Table 4). The increase of *BS* occurred mainly in Australia, and central Asia, but also in South and North America (Fig. 5). The area falling into the *BW* type shows relatively large fluctuations throughout the 20th century (Fig. 4). It is worth noting that during the second half of the 20th century changes in the area of the *BW* type are accompanied by opposite changes in the *BS* type. The first marked phase shift of this kind occurs after around 1936–1965 period and a second one can be identified after the period 1961–1990. As illustrated by Table 4, a large part of these shifts can be explained by mutual replacement of *BW* type with *BS* and vice versa; however, a considerable part is also caused by transitions between other types, especially *BS-Cf* and *BS-Aw*.

With respect to the *C* type, we see only small fluctuations and a slight decrease of the area in the second half of 20th century.

The area of *D* type increased by approximately 0.4% in the first half of the century. This was caused mainly by the spread of those areas falling into type *Dc*. In the past 50 yr, relative changes to the *Dc* and *Do* areas almost compensate for each other; *Dc* has decreased slightly (except most recently since 1970), whereas *Do* has increased. The recent increase in *Dc* is mainly caused by transitions from types *E* and *BS* (Table 4).

Furthermore, we see 2 phases of decrease in the area belonging to type *E*. The first took place between the periods 1901–1930 and 1921–1950, and the second is stronger and occurred after 1969–1998. Between these 2 intervals, a slight increase in the area of type *E* occurred. A similar course can be identified in the case of *Ft*, but in this case in the central period there is no trend and in the final period

the decrease is more pronounced. A decrease of both *E* and *Ft* types can be attributed to the rising surface air temperature. In the Northern Hemisphere, the northward shift of the border between *E* and *Dc* is clearly visible (Fig. 5).

6. DISCUSSION AND CONCLUSIONS

We present a description of the Köppen-Trewartha climate classification (KTC), its comparison with the Köppen classification (KCC), and their application to the most up-to-date CRU dataset version with horizontal resolution of $0.5^\circ \times 0.5^\circ$ over the period 1901–2005. The KTC (Trewartha & Horn 1980), sometimes denoted ‘K-T scheme’, has been used as frequently as the KCC or Köppen-Geiger classification for the analysis of climate model performance and for model projections of future climate change. The advantage of the KTC is a more detailed depiction of climate types (e.g. Fig. 3). This classification has also been proven suitable for the creation of maps of global Ecological Zones (www.fao.org/docrep/006/ad652e/ad652e07.htm) for the Forest Resources Assessment Programme of The United Nations Food and Agriculture Organization (FAO). According to FAO (2001), ‘there is a demonstrated good correspondence between Köppen-Trewartha subzones or climatic types and the natural climax vegetation types and soils within them’.

We originally intended to use only the KTC for our analysis of the outputs of the new generation of GCMs. However, during preparations for this task we encountered much ambiguity in publications and papers dealing with climate classifications. These

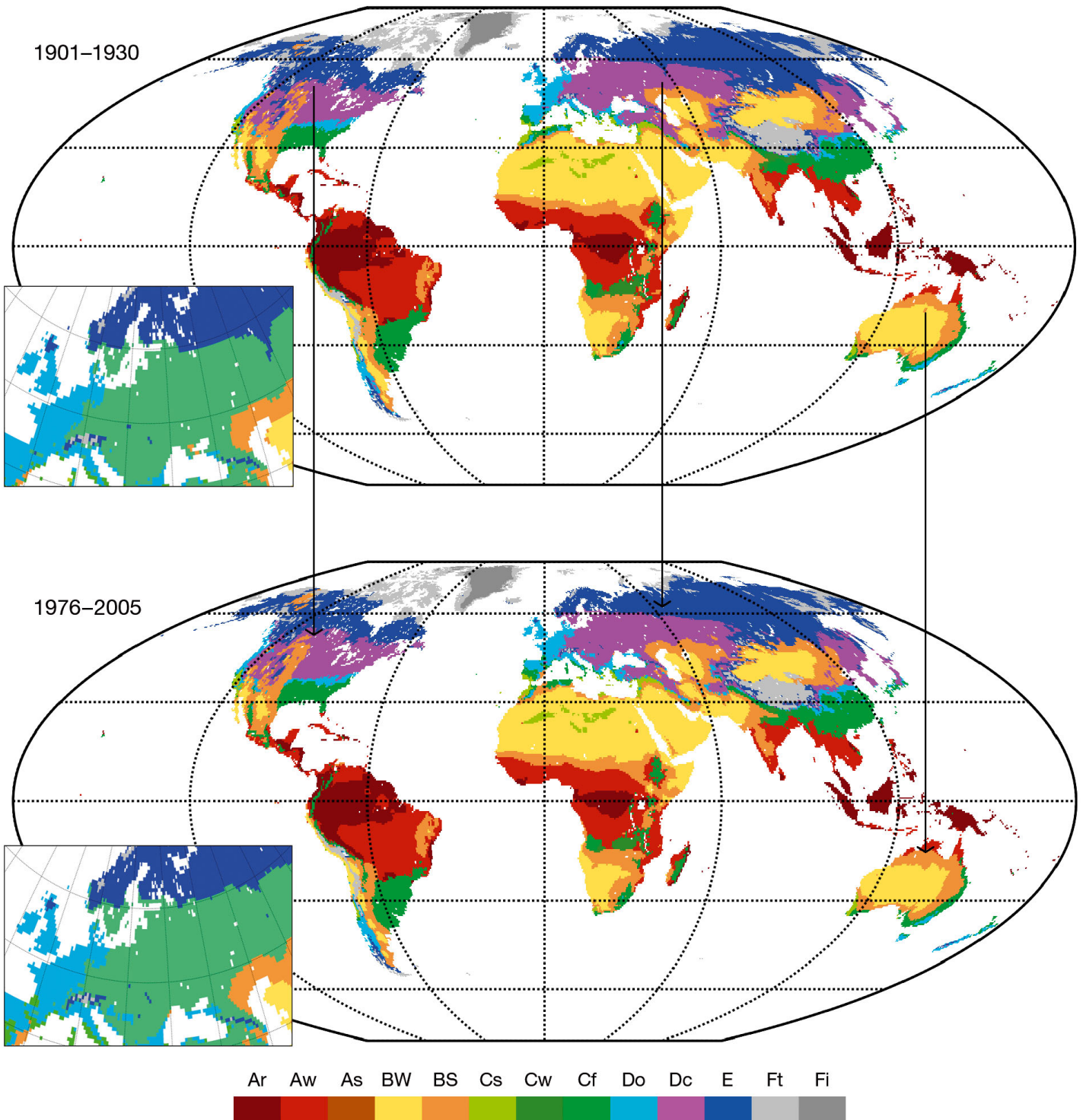


Fig. 5. World maps of Köppen-Trewartha climate classification based on CRU TS 3.10 data for the periods (top) 1901–1930 and (bottom) 1976–2005 on a regular 0.5° latitude/longitude grid. Arrows indicate areas of change

issues related to the designation of the classification (some studies by title suggest the KCC, but actually use the KTC), modified values of thresholds, and different interpretations of classification algorithms, e.g. whether to apply the dryness criteria first or to set apart polar climates. Therefore, we decided to first analyze and describe the KTC in detail, according to Trewartha & Horn (1980) using Patton's criteria of dryness, and compare it to the widely used KCC scheme (Köppen 1936). Following this preparatory study, the analysis of the validation and of future simulated climate change by using the CMIP5 GCM outputs, will follow in subsequent papers.

Another motivation for our study is that the digital maps of Köppen-Geiger climate types are already available in various versions (Kottek et al. 2006, Peel et al. 2007, Rubel & Kottek 2010). However, to our knowledge, digital maps of the KTC climate types for the up-to-date CRU data have not been presented before. We believe that making these maps accessible via the internet will be beneficial to other researchers, not just in the field of climatology, but also in the fields of hydrology and ecology, etc.

It is hardly possible to directly compare our results regarding the spatial distribution of the KTC types and areas belonging to particular climate types with other studies because of the differences in the analyzed datasets and time periods. For example, according to the present study, the order of climate types ranked by the percentage of continents (excluding Antarctica) that they cover in the period 1976–2005 is as follows: *B* (33.04%), *A* (20.44%), *D* (14.98%), *E* (14.78%), *C* (9.74%), and *F* (7.03%). Fraedrich et al. (2001) show that for the period 1981–1995 global tropical zone *A* covers around 22.4% of the continental area. Rubel & Kottek (2010) rank type *B* according to KCC as the most abundant, covering total 29.14% of the global land area (including Antarctica). The ranking derived in this study from the CRU data is different from the one mentioned by Trewartha & Horn (1980), who present type *A* as 'the most widespread of any great climatic groups', estimating the area covered by the type *A* to be around 20% of the land surface.

Regarding the changes in the area covered by individual climate types observed during 1901–2005, we have shown that there are observable changes, especially in subtypes *BS*, *Aw* and *Ft* (Fig. 4). Comparison of our results concerning the temporal evolution of the cover of climate types with other studies is again somewhat difficult. Temporal variations of tundra *Ft* agree well with the findings of Feng et al. (2012), who found a weak trend towards reduced tundra

cover from the beginning of the 20th century to the 1940s and a more abrupt decrease during the past 40 yr. This is also in accordance with trends described by Wang & Overland (2004) and Fraedrich et al. (2001). Furthermore, Feng et al. (2012) describe an expansion of continental temperate climate *Dc* in the area north of 50°N over the past few decades. In our global analysis, the *Dc* area has expanded in the 30-yr periods since 1970 (Fig. 4). Fraedrich et al. (2001) found that the global tropics (*A*) and the tundra (*Ft*) types show statistically significant shifts in the 1901–1995 period. The expansion of the *A* type was replaced by an areal reduction near the end of the period. Similar to our results concerning the *Ft* subtype, they also found a negative trend both at the beginning and at the end of the 20th century.

The analysis of the time development of climate types was, however, not the main goal of the present study; we intended primarily to prepare the background for the validation and the analysis of the CMIP5 GCMs outputs in subsequent papers, where the temporal evolution will be addressed both for simulations of the 20th century and future projections. Therefore, a more detailed examination of this issue is beyond the scope of this study. Here we were only able to show a part of the results obtained during our analysis. Additional materials, including digital maps for various time periods and animations, are accessible at <http://kmop.mff.cuni.cz/projects/trewartha>.

Acknowledgements. The CRU TS 3.10.01 dataset was provided by the Climatic Research Unit, University of East Anglia. This study was supported by project UNCE 204020/2012 funded by the Charles University in Prague and by research plan no. MSM0021620860 funded by the Ministry of Education, Youth and Sports of the Czech Republic. In addition, the work is a part of the activity under the Program of Charles University PRVOUK No. 02 'Environmental Research'.

LITERATURE CITED

- Bailey RG (2009) *Ecosystem geography: from ecoregions to sites*, 2nd edn. Springer, New York, NY
- Baker B, Diaz H, Hargrove W, Hoffman F (2010) Use of the Köppen-Trewartha climate classification to evaluate climatic refugia in statistically derived ecoregions for the People's Republic of China. *Clim Change* 98:113–131
- Daly C, Gibson WP, Taylor GH, Johnson GL, Pasteris P (2002) A knowledge-based approach to the statistical mapping of climate. *Clim Res* 22:99–113
- de Castro M, Gallardo C, Jylha K, Tuomenvirta H (2007) The use of a climate-type classification for assessing climate change effects in Europe from an ensemble of nine regional climate models. *Clim Change* 81:329–341
- Feng S, Ho CH, Hu Q, Oglesby RJ, Jeong SJ, Kim BM (2012)

- Evaluating observed and projected future climate changes for the Arctic using the Köppen-Trewartha climate classification. *Clim Dyn* 38:1359–1373
- Food and Agricultural Organization (FAO) (2001) Global ecological zoning for the Global Forest Resources Assessment 2000. Final Report, Forest Resources Assessment, Working Paper No. 56. FAO, Rome
- Fraedrich K, Gerstengarbe FW, Werner PC (2001) Climate shifts during the last century. *Clim Change* 50:405–417
- Geiger R (1954) Klassifikationen der Klimate nach W. Köppen. In: Landolf-Börnstein: Zahlenwerte und Funktionen aus Physik, Chemie, Astronomie, Geophysik und Technik, (alte Serie), Vol. 3. Springer, Berlin, p 603–607
- Geiger R (1961) bearbeitete Neuauflage von Geiger, R: Köppen-Geiger/Klima der Erde. Wandkarte (wall map) 1:16 Mill. Klett-Perthes, Gotha
- Gerstengarbe FW, Werner PC (2009) A short update on Koeppen climate shifts in Europe between 1901 and 2003. *Clim Change* 92:99–107
- Guetter PJ, Kutzbach JE (1990) A modified Koeppen classification applied to model simulation of glacial and interglacial climates. *Clim Change* 16:193–215
- Harris I, Jones PD, Osborn TJ, Lister DH (in press) Updated high-resolution grids of monthly climatic observations – the CRU TS3.10 dataset. *Int J Clim*, doi: 10.1002/joc.3711
- Jones PD, Wigley TML, Farmer G (1991) Marine and land temperature data sets: a comparison and a look at recent trends. In: Schlesinger ME (ed) Greenhouse-gas-induced climatic change: a critical appraisal of simulations and observations. Elsevier, Amsterdam, p 153–172
- Kalnay E, Kanamitsu M, Kistler R, Collins W and others (1996) The NCEP/NCAR 40-year reanalysis project. *Bull Am Meteorol Soc* 77:437–471
- Kalvová J, Halenka T, Bezpalcová K, Nemešová I (2003) Köppen climate types in observed and simulated climates. *Stud Geophys Geod* 47:185–202
- Köppen W (1923) Die Klimate der Erde. Grundriss der Klimakunde. Walter de Gruyter, Berlin
- Köppen W (1931) Grundriss der Klimakunde. Walter de Gruyter, Berlin
- Köppen W (1936) Das geographische System der Klimate. In: Köppen W, Geiger R (eds) Handbuch der Klimatologie. Gebrüder Borntraeger, Berlin, p 1–44
- Kottek M, Grieser J, Beck C, Rudolf B, Rubel F (2006) World map of the Köppen-Geiger climate classification updated. *Meteorol Z* 15:259–263
- Legates DR, Willmott CJ (1990) Mean seasonal and spatial variability in gauge-corrected, global precipitation. *Int J Climatol* 10:111–127
- Lohmann U, Sausen R, Bengtsson L, Cubash U, Perlwitz J, Roeckner E (1993) The Köppen climate classification as a diagnostic tool for general circulation models. *Clim Res* 3:177–193
- Meehl GA, Covey C, Delworth T, Latif M and others (2007) The WCRP CMIP3 multi-model dataset: a new era in climate change research. *Bull Am Meteorol Soc* 88:1383–1394
- Mitchell TD, Jones PD (2005) An improved method of constructing a database of monthly climate observations and associated high-resolution grids. *Int J Climatol* 25:693–712
- Mitchell TD, Carter TR, Jones PD, Hulme M, New M (2004) A comprehensive set of high-resolution grids of monthly climate for Europe and the globe: the observed records (1901–2000) and 16 scenarios (2001–2100). Working Paper 55, Tyndall Centre of Climate Change Research, Norwich
- Nakicenovic N, Swart R (eds) (2000) Emission scenarios. Cambridge University Press, Cambridge
- New M, Hulme M (1998) Development of an observed monthly surface climate dataset over global land areas for 1901–1995. Report, Climatic Research Unit, University of East Anglia, Norwich
- New M, Hulme M, Jones P (1999) Representing twentieth-century space-time climate variability. I. Development of a 1961–1990 mean monthly terrestrial climatology. *J Clim* 12:829–856
- New M, Hulme M, Jones P (2000) Representing twentieth-century space-time climate variability. II. Development of 1901–96 monthly grids of terrestrial surface temperature. *J Clim* 13:2217–2238
- Patton CP (1962) A note on the classification of dry climate in the Köppen system. *California Geographer* 3:105–112
- Peel MC, Finlayson BL, McMahon TA (2007) Updated world map of the Köppen-Geiger climate classification. *Hydrol Earth Syst Sci* 11:1633–1644
- Peterson TC, Vose RS (1997) An overview of the Global Historical Climatology Network temperature database. *Bull Am Meteorol Soc* 78:2837–2849
- Rubel F, Kottek M (2010) Observed and projected climate shifts 1901–2100 depicted by world maps of the Köppen-Geiger climate classification. *Meteorol Z* 19:135–141
- Taylor K, Stouffer RJ, Meehl GA (2012) An overview of CMIP5 and the experiment design. *Bull Am Meteorol Soc* 93:485–498
- Trewartha GT (1968) An introduction to climate. McGraw-Hill, New York, NY
- Trewartha GT, Horn LH (1980) Introduction to climate, 5th edn. McGraw Hill, New York, NY
- Wang M, Overland JE (2004) Detecting arctic climate change using Köppen climate classification. *Clim Change* 67:43–62

Editorial responsibility: Tim Sparks, Cambridge, UK

*Submitted: June 17, 2013; Accepted: October 21, 2013
Proofs received from author(s): January 17, 2014*



Evaluation of CMIP5 present climate simulations using the Köppen-Trewartha climate classification

Michal Belda^{1,*}, Eva Holtanová¹, Tomáš Halenka¹, Jaroslava Kalvová¹,
Zdeněk Hlávka²

¹Charles University in Prague, Dept. of Atmospheric Physics, 182 00 Prague, Czech Republic

²Charles University in Prague, Dept. of Probability and Mathematical Statistics, 186 75 Prague 8, Czech Republic

ABSTRACT: We used the Köppen-Trewartha classification on the CMIP5 family of global climate model (GCM) simulations and global Climatic Research Unit (CRU) data for comparison. This evaluation provides preliminary insight on GCM performance and errors. For the overall model intercomparison and evaluation, we used 2 simple statistical characteristics: normalized error, which assesses the total relative difference of the area classified by the individual model with respect to the area resulting from CRU data, and overlap, calculating relative area of matching grid boxes in model results and CRU data. With the additional analysis of the classification on world maps, we show that there are some common features in the model results. Many models have problems capturing the rainforest climate type *Ar*, mainly in Amazonia. The desert climate type *BW* is underestimated by as many as half of the models, with Australia being a typical example of a region where the *BW* is not well represented. The boreal climate type *E* is overestimated by many models, mostly spreading over to the areas of observed tundra type *Ft*. All applied metrics indicate that with the current generation of GCMs, there is no clear tendency for models to improve the representation of climate types with higher spatial resolution.

KEY WORDS: Köppen-Trewartha · Köppen · Climate classification · CMIP5 · Global climate model · CRU TS 3.22 dataset · Overlap measure of similarity · Hierarchical cluster analysis

Resale or republication not permitted without written consent of the publisher

1. INTRODUCTION

Recently, a new coordinated set of experiments with global climate models (GCMs) was performed in the framework of the fifth phase of the Coupled Model Intercomparison Project (CMIP5, see Taylor et al. 2012 for project description). The new generation of CMIP5 GCMs differs from the previous (AR4 GCMs, Meehl et al. 2007) in many aspects. The horizontal resolution is finer in most cases, and more physical processes are included in the models. Moreover, in some GCMs, biogeochemical processes are considered in detail and therefore the simulation of a full carbon cycle is possible. Such GCMs are usually called earth system models (ESMs). Examples of

ESMs include MIROC-ESM-CHEM, MPI-ESM-LR, and GFDL-ESM2G (for more details see Section 2 and Table 1). Further progress in comparison to AR4 GCMs is that changes in land use are taken into account in historical simulations of the 20th century (Taylor et al. 2012).

Before future climate changes are estimated based on the outputs of GCMs, it is always necessary to evaluate the model performance in simulating observed climate in a reference period. For such tasks, climate classifications can provide an interesting complement to the commonly used evaluation methods. Climate classifications depict a fairly broad range of climate features in 1 simple characteristic. Most often, the annual and monthly mean values of

*Corresponding author: michal.belda@mff.cuni.cz

air temperature and precipitation and their annual cycle are summarized in the form of climate types and subtypes. For analysis of GCM outputs, the classifications that correspond to vegetation distribution are usually incorporated. One of the most frequently used classifications of this kind was developed by Köppen (1923, 1931, 1936) and modified by various authors (e.g. Geiger 1954, Trewartha & Horn 1980; see Belda et al. 2014 for comparison).

Probably the first paper dealing with the application of a Köppen climate classification (KCC) for the validation of GCM outputs was by Manabe & Holloway (1975), who evaluated a simulation of the GFDL atmospheric general circulation model with a horizontal resolution of about 265 km and 11 vertical levels. Frequently cited work incorporating the Köppen classification is that of Lohmann et al. (1993), who diagnosed the outputs of ECHAM3 (Roeckner et al. 1992) at resolutions T21 and T42. Kalvová et al. (2003) applied the Köppen classification to the simulations of 4 state of the art GCMs, viz. HadCM2 (Mitchell & Johns 1997), ECHAM4 (Roeckner et al. 1996), CSIRO-Mk2b (Hirst et al. 2000), and CGCM1 (Boer et al. 2000). Peel et al. (2007) created digital global maps of Köppen-Geiger climate (KGC) types (Geiger 1954) based on a large amount of long-term monthly precipitation and temperature station data. They also discussed the geographical distribution of KGC types over individual continents as well as the influence of observed temperature trends on results of the classification.

More recently, Rubel & Kottek (2010) created a series of digital world maps of Köppen climate types for the period 1901–2100. These maps are based on Climatic Research Unit (CRU) TS2.1 (Mitchell & Jones 2005), GPCC Version 4 data (<http://gpcc.dwd.de/>) and GCM outputs from the TYN SC 2.0 dataset (Mitchell et al. 2004).

Another broadly used climate classification is the modification of the Köppen system proposed by Trewartha (Trewartha 1968, Trewartha & Horn 1980). They modified original Köppen thermal and dryness criteria to make the climate types better correspond with the observed boundaries of natural landscapes and to eliminate certain vagueness of the KCC definitions. This classification, sometimes referred to as Köppen-Trewartha or K-T classification (denoted as KTC in the following text), provides a more detailed description of climate type distributions than the original Köppen scheme, modifying the thresholds between types and adding a further level of division of types *E* and *F* (see Belda et al. 2014 for more details and a comparison of KCC and KTC). The KTC

scheme was used by e.g. Feng et al. (2012) to analyze observed and projected climate changes and their impact on vegetation for the area north of 50° N over the period 1900–2099. They focused on the Arctic region, and in addition to the observed data, they incorporated the simulations of 16 AR4 GCMs under SRES scenarios B1, A1B, and A2. Another example of the application of KTC on the outputs of GCMs is the study by Guetter & Kutzbach (1990), who investigated the last interglacial and glacial climates (126 000 and 18 000 yr before present) using simulations of an atmospheric general circulation model.

In studies using rule-based classifications, such as KCC or KTC, it is sometimes not obvious which rules were applied first. For example, according to Kottek et al. (2006), the KTC rules determining polar climate class must be applied first, then those for arid climate, and finally those for tropical, temperate, and cold classes. In KTC, the first step selects the polar areas *F*, and dry climate class *B* is evaluated subsequently, i.e. the *B* type cuts across all climate groups except for polar climate *F* (Trewartha & Horn 1980).

A different approach to climate classification is represented by methods based solely on statistical techniques, most often cluster analysis (e.g. Fovell & Fovell 1993, Stern et al. 2000). A disadvantage of such procedures is that the physical interpretation of the results might be difficult. Alternatively, Cannon (2012) used a rule-based clustering algorithm, multivariate regression tree (MRT). He applied the MRT method on long-term monthly mean temperature and precipitation amounts and concluded that the MRT performed significantly better than the Köppen-Geiger classification, which may be suboptimal for applications that are sensitive to spatial variations in precipitation.

For GCM validation, however, the rule-based classification schemes are still preferred, mainly because they are simple, transparent, and easy to interpret, and resulting climate types are related to vegetation distribution, which is important for estimates of climate change impacts.

Most recently, analyses of future climate by means of KTC from the latest generation GCMs were performed by e.g. Mahlstein et al. (2013) and Feng et al. (2014) on a subset of CMIP5 models. However, to our knowledge, no comprehensive study of model validation for the present climate has been conducted using climate classification. Our interest is the evaluation of the new generation GCMs with regard to geographical differences in model skill and inter-comparison of the models. The motivation for such in-depth analysis is manifold. First, one can derive

from it to which extent the latest generation of GCMs improves climate simulations. Second, it lays the groundwork for further assessment of future climate projections by the ensemble of CMIP5 models. Third, and not least important for our application, is the geographical distribution of model errors, which can provide preliminary information to the regional climate modeling communities as to which models may be better suited for driving the regional models in individual regions.

Here we used the KTC to evaluate the performance of CMIP5 GCMs in simulating the climate of the reference period 1961–1990. The KTC scheme used is described only briefly in this text; for a full description see Belda et al. (2014). Additional maps and other graphical materials can be found on a supplementary website at <http://kfa.mff.cuni.cz/projects/trewartha>.

2. DATA

The CRU TS 3.22 dataset (Harris et al. 2014) was used as reference data representing the observed state of the climate in the reference period 1961–1990. We used monthly mean surface air temperature and precipitation to derive the Köppen-Trewartha climate types (see Section 3 for details). Our analysis covers global land areas (excluding Antarctica) for which the CRU TS 3.22 is available at a high spatial resolution of $0.5^\circ \times 0.5^\circ$.

A list of CMIP5 GCM simulations involved in the present study and some basic information about them are provided in Table 1. The data are freely available for non-commercial purposes at <http://cmip-pcmdi.llnl.gov/cmip5/>. We used the outputs from the experiment denoted as ‘historical’. These model runs were forced by observed atmospheric composition changes and time-evolving land cover during the period from the mid-19th century to the near present (Taylor et al. 2012). For ESMs with a carbon cycle, the carbon dioxide concentrations are prescribed in this experiment. Where more ensemble members were available, we chose the ensemble member ‘r1p1i1’.

In some cases, runs from several model versions are available and therefore it is possible to analyze the uncertainty coming from 1 or more aspects in model formulation when these runs are compared. For example, GFDL-ESM2G and GFDL-ESM2M have the same atmosphere component but different formulation of the ocean components (www.gfdl.noaa.gov/cm2m-and-cm2g). Similarly, GISS-E2-H

and GISS-E2-R differ only in the model of the ocean (<http://data.giss.nasa.gov/modelE/ar5/>). IPSL-CM5A and IPSL-CM5B use different physical parameterizations in the atmospheric models. ‘LR’ and ‘MR’ in the abbreviations of these model runs relate to the spatial resolution of the atmospheric component (<http://icmc.ipsl.fr/index.php/icmc-models-2/icmc-ipsl-cm5>). MIROC-ESM-CHEM is the same model as MIROC-ESM, except with an additional interactive model of tropospheric and stratospheric chemistry (Watanabe et al. 2011).

3. METHODS

For validation of CMIP5 GCMs, we applied the Köppen-Trewartha climate classification (for further details about KTC see Trewartha & Horn 1980 and Belda et al. 2014) in the present study. The KTC system has 6 main climate groups. Five of them (denoted *A*, *C*, *D*, *E*, and *F*) are basic thermal zones, and the sixth group (*B*) is the dry climatic zone that cuts across the other climate types, except for the polar climate *F*. The main climate types are, similarly to the Köppen classification scheme, determined according to long-term annual and monthly means of surface air temperature and precipitation amounts. In Belda et al. (2014) and in the present study, we used Patton’s formula (Patton 1962, Trewartha & Horn 1980) for dryness criteria, expressed as:

$$R = 2.3T - 0.64Pw + 41 \quad (1)$$

where R denotes the mean annual precipitation threshold in cm, T is the mean annual air temperature in $^\circ\text{C}$, and Pw is the percentage of annual precipitation concentrated in winter (October to March in the northern hemisphere and April to September in the southern Hemisphere). If the mean annual precipitation amount P_{mean} is lower than R and higher than $0.5R$, type *BS* is defined in such a grid box. Where the mean annual precipitation P_{mean} is lower than $0.5R$, type *BW* is defined. A brief description of climate types and subtypes is provided in Table 2.

The evaluation of the GCM performances in simulating the Köppen-Trewartha climatic types is complicated due to differences in model horizontal resolution. The KTC types were first calculated for both CRU TS 3.22 and CMIP5 GCMs in their original grids, i.e. for each grid point, and based on this information we calculated land areas falling into each climatic subtype (expressed in terms of relative areas, percentage of total global land area except Antarctica). Furthermore, the maps of KTC climatic types for all

Table 1. CMIP5 global climate models analyzed in this paper

CMIP5 model	Resolution	Modeling center
ACCESS1.3	1.88° × 1.24°	Commonwealth Scientific and Industrial Research Organization and Bureau of Meteorology, Australia
BCC-CSM1.1	2.8° × 2.8°	Beijing Climate Center, China Meteorological Administration
BCC-CSM1.1m	1.13° × 1.13°	
CanESM2	2.8° × 2.8°	Canadian Centre for Climate Modelling and Analysis
CCSM4	1.25° × 0.94°	National Center for Atmospheric Research
CESM1-BGC	1.25° × 0.94°	Community Earth System Model Contributors
CESM1-CAM5	1.25° × 0.94°	
CESM1-CAM5.1-FV2	2.50° × 1.88°	
CESM1-FASTCHEM	1.25° × 0.94°	
CESM1-WACCM	2.50° × 1.88°	
CMCC-CESM	3.75° × 3.75°	Centro Euro-Mediterraneo sui Cambiamenti Climatici
CMCC-CM	0.75° × 0.75°	
CNRM-CM5	1.4° × 1.4°	Centre National de Recherches Meteorologiques; Centre Européen de Recherche et Formation Avancées en Calcul Scientifique
CNRM-CM5.2		
CSIRO-Mk3.6.0	1.9° × 1.9°	Commonwealth Scientific and Industrial Research Organisation; Queensland Climate Change Centre of Excellence
EC-EARTH	1.1° × 1.1°	EC-EARTH consortium
FGOALS-g2	2.81° × 3.00°	LASG, Institute of Atmospheric Physics, Chinese Academy of Sciences and CESS, Tsinghua University
GFDL-CM2p1		Geophysical Fluid Dynamics Laboratory
GFDL-CM3	2.5° × 2°	
GFDL-ESM2G	2.5° × 2°	
GFDL-ESM2M	2.5° × 2°	
GISS-E2-H	2.5° × 2°	NASA Goddard Institute for Space Studies
GISS-E2-H-CC	2.5° × 2°	
GISS-E2-R	2.5° × 2°	
GISS-E2-R-CC	2.5° × 2°	
HadCM3	3.75° × 2.5°	Met Office Hadley Centre
HadGEM2-AO		
HadGEM2-CC	1.875° × 1.25°	
HadGEM2-ES	1.875° × 1.25°	
INM-CM4	2° × 1.5°	Institute for Numerical Mathematics
IPSL-CM5A-LR	3.75° × 1.9°	Institut Pierre-Simon Laplace
IPSL-CM5A-MR	2.5° × 1.3°	
IPSL-CM5B-LR	3.75° × 1.9°	
MIROC5	1.4° × 1.4°	Atmosphere and Ocean Research Institute (The University of Tokyo), National Institute for Environmental Studies, and Japan Agency for Marine-Earth Science and Technology
MIROC-ESM	2.8° × 2.8°	Japan Agency for Marine-Earth Science and Technology, Atmosphere and Ocean Research Institute (The University of Tokyo), and National Institute for Environmental Studies
MIROC-ESM-CHEM	2.8° × 2.8°	
MPI-ESM-LR	1.9° × 1.9°	Max Planck Institute for Meteorology
MPI-ESM-MR	1.9° × 1.9°	
MPI-ESM-P	1.9° × 1.9°	
MRI-CGCM3	1.125° × 1.125°	Meteorological Research Institute
MRI-ESM1	1.13° × 1.13°	
NorESM1-M	2.5° × 1.9°	Norwegian Climate Centre
NorESM1-ME	2.5° × 1.9°	

Table 2. Definition of Köppen-Trewartha classification climate types according to Trewartha & Horn (1980), with a dryness threshold defined by Patton (1962). Tmo : long-term monthly mean air temperature; $Tcold$ ($Twarm$): monthly mean air temperature of the coldest (warmest) month; $Pmean$: mean annual precipitation (cm); $Pdry$: monthly precipitation of the driest summer month; R : Patton's precipitation threshold, defined as $R = 2.3T - 0.64Pw + 41$, where T is mean annual temperature ($^{\circ}\text{C}$), and Pw is the percentage of annual precipitation occurring in winter

Type/subtype	Criteria Rainfall/temperature regime
A	$Tcold > 18^{\circ}\text{C}$; $Pmean > R$
<i>Ar</i>	10 to 12 mo wet; 0 to 2 mo dry
<i>Aw</i>	Winter (low-sun period) dry; >2 mo dry
<i>As</i>	Summer (high-sun period) dry; rare in type A climates
B	$Pmean < R$
<i>BS</i>	$R/2 < Pmean < R$
<i>BW</i>	$Pmean < R/2$
C	$Tcold < 18^{\circ}\text{C}$; 8 to 12 mo with $Tmo > 10^{\circ}\text{C}$
<i>Cs</i>	Summer dry; at least 3 times as much rain in winter half year as in summer half-year; $Pdry < 3$ cm; total annual precipitation < 89 cm
<i>Cw</i>	Winter dry; at least 10 times as much rain in summer half-year as in winter half-year
<i>Cf</i>	No dry season; difference between driest and wettest month less than required for <i>Cs</i> and <i>Cw</i> ; $Pdry > 3$ cm
D	4 to 7 mo with $Tmo > 10^{\circ}\text{C}$
<i>Do</i>	$Tcold > 0^{\circ}\text{C}$
<i>Dc</i>	$Tcold < 0^{\circ}\text{C}$
E	1 to 3 mo with $Tmo > 10^{\circ}\text{C}$
F	All months with $Tmo < 10^{\circ}\text{C}$
<i>Ft</i>	$Twarm > 0^{\circ}\text{C}$
<i>Fi</i>	$Twarm < 0^{\circ}\text{C}$

CMIP5 models listed in Table 1 were created and can be found at <http://kfa.mff.cuni.cz/projects/trewartha>.

For the overall model intercomparison and evaluation, we used a simple statistical characteristic normalized error (NE), defined as:

$$NE = \sum_{i=1}^K \frac{|m_i - o_i|}{o} \quad (2)$$

where K is the number of climatic types (13 for KTC incorporated in this study), m_i is the continental area for type i in model m , o_i is the corresponding area according to CRU, and o is the global continental area (according to CRU and the respective models).

The NE was calculated based on both original and re-gridded model data (interpolated to the 0.5° regular grid used in CRU). Although the actual NE values are obviously not equal, the model rank based on NE does not change with re-gridding. In the following analysis, we used NE calculated from the original model data (i.e. not interpolated), to avoid introducing inconsistencies from an arbitrary choice of interpolation method.

To compare spatial representation of the model data, a very simple similarity measure, also known as the overlap, was used. For each model, we calculated the total area of grid points where the model-simulated climate type was the same as the CRU one. The models can be sorted in terms of this matched area, or rather, relatively with respect to the overall continent area providing an overlap characteristic (Table 3). Unlike the NE measure, this method requires interpolating model data to a common grid (in our case a CRU grid) before calculating climate types. The interpolation into the CRU grid was performed using a simple bilinear interpolation method. There is, however, an obvious drawback to such an overlap measure. Clearly, it only takes matching grid points into account without accounting for mismatches, i.e. events when the climate model gives different climate types than CRU (for example, GCM simulates climate type *BS* while CRU gives type *BW*). We did not attempt to correct this problem, since there are many possible ways to assign weights for individual type mismatches. Analyzing these similarity measures in more detail (see e.g. Boriah et al. 2008) is beyond the scope of this paper; therefore, we used no penalization of mismatches during further assessment.

Furthermore, the similarity between any 2 CMIP5 models expressed as overlap can be used for hierarchical cluster analysis. A matrix of pairwise distances is obtained by subtracting the similarity from 100%, i.e. the distance between 2 models is defined as a percentage of the total Earth surface (excluding Antarctica) where the climate types do not agree. The resulting matrix of similarities is visualized by hierarchical cluster analysis. The statistical analysis was performed in the statistical computing environment R (R Core Team 2012). The Ward algorithm (R, library MASS, function `hclust()`) was used to create a dendrogram (see Fig. 2).

All mentioned metrics were calculated for individual models as well as for the ensemble mean, calculated by applying the KTC classification to the ensemble average of temperatures and precipitation. The multi-model mean values are denoted as CMIP5 ENS in the included tables and figures.

Table 3. Model to observation statistics calculated for 1961–1990. CMIP5 ENS: ensemble mean; NE: normalized error of Köppen-Trewartha classification climate type areas for CMIP5 GCMs vs. CRU TS 3.22; NE rank: ranking of the models based on normalized error; Overlap: percentage of continental area, excluding Antarctica, where the model and CRU climate types agree; Overlap rank: ranking of the models based on overlap

Model	NE	NE rank	Overlap (%)	Overlap rank
CMIP5 ENS	0.189	19	70.07	1
ACCESS1.3	0.142	5	66.46	12
BCC-CSM1.1-m	0.111	1	59.21	37
BCC-CSM1.1	0.156	8	62.78	25
CanESM2	0.184	16	65.01	17
CCSM4	0.281	37	63.28	22
CESM1-BGC	0.286	40	63.34	21
CESM1-CAM5	0.253	30	65.29	16
CESM1-CAM5.1-FV2	0.322	43	61.83	29
CESM1-FASTCHEM	0.289	41	63.16	23
CESM1-WACCM	0.298	42	59.18	38
CMCC-CESM	0.174	13	63.41	20
CMCC-CM	0.157	10	66.18	13
CNRM-CM5	0.208	22	67.60	7
CNRM-CM5.2	0.196	20	67.05	10
CSIRO-Mk3.6.0	0.226	23	59.60	35
EC-EARTH	0.236	26	66.13	14
FGOALS-g2	0.257	31	56.50	44
GFDL-CM2p1	0.228	24	59.73	34
GFDL-CM3	0.238	27	63.84	18
GFDL-ESM2G	0.274	34	57.46	41
GFDL-ESM2M	0.235	25	59.41	36
GISS-E2-H	0.158	11	61.51	30
GISS-E2-H-CC	0.156	9	61.26	31
GISS-E2-R	0.153	7	62.36	26
GISS-E2-R-CC	0.144	6	62.18	27
HadCM3	0.172	12	60.82	33
HadGEM2-AO	0.184	17	67.72	6
HadGEM2-CC	0.207	21	67.35	8
HadGEM2-ES	0.177	14	68.94	3
INM-CM4	0.325	44	61.95	28
IPSL-CM5A-LR	0.277	36	63.83	19
IPSL-CM5A-MR	0.251	29	65.73	15
IPSL-CM5B-LR	0.250	28	61.14	32
MIROC-ESM	0.283	39	56.59	43
MIROC-ESM-CHEM	0.271	33	56.83	42
MIROC5	0.281	38	62.98	24
MPI-ESM-LR	0.137	4	67.82	5
MPI-ESM-MR	0.115	2	68.26	4
MPI-ESM-P	0.127	3	68.97	2
MRI-CGCM3	0.187	18	66.82	11
MRI-ESM1	0.180	15	67.20	9
NorESM1-M	0.260	32	58.12	39
NorESM1-ME	0.275	35	57.47	40

4. KTC TYPES FROM CMIP5 GCMS FOR THE PERIOD 1961–1990

As a first look at the results, we show the world maps of classification calculated from CRU TS 3.22 and CMIP5 simulation results (Fig. S1 in the Supplement, www.int-res.com/articles/suppl/c064p201_supp.pdf). The percentages of continental areas (excluding Antarctica) covered by KTC climate types according to CRU TS 3.22 and CMIP5 GCMs are summarized in Fig. 1. In these figures, we present the results based on data in original model grids. The results for re-gridded data do not show significant differences and are presented at the accompanying website (<http://kfa.mff.cuni.cz/projects/trewartha>).

The most frequent KTC type in CRU TS 3.22 is the desert climate *BW*, which covers 19% of the investigated continental area. Twenty out of 43 studied GCMs also give *BW* as the most frequent KTC type. On the other hand, 11 (7) GCMs produce type *E* (*Aw*) as the most abundant. Both versions of NorESM1 give type *Cf* with the highest coverage, and CESM1-FASTCHEM, CESM1-BGC, and HadGEM2-AO produce type *Dc* as the most frequent type.

In addition to *BW*, there are 4 KTC types with more than 10% continental coverage in the observed data: *Aw*, *BS*, *Dc*, and *E*. A similar result is seen for almost all GCMs and the ensemble average. In a few cases, type *Aw* is underestimated. According to 12 GCMs (e.g. most of the CESM1 simulations), type *BS* covers less than 10% of the continental area. Based on the CRU dataset, type *Cf* covers 8.1% of continental area, but approximately half of the GCMs give more than 10% continental coverage for this type. This overestimation results mainly from too large a simulated *Cf* area in southern Africa, South and Central America, northern India, and Australia (Fig. S1).

We will now comment on the skill of the GCMs at simulating the geographical distribution of the most widespread climatic types. About half of the GCMs underestimate the area covered by *BW*. However, as evident in Fig. S1, it does not appear possible to depict one problematic region that is common to all models. For example, all versions of NorESM1, CESM1, FGOALS-g2, and MIROC do not simulate *BW* over Australia, whereas in CRU TS 3.22, most of this continent is covered by this type. On the other hand, INMCM4 represents the distribution of KTC types over Australia correctly, but underestimates *BW* over all other continents. The smallest coverage of *BW* is simulated by FGOALS-g2, which in the southern part of Africa, over Australia, and in central Asia does not simulate any desert at all. The best

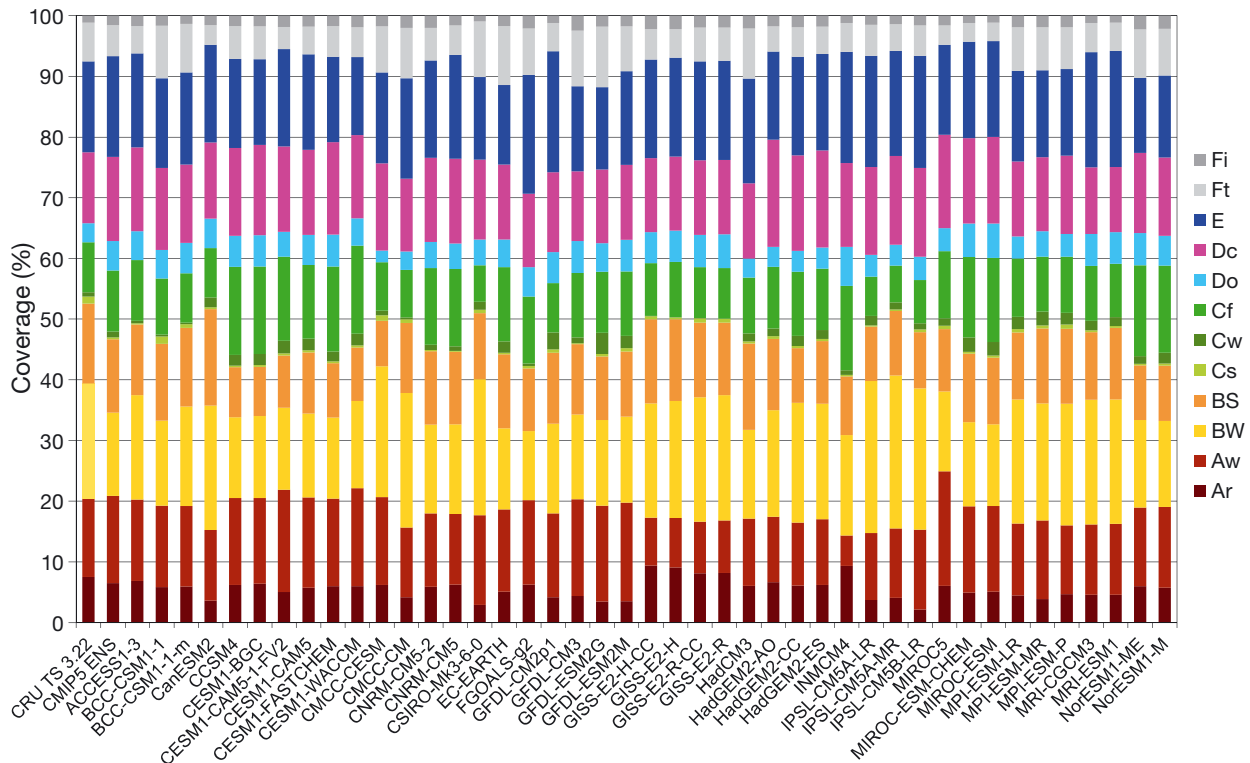


Fig. 1. Percentage of continental area (excluding Antarctica) covered by Köppen-Trewartha classification climate types (see Table 2 for descriptions of climate types) according to CRU TS3.22 and CMIP5 global climate models for the period 1961–1990

results in terms of both total coverage and actual distribution of type *BW* were achieved by MPI-ESM-LR.

Most of the models (39 out of 43 GCMs) underestimate the percentage of global continents covered by *BS*. The exceptions are CanESM2, HadCM3, and GISS-E2-H, GISS-E2-H-CC, which overestimate *BS* mainly over Australia and South America (HadCM3 only over Australia). The area of *BS* is most underestimated by CMCC-CESM, mainly because of a small coverage of this type over North America and Asia. The percentage of continents covered by *BS* is best simulated by GISS-E2-H, and both simulations of BCC-CSM1, but the distribution of this type in these models is not quite correct. They overestimate its area over Australia, while over North America this type is barely present.

Type *Aw* is best simulated by MPI-ESM-MR, IPSL-CM5B-LR, and BCC-CSM1.1m, even though the first 2 overestimate the area covered by *Aw* in South America and underestimate it over Africa and southern Asia. Regarding other GCMs, there is no general tendency to overestimate or underestimate the percentage of continental area belonging to *Aw*. MIROC5 overestimates this type quite strongly (by 6 percentage points, i.e. 6% of the continental area), mostly over Africa, where it pushes the borders of this type

farther from the equator in both directions, and over South America, where it replaces type *Ar* with *Aw*. On the other hand, the model INMCM4 only has 5% of continental areas covered by *Aw*, in comparison to 12.9% in CRU TS 3.22. In equatorial areas over Africa and South America, this model gives *Ar* and *Cf* over areas belonging to *Aw* in the observed data.

Type *Dc* is overestimated by the CMIP5 GCMs. The only exceptions are both MRI simulations and GFDL-CM3, which underestimate the *Dc* coverage, but by less than 1 percentage point. In CRU TS 3.22, *Dc* is found mainly over Europe, central Asia and North America, and these areas are depicted quite well by most of the models. The strongest overestimation of more than 3 percentage points is seen in the HadGEM2 simulations and MIROC5. These models simulate *Dc* over areas that belong to *BS* or *E* in the observed data.

The GCMs tend to overestimate the area covered by type *E* (26 GCMs overestimate type *E* area, 17 underestimate it, and the absolute bias is smaller in the case of underestimation); this is most evident in the simulations of GFDL-CM2p1, FGOALS-g2, and both simulations of MRI. These models give type *E* where, according to observed data, *Ft* should be placed mainly over northern Canada, Alaska (USA),

and north-eastern Asia. FGOALS-g2 and MRI even give *E* over western parts of the USA, where *Dc* or *BS* are present according to the observed data. Interestingly, the model CNRM-CM5, which also overestimates the area of *E* by about 2 percentage points, simulates *E* even on the shores of Greenland and in several grid points over the Arctic islands. Most of these problems are not present in the CNRM-CM5.2 simulation. Following Fig. 1, the closest models to observations in terms of the percentage of continents covered by type *E* are CMCC-CESM and MPI-ESM-LR. The geographical distribution is depicted quite well over Europe and Asia in these 2 models (Fig. S1). However, they fail in distinguishing *E* and *Ft* types over Alaska and northern Canada.

Regarding other climate types (besides the above analyzed 5 most abundant), it is worth denoting that most of the GCMs are not capable of characterizing type *Ar*, mainly over South America. Some of them simulate dry climate types *BS* and *BW* over areas belonging to *Ar* in CRU TS 3.22 over this region (e.g. CanESM2, CSIRO-Mk3.6.0, all MPI simulations). The percentage of global continental area covered by *Ar* is underestimated by most GCMs, sometimes by >50%. The exceptions are the GISS simulations and INMCM4, which overestimate the coverage of *Ar* by up to 1.8 percentage points.

When we assess the overall GCM performance according to the NE (Eq. 2, values shown in Table 3), the models closest to observations are BCC-CSM1.1m, ACCESS1.3, and 3 MPI-ESM.

When we use a simple overlap similarity measure, the rank of the models is different, (last column in Table 3). This metric, when subtracted from 100%, can also be used as a dissimilarity measure for hierarchical cluster analysis. The dendrogram (Fig. 2) suggests that the models on the right-hand side are more similar to CRU than models on the left-hand side. CRU seems to be most similar (closest) to CMCC-CM (within 1 cluster). In the next step, we may add the cluster consisting of INMCM4, MPI-ESM-LR, and MRI-CGCM3 and then clusters of IPSL experiments and CNRM GCMs. In most cases, GCMs originating from 1 modeling center have close locations within the dendrogram, regardless of differences in physical parameterizations and spatial resolution, e.g. models MPI, IPSL, and HadGEM2. One such group of models consists of MRI-CGCM3 and MRI-ESM1, where MRI-ESM1 was basically created from MRI-CGCM3 by adding chemical and biogeochemical modules, and therefore the dynamical and thermodynamical processes are entirely the same in both models (Adachi et al. 2013).

Regarding the performance of the multi-model mean (CMIP5 ENS), we found the following main results. Unlike CRU TS 3.22, CMIP5 ENS gives type *E* as the most abundant climate, and continental coverage of *Cf* is larger than 10%. It underestimates relatively strongly the area of *BW* on practically all continents (by more than 5 percentage points overall). On the other hand, CMIP5 ENS overestimates the area of *Dc*, mainly over North America and the Middle East. The overestimation of type *E* areas by CMIP5 ENS is relatively large, and is mainly due to pushing the northern border of type *E* too far over northern Canada and eastern Asia. For other KTC types, the CMIP5 differences from CRU are mostly smaller than 1.5 percentage points. According to the NE, CMIP5 ENS rank is approximately in the middle of all studied GCMs. On the other hand, based on the overlap characteristic, CMIP5 ENS is in the best agreement with CRU.

5. DISCUSSION AND CONCLUSIONS

We evaluated the skill of CMIP5 GCMs (Taylor et al. 2012) based on the ability of GCMs to represent the climatic types according to the Köppen-Trewartha climate classification (Trewartha & Horn 1980, Belda et al. 2014). The distribution of KTC types was analyzed for the 30 yr reference period 1961–1990. In connection to the choice of averaging period, it is necessary to discuss the influence of natural variability. Since an in-depth analysis of the sources of uncertainty is beyond the scope of this study, we reference our previous study (Belda et al. 2014), where the evolution in 30 yr moving averages was analyzed on CRU data as the first step. Observed changes of KTC types during the 20th century inferred from these values are mostly within a few tenths of percentage points, except for *BS*, which is within ± 0.6 percentage points (i.e. changes of 0.6% of the continental area).

However, Deser et al. (2012) showed that within a large model ensemble, the natural variability contributes considerably to the uncertainty of future climate on the multi-decadal scale (in their case, the period 2006–2060). In our CMIP5 study, we examined the influence of internal climate variability on simulated KTC types by analysis of perturbed initial conditions within a 10-member ensemble of CSIRO-Mk3.6.0 simulations. Areas covered by individual KTC types differ by <0.7% of total continental area between individual ensemble members (not shown). Therefore, in our opinion, the uncertainty connected to the choice of a specific reference period is much

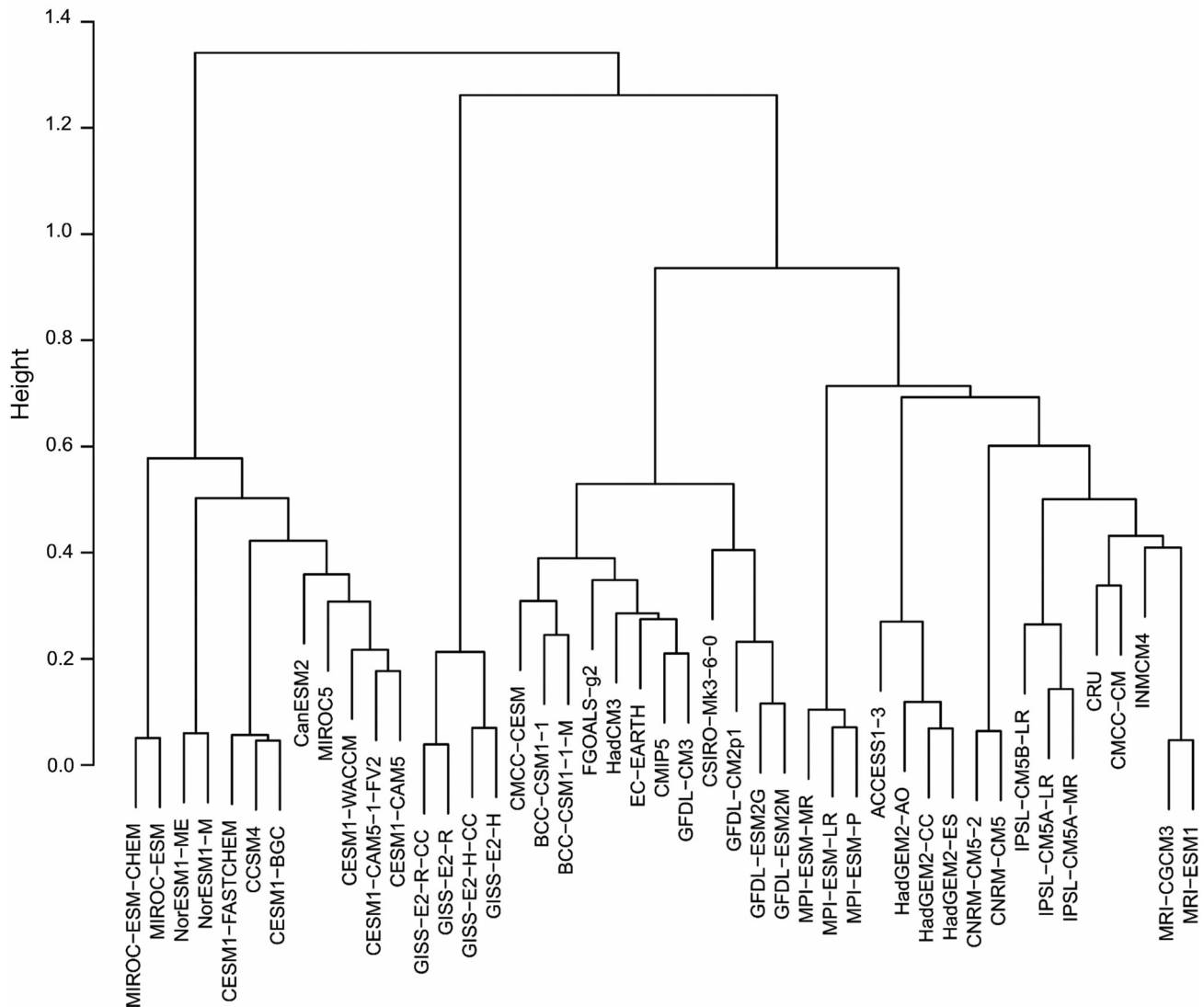


Fig. 2. Cluster dendrogram of model correspondence within the ensemble and with the CRU dataset; the Ward algorithm was used based on overlap measures

lower than model errors; also, the spread of individual models is larger than between different realizations of the selected model CSIRO-Mk3.6.0.

We used several different perspectives of model performance evaluation, ranging from the percentage of continental area (excluding Antarctica) covered by KTC climate types and a simple visual assessment of simulated geographical distribution of climatic types through relative error and overlap, to visualizing the matrix of similarities (the similarity between any 2 climate models is measured by a percentage of overlap of identical climate types) by hierarchical cluster analysis.

The GCMs' performance was assessed according to the percentage of continental areas (excluding Antarctica) covered by KTC climate types. We con-

centrated mainly on the 5 most abundant climate types *BW*, *BS*, *Aw*, *Dc*, and *E*. We can see some general tendencies to overestimate or underestimate areas belonging to individual climate types that seem to be common to most of the GCMs. About half of GCMs underestimate the area covered by *BW* and *Aw*, *BS* is underestimated by most of the models, and *E* and *Dc* are overestimated. However, problematic geographical regions differ between models, e.g. it is not possible to depict a region where most of the models unrealistically simulate the *Aw* type.

In the case of type *BW*, both total coverage and actual distribution are best simulated by MPI-ESM-LR. In terms of area covered by *BS*, models GISS-E2-H and both BCC-CSM1 simulations are closest to the observed state, but the geographical distribution of

this type in these models is not quite realistic. Type *Aw* is best simulated by MPI-ESM-MR, IPSL-CM5B-LR, and BCC-CSM1.1m. Climate type *Dc* occurs mainly over Europe, central Asia, and North America, and most of the models depict these areas quite well. Regarding the total land area covered by type *E*, the closest models to observations are CMCC-CESM and MPI-ESM-LR, but, similarly to *BS*, the geographical distribution of type *E* is not depicted correctly in these 2 models.

Most of the GCMs cannot correctly characterize the equatorial climate over South America, with some of them even giving types *BS* and *BW* over areas belonging to *Ar* in CRU TS 3.22 (e.g. CanESM2, CSIRO-Mk3.6.0, and all MPI simulations). As a whole, the area of tropical rainforest climate *Ar* is underestimated by most CMIP5 GCMs.

The above summarized evaluation of GCMs in terms of the percentage of continental areas (excluding Antarctica) covered by KTC climate types was based on the GCMs' outputs in their original spatial resolution. Calculations with model outputs interpolated into the CRU TS 3.22 grid gave almost identical results. Therefore, we consider the error caused by interpolation negligible.

A GCM can give correct values of global land area fraction belonging to a specific KTC climate type even though the geographical distribution is not well captured by the model. Furthermore, the same GCM can skillfully simulate global land area fractions for some of the climate types but can fail in the case of others.

The evaluation of the models by a specific characteristic depends on what the characteristic depicts, and the results obtained using different metrics can significantly differ. This fact has already been shown in many studies, e.g. Gleckler et al. (2008), Pierce et al. (2009). The agreement of simulated and observed KTC types also depends on the choice of criterion. For example, the model BCC-CSM1.1m is the best model when considering NE of all climate types (Table 3). However, the most widespread type *BW* is not simulated very consistently by this model (Fig. 1); for example, *BW* is absent over Australia according to BCC-CSM1.1m.

A different perspective to the model evaluation is provided by the overlap measure of similarity (Table 3), which is based on the relative area of grid points in which the climate type given by the GCM matches CRU TS 3.22. The best models according to this assessment are MPI-ESM-P, HadGEM2-ES, and MPI-ESM-MR. The cluster dendrogram based on overlap similarity measures showed that the models most similar to CRU TS 3.22 are CMCC-CM,

INMCM4, MPI-ESM-LR, and MRI-CGCM3. The next cluster is formed by IPSL experiments and then by CNRM-CM5 simulations.

The horizontal resolution of GCMs analyzed in our study varies from $0.75^\circ \times 0.75^\circ$ to $3.75^\circ \times 3.75^\circ$. Our results do not indicate any general tendency that GCMs with finer horizontal resolution give better representation of KTC types. For example, we can see in Fig. 2 that in the cluster nearest to CRU TS 3.22 are GCMs with relatively high spatial resolution; however, they were developed in different modeling centers, and it is not clear whether their success is caused by their resolution. On the other hand, model CSIRO-Mk3.6.0 with a relatively high resolution of $1.9^\circ \times 1.9^\circ$ is quite far from that cluster. Both IPSL-CM5A-LR and IPSL-CM5A-MR, which share the same physical parameterizations but differ in their spatial resolution, belong to 1 cluster, indicating a lower effect of resolution on simulated KTC types. The described ambiguous effect of spatial resolution is not particularly surprising because model performance is affected not only by coarse or fine resolution, but also by the parameterizations used, numerical schemes, etc. (e.g. Duffy et al. 2003). However, a clearer benefit of finer resolution might occur if we add another level of subtypes into the classification. This may prove useful especially when applying the classification to regional models rather than GCMs in regions with a much more diverse structure of surface characteristics.

The GCMs coming from the same modeling center are often grouped in the same cluster. A similar result was already described by Knutti et al. (2013). Even though they used a different methodology, their conclusions are quite similar to our results. For example, Knutti et al. (2013) also found that the simulations of CESM1 are close to CCSM4, although most of the major parameterizations were changed going from CCSM4 to CESM1.

According to our results, the multi-model ensemble mean did not outperform all individual GCMs, except for the overlap characteristic. Various previous studies evaluating GCM performances according to different characteristics and metrics indicated superiority of the multi-model mean (e.g. Gleckler et al. 2008, Pierce et al. 2009, Miao et al. 2014). A possible explanation is that unlike usual validation metrics, the climate classification schemes combine various aspects of both air temperature and precipitation fields and therefore no simple cancellation of errors can be expected.

Further analysis of the reasons why the CMIP5 GCMs have problems with simulation of the ob-

served distribution of some KTC types in some regions for the reference period would require a detailed analysis of simulated air temperature and precipitation fields. However, such an investigation is beyond the scope of this paper. We concentrated on the evaluation of CMIP5 GCMs using KTC climate types to show how a climate classification can provide a compact analysis tool integrating important temperature and precipitation characteristics.

Acknowledgements. We acknowledge the World Climate Research Programme's Working Group on Coupled Modelling, which is responsible for CMIP, and we thank the climate modeling groups (listed in Table 1 of this paper) for producing and making available their model outputs. For CMIP, the U.S. Department of Energy's Program for Climate Model Diagnosis and Intercomparison provided coordinating support and led development of software infrastructure in partnership with the Global Organization for Earth System Science Portals. The CRU TS 3.22 dataset was provided by the Climatic Research Unit, University of East Anglia. This study was supported by project UNCE 204020/2012 funded by Charles University in Prague and by research plan no. MSM0021620860 funded by the Ministry of Education, Youth and Sports of the Czech Republic. In addition, the work is part of the activity under the Program of Charles University PRVOUK No. 02 'Environmental Research.'

LITERATURE CITED

- Adachi Y, Yukimoto S, Deushi M, Obata A and others (2013) Basic performance of a new earth system model of the Meteorological Research Institute (MRI-ESM1). *Papers Meteorol Geophys* 64:1–19
- Belda M, Holtanová E, Halenka T, Kalvová J (2014) Climate classification revisited: from Köppen to Trewartha. *Clim Res* 59:1–13
- Boer GJ, Flato G, Reader MC, Ramsden D (2000) A transient climate change simulation with greenhouse gas and aerosol forcing: experimental design and comparison with the instrumental record for the twentieth century. *Clim Dyn* 16:405–427
- Boriah S, Chandola V, Kumar V (2008) Similarity measures for categorical data: a comparative evaluation. *Proceedings of the 8th SIAM International Conference on Data Mining*, p 243–254
- Cannon AJ (2012) Köppen versus the computer: comparing Köppen-Geiger and multivariate regression tree climate classifications in terms of climate homogeneity. *Hydrol Earth Syst Sci* 16:217–229
- Deser C, Knutti R, Solomon S, Phillips AS (2012) Communication of the role of natural variability in future North American climate. *Nat Clim Change* 2:775–779
- Duffy PB, Govindasamy B, Iorio JP, Milovich J and others (2003) High-resolution simulations of global climate. 1. Present climate. *Clim Dyn* 21:371–390
- Feng S, Ho CH, Hu Q, Oglesby RJ, Jeong SJ, Kim BM (2012) Evaluating observed and projected future climate changes for the Arctic using the Köppen-Trewartha climate classification. *Clim Dyn* 38:1359–1373
- Feng S, Hu Q, Chen F, Ho CH, Li R, Tang Z (2014) Projected climate shift under future global warming from multi-model, multi-scenario, CMIP5 simulations. *Global Planet Change* 112:41–52
- Fovell RG, Fovell MYC (1993) Climate zones of the conterminous United States defined using cluster-analysis. *J Clim* 6:2103–2135
- Geiger R (1954) *Landolt-Börnstein — Zahlenwerte und Funktionen aus Physik, Chemie, Astronomie, Geophysik und Technik, alte Serie Vol 3*. Springer, Berlin
- Gleckler PJ, Taylor KE, Doutriaux C (2008) Performance metrics for climate models. *J Geophys Res* 113:D06104, doi:10.1029/2007JD008972
- Guetter PJ, Kutzbach JE (1990) A modified Koeppen classification applied to model simulation of glacial and interglacial climates. *Clim Change* 16:193–215
- Harris I, Jones PD, Osborn TJ, Lister DH (2014) Updated high-resolution grids of monthly climatic observations — the CRU TS3.10 dataset. *Int J Climatol* 34:623–642
- Hirst AC, O'Farrell SP, Siobhan P, Gordon HB (2000) Comparison of a coupled ocean-atmosphere model with and without oceanic eddy-induced advection. 1. Ocean spinup and control integrations. *J Clim* 13:139–163
- Kalvová J, Halenka T, Bezpalcová K, Nemešová I (2003) Köppen climate types in observed and simulated climates. *Stud Geophys Geod* 47:185–202
- Knutti R, Masson D, Gettelman A (2013) Climate model genealogy: generation CMIP5 and how we got there. *Geophys Res Lett* 40:1194–1199
- Köppen W (1923) *Die Klimate der Erde: Grundriss der Klimakunde*. Walter de Gruyter & Co., Berlin
- Köppen W (1931) *Grundriss der Klimakunde*. Walter de Gruyter & Co., Berlin
- Köppen W (1936) *Das geographische System der Klimate*. In: Köppen W, Geiger R (eds) *Handbuch der Klimatologie*. Gebrüder Borntraeger, Berlin, p C1–C44
- Kottek M, Grieser J, Beck C, Rudolf B, Rubel F (2006) World map of the Köppen-Geiger climate classification updated. *Meteorol Z* 15:259–263
- Lohmann U, Sausen R, Bengtsson L, Cubasch U, Perlwitz J, Roeckner E (1993) The Köppen climate classification as a diagnostic tool for general circulation models. *Clim Res* 3:177–193
- Mahlstein I, Daniel JS, Solomon S (2013) Pace of shifts in climate regions increases with global temperature. *Nat Clim Change* 3:739–743
- Manabe S, Holloway JL Jr (1975) The seasonal variation of the hydrological cycle as simulated by a global model of the atmosphere. *J Geophys Res* 80:1617–1649
- Meehl GA, Covey C, Delworth T, Latif M and others (2007) The WCRP CMIP3 multi-model dataset: a new era in climate change research. *Bull Am Meteorol Soc* 88:1383–1394
- Miao C, Duan Q, Sun Q, Huang Y and others (2014) Assessment of CMIP5 climate models and projected temperature changes over Northern Eurasia. *Environ Res Lett* 9:055007, doi:10.1088/1748-9326/9/5/055007
- Mitchell JFB, Johns TC (1997) On modification of global warming by sulphate aerosols. *J Clim* 10:245–267
- Mitchell TD, Jones PD (2005) An improved method of constructing a database of monthly climate observations and associated high-resolution grids. *Int J Climatol* 25:693–712
- Mitchell TD, Carter TR, Jones PD, Hulme M, New M (2004) A comprehensive set of high-resolution grids of monthly climate for Europe and the globe: the observed records (1901–2000) and 16 scenarios (2001–2100). Working

- paper 55. Tyndall Centre of Climate Change Research, Norwich
- Patton CP (1962) A note on the classification of dry climate in the Köppen system. *Calif Geogr* 3:105–112
- Peel MC, Finlayson BL, McMahon TA (2007) Updated world map of the Köppen-Geiger climate classification. *Hydrol Earth Syst Sci* 11:1633–1644
- Pierce DW, Barnett TP, Santer BD, Gleckler PJ (2009) Selecting global climate models for regional climate change studies. *Proc Natl Acad Sci USA* 106:8441–8446
- R Core Team (2012) R: a language and environment for statistical computing. R Foundation for Statistical Computing, Vienna. www.R-project.org/
- Roeckner E, Arpe K, Bengtsson L, Brinkop S and others (1992) Simulation of the present-day climate with ECHAM model: impact of model physics and resolution. Rep 93. Max-Planck-Institut für Meteorologie, Hamburg
- Roeckner E, Arpe K, Bengtsson L, Christoph M and others (1996) The atmospheric general circulation model ECHAM-4: model description and simulation of present-day climate. Rep 218. Max-Planck-Institut für Meteorologie, Hamburg
- Rubel F, Kottek M (2010) Observed and projected climate shifts 1901–2100 depicted by world maps of the Köppen-Geiger climate classification. *Meteorol Z* 19:135–141
- Stern H, De Hoedt G, Ernst J (2000) Objective classification of Australian climates. *Aust Meteorol Mag* 49:87–96
- Taylor K, Stouffer RJ, Meehl GA (2012) An overview of CMIP5 and the experiment design. *Bull Am Meteorol Soc* 93:485–498
- Trewartha GT (1968) *An introduction to climate*. McGraw-Hill, New York, NY
- Trewartha GT, Horn LH (1980) *Introduction to climate*, 5th edn. McGraw Hill, New York, NY
- Watanabe S, Hajima T, Sudo K, Nagashima T and others (2011) MIROC-ESM 2010: model description and basic results of CMIP5-20c3m experiments. *Geosci Model Dev* 4:845–872

Editorial responsibility: Tim Sparks, Cambridge, UK

*Submitted: October 6, 2014; Accepted: May 27, 2015
Proofs received from author(s): August 11, 2015*



Global warming-induced changes in climate zones based on CMIP5 projections

Michal Belda*, Eva Holtanová, Jaroslava Kalvová, Tomáš Halenka

Charles University in Prague, Dept. of Meteorology and Environment Protection, 18200, Prague, Czech Republic

ABSTRACT: Climate classifications can provide an effective tool for integrated assessment of climate model results. We present an analysis of future global climate projections performed in the framework of the Coupled Model Intercomparison Project Phase 5 (CMIP5) project by means of Köppen-Trewartha classification. Maps of future climate type distributions were created along with the analysis of the ensemble spread. The simulations under scenarios with representative concentration pathway (RCP) 4.5 and RCP8.5 showed a substantial decline in ice cap, tundra, and boreal climate in the warming world, accompanied by an expansion of temperate climates, dry climates, and savanna, nearly unanimous within the CMIP5 ensemble. Results for the subtropical climate types were generally not conclusive. Changes in climate zones were also analyzed in comparison with the individual model performance for the historical period 1961–1990. The magnitude of change was higher than model errors only for tundra, boreal, and temperate continental climate types. For other types, the response was mostly smaller than model error, or there was considerable disagreement among the ensemble members. Altogether, around 14% of the continental area is expected to change climate types by the end of the 21st century under the projected RCP4.5 forcing and 20% under the RCP8.5 scenario.

KEY WORDS: Köppen-Trewartha climate classification · Coupled Model Intercomparison Project Phase 5 · CMIP5 · Global climate model · Climate type change · Representative concentration pathways

1. INTRODUCTION

The outputs of state-of-the-art global climate models are currently available within the Coupled Model Intercomparison Project Phase 5 (CMIP5, Taylor et al. 2012b), which served as the basis for the IPCC's Fifth Assessment Report, published in September 2013 (available online at www.ipcc.ch). Besides the global climate models (GCMs) themselves, which were improved, e.g. toward higher resolution and in some cases by including new processes and interactions such as so-called Earth System Models (ESMs), the methodology regarding the construction of projection scenarios also changed in comparison to previous GCM experiments (CMIP3 GCMs, Meehl et al. 2007). For the core CMIP5 GCM experiments, 4 representative concentration pathways (RCPs) with

radiative forcing ranging from 2.6 to 8.5 W m⁻² in the year 2100 were chosen, designated as RCP2.6, RCP4.5, RCP6.0, and RCP8.5 (Moss et al. 2010).

Each generation of climate models must inevitably be subject to tests of how realistic the models are in simulating the observed climate characteristics in the recent past. The climate classifications can serve, inter alia, as effective tools for analysis of model performance. The Köppen classification (Köppen 1923, 1931, 1936, Geiger 1954) or Köppen-Trewartha classification (KTC, Trewartha 1968, Trewartha & Horn 1980) have most often been used for this purpose. The climate types are based on long-term climatological means of near-surface air temperature and precipitation that are easily obtained from the outputs of GCMs. The KTC provides a slightly more detailed description of climate type distributions than the original

*Corresponding author: Michal.Belda@mff.cuni.cz

Köppen scheme (de Castro et al. 2007). Belda et al. (2014) reviewed the KTC and its differences from the original Köppen scheme, and analyzed observed patterns in climate types and their changes during the 20th century.

Climate types derived from GCM projections of future climate are useful for a variety of sectors and scientific fields. They provide an idea of what changes can be expected in the areas of individual climate types. Due to their strong relationship with the distribution of natural vegetation zones (e.g. Trewartha & Horn 1980, Bailey 2009), it is possible to assess the development of different ecoregions, even though further information on e.g. edaphic and topographic properties (Baker et al. 2010, Hargrove & Hoffman 2004) is needed for such assessments.

Projected changes in climate types have previously been analyzed in various studies using different climate models and emission scenarios. Lohmann et al. (1993) assessed the outputs of the atmospheric general circulation model ECHAM3 using the Köppen classification, and derived shifts in climate zones in greenhouse gas warming simulations over 100 model years. They projected a retreat of the permafrost climate and an extension of both the tropical rainy climate and dry climate.

Kalvová et al. (2003) applied the Köppen classification to simulations of 4 GCMs, namely HadCM2, ECHAM4, CSIRO-Mk2b, and CGCM1, for the present and future periods. They confirmed the results described by Lohmann et al. (1993) regarding tropical and dry climates and described a decline in the area of boreal and cold climates.

More recently, Rubel & Kottek (2010) created a series of digital world maps of Köppen climate types for the period 1901–2100 based on observed data (CRU TS2.1, GPCP Version 4) and 20 simulations of 5 GCMs (each GCM with 4 Special Report on Emission Scenarios [SRES] emission scenarios). In the case of the emission scenario with the highest rate of emission increase (A1FI), the results showed an increase in the areas covered by tropical, dry, and temperate climates, and a decrease in the coverage of cold and boreal climates. Projected changes for the milder emissions scenario (B1) were significantly smaller.

Baker et al. (2010) compared KTC types over China for historical (1961–1990) and projected future climates (2041–2070) simulated by HadCM3 for the SRES A1FI scenario. They showed that the spatial patterns of climate change resulted in a northern migration of warmer climatic types as well as a slight expansion in the high-latitude desert and arid shrubland regions in northwestern China.

Mahlstein et al. (2013) used simulations of 13 CMIP5 GCMs for determination of Köppen-Geiger climate types and analyzed their changes during 1900–2098. They found that under the RCP8.5 forcing, for which the mean warming reaches about 4.5°C by the end of the 21st century (Rogelj et al. 2012), approximately 20% of the global land area would undergo a shift in the original climate zones. Frost climates are projected to largely decline, some arid climatic zones are expected to expand, and large parts of the global land area with cool summers will experience a change to climates with hot summers. However, Mahlstein et al. (2013) also emphasized large model uncertainties and reported that the pace of the climate type shifts increases with increasing global mean temperature.

Feng et al. (2012) analyzed observed and projected climate changes and their impact on vegetation for the area north of 50°N over the period of 1900–2099 using the KTC scheme. To estimate the future changes, they used the simulations of 16 CMIP3 GCMs for 3 SRES emission scenarios (B1, A1B, and A2). Their results showed a decrease in areas classified as tundra, ice cap, and subarctic continental climates, and an expansion of the temperate and boreal oceanic climates. Moreover Feng et al. (2012) projected that arid, warm temperate, and snow and polar climates will successively shift to the north in the northern hemisphere.

Feng et al. (2014) focused on shifts in KTC climate types in 1900–2100. In contrast to Feng et al. (2012), the analysis was done for the whole global land area and model simulations of 20 CMIP5 GCMs for RCP4.5 and RCP8.5 pathways. Feng et al. (2014) found that during the 21st century, the KTC types would shift toward warmer and drier types, with the largest changes in the northern hemisphere north of 30°N. They also concluded that temperature changes are the dominant factor causing the projected shifts in climate types during the 21st century.

Here we used the KTC to assess changes in climate type areas simulated by a suite of 30 CMIP5 GCMs for the period of 2006–2100 and 2 RCPs (RCP4.5 and RCP8.5). Our study follows previous papers, i.e. Belda et al. (2014) mentioned above and Belda et al. (2015), wherein we assessed the performance of 43 CMIP5 GCMs in simulating the KTC climate types in the reference period 1961–1990. One of the main conclusions of Belda et al.'s (2015) analysis was that models generally had problems capturing the rainforest climate type *Ar* (see Table 2 for climate types), mainly in Amazonia. The desert climate type *BW* was underestimated by half of the models. Boreal climate

type *E* was overestimated by many models, mostly spreading over to the areas of observed tundra type *Ft*. Further, Belda et al. (2015) indicated that CMIP5 GCMs did not show any clear tendency to improve the representation of climate types with increasing spatial resolution.

In addition to previous analyses of CMIP5 models in terms of Köppen classification by Mahlstein et al. (2013) and Feng et al. (2014), here we use the largest possible set of GCMs, describe the temporal evolution of KTC types for individual GCMs, and present simulated changes in the context of model performance for the present climate. We also add an analysis of future climate uncertainty in terms of ensemble spread throughout the scenario simulations.

Various supplementary graphical products, including figures describing the model performance of CMIP5 GCMs used by Belda et al. (2015) are available at <http://kfa.mff.cuni.cz/projects/trewartha/>.

2. DATA AND METHODS

2.1. Data

A suite of CMIP5 GCM simulations is employed here, selected based on the availability of data for both RCP4.5 and RCP8.5 scenarios. Basic information on all model simulations incorporated here is presented in Table 1. The data are available at <http://cmip-pcmdi.llnl.gov/cmip5/>; we used monthly mean surface air temperature and precipitation to classify the KTC types. The outputs from the experiment denoted as ‘historical’ were used for the reference period 1961–1990. For the future time period 2006–2100, we considered 2 alternative simulations, RCP4.5 and RCP8.5. RCP4.5 assumes radiative forcing of 4.5 W m^{-2} at stabilization after 2100, whereas RCP8.5 represents a ‘rising pathway’ with radiative forcing higher than 8.5 W m^{-2} after 2100. For more details on RCPs, see Moss et al. (2010). Where more ensemble members were available, we chose the ensemble member r1i1p1 (considered a baseline simulation of the subensemble for the purposes of this analysis) (Taylor et al. 2012a).

As one of the indicators of uncertainty in the climate signal, errors in the historical experiment during the reference period were considered in terms of KTC types based on monthly mean surface air temperature and precipitation provided by the Climatic Research Unit (CRU) TS 3.22 dataset (Harris et al. 2014, hereafter TS3) available in spatial resolution of $0.5^\circ \times 0.5^\circ$ over global land areas excluding Ant-

arctica. As a part of the uncertainty analysis, a comparison of the classification based on 2 versions of CRU (TS 3.22 and TS 3.1.10) and the University of Delaware dataset version 4.01 (UDEL; Willmott & Matsuura 2001) was performed with the conclusion that the differences between these datasets are considerably smaller than the spread of the model simulations, and thus the impact of the choice of the observational dataset on GCM performance evaluation is negligible.

2.2. Methods

The KTC system (Trewartha & Horn 1980, Belda et al. 2014) has 6 main climate groups. Five of them (*A*, *C*, *D*, *E*, and *F*) are basic thermal zones. The sixth group, *B*, is the dry climatic zone that cuts across the other climate types, except for the polar climate *F*. Similarly to original Köppen classification scheme, the main climate types are determined according to long-term annual and monthly means of surface air temperature and precipitation amounts. The dryness threshold distinguishing group *B* is based on the definition by Patton (1962). A brief summary of climate types and subtypes is provided in Table 2.

The KTC climate types were calculated in the original model grids for the reference period 1961–1990 and for running 30 yr periods during the 21st century, beginning with 2006–2035 until 2071–2100 or 2070–2099 (as data for some of the model runs are only available until the year 2099). Land areas falling into each climate type/subtype were expressed in terms of relative areas, i.e. as a percentage of the whole global land area (excluding Antarctica). Simulated changes of KTC types for both RCP4.5 and RCP8.5 were assessed in several different ways. An overall picture of the multi-model ensemble evolution in time is provided as medians and 10th and 90th percentiles of changes of relative areas with respect to the values simulated for the reference period 1961–1990.

Further, we pay special attention to 3 selected time periods denoted as near future (2006–2035), mid-century (2020–2050), and far future (2071–2100 or 2070–2099 based on the simulation period). We demonstrate changes in selected climate type areas for each of these periods simulated by individual GCMs together with model errors in the reference period indicating the reliability of the climate change signal. All changes are expressed in percentage of area simulated by the respective GCMs in the reference period. The model errors are defined as differences in

Table 1. CMIP5 global climate models analyzed in this study with model versions explained (where applicable)

No.	CMIP5 model	Resolution	Modeling center/model versions
1	ACCESS1.3	1.88° × 1.24°	Commonwealth Scientific and Industrial Research Organisation (CSIRO) and Bureau of Meteorology, Australia
2	CanESM2	2.8° × 2.8°	Canadian Centre for Climate Modelling and Analysis
3	CCSM4	1.25° × 0.94°	National Center for Atmospheric Research
4	CESM1-BGC	1.25° × 0.94°	Community Earth System Model Contributors BGC: BioGeoChemistry CAM5: Community Atmospheric Model v5 FV2: Finite volume 2degree
5	CESM1-CAM5	1.25° × 0.94°	
6	CESM1-CAM5.1-FV2	2.50° × 1.88°	
7	CNRM-CM5	1.4° × 1.4°	Centre National de Recherches Météorologiques; Centre Européen de Recherche et Formation Avancées en Calcul Scientifique
8	CSIRO-Mk3.6.0	1.9° × 1.9°	CSIRO; Queensland Climate Change Centre of Excellence
9	FGOALS-g2	2.81° × 3.00°	LASG, Institute of Atmospheric Physics, Chinese Academy of Sciences and CESS, Tsinghua University
10	GFDL-CM3	2.5° × 2°	Geophysical Fluid Dynamics Laboratory
11	GFDL-ESM2G	2.5° × 2°	
12	GFDL-ESM2M	2.5° × 2°	
13	GISS-E2-H	2.5° × 2°	NASA Goddard Institute for Space Studies H: Hycom Ocean Model R: Russell Ocean Model CC: interactive terrestrial carbon cycle, ocean biogeochemistry
14	GISS-E2-H-CC	2.5° × 2°	
15	GISS-E2-R	2.5° × 2°	
16	GISS-E2-R-CC	2.5° × 2°	
17	HadGEM2-AO		Met Office Hadley Centre AO: aerosols, ocean & sea-ice CC: AO+terrestrial carbon cycle, ocean biogeochemistry ES: CC+chemistry
18	HadGEM2-CC	1.875° × 1.25°	
19	HadGEM2-ES	1.875° × 1.25°	
20	INM-CM4	2° × 1.5°	Institute for Numerical Mathematics
21	IPSL-CM5A-MR	2.5° × 1.3°	Institut Pierre-Simon Laplace MR: Medium resolution LR: Low resolution
22	IPSL-CM5B-LR	3.75° × 1.9°	
23	MIROC5	1.4° × 1.4°	Atmosphere and Ocean Research Institute (The University of Tokyo), National Institute for Environmental Studies, and Japan Agency for Marine-Earth Science and Technology
24	MIROC-ESM	2.8° × 2.8°	Japan Agency for Marine-Earth Science and Technology, Atmosphere and Ocean Research Institute (The University of Tokyo), and National Institute for Environmental Studies CHEM: added atmospheric chemistry
25	MIROC-ESM-CHEM	2.8° × 2.8°	
26	MPI-ESM-LR	1.9° × 1.9°	Max Planck Institute for Meteorology MR: Medium resolution LR: Low resolution
27	MPI-ESM-MR	1.9° × 1.9°	
28	MRI-CGCM3	1.125° × 1.125°	Meteorological Research Institute
29	NorESM1-M	2.5° × 1.9°	Norwegian Climate Centre M: intermediate resolution ME: M+carbon cycle
30	NorESM1-ME	2.5° × 1.9°	

Table 2. Definition of Köppen-Trewartha classification (KTC) climate types according to Trewartha & Horn (1980), with dryness threshold defined by Patton (1962). T_{mo} : long-term monthly mean air temperature; T_{cold} (T_{warm}): monthly mean air temperature of the coldest (warmest) month; P_{mean} : mean annual precipitation (cm); P_{dry} : mean precipitation of the driest summer month; R : Patton's precipitation threshold, defined as $R = 2.3T - 0.64P_w + 41$, where T is mean annual temperature ($^{\circ}\text{C}$) and P_w is the percentage of annual precipitation occurring in winter

Type	Criteria
Subtype	Precipitation/temperature regime
A	$T_{cold} > 18^{\circ}\text{C}$; $P_{mean} > R$
Ar	10 to 12 mo wet; 0 to 2 mo dry
Aw	Winter (low-sun period) dry; > 2 mo dry
As	Summer (high-sun period) dry; rare in type A climates
B	$P_{mean} < R$
BS	$R/2 < P_{mean} < R$
BW	$P_{mean} < R/2$
C	$T_{cold} < 18^{\circ}\text{C}$; 8 to 12 mo with $T_{mo} > 10^{\circ}\text{C}$
Cs	Summer dry; at least 3 times as much precipitation in winter half-year as in summer half-year; $P_{dry} < 3$ cm; total annual precipitation < 89 cm
Cw	Winter dry; at least 10 times as much precipitation in summer half-year as in winter half-year
Cf	No dry season; difference between driest and wettest month less than required for Cs and Cw; $P_{dry} > 3$ cm
D	4 to 7 mo with $T_{mo} > 10^{\circ}\text{C}$
Do	$T_{cold} > 0^{\circ}\text{C}$
Dc	$T_{cold} < 0^{\circ}\text{C}$
E	1 to 3 mo with $T_{mo} > 10^{\circ}\text{C}$
F	All months with $T_{mo} < 10^{\circ}\text{C}$
Ft	$T_{warm} > 0^{\circ}\text{C}$
Fi	$T_{warm} < 0^{\circ}\text{C}$

simulated and observed CRU TS3.22 areas expressed as a percentage of observed values.

For illustration of the geographical distribution of changes simulated for the far-future period, maps of projected distributions of KTC types are shown for both RCPs. Climate zones in the future period were calculated based on temperature and precipitation scenarios constructed using the delta method (Deque 2007). Ensemble mean values in the periods 2070–2099 and 1961–1990 were used to calculate deltas that were then added (multiplied) to the present climate state represented by the temperature (precipitation) from the CRU TS3.22 database. KTC was then applied, which provided spatial distributions of climate zones in the scenarios.

3. RESULTS

The geographical distribution of observed KTC types and its simulated changes are illustrated in Figs. 1–3. The climate change signal patterns are similar for both scenarios, with stronger manifestation under stronger forcing of RCP8.5. In the northern hemisphere, the most remarkable feature is the northward shift of the border between *Dc* and *E* types, with an increase in the area of *Dc* and shrinking of the *E* type. The shift of the southern border of *Dc* is not as evident; only in Europe, an eastward shift of the *Dc*–*Do* border is projected, inducing expansion of the *Do* area over western and central Europe. Further, a global feature is shrinking of the *Ft* area, not only in the high latitudes, but also in high-elevation regions of the Himalayas and the Andes. In South America, the *Ft* type is projected to disappear by the end of the century under both RCPs. Another distinct pattern of change in South America is the expansion of the dry types *BW* and *BS*. In Africa and Australia, the GCMs project an increase in the *BW* area and shrinking of the *C* types. In southeastern Asia, our results suggest an expansion of the *Aw* type, which might be connected to increased strength of the Indian summer monsoon as documented e.g. by Menon et al. (2013).

The values of multi-model medians of simulated changes, 10th and 90th percentiles, and the range between them for the period 2071–2100 under both RCP4.5 and RCP8.5 forcings are summarized in Table 3.

The KTC climate types can be divided into 3 groups (decreasing area, increasing area and no conclusive change) based on the temporal behavior of simulated continental areas belonging to respective KTC types during the 21st century under the RCP4.5 and RCP8.5 forcing. The first group comprises boreal climate *E*, tundra *Ft*, and ice cap climate *Fi* that, according to the GCMs analyzed in our study, are expected to retreat. These 3 types occur at high latitudes or altitudes.

All GCMs simulate a decrease in the continental coverage (Antarctica not included in the analysis) of ice cap climate *Fi* (Fig. 4), which is clearly seen for the multi-model median (M-MED). Under the RCP4.5 forcing, the relative area of *Fi* decreases to 73 % (Table 3) of the value simulated for the reference period 1961–1990. In the case of RCP8.5, the decrease is even stronger, as the *Fi* area decreases to 52 % of its reference value. The decrease to less than 90 % is already expected in the period 2006–2035 for both scenarios. The multi-model spread of simulated

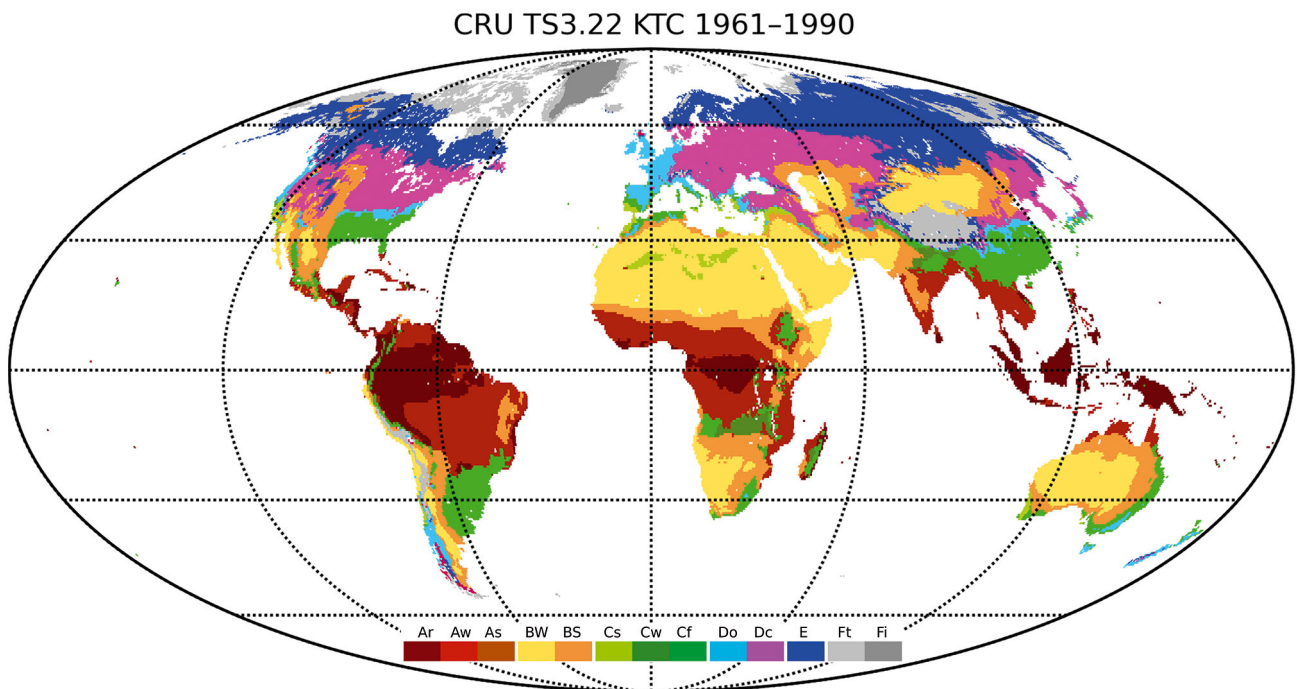


Fig. 1. Köppen-Trewartha climate types derived from observations (CRU TS3.22) for the period 1961–1990

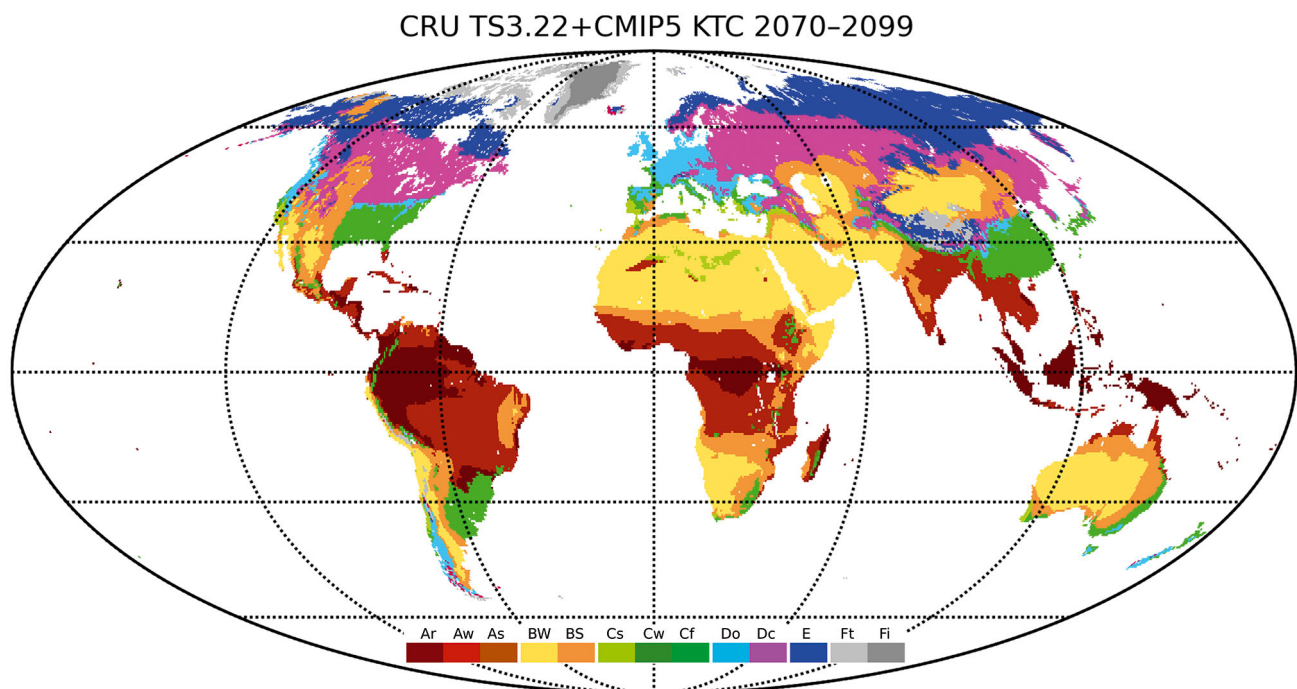


Fig. 2. Köppen-Trewartha climate types for the period 2070–2099, derived from the CRU TS3.22 observational dataset and the CMIP5 ensemble RCP4.5 scenario using the delta method

changes is quite large and is the same for both RCPs. In the case of RCP4.5, the decrease is often fastest during the first half of this century; in the second half it is rather slow, whereas the stronger forcing of RCP8.5 leads to more pronounced decline during the

whole century. The decrease in relative area occupied by type *Fi* is solely due to transformation to tundra, *Ft*. Regarding the comparison of simulated changes to model errors in the reference period, all GCMs (except for CSIRO-Mk3-6-0 and MIROC-

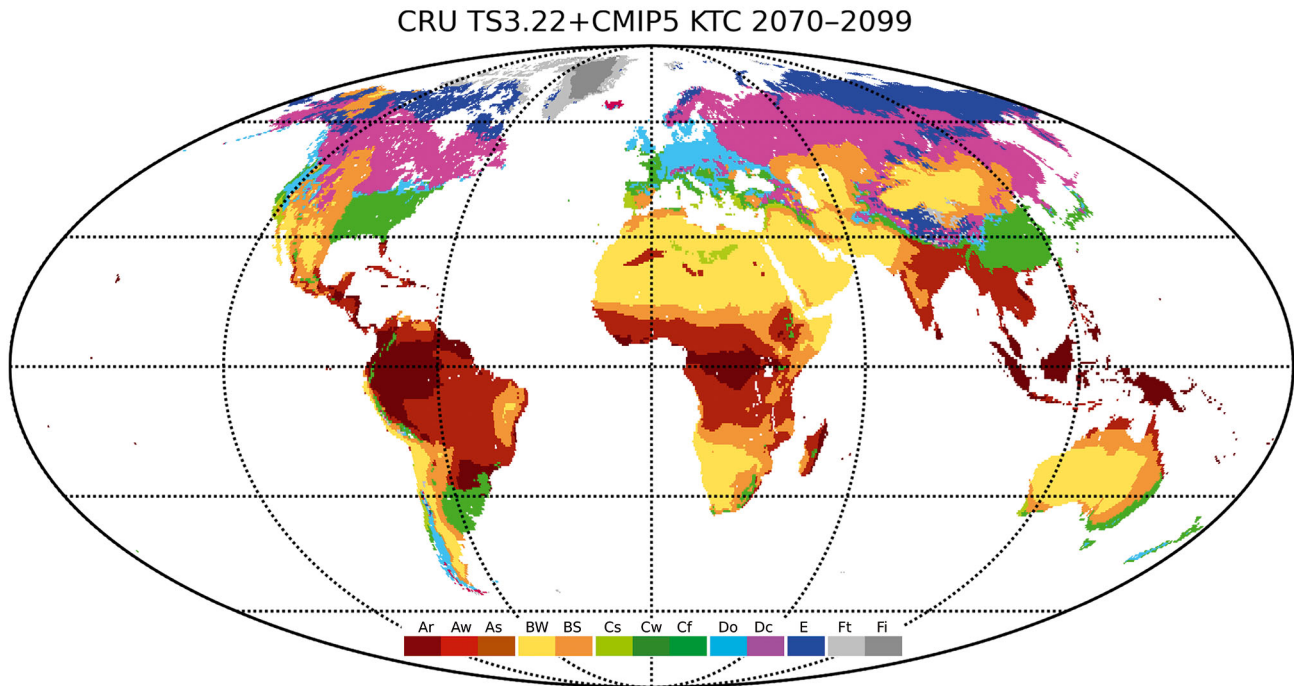


Fig. 3. Köppen-Trewartha climate types for the period 2070–2099, derived from the CRU TS3.22 observational dataset and the CMIP5 ensemble RCP8.5 scenario using the delta method

ESM) overestimate the observed area of *Fi*. Only in 37 out of 180 cases (3 periods, 2 RCPs, 30 GCMs) are the projected changes larger (in absolute value) than model errors (Fig. 5).

Similarly, all GCMs simulate a decrease in tundra climate type *Ft*, and under the RCP4.5 forcing, a faster rate of change occurs in the first half of the century (Fig. 4). According to M-MED, the relative area of *Ft* decreases by the end of the 21st century to 63 %

(42 %) for RCP4.5 (RCP8.5), and the multi-model range is larger for RCP8.5 (Table 3). Models MIROC-ESM, MIROC-ESM-CHEM, and INMCM4 simulate the slowest decline in *Ft* (Fig. 5), even though the first 2 of these GCMs are the most sensitive to *Fi* changes. The largest change in *Ft* for the far future period is simulated by GFDL-CM3, which shows a decrease to 30 % of the reference under RCP4.5 and 19 % under RCP8.5. Projected changes are larger than model errors in 60 % of all cases for RCP4.5, and in 90 % for RCP8.5 at the end of the century. The *Ft* climate type is expected to transform into boreal climate *E*, although under RCP8.5, transitions of smaller areas to *Dc* and *Do* climate types are also simulated.

Table 3. Multi-model statistics of the percentage changes of Köppen-Trewartha classification (KTC; see Table 2 for definitions) climate type areas in the future with respect to the reference period (1961–1990) for the RCP4.5 and RCP8.5 scenarios. M-MED: multi-model median, p10: 10th percentile, p90: 90th percentile, range: range between p10 and p90

KTC type	RCP4.5				RCP8.5			
	M-MED	p10	p90	Range	M-MED	p10	p90	Range
<i>Fi</i>	73	57	85	28	52	40	68	28
<i>Ft</i>	63	45	77	32	42	28	66	38
<i>E</i>	83	67	97	30	64	36	86	50
<i>Dc</i>	115	106	127	21	130	116	145	29
<i>Do</i>	112	96	122	26	115	100	134	34
<i>BW</i>	108	103	117	14	113	108	123	15
<i>BS</i>	108	100	120	20	113	101	131	30
<i>Aw</i>	117	100	125	25	120	101	137	36
<i>Ar</i>	103	96	109	13	103	89	116	27
<i>Cf</i>	95	85	100	15	98	80	106	26
<i>Cw</i>	41	7	79	72	20	7	59	52
<i>Cs</i>	122	77	156	79	121	52	214	162

According to the outputs of all analyzed CMIP5 GCMs (except for GFDL-ESM2G and NorESM1-ME), the continental area occupied by boreal climate *E* is also expected to decrease (Fig. 5, Table 3). Time evolution of *E* type area in the running 30 yr periods according to individual GCMs shows a gradual monotonic decrease or only small fluctuations (Fig. 4). The exception is model CESM1-CAM5-1-FV2, which for both RCPs shows a negative peak around the year 2061 preceded by a steep decrease after 2045 and fol-

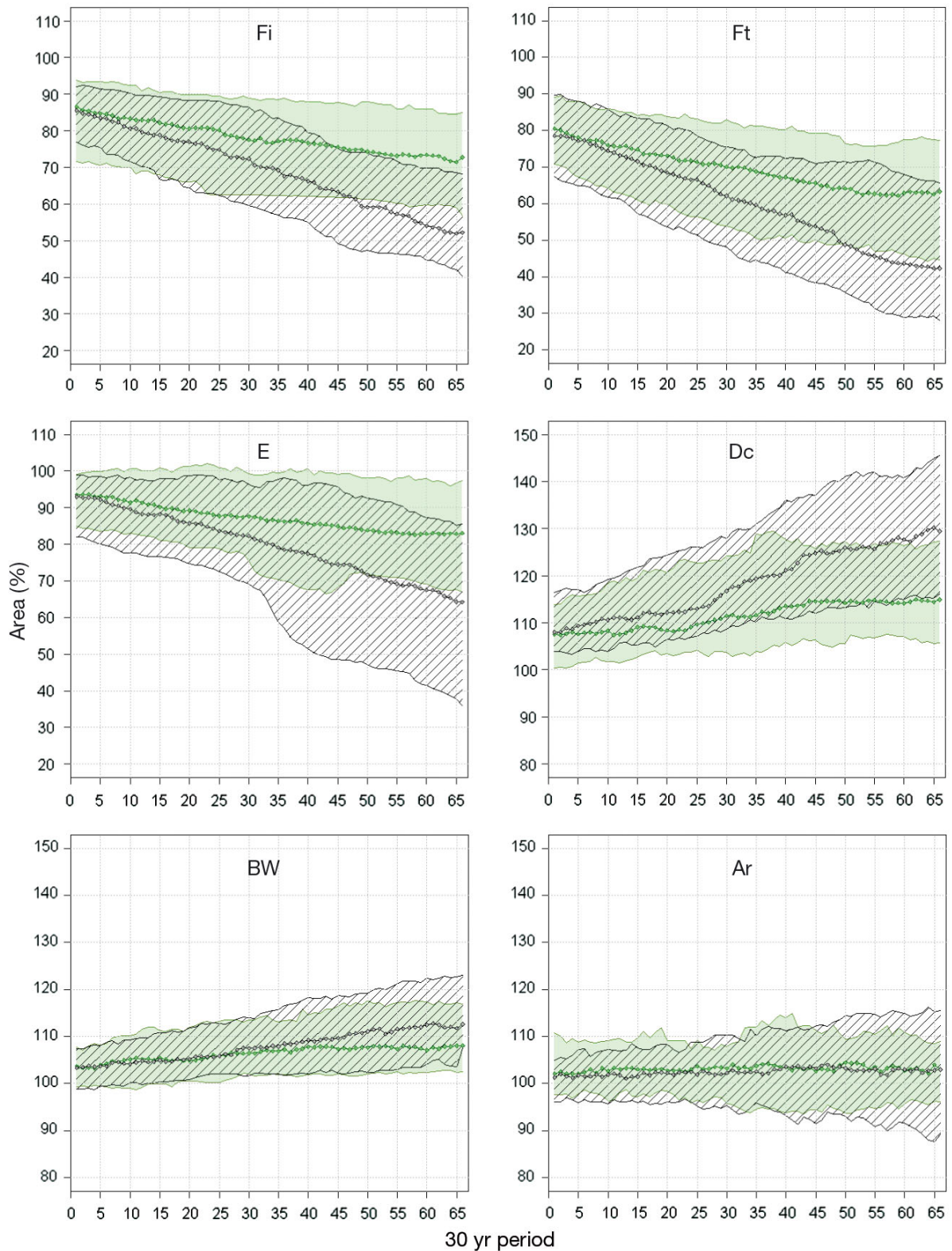


Fig. 4. Temporal evolution of continental area belonging to selected climate types (*Fi*, *Ft*, *E*, *Dc*, *BW*, and *Ar*; see Table 2 for definitions) for moving 30 yr periods throughout the 21st century relative to the reference period 1961–1990 (100% means no change); x-axis: 30 yr periods (period 1 is 2006–2035, period 66 is 2071–2100); squares: multi-model medians calculated from the ensemble of 30 selected CMIP5 GCMs (green for RCP4.5, black for RCP8.5); green area (diagonal hatching): values between the 10th and 90th percentiles of the multi-model ensemble for RCP4.5 (RCP8.5)

lowed by a steep rise until 2073 and a moderate decrease afterwards (not shown). This pattern both affects the spread of the results and is reflected in some other types (*Do*, *Dc*, *Ar*). Even though all GCMs simulated the observed area of type *E* with the smallest errors, their reactions to radiative forcing are quite diverse. The spread of the multi-model ensemble is larger for the stronger forcing of RCP8.5 than for RCP4.5 (Table 3). The decrease in continental area for type *E* by the end of the century seems to be the most convincing (in comparison to model errors, Fig. 5) of all climate types that are expected to decrease. Boreal climate transforms mainly to temperate continental climate *Dc*. For RCP8.5 the losses, generally from the southern extent of type *E* in the northern hemisphere, are >4 times larger than the gains of the area from tundra climate *Ft*.

The second group of KTC types consists of *Dc*, *Do*, *BW*, *BS*, and *Aw* that are all expected to increase their relative continental areas, according to most of the GCMs and both RCPs. All GCMs considered in our study (except for CESM1-CAM5-1-FV2) give a gradual expansion of continental temperate climate *Dc* during 2006–2100. Based on M-MED, the relative area occupied by *Dc* for RCP4.5 (RCP8.5) increases to approx. 115 % (130 %) of the area in the reference period by the end of the century (Fig. 5, Table 3). The stronger forcing of RCP8.5 leads to a higher increase in *Dc* area but also to a somewhat larger multi-model spread (Fig. 4, Table 3). Regarding the model errors, the GCMs tend to overestimate the observed area of *Dc*, but the errors are generally smaller in comparison to other KTC types. In the far-future period under RCP8.5, most of the simulated changes are larger than corresponding model errors (Fig. 5). The expansion of *Dc* is given mainly by the transition from *E*; for RCP8.5, a small portion also comes from *Ft*.

The expected increase in dry climate types *BW* and *BS* is not as convincing and well-marked as the increase in type *Dc*. According to M-MED, the relative continental area of desert climate *BW* grows by the end of the century to ~108 % (113 %) for RCP4.5 (RCP8.5) (Fig. 4, Table 3). Some of the GCMs, e.g. FGOALS-g2 and MRI-CGCM3, give a similar relative continental area for *BW* at the end of the 21st century as in the reference period (Fig. 5). The patterns in temporal behavior differ considerably among GCMs. Some models simulate a steady rise in *BW* area, others project a slight decrease during first decades followed by an increase or an increase followed by a short decline and a final rise. However, the multi-model spread of changes simulated for the end of the 21st century is one of the lowest of all KTC types. Both the

simulated increase and the multi-model spread are larger for the RCP8.5 scenario. The simulated changes are larger than model errors for 50 % (30 %) of the GCMs for RCP8.5 (RCP4.5) in 2071–2100. Regarding the transitions between climate types, the *BW* gains the area mainly from *BS*. However, a small part of the *BW* area transforms into *BS*.

Our findings for steppe climate type *BS* are similar to *BW*. Most of the GCMs simulate a larger or similar relative continental area for *BS* at the end of the century with respect to the reference period (see Fig. S15 in the Supplement at www.int-res.com/articles/suppl/c071p017_supp.pdf). The multi-model median of changes represents an increase to 108 % (113 %) for RCP4.5 (RCP8.5) (Fig. S3, Table 3). For about half of the GCMs, under RCP8.5 in the far future, the expected change is greater than the model error. The expected climate changes lead to transition of *Cf* and *Aw* into *BS* and from *BS* into *BW*.

For savanna climate type *Aw*, most GCMs project a moderate expansion with M-MED of 117 % (120 %) for RCP4.5 (RCP8.5) (Fig. S2, Table 3). An exception is the model CanESM2, which projects a slight decrease in *Aw* area. Model errors are smaller than simulated changes for 2071–2100 according to 30 % (50 %) of simulations under RCP4.5 (RCP8.5). Similar to the case of boreal climate *E*, even though model performance in simulating *Aw* in the reference period is relatively good, the reactions to radiative forcing differ considerably among models. Part of the continental area occupied by *Aw* undergoes a transition to *BS* and a part of *Cf* area transforms into *Aw*.

Expected temporal evolution of relative continental area occupied by oceanic temperate climate *Do* differs between individual GCMs. Some of them project an increase in the area, others project an initial decrease and then a slow rise to approximately the same *Do* extent as simulated for the reference period. The time development of the 10th percentile (Fig. S8) shows that some GCMs even project a decrease in *Do* area in the far future, especially for RCP4.5. M-MED shows an overall change to 112 % of the reference area for RCP4.5 and 115 % for RCP8.5. Simulated changes in *Do* are smaller than model errors (Fig. S20), except for IPSL-CM5A-MR and HadGEM2-AO. Regarding the transitions between climate types, *Do* is expected to transform mainly into *Cf*.

Until now we have dealt with KTC types that are expected to decline or increase their area according to most CMIP5 GCMs, even though the sensitivity of the models was different and multi-model spread was quite large in some cases. Results for the remaining KTC types are less conclusive. Regarding the tropical

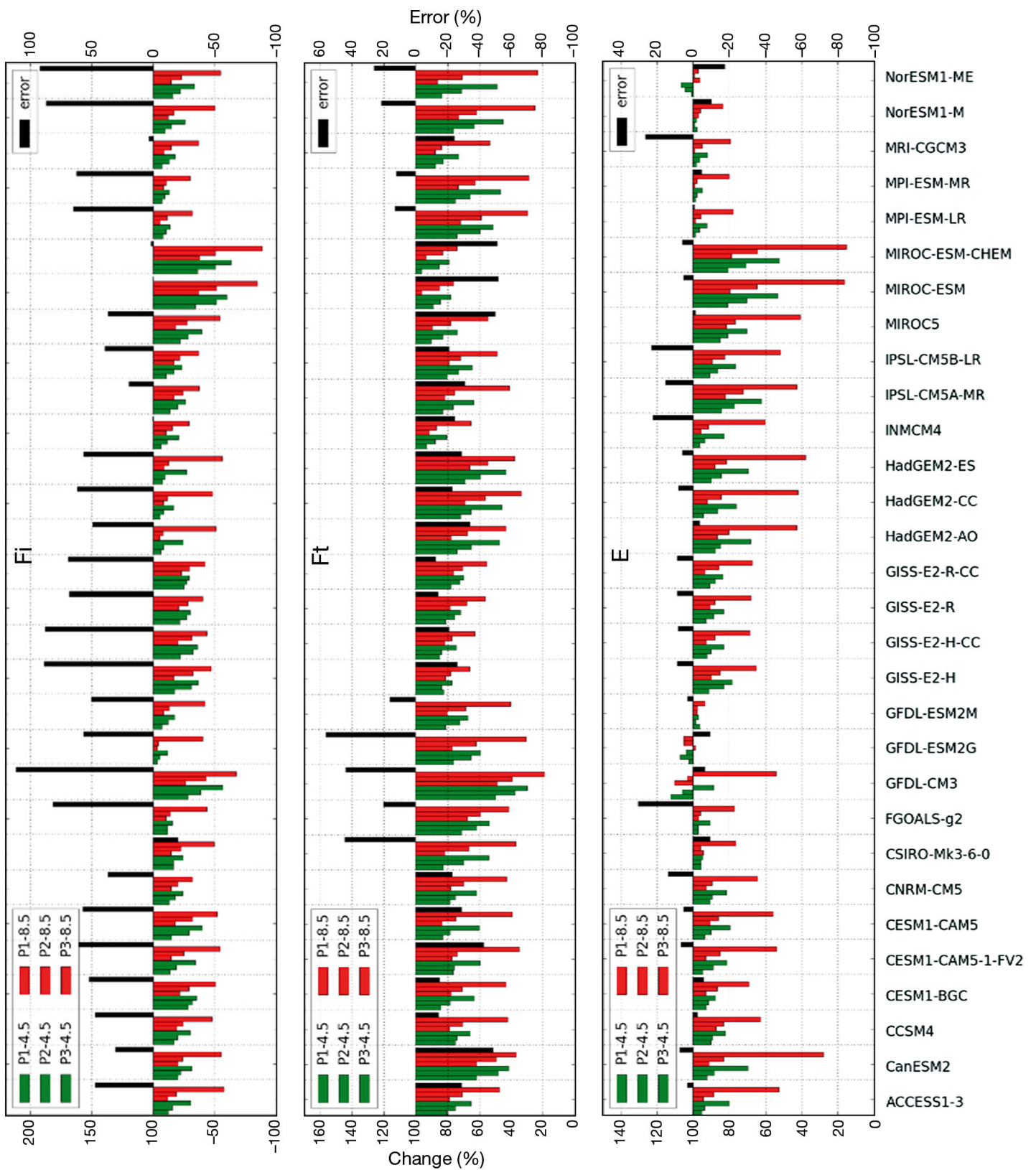


Fig. 5. Changes in relative continental areas of selected Köppen-Trewartha classification (KTC) climate types (*Fi*, *Ft*, *E*, *Dc*, *BW*, *Ar*; see Table 2 for definitions) projected for the periods 2006–2035 (P1), 2021–2050 (P2), and 2071–2100 (P3) relative to the reference period 1961–1990 (100% means no change) based on the ensemble of 30 selected CMIP5 GCMs for RCP4.5 (green) and RCP8.5 (red); error: model error in the reference period expressed as the difference between simulated and observed (based on CRU TS3.22) relative area in the percentage of the observed value

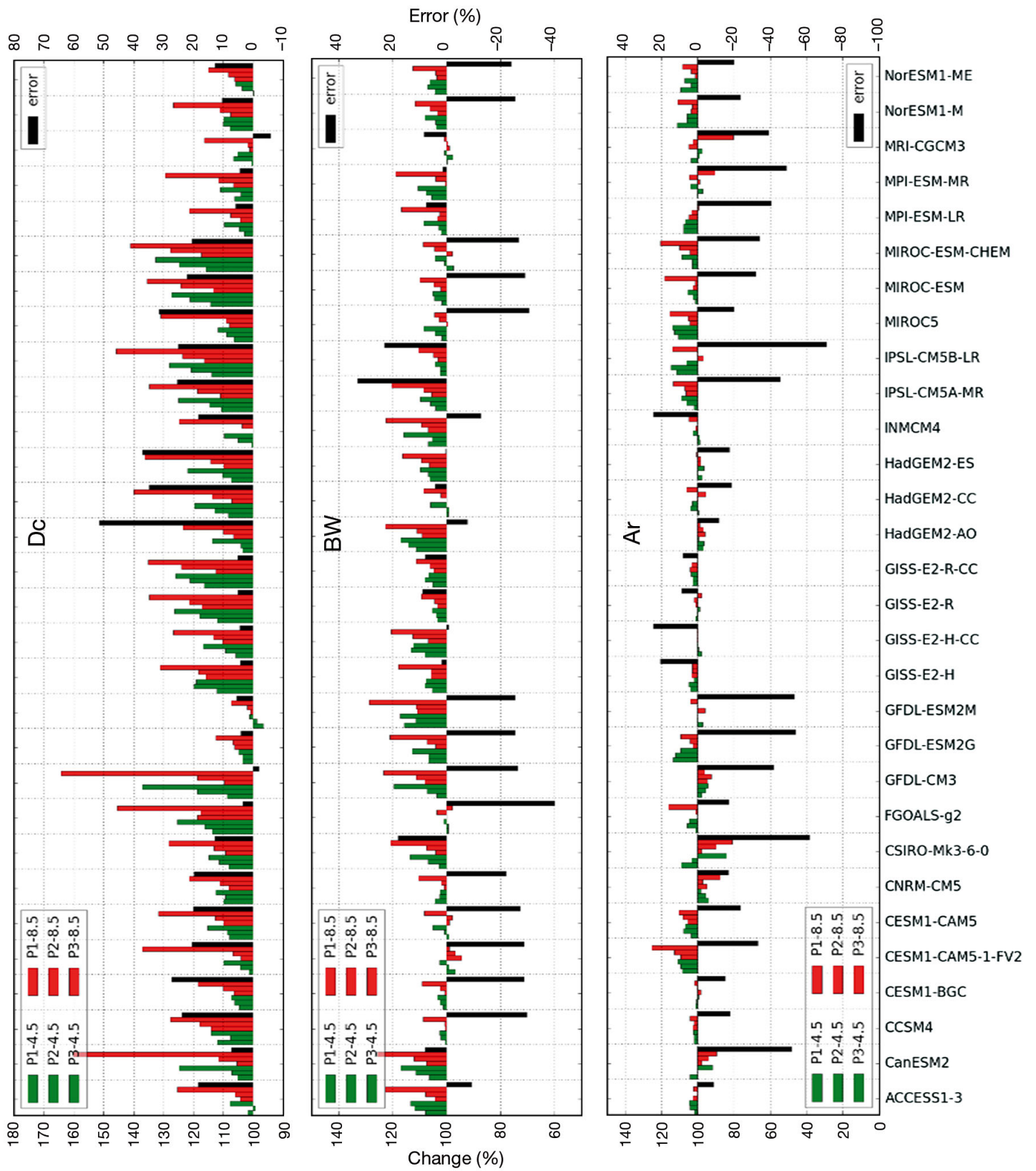


Fig. 5. (continued)

rainforest climate *Ar*, the ensemble does not show any significant signal, with ambiguous signs of change for individual GCM simulations (Fig. 5, Table 3). For both RCPs, the spread is rather small, similar to *BW* and *Cf*. The model errors are larger than simulated changes for all GCMs. The changes of *Ar* are given by transitions from *Aw* and *Cf* and into *Aw*.

Most of the GCMs simulate a decline in the area occupied by the subtropical humid climate *Cf* in 2006–2035, to ca. 95% of reference value according to M-MED. Thereafter, M-MED does not vary considerably, even though the multi-model spread grows throughout the century (Fig. S5). Simulated changes are mostly smaller than model errors, except for GISS-E2-R, GISS-E2-R-CC, and CanESM2 (Fig. S17). The subtropical humid climate *Cf* transforms mainly to *Aw* and *BS*. The area of type *Cf* increases due to gains from *Do*, *Dc*, and *BS*.

We do not discuss the results for *Cw* and *Cs*, as they both occupy a small fraction of global land area, and the spread of the model results is quite large. Therefore, it is difficult to draw any conclusions about their projected changes.

Overall, the GISS models and MRI-CGCM3, ACCESS1-3, GFDL-ESM2M, and NorESM1 have the least pronounced response to radiative forcing. For RCP8.5, these models simulate changes of ca. 16% of continental area (not including Antarctica). On the other hand, MIROC-ESM, MIROC-ESM-CHEM, GFDL-CM3, and CanESM2 show the largest KTC type changes. According to these GCMs, more than 30% of the considered land area will undergo a change of KTC type by the end of the 21st century. However, for individual KTC types, the models simulating the largest or smallest changes differ. For example, MIROC-ESM and MIROC-ESM-CHEM show the largest reduction in *Fi* but the slowest decline of *Ft*. It is noteworthy that GCMs developed in the same modeling center do not necessarily yield similar results. For example, GFDL-CM3 shows the most sensitive response of *Dc* area to radiative forcing, whereas GFDL-ESM2M gives a change of only 1% (7%) for RCP4.5 (RCP8.5) at the end of the century.

4. DISCUSSION AND CONCLUSIONS

We assessed changes in the global distributions of Köppen-Trewartha climate types throughout the 21st century as simulated by a suite of 30 CMIP5 global climate models for 2 representative concentration pathways, RCP4.5 and RCP8.5. Ice cap climate *Fi*, tundra *Ft*, and boreal climate *E* are expected to

decline (Fig. 4). On the other hand, the relative continental area occupied by temperate climates *Dc* and *Do*, dry climates *BW* and *BS*, and savanna climate *Aw* will increase (with a few exceptions). The results for 2 remaining climate types, *Ar* and *Cf*, are less convincing; the changes are rather small, and the models do not even agree on the sign of the changes. Nevertheless, most of the GCMs simulate a slight decrease or increase at the beginning of the 21st century and very small changes thereafter. The types *Cs* and *Cw* cover only a small portion of the total continental area, and simulated changes have a large spread; therefore we will not discuss these types in detail.

Our conclusions about a decrease in *Fi* and *Ft* area and an increase in *Dc* and *Do* extent are consistent with the expected rise in near-surface air temperature and are in agreement with results described by other recent studies based on CMIP5 GCMs, e.g. by Feng et al. (2014), and also by studies for the previous generation of GCMs, e.g. Rubel & Kottek (2010).

Regarding the temporal evolution of relative continental areas covered by specific KTC types during the 21st century based on M-MED of simulated changes, a distinct difference in comparison to the reference period is already apparent for the first 30 yr time window of 2006–2035, and in most cases (except for *Ar* and *Cf*), the magnitude of simulated changes increases throughout the century. This pattern is more pronounced for RCP8.5. The course of simulated changes is not always smooth; for example, under RCP4.5 forcing, the decrease in area covered by *Ft* is faster during the first half of the century, while for RCP8.5 the decline is more stable. Similarly, under RCP4.5, the rate of increase/decrease of *BW*, *Dc*, and *Ar* is slower in the last third of the century. This might be partly due to differences in the RCPs; RCP4.5 represents a stabilization scenario with radiative forcing reaching its maximum in the second half of the 21st century; in contrast, under RCP8.5, radiative forcing increases throughout the whole 21st century (IPCC 2013). However, the influence of RCPs cannot be simply generalized. For example, the expansion of *Do* shows almost the same rate under both RCPs.

Considering the projections given by individual GCMs, for some KTC types the GCMs agree on the sign and general pattern of changes; however, the sensitivity of models to the radiative forcing differs for different KTC types (Fig. 5). For example, the models MIROC-ESM and MIROC-ESM-CHEM give the smallest change in *Ft* and the largest change in *Fi* (Fig. S24). The course of simulated changes is quite

smooth for some of the GCMs, while for others it exhibits wave-like behavior, breaks, and jumps even when using 30 yr running means.

The magnitude of changes for 3 selected time periods (near future, mid-century, far future) were compared to model errors in the reference period 1961–1990 (Fig. 5). The errors were evaluated from comparison of relative land areas of KTC types derived from GCM simulations and from CRU TS3.22 observations; in this way, they could be interpreted as biases as well. Regarding the end of the 21st century (far future), only for 3 out of 12 KTC types, viz. *Ft*, *E*, and *Dc*, the changes are higher than the model errors (according to most of GCMs under RCP8.5; under RCP4.5, half of the GCMs show that changes are higher than errors for *Dc*, and ca. 75% of GCMs indicate that this is the case for *E* and *Ft*). Thus, considering the model errors, the simulated decrease in relative continental area is clearly pronounced in the case of boreal climate *E* and tundra climate *Ft*, and the increase is pronounced in the case of continental temperate climate *Dc*. Regarding the expected decrease in *Fi* area, the simulated changes are larger than model errors according to only one-third of the GCMs for both RCP 8.5 and RCP 4.5. Further, in case of savanna climate *Aw*, dry climates *BW*, and steppe climate *BS*, the simulated changes in the far future are larger than model errors according to about half of the GCMs for both RCPs, except for dry climate *BW* under RCP4.5 (one-third of the models) and steppe climate *BS* under the same scenario (only 13%).

For *Cf* and *Do*, the simulated changes are larger than model errors according to only 6 and 4 out of 30 GCMs, respectively. The type *Ar* is the only KTC type for which the simulated changes are smaller than model errors for both RCPs and all 3 time periods. We found no straightforward relationship between the model performance and the strength of the climate signal in projected changes.

Besides a comparison of simulated changes to model errors, we assessed the uncertainty stemming from necessary choices in GCM structure. We used the range between the 10th and 90th percentile of the multi-model ensemble to assess this uncertainty. The smallest multi-model spread of simulated changes is seen for the *BW* type (Table 3), the largest for *E* and *Ft*. The simulated changes of *Ar*, *Cf*, and *Do* types are ambiguous in the sense that the multi-model ranges include a ‘zero change’.

Considering the changes in relative areas for the KTC types all together, the lowest sensitivity to radiative forcing under RCP4.5 is seen for MRI-CGCM3, with 8% of total continental area undergoing a KTC

type change until the end of the 21st century. Then follows a group of models with simulated changes of <12% (3 GISS GCMs, Nor-ESM1-M, Nor-ESM1-ME, GFDL-ESM2M, ACCESS1-3). For RCP8.5, the lowest sensitivity was found for all GISS models and MRI-CGCM3, with changes of 16–17%. The largest sensitivity was found for MIROC-ESM and MIROC-ESM-CHEM, with nearly a quarter of the global continental area (without Antarctica) showing changed KTC types under RCP4.5 and about 35% under RCP8.5. According to M-MED for RCP4.5 (RCP8.5), 14% (22%) of the continental area is expected to change its climate type by the end of the century. Our results are in agreement with Mahlstein et al. (2013), who projected that approximately 20% of global land will experience a change in climate type until 2100 under RCP8.5 forcing, although their study was based on a smaller number of models than ours. According to Feng et al. (2014), a larger portion of the continental area is expected to undergo a change in climate type (31% for RCP 4.5 and 46% for RCP8.5).

Regarding the shifts in the 6 major climate types, the changes projected for the far-future period under RCP8.5 based on our results and the study of Feng et al. (2014) are summarized in Table 4. The values are shown as a percentage of the respective KTC type area in the reference period 1961–1990. The simulated changes are more distinct for types *D*, *E*, and *F* than for other KTC types. For these 3 types, 25–50% of the reference area is expected to shift to another KTC type. This likely points to a more important influence of air temperature changes than precipitation changes on the KTC type shifts, which was shown by Feng et al. (2014) and Mahlstein et al. (2013).

Table 4. Comparison of multi-model statistics aggregated for the main Köppen-Trewartha classification (KTC) climate types (*A–F*, see Table 2 for definitions) in this study (rows 1–5) and in Feng et al. (2014, rows 6–9). Values are given as a percentage of the respective KTC type area in the reference period 1961–1990. M-MED: multi-model median, M-mean: multi-model mean, SD: standard deviation, F: Feng et al. (2014) values

	A	B	C	D	E	F
1 M-MED	17.4	13.2	-11.2	24.7	-37.4	-50.0
2 M-mean	14.9	15.6	-13.5	26.3	-39.4	-61.0
3 SD	10.1	6.3	12.7	9.3	22.3	27.4
4 M-mean – SD	4.9	9.3	-26.2	17.0	-61.7	-88.5
5 M-mean + SD	25.0	21.9	-0.8	35.5	-17.1	-33.6
6 Fmean	11.6	15.9	-13.4	40.0	-50.4	-59.2
7 FSD	4.0	5.3	7.9	13.7	16.9	10.8
8 Fmean – FSD	7.6	10.6	-21.3	26.3	-67.3	-70.0
9 Fmean + FSD	15.6	21.2	-5.5	53.7	-33.5	-48.4

For the purpose of comparing our results to the study of Feng et al. (2014), the multi-model mean (M-mean) and standard deviation (SD) were calculated for the 6 main climate types (Table 4). M-mean differs from M-MED most prominently for the *F* climate type, for which the SD has also the highest value. The values of M-mean according to our results and Feng et al. (2014) are fairly similar except for *D* and *E*, where Feng et al. (2014) found larger changes than presented in our analysis. The SD values according to Feng et al. (2014) are all smaller than our SD values, except for type *D*. In our study, we prefer the median and range between the 10th and 90th percentile to characterize the distribution of the multi-model ensemble, as the distribution of simulated KTC type changes is generally not symmetrical.

There are several possible reasons for the differences between our results and the results of Feng et al. (2014). The analyses are based on different groups of GCMs which may significantly influence the results, as individual models show different changes in KTC types in reaction to a given forcing. Further, we used model outputs in the original model grids, but Feng et al. (2014) applied a downscaling procedure to the GCM outputs. The fact that we investigated all continental areas excluding Antarctica, whereas Feng et al. (2014) only considered global continents north of 60° S, and the different observational datasets used could also play a role, although, as discussed previously, the differences are very small compared to the ensemble spread.

A change in relative continental areas of climate types is not the only expected impact of climate change. Potential geographical shifts are also very important. Our results indicate a poleward shift of *Ft*, *E*, *Do*, *Dc*, and *Cf* types (not shown). On the other hand, *Ar* and *Aw* types, which are found near the equator, did not experience any latitudinal shift. Regarding the dry climates, the GCMs do not agree entirely, especially in the case of *BW*. A detailed analysis of these shifts, however, is beyond the scope of this study and will be the subject of future investigations.

Acknowledgement. We acknowledge the World Climate Research Programme's Working Group on Coupled Modelling, which is responsible for CMIP, and we thank the climate modeling groups for producing and making available their model outputs. For CMIP the US Department of Energy's Program for Climate Model Diagnosis and Intercomparison provides coordinating support and led development of software infrastructure in partnership with the Global Organization for Earth System Science Portals. The CRU TS 3.22 dataset was provided by the Climatic Research

Unit, University of East Anglia. This study was supported by project UNCE 204020/2012, funded by Charles University in Prague, and by research plan no. MSM0021620860 funded by the Ministry of Education, Youth and Sports of the Czech Republic. In addition, the work is part of the activity under the Program of Charles University PRVOUK No. 02 'Environmental Research'.

LITERATURE CITED

- Bailey RG (2009) *Ecosystem geography: from ecoregions to sites*, 2nd edn. Springer, New York, NY
- Baker B, Diaz H, Hargrove W, Hoffman F (2010) Use of the Köppen-Trewartha climate classification to evaluate climatic refugia in statistically derived ecoregions for the People's Republic of China. *Clim Change* 98:113–131
- Belda M, Holtanová E, Halenka T, Kalvová J (2014) Climate classification revisited: from Köppen to Trewartha. *Clim Res* 59:1–13
- Belda M, Holtanová E, Halenka T, Kalvová J, Hálvka Z (2015) Evaluation of CMIP5 present climate simulations using the Köppen-Trewartha climate classification. *Clim Res* 64:201–212
- de Castro M, Gallardo C, Jylha K, Tuomenvirta H (2007) The use of a climate-type classification for assessing climate change effects in Europe from an ensemble of nine regional climate models. *Clim Change* 81:329–341
- Deque M (2007) Frequency of precipitation and temperature extremes over France in an anthropogenic scenario: model results and statistical correction according to observed values. *Global Planet Change* 57:16–26
- Feng S, Ho CH, Hu Q, Oglesby RJ, Jeong SJ, Kim BM (2012) Evaluating observed and projected future climate changes for the Arctic using the Köppen-Trewartha climate classification. *Clim Dyn* 38:1359–1373
- Feng S, Hu Q, Huang W, Ho CH, Li R, Tang Z (2014) Projected climate regime shift under future global warming from multi-model, multi-scenario CMIP5 simulation. *Global Planet Change* 112:41–52
- Geiger R (1954) Klassifikationen der Klimate nach W. Köppen. In: Bartels J, ten Bruggencate P (eds) *Landolt-Börnstein: Zahlenwerte und Funktionen aus Physik, Chemie, Astronomie, Geophysik und Technik (alte Serie)*, Vol 3. Springer, Berlin, p 603–607
- Hargrove WW, Hoffman FM (2004) Potential of multivariate quantitative methods for delineation and visualization of ecoregions. *Environ Manag* 34:S39–S60
- Harris I, Jones PD, Osborn TJ, Lister DH (2014) Updated high-resolution grids of monthly climatic observations—the CRU TS3.10 dataset. *Int J Climatol* 34:623–642
- IPCC (Intergovernmental Panel on Climate Change) (2013) *Climate Change 2013: the physical science basis*. Cambridge University Press, Cambridge
- Kalvová J, Halenka T, Bezpalcová K, Nemešová I (2003) Köppen climate types in observed and simulated climates. *Stud Geophys Geod* 47:185–202
- Köppen W (1923) *Die Klimate der Erde*. Grundriss der Klimakunde. Walter de Gruyter & Co., Berlin
- Köppen W (1931) *Grundriss der Klimakunde*. Walter de Gruyter & Co., Berlin
- Köppen W (1936) *Das geographische System der Klimate*. In: Köppen W, Geiger R (eds) *Handbuch der Klimatologie*. Gebrüder Borntraeger, Berlin, p C1–C44
- Lohmann U, Sausen R, Bengtsson L, Cubasch U, Perlwitz J,

- Roeckner E (1993) The Köppen climate classification as a diagnostic tool for general circulation models. *Clim Res* 3:177–193
- Mahlstein I, Daniel JS, Solomon S (2013) Pace of shifts in climate regions increases with global temperature. *Nat Clim Change* 3:739–743
 - Meehl GA, Covey C, Delworth T, Latif M and others (2007) The WCRP CMIP3 multi-model dataset: a new era in climate change research. *Bull Am Meteorol Soc* 88: 1383–1394
 - Menon A, Levermann A, Schewe J, Lehmann J, Frieler K (2013) Consistent increase in Indian monsoon rainfall and its variability across CMIP-5 models. *Earth Syst Dyn* 4:287–300
 - Moss RH, Edmonds JA, Hibbard KA, Manning MR and others (2010) The next generation of scenarios for climate change research and assessment. *Nature* 463: 747–756
 - Patton CP (1962) A note on the classification of dry climate in the Köppen system. *Calif Geogr* 3:105–112
 - Rogelj J, Meinshausen M, Knutti R (2012) Global warming under old and new scenarios using IPCC climate sensitivity range estimates. *Nat Clim Change* 2:248–253
 - Rubel F, Kottek M (2010) Observed and projected climate shifts 1901–2100 depicted by world maps of the Köppen-Geiger climate classification. *Meteorol Z* 19:135–141
 - Taylor K, Balaji V, Hankin S, Juckes M, Lawrence B, Pascoe S (2012a) CMIP5 Data Reference Syntax (DRS) and controlled vocabularies. http://pcmdi-cmip.llnl.gov/xmip5/docs/cmip5_data_refernce_syntax.pdf (accessed 7 Nov 2016)
 - Taylor K, Stouffer RJ, Meehl GA (2012b) An overview of CMIP5 and the experiment design. *Bull Am Meteorol Soc* 93:485–498
 - Trewartha GT (1968) *An introduction to climate*. McGraw-Hill, New York, NY
 - Trewartha GT, Horn LH (1980) *Introduction to climate*, 5th edn. McGraw Hill, New York, NY
 - Willmott CJ, Matsuura K (2001) Terrestrial air temperature and precipitation: monthly and annual time series (1950–1999). http://climate.geog.udel.edu/~climate/html_pages/README.ghcn_ts2.html

Editorial responsibility: Tim Sparks, Cambridge, UK

*Submitted: February 22, 2016; Accepted: July 24, 2016
Proofs received from author(s): November 3, 2016*



CECILIA regional climate simulations for the present climate: validation and inter-comparison

Petr Skalák^{1,2,*}, Michel Déqué³, Michal Belda⁴, Aleš Farda^{1,2}, Tomáš Halenka⁴,
Gabriella Csima⁵, Judit Bartholy⁶, Mihaela Caian⁷, Valery Spiridonov⁸

¹Czech Hydrometeorological Institute, 14306 Prague, Czech Republic

²Global Change Research Centre, Academy of Science of the Czech Republic, 60300 Brno, Czech Republic

³Météo-France, Centre National de Recherches Météorologiques, 31057 Toulouse, France

⁴Charles University in Prague, Department of Meteorology and Environment Protection, 18200 Prague, Czech Republic

⁵Hungarian Meteorological Service, 1525 Budapest, Hungary

⁶Eötvös Loránd University, Dept. of Meteorology, 1518 Budapest, Hungary

⁷Rosby Centre, Swedish Meteorological and Hydrological Institute, 60176 Norrköping, Sweden

⁸National Institute of Meteorology and Hydrology, 1784 Sofia, Bulgaria

ABSTRACT: We investigated high-resolution simulations of regional climate models (RCMs) driven by ERA-40 reanalyses over areas of selected European countries (Austria, Czech Republic, Hungary, Slovakia and Romania) for the period 1961–1990. RCMs were run at a spatial resolution of 10 km in the framework of the CECILIA project, and their outputs were compared with the E-OBS dataset of gridded observations and RCM simulations at coarser 25 km resolution from the ENSEMBLES project to identify a possible gain from the CECILIA experiments over ENSEMBLES. Cold biases of air temperature and wet biases of precipitation dominate in the CECILIA simulations. Spatial variability and distribution of the air temperature field are well captured. The precipitation field, relative to observations, often shows inadequately small spatial variability and lowered correlations but is nevertheless comparable to the ENSEMBLES model. Inter-annual variability (IAV) of air temperature is captured differently among seasons but mostly improved in CECILIA compared with ENSEMBLES. Precipitation IAV shows a similar or worse score. The detected weaknesses found within the validation of the CECILIA RCMs are attributed to the resolution dependence of the set of physical parameterizations in the models and the choice of integration domain. The gain obtained by using a high resolution over a small domain (as in CECILIA) relative to a lower resolution (25 km) over a larger domain (as in ENSEMBLES) is clear for air temperature but limited for precipitation.

KEY WORDS: RCM · Model performance · Validation · CECILIA · ALADIN-Climate · RegCM3

— Resale or republication not permitted without written consent of the publisher —

1. INTRODUCTION

Regional climate models (RCMs) are widely used tools for the assessment of regional aspects of climate change. They have emerged in the last 2 decades as an answer to an increased demand for information about climate change and its impact on a regional scale. This information cannot be obtained directly from global climate models (GCMs) because of their relatively coarse horizontal spatial resolution. Dy-

namical downscaling of GCM simulations by RCMs is one of the current approaches to simulate climate conditions on a regional scale. The basis of regional modeling has been widely described since the 1990s, e.g. in Giorgi & Mearns (1991, 1999).

The current generation of RCMs typically operates at horizontal resolutions from ~50 to 10 km. The benefits of a finer resolution are mainly found in regions where complex topography or surface physiographic features affect the local climate. Some simulated

*Corresponding author: skalak@chmi.cz

properties, e.g. precipitation, are particularly sensitive to an increased resolution and a better surface description. While the dynamical part of RCMs is coded irrespective of resolution, a package of physical parameterizations can require an adaptation for a particular range of spatial scales. This has been proved during the development of RCMs (Laprise 2008). Recent studies also suggest that even if the overall quality of GCM and RCM simulations improves or at least remains unchanged with a higher model resolution (Reichler & Kim 2008, Meissner et al. 2009), the use of a higher resolution may present some discrepancies as well.

The analysis of resolution effects on precipitation in an ensemble of RCM simulations over Europe (Rauscher et al. 2010) revealed larger precipitation amounts at a higher resolution, especially in the summer, leading to a slight increase of wet biases relative to the coarser resolution. The tendency of most RCMs to simulate more precipitation and increase wet biases in some regions and seasons under higher resolutions was also reported by other authors (e.g. Halenka et al. 2006, Bergant et al. 2007, Jaeger et al. 2008, Suklitsch et al. 2011). However, some systematic errors in models can stem from insufficient density of reference observed data, resulting in an inability to capture fine-scale climate signals (Kyselý & Plavcová 2010, Rauscher et al. 2010), and can also be artificially amplified by the lack of a rain gauge correction in the observations, especially in the winter (Adam & Lettenmaier 2003, Yang et al. 2005).

The other effects of higher resolution on simulated precipitation include larger spatial variability and inter-annual variability (IAV), and better resolved fine-scale precipitation structures corresponding more closely with observations (Jaeger et al. 2008, Rauscher et al. 2010). The evaluation of RCM simulations over the Alpine region also showed that the error characteristics of precipitation can worsen when analyzed on smaller scales (subdomains), while for air temperature, error characteristics remain similar to those of a larger evaluation region (Suklitsch et al. 2011).

Although air temperature characteristics are usually improved in high-resolution simulations, RCMs often simulate a summer climate that is too dry and warm in southeastern Europe when driven by both reanalysis (Hagemann et al. 2004) and GCM (Jacob et al. 2007). These errors have been attributed to deficiencies in land surface parameterizations as well as systematic errors in the dynamics (Hagemann et al. 2004). Some features of temperature biases over Europe may depend on the ability of RCMs to properly capture the atmospheric circulation (Sanchez-

Gomez et al. 2009, Kjellström et al. 2011, Plavcová & Kyselý 2011). In addition, most RCMs also overestimate summer temperature IAV in central, eastern and southeastern Europe (Jacob et al. 2007, Lenderink et al. 2007, Vidale et al. 2007).

The forthcoming Fifth Assessment Report of the Intergovernmental Panel on Climate Change will present new findings on a regional climate change that, among other things, will be built on a set of regional climate model simulations prepared within the Coordinated Regional Downscaling Experiment (CORDEX, see Giorgi et al. 2009 for more information). For Europe, many of those simulations will be performed at a very high resolution of ~10 km to provide new insight into local climate and its possible future evolution. In the region of central and eastern Europe (CEE) a similar effort, with emphasis on climate change impacts and assessment of vulnerability, has already been carried out within 2 recent projects of the European Commission's 6th Framework Programme (FP6): CECILIA (Central and Eastern Europe Climate Change Impact and Vulnerability Assessment, www.cecilia-eu.org) and CLAVIER (Climate Change and Variability: Impact on Central and Eastern Europe, www.clavier-eu.org). In both projects, one of the key objectives was to deliver information on climate change in the region of CEE by means of RCM simulations at a very high resolution of 10 km (see Halenka 2008 and Jacob et al. 2008 for more details).

The present study focuses on testing the ability of CECILIA RCMs to capture the main features of the climate in CEE for the period 1961–1990. For this purpose, the RCMs were driven by European Centre for Medium-Range Weather Forecasts (ECMWF) ERA-40 reanalyses (Uppala et al. 2005), and the results were validated against the E-OBS version 6.0 gridded dataset of station observations (Haylock et al. 2008). Our goal was to evaluate the gain obtained by using a high resolution over a small domain in comparison to a lower resolution (25 km) over a larger domain as in the FP6 ENSEMBLES project (ENSEMBLE-based Predictions of Climate Changes and their Impacts, www.ensembles-eu.org, see van der Linden & Mitchell 2009 for more details).

2. DATA AND ANALYSIS METHODS

We used the results prepared by 5 CECILIA teams from the following institutions: Czech Hydrometeorological Institute (CHMI), Czech Republic; Charles University in Prague (CUNI), Czech Republic; Eötvös

Loránd University (ELU), Hungary; Hungarian Meteorological Service (OMSZ), Hungary; and National Meteorological Administration (NMA), Romania. These teams employed 4 regional climate models: 2 versions of ALADIN-Climate (Farda et al. 2010) and 2 versions of RegCM3 (Pal et al. 2007).

The two versions of ALADIN-Climate correspond to cycles 24 and 28 of the ARPEGE/IFS code. Their physical parameterizations are different. While the original version of ALADIN-Climate (cycle 24) developed by Météo-France has a physical parameterization package derived directly from the one used in GCM ARPEGE-CLIMAT 4 (Déqué 2007), the other version, ALADIN-Climate/CZ (cycle 28), is based on the numerical weather prediction version of the ALADIN model in operational use at CHMI in 2002 and 2003. The major differences in the Czech version include new radiation and planetary boundary layer process schemes, different cloudiness and large-scale precipitation schemes and improved deep convection and gravity wave drag schemes with the parameterization of mountain blocking and lift effects based on mean orography. For more detailed information on both ALADIN-Climate versions, we refer to Farda et al. (2010).

The two versions of RegCM3 differ in some aspects of the physical parameterizations, one in the original setting described by Pal et al. (2007), named *alpha* for distinction, and the other, called *beta*, with applied changes in large-scale precipitation schemes. The modifications in the *beta* version were motivated by a large bias of precipitation found during sensitivity tests conducted with the RegCM3 *alpha* model over the Carpathian Basin (Torma et al. 2008) and included a decrease in the cloud-to-rain autoconversion rate by half, increasing the raindrop evaporation rate coefficient by a factor of 50 and reducing the raindrop accretion rate by half. More information on the applied changes and their justification can be found in Torma et al. (2008, 2011).

The spatial resolution of the CECILIA simulations was 10 km, and the integration period, after excluding a necessary spin-up period (year 1960 for most models, years 1958–1960 for ALADIN-Climate), covered the years 1961–1990. All models were driven by ECMWF ERA-40 reanalyses, either directly or via a double-nesting technique. The latter means that the model is first driven by ECMWF ERA-40 reanalyses in a coarser resolution (e.g. 50 km) over a larger geographical domain, and then the resulting simulation is taken to drive the same model again but in the finer spatial resolution mode (10 km in this case), hence covering a smaller integration domain. ALADIN-

Climate/CZ and RegCM3 *alpha* of the CUNI team were the only models where the double nesting was employed, with driving RCM simulations having a horizontal resolution of either 50 (ALADIN-Climate/CZ) or 25 km (RegCM3 *alpha*) and originally coming from the FP6 project ENSEMBLES. An overview of CECILIA teams, their models, integration domains and driving data is given in Table 1. Some parameterization settings of the CECILIA models are in Table 2. The integration domains are also shown in Fig. 1.

Except for the CECILIA RCMs, we also considered the data from 5 models involved in the FP6 project ENSEMBLES that run their RCMs at a resolution of about 25 km over the common integration domain covering all of Europe (Christensen et al. 2010). This was done to enable the comparison of the very high resolution CECILIA RCMs data with those of ENSEMBLES and possibly identify benefits of running RCMs in a configuration of the CECILIA experiments. The overview of ENSEMBLES teams/models is also in Table 1. Three of 5 ENSEMBLES RCMs were selected because of their use in both projects, thus allowing a comparison of RCM qualities in different configurations. The remaining 2 RCMs (HIRHAM5 model of the Danish Meteorological Institute, Denmark, and CLM 2.4.6 model of the Swiss Federal Institute of Technology Zurich, Switzerland) were chosen because the relevant teams (but not RCMs) were also involved in the CECILIA project.

The investigation of model performance was based on a comparison of simulated properties of seasonal mean air temperature and seasonal sum of precipitation against observations represented by the E-OBS dataset. The validation was carried out over areas of the selected CEE countries (Austria, Czech Republic, Hungary, Romania and Slovakia), each country separately, for the period 1961–1990. The detailed listing of RCMs and individual countries covered within their integration domains is in Table 1. Before the validation, we first transformed the RCM data from their native grids to the regular 0.25° latitude-longitude grid of the E-OBS dataset. Transformation was done in 2 steps. First, a bilinear interpolation was used to remap the data on the regular 0.125° latitude-longitude grid, and then we averaged four 0.125° grid points to the final resolution. The same procedure was applied on the orography, and the resulting difference between the model and E-OBS orography was multiplied by the climatological temperature lapse rate (-6.5 K km^{-1}) to correct the RCM air temperature data.

For each season and country, we derived 1961–1990 climatology mean fields of air temperature (or

Table 1. CECILIA and ENSEMBLES partners, regional climate models (RCMs), settings and central and eastern European countries where RCM performance is tested (domain size in points and number of vertical levels). A = Austria; BG = Bulgaria; CHMI = Czech Hydrometeorological Institute, Czech Republic; CNRM = Centre National de Recherches Météorologiques, France; CUNI = Charles University in Prague, Czech Republic; CZ = Czech Republic; DMI = Danish Meteorological Institute, Denmark; ELU = Eötvös Loránd University, Hungary; ETH = Swiss Federal Institute of Technology Zurich, Switzerland; H = Hungary; ICTP = International Centre for Theoretical Physics, Italy; NMA = National Meteorological Administration, Romania; OMSZ = Hungarian Meteorological Service, Hungary; RO = Romania; SK = Slovakia

Partner	Model	Acronym	Resolution (km)	Domain size	Boundary forcing	Analyzed area
CECILIA						
CUNI	RegCM3 <i>alpha</i>	Ra	10	184 × 164 × 23	ERA 40 RegCM3@25	A, CZ, H, SK
CHMI	ALADIN-Climate/CZ	Az	10	160 × 102 × 43	ERA 40 ALADIN-Climate/CZ@50	A, CZ, H, SK
NMA	RegCM3 <i>alpha</i>	Ra2	10	156 × 102 × 18	ERA 40	RO, SK
OMSZ	ALADIN-Climate	A	10	108 × 72 × 31	ERA 40	H, SK
ELU	RegCM3 <i>beta</i>	Rb	10	120 × 100 × 18	ERA 40	H, SK
ENSEMBLES						
CHMI	ALADIN-Climate/CZ	Az	25	183 × 205 × 31	ERA 40	A, CZ, H, RO, SK
CNRM	ALADIN-Climate	A	25	229 × 229 × 31	ERA 40	A, CZ, H, RO, SK
DMI	HIRHAM5	H	25	194 × 210 × 19	ERA 40	A, CZ, H, RO, SK
ETHZ	CLM 2.4.6	C	25	193 × 201 × 32	ERA 40	A, CZ, H, RO, SK
ICTP	RegCM3 <i>alpha</i>	Ra	25	190 × 206 × 18	ERA 40	A, CZ, H, RO, SK

Table 2. Physical parameterization settings for the CECILIA regional climate models. NIMH = National Institute of Meteorology and Hydrology, Bulgaria; other partner names defined in Table 1

Partner	Model	Numeric	Vertical coordinate	Radiation scheme	Convection scheme	Surface scheme
CUNI	RegCM3 <i>alpha</i>	Difference	Sigma	CCM3	Grell (Fritsch & Chappell)	BATS
CHMI	ALADIN-Climate/CZ	Spectral	Hybrid	ACRANEB	Bougeault	ISBA
NMA	RegCM3 <i>alpha</i>	Difference	Sigma	CCM3	Grell (Fritsch & Chappell)	BATS
NIMH	ALADIN-Climate	Spectral	Hybrid	FMR	Bougeault	ISBA
OMSZ	ALADIN-Climate	Spectral	Hybrid	FMR	Bougeault	ISBA
ELU	RegCM3 <i>beta</i>	Difference	Sigma	CCM3	Grell (Fritsch & Chappell)	BATS

precipitation) and analyzed their spatial variability and spatial correlation (between simulated and observed fields). We also determined a systematic error (bias) and averaged it over the territory of the country to gain a single characteristic. To assess RCM simulations from a temporal aspect, we studied the IAV of area-averaged seasonal mean air temperature (or sum of precipitation) within the 1961–1990 period. Standard deviations of time series consisting of 30 seasons (29 for winter) for a model (σ_{TM}) and observations (σ_{TO}) were calculated, and their ratio (σ_{TM}/σ_{TO}) was used as a benchmark of the IAV of air temperature. For precipitation, we used the coefficient of variation (a ratio between standard deviation and mean). To study the spatial variability of climatology mean fields, we used either the standard deviation or again the coefficient of variation (only for precipitation).

3. RESULTS

3.1. Air temperature

The area-averaged systematic error (bias) of long-term seasonal temperature for the CECILIA and ENSEMBLES models, as well as for the ERA-40 driving data over CEE countries, is summarized in Table 3. The statistically significant bias, identified using the *t*-test of time series of yearly bias values, is highlighted in bold in Table 3. The systematic errors of the CECILIA models are usually within the $\pm 1^\circ\text{C}$ range, with cold bias dominating. Significant cold bias is detected in 3 out of 4 seasons (winter, spring, autumn) in the ALADIN-Climate (A) simulation and in spring in the ALADIN-Climate/CZ (Az) and CUNI RegCM3 *alpha* (Ra) simulations. Significant warm

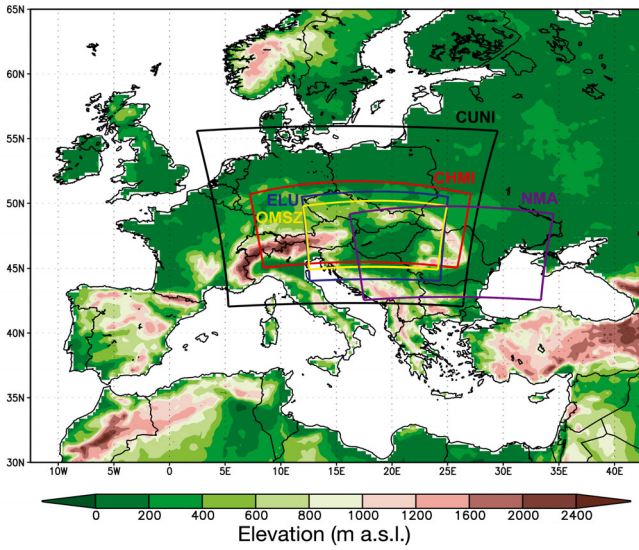


Fig. 1. E-OBS orography in 0.25° spatial resolution with integration domains of the CECILIA regional climate models a.s.l. = above sea level

biases of summer temperature detected in southeastern Europe by earlier studies (e.g. Hagemann et al. 2004) are present in some ENSEMBLES RCMs but not in the CECILIA RCMs. When the same models are compared, systematic errors of the CECILIA RCMs are usually smaller in magnitude than in the ENSEMBLES simulations. The only exception is ALADIN-Climate (A), whose systematic errors in the CECILIA experiment are always 1.5–3 K lower than those in the ENSEMBLES simulation, thus making it too cold in most seasons and often worse than the other ENSEMBLES RCMs.

The spatial variability of air temperature and its spatial correlation with observations are summarized in Fig. S1 (in the Supplement at www.int-res.com/articles/suppl/c060p001_supp.pdf) in the form of a Taylor diagram (Taylor 2001). The CECILIA RCMs mostly show comparable or slightly better spatial correlations with observations than the ENSEMBLES models, often higher than 90%. The RegCM3 *alpha*

Table 3. Bias of seasonal temperature in the CECILIA and ENSEMBLES models over central and eastern European countries for the 1961–1990 period. **Bold**: statistically significant bias. DJF = winter, MAM = spring, JJA = summer, SON = autumn. Further abbreviations in Table 1

Country	Season	Air temperature bias (°C)										
		CECILIA models					ENSEMBLES models					ERA40
		Az	Ra	Rb	Ra2	A	Az	A	H	C	Ra	
Austria	DJF	-0.3	-0.2				-0.5	0.1	-0.9	-1.1	-1.1	0.2
	MAM	-1.3	-1.1				-1.7	0.9	-0.5	-1.3	-1.5	1.4
	JJA	-0.6	-0.9				-0.8	1.6	0.3	0.2	-0.6	1.8
	SON	-0.7	-0.7				-1.1	-1.0	0.0	-0.8	-1.3	0.6
Czech Republic	DJF	0.1	0.2				-0.2	0.9	-1.0	-0.1	-0.7	0.6
	MAM	-0.8	-0.6				-1.1	1.1	0.3	0.1	-1.0	0.8
	JJA	0.2	-0.8				0.3	1.5	0.8	1.2	-0.1	0.8
	SON	0.4	0.0				0.2	-0.6	0.5	0.2	-0.6	0.7
Hungary	DJF	0.0	0.5	1.3		-0.9	-0.4	0.7	-0.8	0.0	-0.6	0.2
	MAM	-1.3	-1.2	-0.5		-2.2	-1.6	0.5	0.4	0.1	-1.4	0.2
	JJA	1.0	-0.8	-0.5		-0.6	1.2	2.3	1.5	2.7	0.2	0.0
	SON	0.9	-0.4	0.0		-2.6	0.6	-0.9	0.6	0.3	-1.0	0.4
Romania	DJF				1.3		0.2	0.6	0.0	0.4	-0.5	0.4
	MAM				-0.3		-1.7	-0.4	0.6	0.4	-1.3	0.4
	JJA				-1.0		0.2	1.1	1.4	2.5	0.0	0.5
	SON				-0.4		0.0	-1.8	0.4	0.3	-1.4	0.3
Slovakia	DJF	0.3	0.0	0.9	1.2	-0.9	0.1	1.1	-1.0	-0.1	-1.0	0.7
	MAM	-1.2	-1.0	-0.4	0.2	-2.2	-1.5	0.6	0.1	-0.1	-1.3	1.0
	JJA	0.6	-0.7	-0.2	0.0	-0.2	0.7	1.9	1.1	1.7	0.1	1.4
	SON	0.4	-0.3	0.0	0.4	-2.3	0.2	-0.6	0.4	0.2	-0.9	2.1



(Ra2) simulation of NMA is the only exception to the previous, with slightly lowered correlations over Romania and Slovakia compared to the ENSEMBLES RCMs. Spatial variability of the CECILIA RCMs is mostly within the 0.8–1.2 range of the observed spatial variability (= 1), and there is no systematic improvement in the CECILIA simulations as in the case of biases or spatial correlations. However, the CECILIA RCMs are within the range of spatial variability of the ENSEMBLES RCMs. Agreement of the simulated spatial characteristics with observations is the worst in Hungary, where the simulations substantially overestimate spatial variability in all seasons except winter.

The IAV of the CECILIA and ENSEMBLES models as well as the ERA-40 driving data over CEE countries is summarized in Table 4. In transient seasons (spring, autumn), the IAV of the CECILIA RCMs is often within the 0.9–1.1 range of the observed IAV (= 1). The only exception is the CUNI RegCM3 *alpha* (Ra) simulation that exhibits increased IAV in spring.

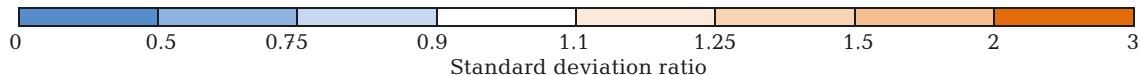
In winter, the CECILIA RCMs, except CUNI RegCM3 *alpha* (Ra), show decreased IAV (IAV ratio 0.4–0.9), with models of the ALADIN family being worse than RegCM3 models. An overestimation of summer temperature IAV in CEE reported by earlier studies (Jacob et al. 2007, Lenderink et al. 2007, Vidale et al. 2007) is present in all ENSEMBLES RCMs, but in only some CECILIA RCMs, namely ALADIN-Climate/CZ (Az) and RegCM3 *alpha* (Ra) of CUNI. When all seasons are considered, IAV is mostly captured better in the CECILIA than ENSEMBLES models.

3.2. Precipitation

The area-averaged systematic error (bias) of long-term seasonal precipitation sums over CEE countries for the CECILIA and ENSEMBLES models and their driving ERA-40 data is summarized in Table 5. The statistically significant bias, detected by the same cri-

Table 4. Inter-annual variability of seasonal temperature in the CECILIA and ENSEMBLES models expressed as a relative fraction of observed inter-annual standard deviation over central and eastern European countries for the 1961–1990 period. DJF = winter, MAM = spring, JJA = summer, SON = autumn

Country	Season	Inter-annual standard deviation ratio										
		CECILIA models					ENSEMBLES models					ERA40
		Az	Ra	Rb	Ra2	A	Az	A	H	C	Ra	
Austria	DJF	0.51	1.16				0.52	0.59	1.18	1.03	1.20	1.00
	MAM	0.89	1.34				0.96	1.11	1.27	1.20	1.45	0.92
	JJA	1.29	1.38				1.25	1.69	1.78	1.66	1.60	0.91
	SON	0.91	1.06				0.93	0.85	1.27	1.11	1.13	1.00
Czech Republic	DJF	0.54	1.11				0.57	0.61	1.26	1.01	1.16	1.03
	MAM	1.08	1.36				1.20	1.30	1.36	1.16	1.52	0.98
	JJA	1.20	1.01				1.29	1.56	1.39	1.77	1.32	0.96
	SON	0.99	1.01				1.04	0.96	1.26	1.18	1.11	0.98
Hungary	DJF	0.48	1.01	0.77		0.63	0.49	0.69	1.13	0.89	1.06	0.94
	MAM	1.08	1.19	1.05		1.06	1.24	1.27	1.18	1.16	1.39	0.95
	JJA	2.00	2.13	1.02		1.27	1.93	2.47	1.92	2.19	1.89	1.07
	SON	1.07	0.95	1.05		1.07	1.13	1.02	1.17	1.03	1.00	1.06
Romania	DJF				0.80		0.50	0.61	0.96	0.85	1.01	0.97
	MAM				0.98		1.02	1.02	1.08	1.07	1.14	0.95
	JJA				1.29		1.43	1.71	1.88	2.12	1.58	1.02
	SON				1.05		1.24	0.78	1.13	1.22	1.09	1.01
Slovakia	DJF	0.45	1.08	0.82	0.85	0.66	0.45	0.59	1.11	0.95	1.13	1.02
	MAM	0.98	1.24	1.03	1.01	0.94	1.07	1.17	1.20	1.09	1.40	0.96
	JJA	1.36	1.32	1.00	1.02	1.04	1.48	1.87	1.57	1.98	1.53	1.03
	SON	0.98	0.90	0.97	0.88	0.89	1.02	0.88	1.11	1.05	0.96	0.95



terion as for air temperature, is again highlighted in bold in Table 5. The CECILIA RCMs simulate more precipitation than is observed. The excess of seasonal precipitation is smaller (<~50%) for ALADIN-Climate/CZ (Az) and RegCM3 *beta* (Rb) models, whereas RegCM3 *alpha* (Ra, Ra2) models overestimate precipitation in all seasons, sometimes by more than 100%. ALADIN-Climate (A) models capture winter and autumn precipitation very well but double seasonal precipitation sums in spring and summer. The CECILIA RCMs generate higher (and less realistic in the majority of cases) seasonal sums of precipitation than their relevant ENSEMBLES counterparts or the ENSEMBLES models in general. Dry summer conditions in southeastern Europe detected in RCM simulations by earlier studies (e.g. Hagemann et al. 2004, Jacob et al. 2008) are partly present in some ENSEMBLES RCMs but not in the CECILIA RCMs.

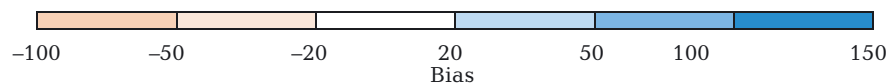
Spatial variability of precipitation and its spatial

correlation with observations is again summarized in the form of a Taylor diagram in Fig. S2 in the Supplement. Spatial correlations with observed precipitation vary strongly among the CECILIA models (and the ENSEMBLES models), seasons and assessed areas. For example, the spatial correlation of the CUNI RegCM3 *alpha* (Ra) summer precipitation in Hungary is only 28%, but over neighboring Slovakia, it reaches 87%. RegCM3 *beta* (Rb) is the only model where improvements prevail when compared to its ENSEMBLES counterpart (International Centre for Theoretical Physics, Italy, RegCM3 *alpha*, Ra). For other CECILIA RCMs, we detect worsening of a different magnitude or no significant changes in any direction. However, in general, all CECILIA RCMs are within the range of spatial correlations of the ENSEMBLES models.

Spatial variability of the precipitation field, when accessed by a standard deviation ratio as in the Tay-

Table 5. Bias of seasonal precipitation in the CECILIA and ENSEMBLES models over central and eastern European countries for the 1961–1990 period. **Bold**: statistically significant bias. DJF = winter, MAM = spring, JJA = summer, SON = autumn

Country	Season	Precipitation bias (%)										
		CECILIA models					ENSEMBLES models					ERA40
		Az	Ra	Rb	Ra2	A	Az	A	H	C	Ra	
Austria	DJF	21	114				6	-35	68	38	68	-36
	MAM	26	79				9	9	45	16	46	-29
	JJA	35	22				13	12	2	-10	-7	-30
	SON	13	46				-3	-46	20	6	15	-37
Czech Republic	DJF	35	119				31	-18	82	50	90	25
	MAM	32	107				17	12	39	28	62	-1
	JJA	33	62				14	12	11	-5	9	-13
	SON	13	77				2	-41	36	24	42	-10
Hungary	DJF	42	60	38		10	34	-43	48	34	65	23
	MAM	37	102	40		82	24	4	12	19	59	-6
	JJA	5	62	34		98	-9	-9	-20	-21	11	-23
	SON	13	40	7		-7	2	-62	4	6	22	-14
Romania	DJF				119		48	-25	109	78	130	14
	MAM				125		41	13	35	42	87	8
	JJA				106		25	14	-8	-18	4	18
	SON				83		10	-47	30	24	46	-12
Slovakia	DJF	25	105	46	63	12	12	-34	74	41	80	-1
	MAM	29	103	34	83	91	13	-6	36	26	59	-17
	JJA	13	37	-1	71	105	-7	-11	-7	-21	-10	-29
	SON	7	67	14	40	-2	-10	-60	26	7	39	-31

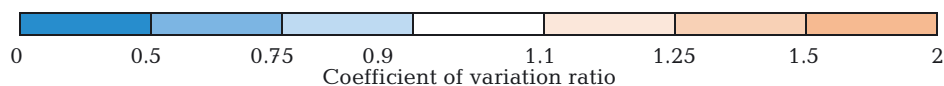


lor diagram, is mostly larger in the CECILIA RCMs than in their ENSEMBLES counterparts and is also larger than in observations, especially in countries with complex topography (all except Hungary). This is mainly in the ALADIN-Climate (A) and both RegCM3 *alpha* (Ra, Ra2) models. On the other hand, RegCM3 *beta* (Rb) shows unchanged or even reduced spatial variability of precipitation, and ALADIN-Climate/CZ (Az) shows changes in both directions that seem to be partly related to the height of orography over the country. When the spatial variability of the precipitation field is assessed by using a coefficient of variation ratio to rule out the effect of precipitation bias, all CECILIA RCMs (even those with significant wet biases) show spatial variability close to the observed one (not shown). Their spatial variability, when the same models are compared, is mostly slightly reduced and worse but, in general, is still very close to that of the ENSEMBLES models (not shown).

The IAV of area-averaged precipitation is described by the coefficient of variation ratio (model to observation) and is presented in Table 6. With values predominantly in the 0.5–0.9 range of the observed IAV (= 1), the CECILIA RCMs tend to underestimate precipitation IAV. ALADIN-Climate/CZ (Az) has the best agreement with the observed IAV from all CECILIA RCMs. NMA RegCM3 *alpha* (Ra2) substantially overestimates summer precipitation IAV. It is also the only CECILIA RCM where IAV is increased compared to its ENSEMBLES counterpart. For other CECILIA RCMs, we rather see the opposite, i.e. a reduction of precipitation IAV. In seasons when precipitation IAV is lessened in the ERA-40 driving data, we also find smaller IAV in CECILIA (and some ENSEMBLES) RCMs. Otherwise, there is no noticeable feature in simulated precipitation IAV like that in air temperature. When all seasons, countries and models are considered, the capture of IAV is similar or slightly worse in the CECILIA models compared with ENSEMBLES models.

Table 6. Inter-annual variability of seasonal precipitation in the CECILIA and ENSEMBLES models expressed as relative fraction of observed inter-annual coefficient of variation over central and eastern European countries for the 1961–1990 period. DJF = winter, MAM = spring, JJA = summer, SON = autumn

Country	Season	Inter-annual coefficient of variation ratio										
		CECILIA models					ENSEMBLES models					ERA40
		Az	Ra	Rb	Ra2	A	Az	A	H	C	Ra	
Austria	DJF	0.92	0.85				0.86	1.75	0.82	0.81	0.82	0.92
	MAM	0.68	0.58				0.70	0.80	0.84	0.64	0.65	0.76
	JJA	0.72	0.79				0.84	0.71	1.56	1.10	1.18	1.06
	SON	1.14	1.08				1.19	1.63	1.10	1.24	1.23	1.06
Czech Republic	DJF	0.86	0.70				0.89	1.26	0.72	0.80	0.72	0.79
	MAM	0.84	0.48				0.84	1.18	1.25	0.94	0.76	0.85
	JJA	0.86	0.56				0.93	0.68	1.04	1.17	0.84	0.87
	SON	1.25	0.91				1.45	1.29	0.93	1.15	1.15	1.09
Hungary	DJF	0.87	0.61	0.74		0.87	0.89	1.48	0.78	0.69	0.66	0.66
	MAM	0.74	0.62	0.76		0.69	0.81	1.11	1.09	0.93	0.87	1.02
	JJA	1.08	1.05	0.88		0.67	0.97	1.02	1.15	1.01	1.16	1.18
	SON	0.80	0.83	0.88		0.87	0.89	1.25	0.79	0.91	0.92	0.98
Romania	DJF				0.68		1.02	1.05	0.81	0.81	0.74	0.71
	MAM				0.98		0.81	0.87	0.97	1.05	0.88	1.03
	JJA				1.53		0.93	0.91	1.78	1.59	1.28	1.25
	SON				1.01		0.98	1.27	0.74	0.95	0.69	1.05
Slovakia	DJF	1.07	0.67	0.80	0.77	0.87	0.99	1.50	0.86	0.82	0.71	0.73
	MAM	1.02	0.84	1.00	1.11	0.74	1.03	1.14	1.28	0.99	1.06	0.93
	JJA	0.98	0.80	0.87	1.40	0.64	1.07	0.97	1.00	1.07	1.02	1.23
	SON	0.97	0.79	0.83	0.87	0.78	1.03	1.23	0.83	0.91	0.84	1.32



4. DISCUSSION

Analysis of the CECILIA RCM simulations reveals that the models are able to capture the main features of the climate in CEE. We find both improvement and degradation of climate description provided by the high-resolution CECILIA simulations on small domains compared to the lower resolution ENSEMBLES simulations on a larger domain.

Although the assessed quality of the CECILIA and ENSEMBLES simulations is often similar, we see the majority of CECILIA simulations improve on ENSEMBLES simulations for air temperature characteristics. The biases are usually reduced, and the warm anomaly of summer temperature in southeastern Europe reported by earlier studies (e.g. Hagemann et al. 2004) is not present in the CECILIA RCMs. However, the decrease of warm summer air temperature bias is accompanied by a larger wet precipitation bias in all CECILIA RCMs except ALADIN-Climate/CZ (Az). Therefore, the better score for the CECILIA RCMs in simulated summer air temperature could be a consequence of their tendency to simulate excessive precipitation amounts. The increased summer temperature IAV described by other authors (Jacob et al. 2007, Lenderink et al. 2007, Vidale et al. 2007) is present in only some CECILIA simulations. The significant feature of simulated IAV is its underestimate in the ALADIN family models in winter. Referring to the results of Sanchez-Gomez et al. (2009), we suggest that this may be caused by underestimating the mean persistence of anticyclonic weather regime episodes, which bring cold arctic air from the north and east to CEE. Suppressing the episodes of the cold weather could also be reflected in relatively small cold (or even warm) biases of winter temperature in the affected simulations. The spatial pattern of seasonal air temperature is well captured in all simulations, and further improved by the CECILIA RCMs. A slightly worse score over Hungary is rather a consequence of comparing relatively smooth spatial temperature fields, where even a small difference between a model and observations can deteriorate spatial variability or correlation.

The CECILIA RCMs show clear worsening in simulated properties of precipitation. Similarly, as in previous studies (e.g. Jaeger et al. 2008, Rauscher et al. 2010), we detect larger precipitation amounts (compared to ENSEMBLES RCMs) and significant wet biases in all high-resolution CECILIA simulations. Spatial properties of the precipitation field as well as the IAV of precipitation are also less realistic in some regions and RCMs, although some minor

improvements can be detected as well. Our investigation suggests that the results and possible gain (or loss) from the CECILIA experiments over the ENSEMBLES models are strongly dependent on which particular simulation is assessed. Because of the variety of models and their different settings, we cannot unambiguously identify the reasons explaining the performance of the CECILIA RCMs. We suspect that 3 major effects play important roles.

First, some physical parameterizations of RCMs can be sensitive on different scales of spatial resolution, and they can require further adaptation before models are run at a very high resolution of 10 km. All CECILIA teams employing the RegCM3 model detected significant wet biases regardless of other factors, e.g. coupling with the ERA-40 data or domain setting. This led to the development of the new version of the RegCM3 model (here referred to as the *beta* version) with adjusted parameters of the large-scale precipitation scheme that has reduced the precipitation bias and improved other properties of simulated precipitation (Georgescu et al. 2009) as well as air temperature (Torma et al. 2008, 2011). The decrease in the precipitation bias with the RegCM3 *beta* version is shown here in the results of the ELU team (Rb), but it was also reported later by CUNI and NMA teams (M. Belda, M. Caian pers. comm.). However, in this study, we present only original CUNI and NMA RegCM3 *alpha* (Ra, Ra2) simulations that are available on the project public data archive. Fragmentation of the ALADIN-Climate/CZ (Az) simulated precipitation field (Fig. 2) in central Europe, which is strong in winter and reflected in very low spatial correlation with observations in this season, also points out some weak points in the model physics. We suspect that an imperfection in the horizontal diffusion of humidity in the model may be a source of the fragmentation of the simulated precipitation in both the CECILIA and ENSEMBLES experiments, but this hypothesis must still be investigated further.

Second, coupling of the relatively coarse ERA-40 data with an RCM of 10 km spatial resolution over a small domain could limit the ability of the RCM to produce high-resolution features, and deteriorate results because of the proximity of the coupling zone to the inner part of the domain. This could be further amplified by the presence of mountain ranges on the domain boundary. CECILIA ALADIN-Climate (A) simulation was driven directly by ERA-40 reanalyses over a small domain with mountains on its edges. Following the results of earlier studies by Csima & Horányi (2008) and mainly Farda et al. (2010), who studied the

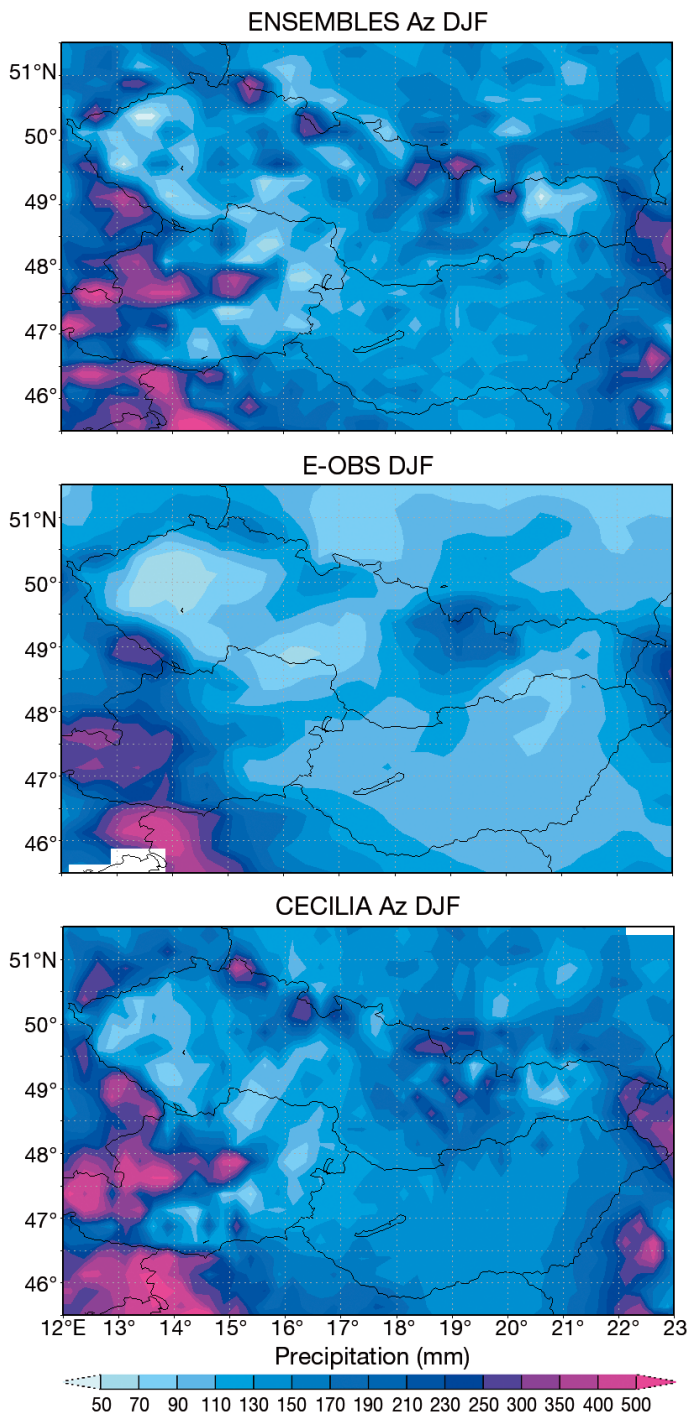


Fig. 2. Comparison of winter (DJF) mean precipitation sums over central Europe in the E-OBS gridded observation dataset (middle) and 2 ALADIN-Climate/CZ (Az) simulations from the ENSEMBLES (left) and CECILIA (right) projects

effect of domain size on the quality of ALADIN-Climate simulations over Bulgaria, we hypothesize that high deviations of CECILIA ALADIN-Climate (A) simulations from observations are at least partly

caused by the setting of the integration domain. In CECILIA ALADIN-Climate (A) simulations, the integration domain and its coupling zone are perhaps too small compared to the resolution of the ERA-40 driving data, and there is a risk of imbalance between spatial and temporal resolution of the coupling zone. Especially fast-travelling synoptic systems could enter the domain's interior without being captured properly by a coupling procedure working with 6 h frequency. In the case of RegCM3 *alpha* (Ra, Ra2) models, the excessive precipitation could be associated with not only an internal model design (as discussed above) but also a domain setting. Sensitivity tests with RegCM3 models (not shown here) performed in the early stage of the CECILIA project showed a significant response of precipitation to the choice of the domain for the same model and configuration (CECILIA WP2 Deliverable D2.1 2008). The complex land cover, including a sea surface, within the integration domain of this CECILIA simulation (see Fig. 1) could affect simulated precipitation and air temperature, e.g. by forcing the model climate systematically towards predefined sea surface temperature.

Finally, properties of the E-OBS dataset could also affect validation results. The E-OBS dataset was developed in the framework of the ENSEMBLES project to enable validation of RCM simulations at 50 and 25 km resolution. The previous studies carried out over the Czech Republic detected low spatial variability of air temperature (Kyselý & Plavcová 2010) and precipitation (Zíková et al. 2012) in the E-OBS dataset. The highest deficiencies of E-OBS were detected mainly over mountain areas. The density of an underlying station network in the E-OBS dataset is one of the key factors affecting its properties and the consequent results of climate model validation (Kyselý & Plavcová 2010, Rauscher et al. 2010). During preparation of this study, we detected an improvement in the validation of the CECILIA RCMs in central Europe when the E-OBS dataset version 6.0, based on a higher number of stations, was used instead of version 2.0 (not shown). Despite some recent updates, the density of station data available for E-OBS still remains very low in many CEE countries, and needs to be further increased to enhance the suitability of the E-OBS dataset for the evaluation of high-resolution RCMs.

5. CONCLUSIONS

The aim of this paper was to evaluate 1961–1990 simulations of regional climate models at a high spa-

tial resolution of 10 km over small integration domains, and identify their possible gain relative to simulations of a lower resolution (25 km), but carried out over larger integration domains. This was done by comparing 2 sets of RCM simulations from the FP6 CECILIA and FP6 ENSEMBLES projects with observations represented by the E-OBS dataset.

We found that the CECILIA models at 10 km resolution are capable of capturing the main features of recent climate in the target region of CEE, and that they in many aspects reach similar or even better measures of quality as the lower resolution ENSEMBLES models. The major improvements are found in the properties of simulated air temperature. Still, we have detected several weaknesses. Compared with the ENSEMBLES simulations, the CECILIA experiments do not provide any significant gain in the quality of precipitation description and rather bring more drawbacks than improvements.

We suspect 3 major reasons for the worsening quality of simulated precipitation. (1) An internal design of some models, especially their package of physical parameterizations, is sensitive to a spatial scale at which the model is employed. (2) Coupling of the coarse ERA-40 data with an RCM over a small domain may limit the ability of the model to produce high-resolution features. In addition, the choice of the integration domain in some CECILIA simulations could cause a propagation of errors related to coupling into the interior of the integration domain and thus deteriorate the results. Finally, (3) one reason for the apparently worse performance of the CECILIA models can be associated with imperfections of the reference E-OBS dataset rather than the model simulations themselves. Testing the CECILIA models at the very high resolution of 10 km would perhaps require new, even more developed datasets of station observations than E-OBS, currently considered the best pan-European gridded station dataset.

Even though the CECILIA simulations show no overall but only partial improvement over the ENSEMBLES models, we believe it still makes sense to carry out similar experiments with high-resolution RCMs. Such experiments may better account for details not obvious from comparison with E-OBS, and also enhance topographic features important for climate impact studies. In addition, even high systematic errors in control climate simulations may not significantly affect the simulation of climate change as the analysis of CECILIA scenario simulations implies.

Using reanalysis-driven RCM simulations is a fruitful step for evaluating the role of resolution and domain design. The new ERA-Interim reanalysis at

higher resolution will help to reduce the problem of a jump in resolution in the perfect boundary condition experiments. In the forthcoming CORDEX project (Giorgi et al. 2009), led by the World Climate Research Programme, the perfect boundary condition approach will be systematized.

Acknowledgements. We acknowledge the E-OBS dataset from the EU-FP6 project ENSEMBLES (<http://ensembles-eu.metoffice.com>) and the data providers in the ECA&D project (<http://eca.knmi.nl>). This study was performed within the CECILIA project, funded by the European Commission's 6th Framework Programme under contract number 037013. The authors also gratefully acknowledge the financial support of the following foundations and research programs: CzechGlobe Centre (CZ.1.05/1.1.00/02.0073) and projects CZ.1.07/2.4.00/31.0056 (Operational Programme of Education for Competitiveness of Ministry of Education, Youth and Sports of the Czech Republic) and P209/11/2405 (Czech Science Foundation). Partial support was also provided under the Research Plan of MSMT (No. MSM 0021620860) and through the COST 734 activity locally supported by MSMT grant OC10061.

LITERATURE CITED

- Adam JC, Lettenmaier DP (2003) Adjustment of global gridded precipitation for systematic bias. *J Geophys Res* 108: 4257, doi:10.1029/2002JD002499
- Bergant K, Belda M, Halenka T (2007) Systematic errors in the simulation of European climate (1961–2000) with RegCM3 driven by NCEP/NCAR reanalysis. *Int J Climatol* 27:455–472
- CECILIA (2008) D2.1: RCM simulations forced by observations. Accessed 10 Nov 2011. Available at www.cecilia-eu.org/restricted/deliverables.php
- Christensen JH, Kjellström E, Giorgi F, Lenderink G, Rummukainen M (2010) Weight assignment in regional climate models. *Clim Res* 44:179–194
- Csima G, Horányi A (2008) Validation of the ALADIN-Climat model at the Hungarian Meteorological Service. *Időjárás* 112:155–178
- Déqué M (2007) Frequency of precipitation and temperature extremes over France in an anthropogenic scenario: model results and statistical correction according to observed values. *Glob Planet Change* 57:16–26
- Farda A, Déqué M, Somot S, Horányi A, Spiridonov V, Tóth H (2010) Model ALADIN as regional climate model for Central and Eastern Europe. *Stud Geophys Geod* 54: 313–332
- Georgescu F, Tascu S, Caian M, Banciu D (2009) A severe blizzard event in Romania—a case study. *Nat Hazards Earth Syst Sci* 9:623–634
- Giorgi F, Mearns LO (1991) Approaches to regional climate change simulation: a review. *Rev Geophys* 29:191–216
- Giorgi F, Mearns LO (1999) Introduction to special section: regional climate modeling revisited. *J Geophys Res* 104: 6335–6352
- Giorgi F, Jones C, Asrar GR (2009) Addressing climate information needs at the regional level: the CORDEX framework. *WMO Bulletin* 58:175–183
- Hagemann S, Machenhauer B, Jones R, Christensen OB,

- Déqué M, Jacob D, Vidale PL (2004) Evaluation of water and energy budgets in regional climate models applied over Europe. *Clim Dyn* 23:547–567
- Halenka T (2008) Regional climate modeling activities in CECILIA project: introduction. *Időjárás* 112:III–IX
- Halenka T, Kalvová J, Chládková Z, Demeterová A, Zemánková K, Belda M (2006) On the capability of RegCM to capture extremes in long term regional climate simulation — comparison with the observations for Czech Republic. *Theor Appl Climatol* 86:125–145
- Haylock MR, Hofstra N, Klein Tank AMG, Klok EJ, Jones PD, New M (2008) A European daily high-resolution gridded dataset of surface temperature and precipitation for 1950–2006. *J Geophys Res* 113:D20119, doi:10.1029/2008JD10201
- Jacob D, Bärring L, Christensen OB, Christensen JH and others (2007) An inter-comparison of regional climate models for Europe: model performance in present-day climate. *Clim Change* 81:31–52
- Jacob D, Kotova L, Lorenz P, Moseley Ch, Pfeifer S (2008) Regional climate modeling activities in relation to CLAVIER project. *Időjárás* 112:141–153
- Jaeger EB, Anders I, Lüthi D, Rockel B, Schär C, Seneviratne S (2008) Analysis of ERA40-driven CLM simulations for Europe. *Meteorol Z* 17:349–367
- Kjellström E, Nikulin G, Hansson U, Strandberg G, Ullerstig A (2011) 21st century changes in the European climate: uncertainties derived from an ensemble of regional climate model simulations. *Tellus* 63:24–40
- Kyselý J, Plavcová E (2010) A critical remark on the applicability of E-OBS European gridded temperature data set for validating control climate simulations. *J Geophys Res* 115:D23118, doi:10.1029/2010JD014123
- Laprise R (2008) Regional climate modelling. *J Comput Phys* 227:3641–3666
- Lenderink G, van Ulden A, van den Hurk B, van Meijgaard E (2007) Summertime inter-annual temperature variability in an ensemble of regional climate model simulations: analysis of the surface energy budget. *Clim Change* 81:233–247
- Meissner C, Schädler G, Panitz HJ, Feldmann H, Kottmeier C (2009) High-resolution sensitivity studies with the regional climate model COSMO-CLM. *Meteorol Z* 18:543–557
- Pal JS, Giorgi F, Bi X, Elguindi N and others (2007) Regional climate modeling for the developing world: the ICTP RegCM3 and RegCNET. *Bull Am Meteorol Soc* 88:1395–1409
- Plavcová E, Kyselý J (2011) Evaluation of daily temperatures in Central Europe and their links to large-scale circulation in an ensembles of regional climate models. *Tellus* 63:763–781
- Rauscher SA, Coppola E, Piani C, Giorgi F (2010) Resolution effects on regional climate model simulations of seasonal precipitation over Europe. *Clim Dyn* 35:685–711
- Reichler T, Kim J (2008) How well do coupled models simulate today's climate? *Bull Am Meteorol Soc* 89:303–311
- Sanchez-Gomez E, Somot S, Déqué M (2009) Ability of an ensemble of regional climate models to reproduce weather regimes over Europe-Atlantic during the period 1961–2000. *Clim Dyn* 33:723–736
- Suklitsch M, Gobiet A, Truhetz H, Awan NK, Göttel H, Jacob D (2011) Error characteristics of high resolution regional climate models over the Alpine area. *Clim Dyn* 37:377–390
- Taylor K (2001) Summarizing multiple aspects of model performance in a single diagram. *J Geophys Res* 106:7183–7192
- Torma C, Bartholy J, Pongrácz R, Barcza Z, Coppola E, Giorgi F (2008) Adaptation of the RegCM3 climate model for the Carpathian Basin. *Időjárás* 112:233–247
- Torma C, Coppola E, Giorgi F, Bartholy J, Pongrácz R (2011) Validation of a high-resolution version of the regional climate model RegCM3 over the Carpathian Basin. *J Hydrometeorol* 12:84–100
- Uppala SM, Kållberg PW, Simmons AJ, Andrae U and others (2005) The ERA-40 re-analysis. *QJR Meteorol Soc* 131:2961–3012
- van der Linden P, Mitchell JFB (eds) (2009) ENSEMBLES: climate change and its impacts: summary of research and results from the ENSEMBLES project. Met Office Hadley Centre, Exeter
- Vidale PL, Lüthi D, Wegmann R, Schär C (2007) European summer climate variability in a heterogeneous multi-model ensemble. *Clim Change* 81:209–232
- Yang D, Kane D, Zhang Z, Legates D, Goodison B (2005) Bias correction of long-term (1973–2004) daily precipitation data over the northern regions. *Geophys Res Lett* 32:L19501, doi:10.1029/2005GL024057
- Zíková N, Holtanová E, Kalvová J (2013) Annual precipitation cycle in regional climate models: the influence of horizontal resolution. *Theor Appl Climatol* 112:521–533

Editorial responsibility: Filippo Giorgi, Trieste, Italy

*Submitted: December 2, 2011; Accepted: November 11, 2013
Proofs received from author(s): April 25, 2014*

Research Article

CECILIA Regional Climate Simulations for Future Climate: Analysis of Climate Change Signal

Michal Belda,¹ Petr Skalák,^{2,3} Aleš Farda,^{2,3} Tomáš Halenka,¹
Michel Déqué,⁴ Gabriella Csima,⁵ Judit Bartholy,⁶ Csaba Torma,⁷
Constanta Boroneant,⁸ Mihaela Caian,⁹ and Valery Spiridonov¹⁰

¹ Department of Meteorology and Environment Protection, Charles University in Prague, 18200 Prague, Czech Republic

² Czech Hydrometeorological Institute, 14306 Prague, Czech Republic

³ Global Change Research Centre, Academy of Science of the Czech Republic, 60300 Brno, Czech Republic

⁴ National Centre for Meteorological Research, Météo France, 31057 Toulouse, France

⁵ Hungarian Meteorological Service, Budapest 1525, Hungary

⁶ Department of Meteorology, Eötvös Loránd University, Budapest 1518, Hungary

⁷ The Abdus Salam International Centre for Theoretical Physics, 34151 Trieste, Italy

⁸ Centre for Climate Change, Rovira i Virgili University, 43500 Tarragona, Spain

⁹ Rossby Centre, SMHI, 60176 Norrköping, Sweden

¹⁰ National Institute of Meteorology and Hydrology, 1784 Sofia, Bulgaria

Correspondence should be addressed to Michal Belda; michal.belda@mff.cuni.cz

Received 24 April 2014; Revised 8 August 2014; Accepted 11 August 2014

Academic Editor: Lian Xie

Copyright © 2015 Michal Belda et al. This is an open access article distributed under the Creative Commons Attribution License, which permits unrestricted use, distribution, and reproduction in any medium, provided the original work is properly cited.

Regional climate models (RCMs) are important tools used for downscaling climate simulations from global scale models. In project CECILIA, two RCMs were used to provide climate change information for regions of Central and Eastern Europe. Models RegCM and ALADIN-Climate were employed in downscaling global simulations from ECHAM5 and ARPEGE-CLIMAT under IPCC A1B emission scenario in periods 2021–2050 and 2071–2100. Climate change signal present in these simulations is consistent with respective driving data, showing similar large-scale features: warming between 0 and 3°C in the first period and 2 and 5°C in the second period with the least warming in northwestern part of the domain increasing in the southeastern direction and small precipitation changes within range of +1 to –1 mm/day. Regional features are amplified by the RCMs, more so in case of the ALADIN family of models.

1. Introduction

Regional climate models (RCMs) are tools that greatly enhance the usability of climate projections made by global climate models (GCMs) for studying climate and its change and impacts on a regional scale. Following the methodology of dynamical downscaling [1, 2], the outputs of GCMs can be used as driving fields for the nested RCMs running with higher resolution, allowing capturing the local features of the climate.

The Fifth Assessment Report of the Intergovernmental Panel on Climate Change [3] suggests changes in regional climate conditions in the 21st century over Central and Eastern

Europe (CEE). The Coupled Model Intercomparison Project Phase 5 (CMIP5) projections generally agree on warming in all seasons in Europe during the 21st century, while precipitation projections are more variable across different parts of Europe and seasons. CEE is a region where precipitation changes remain still uncertain. Even the findings of recent coordinated downscaling experiments in Europe, for example, projects PRUDENCE (Prediction of Regional Scenarios and Uncertainties for Defining European Climate Change Risks and Effects) [4] or ENSEMBLES (ENSEMBLE based predictions of climate changes and their impacts) [5] using RCM simulations of 25–50 km horizontal resolution,

are consistent with the CMIP5 (Coupled Model Intercomparison Project Phase 5) projections and do not indicate any significant precipitation change in CEE. Although regional climate change amplitudes of temperature and precipitation follow global trends in Europe, they can be also affected by changes in the large-scale circulation and regional feedback processes [6]. Recent studies have also clearly identified importance of soil moisture changes and their impact on amplification of temperature extremes in Europe [7, 8]. Similar processes and meteorological extremes in general have strong consequences on local scale climate conditions and they can be only hardly captured by coarser resolution GCMs. Downscaling methods, both statistical and dynamical based on RCMs, may thus provide valuable information on climate change for assessing its regional impacts, detecting possible vulnerabilities, and adopting the relevant adaptation measures.

Climate change impacts and vulnerability assessment were the key objectives of two recent projects supported by European Commission's 6th Framework Programme: CECILIA (Central and Eastern Europe Climate Change Impact and Vulnerability Assessment, <http://www.cecilia-eu.org/>) [9–12] and CLAVIER (Climate Change and Variability: Impact on Central and Eastern Europe, <http://www.clavier-eu.org/>) [13]. The emphasis of both projects on CEE was not only due to uncertainties in the future climate evolution in this region. It also reflected the fact that CEE countries are relatively young and emerging market economies and thus potentially more vulnerable than developed Western Europe countries. The novel aspect of both projects was to deliver information on the climate change in the region of CEE by means of RCMs simulations at very high resolution of 10 km on a relatively small domain. Advantages of such model setup and ability of the CECILIA RCMs to capture the main features of the climate in the CEE in the past period 1961–1990 have been tested by several studies [14–16]. Skalák et al. [14] analysed the performance of CECILIA models driven by ERA-40 reanalysis (“perfect-boundary” experiment). They concluded that the gain of using a high resolution RCM on a small domain (as in the CECILIA project) with respect to a lower resolution (25 km) over a larger domain (as in the ENSEMBLES project) is clear for air temperature but very limited for precipitation. The authors have also confirmed findings of previous studies, for instance, [17–19], validating influence of model resolution on simulated temperature and precipitation. Despite high systematic errors of RCMs in control climate simulations, those may not significantly affect the simulation of climate change and rule out RCMs from providing useful information on the future climate state. This study follows up on the paper by Skalák et al. [14] and presents the analysis of CECILIA climate change simulations in the region of CEE for 2021–2050 and 2071–2100 periods and compares the results of high resolution RCMs with their driving data.

2. Modeling Setup

The CECILIA modeling system consists of six individual simulations over various domains in Central and Eastern

Europe. Based on previous experience and experiment testing performed in the first stage of the project, six project partners (institutions) were involved in the Work Package 2 of the CECILIA project: Charles University in Prague, Czech Republic (CUNI), Czech Hydrometeorological Institute, Czech Republic (CHMI), Eötvös Loránd University, Hungary (ELU), Hungarian Meteorological Service, Hungary (OMSZ), National Meteorological Administration, Romania (NMA), and National Institute of Meteorology and Hydrology, Bulgaria (NIMH). The partners picked four RCMs for the climate studies, two versions of ALADIN-Climate [20] and two versions of RegCM3 [21], and made their choice of model and domain setup.

Two versions of ALADIN-Climate correspond to cycle 24 and cycle 28 of the ARPEGE/IFS code. Their physical parameterizations are different. While the original version of ALADIN-Climate (cycle 24) developed by Météo-France has a physical parameterization package derived directly from the one used in GCM ARPEGE-CLIMAT 4 [22], the other version, ALADIN-Climate/CZ (cycle 28), is based on the numerical weather prediction version of the ALADIN model in operational use at the Czech Hydrometeorological Institute in 2002 and 2003.

Two versions of RegCM3 differ in some aspects of the physical parameterizations: one in the original setting described by Pal et al. [21], named *alpha* for distinction, and the other, called *beta*, with applied changes into the large-scale precipitation schemes. The modifications in the *beta* version were motivated by a large bias of precipitation found during sensitivity tests conducted with the RegCM3 *alpha* model over the Carpathian Basin and their justification can be found in Torma et al. [23, 24].

In order to produce scenarios of the 21st century with CECILIA high resolution RCMs, two types of boundary conditions were taken. ALADIN-Climate models were driven by the boundary condition of 50 km horizontal resolution coming from a “stretch mesh” version of ARPEGE-CLIMAT 4 GCM. This version of the GCM has a variable horizontal resolution being around 50 km over Southern Europe and decreasing to ca 300 km at the antipode. In case of RegCM3 models, a double nesting technique was applied. The CECILIA RegCM3 10 km experiments were driven by another RegCM3 simulation of 25 km resolution that was forced by ECHAM5 GCM. The RegCM3 25 km simulation was originally produced by the Abdus Salam International Centre for Theoretical Physics (ICTP) in the frame of the ENSEMBLES project. All CECILIA simulations undertaken are summarized in Table 1. Modeling domains of individual groups are illustrated in Figure 1.

CUNI was the only partner using the original version of RegCM3 *alpha*. The reason for not using the improved *beta* version was rather technical, since the modification was introduced after a big part of CUNI simulations had been carried out and it was not computationally feasible to repeat all the simulations within the scope of the project. The RegCM3 *beta* was however used by CUNI to prepare meteorological fields for coupling with chemical model CAMx for air quality studies in Work Package 7 of the CECILIA project (see Huszar et al. [11] for details).

TABLE 1: CECILIA RCM-GCM setup.

Partner	Regional model	Acronym	Horizontal resolution	Domain size [points and vertical levels]	Boundary forcing (GCM)
CUNI	RegCM3 <i>alpha</i>	Ra	10 km	184 × 164 × 23	RegCM3 @ 25 km (ECHAM5)
CHMI	ALADIN-Climate/CZ	Az	10 km	160 × 102 × 43	ARPEGE-CLIMAT
ELU	RegCM3 <i>beta</i>	Rb	10 km	120 × 100 × 18	RegCM3 @ 25 km (ECHAM5)
NIMH	ALADIN-Climate	A2	10 km	105 × 80 × 31	ARPEGE-CLIMAT
NMA	RegCM3 <i>beta</i>	Rb2	10 km	156 × 102 × 18	RegCM3 @ 25 km (ECHAM5)
OMSZ	ALADIN-Climate	A	10 km	108 × 72 × 31	ARPEGE-CLIMAT

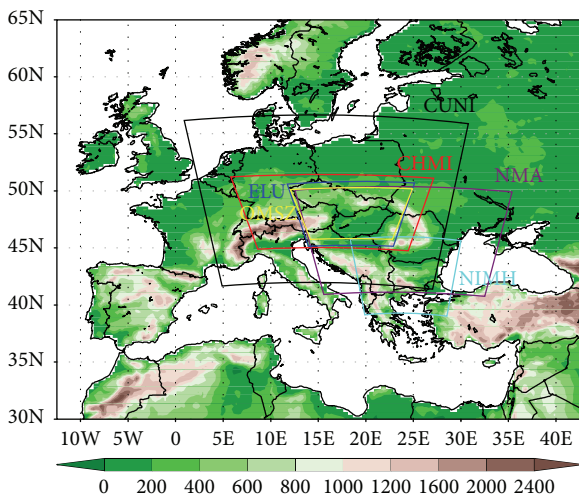


FIGURE 1: Integration domains of CECILIA simulations; shading: orography from E-OBS (0.25 deg).

Four areas were identified for which the RCM simulations were performed: Central Europe (CHMI, CUNI), Carpathian Basin (OMSZ, ELU), Romania and Black Sea (NMA), and Bulgaria (NIMH). For the climate change projections, all partners were obliged to run the models for three time slices: 1961–1990 (present climate control run, CTL), 2021–2050 (near future run, NF), and 2071–2100 (far future run, FF). All future simulations were carried out using CO₂ concentrations as described by the IPCC A1B scenario [25]. This scenario was the only possible choice due to the fact that the driving ENSEMBLES simulations were conducted for A1B scenario only.

3. Climate Projections

The following text analyses basic climate properties in the regional climate simulations of CECILIA models with focus on average precipitation and 2 m temperature. Main features of these variables in terms of yearly averages were analysed in three regions: composite of all model domains in CECILIA (i.e., in areas where at least one model simulation can be evaluated, used in Figures 2 and 9), Central European part of the domain (longitude: 10–24, latitude: 45.5–51.5, covered by simulations of CUNI, CHMI, ELU, and OMSZ), and the

region in Bulgaria and Romania where the modeled domains of NIMH and NMA overlap (lon.: 21–28.5, lat.: 43–45.5). The results for each simulation were first interpolated to a common regular grid and then averaged separately for ALADIN and RegCM models giving two sets of results referred to as Aladin set and RegCM set. No weighting of models was applied for the calculation of averages. All of the analyses were carried out using only those grid points from the inner modeling domains; that is, grid points from the boundary zone were discarded first.

For both 2 m temperature and precipitation, we show first overall change of the respective variable between control period and future periods as the difference in 30-year averages over the common area. Changes in the seasonal average values are discussed in more detail showing the correspondence between high resolution regional models and their driving fields. Results of CECILIA models are compared with the simulations of ICTP and CNRM that were used as driving fields for CECILIA simulations along with the average of 14 model runs from the ENSEMBLES project as a reference [26]. From the total number of 25 ENSEMBLES regional simulations, only those that were available for both near and far future periods were used for comparison.

Seasonal values were calculated as country averages. Five countries were picked, Czech Republic, Slovakia, Hungary, Romania, and Bulgaria, for which the values were computed by averaging values in the grid points covered by the respective country area. Regions of Slovakia and Hungary were covered by five modeling groups (CHMI, CUNI, ELU, OMSZ, and NMA); Czech Republic was covered by four groups (CHMI, CUNI, ELU, and OMSZ). Countries from the Eastern European part of the area, Romania and Bulgaria, were each included only in the modeling domain of their respective WP2 partner, NMA and NIMH.

3.1. Climate Response for 2 m Temperature. Annual 2 m temperature changes as represented in scenario runs of CECILIA models are shown in Figure 2. Both Aladin and RegCM set of the models agree in the basic features: warming up to 3°C in near future and between +2 and +5°C in far future. The spatial pattern of the changes is consistent with warming values increasing in the southeastern direction. In general, the warming is stronger in Aladin model set in all domain parts.

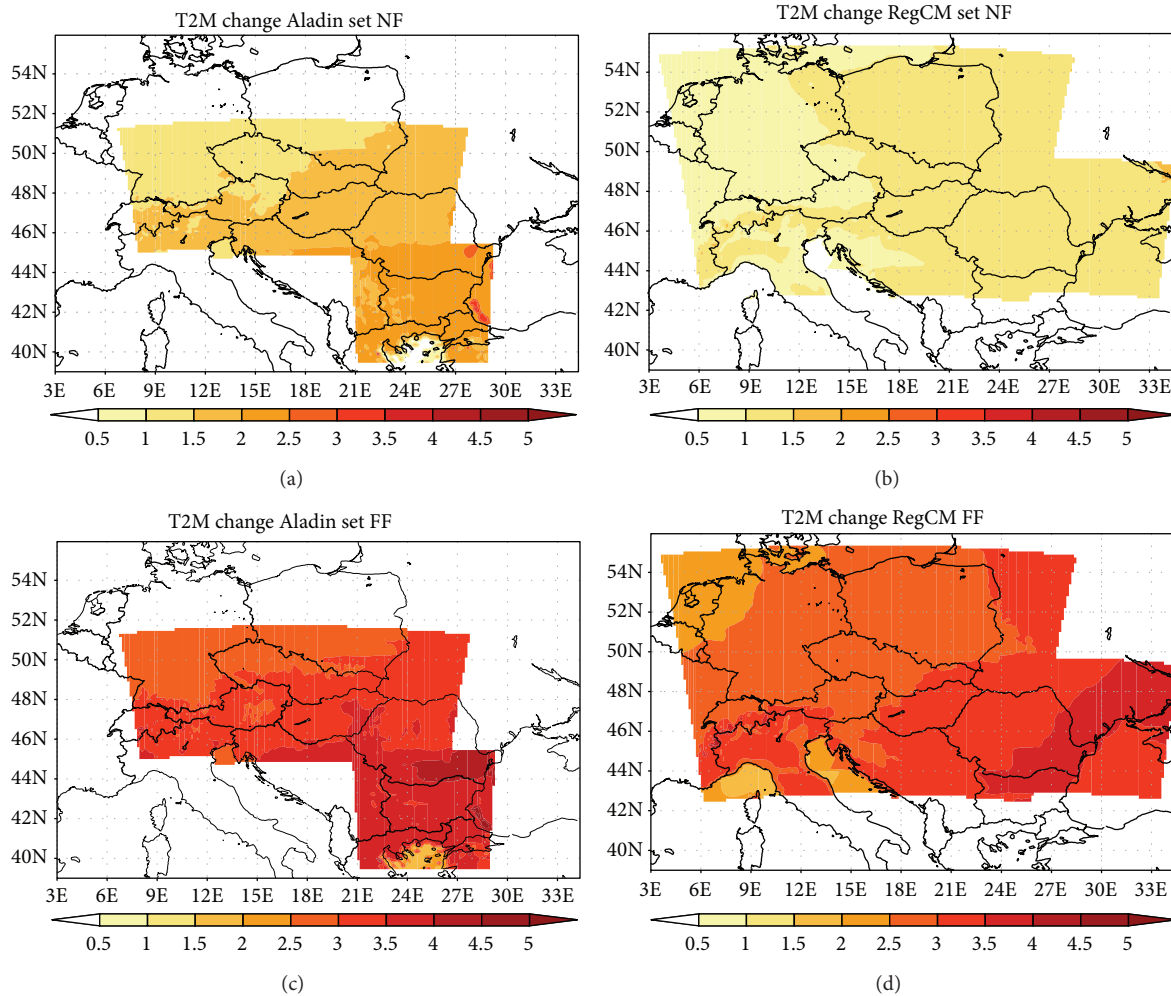


FIGURE 2: Change in annual 2 m temperature in Aladin (a, c) and RegCM (b, d) set between 2021–2050 and 1961–1990 (a, b) and 2071–2100 and 1961–1990 (c, d). Units are °C.

Changes of seasonal 2 m temperature in near future lie within the range between 0 and +3°C (Figures 3, 4, 5, 6, and 7, left). Aladin models give higher rise in temperature than RegCM models in summer and fall season. In winter and spring, there is small difference between model sets. In all analysed countries, RegCM models usually preserve the interseasonal structure of their driving fields with the highest values in spring and winter and the smallest in summer. In autumn, the response is weaker in RegCM models, while the driving ICTP model gives the strongest response. Aladin models agree with the warming present in their driving Arpege model except for summer when the response in the high resolution Aladin is stronger over Hungary, Slovakia, and Bulgaria.

In the far future time slice (Figures 3–7, right), this behaviour is even more pronounced. Warming present in the high resolution RegCM models is very similar to the response in their driving ICTP model with the values between +2.5

and +3.5°C. For countries in the northern part of the domain (Czech Rep. and Slovakia), the temperature increase is the highest in winter; in southern countries (Hungary, Romania), the highest increase occurs in summer season. Aladin models tend to give higher increase in temperature than the global Arpege model in all seasons except winter. In winter, Aladin models show lower response than RegCM models.

While the models generally agree on the spatial structure of mean changes, there is quite significant difference in the representation of changes in interannual variability, shown in Figure 8 as interannual standard deviation of seasonal temperature. During summer months, there is a consistent signal of increased variability in all parts of the domain. Other seasons exhibit much larger spread between model sets and time slice. RegCM models tend to prefer bipolar structure with increased variability in the southern part and decreased (or not changed) variability in the northern part of the domain.

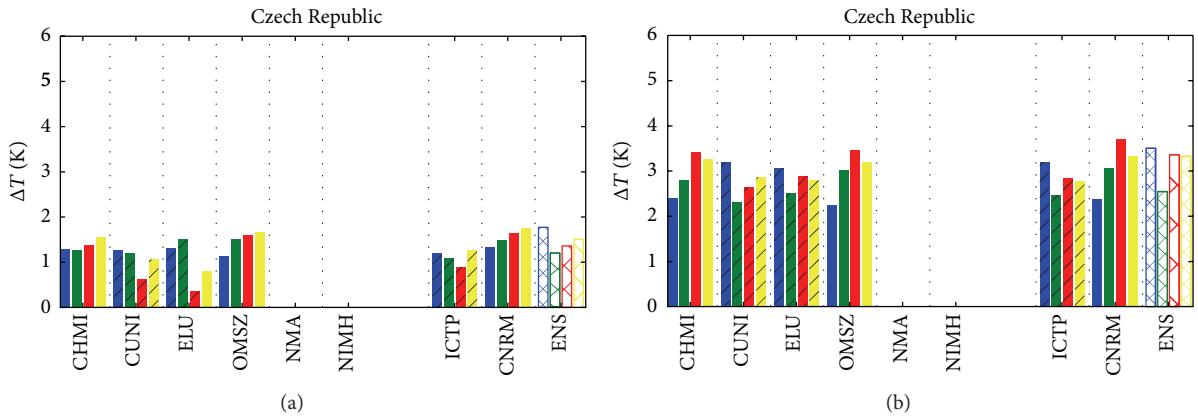


FIGURE 3: Change in 2 m temperature over Czech Republic between 2021–2050 and 1961–1990 (a) and 2071–2100 and 1961–1990 (b); blue = DJF, green = MAM, red = JJA, yellow = SON, hatched = RegCM-ECHAM couple, plain = Aladin-Arpege couple, and ENS = average of 14 ENSEMBLES models.

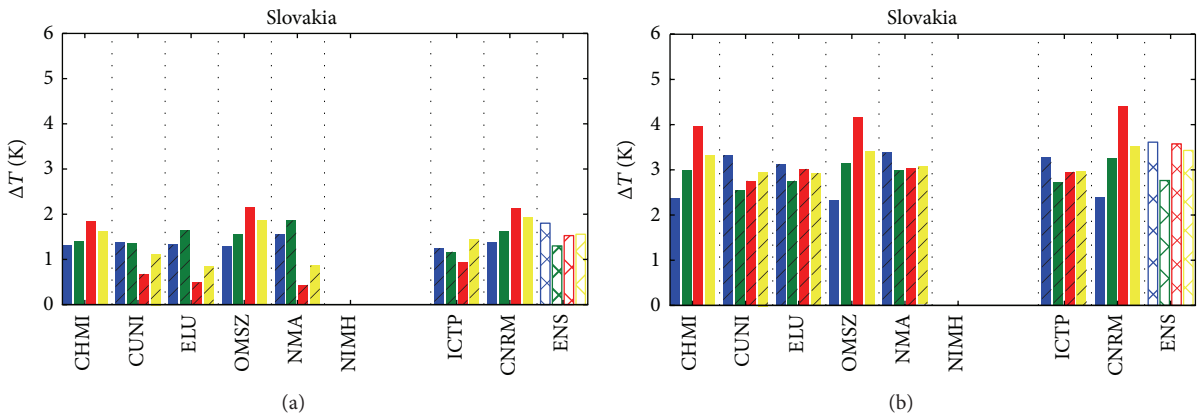


FIGURE 4: As Figure 3 for Slovakia.

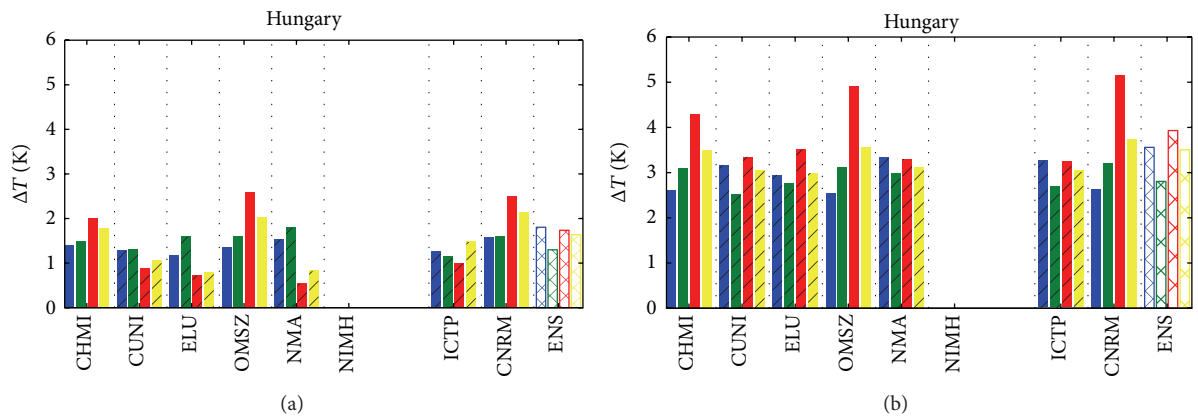


FIGURE 5: As Figure 3 for Hungary.

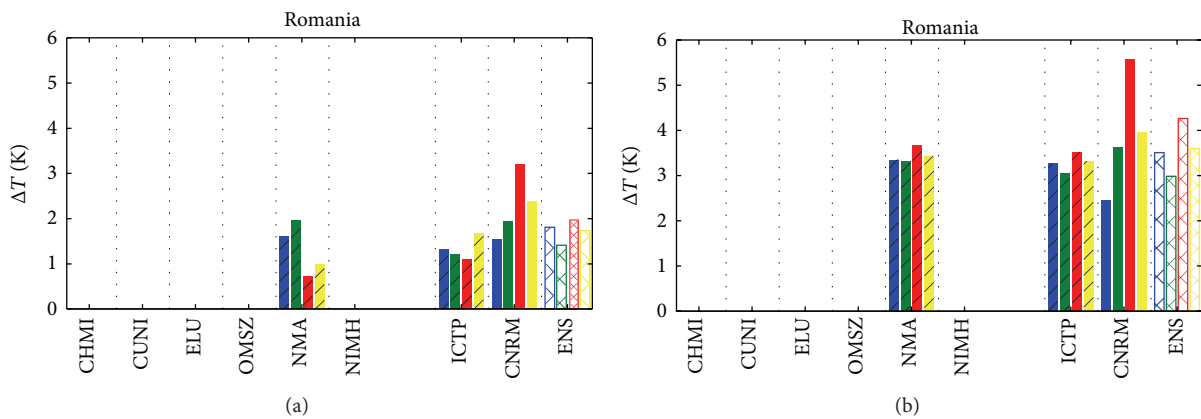


FIGURE 6: As Figure 3 for Romania.

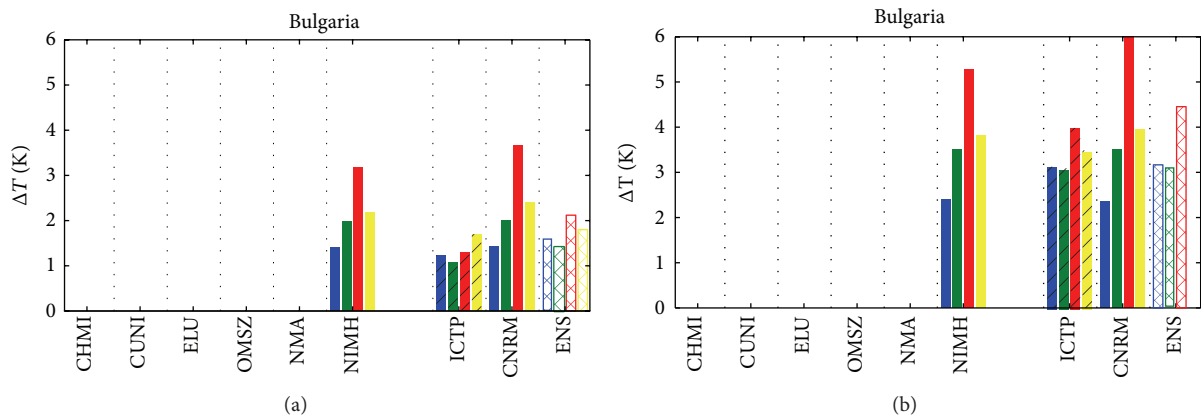


FIGURE 7: As Figure 3 for Bulgaria.

3.2. Climate Response for Precipitation. Changes in precipitation are more varied between models and integration domains. Overall pattern of total precipitation (Figure 9) present in both model sets is that of small changes (between -0.25 and $+0.25$ mm/day) with significant decrease in mountainous areas (RegCM) and near domain borders (Aladin) where the modelled precipitation exhibits large biases.

During individual seasons, RegCM models generally copy the patterns present in the driving ICTP simulation. This pattern is characterised by small increase in precipitation (up to 0.3 mm/day) in winter, summer, and autumn and decrease (up to -0.3 mm/day) in spring in the near future time slice (Figures 10, 11, 12, 13, and 14, left). Over Hungary and Slovakia, the ELU simulation changes the sign of the response, giving small decrease in winter and autumn (around -0.2 mm/day). In near future, Aladin simulations mostly decrease precipitation in winter with values ranging from -0.1 mm/day to -0.3 mm/day and increase precipitation up to 0.25 mm/day in other seasons. The exceptions are OMSZ simulation over Hungary which decreases precipitation in summer and Bulgaria where NIMH simulation gives decrease in all seasons except autumn.

For the late 21st century period (Figures 10–14, right), the response is generally higher in absolute values. All RegCM models agree on increasing precipitation in winter and autumn (0.15 – 0.76 mm/day) and decreasing it in summer (up to -0.45 mm/day) with the exception of ELU simulation showing almost no change in autumn over Slovakia and NMA simulation that gives slight increase in summer over Hungary. Spring precipitation is increased over Czech Republic, decreased over Hungary, decreased over Slovakia by ELU and NMA simulations, and increased by CUNI simulation. Aladin models are consistently decreasing precipitation in summer (up to -0.84 mm/day) and slightly in winter (up to -0.1 mm/day). In spring, the precipitation is increased over Czech Republic, Slovakia, and Hungary and decreased over Bulgaria. Autumn precipitation is mostly slightly decreased except for Hungary and Czech Republic.

As a measure of interannual variability for precipitation, coefficient of variation was adopted after [27]. Figure 15 shows changes of variability in seasons. The signal is not very strong; only in summer and autumn season a tendency towards higher variability in eastern part of the domain can be identified. The highest increase, though, is again present

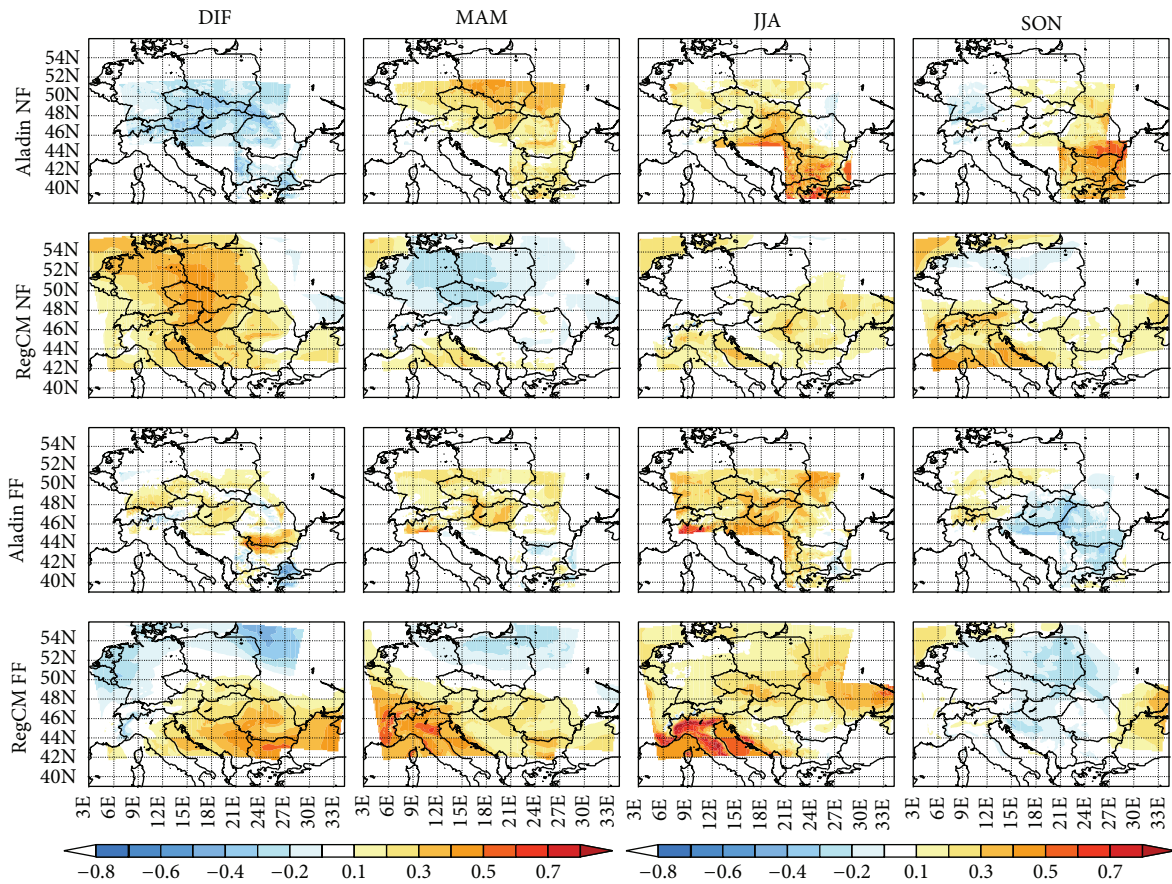


FIGURE 8: Change in 2 m temperature interannual standard deviation. Units are °C.

in the border parts of the domain, which may indicate a nonphysical cause of such behaviour.

From previous analyses (e.g., [14]), the RegCM *alpha* simulations forced by ERA40 are known to have large bias in precipitation (up to 200% in some cases). The same situation occurs in case of ECHAM forced runs and is evident from Figures 16, 17, and 18. Precipitation simulated from the RegCM model set is systematically higher by around +0.5 mm/day in the Central European part of the domain where CUNI simulations made with the *alpha* version of RegCM model are present. In the southeastern area, where only RegCM *beta* simulations of NMA are available, there is only small difference between Aladin and RegCM results. This fact raises a question of reliability of the future period simulations performed by RegCM *alpha* model. Strictly speaking, poor performance of the model in the “perfect-boundary” conditions renders the results of GCM-forced simulation less credible. However, we argue that, considering the consistency of future response between *alpha* and *beta* version, the results of RegCM *alpha* are applicable for climate change assessment and after applying proper statistical processing methods even for impact studies.

4. Summary and Conclusions

In this paper, we presented basic properties of climate change scenarios downscaled by high resolution regional climate models for the area of Central and Eastern Europe under the IPCC A1B scenario. Regional models used were RegCM3 and ALADIN-Climate forced by lateral boundary conditions from global models ECHAM and ARPEGE-CLIMAT, respectively. Periods simulated were 2021–2050 (near future) and 2071–2100 (far future) with the reference period 1961–1990. Climate response for 2 m temperature and precipitation was analysed in terms of annual and seasonal mean change and interannual variability.

Both models show the same general features: warming between 0 and 3°C in near future and 2 and 5°C in far future with least warming in the northwestern part of the domain increasing towards the southeast. The seasonal values are more varied between model sets, with RegCM3 having more consistent results with its forcing model. This behaviour is persistent in all analyses and can be partly attributed to the fact that ALADIN-Climate uses boundary conditions directly from global ARPEGE-CLIMAT with horizontal resolution of 50 km. On the other hand, RegCM3 model is used

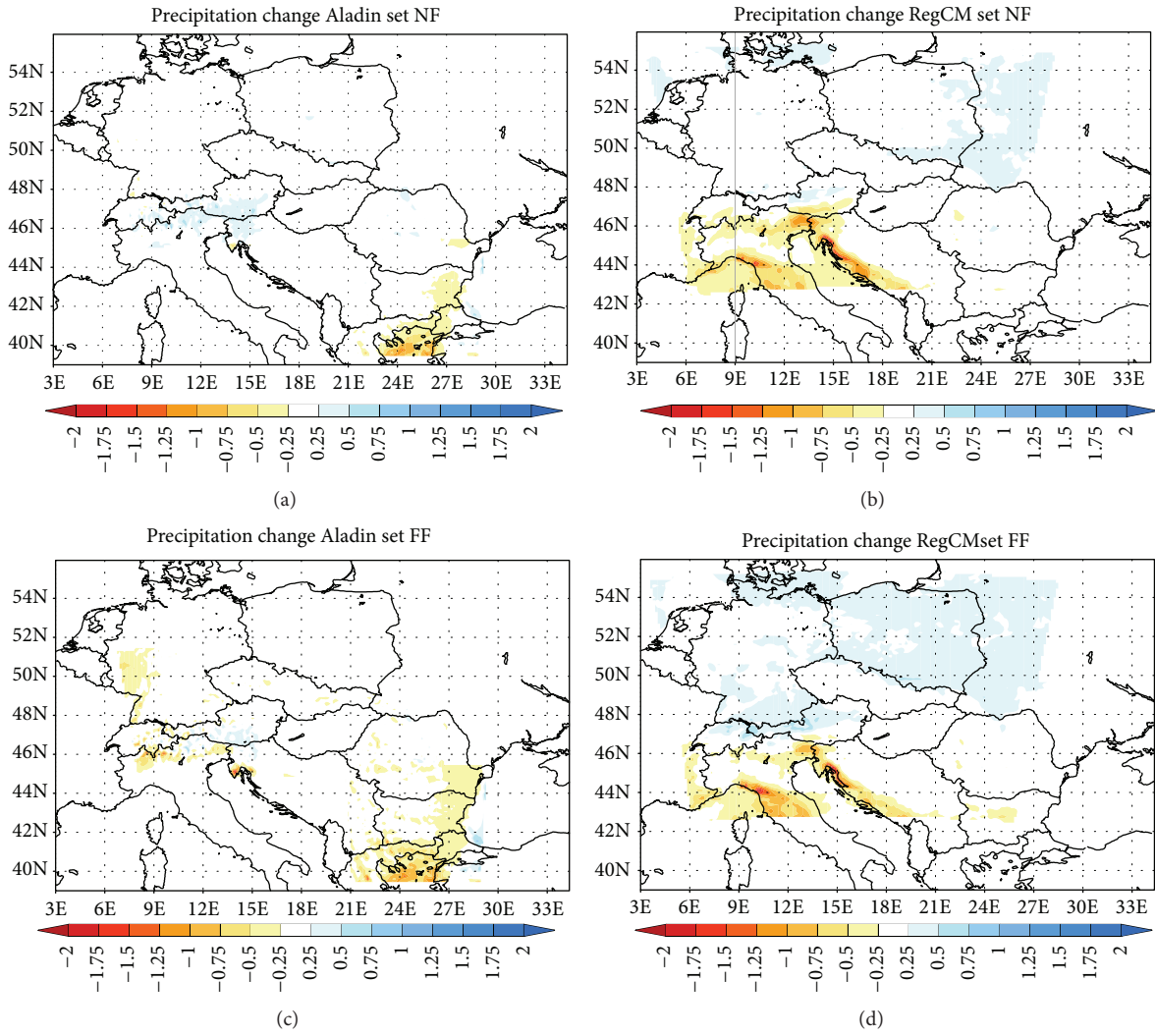


FIGURE 9: Change in total precipitation in Aladin (a, c) and RegCM (b, d) set between 2021–2050 and 1961–1990 (a, b) and 2071–2100 and 1961–1990 (c, d). Units are mm/day.

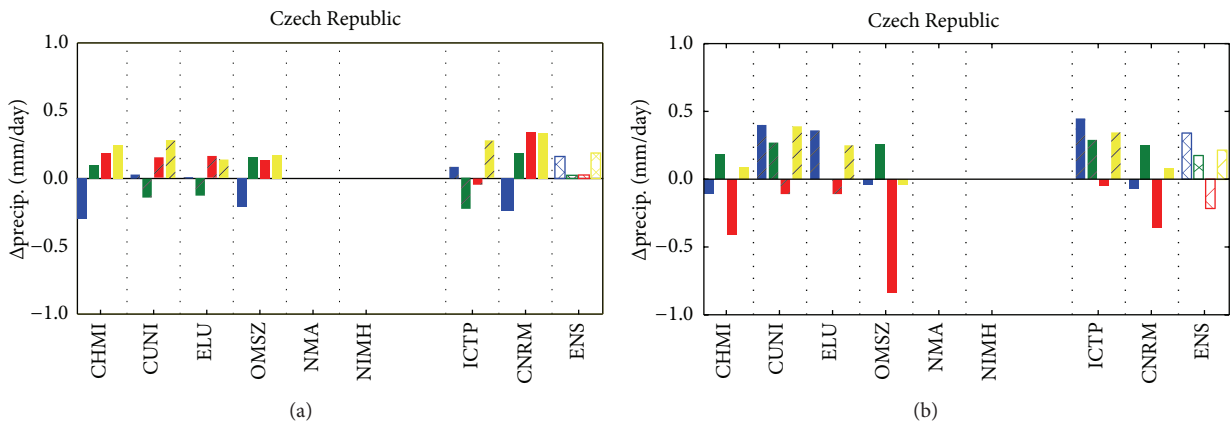


FIGURE 10: Change in total precipitation over Czech Republic between 2021–2050 and 1961–1990 (a) and 2071–2100 and 1961–1990 (b); blue = DJF, green = MAM, red = JJA, yellow = SON, hatched = RegCM-ECHAM couple, plain = Aladin-Arpege couple, and ENS = average of 14 ENSEMBLES models.

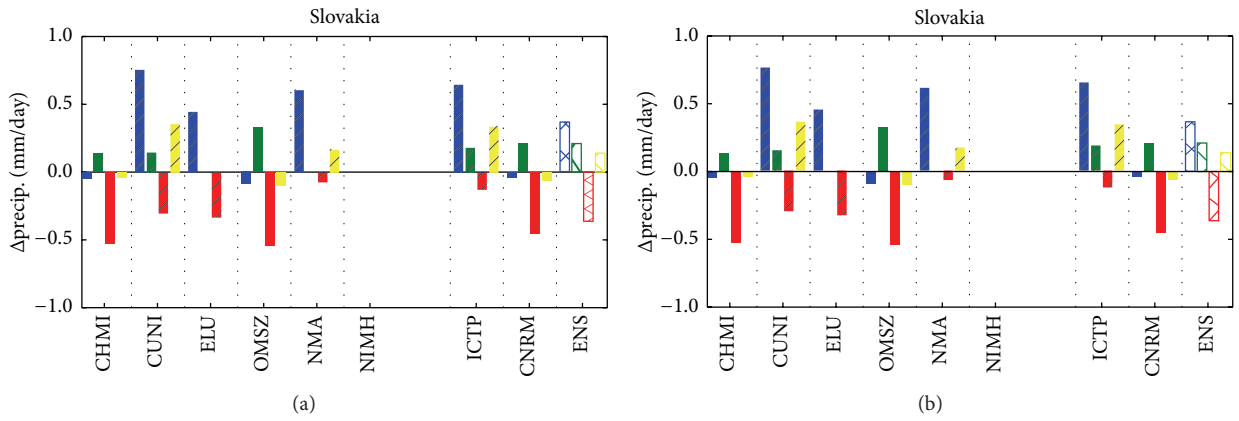


FIGURE 11: As Figure 10 for Slovakia.

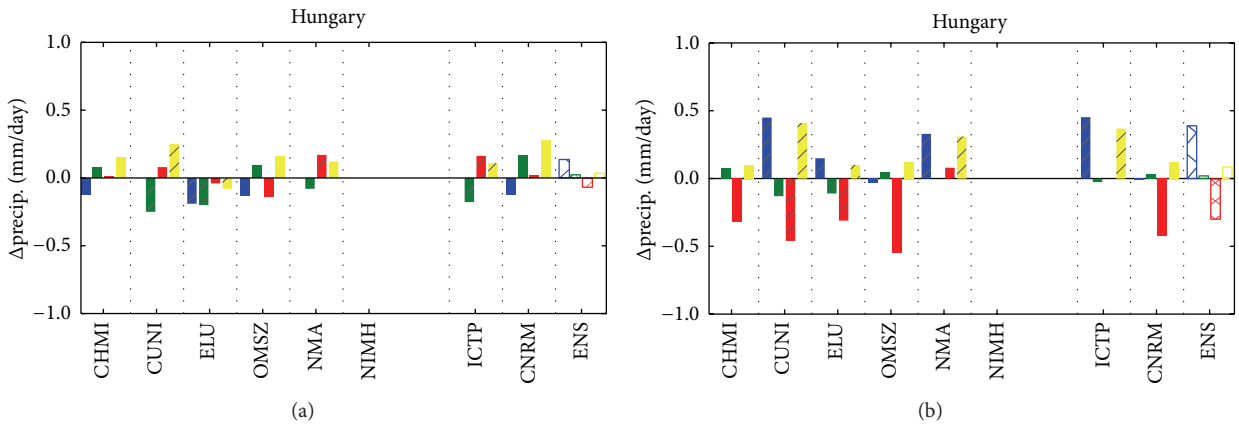


FIGURE 12: As Figure 10 for Hungary.

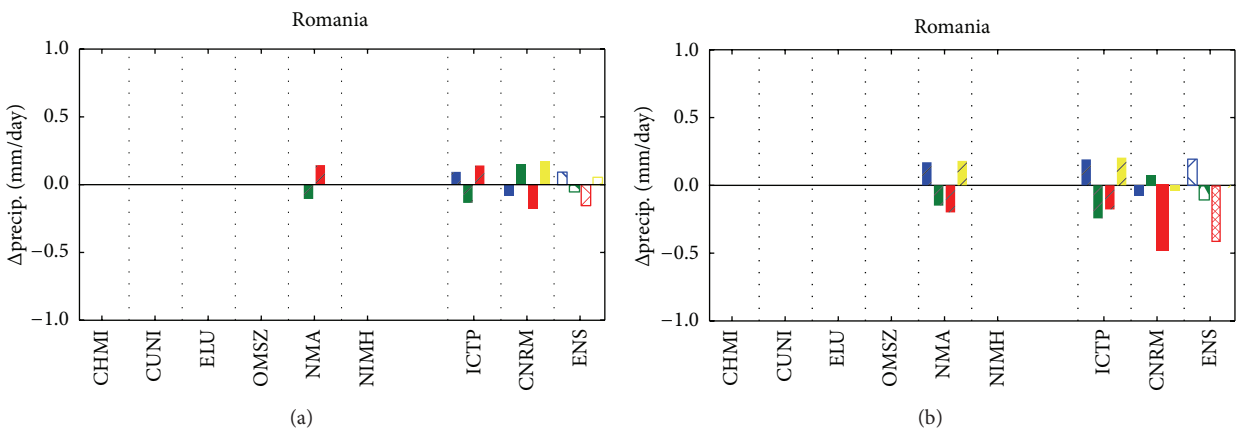


FIGURE 13: As Figure 10 for Romania.

in double-nested mode, taking boundary conditions from 25 km RegCM3 simulation forced by global ECHAM model.

Precipitation is projected to undergo very small changes in the first half of the century. The response is larger for

the end of the century with values within the range +1 to -1 mm/day. The signal is also very consistent in the high resolution simulations with the models used for driving; generally, the RegCM model family show more consistency, while

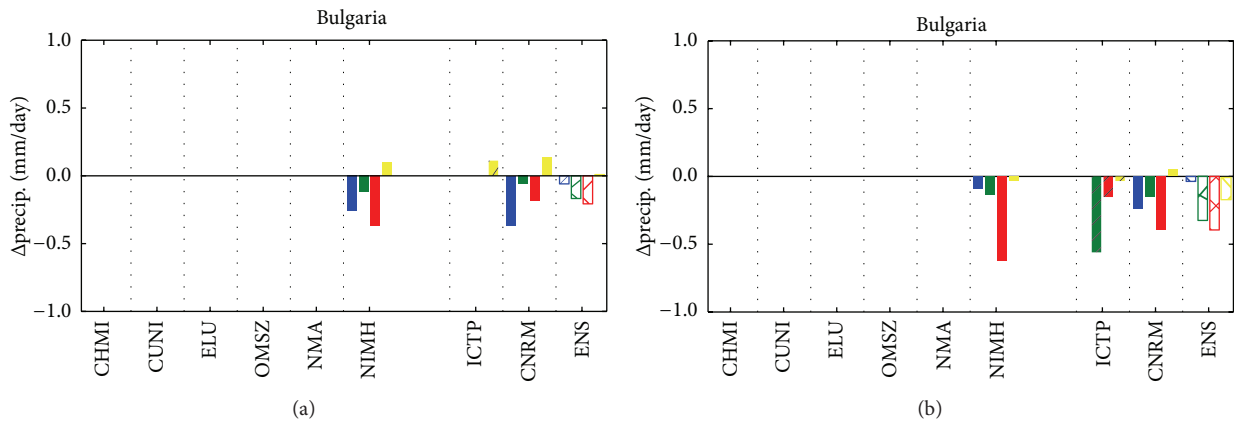


FIGURE 14: As Figure 10 for Bulgaria.

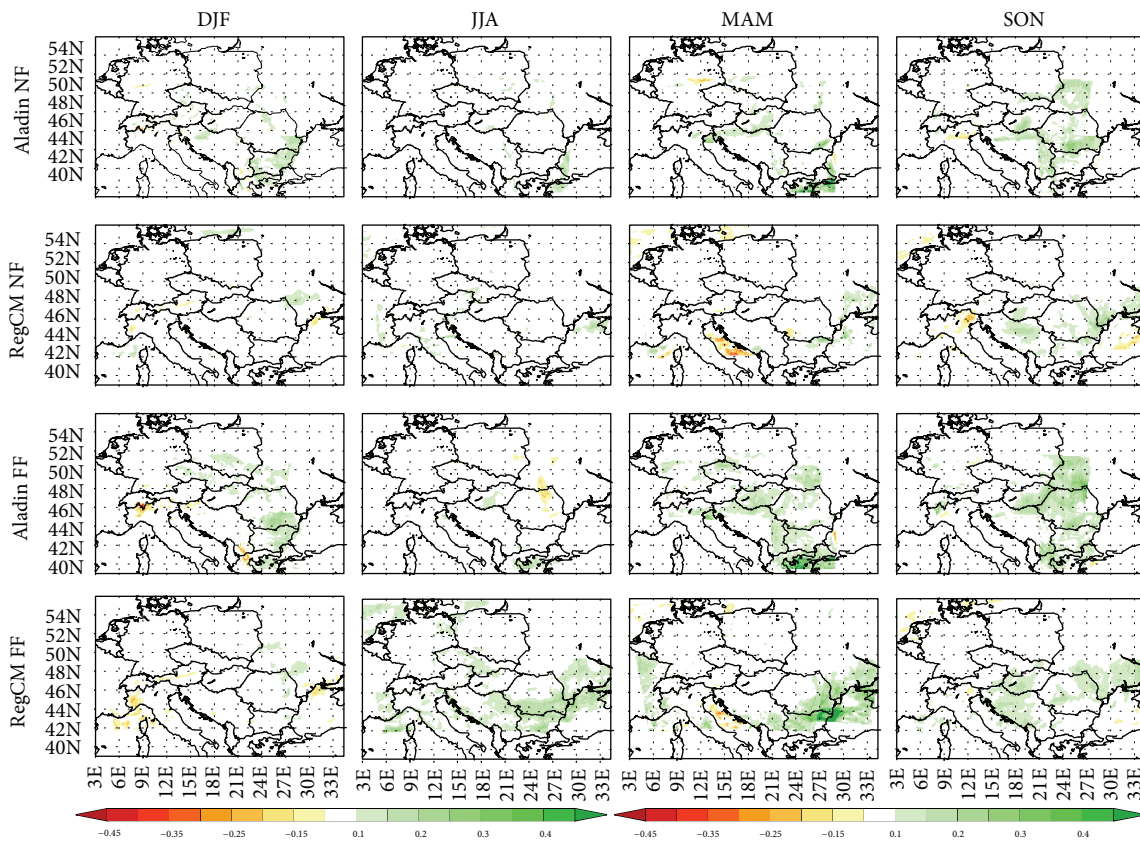


FIGURE 15: Change in precipitation interannual coefficient of variation. Units are percent.

Aladin family in some cases alter not only the magnitude of the change but also the sign.

The climate change signal present in the CECILIA simulations is comparable to previous regional-scale projections carried out within projects such as PRUDENCE or ENSEMBLES (see, e.g., [5, 28]). The high resolution models focusing on specific regions are capable of retaining the same large-scale patterns that are found in their lower resolution counterparts, while adding some local features that cannot

be identified in the driving fields. Interestingly, this added information is not confined only to regions with major orographic features but is consistent across the whole domain of interest.

The results analysed in this paper show that the modeling system employed within the CECILIA project is capable of delivering regionalized climate information beyond simple interpolation of GCM outputs. Even though the models exhibit nonnegligible biases [14], the simulations carried out

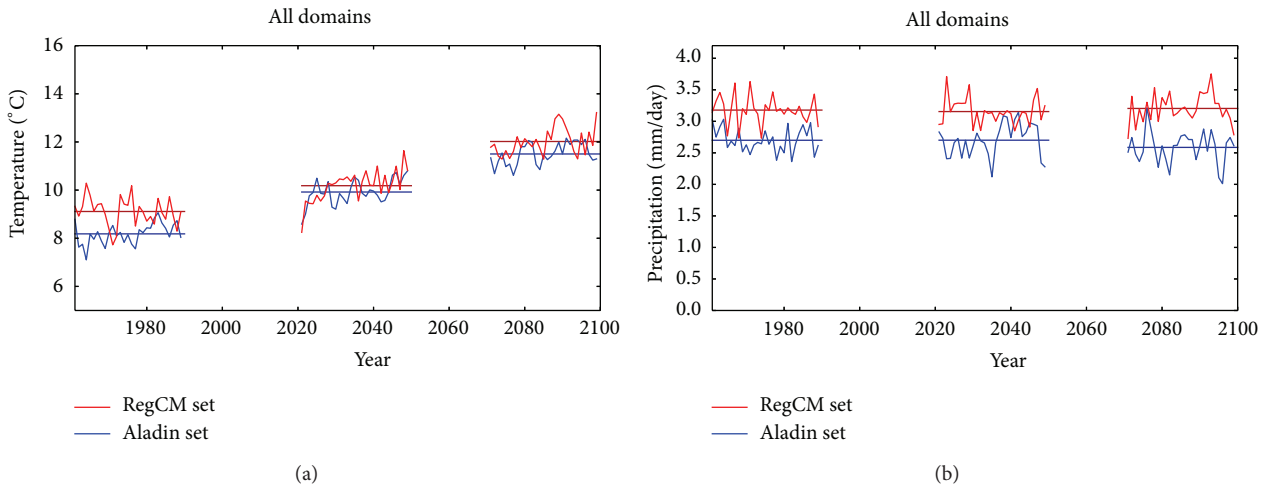


FIGURE 16: Average 2 m temperature (a) and precipitation (b) over common CECILIA domain; annual average (thin line) and 30-year average (thick line).

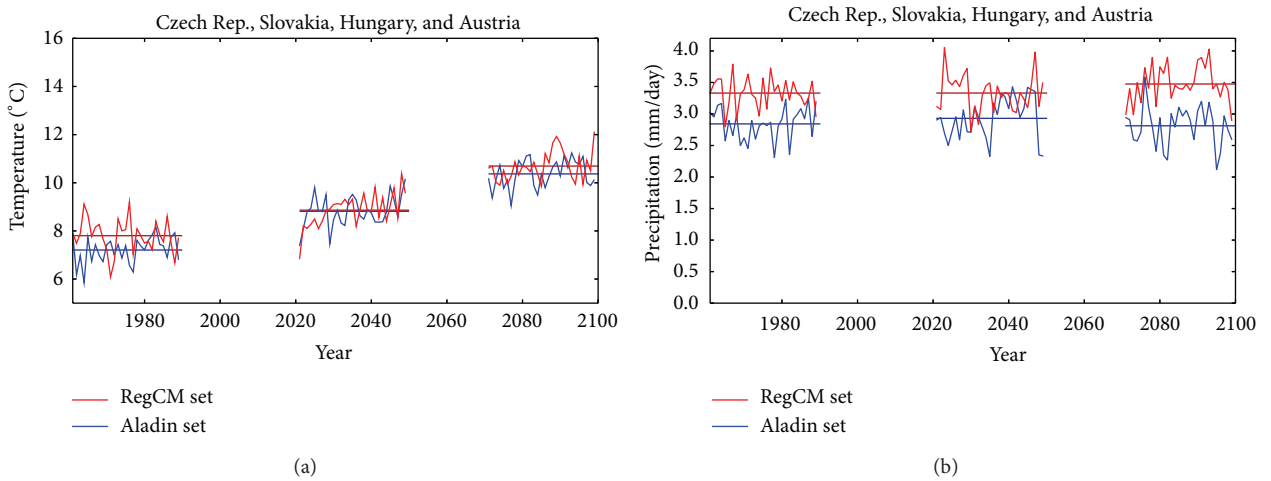


FIGURE 17: Average 2 m temperature (a) and precipitation (b) over Central Europe; annual average (thin line) and 30-year average (thick line).

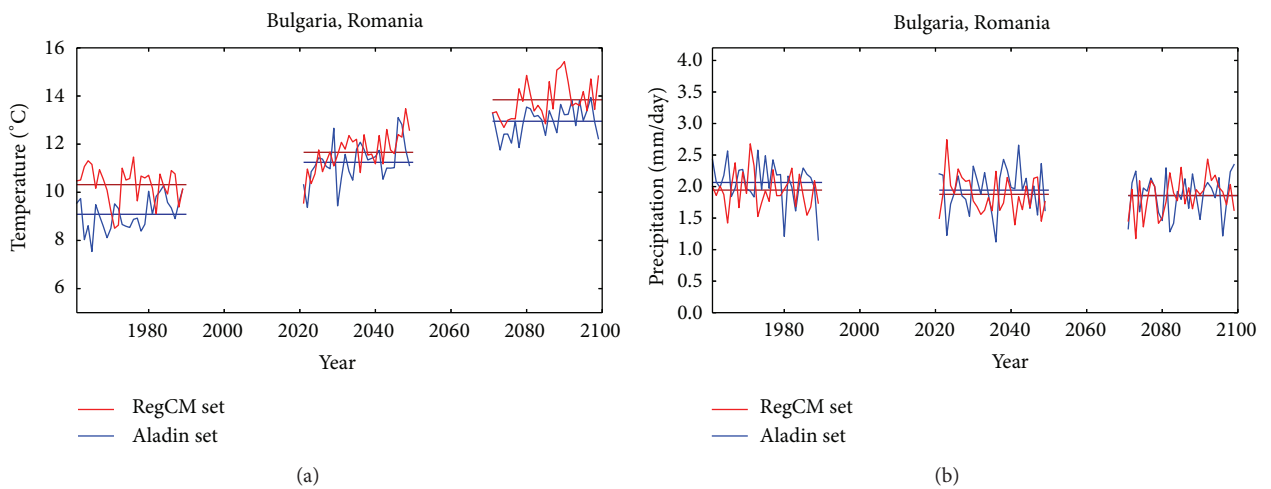


FIGURE 18: Average 2 m temperature (a) and precipitation (b) over common area of Bulgaria and Romania; annual average (thin line) and 30-year average (thick line).

provide good basis for further model development and use in climate change assessment.

Conflict of Interests

The authors declare that there is no conflict of interests regarding the publication of this paper.

Acknowledgments

This study was performed within the CECILIA project, funded by European Commission's 6th Framework Programme under Contract no. 037013. The authors also gratefully acknowledge the financial support of the following foundations and research programs: CzechGlobe Centre (CZ.1.05/1.1.00/02.0073) and projects CZ.1.07/2.3.00/20.0248 (Operational Programme of Education for Competitiveness of Ministry of Education, Youth and Sports of the Czech Republic) and P209/11/2405 (Czech Science Foundation). The authors also acknowledge the ENSEMBLES project, funded by European Commission's 6th Framework Programme through Contract GOCE-CT-2003-505539.

References

- [1] F. Giorgi and L. O. Mearns, "Approaches to the simulation of regional climate change: a review," *Reviews of Geophysics*, vol. 29, no. 2, pp. 191–216, 1991.
- [2] F. Giorgi and L. O. Mearns, "Introduction to special section: regional climate modeling revisited," *Journal of Geophysical Research*, vol. 104, pp. 6335–6352, 1999.
- [3] Intergovernmental Panel on Climate Change, *Climate Change 2013: The Physical Science Basis*, Cambridge University Press, Cambridge, UK, 2013.
- [4] J. H. Christensen, T. R. Carter, M. Rummukainen, and G. Amanatidis, "Evaluating the performance and utility of regional climate models: the PRUDENCE project," *Climatic Change*, vol. 81, no. 1, pp. 1–6, 2007.
- [5] P. van der Linden and J. F. B. Mitchell, Eds., *ENSEMBLES: Climate Change and Its Impacts: Summary of Research and Results from the ENSEMBLES Project*, Met Office Hadley Centre, London, UK, 2009.
- [6] E. Kjellstrom, G. Nikulin, U. Hansson, G. Strandberg, and A. Ullerstig, "21st century changes in the European climate: uncertainties derived from an ensemble of regional climate model simulations," *Tellus, Series A: Dynamic Meteorology and Oceanography*, vol. 63, no. 1, pp. 24–40, 2011.
- [7] E. B. Jaeger and S. I. Seneviratne, "Impact of soil moisture-atmosphere coupling on European climate extremes and trends in a regional climate model," *Climate Dynamics*, vol. 36, no. 9–10, pp. 1919–1939, 2011.
- [8] M. Hirschi, S. I. Seneviratne, V. Alexandrov et al., "Observational evidence for soil-moisture impact on hot extremes in southeastern Europe," *Nature Geoscience*, vol. 4, no. 1, pp. 17–21, 2011.
- [9] T. Halenka, "Regional climate modeling activities in CECILIA project: introduction," *Időjárás*, vol. 112, pp. III–IX, 2008.
- [10] T. Hlásny, Z. Barcza, M. Fabrika et al., "Climate change impacts on growth and carbon balance of forests in Central Europe," *Climate Research*, vol. 47, no. 3, pp. 219–236, 2011.
- [11] P. Huszar, K. Juda-Rezler, T. Halenka et al., "Effects of climate change on ozone and particulate matter over Central and Eastern Europe," *Climate Research*, vol. 50, no. 1, pp. 51–68, 2011.
- [12] K. Juda-Rezler, M. Reizer, P. Huszar et al., "Modelling the effects of climate change on air quality over Central and Eastern Europe: concept, evaluation and projections," *Climate Research*, vol. 53, no. 3, pp. 179–203, 2012.
- [13] D. Jacob, L. Kotova, P. Lorenz, C. Moseley, and S. Pfeifer, "Regional climate modeling activities in relation to CLAVIER project," *Időjárás*, vol. 112, pp. 141–153, 2008.
- [14] P. Skalák, M. Déqué, M. Belda et al., "CECILIA regional climate simulations for the present climate: validation and inter-comparison," *Climate Research*, vol. 60, no. 1, pp. 1–12, 2014.
- [15] P. Skalák, P. Štěpánek, and A. Farda, "Validation of ALADIN-Climate/CZ for present climate (1961–1990) over the Czech Republic," *Időjárás*, vol. 112, pp. 191–202, 2008.
- [16] G. Csima and A. Horányi, "Validation of the ALADIN-Climate regional climate model at the Hungarian Meteorological Service," *Időjárás*, vol. 112, pp. 155–178, 2008.
- [17] E. B. Jaeger, I. Anders, D. Lüthi, B. Rockel, C. Schär, and S. I. Seneviratne, "Analysis of ERA 40-driven CLM simulations for Europe," *Meteorologische Zeitschrift*, vol. 17, no. 4, pp. 349–367, 2008.
- [18] C. Meissner, G. Schädler, H.-J. Panitz, H. Feldmann, and C. Kottmeier, "High-resolution sensitivity studies with the regional climate model COSMO-CLM," *Meteorologische Zeitschrift*, vol. 18, no. 5, pp. 543–557, 2009.
- [19] S. A. Rauscher, E. Coppola, C. Piani, and F. Giorgi, "Resolution effects on regional climate model simulations of seasonal precipitation over Europe," *Climate Dynamics*, vol. 35, no. 4, pp. 685–711, 2010.
- [20] A. Farda, M. Déqué, S. Somot, A. Horányi, V. Spiridonov, and H. Tóth, "Model ALADIN as regional climate model for Central and Eastern Europe," *Studia Geophysica et Geodaetica*, vol. 54, no. 2, pp. 313–332, 2010.
- [21] J. S. Pal, F. Giorgi, X. Bi et al., "Regional climate modeling for the developing world: the ICTP RegCM3 and RegCM3," *Bulletin of the American Meteorological Society*, vol. 88, no. 9, pp. 1395–1409, 2007.
- [22] M. Déqué, "Frequency of precipitation and temperature extremes over France in an anthropogenic scenario: model results and statistical correction according to observed values," *Global and Planetary Change*, vol. 57, no. 1–2, pp. 16–26, 2007.
- [23] C. Torma, J. Bartholy, R. Pongrácz, Z. Barcza, E. Coppola, and F. Giorgi, "Adaptation of the RegCM3 climate model for the Carpathian Basin," *Időjárás*, vol. 112, pp. 233–247, 2008.
- [24] C. Torma, E. Coppola, F. Giorgi, J. Bartholy, and R. Pongrácz, "Validation of a high-resolution version of the regional climate model RegCM3 over the Carpathian basin," *Journal of Hydrometeorology*, vol. 12, no. 1, pp. 84–100, 2011.
- [25] N. Nakicenovic, *Intergovernmental Panel on Climate Change: Emission Scenarios, a Special Report of Working Group III of the Intergovernmental Panel on Climate Change*, Cambridge University Press, Cambridge, UK, 2000.
- [26] J. H. Christensen, M. Rummukainen, and G. Lenderink, "Formulation of very-high-resolution regional climate model ensembles for Europe," in *ENSEMBLES: Climate Change and its Impacts: Summary of Research and Results from the ENSEMBLES Project*, pp. 47–58, Met Office Hadley Centre, Exeter, UK, 2009.

- [27] F. Giorgi, X. Bi, and J. Pal, "Mean, interannual variability and trends in a regional climate change experiment over Europe. II: climate change scenarios (2071–2100)," *Climate Dynamics*, vol. 23, no. 7-8, pp. 839–858, 2004.
- [28] J. Bartholy, R. Pongrácz, G. Gelybó, and P. Szépszó, "Analysis of expected climate change in the Carpathian Basin using the PRUDENCE results," *Időjárás*, vol. 112, pp. 249–264, 2008.



Regional climate downscaling over Europe: perspectives from the EURO-CORDEX community

Daniela Jacob¹ · Claas Teichmann¹ · Stefan Sobolowski² · Eleni Katragkou³ · Ivonne Anders⁴ · Michal Belda⁵ · Rasmus Benestad⁶ · Fredrik Boberg⁷ · Erasmo Buonomo^{8,9} · Rita M. Cardoso¹⁰ · Ana Casanueva¹¹ · Ole B. Christensen⁷ · Jens Hesselbjerg Christensen^{2,12} · Erika Coppola¹³ · Lesley De Cruz¹⁴ · Edouard L. Davin¹⁵ · Andreas Dobler⁶ · Marta Domínguez¹⁶ · Rowan Fealy¹⁷ · Jesus Fernandez¹¹ · Miguel Angel Gaertner¹⁸ · Markel García-Díez¹¹ · Filippo Giorgi¹³ · Andreas Gobiet⁴ · Klaus Goergen^{19,20} · Juan José Gómez-Navarro²¹ · Juan Jesús González Alemán¹⁸ · Claudia Gutiérrez¹⁸ · José M. Gutiérrez²² · Ivan Güttler²³ · Andreas Haensler¹ · Tomáš Halenka⁵ · Sonia Jerez²¹ · Pedro Jiménez-Guerrero²¹ · Richard G. Jones⁸ · Klaus Keuler²⁴ · Erik Kjellström²⁵ · Sebastian Knist^{20,26} · Sven Kotlarski²⁷ · Douglas Maraun²⁸ · Erik van Meijgaard²⁹ · Paola Mercogliano^{30,31} · Juan Pedro Montávez²¹ · Antonio Navarra³⁰ · Grigory Nikulin²⁵ · Nathalie de Noblet-Ducoudré³² · Hans-Juergen Panitz³³ · Susanne Pfeifer¹ · Marie Piazza²⁸ · Emanuela Pichelli¹³ · Joni-Pekka Pietikäinen^{1,34} · Andreas F. Prein³⁵ · Swantje Preuschmann¹ · Diana Rechid¹ · Burkhardt Rockel³⁶ · Raquel Romera¹⁷ · Enrique Sánchez¹⁷ · Kevin Sieck¹ · Pedro M. M. Soares¹⁰ · Samuel Somot³⁷ · Lidija Srnc²³ · Silje Lund Sørland¹⁵ · Piet Termonia^{14,38} · Heimo Truhetz²⁸ · Robert Vautard³² · Kirsten Warrach-Sagi³⁹ · Volker Wulfmeyer³⁹

Received: 17 May 2019 / Accepted: 13 November 2019 / Published online: 23 April 2020
© The Author(s) 2020

Abstract

The European CORDEX (EURO-CORDEX) initiative is a large voluntary effort that seeks to advance regional climate and Earth system science in Europe. As part of the World Climate Research Programme (WCRP) - Coordinated Regional Downscaling Experiment (CORDEX), it shares the broader goals of providing a model evaluation and climate projection framework and improving communication with both the General Circulation Model (GCM) and climate data user communities. EURO-CORDEX oversees the design and coordination of ongoing ensembles of regional climate projections of unprecedented size and resolution (0.11° EUR-11 and 0.44° EUR-44 domains). Additionally, the inclusion of empirical-statistical downscaling allows investigation of much larger multi-model ensembles. These complementary approaches provide a foundation for scientific studies within the climate research community and others. The value of the EURO-CORDEX ensemble is shown via numerous peer-reviewed studies and its use in the development of climate services. Evaluations of the EUR-44 and EUR-11 ensembles also show the benefits of higher resolution. However, significant challenges remain. To further advance scientific understanding, two flagship pilot studies (FPS) were initiated. The first investigates local-regional phenomena at convection-permitting scales over central Europe and the Mediterranean in collaboration with the Med-CORDEX community. The second investigates the impacts of land cover changes on European climate across spatial and temporal scales. Over the coming years, the EURO-CORDEX community looks forward to closer collaboration with other communities, new advances, supporting international initiatives such as the IPCC reports, and continuing to provide the basis for research on regional climate impacts and adaptation in Europe.

Keywords EURO-CORDEX · CORDEX · Climate change · Regional climate models · Regional climate modelling

✉ Daniela Jacob
daniela.jacob@hzg.de

Extended author information available on the last page of the article.

Introduction

The World Climate Research Programme (WCRP) established the Task Force for Regional Climate Downscaling (TFRCDD) in 2009, which created the Coordinated Regional

climate Downscaling Experiment (CORDEX) initiative to advance and coordinate the science and application of regional climate downscaling through global partnerships (Giorgi et al. 2009). The major goals of CORDEX are as follows: (i) to better understand relevant regional/local climate phenomena, their variability and changes, through downscaling, (ii) to evaluate and improve regional climate downscaling models and techniques, (iii) to produce coordinated sets of regional downscaled projections worldwide, and (iv) to foster communication and knowledge exchange with users of regional climate information. Working towards these goals also helps address WCRP Grand Challenges such as: Water for the food baskets of the world, Clouds circulation and climate sensitivity, Weather and climate extremes, Carbon feedbacks in the climate system, Melting ice and global consequences, and Regional sea-level change and coastal impacts. CORDEX was recently added as a major project under the WCRP auspices and is also included as a diagnostic Model Intercomparison Project (MIP) in CMIP6 (Gutowski et al. 2016). Each regional team can coordinate its own simulations and associated research activities. The EURO-CORDEX community, in particular, has established itself as a key contributor to CORDEX, with more than 30 modelling groups collaborating in the simulation of the European climate, across all scenarios, and making the regional climate model (RCM) data publicly available and accessible in particular via the Earth System Grid Federation (ESGF). Further, many of the groups in the EURO-CORDEX community have contributed with a wide range of simulations of regional climates in other CORDEX regions and have played an instrumental role in defining standards for the ESGF publication.

This community is organized in a way that allows both a high level of coordination as well as flexibility (e.g., dynamic structures to address emergent scientific challenges). EURO-CORDEX celebrated 10 years as an active consortium in 2019. The scientific output along with the substantial contributions to open archives (e.g., Earth System Grid Federation, <https://esgf.llnl.gov>) marks EURO-CORDEX as a success. However, Europe enjoys many financial and institutional advantages compared with other regions that should not be ignored. Despite this, there are many aspects to EURO-CORDEX's success that do not rely on these advantages but rather on the members' commitment to a strongly coordinated, organized and community-based effort. The authors hope that the lessons learned from the experience of the EURO-CORDEX community can be applied as a model for other CORDEX regions as they evolve.

EURO-CORDEX is driven by scientific challenges, aligned with the first two goals of the WCRP-CORDEX

initiative. EURO-CORDEX has made substantial progress in addressing the following specific challenges:

- Added value of regional downscaling with respect to scale, uncertainty, processes, and phenomena (Torma et al. 2015; Giorgi and Gutowski 2015; Prein and Gobiet 2016; Fantini et al. 2018; Coppola et al. 2018a; Soares and Cardoso 2017).
- Impacts of coupled processes and land-atmosphere (L-A) feedbacks in a regional context, Knist et al. (2017) and Davin et al. (2020).
- Improve the understanding of regional phenomena in a climate change context, in particular extreme weather events e.g., heat waves, storms, winds, floods, droughts, precipitation, Termonia et al. (2018) and Belušić et al. (2017) and their attribution to human activities (Stott et al. 2015; Luu et al. 2018; Philip et al. 2018; Kew et al. 2018).
- Cross cutting themes: e.g., water resources/hydrological cycle (Donnelly et al. 2017), energy-climate nexus (Jerez et al. 2015; Tobin et al. 2016; Tobin et al. 2018)

The strategic challenges confronting EURO-CORDEX are closely aligned with the goals of CORDEX mentioned above. Although progress on point (i) has been demonstrated, substantial gaps remain and EURO-CORDEX will need to address the following issues related to point (ii) over the coming years:

- Quality control: EURO-CORDEX certified process-based assessments, which seek to attribute model performance to emerging processes, e.g., conditions originating from the interaction of components of a complex system.
- Creation of climate information through
 - stronger involvement of the statistics community and “big data” analytics strategies as well as stronger engagement with programs and bodies which focus on vulnerability, impacts, adaptation and climate services (VIACS) such as GEWEX (www.gewex.org), Copernicus Climate Change Service (C3S; <https://climate.copernicus.eu>) and Future Earth (www.futureearth.org).
 - development of approaches to assess the credibility and robustness of multi-model-multi-method ensemble projections, and to synthesize these into user-relevant narratives (Benestad et al. 2017a)
- Knowledge transfer and exchange with the GCM community, in particular by contributing to the WCRP

Grand Challenges relevant for Europe and by quantifying the GCM limitations induced by simulating the climate at low resolution (Giorgi et al. 2016).

As the needs of researchers and policy makers become ever more focused on local to regional impacts and phenomena (including features such as urban environments, hydrology, vegetation, land use) so must EURO-CORDEX evolve.

This manuscript is meant to provide a brief history of EURO-CORDEX and its predecessors (“[A brief history of EURO-CORDEX](#)”), the evolution of the community and its current organization (“[Organizational structure of EURO-CORDEX](#)”), the EURO-CORDEX modelling framework (“[EURO-CORDEX modelling framework](#)”), its scientific advances to date (“[Scientific advances](#)”) and what these advances mean for the future (“[Key messages and outlook](#)”).

A brief history of EURO-CORDEX

EURO-CORDEX stems from the achievements of former EU projects on regional climate modelling such as PRUDENCE and ENSEMBLES (Christensen et al. 2007; van der Linden and Mitchell 2009). In launching the CORDEX initiative, WCRP recognized that in order to produce, maintain and continuously analyze large ensembles of regional climate simulations, a large, long-lasting and coordinated community effort is needed. Therefore the EURO-CORDEX community was formed in order to sustain and provide a structure for these activities concentrated on the European domain. As such, EURO-CORDEX has always been a voluntary, self-organized and dynamic community that can grow and evolve with the changing landscape of climate research, high-performance computing and user needs. Due to the fact that EURO-CORDEX builds on the efforts of previous projects and incorporates their lessons, it is also a role model for other CORDEX communities who are engaging in this type of effort for the first time.

Being a voluntary effort without base funding (similar to the larger CORDEX initiative and other endeavors such as CMIP), EURO-CORDEX nevertheless leverages its activities to obtain national and European funding. It also relies heavily on the enthusiasm and engagement of the participating researchers and institutions. The EURO-CORDEX consortium meets yearly in the Climate Service Center in Hamburg, Germany (GERICS). The number of registered participants from the 1st General Assembly (GA) in 2011 to the 8th GA in 2018 grew from 40 to 64, with representatives from 18 European countries (Table 1). At the first meeting, the foundation for the

activities of the upcoming years has been laid, including the modelling protocol that forms the backbone of the EURO-CORDEX ensemble. Since then, yearly meetings have provided an opportunity for presenting and discussing the major EURO-CORDEX activities and outcomes, and to decide about future plans and strategies. The EURO-CORDEX community also provided a strong contribution to the two International Conferences on Regional Climate - CORDEX (Brussels, November 2013 and Stockholm, May 2016). In preparation for the Brussels conference the EURO-CORDEX community produced a press release to announce the release of the EURO-CORDEX data (based on studies by Jacob et al. 2014 and Vautard et al. 2013) entitled “New, detailed climate projections for Europe reveal changes in extreme events and open the way for climate change impact studies.” Further research activities were discussed including the analysis of low emission scenarios, including the + 1.5 °C and + 2 °C global warming targets, which resulted in recent studies that use many EURO-CORDEX simulations to assess the impacts of these warming targets over Europe (Jacob et al. 2018; Kjellström et al. 2018; Teichmann et al. 2018). General assemblies are also an opportunity to reflect critically on the work performed and address emergent challenges.

EURO-CORDEX is conceived as both a dynamical and a statistical downscaling activity. Modelling groups focusing on dynamical downscaling are using the following regional climate modelling systems: ALADIN-Climate (Colin et al. 2010), CCLM (Böhm et al. 2006; Will et al. 2017; Rockel et al. 2008), HIRHAM (Christensen et al. 2007), RACMO (Van Meijgaard et al. 2012), RCA (Samuelsson et al. 2011), RegCM (Giorgi et al. 2012), REMO (Jacob et al. 2012, 2014), PROMES (Domínguez et al. 2010; Domínguez et al. 2013), WRF (Skamarock and Klemp 2008), and ALARO-0 (Giot et al. 2016; Termonia et al. 2018).

Modelling groups focusing on empirical statistical downscaling (ESD) employ a wide range of approaches (Benestad et al. 2017a; Maraun et al. 2015, 2018; Gutiérrez et al. 2018; Hertig et al. 2018; Soares et al. 2018; Widmann et al. 2019). The two approaches to downscaling are seen as complementary within the EURO-CORDEX community, each with its relative strengths.

Organizational structure of EURO-CORDEX

In order to evolve and adequately address emerging challenges, the EURO-CORDEX community has refined its structure during its existence. Initially, two coordinators were sufficient to manage the dynamically downscaled ensemble. However, new challenges meant that it was necessary to expand the number of coordinating members.

Table 1 EURO-CORDEX General Assembly (GA) participation and milestones

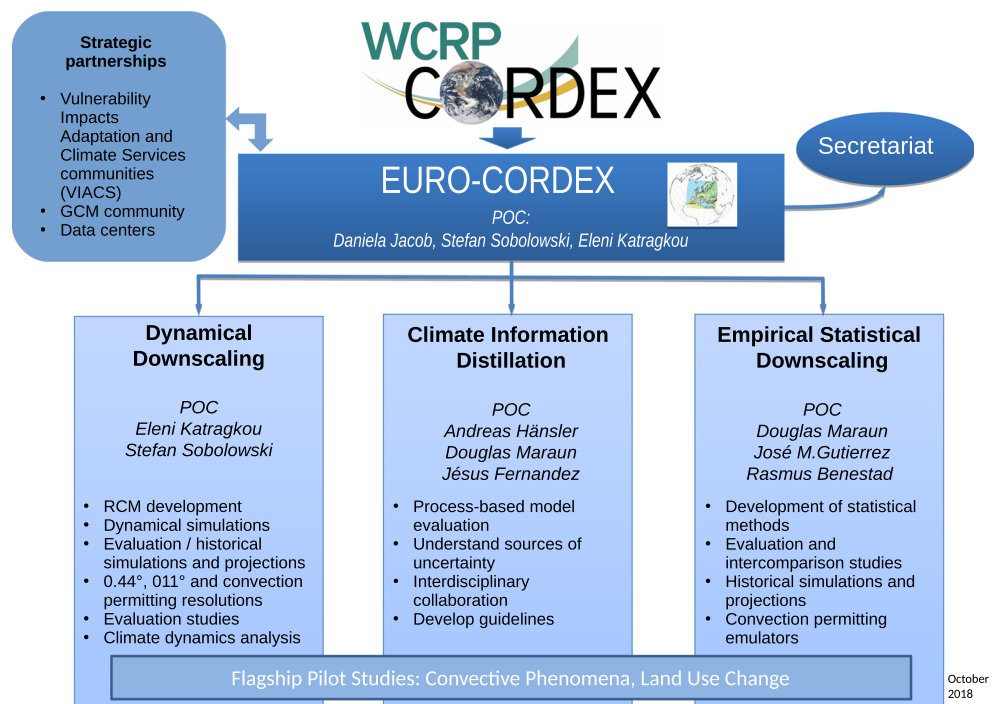
Date	General Assembly	Decisions/milestones	Participants	Countries
11/2011	First	Organize modelling and evaluation activities; create databases in ESGF format, experimental design, requirements for simulations	37	14
01/2012	Second	Collect observational datasets; application of statistical downscaling techniques	44	13
10/2013	Third	Preparation for the International CORDEX conference 2013	28	13
03/2014	Fourth	Enhance integration with impact modelling; focus on science	30	12
01/2015	Fifth	Encompass both statistical and dynamical downscaling methods; scientific focus on land use change impacts	47	13
01/2016	Sixth	New organizational structure; Prepare for 2nd EURO-CORDEX phase; FPS preparations	49	16
01/2017	Seventh	Launch of flagship pilot studies	55	17
01/2018	Eighth	Establish new research themes	64	18

The new structure, shown in Fig. 1, is an outcome of the 6th GA in 2016. There, the EURO-CORDEX community acknowledged that downscaling is achievable through different approaches, and that dynamical and statistical approaches are complementary to each other with different strengths and weaknesses. Both approaches are needed to address the challenges ahead. As a result, there are now two working groups devoted to specifically tackle

issues related to dynamical and statistical downscaling, respectively, although they interact with each other.

Further, a third working group was formed explicitly focussing on Climate Information Distillation (CID). As discussed previously, this activity emerged as the scientific community acknowledged the challenges that users face when adopting climate data in decision-making contexts. The vast amounts of data produced from multi-model

Fig. 1 Organizational structure of EURO-CORDEX based on the decision in the 6th GA. Point of contacts (POCs) are shown for each of the EURO-CORDEX pillars



ensembles with different model combinations make state-of-the-art statistical methods necessary in order to make sense of all the data, however, the statistics community has not yet been widely engaged in the analysis of the data (Benestad et al. 2017b). This activity is seen as crucial to the effective integration and collaboration between EURO-CORDEX and the VIACS/policy communities, as this is where the output of the scientific activity makes its way into decision-making. Deser et al. (2012) pointed out that GCMs produce pronounced chaotic variations on regional scales even over decades, and demonstrated that one model with slightly different initial conditions could produce a wide range of local scenarios. One important question therefore concerns the minimum size of a reliable ensemble that is not susceptible to random fluctuations and the law of small numbers (Benestad et al. 2017b). Given the multiplicity of messages, users may be inadequately prepared to incorporate state-of-the-art climate information or may make inappropriate decisions if messages from limited, non-robust, unreliable subsets of data are adopted (Fernández et al. 2019). Currently, a group of scientists is forming to tackle the issue of CID, including dynamical and statistical downscaling researchers from EURO-CORDEX, but also global climate modelers, atmospheric dynamicists, climate service providers and philosophers. Initial teleconferences

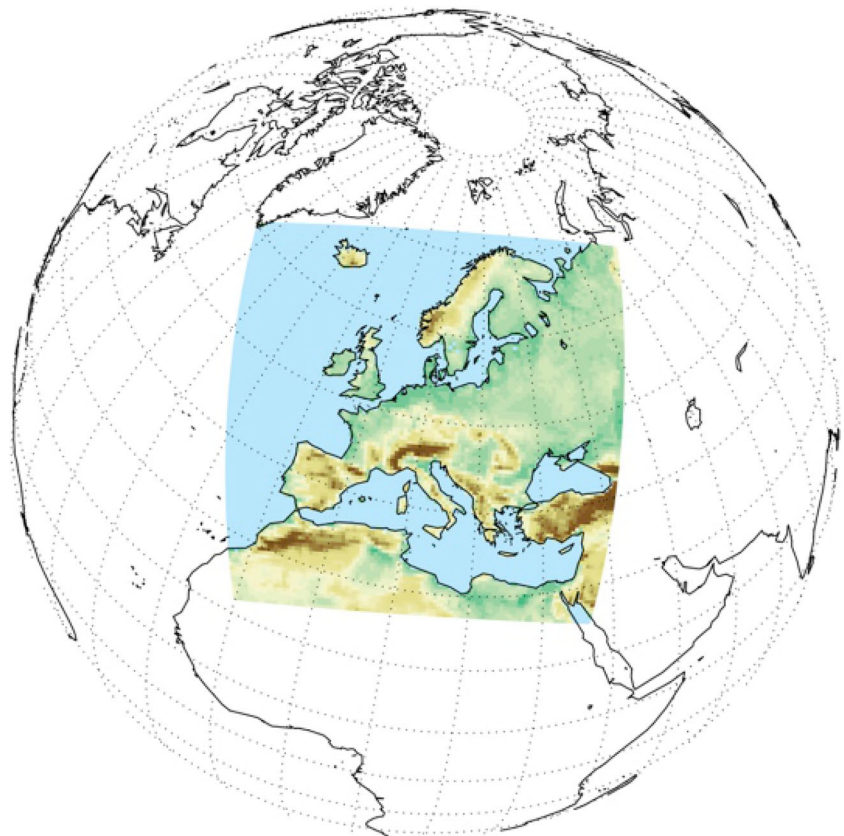
took place during spring of 2018 and additional activities are planned.

EURO-CORDEX modelling framework

In order to assure a high-quality and easy to handle ensemble of simulations, the EURO-CORDEX modelling strategy was implemented at the first GA. It consists of a controlled experiment setup containing a fixed simulation domain (Fig. 2), predefined horizontal grid spacings, an evaluation simulation for each model used within EURO-CORDEX and a historical and climate change simulations, following the endorsed CORDEX protocol (Giorgi and Gutowski 2015). The following are the time periods covered by the simulations: Evaluation (ERA-Interim), 1989–2008; Control, 1951–2005; Scenarios, 2006–2100.

Within EURO-CORDEX, one domain with two resolutions is used for the RCM simulations: the EUR-44 domain at 0.44° grid spacing, which is similar to what is used in the first phase of CORDEX experiments, and the EUR-11 domain at 0.11° grid spacing. Therefore, together with an ensemble at the CORDEX standard resolution (at 0.44°), an ensemble of high-resolution regional climate simulations has been created (at 0.11°), aiming at better resolving

Fig. 2 EURO-CORDEX model domain at 0.11° resolution

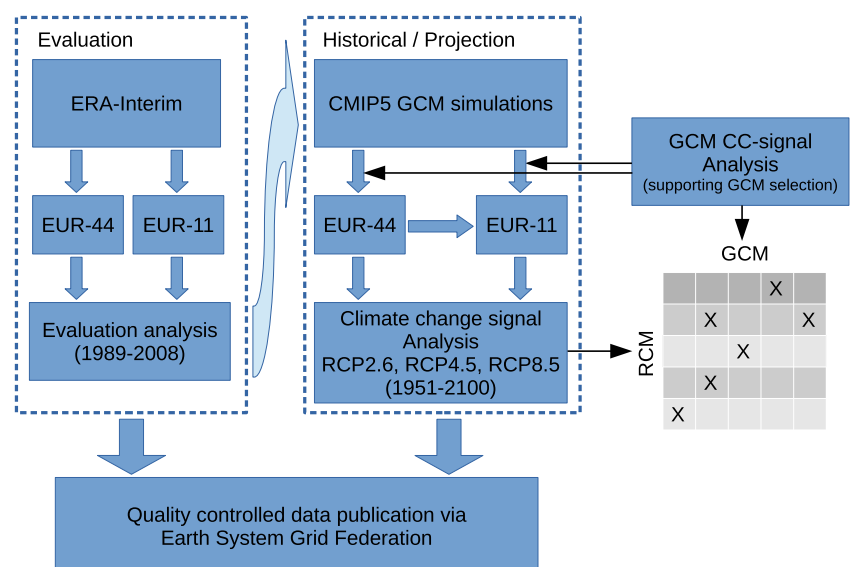


meteorological phenomena, including extreme events, over Europe. At both resolutions, three types of experiments are performed: reanalysis-driven evaluation runs designed to assess RCM capacity to properly simulate regional climate in a “perfect” boundary conditions setup, GCM-driven historical simulations, and GCM-driven climate projections designed to assess current and future climate change. GCM simulations are directly downscaled using RCMs (GCM to EUR-11) or via an intermediate step using a EUR-44 simulation which is then downscaled to EUR-11 (GCM to EUR-44 to EUR-11) (Fig. 3). Simulations are accessible via the ESGF data distribution facility at both a resolution of 0.44° , but also at a higher resolution of 0.11° which is unique within the CORDEX framework.

All regional models used in EURO-CORDEX are evaluated using reanalysis-forced simulations (left hand side in Fig. 3) before running regional climate change projections driven by GCM forcing (right hand side in Fig. 3). Evaluation simulations are driven by “quasi-observational” data (ERA-Interim reanalysis; Dee et al. 2011) offering a robust basis for joint evaluation studies, atmospheric process analysis, comparison with previous projects, e.g., ENSEMBLES, and detailed evaluation against observational data. This provides some information about the performance of the individual RCMs over Europe, along with the presence of common systematic biases. Data are quality controlled before being uploaded to the ESGF repository, and best practices on the use of the regionally downscaled ensembles are provided (see <https://euro-cordex.net>). Furthermore, a joint errata service, accessible via <https://euro-cordex.net>, has been set in place in order to inform users on erroneous or equivocal simulation output.

In EURO-CORDEX, the choice of the driving GCM for the climate projection runs is largely up to each participating modelling group, given that it is a voluntary effort. This kind of approach can result in an ensemble of opportunity that might suffer from inconsistent climate change signals (Turco et al. 2013) or be biased towards a few preferred GCMs (Fernández et al. 2019). To avoid this, there has been a strong effort within EURO-CORDEX, and also from other initiatives, to analyze the driving GCMs, both regarding their performance (e.g., Cattiaux et al. 2013; McSweeney et al. 2014; Brands et al. 2013; Belda et al. 2015) and the spread of their mean seasonal temperature and precipitation changes (following the methods of Mendlik and Gobiet (2015) and McSweeney et al. (2014), or using a climate classification in Belda et al. (2016) or for their changes in weather regime frequency (Cattiaux et al. 2013). These analyses serve as support in the selection of forcing GCMs, in the sense of performance under current climate, but also in order to span the full spread of the GCM climate change signals over Europe. So while EURO-CORDEX does not explicitly follow a systematic experimental design as proposed by McSweeney et al. (2014) it does incorporate selection criteria. Further, most of the GCMs used in EURO-CORDEX are among those listed as well performing by McSweeney et al. (2014) for Europe. Nevertheless, the GCM-RCM simulation matrix is sparse. Therefore, national projects such as ReKlies-DE (<http://reklies.hlnug.de>) and international activities such as the EU-funded Copernicus Climate Change Services (C3S; <https://climate.copernicus.eu>) are supporting EURO-CORDEX in filling this GCM-RCM-simulation matrix in a coordinated effort. There have also been C3S projects for the evaluation and quality control (EQC) of climate model data (<https://climatedatasite.net/>).

Fig. 3 Schematic description of the EURO-CORDEX experiment protocol. For further details refer to the text



Scientific advances

Early on, EURO-CORDEX committed itself to make data available through open access services such as the ESGF (<https://esg-dn1.nsc.liu.se/projects/esgf-liu/>) and climate impact web portals (<https://climate4impact.eu>). The availability of a large multi-model ensemble in a coordinated framework (evaluation, historical and future simulations), on different spatial resolutions and for a range of Representative Concentration Pathways (RCPs) is a significant contribution to the climate science community. It has provided the researchers with a solid basis from which to investigate present and future European climate, and assess uncertainty on continental to regional scales.

At the eighth GA (January 2018), a renewed commitment was made towards community-driven research on high-impact topics with a focus on contributing to the next IPCC assessment report. These topics include the following: urban scale issues, added value, impacts (with a focus on extremes), emergent constraints, interactions/feedbacks, and dynamics/thermodynamics. Another outcome of the GA was the establishment of a EURO-CORDEX errata page where issues noted by modelling teams and users are gathered, described and addressed in an accessible and transparent manner. A third decision was to update and improve model/experiment documentation. This will include synchronizing EURO-CORDEX documentation with ongoing C3S-funded projects.

Evaluation studies and projections of future European climate

The EURO-CORDEX evaluation simulations have served as the data-pool for a series of investigations concerning current European climate and the ability of regional models to accurately represent its state, its range of uncertainty and systematic model biases on a continental (e.g., Kotlarski et al. 2014; Katragkou et al. 2015; García-Díez et al. 2015) or regional level (e.g., Belušić et al. 2017; Dyrørdal et al. 2017). These simulations also provide a basis for assessing the added value, or lack thereof, of regional climate models. One way to look at downscaling is that information is added, with an improved physical understanding (i.e., though explicit inclusion of more processes/phenomena) and more geographical detail. At the same time, the downscaling can also introduce new errors and biases (e.g., additional uncertainties, mismatches between GCM and RCM in terms of parameterizations). The case for added value is where the addition of information dominates over the addition of uncertainty. However, the question of added value also depends on how the results are being used. For example, there is recent work that shows that the biases

and uncertainty in GCM-RCM chains are not additive, i.e., uncertainty does not increase with each downscaling step and that RCMs in the EURO-CORDEX framework improve on the GCMs even at larger scales (Sørland et al. 2018).

The added value of higher resolution simulations was also addressed, both directly and indirectly, in a number of studies including dynamical downscaling (Warrach-Sagi et al. 2013; Torma et al. 2015; Casanueva et al. 2016b; Coppola et al. 2018a; Prein and Gobiet 2016; Ivanov et al. 2017; Soares and Cardoso 2017; Fantini et al. 2018; Sørland et al. 2018) and statistical methods (Casanueva et al. 2016a; Soares et al. 2018). Joint evaluation studies also focused on extreme climate events, such as heat waves (Vautard et al. 2013; Lhotka et al. 2017) and extreme precipitation (Fantini et al. 2018), medicanes (Gaertner et al. 2018) or physical process analysis, such as land-atmosphere interactions (e.g., Davin et al. 2016; Knist et al. 2017) and coastal circulations (Cardoso et al. 2016). Many of these examples point to an added value of regional downscaling by including processes or phenomena that are missing from coarser resolution models (e.g., Prein et al. 2015; Cardoso et al. 2016; Davin et al. 2016; Knist et al. 2017; Fantini et al. 2018). In other cases, such as in studies focusing on mean climate conditions involving spatially or temporally averaged fields (e.g., Kotlarski et al. 2014; Casanueva et al. 2016b) and/or phenomena with strong links to large scale circulation (Vautard et al. 2013), the added value is less apparent. However, a comprehensive assessment of added value in CORDEX RCM simulations is still lacking.

The historical and projection simulation datasets are the basis for the investigation of current and future European climate, including investigation of uncertainty stemming from model variability and projection scenarios. Jacob et al. (2014) used the higher resolution (0.11°) EURO-CORDEX simulations to show the overall spatial patterns for temperature and precipitation changes and related indices are similar to those of ENSEMBLES, with a slightly stronger mean precipitation increase over most of Europe and a reduced northwards shift of Mediterranean drying evolution. Bador et al. (2017) investigated the evolution of the record temperatures showing that maximum temperatures above 50 °C can occur at the end of the 21st century under the RCP8.5 scenario. Trambly and Somot (2018) used the EUR-11 EURO-CORDEX ensemble to investigate the intensity and the time of emergence of the response of Mediterranean extreme precipitation to climate change. They showed a robust north-south pattern with increase (resp. decrease) in the North (resp. South) of the basin. Related to these projected shifts are projected changes in extreme dry spells, which may increase in duration and extent over the Mediterranean basin (Raymond et al. 2019). Jerez et al. (2015) and

Bartók et al. (2017) compared changes in solar radiation projected by global and regional EURO-CORDEX climate models and reported a discrepancy between the results in the GCM/RCM ensembles, namely increasing/decreasing trends for the period 2006–2100 over Europe under RCP8.5. Tobin et al. (2016) analyzed changes in surface wind speed and wind power in Europe, using EURO-CORDEX simulations, and Tobin et al. (2018) assessed general changes in electricity production in Europe. Others have also investigated renewable energy projections and note a more challenging environment for wind energy management in the future (Moemken et al. 2018). Several other studies used the EURO-CORDEX projections to focus on regional/national level (e.g., Smiatek et al. 2016; Rulfová et al. 2016; Ouzeau et al. 2016; Soares and Cardoso 2017; Hosseinzadehtalaei et al. 2018; Bador et al. 2017; Fernández et al. 2019; Huebener et al. 2017; Kjellström et al. 2016; Rajczak and Schär 2017; Púčik et al. 2017; Frei et al. 2018; Termonia et al. 2018; Prein and Gobiet 2016; Stepanek et al. 2016; Cardoso et al. 2018) others applied statistical downscaling methods, to further downscale the regional climate information (e.g., Dosio 2016; Mezghani et al. 2017) while others, after adopting bias adjustment techniques, use EURO-CORDEX data for local applications (Reder et al. 2018; Croce et al. 2018).

EURO-CORDEX simulations were recently used to assess the human influence in recent individual extreme events, together with other projection ensembles, a type of analysis which is called “event attribution” (Stott et al. 2015). EURO-CORDEX does not include pre-industrial simulations but changes between an earlier historical period (e.g., 1971–2000) and a “current climate” period (e.g., 2001–2030) allows to estimate a lower bound of human influence on regional climate events. In this way, Kew et al. (2018) showed that heat waves such as the 2017 summer “Lucifer” heat wave in Southern Europe had a probability that had strongly increased due to human influence. Other cases were studied using EURO-CORDEX, such as the extreme precipitations over the Cévennes mountains range (Luu et al. 2018), the European drought of Summer 2015 in Central Europe (Hauser et al. 2017) the extreme wind stagnation of December 2016 (Vautard et al. 2018), and the winter wind storms of January 2018 (Vautard et al. 2019). The added value of high resolution was demonstrated in particular for the Mediterranean heavy precipitations. As a final example, Giorgi et al. (2016) showed the added value of high-resolution RCMs in the projection of summer precipitation changes over high mountainous areas (e.g., the Alps). An overview of EURO-CORDEX publications can be found in the EURO-CORDEX publication web pages (<http://euro-cordex.net>).

Flagship pilot studies

The flagship pilot studies (FPS) initiative was established by the CORDEX Scientific Advisory Team as an additional activity to the core work of CORDEX, analogous to the MIPs of Coupled Model Intercomparison Project (CMIP) (Gutowski et al. 2016). These are “bottom up” initiatives and benefit the larger CORDEX/Working Group on Regional Climate (WGRC, <https://www.wcrp-climate.org/regional-climate>) bodies through linking to the wider climate research community, such as the newly established MIPs and other WCRP core projects. The EURO-CORDEX community submitted two successful FPS applications, one on the climatic impacts of land cover changes and one jointly with the Med-CORDEX community (Ruti et al. 2016; Somot et al. 2018) on convective phenomena through the use of very high-resolution convection-permitting regional climate models (CPRCMs). These computationally intensive projects started up in 2017 and just recently begun to produce results.

FPS I Land Use and Climate Across Scales

Land Use and Climate Across Scales (LUCAS) is a new initiative on coordinated regional climate experiments for Europe including land use change forcing (https://www.hzg.de/ms/cordex_fps_lucas/). It was initiated jointly by EURO-CORDEX and LUCID (Land-Use and Climate, IDentification of robust impacts, <http://www.lucidproject.org.au>). Land use change (including land cover and/or land management changes) is an important anthropogenic forcing on climate, and its direct biophysical effect on temperature can locally or regionally be of the same order of magnitude as the effect from global greenhouse gas forcing, but there are still uncertainties in magnitude and sign of many land-induced changes (de Noblet-Ducoudré et al. 2012; Lejeune et al. 2017; Perugini et al. 2017; Cherubini et al. 2018). Even more important for impact studies, many numerical experiments have highlighted the strong impact land uses may have on extreme events (e.g., Pitman et al. 2012; Davin et al. 2014; Thiery et al. 2017; Lejeune et al. 2018; Berckmans et al. 2019).

The LUCAS initiative is complementary to the Land Use Model Intercomparison Project (Lawrence et al. 2016) in that LUMIP focuses on the global scale, while LUCAS investigates regional impacts, using higher resolution, closer to the scale at which the biogeophysical effect of LUC has the strongest impacts. Up till now, this human forcing is not accounted for in RCM climate change projections. RCMs have been applied individually for investigating impacts of land use changes on regional climate in different world

regions (e.g., see reviews of Pielke et al. 2011; Lawrence and Vandecar 2015; Santanello et al. 2018). Most results are model specific and therefore do not allow one to derive robust conclusions. In LUCAS, for the first time an ensemble of RCMs will be used in coordinated land use change (LUC) experiments, focusing on anthropogenic land cover conversions and potentially on land management practices during its later phase. The LUCAS modelling framework is visualized in Fig. 4.

The overall objectives of LUCAS are (i) to identify robust biophysical impacts of land use change on climate across regional-to-local spatial scales and at various time scales, from extreme events to multi-decadal trends, and (ii) to provide robust information in support of effective land use practices and also help guide decisions on land management from unintended consequences. The questions to be addressed are:

- How sensitive are regional climate models to land use change and how is this interrelated to land-atmosphere coupling in different regions among the suite of models?
- How large is the relative contribution of land use change compared with other forcings in the detection of past and potential future climate trends?
- How do land use practices modulate climate variability? Can local land use change modulate extreme climate conditions?
- What is the effect of spatial resolution on the magnitude and robustness of land use change-induced climate changes?
 - What errors do we make on the downscaled climate change if we ignore land use change? This is especially important for subsequent impact studies.

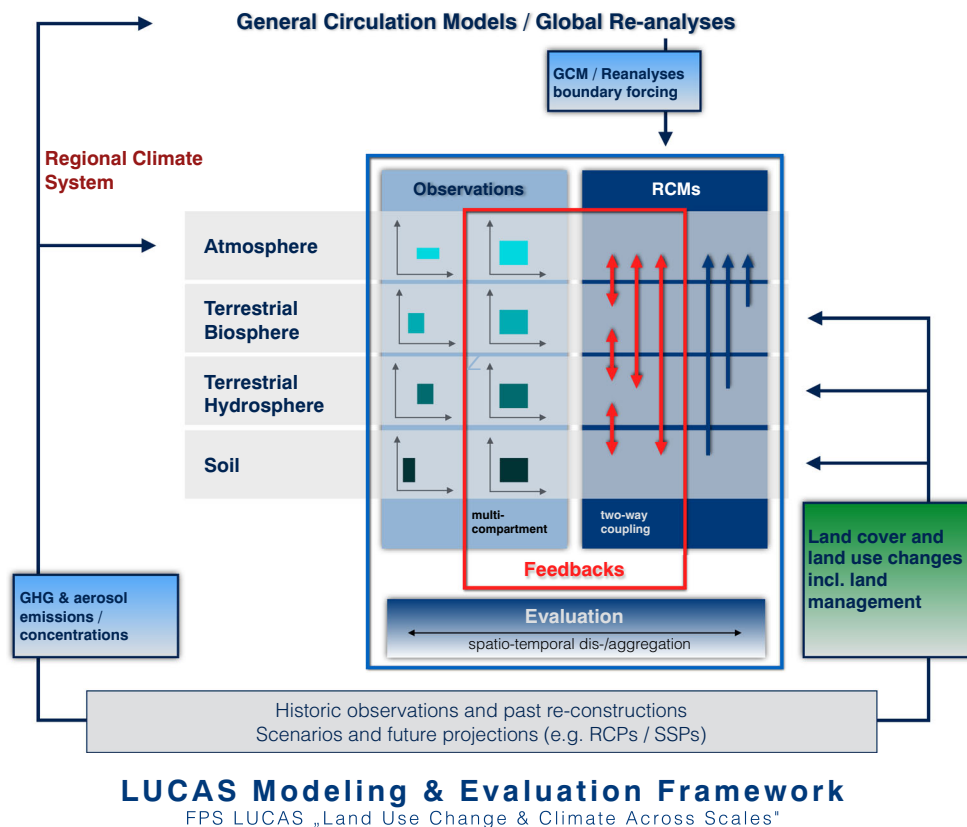


Fig. 4 LUCAS modelling framework. Land use and climate change experiments are performed with several RCMs. They represent processes in atmosphere, terrestrial biosphere, hydrosphere and pedosphere. RCMs which apply a two-way coupling between the atmosphere and the terrestrial components, enable the investigation of land-atmosphere feedbacks. The evaluation experiments are driven by reanalysis data and compared with observational data. Multi-compartment observational data on consistent temporal and spatial scales enable the evaluation of land-atmosphere feedbacks. The climate change experiments are driven by GCMs. Greenhouse gas (GHG)

and aerosol concentrations are prescribed to the model simulations according to observed past concentrations for historical time periods, and according to different RCPs for climate change projections. Land cover and land use changes are implemented into the RCMs according to observed past re-constructions for historical time periods, and according to different Shared Socio-Economic Pathways (SSPs), which are linked to certain RCPs, respectively. Additional land use change experiments are designed, for which specific land use forcings are developed and implemented

It is clear that the outcome of these simulations will be limited as long as the representation of surface fluxes, boundary layer turbulence, and cloud microphysics cannot be verified and improved. Therefore, these modelling efforts will be accompanied by field experiments on land-atmosphere feedback (Wulfmeyer et al. 2018), which are currently being evaluated or prepared, e.g., at the TERENO sites (Bogena 2016) and the new Land-Atmosphere Feedback Observatory (LAFO; see <https://lafo.uni-hohenheim.de>).

Cropland management as well as human water use by water extraction and irrigation is an emerging topic and has the potential to either enhance or dampen temperature extremes (Becker et al. 2013; Davin et al. 2014; Thiery et al. 2017; Keune et al. 2018). Also, the collaboration between the FPS LUCAS on land-atmosphere feedback, the WRCP LoCo community (Santanello et al. 2018) and experiments on land-atmosphere feedback (Wulfmeyer et al. 2018) including groundwater dynamics (Keune et al. 2016) should be intensified.

FPS II convective phenomena at high resolution over Europe and the Mediterranean

The second FPS mobilizes the EURO- and MED-CORDEX communities and aims to bring fresh perspectives and expertise on issues surrounding convective phenomena. Present and future convective extremes and their processes are under investigation with convection-permitting regional climate models (CPRCMs), at resolutions finer than 3 km, over selected sub-regions of Europe and the Mediterranean (Fig. 5). Advanced statistical techniques will also be employed in parallel to evaluate the performance

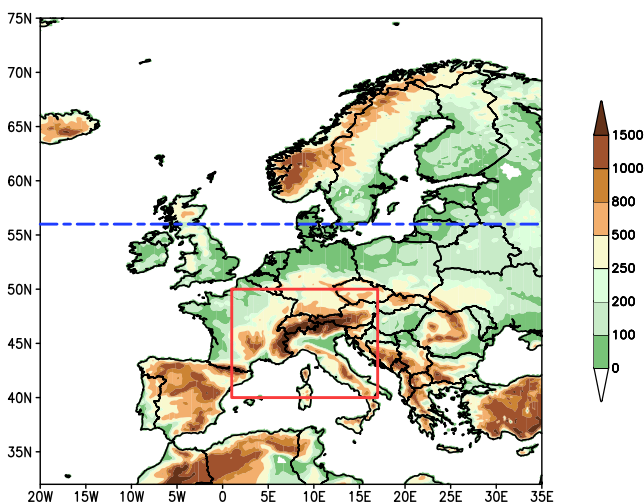


Fig. 5 Mandatory domain for the FPS on convective phenomena (red box). The dashed blue line corresponds to the northern boundary of the Med-CORDEX domain

of dynamical models, to potentially serve as emulators of convective extremes, and to detect and attribute their changes. These so-called emulators use empirical relationships between large scale features and local phenomena such as precipitation in ways similar to statistical downscaling but then add additional detail to obtain, e.g., sub-daily rainfall (Mezghani et al. 2019). The FPS aims to extend these to also include information from the dynamical downscaling. The added value of CPRCMs is well established now, especially for mesoscale convective systems, rainfall extremes, diurnal cycles, regional snow cover, etc. (see Ban et al. 2014; Prein et al. 2015, 2017a; Berthou et al. 2018; Sørland et al. 2018; Lüthi et al. 2019; Scaff et al. 2019). What has not been done as yet, is to explore these advances in an ensemble framework, which will allow us to better estimate uncertainty, quantify robustness and elucidate key driving processes. The added value of explicitly simulating deep convection will be rigorously evaluated with respect to both coarser resolution simulations up to GCM scales and VIACS applications. The CPRCM simulations will also serve as references and help developing convection parameterizations in standard RCMs and GCMs. The availability of observational datasets at very high resolutions in both space and time allows unprecedented evaluation opportunities (e.g., Lussana et al. 2018; Hiebl and Frei 2016, 2018; Frei 2014).

This FPS has three main scientific questions with many attendant sub-topics and questions:

- How do convective events and associated damaging phenomena (heavy precipitation, wind storms, flash-floods) respond to changing climate conditions in different climatic regions of Europe?
- Does an improved representation of convective processes and precipitation at convection-permitting scales lead to downscaled as well as upscaled added value?
- To what extent do lateral boundaries affect convection-permitting model (CPM) performance and how can corresponding errors be reduced?
- Is it possible to complement costly convection-permitting experiments with physically defensible statistical downscaling approaches such as “convection emulators” that mimic CPMs and are fed by output from conventional-scale climate models?

Convective extreme events are a priority under the WCRP Grand Challenge on weather and climate extremes, because they carry both society-relevant and scientific challenges that can be tackled in the coming years. Further, “coordinated modelling programs are crucially needed to advance parameterizations of unresolved physics and to assess the full potential of CPMs” (Prein et al. 2015). The project involves over 20 modelling teams and consists

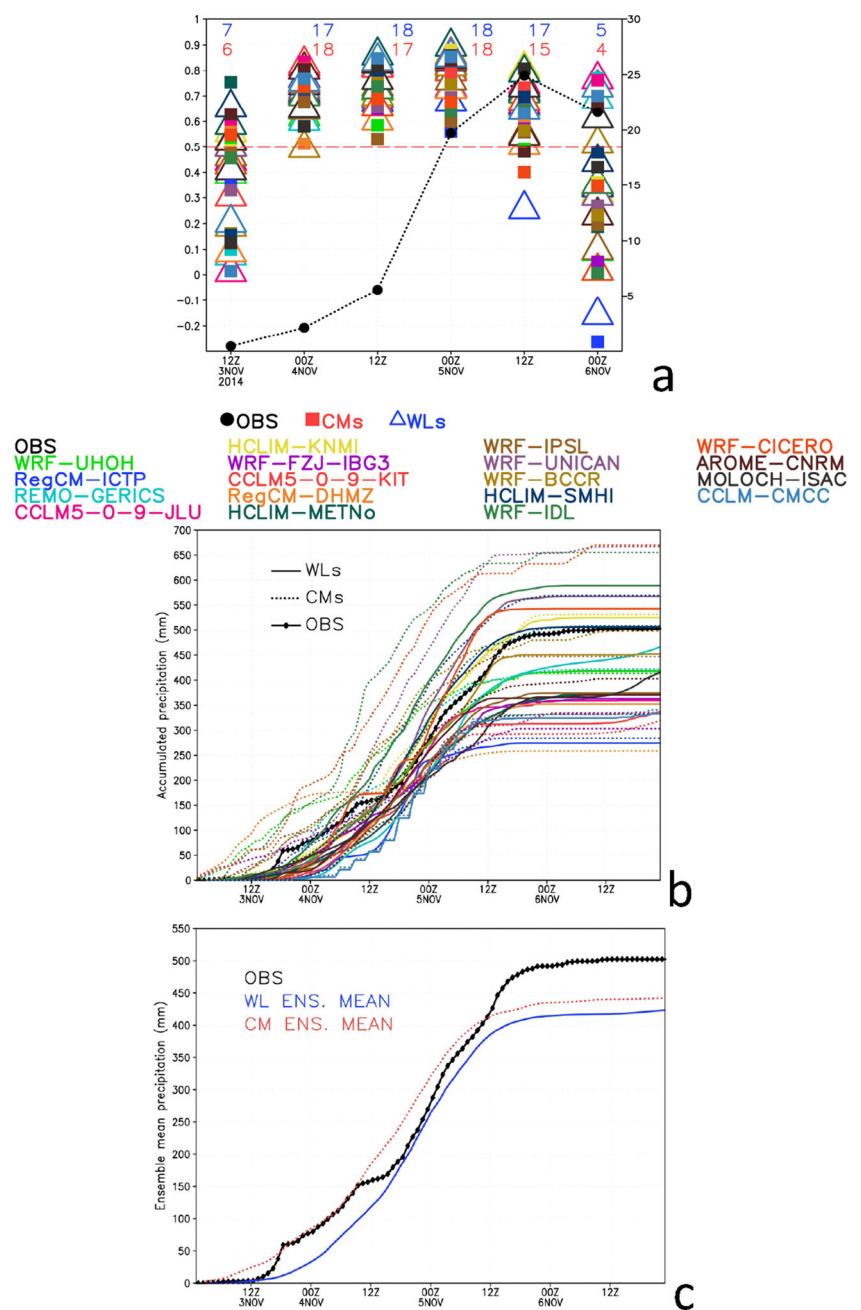
of three modelling steps: test cases, evaluation runs and scenario runs. A presentation of the project and preliminary results appear in Coppola et al. (2018b). Figure 6 shows results from a test case over Switzerland and highlights the ensemble performance in reproducing an extreme Foehn event in November of 2014. The ensemble mean spatial pattern correlations for this event were over 0.90. However, the ensemble exhibits much larger spread for events that are more weakly forced by the synoptic background state and have strong orographic and/or land-ocean interactions. Simulations over climate scales (10 years time slices) under present and future conditions are ongoing. A small ensemble has recently been completed (fall 2019) and a

number of investigations are underway with results expected in late 2019/early 2020.

Key messages and outlook

The scientific challenges EURO-CORDEX faces will require broad community-based research. Given the fragmented nature of funding for EURO-CORDEX and CORDEX generally, there is a need for funding that targets these types of research initiatives. Only in this way will significant improvements in fundamental understanding emerge. A non-exhaustive list of directed research

Fig. 6 Time series of 12 hourly accumulated precipitation for a Foehn event over southern Switzerland (black line/dots, in mm on the right hand y-axis) during the event and temporal evolution of the spatial correlation (lefthand y-axis) of the accumulated 12 hourly precipitation between the simulations and observations, panel a. Number of models with a correlation greater than 0.5 for WL simulation (in blue) and CM simulation (in red). Time series of the accumulated precipitation averaged over the region covered by the observations for each model (colored lines) versus observations (black line), panel b. Time series of accumulated hourly precipitation for the ensemble means of the WL and CM simulations versus observations (blue, red and black lines, respectively), panel c (Reproduced from Coppola et al. (2018b))



recommendations are presented below. These are followed by more detailed descriptions of key messages and the future outlook from the EURO-CORDEX community, which include not only research but also necessary expansion of the community to include additional perspectives.

- Research towards a more comprehensive and improved understanding of regional climate processes and their drivers, in particular with respect to extremes and place these within the context of the Sustainable Development Goals and WCRP Grand Challenges.
- Research towards transient continental-scale ensemble kilometer scale modelling (i.e., convection permitting) has the potential to substantially reduce uncertainties in future climate projections and enhance our understanding of high-impact weather events under climate change; the community is moving in this direction but such initiatives require significant and sustained investment in personnel and resources
- Research support for the interdisciplinary community that will be needed to further develop Regional Earth system models that are able to better simulate the human impact on local and regional climate (e.g., vegetation feedbacks, hydrology and water resources, irrigation for agricultural production, urban climate, regional sea-level rise, storm surge modelling, coupled glacier modelling)
- Research that explicitly links observations to model development and improvement through collaborative community efforts that focus on regional and local process studies that make use of, e.g., field campaign data to improve the representation of processes and feedbacks in regional models.

Linking with climate services

In addition to generating a unique dataset to address many scientific issues pertaining to climate downscaling, the first phase of EURO-CORDEX has already had a tremendous impact on the provision of regional climate services. For example, several “official” national climate scenarios (examples include France (<http://www.drias-climat.fr>), Switzerland (www.ch2018.ch), Austria, Norway (<https://klimaservicesenter.no>), Spain (<http://escenarios.adaptecca.es>) and Belgium (<http://www.euro-cordex.be>) for national climate change adaptation strategies are nowadays based on EURO-CORDEX. In addition, EURO-CORDEX will be at the heart of the coming C3S European climate service for future projections (e.g., the Copernicus Climate Change Service project C3S34b, PRINCIPLES, <https://climate.copernicus.eu>). It has also been used in proof-of-concept European climate services, for instance to help the energy sector facing climate change impacts and climate

variability in developing renewable energies, or water, such as in the C3S CLIM4ENERGY and SWICCA projects (<https://climate.copernicus.eu>). Operational implementation is currently underway.

Despite the scientific progress and overall success of the EURO-CORDEX initiative, there are a number of challenges confronting it. These challenges are of both scientific and strategic nature. For example, simply generating and disseminating downscaled regional climate projections in the absence of good experimental design and without proper context, guidance and tailoring, will, at best, not serve user communities’ needs optimally and, at worst, potentially lead to misleading strategies (Dilling and Berggren 2014). Avoiding such pitfalls will require both scientific advances on uncertainty quantification and verification metrics needed to produce robust and reliable projections, as well as strategic partnerships with outside collaborators in the VIACS communities. EURO-CORDEX is directly addressing these challenges through the establishment of strategic partnerships (e.g., with the CMIP6-endorsed VIACS advisory board (Ruane et al. 2016) and a dedicated effort on CID (Fig. 1).

In the second phase of EURO-CORDEX, the ensemble of EUR-44 and EUR-11 simulations will be extended to serve as a robust basis for further studies and VIACS applications. Additional EURO-CORDEX objectives are to foster the creation of climate information including the interface to users and to integrate empirical statistical downscaling. The new structure of EURO-CORDEX (see Fig. 1) reflects these aims and gives us a good basis for future cooperation and collaborations with the broader community of climate change, sustainability and social transformations researchers. It is an ambitious and exciting platform but one that is timely and has a proven and dedicated community of practice built to support it.

Integrating statistical methods

As noted previously, the volume of data produced in the EURO-CORDEX downscaling activities requires advanced statistical techniques for robust analyses (Benestad et al. 2017a, b). Better integration of these techniques and collaboration with external experts is a key strategic aim for EURO-CORDEX. Steps have already been taken with participation of EURO-CORDEX teams in the EU COST Action ES1102 “VALUE” (Maraun et al. 2015), where statistical downscaling groups organized themselves to systematically investigate statistical downscaling and bias correction methods. In a first experiment, VALUE investigated the downscaling skill of some 50 statistical methods for present climate, when driven with reanalysis-based predictors. These results have recently been published in a special issue (Maraun et al. 2017, 2018; Gutiérrez et al. 2018;

Hertig et al. 2018; Soares et al. 2018). These types of activities have been integrated into the ESD pillar into EURO-CORDEX (Fig. 1), and a new call for the next experiment will be issued shortly. This experiment will investigate the overall skill of statistically downscaled GCMs in present climate and the plausibility and uncertainties of future projections based on statistical downscaling.

Receiving support from computer science

The fields of climate science and climate change impacts heavily rely on computationally-intensive simulations and data centers should be aware of the wealth of data that is to come from the EURO-CORDEX community due to increasing ensemble sizes and heading towards convection-permitting resolutions. For instance, the effort in the setup and performance of CPM simulations was exemplified in latitude-belt runs by Schwitalla et al. (2017) or European, CPM simulations by Leutwyler et al. (2016) and on global scales by Heinzeller et al. (2016). On the other hand the climate modelling community, enabled by ever increasing high-performance computing resources, is facing large challenges related to new, emerging computing paradigms using, e.g., new microarchitectures such as GPUs (Lawrence et al. 2018) and finding more efficient ways to handle and store the massive amounts of data produced by CPM simulations. Additionally, there will be even more requests from VIACS communities for this data and online processing services to reduce the data volume on the server side. VIACS will have to bring together the large amount of high-resolution climate data and the requests of their customers for local climate information. They are challenged by the need of quick answers on the one hand and the desire to deliver high-quality well thought out and crafted products on the other. To address this issue targeted research and development to simplify and democratize data access and analysis and improve guidance for end-users in an era of data volume explosion will be needed. Here, a closer collaboration with the EURO-CORDEX community will help to address the challenges and fulfill mutual requirements.

Fostering cooperation with WCRP activities

The regional activities in WCRP are receiving increased visibility at present, and it is incumbent upon all involved to look for synergies across these activities. EURO-CORDEX, and CORDEX more generally, has a critical role to play in realizing WCRP's new scientific objectives, in particular objective 4 "Bridging science and society" (WCRP Joint Scientific Committee (JSC) 2019). The EURO-CORDEX community itself is also challenged by the WCRP and CORDEX-specific grand scientific challenges. Some of

them can be addressed together with other communities, such as VIACS or the larger climate science community including CMIP6. Here, closer and more active interaction is essential. Besides the scientific challenges, it is also necessary to support VIACS communities by providing well designed, large ensembles of climate simulations in a well-documented and usable way. As a promising development, a robust community has formed around convection-permitting modelling and two successful WCRP-GEWEX sponsored workshops, with strong participation from the EURO-CORDEX community, have been held in Boulder, Colorado. While advances are coming quickly, there are a number of challenges for this community to address (Prein et al. 2017b). EURO-CORDEX and its affiliated Flagship Pilot Studies are right at the forefront of this effort.

Collaboration with the GCM community

Finally, there is a tremendous strategic opportunity for EURO-CORDEX to pursue synergies with climate research activities mainly focused on GCM modelling through the establishment of CORDEX as a diagnostic MIP within the CMIP6 framework. This is also a non-trivial task, since institutional, disciplinary and philosophical barriers often remain between the two communities. However, increasing collaboration is very important, as CPMs are approaching the global scale and can be operated without lateral boundaries (e.g., Schwitalla et al. 2017). There exist a number of opportunities to evaluate upscaled added value, investigate emergent constraints on climate change at regional scales, provide feedback into GCMs to improve parameterizations, and for collaboration with higher resolution, convection-permitting GCMs.

Acknowledgments We acknowledge all participating institutions for their voluntary effort and contribution to EURO-CORDEX. We also thank the developers and maintainers of the ESGF-nodes who make it possible to store and distribute EURO-CORDEX data. S.S. acknowledges the support of NOTUR/NORSTORE projects NN9280K/NS9001K and the Research Council of Norway and its basic institute support of the strategic project on Climate Services. E.K. acknowledges the support of the Greek Research & Technology Network (GRNET) for provision of technical support and facilities (HPC-ARIS). L.S. and I.G. acknowledge the support of Croatian Science Foundation project CARE (2831) and Ministry of Environment and Energy project TF/HR/P3-M1-O1-0101 (www.prilagodba-klimi.hr). J. F. acknowledges support from the Spanish R+D Programme through grant INSIGNIA (CGL2016-79210-R), co-funded by ERDF/FEDER, and the Altamira Supercomputer at Instituto de Física de Cantabria (IFCA-CSIC), member of the Spanish Supercomputing Network. P.T. acknowledges support from the Belgian Science Policy (BELSPO) within the CORDEX.be (BR/143/A2) project, and the VSC (Flemish Supercomputer Center), funded by the Research Foundation - Flanders (FWO) and the Flemish Government - department EWI.M.A.G. acknowledges support from the Spanish R+D Programme through grants CGL2013-47261-R and CGL2017-89583-R, co-funded by the European Regional Development Fund. RF acknowledges support provided by ICHEC (Irish Centre for High

End Computing) and the Irish Environmental Protection Agency. K.G. and S.K. gratefully acknowledge the computing time granted through JARA-HPC on the supercomputers JUROPA and JURECA at Forschungszentrum Jülich. M.B. and T.H. acknowledge support by The Ministry of Education, Youth and Sports from the Large Infrastructures for Research, Experimental Development and Innovations project “IT4Innovations National Supercomputing Center – LM2015070” and the INTER-EXCELLENCE program LTT17007, and support by Charles University from the PROGRES Q16 program. We acknowledge the approval and support of the two Flagship Pilot Studies (the FPS on Convective phenomena at high resolution over Europe and the Mediterranean and the FPS on Land Use and Climate Across Scales) by WRCP CORDEX. We thank Merja Tölle for providing simulation CCLM5-0-9-JLU as contribution to the CORDEX-FPS “Convective phenomena at high resolution over Europe and the Mediterranean”.

D. M., M.P., and H.T. gratefully acknowledge the support received via the projects HighEnd:Extremes, SPIRIT, and reclip:convex, funded by the Austrian Climate Research Programme (ACRP) of the Klima- und Energiefonds (nos. B368608, B960272, and B769999, respectively), as well as the Jülich Supercomputing Centre (JSC) for compute time on JURECA through the grant JJSC39 and the Vienna Scientific Cluster (VSC) through the grants 70992 and 71193.

Funding Information Open Access funding provided by Projekt DEAL.

Compliance with ethical standards

Conflict of interest The authors declare that they have no conflict of interest.

Open Access This article is licensed under a Creative Commons Attribution 4.0 International License, which permits use, sharing, adaptation, distribution and reproduction in any medium or format, as long as you give appropriate credit to the original author(s) and the source, provide a link to the Creative Commons licence, and indicate if changes were made. The images or other third party material in this article are included in the article’s Creative Commons licence, unless indicated otherwise in a credit line to the material. If material is not included in the article’s Creative Commons licence and your intended use is not permitted by statutory regulation or exceeds the permitted use, you will need to obtain permission directly from the copyright holder. To view a copy of this licence, visit <http://creativecommons.org/licenses/by/4.0/>.

References

- Bador M, Terray L, Boé J, Somot S, Alias A, Gibelin A-L, Dubuisson B (2017) Future summer mega-heatwave and record-breaking temperatures in a warmer France climate. *Environ Res Lett* 12(7):074025. <https://doi.org/10.1088/1748-9326/aa751c>
- Ban N, Schmidli J, Schär C (2014) Evaluation of the convection-resolving regional climate modeling approach in decade-long simulations. *J Geophys Res* 119(13):7889–7907. <https://doi.org/10.1002/2014JD021478>
- Bartók B, Wild M, Folini D, Lüthi D, Kotlarski S, Schär C, Vautard R, Jerez S, Imecs Z (2017) Projected changes in surface solar radiation in CMIP5 global climate models and in EURO-CORDEX regional climate models for Europe. *Clim Dyn* 49(7–8):2665–2683. <https://doi.org/10.1007/s00382-016-3471-2>
- Becker K, Wulfmeyer V, Berger T, Gebel J, Münch W (2013) Carbon farming in hot, dry coastal areas: an option for climate change mitigation. *Earth Syst Dyn* 4(2):237–251. <https://doi.org/10.5194/esd-4-237-2013>
- Belda M, Holtanová E, Halenka T, Kalvová J, Hlávka Z (2015) Evaluation of CMIP5 present climate simulations using the Köppen-Trewartha climate classification. *Clim Res* 64(3):201–212. <https://doi.org/10.3354/cr01316>
- Belda M, Holtanová E, Kalvová J, Halenka T (2016) Global warming-induced changes in climate zones based on CMIP5 projections. *Clim Res* 71(1):17–31. <https://doi.org/10.3354/cr01418>
- Belušić A, Prtenjak MT, Güttler I, Ban N, Leutwyler D, Schär C (2017) Near-surface wind variability over the broader Adriatic region: Insights from an ensemble of regional climate models. *Clim Dyn* 50(11–12):4455–4480. <https://doi.org/10.1007/s00382-017-3885-5>
- Benestad R, Parding K, Dobler A, Mezghani A (2017a) A strategy to effectively make use of large volumes of climate data for climate change adaptation. *Clim Serv* 6:48–54. <https://doi.org/10.1016/j.cliser.2017.06.013>
- Benestad R, Sillmann J, Thorarinsdottir TL, Guttorp P, d S Mesquita M, Tye MR, Uotila P, Fox Maule C, Thejll P, Drews M, Parding KM (2017b) New vigour involving statisticians to overcome ensemble fatigue. *Nat Clim Change* 7(10):697–703. <https://doi.org/10.1038/nclimate3393>
- Berckmans J, Hamdi R, Dendoncker N (2019) Bridging the gap between policy-driven land use changes and regional climate projections. *J Geophys Res Atmos* 124(12):5934–5950. <https://doi.org/10.1029/2018JD029207>
- Berthou S, Kendon EJ, Chan SC, Ban N, Leutwyler D, Schär C, Fosser G (2018) Pan-european climate at convection-permitting scale: a model intercomparison study. *Clim Dyn*, 1–25. <https://doi.org/10.1007/s00382-018-4114-6>
- Bogena HR (2016) TERENO: German network of terrestrial environmental observatories. *J Large-Scale Res Facilities JLSRF* 2:A52. <https://doi.org/10.17815/jlsrf-2-98>
- Böhm U, Kücken M, Ahrens W, Block A, Hauffe D, Keuler K, Rockel B, Will A (2006) CLM — the climate version of LM: brief description and long-term applications. *COSMO Newsletter* 6:225–235
- Brands S, Herrera S, Fernández J, Gutiérrez JM (2013) How well do CMIP5 Earth System Models simulate present climate conditions in Europe and Africa? *Clim Dyn* 41(3–4):803–817. <https://doi.org/10.1007/s00382-013-1742-8>
- Cardoso RM, Soares PMM, Lima DCA, Semedo A (2016) The impact of climate change on the Iberian low-level wind jet: EURO-CORDEX regional climate simulation. *Tellus, Series A: Dynamic Meteorology and Oceanography*, 68:1. <https://doi.org/10.3402/tellussa.v68.29005>
- Cardoso RM, Soares PMM, Lima DCA, Miranda PMA (2018) Mean and extreme temperatures in a warming climate: EURO CORDEX and WRF regional climate high-resolution projections for Portugal. *Clim Dyn* 52:129–157. <https://doi.org/10.1007/s00382-018-4124-4>
- Casanueva A, Herrera S, Fernández J, Gutiérrez JM (2016a) Towards a fair comparison of statistical and dynamical downscaling in the framework of the EURO-CORDEX initiative. *Clim Change* 137(3–4):411–426. <https://doi.org/10.1007/s10584-016-1683-4>
- Casanueva A, Kotlarski S, Herrera S, Fernández J, Gutiérrez JM, Boberg F, Colette A, Christensen OB, Goergen K, Jacob D, Keuler K, Nikulin G, Teichmann C, Vautard R (2016b) Daily precipitation statistics in a euro-cordex rcm ensemble: Added value of raw and bias-corrected high-resolution simulations. *Clim Dyn* 47(3):719–737. <https://doi.org/10.1007/s00382-015-2865-x>
- Cattiaux J, Douville H, Peings Y (2013) European temperatures in CMIP5: origins of present-day biases and future uncertainties.

- Clim Dyn 41(11–12):2889–2907. <https://doi.org/10.1007/s00382-013-1731-y>
- Cherubini F, Huang B, Hu X, Tölle MH, Strømman AH (2018) Quantifying the climate response to extreme land cover changes in Europe with a regional model. *Environ Res Lett* 13(7):074002. <https://doi.org/10.1088/1748-9326/aac794>
- Christensen JH, Carter TR, Rummukainen M, Amanatidis G (2007) Evaluating the performance and utility of regional climate models: the PRUDENCE project. *Clim Change* 81(SUPPL. 1):1–6. <https://doi.org/10.1007/s10584-006-9211-6>
- Colin J, Déqué M, Radu R, Somot S (2010) Sensitivity study of heavy precipitation in limited area model climate simulations: influence of the size of the domain and the use of the spectral nudging technique. *Tellus, Series A: Dynamic Meteorology and Oceanography* 62(5):591–604. <https://doi.org/10.1111/j.1600-0870.2010.00467.x>
- Coppola E, Raffaele F, Giorgi F (2018a) Impact of climate change on snow melt driven runoff timing over the Alpine region. *Clim Dyn* 51:1259–1273. <https://doi.org/10.1007/s00382-016-3331-0>
- Coppola E, Sobolowski S, Pichelli E, Raffaele F, Ahrens B, Anders I, Ban N, Bastin S, Belda M, Belusic D, Caldas-Alvarez A, Cardoso RM, Davolio S, Dobler A, Fernandez J, Fita L, Fumiere Q, Giorgi F, Goergen K, Güttler I, Halenka T, Heinzeller D, Hodnebrog Ø, Jacob D, Kartsios S, Katragkou E, Kendon E, Khodayar S, Kunstmann H, Knist S, Lavín-Gullón A, Lind P, Lorenz T, Maraun D, Marelle L, van Meijgaard E, Milovac J, Myhre G, Panitz H-J, Piazza M, Raffa M, Raub T, Rockel B, Schär C, Sieck K, Soares PMM, Somot S, Srnec L, Stocchi P, Tölle MH, Truhetz H, Vautard R, de Vries H, Warrach-Sagi K (2018b) A first-of-its-kind multi-model convection permitting ensemble for investigating convective phenomena over Europe and the Mediterranean. *Clim Dyn*. <https://doi.org/10.1007/s00382-018-4521-8>
- Croce P, Formichi P, Landi F, Mercogliano P, Bucchignani E, Dosio A, Dimova S (2018) The snow load in Europe and the climate change. *Clim Risk Manag* 20:138–154. <https://doi.org/10.1016/j.crm.2018.03.001>
- Davin EL, Seneviratne SI, Ciais P, Ollio A, Wang T (2014) Preferential cooling of hot extremes from cropland albedo management. *Proc National Academy Sci* 111(27):9757–9761. <https://doi.org/10.1073/pnas.1317323111>
- Davin EL, Maisonnave E, Seneviratne SI (2016) Is land surface processes representation a possible weak link in current regional climate models? *Environ Res Lett* 11(7):074027. <https://doi.org/10.1088/1748-9326/11/7/074027>
- Davin EL, Rechid D, Breil M, Cardoso RM, Coppola E, Hoffmann P, Jach LL, Katragkou E, de Noblet-Ducoudré N, Radtke K, Raffa, M, Soares PMM, Sofiadis G, Strada S, Strandberg G, Tölle MH, Warrach-Sagi K, Wulfmeyer V (2020) Biogeophysical impacts of forestation in Europe: First results from the LUCAS Regional Climate Model intercomparison. *Earth Syst Dyn* 11:183–200. <https://doi.org/10.5194/esd-11-183-2020>
- de Noblet-Ducoudré N, Boisier J-P, Pitman A, Bonan GB, Brovkin V, Cruz F, Delire C, Gayler V, van den Hurk BJM, Lawrence PJ, van der Molen MK, Müller C, Reick CH, Strengers BJ, Voltaire A (2012) Determining robust impacts of land-use-induced land cover changes on surface climate over North America and Eurasia: results from the first set of LUCID experiments. *J Clim* 25(9):3261–3281. <https://doi.org/10.1175/jcli-d-11-00338.1>
- Dee DP, Uppala SM, Simmons AJ, Berrisford P, Poli P, Kobayashi S, Andrae U, Balmaseda MA, Balsamo G, Bauer P, Bechtold P, Beljaars ACM, van de Berg L, Bidlot J, Bormann N, Delsol C, Dragani R, Fuentes M, Geer AJ, Haimberger L, Healy SB, Hersbach H, Hólm EV, Isaksen L, Kållberg P, Köhler M, Matricardi M, McNally AP, Monge-Sanz BM, Morcrette J-J, Park B-K, Peubey C, de Rosnay P, Tavalato C, Thépaut J-N, Vitart F (2011) The ERA-Interim reanalysis: configuration and performance of the data assimilation system. *Quarterly J Royal Meteorol Soc* 137(656):553–597. <https://doi.org/10.1002/qj.828>
- Deser C, Knutti R, Solomon S, Phillips AS (2012) Communication of the role of natural variability in future North American climate. *Nat Clim Change* 2(11):775–779. <https://doi.org/10.1038/nclimate1562>
- Dilling L, Berggren J (2014) What do stakeholders need to manage for climate change and variability? A document-based analysis from three mountain states in the Western USA. *Reg Environ Change* 15(4):657–667. <https://doi.org/10.1007/s10113-014-0668-y>
- Domínguez M, Gaertner MA, de Rosnay P, Losada T (2010) A regional climate model simulation over West Africa: parameterization tests and analysis of land-surface fields. *Clim Dyn* 35(1):249–265. <https://doi.org/10.1007/s00382-010-0769-3>
- Domínguez M, Romera R, Sánchez E, Fita L, Fernández J, Jiménez-Guerrero P, Montávez J, Cabos W, Liguori G, Gaertner M (2013) Present-climate precipitation and temperature extremes over Spain from a set of high resolution RCMs. *Clim Res* 58(2):149–164. <https://doi.org/10.3354/cr01186>
- Donnelly C, Greuell W, Andersson J, Gerten D, Pisacane G, Roudier P, Ludwig F (2017) Impacts of climate change on European hydrology at 1.5, 2 and 3 degrees mean global warming above preindustrial level. *Clim Change* 143:13–26. <https://doi.org/10.1007/s10584-017-1971-7>
- Dosio A (2016) Projections of climate change indices of temperature and precipitation from an ensemble of bias-adjusted high-resolution EURO-CORDEX regional climate models. *J Geophys Res Atmos* 121(10):5488–5511. <https://doi.org/10.1002/2015jd024411>
- Dyrddal AV, Stordal F, Lussana C (2017) Evaluation of summer precipitation from EURO-CORDEX fine-scale RCM simulations over Norway. *Int J Climatol* 38(4):1661–1677. <https://doi.org/10.1002/joc.5287>
- Fantini A, Raffaele F, Torma C, Bacer S, Coppola E, Giorgi F, Ahrens B, Dubois C, Sanchez E, Verdecchia M (2018) Assessment of multiple daily precipitation statistics in ERA-Interim driven Med-CORDEX and EURO-CORDEX experiments against high resolution observations. *Clim Dyn* 51(3):877–900. <https://doi.org/10.1007/s00382-016-3453-4>
- Fernández J, Frías MD, Cabos WD, Cofiño AS, Domínguez M, Fita L, Gaertner MA, García-Díez M, Gutiérrez JM, Jiménez-Guerrero P, Liguori G, Montávez JP, Romera R, Sánchez E (2019) Consistency of climate change projections from multiple global and regional model intercomparison projects. *Clim Dyn* 52(1):1139–1156. <https://doi.org/10.1007/s00382-018-4181-8>
- Frei C (2014) Interpolation of temperature in a mountainous region using nonlinear profiles and non-Euclidean distances. *Int J Climatol* 34(5):1585–1605. <https://doi.org/10.1002/joc.3786>
- Frei P, Kotlarski S, Liniger MA, Schär C (2018) Future snowfall in the Alps: projections based on the EURO-CORDEX regional climate models. *The Cryosphere* 12(1):1–24. <https://doi.org/10.5194/tc-12-1-2018>
- Gaertner MÁ, González-Alemán JJ, Romera R, Domínguez M, Gil V, Sánchez E, Gallardo C, Miglietta MM, Walsh KJE, Sein DV, Somot S, Dell’Aquila A, Teichmann C, Ahrens B, Buonomo E, Colette A, Bastin S, van Meijgaard E, Nikulin G (2018) Simulation of medicanes over the Mediterranean Sea in a regional climate model ensemble: impact of ocean-atmosphere coupling and increased resolution. *Cli Dyn* 51:1041–1057. <https://doi.org/10.1007/s00382-016-3456-1>
- García-Díez M, Fernández J, Vautard R (2015) An RCM multi-physics ensemble over Europe: multi-variable evaluation to avoid error compensation. *Clim Dyn* 45(11–12):3141–3156. <https://doi.org/10.1007/s00382-015-2529-x>

- Giorgi F, Coppola E, Solmon F, Mariotti L, Sylla MB, Bi X, Elguindi N, Diro GT, Nair V, Giuliani G, Turuncoglu UU, Cozzini S, Güttler I, O'Brien TA, Tawfik AB, Shalaby A, Zakey AS, Steiner AL, Stordal F, Sloan LC, Brankovic C (2012) RegCM4: model description and preliminary tests over multiple CORDEX domains. *Clim Res* 52(1):7–29. <https://doi.org/10.3354/cr01018>
- Giorgi F, Gutowski WJ (2015) Regional dynamical downscaling and the CORDEX Initiative. *Annu Rev Environ Res* 40:467–490. <https://doi.org/10.1146/annurev-environ-102014-021217>
- Giorgi F, Jones C, Asrar G (2009) Addressing climate information needs at the regional level: the CORDEX framework. *WMO Bull* 58(3):175–183
- Giorgi F, Torma C, Coppola E, Ban N, Schär C, Somot S (2016) Enhanced summer convective rainfall at Alpine high elevations in response to climate warming. *Nat Geosci* 9(8):584–589. <https://doi.org/10.1038/ngeo2761>
- Giot O, Termonia P, Degrauwe D, De Troch R, Caluwaerts S, Smet G, Berckmans J, Deckmyn A, De Cruz L, De Meutter P, Duerinckx A, Gerard L, Hamdi R, Van den Bergh J, Van Ginderachter M, Van Schaybroeck B (2016) Validation of the ALARO-0 model within the EURO-CORDEX framework. *Geosci Model Dev* 9(3):1143–1152. <https://doi.org/10.5194/gmd-9-1143-2016>
- Gutiérrez JM, Maraun D, Widmann M, Huth R, Hertig E, Benestad R, Roessler O, Wibig J, Wilcke R, Kotlarski S, San Martín D, Herrera S, Bedia J, Casanueva A, Manzanar R, Iturbide M, Vrac M, Dubrovsky M, Ribalaygua J, Pórtolas J, Rätty O, Räisänen J, Hingray B, Raynaud D, Casado MJ, Ramos P, Zerenner T, Turco M, Bosshard T, Štěpánek P, Bartholy J, Pongracz R, Keller DE, Fischer AM, Cardoso RM, Soares PMM, Czernecki B, Pagé C (2018) An intercomparison of a large ensemble of statistical downscaling methods over Europe: results from the VALUE perfect predictor cross-validation experiment. *Int J Climatol*. <https://doi.org/10.1002/joc.5462>
- Gutowski JW, Giorgi F, Timbal B, Frigon A, Jacob D, Kang HS, Raghavan K, Lee B, Lennard C, Nikulin G, O'Rourke E, Rixen M, Solman S, Stephenson T, Tangang F (2016) WCRP coordinated regional downscaling experiment (CORDEX): a diagnostic MIP for CMIP6. *Geosci Model Dev* 9(11):4087–4095. <https://doi.org/10.5194/gmd-9-4087-2016>
- Hauser M, Gudmundsson L, Orth R, Jézéquel A, Hausteiner K, Vautard R, van Oldenborgh GJ, Wilcox L, Seneviratne SI (2017) Methods and model dependency of extreme event attribution: the 2015 European drought. *Earth's Future* 5(10):1034–1043. <https://doi.org/10.1002/2017EF000612>
- Heinzeller D, Duda MG, Kunstmann H (2016) Towards convection-resolving, global atmospheric simulations with the Model for Prediction Across Scales (MPAS) v3.1: an extreme scaling experiment. *Geosci Model Dev* 9(1):77–110. <https://doi.org/10.5194/gmd-9-77-2016>
- Hertig E, Maraun D, Bartholy J, Pongracz R, Vrac M, Mares I, Gutiérrez JM, Wibig J, Casanueva A, Soares PMM (2018) Comparison of statistical downscaling methods with respect to extreme events over Europe: validation results from the perfect predictor experiment of the COST action VALUE. *Int J Climatol*. <https://doi.org/10.1002/joc.5469>
- Hiebl J, Frei C (2016) Daily temperature grids for Austria since 1961—concept, creation and applicability. *Theor Appl Climatol* 124(1–2):161–178. <https://doi.org/10.1007/s00704-015-1411-4>
- Hiebl J, Frei C (2018) Daily precipitation grids for Austria since 1961—development and evaluation of a spatial dataset for hydroclimatic monitoring and modelling. *Theor Appl Climatol* 132(1–2):327–345. <https://doi.org/10.1007/s00704-017-2093-x>
- Hosseinzadehtalaei P, Tabari H, Willems P (2018) Precipitation intensity–duration–frequency curves for central Belgium with an ensemble of EURO-CORDEX simulations, and associated uncertainties. *Atmos Res* 200:1–12. <https://doi.org/10.1016/j.atmosres.2017.09.015>
- Huebener H, Hoffmann P, Keuler K, Pfeifer S, Ramthun H, Spekat A, Steger C, Warrach-Sagi K (2017) Deriving user-informed climate information from climate model ensemble results. *Adv Sci Res* 14:261–269. <https://doi.org/10.5194/asr-14-261-2017>
- Ivanov M, Warrach-Sagi K, Wulfmeyer V (2017) Field significance of performance measures in the context of regional climate model evaluation. Part 1: temperature. *Theor Appl Climatol* 132(1–2):219–237. <https://doi.org/10.1007/s00704-017-2100-2>
- Jacob D, Elizalde A, Haensler A, Hagemann S, Kumar P, Podzun R, Rechid D, Remedio AR, Saeed F, Sieck K, Teichmann C, Wilhelm C (2012) Assessing the transferability of the regional climate model REMO to different COordinated regional climate downscaling EXperiment (CORDEX) regions. *Atmosphere* 3(1):181–199. <https://doi.org/10.3390/atmos3010181>
- Jacob D, Petersen J, Eggert B, Alias A, Christensen OB, Bouwer LM, Braun A, Colette A, Déqué M, Georgievski G, Georgopoulou E, Gobiet A, Menut L, Nikulin G, Haensler A, Hempelmann N, Jones C, Keuler K, Kovats S, Kröner N, Kotlarski S, Kriegsmann A, Martin E, van Meijgaard E, Moseley C, Pfeifer S, Preuschmann S, Radermacher C, Radtke K, Rechid D, Rounsevell M, Samuelsson P, Somot S, Soussana J-F, Teichmann C, Valentini R, Vautard R, Weber Brn, Yiou P (2014) EURO-CORDEX: new high-resolution climate change projections for European impact research. *Reg Environ Change* 14(2):563–578. <https://doi.org/10.1007/s10113-013-0499-2>
- Jacob D, Kotova L, Teichmann C, Sobolowski SP, Vautard R, Donnelly C, Koutroulis AG, Grillakis MG, Tsanis IK, Damm A, Sakalli A, van Vliet MTH (2018) Climate Impacts in Europe Under +1.5 °C Global Warming. *Earth's Future* 6(2):264–285. <https://doi.org/10.1002/2017ef000710>
- Jerez S, Tobin I, Vautard R, Montávez JP, López-Romero JM, Thais F, Bartok B, Christensen OB, Colette A, Déqué M, Nikulin G, Kotlarski S, van Meijgaard E, Teichmann C, Wild M (2015) The impact of climate change on photovoltaic power generation in Europe. *Nat Commun* 6(1):10014. <https://doi.org/10.1038/ncomms10014>
- Katragkou E, García-Díez M, Vautard R, Sobolowski S, Zanits P, Alexandri G, Cardoso RM, Colette A, Fernandez J, Gobiet A, Goergen K, Karacostas T, Knist S, Mayer S, Soares PMM, Pytharoulis I, Tegoulas I, Tsikerdekis A, Jacob D (2015) Regional climate hindcast simulations within EURO-CORDEX: evaluation of a WRF multi-physics ensemble. *Geosci Model Dev* 8(3):603–618. <https://doi.org/10.5194/gmd-8-603-2015>
- Keune J, Gasper F, Goergen K, Hense A, Shrestha P, Sulis M, Kollet S (2016) Studying the influence of groundwater representations on land surface-atmosphere feedbacks during the European heat wave in 2003. *J Geophys Res Atmos* 121(22):13,301–13,325. <https://doi.org/10.1002/2016jd025426>
- Keune J, Sulis M, Kollet S, Siebert S, Wada Y (2018) Human water use impacts on the strength of the continental sink for atmospheric water. *Geophys Res Lett* 45(9):4068–4076. <https://doi.org/10.1029/2018gl077621>
- Kew SF, Philip SY, van Oldenborgh GJ, Otto FEL, Vautard R, van der Schrier G, Tebaldi C (2018) Attribution of the exceptional summer heat wave in Southern Europe 2017. *Bull Am Meteor Soc*. in press
- Kjellström E, Bärring L, Nikulin G, Nilsson C, Persson G, Strandberg G (2016) Production and use of regional climate model projections – a Swedish perspective on building climate services. *Clim Serv* 2–3:15–29. <https://doi.org/10.1016/j.cliser.2016.06.004>
- Kjellström E, Nikulin G, Strandberg G, Christensen OB, Jacob D, Keuler K, Lenderink G, van Meijgaard E, Schär C, Somot S, Sørland SL, Teichmann C, Vautard R (2018) European climate


- change at global mean temperature increases of 1.5 and 2 °C above pre-industrial conditions as simulated by the EURO-CORDEX regional climate models. *Earth Syst Dyn* 9(2):459–478. <https://doi.org/10.5194/esd-9-459-2018>
- Knist S, Goergen K, Buonomo E, Christensen OB, Colette A, Cardoso RM, Fealy R, Fernández J, García-Díez M, Jacob D, Kartsios S, Katragkou E, Keuler K, Mayer S, van Meijgaard E, Nikulin G, Soares PMM, Sobolowski S, Szepszo G, Teichmann C, Vautard R, Warrach-Sagi K, Wulfmeyer V, Simmer C (2017) Land-atmosphere coupling in EURO-CORDEX evaluation experiments. *J Geophys Res Atmos* 122(1):79–103. <https://doi.org/10.1002/2016jd025476>
- Kotlarski S, Keuler K, Christensen OB, Colette A, Déqué M, Gobiet A, Goergen K, Jacob D, Lüthi D, van Meijgaard E, Nikulin G, Schär C, Teichmann C, Vautard R, Warrach-Sagi K, Wulfmeyer V (2014) Regional climate modeling on European scales: a joint standard evaluation of the EURO-CORDEX RCM ensemble. *Geosci Model Dev* 7(4):1297–1333. <https://doi.org/10.5194/gmd-7-1297-2014>
- Lawrence D, Vandecar K (2015) Effects of tropical deforestation on climate and agriculture. *Nat Clim Change* 5(1):27–36. <https://doi.org/10.1038/nclimate2430>
- Lawrence DM, Hurtt GC, Arneth A, Brovkin V, Calvin KV, Jones AD, Jones CD, Lawrence PJ, de Noblet-Ducoudré N, Pongratz J, Seneviratne SI, Shevliakova E (2016) The land use model intercomparison project (LUMIP) contribution to CMIP6: rationale and experimental design. *Geosci Model Dev* 9(9):2973–2998. <https://doi.org/10.5194/gmd-9-2973-2016>
- Lawrence BN, Rezný M, Budich R, Bauer P, Behrens Jrg, Carter M, Deconinck W, Ford R, Maynard C, Mullerworth S, Osuna C, Porter A, Serradell K, Valcke S, Wedi N, Wilson S (2018) Crossing the chasm: how to develop weather and climate models for next generation computers? *Geosci Model Dev* 11(5):1799–1821. <https://doi.org/10.5194/gmd-11-1799-2018>
- Lejeune Q, Seneviratne SI, Davin EL (2017) Historical land-cover change impacts on climate: Comparative assessment of LUCID and CMIP5 multimodel experiments. *J Clim* 30(4):1439–1459. <https://doi.org/10.1175/jcli-d-16-0213.1>
- Lejeune Q, Davin EL, Gudmundsson L, Winckler J, Seneviratne SI (2018) Historical deforestation locally increased the intensity of hot days in northern mid-latitudes. *Nat Clim Change* 8(5):386–390. <https://doi.org/10.1038/s41558-018-0131-z>
- Leutwyler D, Fuhrer O, Lapillonne X, Lüthi D, Schär C (2016) Towards European-scale convection-resolving climate simulations with GPUs: a study with COSMO 4.19. *Geosci Model Dev* 9(9):3393–3412. <https://doi.org/10.5194/gmd-9-3393-2016>
- Lhotka O, Kyselý J, Plavcová E (2017) Evaluation of major heat waves' mechanisms in EURO-CORDEX RCMs over Central Europe. *Clim Dyn* 50(11–12):4249–4262. <https://doi.org/10.1007/s00382-017-3873-9>
- Lussana C, Saloranta T, Skaugen T, Magnusson J, Einar Tveito O, Andersen J (2018) SeNorge2 daily precipitation, an observational gridded dataset over Norway from 1957 to the present day. *Earth Syst Sci Data* 10(1):235–249. <https://doi.org/10.5194/essd-10-235-2018>
- Luu LN, Vautard R, Yiou P, van Oldenborgh GJ, Lenderink G (2018) Attribution of extreme rainfall events in the South of France using EURO-CORDEX simulations. *Geophysical Research Letters*. <https://doi.org/10.1029/2018gl077807>
- Lüthi S, Ban N, Kotlarski S, Steger CR, Jonas T, Schär C (2019) Projections of alpine snow-cover in a high-resolution climate simulation. *Atmosphere* 10(8):463. <https://doi.org/10.3390/atmos10080463>, <https://www.mdpi.com/2073-4433/10/8/463>
- Maraun D, Huth R, Gutiérrez JM, Martín DS, Dubrovsky M, Fischer A, Hertig E, Soares PMM, Bartholy J, Pongrácz R, Widmann M, Casado MJ, Ramos P, Bedia J (2017) The VALUE perfect predictor experiment: evaluation of temporal variability. *International Journal of Climatology*. <https://doi.org/10.1002/joc.5222>
- Maraun D, Widmann M, Gutiérrez JM, Kotlarski S, Chandler RE, Hertig E, Wibig J, Huth R, Wilcke RAI (2015) VALUE: a framework to validate downscaling approaches for climate change studies. *Earth's Future* 3(1):1–14. <https://doi.org/10.1002/2014ef000259>
- Maraun D, Widmann M, Gutierrez JM (2018) Statistical downscaling skill under present climate conditions: a synthesis of the VALUE perfect predictor experiment. *International Journal of Climatology*. <https://doi.org/10.1002/joc.5877>
- McSweeney CF, Jones RG, Lee RW, Rowell DP (2014) Selecting CMIP5 GCMs for downscaling over multiple regions. *Clim Dyn* 44(11–12):3237–3260. <https://doi.org/10.1007/s00382-014-2418-8>
- Mendlik T, Gobiet A (2015) Selecting climate simulations for impact studies based on multivariate patterns of climate change. *Clim Change* 135(3–4):381–393. <https://doi.org/10.1007/s10584-015-1582-0>
- Mezghani A, Dobler A, Haugen JE, Benestad RE, Parding KM, Piniewski M, Kardel I, Kundzewicz ZW (2017) CHASE-PL climate projection dataset over Poland - bias adjustment of EURO-CORDEX simulations. *Earth Syst Sci Data* 9(2):905–925. <https://doi.org/10.5194/essd-9-905-2017>
- Mezghani A, Dobler A, Benestad R, Haugen JE, Parding KM, Piniewski M, Kundzewicz ZW (2019) Subsampling impact on the climate change signal over Poland based on simulations from statistical and dynamical downscaling. *J Appl Meteorol Climatol* 58(5):1061–1078. <https://doi.org/10.1175/JAMC-D-18-0179.1>
- Moemken J, Reyers M, Feldmann H, Pinto JG (2018) Future changes of wind speed and wind energy potentials in EURO-CORDEX ensemble simulations. *J Geophys Res Atmos* 123(12):6373–6389. <https://doi.org/10.1029/2018JD028473>
- Ouzeau G, Soubeyroux J-M, Schneider M, Vautard R, Planton S (2016) Heat waves analysis over France in present and future climate: Application of a new method on the EURO-CORDEX ensemble. *Clim Serv* 4:1–12. <https://doi.org/10.1016/j.cliser.2016.09.002>
- Perugini L, Caporaso L, Marconi S, Cescatti A, Quesada B, de Noblet-Ducoudré N, House JJ, Arneth A (2017) Biophysical effects on temperature and precipitation due to land cover change. *Environ Res Lett* 12(5):053002. <https://doi.org/10.1088/1748-9326/aa6b3f>
- Philip S, Kew SF, van Oldenborgh GJ, Aalbers E, Vautard R, Otto F, Haustein K, Habets F, Singh R (2018) Validation of a rapid attribution of the May/June 2016 flood-inducing precipitation in France to climate change. *Journal of Hydrometeorology*. <https://doi.org/10.1175/jhm-d-18-0074.1>
- Pielke RA, Pitman A, Niyogi D, Mahmood R, McAlpine C, Hossain F, Klein Goldewijk K, Nair U, Betts R, Fall S, Reichstein M, Kabat P, de Noblet N (2011) Land use/land cover changes and climate: modeling analysis and observational evidence. *Wiley Interdiscip Rev Clim Change* 2(6):828–850. <https://doi.org/10.1002/wcc.144>
- Pitman AJ, de Noblet-Ducoudré N, Avila FB, Alexander LV, Boisier J-P, Brovkin V, Delire C, Cruz F, Donat MG, Gayler V, van den Hurk B, Reick C, Voldoire A (2012) Effects of land cover change on temperature and rainfall extremes in multi-model ensemble simulations. *Earth Syst Dyn* 3(2):213–231. <https://doi.org/10.5194/esd-3-213-2012>
- Prein AF, Langhans W, Fosser G, Ferrone A, Ban N, Goergen K, Keller M, Tölle M, Gutjahr O, Feser F, Brisson E, Kollet S, Schmidli J, van Lipzig NPM, Leung R (2015) A review on regional convection-permitting climate modeling: demonstrations, prospects, and challenges. *Rev Geophys* 53(2):323–361. <https://doi.org/10.1002/2014rg000475>

- Prein AF, Gobiet A (2016) Impacts of uncertainties in European gridded precipitation observations on regional climate analysis. *Int J Climatol* 37(1):305–327. <https://doi.org/10.1002/joc.4706>
- Prein AF, Liu C, Ikeda K, Bullock R, Rasmussen RM, Holland GJ, Clark M (2017a) Simulating north american mesoscale convective systems with a convection-permitting climate model. *Clim Dyn* 28:1–16. <https://doi.org/10.1007/s00382-017-3993-2>
- Prein AF, Rasmussen R, Stephens G (2017b) Challenges and advances in convection-permitting climate modeling. *Bull Am Meteorol Soc* 98(5):1027–1030. <https://doi.org/10.1175/bams-d-16-0263.1>
- Pučík T, Groenemeijer P, Rädler AT, Tijssen L, Nikulin G, Prein AF, van Meijgaard E, Fealy R, Jacob D, Teichmann C (2017) Future changes in European severe convection environments in a regional climate model ensemble. *J Clim* 30(17):6771–6794. <https://doi.org/10.1175/jcli-d-16-0777.1>
- Rajczak J, Schär C (2017) Projections of future precipitation extremes over Europe: a multimodel assessment of climate simulations. *J Geophys Res Atmos* 122(20):10,773–10,800. <https://doi.org/10.1002/2017jd027176>
- Raymond F, Ullmann A, Trambly Y, Drobinski P, Camberlin P (2019) Evolution of mediterranean extreme dry spells during the wet season under climate change. *Reg Environ Change*. <https://doi.org/10.1007/s10113-019-01526-3>
- Reder A, Iturbide M, Herrera S, Rianna G, Mercogliano P, Gutiérrez JM (2018) Assessing variations of extreme indices inducing weather-hazards on critical infrastructures over Europe—the INTACT framework. *Clim Change* 148(1-2):123–138. <https://doi.org/10.1007/s10584-018-2184-4>
- Rockel B, Will A, Hense A (2008) The regional climate model COSMO-CLM (CCLM). *Meteorologische Zeitschrift* 17(4):347–348
- Ruane AC, Teichmann C, Arnell NW, Carter TR, Ebi KL, Frieler K, Goodess CM, Hewitson B, Horton R, Kovats RS, Lotze HK, Mearns LO, Navarra A, Ojima DS, Riahi K, Rosenzweig C, Themessl M, Vincent K (2016) The vulnerability, impacts, adaptation and climate services advisory board (VIACS AB v1.0) contribution to CMIP6. *Geosci Model Dev* 9(9):3493–3515. <https://doi.org/10.5194/gmd-9-3493-2016>
- Rulfová Z, Beranová R, Kyselý J (2016) Climate change scenarios of convective and large-scale precipitation in the Czech Republic based on EURO-CORDEX data. *Int J Climatol* 37(5):2451–2465. <https://doi.org/10.1002/joc.4857>
- Ruti PM, Somot S, Giorgi F, Dubois C, Flaounas E, Obermann A, Dell'Aquila A, Pisacane G, Harzallah A, Lombardi E, Ahrens B, Akhtar N, Alias A, Arsouze T, Aznar R, Bastin S, Bartholy J, Béranger K, Beuvier J, Bouffies-Cloché S, Brauch J, Cabos W, Calmanti S, Calvet J-C, Carillo A, Conte D, Coppola E, Djurdjevic V, Drobinski P, Elizalde-Arellano A, Gaertner M, Galàn P, Gallardo C, Gualdi S, Goncalves M, Jorba O, Jordà G, L'Heveder B, Lebeaupin-Brossier C, Li L, Liguori G, Lionello P, Maciàs D, Nabat P, nol B, Raikovic B, Ramage K, Sevaut F, Sannino G, Struglia MV, Sanna A, Torma C, Vervatis V (2016) Med-CORDEX initiative for mediterranean climate studies. *Bull Am Meteorol Soc* 97(7):1187–1208. <https://doi.org/10.1175/bams-d-14-00176.1>
- Samuelsson P, Jones CG, Willén U, Ullerstig A, Gollvik S, Hansson U, Jansson C, Kjellström E, Nikulin G, Wyser K (2011) The Rossby Centre regional climate model RCA3: model description and performance. *Tellus A: Dynamic Meteorology and Oceanography* 63(1):4–23. <https://doi.org/10.1111/j.1600-0870.2010.00478.x>
- Santanello JA, Dirmeyer PA, Ferguson CR, Findell KL, Tawfik AB, Berg A, Ek M, Gentile P, Guillod BP, van Heerwaarden C, Roundy J, Wulfmeyer V (2018) Land–atmosphere interactions: the LoCo perspective. *Bull Am Meteorol Soc* 99(6):1253–1272. <https://doi.org/10.1175/bams-d-17-0001.1>
- Scaff L, Prein AF, Li Y, Liu C, Rasmussen R, Ikeda K (2019) Simulating the convective precipitation diurnal cycle in north america's current and future climate. *Climate Dynamics*. <https://doi.org/10.1007/s00382-019-04754-9>
- Schwitalla T, Bauer HS, Wulfmeyer V, Warrach-Sagi K (2017) Continuous high-resolution midlatitude-belt simulations for July–August 2013 with WRF. *Geosci Model Dev* 10(5):2031–2055. <https://doi.org/10.5194/gmd-10-2031-2017>
- Skamarock WC, Klemp JB (2008) A time-split nonhydrostatic atmospheric model for weather research and forecasting applications. *J Comput Phys* 227(7):3465–3485. <https://doi.org/10.1016/j.jcp.2007.01.037>
- Smiattek G, Kunstmann H, Senatore A (2016) EURO-CORDEX regional climate model analysis for the greater alpine region: performance and expected future change. *J Geophys Res Atmos* 121(13):7710–7728. <https://doi.org/10.1002/2015jd024727>
- Soares PMM, Cardoso RM (2017) A simple method to assess the added value using high-resolution climate distributions: application to the EURO-CORDEX daily precipitation. *Int J Climatol* 38(3):1484–1498. <https://doi.org/10.1002/joc.5261>
- Soares PMM, Maraun D, Brands S, Jury MW, Gutiérrez JM, San Martín D, Hertig E, Huth R, Belušić A, Cardoso RM, Kotlarski S, Drobinski P, Obermann-Hellhund A (2018) Process-based evaluation of the VALUE perfect predictor experiment of statistical downscaling methods. *Int J Climatol* 39:3868–3893. <https://doi.org/10.1002/joc.5911>. <https://rmets.onlinelibrary.wiley.com/doi/pdf/10.1002/joc.5911>
- Somot S, Ruti P, Ahrens B, Coppola E, Jordà G, Sannino G, Solmon F (2018) Editorial for the Med-CORDEX special issue. *Clim Dyn* 51(3):771–777. <https://doi.org/10.1007/s00382-018-4325-x>
- Sørland SL, Schär C, Lüthi D, Kjellström E (2018) Bias patterns and climate change signals in GCM-RCM model chains. *Environ Res Lett* 13(7):074017. <https://doi.org/10.1088/1748-9326/aacc77>
- Stepanek P, Zahradníček P, Farda A, Skalák P, Trnka M, Meitner J, Rajdl K (2016) Projection of drought-inducing climate conditions in the Czech Republic according to euro-CORDEX models. *Clim Res* 70(2-3):179–193. <https://doi.org/10.3354/cr01424>
- Stott PA, Christidis N, Otto FEL, Sun Y, Vanderlinden JP, van Oldenborgh GJ, Vautard R, von Storch H, Walton P, Yiou P, Zwiers FW (2015) Attribution of extreme weather and climate-related events. *Wiley Interdiscip Rev Clim Change* 7(1):23–41. <https://doi.org/10.1002/wcc.380>
- Teichmann C, Bülow K, Otto J, Pfeifer S, Rechid D, Sieck K, Jacob D (2018) Avoiding Extremes: Benefits of Staying below +1.5 °C Compared to +2.0 °C and +3.0 °C Global Warming. *Atmosphere* 9(4):115. <https://doi.org/10.3390/atmos9040115>
- Termonia P, Van Schaeuybroeck B, De Cruz L, De Troch R, Caluwaerts S, Giot O, Hamdi R, Vannitsem S, Duchêne F, Willems P, Tabari H, Van Uytven E, Hosseinzadehtalaei P, Van Lipzig N, Wouters H, Vanden Broucke S, van Ypersele J-P, Marbaix P, Villanueva-Birriel C, Fettweis X, Wyard C, Scholzen C, Doutreloup S, De Ridder K, Gobin A, Lauwaet D, Stavrakou T, Bauwens M, Müller J-F, Luyten P, Ponsar S, Van den Eynde D, Pottiaux E (2018) The CORDEX.be initiative as a foundation for climate services in Belgium. *Climate Services*. <https://doi.org/10.1016/j.cliser.2018.05.001>
- Thiery W, Davin EL, Lawrence DM, Hirsch AL, Hauser M, Seneviratne SI (2017) Present-day irrigation mitigates heat extremes. *J Geophys Res Atmos* 122(3):1403–1422. <https://doi.org/10.1002/2016jd025740>
- Tobin I, Jerez S, Vautard R, Thais F, van Meijgaard E, Prein A, Déqué M, Kotlarski S, Fox Maule C, Nikulin G, Noël T, Teichmann C (2016) Climate change impacts on the power generation potential of a European mid-century wind farms scenario. *Environ Res Lett* 11(3):034013. <http://stacks.iop.org/1748-9326/11/i=3/a=034013>

- Tobin I, Greuell W, Jerez S, Ludwig F, Vautard R, van Vliet MTH, Bréon FM (2018) Vulnerabilities and resilience of European power generation to 1.5 °C, 2 °C and 3 °C warming. *Environ Res Lett* 13(4):044024. <http://stacks.iop.org/1748-9326/13/i=4/a=044024>
- Torma C, Giorgi F, Coppola E (2015) Added value of regional climate modeling over areas characterized by complex terrain-precipitation over the Alps. *J Geophys Res Atmos* 120(9):3957–3972. <https://doi.org/10.1002/2014jd022781>
- Tramblay Y, Somot S (2018) Future evolution of extreme precipitation in the mediterranean. *Clim Change* 151(2):289–302. <https://doi.org/10.1007/s10584-018-2300-5>
- Turco M, Sanna A, Herrera S, Llasat MC, Gutiérrez JM (2013) Large biases and inconsistent climate change signals in ENSEMBLES regional projections. *Clim Change* 120(4):859–869. <https://doi.org/10.1007/s10584-013-0844-y>
- van der Linden P, Mitchell JFB (2009) ENSEMBLES: Climate change and its impacts - summary of research and results from the ENSEMBLES project. Tech. rep., Met Office Hadley Centre, Exeter, United Kingdom. <http://mfkp.org/INRMM/article/14257308>
- Van Meijgaard E, Van Ulft L, Lenderink G, De Roode S, Wipfler EL, Boers R, van Timmermans R (2012) Refinement and application of a regional atmospheric model for climate scenario calculations of western europe. KVR 054/12 KVR
- Vautard R, Gobiet A, Jacob D, Belda M, Colette A, Déqué M, Fernández J, García-Díez M, Goergen K, Güttler I, Halenka T, Karacostas T, Katragkou E, Keuler K, Kotlarski S, Mayer S, van Meijgaard E, Nikulin G, Patarčić M, Scinocca J, Sobolowski S, Suklitsch M, Teichmann C, Warrach-Sagi K, Wulfmeyer V, Yiou P (2013) The simulation of European heat waves from an ensemble of regional climate models within the EURO-CORDEX project. *Clim Dyn* 41(9–10):2555–2575. <https://doi.org/10.1007/s00382-013-1714-z>
- Vautard R, Colette A, van Meijgaard E, Meleux F, van Oldenborgh GJ, Otto F, Tobin I, Yiou P (2018) 14. Attribution of wintertime anticyclonic stagnation contributing to air pollution in western Europe. *Bull Am Meteorol Soc* 99(1):S70–S75. <https://doi.org/10.1175/BAMS-D-17-0113.1>
- Vautard R, Jan Van Oldenborgh G, Otto FEL, Yiou P, De Vries H, Van Meijgaard E, Stepek A, Soubeyroux J-M, Philip S, Kew SF, Costella C, Singh R, Tebaldi C (2019) Human influence on european winter wind storms such as those of January 2018. *Earth Syst Dyn* 10(2):271–286. <https://doi.org/10.5194/esd-10-271-2019>
- Warrach-Sagi K, Schwitalla T, Wulfmeyer V, Bauer H-S (2013) Evaluation of a climate simulation in Europe based on the WRF–NOAH model system: precipitation in Germany. *Clim Dyn* 41(3–4):755–774. <https://doi.org/10.1007/s00382-013-1727-7>
- WCRP Joint Scientific Committee (JSC) (2019) World Climate Research Programme Strategic Plan 2019–2028. WCRP Publication 1/2019
- Widmann M, Bedia J, Gutiérrez JM, Bosshard T, Hertig E, Maraun D, Casado MJ, Ramos P, Cardoso RM, Soares PMM, Ribalaygua J, Pagé C, Fischer AM, Herrera S, Huth R (2019) Validation of spatial variability in downscaling results from the VALUE perfect predictor experiment. *Int J Climatol* 39(9):3819–3845. <https://doi.org/10.1002/joc.6024>
- Will A, Akhtar N, Brauch J, Breil M, Davin E, Ho-Hagemann HTM, Maisonnave E, Thürkow M, Weiher S (2017) The COSMO-CLM 4.8 regional climate model coupled to regional ocean, land surface and global earth system models using OASIS3-MCT: description and performance. *Geosci Model Dev* 10(4):1549–1586. <https://doi.org/10.5194/gmd-10-1549-2017>
- Wulfmeyer V, Turner DD, Baker B, Banta R, Behrendt A, Bonin T, Brewer WA, Cuban M, Choukulkar A, Dumas R, Hardesty RM, Heus T, Ingwersen J, Lange D, Lee TR, Metzendorf S, Muppa SK, Meyers T, Newsom R, Osman M, Raasch S, Santanello J, Senff C, Späth F, Wagner T, Weckwerth T (2018) A new research approach for observing and characterizing land-atmosphere feedback. *Bull Am Meteorol Soc* 99(8):1639–1667. <https://doi.org/10.1175/BAMS-D-17-0009.1>

Publisher's note Springer Nature remains neutral with regard to jurisdictional claims in published maps and institutional affiliations.

Affiliations

Daniela Jacob¹ · Claas Teichmann¹  · Stefan Sobolowski² · Eleni Katragkou³ · Ivonne Anders⁴ · Michal Belda⁵ · Rasmus Benestad⁶ · Fredrik Boberg⁷ · Erasmo Buonomo^{8,9} · Rita M. Cardoso¹⁰ · Ana Casanueva¹¹ · Ole B. Christensen⁷ · Jens Hesselbjerg Christensen^{2,12} · Erika Coppola¹³ · Lesley De Cruz¹⁴ · Edouard L. Davin¹⁵ · Andreas Dobler⁶ · Marta Domínguez¹⁶ · Rowan Fealy¹⁷ · Jesus Fernandez¹¹ · Miguel Angel Gaertner¹⁸ · Markel García-Díez¹¹ · Filippo Giorgi¹³ · Andreas Gobiet⁴ · Klaus Goergen^{19,20} · Juan José Gómez-Navarro²¹ · Juan Jesús González Alemán¹⁸ · Claudia Gutiérrez¹⁸ · José M. Gutiérrez²² · Ivan Güttler²³ · Andreas Haensler¹ · Tomáš Halenka⁵ · Sonia Jerez²¹ · Pedro Jiménez-Guerrero²¹ · Richard G. Jones⁸ · Klaus Keuler²⁴ · Erik Kjellström²⁵ · Sebastian Knist^{20,26} · Sven Kotlarski²⁷ · Douglas Maraun²⁸ · Erik van Meijgaard²⁹ · Paola Mercogliano^{30,31} · Juan Pedro Montávez²¹ · Antonio Navarra³⁰ · Grigory Nikulin²⁵ · Nathalie de Noblet-Ducoudré³² · Hans-Juergen Panitz³³ · Susanne Pfeifer¹ · Marie Piazza²⁸ · Emanuela Pichelli¹³ · Joni-Pekka Pietikäinen^{1,34} · Andreas F. Prein³⁵ · Swantje Preuschmann¹ · Diana Rechid¹ · Burkhardt Rockel³⁶ · Raquel Romera¹⁷ · Enrique Sánchez¹⁷ · Kevin Sieck¹ · Pedro M. M. Soares¹⁰ · Samuel Somot³⁷ · Lidija Srnec²³ · Silje Lund Sørland¹⁵ · Piet Termonia^{14,38} · Heimo Truhetz²⁸ · Robert Vautard³² · Kirsten Warrach-Sagi³⁹ · Volker Wulfmeier³⁹

¹ Climate Service Center Germany (GERICS), Helmholtz-Zentrum Geesthacht, Fischertwiete 1 20095 Hamburg, Germany

² NORCE Norwegian Research Centre, The Bjerknes Centre for Climate Research, Bergen, Norway

³ Department of Meteorology and Climatology, School of Geology, Aristotle University of Thessaloniki, Thessaloniki, Greece

⁴ Central Institute for Meteorology and Geodynamics (ZAMG), Vienna, Austria

⁵ Department of Atmospheric Physics, Faculty of Mathematics and Physics, Charles University, Prague, Czech Republic

⁶ The Norwegian Meteorological Institute, Oslo, Norway

⁷ Danish Meteorological Institute (DMI), Copenhagen, Denmark

⁸ Met Office Hadley Centre, Fitzroy Road, Exeter, EX1 2HF, UK

⁹ School of Geography and the Environment, University of Oxford, South Parks Road, Oxford, OX1 3QY, UK

¹⁰ Instituto Dom Luiz (IDL), Faculdade de Ciências, Universidade de Lisboa, 1749-016 Lisbon, Portugal

¹¹ Meteorology Group, Department of Applied Mathematics and Computer Science, Universidad de Cantabria, Santander, Spain

¹² Niels Bohr Institute, University of Copenhagen, Copenhagen, Denmark

¹³ International Centre for Theoretical Physics (ICTP), Trieste, Italy

¹⁴ Royal Meteorological Institute of Belgium (RMIB), Brussels, Belgium

¹⁵ Institute for Atmospheric and Climate Science, ETH Zurich, Zurich, Switzerland

¹⁶ Agencia Estatal de Meteorología, Madrid, Spain

¹⁷ ICARUS, Department of Geography, Maynooth University, Maynooth, Co. Kildare, Ireland

¹⁸ University of Castilla-La Mancha, Toledo, Spain

¹⁹ Institute of Bio- and Geosciences, Agrosphere (IBG-3), Research Centre Jülich, Jülich, Germany

²⁰ Centre for High-Performance Scientific Computing in Terrestrial Systems, Geoverbund ABC/J, Jülich, Germany

²¹ Regional Atmospheric Modeling Group, Department of Physics, University of Murcia, Murcia, Spain

²² Meteorology Group, Instituto de Física de Cantabria (CSIC-Universidad de Cantabria), Santander, Spain

²³ Croatian Meteorological and Hydrological Service, Zagreb, Croatia

²⁴ Chair of Atmospheric Processes, Brandenburg University of Technology Cottbus - Senftenberg, Cottbus, Germany

²⁵ Swedish Meteorological and Hydrological Institute, Norrköping, Sweden

²⁶ Meteorological Institute, University of Bonn, Bonn, Germany

²⁷ Federal Office of Meteorology and Climatology MeteoSwiss, Zurich-Airport, Switzerland

²⁸ Wegener Center for Climate and Global Change, University of Graz, Graz, Austria

²⁹ Royal Netherlands Meteorological Institute (KNMI), De Bilt, The Netherlands

³⁰ Centro Euro-Mediterraneo sui Cambiamenti Climatici (CMCC), Lecce, Italy

³¹ C.I.R.A., Capua, Italy

³² Laboratoire des Sciences du Climat et de l'Environnement, IPSL, Unité Mixte CEA-CNRS-UVSQ, Université Paris-Saclay, Orme des Merisiers, 91191 Gif-sur-Yvette cédex, France

³³ Institute of Meteorology and Climate Research, Karlsruhe Institute of Technology, Karlsruhe, Germany

³⁴ Finnish Meteorological Institute (FMI), Helsinki, Finland

³⁵ National Center for Atmospheric Research, Boulder, CO, USA

³⁶ Helmholtz-Zentrum Geesthacht, Geesthacht, Germany

³⁷ CNRM, Université de Toulouse, Météo-France, CNRS, Toulouse, France

³⁸ Department of Physics and Astronomy, Ghent University, Ghent, Belgium

³⁹ Institute of Physics and Meteorology, University of Hohenheim, Stuttgart, Germany



PALM-USM v1.0: A new urban surface model integrated into the PALM large-eddy simulation model

Jaroslav Resler^{1,2}, Pavel Krč^{1,2}, Michal Belda^{1,2,4}, Pavel Juruš^{1,2}, Nina Benešová^{1,3}, Jan Lopata^{1,3}, Ondřej Vlček^{1,3}, Daša Damašková^{1,3}, Kryštof Eben^{1,2}, Přemysl Derbek¹, Björn Maronga⁵, and Farah Kanani-Sühring⁵

¹Faculty of Transportation Sciences, Czech Technical University in Prague, Prague, Czech Republic

²Institute of Computer Science, The Czech Academy of Sciences, Prague, Czech Republic

³Air Quality Protection Division, Czech Hydrometeorological Institute, Prague, Czech Republic

⁴Department of Atmospheric Physics, Faculty of Mathematics and Physics, Charles University, Prague, Czech Republic

⁵Institute of Meteorology and Climatology, Leibniz Universität Hannover, Hannover, Germany

Correspondence to: Jaroslav Resler (reslejar@fd.cvut.cz)

Received: 9 March 2017 – Discussion started: 15 March 2017

Revised: 11 August 2017 – Accepted: 31 August 2017 – Published: 9 October 2017

Abstract. Urban areas are an important part of the climate system and many aspects of urban climate have direct effects on human health and living conditions. This implies that reliable tools for local urban climate studies supporting sustainable urban planning are needed. However, a realistic implementation of urban canopy processes still poses a serious challenge for weather and climate modelling for the current generation of numerical models. To address this demand, a new urban surface model (USM), describing the surface energy processes for urban environments, was developed and integrated as a module into the PALM large-eddy simulation model. The development of the presented first version of the USM originated from modelling the urban heat island during summer heat wave episodes and thus implements primarily processes important in such conditions. The USM contains a multi-reflection radiation model for shortwave and long-wave radiation with an integrated model of absorption of radiation by resolved plant canopy (i.e. trees, shrubs). Furthermore, it consists of an energy balance solver for horizontal and vertical impervious surfaces, and thermal diffusion in ground, wall, and roof materials, and it includes a simple model for the consideration of anthropogenic heat sources. The USM was parallelized using the standard Message Passing Interface and performance testing demonstrates that the computational costs of the USM are reasonable on typical clusters for the tested configurations. The module was fully integrated into PALM and is available via its online repository under the GNU General Public License (GPL). The

USM was tested on a summer heat-wave episode for a selected Prague crossroads. The general representation of the urban boundary layer and patterns of surface temperatures of various surface types (walls, pavement) are in good agreement with in situ observations made in Prague. Additional simulations were performed in order to assess the sensitivity of the results to uncertainties in the material parameters, the domain size, and the general effect of the USM itself. The first version of the USM is limited to the processes most relevant to the study of summer heat waves and serves as a basis for ongoing development which will address additional processes of the urban environment and lead to improvements to extend the utilization of the USM to other environments and conditions.

1 Introduction

1.1 Urban climate

As more than half of the human population resides in cities, and this figure is expected to keep increasing in future (United Nations, 2014), the influence of urban surfaces on the local urban climate gains more importance. Many aspects of urban climate have direct effects on human health and living conditions, the most prominent examples being thermal comfort and air quality.

One major phenomenon related to the urban climate is the urban heat island (UHI), i.e. the fact that an urban area may be significantly warmer than its surrounding rural areas, which mainly appears during evening and early night hours (Oke, 1982). The higher temperature is linked to the absorption and retention of energy by urban surfaces and to anthropogenic heat emissions, which can cause urban-to-rural temperature differences of several degrees Celsius. Moreover, buildings and other urban components can locally decrease the ventilation (e.g. Letzel et al., 2012), thus adding to thermal discomfort. Chemical processes, and consequently air quality, are also affected by the urban environment.

Effects of the urban heat island on living conditions have been the focus of urban planning for several decades in various cities, as it is anticipated that careful planning can alleviate some of these effects. However, developing adaptation and mitigation strategies requires state-of-the-art tools applicable for urban climatology studies. The work presented in this paper started in the larger framework of the Urban Adapt¹ project, which focused on the development of such strategies for three major cities in the Czech Republic (Prague, Brno, and Pilsen). The aim was to provide as detailed a description of the street canyon conditions as possible, going to the resolution of the order of a few metres. Below we provide a brief description of the methods typically used for such a task and the motivation for developing a new urban surface model (USM).

Several possible approaches for studying urban climate have been used, ranging from observation analyses, over physical modelling, to numerical simulations (for a comprehensive review, see e.g. Mirzaei and Haghighat, 2010; Moonen et al., 2012). In this context, a number of physical processes and their complex interactions must be taken into account (e.g. Arnfield, 2003). Urban surfaces are affected by shortwave and longwave radiation, and energy is exchanged between the urban canopy and the atmosphere in various forms, including sensible and latent heat fluxes. These fluxes in turn, together with boundary layer processes and large-scale synoptic conditions, affect the turbulent flow of air. The complexity is further increased by the presence of vegetation and the pronounced heterogeneity of urban surface materials.

For numerical modelling of urban climate processes, various models and frameworks have been used (Mirzaei and Haghighat, 2010; Moonen et al., 2012; Mirzaei, 2015). One possible approach is to use a regional meteorological or climate model. However, these models typically operate with horizontal resolutions of the order of hundreds of metres to tens of kilometres, and urban processes are treated using bulk parameterizations or single-/multi-layer urban canopy models (e.g. Kusaka et al., 2001; Martilli et al., 2002). Thus, these models are much better suited to assessing the influence of urban environments on the larger-scale meteorology.

A second approach is represented by standalone parameterized models, e.g. the SOLWEIG model (Lindberg et al., 2008), RayMan (Matzarakis et al., 2010), the TUF-3D model (Krayenhoff and Voogt, 2007), the TUF-IOBES model (Yaghoobian and Kleissl, 2012, based on TUF-3D), TEB (Masson, 2000), or SUEWS (Järvi et al., 2011). These models treat some physical processes (e.g. radiation, latent heat flux, water balance), while they parameterize the air flow by means of statistical and climatological models or meteorological measurements.

The most complex approach is represented by a group of computational fluid dynamics (CFD) models. The explicit simulation of the turbulent flow is computationally expensive; thus, different techniques have to be adapted to make calculations feasible, usually based on limiting the range of the resolved length scales and timescales of the turbulent flow. Most of the CFD models applied for urban climatology studies today are models based on the Reynolds-averaged Navier–Stokes (RANS) equations, e.g. ENVI-met (ENVI-met, 2009), MITRAS (Schlünzen et al., 2003), MIMO (Ehrhard et al., 2000), and MUKLIMO_3 (Sievers, 2012, 2014). In RANS models, the entire turbulence spectrum is parameterized, and thus only the mean flow is predicted. This allows for use of relatively large time steps leading to moderate computational demands, but it implies physical limitations as interactions of turbulent eddies with the urban canopy cannot be explicitly treated. In order to overcome this deficiency, large-eddy simulation (LES) models can be employed. They use a scale separation approach to resolve the bulk of the turbulence spectrum explicitly, while parameterizing only the smallest eddies in a so-called subgrid-scale model. Examples of such models are e.g. PALM (Maronga et al., 2015), which can incorporate buildings as explicit obstacles, the OpenFoam² modelling system, which can use both LES and RANS solvers, or DALES (Heus et al., 2010).

However, many of the CFD models do not contain appropriate urban canopy energy balance models with an explicit treatment of radiative fluxes. To overcome this deficiency, stand-alone energy balance models can be coupled to CFD models, recent examples being SOLENE-microclimat (Musy et al., 2015) or TUF-IOBES, which was coupled to PALM (Yaghoobian et al., 2014). These are usually one-way coupled systems in which the stand-alone model is used for the calculation of incoming/outgoing energy fluxes to/from any surface element, which are then imported into the CFD model. This means that CFD model dynamics are not considered for the calculation of the energy fluxes, making this approach less precise than fully two-way integrated models.

Most of the CFD models are closed-source in-house solutions, complicating their scientific and technical validation. Furthermore, many of them are not designed to work on high-performance computing systems (HPC) with hundreds

¹<http://urbanadapt.cz/en>

²<http://www.openfoam.org>

to thousands of processor cores, limiting their range of applications. Notable exceptions are the models PALM, OpenFoam, and DALES, which are available under a free license and can be run on HPC.

Regarding the task at hand, i.e. providing detailed information on the influence of urban surfaces and vegetation on pedestrian-level thermal comfort and air quality, LES models can be considered to be the most appropriate and future-oriented since they can predict the turbulent air flow over a very complex surface with sufficient resolution. However, according to the authors' research at the beginning of the study, there was no open-source LES model with an integrated energy balance solver for urban surfaces that would be able to account for the realistic implementation of various processes inside an urban canopy. Our attempts to integrate some of the existing energy models (e.g. TUF-3D) into PALM led to serious technical difficulties due to the different scientific approaches of the particular models, incompatible data structures, difficult parallelization, and other issues. The license compatibility was another issue. Therefore, we decided to start from scratch, extending existing LES model PALM with a new fully integrated USM module that explicitly describes energy exchanges in the urban environment. Due to the complexity of this task, the first version of PALM-USM was deliberately limited to the most important processes for modelling summer heat-wave episodes in fully urbanized areas. Further improvements and additions to this module are a current work in progress and will be realized within the next years (see also Sect. 6).

1.2 LES model PALM

PALM³ is designed to simulate the turbulent flow in atmospheric and oceanic boundary layers. A highlight of PALM is its outstanding scalability on massively parallel computer architectures (Maronga et al., 2015). The model solves the non-hydrostatic incompressible Navier–Stokes equations in Boussinesq approximation. Subgrid-scale processes that cannot be resolved implicitly based on the numerical grid resolution are parameterized according to the 1.5-order Deardorff closure scheme (Deardorff, 1980) with the modification of Moeng and Wyngaard (1988) and Saiki et al. (2000), assuming that the energy transport by subgrid-scale eddies is proportional to the local gradients of the mean quantities.

Prognostic equations are solved numerically, primarily using an upwind biased fifth-order differencing scheme (Wicker and Skamarock, 2002) and a third-order Runge–Kutta time-stepping scheme following Williamson (1980). Discretization in space is achieved using finite differences on a staggered Cartesian Arakawa-C grid (Arakawa and Lamb, 1977).

PALM includes several features, such as cloud microphysics, a plant canopy model, and an embedded Lagrangian

particle model. In connection with the urban application, four other relevant schemes have already been implemented: a Cartesian topography scheme, representation of radiative exchange at the surface, large-scale forcing, and land-surface interactions with the atmosphere. The Cartesian topography scheme covers solid, impermeable, fixed flow obstacles (e.g. buildings) as well as terrain elevations (mountains, hills), with a constant-flux layer assumed between each surface element and the first grid level adjacent to the respective surface in order to account for friction effects. The representation of radiative exchange at the surface contains options to use either a simple clear-sky radiation parameterization or employ the Rapid Radiation Transfer Model for Global Models (RRTMG, e.g. Clough et al., 2005), which is coupled to PALM and is applied as a single-column model for each vertical column in the PALM domain. The large-scale forcing option enables forcing with data e.g. from mesoscale models via additional tendency terms, including an option for nudging of the mean profiles. Finally, the implementation of land-surface interactions with the atmosphere is based on a simplified version of the Tiled European Centre for Medium-Range Weather Forecasts Scheme for Surface Exchanges over Land (TESSEL/HTESSEL, Balsamo et al., 2009) and its derivative implementation on the DALES model (Heus et al., 2010). PALM's land-surface submodel (Maronga and Bosveld, 2017), hereafter referred to as PALM-LSM, further extends the surface parameterizations for impervious surfaces on the ground (pavements, roads) by replacing upper soil layers with a pavement layer attributed with a specific heat capacity and heat conductivity.

However, none of the included schemes are suited for treating complex effects of the urban environment driven by the diverse physical properties of different urban surfaces (both horizontal and vertical), heat transfer within building walls, and heat fluxes between the urban surfaces and the atmosphere. Also, the description of shortwave and longwave radiation budgets including shading and multi-reflection between surfaces, as well as the absorption of radiation by plant canopies, have not been treated by PALM so far. Therefore, we developed the USM for PALM that is able to treat these processes using approaches described in the following section.

2 Urban surface model

In this section, the first version of the new USM for PALM is described. The USM consists of a solver for the energy balance of all horizontal and vertical urban surface elements, including building walls and roofs, as well as pavements. The energy balance solver predicts the skin layer temperature, and it simultaneously calculates the near-surface turbulent flux of sensible heat and the subsurface conductive heat flux. The latter is calculated by means of a multi-layer model predicting heat diffusion through solid material. Moreover,

³<https://palm.muk.uni-hannover.de>

a multi-reflection radiative transfer model (RTM) for the urban canopy layer was developed, and coupled to the plant canopy model in order to calculate realistic surface radiative fluxes as input for the energy balance solver.

This first version of the USM was designed with the focus on modelling summer heat-wave episodes in built-up urban areas. The newly implemented methods hence concentrated on the most relevant processes for such conditions. Limitations of the current version are e.g. no treatment of reflective surfaces and windows; only a basic building energy model; simplification of some radiation-related processes (see Sect. 2.2.1 for details); a missing plant-canopy evapotranspiration model; and surfaces impervious to water. Possible impacts of these limitations are discussed in Sect. 4. Improvements of the USM and related PALM components are subject to ongoing development within the PALM community.

2.1 Energy balance solver

The surface energy balance correlates radiative energy fluxes with sensible and latent heat fluxes between the surface skin layer and the atmosphere, as well as with the storage heat fluxes into soil and walls. In this first PALM-USM version, latent heat fluxes were omitted, since the purpose of this version was to simulate heat-wave episodes in fully urbanized areas. This limitation is discussed in Sect. 4.1. The energy budget is expressed in the form

$$C_0 \frac{dT_0}{dt} = R_n - H - G, \quad (1)$$

where C_0 and T_0 are the heat capacity and temperature of the surface skin layer, respectively, t is the time, R_n is the net radiation, H is the turbulent sensible heat flux near the surface, and G is the heat flux from the surface skin layer into the ground or material (i.e. pavement, walls, roofs). The list of all used symbols, their descriptions, and units can be found in the Supplement in Table S1.

The calculation of the heat transfer H between the surface skin layer and the air is based on the equation

$$H = h(\theta_1 - \theta_0), \quad (2)$$

where θ_0 is the potential temperature at the surface and θ_1 is the potential temperature of the air layer adjacent to the surface; and h is the so-called heat flux coefficient, which is parameterized for vertical surfaces according to Krayenhoff and Voogt (2007), while for horizontal surfaces the parameterization of h follows the default PALM-LSM formulation based on Monin–Obukhov similarity theory (Obukhov, 1971). The latter involves the calculation of a local friction velocity, for which stability effects are considered for horizontal surfaces, while stability for vertical surfaces is treated as neutral (i.e. law-of-the-wall scaling is used). The friction velocity is used to calculate both the surface momentum flux for each individual surface element and the coefficient h for

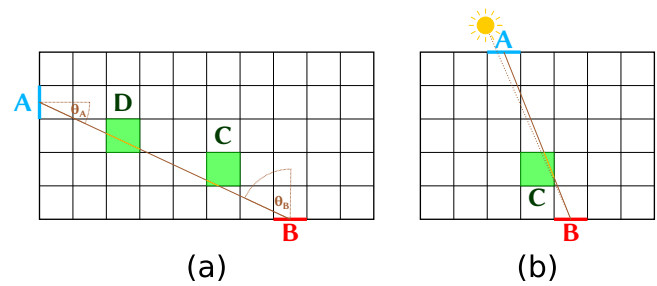


Figure 1. (a) View factor calculation (2-D simplification); (b) direct solar irradiation.

horizontal surface elements. The application of MOST for finite-sized surfaces is debatable as the theory is based on the assumption of horizontal homogeneity of the surface and flow, which is violated in urban areas. However, for lack of alternatives, it is the common modelling approach used in all state-of-the-art surface parameterization schemes (e.g. TUF-3D, Krayenhoff and Voogt, 2007; SUEWS, Järvi et al., 2011). The use of MOST in PALM as a boundary condition for buildings has been validated for neutral stratification by Letzel et al. (2008) and Kanda et al. (2013). Moreover, Park and Baik (2013) validated their LES results for non-neutral stratification against wind-tunnel data.

The heat transfer between surface skin layer and subsurface layers follows the general formulation for the heat flux G :

$$G = \Lambda(T_0 - T_{\text{matter},1}), \quad (3)$$

where T_0 is the temperature of the surface skin layer, $T_{\text{matter},1}$ is the temperature of the outermost layer of the material, and Λ is an empirical heat conductivity between the skin layer and the first grid level in the material.

The heat transfer within the material layers is calculated via the Fourier law of diffusion. This approach has been generalized for different material types of the pavements, walls, and roofs, each structured into four layers; each layer of each material is described by its own properties (thickness, volumetric thermal capacity, and thermal conductivity). The diffusion equation is solved numerically describing the heat transfer from the surface into the inner layers. Boundary conditions of the deepest layer are prescribed in the configuration for particular types of surfaces and are kept constant throughout the simulation. The flux G , calculated in the surface energy balance model, serves as a boundary condition for the outermost material layer.

All non-linear terms in Eq. (1) are linearized to avoid the need for an iteration method to solve for the skin temperature (see Maronga and Bosveld, 2017). Equation (1) is then solved by PALM's default Runge–Kutta scheme. The near-surface heat fluxes are evaluated based on the new prognostic skin layer temperature.

2.2 Radiative transfer model

2.2.1 General concept

The USM receives radiation from the standard PALM solar radiation model at the top boundary of the urban canopy layer. Depending on the chosen radiation module in PALM, the separate direct and diffuse components of the downward shortwave radiation flux may or may not be available. In the latter case, a simple statistical splitting is applied based on Boland et al. (2008). The USM then adds a description of radiation processes in the urban canopy layer where multiple reflections are considered.

Radiation processes are modelled separately for shortwave (SW) and longwave (LW) radiation. Direct and diffuse SW solar radiation along with the relative position of the Sun, as well as the LW radiation from the atmosphere, is provided by PALM's solar radiation model. Thermal emission from the ground, walls, and roofs is added as a source of longwave radiation. For each time step, radiation is propagated through the 3-D geometry of the urban canopy layer for a finite number of reflections, after which all of the radiation is considered fully absorbed by the surfaces. All reflections are treated as diffuse (Lambertian), and in each reflection, a portion of radiation is absorbed by the respective surface according to its properties (albedo and emissivity). The urban layer may contain an arbitrarily located plant canopy (trees and shrubs) described by a 3-D structure of leaf area density (LAD), which is treated as semi-opaque for the modelled SW radiation and transforms the absorbed radiation to heat (see Sect. 2.2.4).

Some radiation-related processes have been omitted in this first version, including absorption, emission, and scattering by air within the urban canopy layer, interaction of LW radiation with plant canopy, and thermal capacity of plant leaves (plant canopy is assumed to have the temperature of the surrounding air). The effects of these simplifications are discussed in Sect. 4.

2.2.2 Calculation of view factors and canopy sink factors

For the calculation of irradiation of each face⁴ from diffuse solar radiation, thermal radiation, and reflected radiation, mutual visibility between faces of both real surfaces and virtual surfaces (top and lateral domain boundaries) has to be known. It is calculated using a ray tracing algorithm. Since this process is computationally expensive and hard to parallelize (as rays can travel through the entire domain which is distributed on different processors), both the view factors (SVF) and the plant-canopy sink factors (CSF) are precomputed during the model initialization. These factors can be

⁴A face is a unit of surface according to discretization by grid; it is a boundary between a grid box with terrain/building and an adjacent air-filled grid box.

saved to file and used for other simulations with the same surface geometry, or for the calculation of the mean radiant temperature (MRT) in the postprocessing.

For any two faces A and B with mutual visibility, the *view factor* $F_{A \rightarrow B}$ represents the fraction between that part of the radiant flux from face A that strikes face B and the total radiant flux leaving face A . For infinitesimally small areas of A and B , a *differential view factor* $F_{A \rightarrow B}^d$ can be written as

$$F_{A \rightarrow B}^d = \frac{dF_{A \rightarrow B}}{d\mathcal{A}(B)} = \frac{\cos\theta_A \cos\theta_B}{\pi s^2}, \quad (4)$$

where $\mathcal{A}(B)$ is the surface area of face B , θ_A and θ_B are the angles between the respective face normals and the connecting ray, and s is the separation distance (ray length) (Howell et al., 2010); see Fig. 1a. Under the assumption that s is much larger than the grid resolution, differential view factors are precomputed for all mutually visible face centres and used in place of view factors divided by target area. At the end, the differential view factors are normalized such that the sum of all normalized differential view factors with the same target face (B) multiplied by source area equals 1:

$$\widehat{F}_{A \rightarrow B}^d = \frac{F_{A \rightarrow B}^d}{\sum_{A'} F_{A' \rightarrow B}^d \mathcal{A}(A')}. \quad (5)$$

If the view factors were known exactly, the sum $\sum_{A'} \frac{F_{A' \rightarrow B}^d \mathcal{A}(A')}{\mathcal{A}(B)}$ would equal 1 (from the reciprocity rule $\mathcal{A}(A)F_{A \rightarrow B} = \mathcal{A}(B)F_{B \rightarrow A}$). Therefore, the normalization guarantees that, in total, no radiation is lost or created by simplification due to discretization. Since the part of face B 's irradiance that comes from face A is computed as

$$J_{e,A \rightarrow B} = E_{e,A} \mathcal{A}(A) \widehat{F}_{A \rightarrow B}^d, \quad (6)$$

where $E_{e,A}$ is the radiosity of face A , we specifically precompute and store the value of

$$\text{SVF}_{A \rightarrow B} = \mathcal{A}(A) \widehat{F}_{A \rightarrow B}^d \quad (7)$$

which we call the *irradiance factor*. In case the ray tracing algorithm encounters an obstacle (i.e. wall or roof), the view-factor entry is not stored, indicating the absence of mutual visibility between the two respective faces.

The equations above describe radiative fluxes before accounting for plant canopy. For every ray that crosses a grid box containing plant canopy (i.e. a partially opaque box), a dimensionless *ray canopy sink factor* (RCSF) represents the radiative flux absorbed within the respective grid box normalized by the total radiative flux carried by the ray at its origin. For a ray $A \rightarrow B$ and a grid box C , the RCSF is calculated as

$$\text{RCSF}_{C,A \rightarrow B} = \left(1 - \sum_D \text{RCSF}_{D,A \rightarrow B}\right) (1 - e^{-\alpha a_C s_C}), \quad (8)$$

where a_C is the leaf area density of grid box C , s_C is the length of the ray's intersection with box C , and α is the

extinction coefficient. The sum in the first term represents cumulative absorption by all plant-canopy-containing grid boxes D that have already been encountered on the ray's path before reaching grid box C (Fig. 1a).

After the entire ray is traced, the total transmittance T of the ray $A \rightarrow B$ passing through plant canopy grid boxes C

$$T_{A \rightarrow B} = 1 - \sum_C \text{RCSF}_{C,A \rightarrow B} \quad (9)$$

is stored along with $\text{SVF}_{A \rightarrow B}$. Later in the modelling, when the radiant flux transmitted through $\text{SVF}_{A \rightarrow B}$ is calculated, it is multiplied by $T_{A \rightarrow B}$ to account for the absorbed flux.

The actual radiant flux Φ_e received by the grid box C from the ray $A \rightarrow B$ is equal to

$$\Phi_{e,C,A \rightarrow B} = E_{e,A} \cdot \text{SVF}_{A \rightarrow B} \cdot \mathcal{A}(B) \cdot \text{RCSF}_{C,A \rightarrow B}. \quad (10)$$

The radiosity $E_{e,A}$ of the source face is the only time-dependent variable in this equation. Therefore, the rest of this product can be precomputed during initialization, and summed up per source face in the form of a *canopy sink factor* (CSF):

$$\text{CSF}_{C,A} = \sum_B \text{SVF}_{A \rightarrow B} \cdot \mathcal{A}(B) \cdot \text{RCSF}_{C,A \rightarrow B}. \quad (11)$$

CSF represents the ratio between the radiant flux absorbed within plant canopy box C originating from face A and the radiosity of face A .

2.2.3 Calculation of per-face irradiation

At each time step, the total incoming and outgoing radiative fluxes of each face are computed iteratively, starting from the first pass of radiation from sources to immediate targets, followed by consecutive reflections.

In the first pass, the virtual surfaces (sky and domain boundaries) are used as sources of radiation by representing components of diffuse shortwave solar radiation and longwave radiation from the sky. At this point, the real surfaces (wall facades, roofs, ground) are set to emit longwave radiation according to their surface temperature and emissivity. The precomputed view factors are then used to cast the shortwave and longwave radiation from source to target faces.

Solar visibility has to be calculated for the quantification of the direct part of shortwave solar radiation. The solar angle is discretized for this purpose so that the solar ray always originates from the centre of the virtual face at the top of the urban layer or at lateral domain boundaries (see the real location of the Sun vs. the discretized location (centre of face A) in Fig. 1b). We have decided not to do the computationally expensive ray tracing after the precomputation phase is over; moreover, the total transmittance stored alongside the precomputed view factor (see Eq. 9) is readily available. If there is no such view factor entry, it means that the discretized ray path is blocked by a wall or roof and the target face receives

no direct solar irradiation. For the purpose of calculating the actual amount of direct solar irradiation, an exact solar angle is used, not the discretized one.

After the aforementioned first pass of radiation from source to target surfaces has been computed, reflection is applied iteratively. At each iteration, a fraction of each surface's irradiation from the previous iteration is reflected and the remainder is considered absorbed. The reflected fraction is determined by the surface's albedo for shortwave radiation and by the surface's emissivity ε for longwave radiation, where the longwave reflectivity results from $(1 - \varepsilon)$ according to Kirchhoff's law. The reflected part is then again distributed onto visible faces using the precomputed view factors. After the last iteration, all residual irradiation is considered absorbed. The number of iterations is configurable, and the amount of residual absorbed radiation can be displayed in the model output. In our experience, three to five iterations lead to negligible residue.

2.2.4 Absorption of radiation in the plant canopy

The fraction of SW radiative flux absorbed by the plant canopy is calculated for the first pass as well as for all the successive reflection steps (these are described in Sect. 2.2.3).

For diffuse and reflected shortwave radiation, the amount of radiative flux absorbed by each grid box with plant canopy is determined using the precomputed CSF and radiosity of the source face (i.e. reflected radiosity for a real surface or diffuse solar irradiance for a virtual surface; see Eq. 10).

For the direct solar irradiance, the nearest precomputed ray path from the urban-layer bounding box (represented by virtual face A in Fig. 1b) to the respective plant canopy grid box C is selected similarly to the direct surface irradiation described in Sect. 2.2.3. In case the grid box C is fully shaded, no ray path is available. Otherwise, the transmittance of the path is known. The absorbed direct solar flux for the grid box C is equal to

$$\Phi_{e,C} = E_{e,\text{dir}} \cdot T_{A \rightarrow C} \cdot \frac{\iint_b (1 - e^{-\alpha_{ac}s_b}) db}{\mathcal{A}'_C}, \quad (12)$$

where $E_{e,\text{dir}}$ is the direct solar irradiance and \mathcal{A}'_C is the cross-sectional area of C viewed from the direction of the solar radiation. The fraction in Eq. (12) represents the absorbed proportion of radiative flux, averaged over each ray b that intersects the grid box C , and is parallel to the direction of the solar radiation; s_b is the length of the intersection. Since all grid boxes have the same dimensions, this fraction is precomputed based on the solar direction vector at the beginning of each time step using discrete approximation.

Once the total absorbed radiative flux is known, it is stored as plant canopy heat rate for the respective grid box. Since the plant canopy is considered to have zero thermal capacity, all of the heating power is applied immediately to the grid box's air volume.

2.3 Anthropogenic heat

The prescribed anthropogenic heat is assigned to the appropriate layer of the air, where it increases the potential-temperature tendencies at each time step. This process takes place after the surface energy balance is solved. The heat is calculated from daily total heat released into any particular grid box, and from the daily profile of the release specified for every layer to which anthropogenic heat is released.

2.4 USM module integration into PALM

The USM was fully integrated into PALM, following its modular concept, as an optional module, which directly utilizes the model values of wind flow, radiation, temperature, energy fluxes, and other required values. The USM returns the predicted surface heat fluxes back to the PALM core, where they are used in the corresponding prognostic equations. It also adjusts the prognostic tendencies of air according to released anthropogenic heat.

Descriptions of real and virtual surfaces and their properties are stored in 1-D arrays indexed to the 3-D model domain. The crucial challenge of this part of the design is to ensure an efficient parallelization of the code, including an efficient handling and access of data stored in the memory during the simulation. The values are stored locally in particular processes of the Message Passing Interface (MPI⁵), corresponding to the parallelization of the PALM core. Necessary access to values stored in other processes is enabled by means of MPI routines, including interfaces for one-sided MPI communication.

The configuration of the USM module is compatible with other PALM modules. Variables for instantaneous and time-averaged outputs of the USM are integrated into PALM's standard 3-D NetCDF output files, and they are configured in the same way as the rest of the model output variables. The configuration options as well as the structure of input and output files are described in the Supplement to this article. The Supplement also contains the list and description of needed surface and material parameters of urban surfaces, plant-canopy data, and anthropogenic-heat data. The model PALM with its USM module is hereafter referred to as PALM-USM, which is freely available under the GNU General Public License (see the Code availability section).

3 Evaluation and sensitivity tests of the USM

In order to evaluate how well the USM represents urban surfaces' temperatures (of e.g. walls, roofs, and streets), a summer heat-wave observation campaign in an urban quarter of Prague, Czech Republic, was carried out (see Sect. 3.1). By means of PALM-USM, urban-quarter characteristics and the campaign's meteorological conditions were simulated (see

Sect. 3.2) and model results evaluated against the observations (see Sect. 3.3).

3.1 Observation campaign

The campaign was carried out at the crossroads of Dělňnická street and Komunardů street in Prague, Czech Republic (50.10324° N, 14.44997° E; terrain elevation 180 m a.s.l.). This location was selected in coordination with the Prague Institute of Planning and Development as a case study area for urban heat island adaptation and mitigation strategies. This particular area represents a typical residential area in a topographically flat part of the city of Prague with a combination of old and new buildings and a variety of other urban components (such as yards or parking spaces). The streets are oriented in the north–south (Komunardů) and west–east (Dělňnická) directions, roughly 20 and 16 m wide, respectively. The building heights alongside the streets range approximately from 10 to 25 m. The area does not contain much green vegetation and the majority of the trees is located in the yards. The neighbourhood in the extent of approximately 1 km² has similar characteristics to the study area (see the aerial photo in Fig. 2).

Measurements were conducted from 2 July 2015, 14:00 UTC to 3 July 2015, 17:00 UTC. The timing of the measurement campaign was chosen to cover a typical summer heat-wave episode.

3.1.1 Measurements

Wall and ground surface temperatures were measured by an infrared camera – FLIR SC660 (FLIR, 2008). The thermal sensor of the camera has a field of view of 24 by 18° and a spatial resolution (given as an instantaneous field of view) of 0.65 mrad. The spectral range of the camera is 7.5 to 13 μm, and the declared thermal sensitivity at 30 °C is 45 mK. The measurement accuracy for an object with a temperature between +5 and +120 °C, and given an ambient air temperature between +9 and +35 °C, is ±1 °C, or ±1 % of the reading. The camera offers a built-in emissivity-correction option, which was not used for this study. Apart from the infrared pictures, the camera allows us to take pictures in the visible spectrum simultaneously.

Observation locations are shown in Fig. 3, eight of them (Nos. 1–7 and 9) representing temperature measurements of the walls on the opposite side of the street, and one of them (No. 8) representing the ground-temperature measurement on the road. The camera was always placed on a tripod at about 1.6 m above ground, with its orientation approximately perpendicular to the opposite walls, at a distance of 14–18 m depending on the street width. For scans of the ground, the picture's centre was viewed under an angle of about 15° (the closest point was approx. 2 m away and the most distant point 30 m, resulting in view angles of 38 and 3°, respectively). Pictures in both the infrared and visible spectra were taken

⁵<http://mpi-forum.org>

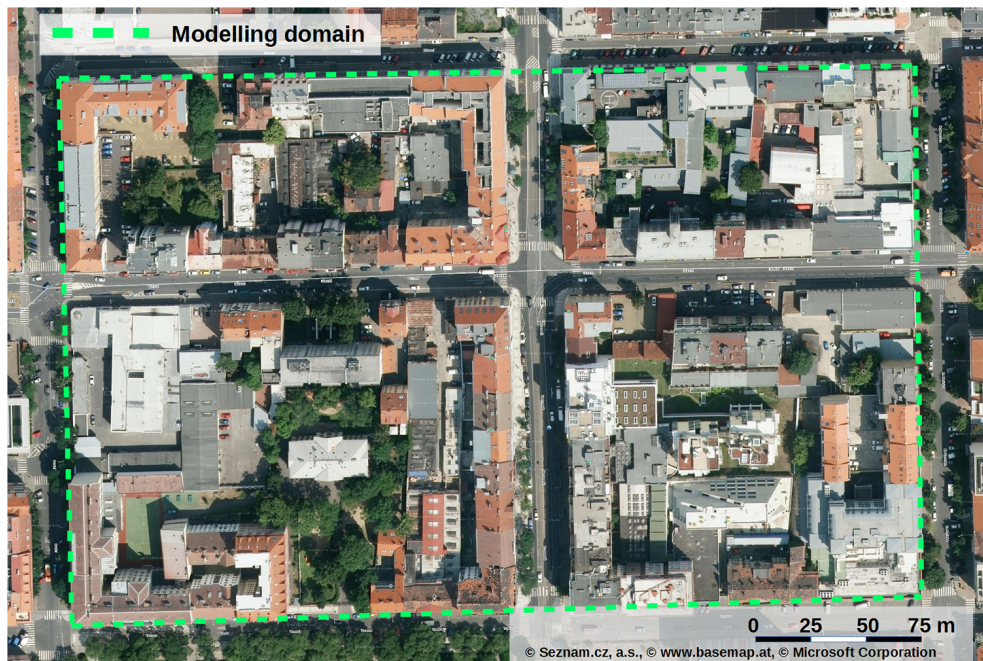


Figure 2. Aerial photo of the studied area.

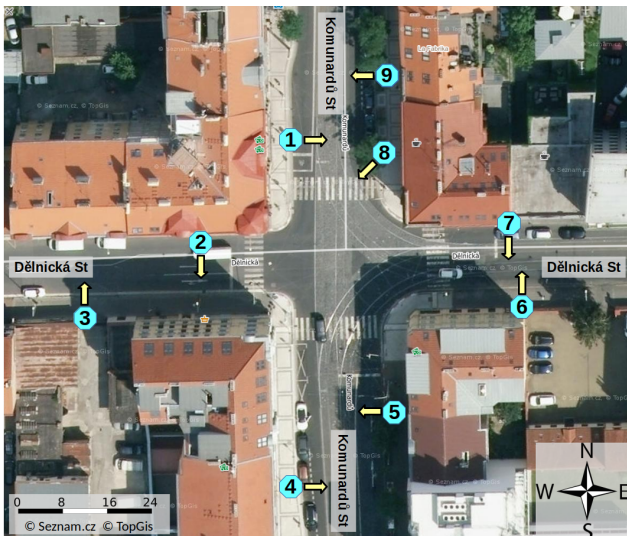


Figure 3. Observation locations. Arrows depict the orientation of the camera view. Url of the map: <https://mapy.cz/s/12Qd8>.

simultaneously, starting at observation location 1 every full hour and continuing through observation locations 2, 3, etc. This provided a series of 28 temperature snapshots per location with an approximately 1 h time step. The exact recording time of each picture was used for further processing and evaluation of the model.

The pictures were further postprocessed. First, the infrared pictures were converted into a common temperature scale +10 to +60°C. Second, the pictures were transformed to

overlap each other in order to correct for slight changes in camera position between the measurements, as the camera was carried from one location to another. Third, several evaluation points were selected for each view to cover various surface types in order to evaluate the model performance under different surface parameter settings (different surface materials and colours) and under different situations (fully irradiated or shaded areas). That is, selected surface materials comprised old and new plastered brick house walls as well as modern insulated facades for vertical surfaces, and pavement or asphalt for the ground observation location. With regard to colours, the evaluation points were placed on both dark and light surfaces, with special interest in places where light and dark materials are located side-by-side, thus allowing one to inspect different albedo settings under roughly the same irradiance conditions. Some points were placed on wall areas, which are temporarily (in the diurnal cycle) shaded by trees or buildings, in order to test how the shading works in the model.

Apart from infrared camera scanning, the air temperature was measured once an hour at observation location 1 at the edge of the pavement, about 2 m apart from the wall and 2 m above ground, and not in direct sunlight. A digital thermometer with an external NTC-type thermistor measuring probe (resolution of 0.1 K and declared accuracy of 1 K) was used. This on-site measurement did not meet requirements for the standard meteorological measurement; therefore, we refer to it as the indicative measurement later in the text.

Further meteorological data were acquired from the official weather monitoring network, including stations

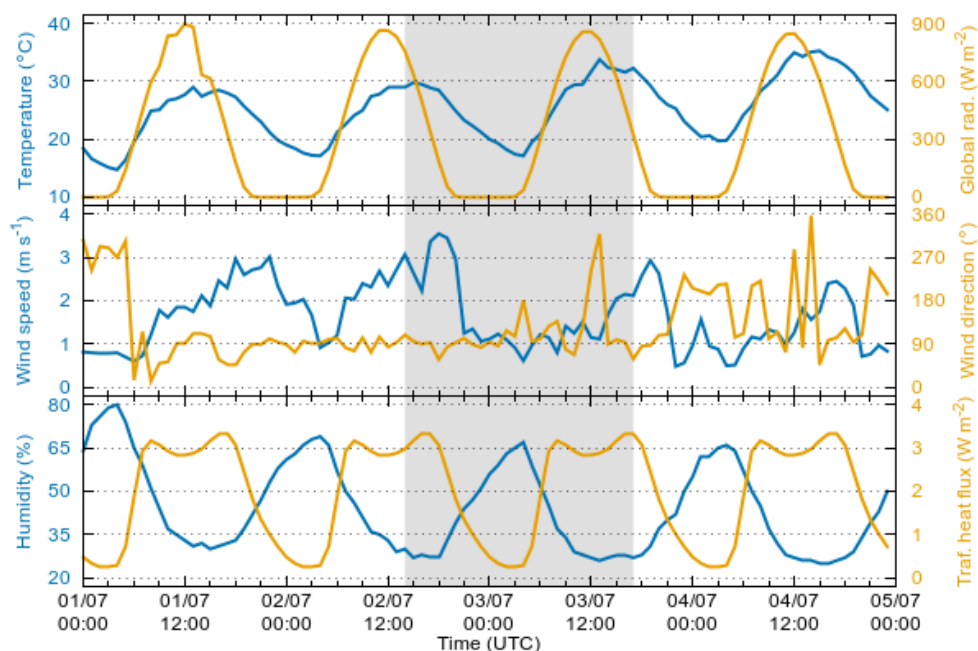


Figure 4. Meteorological conditions from station Prague, Karlov, and spatially averaged traffic heat flux from 1 to 4 July. The shaded area marks the time of the observation campaign.

Prague, Klementinum; Prague, Karlov; Prague, Kbely; and Prague, Libuš. Station Prague, Klementinum (50.08636° N, 14.41634° E; terrain elevation 190 m a.s.l., 3 km away from the crossroads of interest) was used as supplementation to the on-site indicative measurement. The temperature at this station is measured on the north-facing wall, 10 m above the courtyard of the historical building complex, and it can be used as another reference for the air temperature inside the urban canopy. Station Prague, Karlov (50.06916° N, 14.42778° E, 232 m a.s.l.; 4.3 km away), can be considered representative for the city core of Prague as it is located in the centre of the city. Station Prague, Kbely (50.12333° N, 14.53806° E, 285 m a.s.l.; 6.7 km away), is located at the border of the city and serves as a reference for regional background suburban meteorological conditions. Station Prague, Libuš (50.00778° N, 14.44694° E, 302 m a.s.l.; 10 km away), is located in the city suburb and it is the only station with sounding measurements in the area. Radiosondes are released three times a day (00:00, 06:00, 12:00 UTC).

3.1.2 Weather conditions

The weather during the campaign was influenced by a high-pressure system centred above the Baltic Sea. The meteorological conditions at Prague, Karlov station, are shown in Fig. 4. Winds above rooftop were weak, mostly below 2.5 m s^{-1} , and often as low as 1 m s^{-1} from easterly directions. The maximum measured wind speeds of $3\text{--}4 \text{ m s}^{-1}$ were observed in the afternoons at the beginning and at the end of the campaign. According to the atmospheric sounding,

a low-level jet from the south and south-east was observed during the night, with a maximum wind speed of 10 m s^{-1} at 640 m a.s.l. (950 hPa) (not shown). The temperature exceeded 30°C in the afternoons and dropped to 20°C at night. The sky was mostly clear with some clouds during the daytime on 1 July and high-altitude cirrus forming in the morning and afternoon on 3 July. The highest values of relative humidity occurred at night (65%), dropping to 30% during the day. The time of the sunset was 19:15 UTC on 2 July 2015, and the time of sunrise and solar noon on 3 July was 02:58 and 11:06 UTC.

3.2 Model set-up and input data for USM

To assess the validity of the model formulation and its performance in real conditions, the model was set up to simulate the measured summer episode described in Sect. 3.1. The total simulation time span was 48 h, starting on 2 July 2015, 00:00 UTC.

3.2.1 Model domain

The horizontal size of the model domain was $376 \text{ m} \times 226 \text{ m}$ (see Fig. 2) at a resolution of $2.08 \text{ m} \times 2.08 \text{ m}$. The vertical grid spacing was 2.08 m within the first 50 m, and above this level, a vertical stretching factor of 1.08 between two adjacent levels was used with a maximum grid spacing of 20 m. The resulting total domain height was about 3.5 km. The relatively small horizontal model domain was chosen due to available data of surface parameters and to keep com-

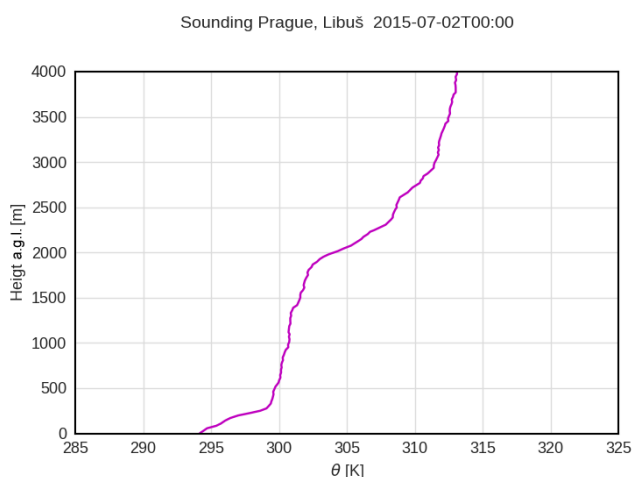


Figure 5. Initial vertical profile of potential temperature (θ) as used for initialization of PALM.

putational demands feasible. This poses some limitation to the turbulence development during the daytime, where the largest eddies usually scale with the height of the boundary layer. These eddies could not be captured well with this configuration. The effects of the limited horizontal size of the domain on model results will be discussed in Sect. 4.

3.2.2 Boundary and initial conditions

Lateral domain boundaries were cyclic, which can be envisioned as an infinite repetition of the simulated urban quarter. This is a reasonable approximation, since the surrounding area has similar characteristics to the model domain; thus, the character of the flow can be considered similar. The bottom boundary was driven by the heat fluxes as calculated by the energy balance solver (see Sect. 2.1). At the top of the domain, Neumann boundary conditions were applied for potential temperature and relative humidity, while a Dirichlet boundary was set for the horizontal wind. A weak Rayleigh damping with a factor of 0.001 was applied to levels above 3000 m. The indoor temperature was fixed at 22 °C during the entire simulation.

The initial vertical profile of potential temperature of air was derived from the sounding measurement in the outskirts of Prague, Libuš station, from 2 July 2015, 00:00 UTC (see Fig. 5). At midnight, a stable layer had developed near the surface, extending to a height of about 300 m. Above, a residual layer with slightly stable stratification ranged up to the inversion at around 1900 m. The capping inversion had a strength of about 5 K, with the stable free atmosphere aloft. The temperature of walls, grounds, and roofs was initialized from a 24 h spin-up simulation.

3.2.3 Large-scale forcing

To account for the processes occurring on larger scales than the modelling domain but still affecting the processes inside the domain, the large-scale forcing option of PALM was used. The effect of large-scale conditions is included via geostrophic wind and large-scale advection tendencies for temperature and humidity. The forcing quantities can depend on both height and time while being horizontally homogeneous. Nudging of PALM quantities towards the large-scale conditions was enabled for the free atmosphere layers with a relaxation time of 7 h. Inside the boundary layer nudging was disabled. Large-scale forcing and nudging data were generated based on a run with the WRF meso-scale numerical weather prediction model (version 3.8.1, Skamarock et al., 2008). The WRF simulation domain covered a large part of Europe (-1.7 – 34.7° longitude, 41.4 – 56.7° latitude; 9 km horizontal resolution, 49 vertical levels). Standard physics parameterizations were used, including the RRTMG radiation scheme, the Yonsei University PBL scheme (Hong et al., 2006), a Monin–Obukhov similarity surface layer, and the Noah land surface model (Tewari et al., 2004). The urban parameterization was not enabled, in order to avoid double counting of the urban canopy effect which is treated by PALM-USM. The configuration of the WRF model corresponds to the prediction system routinely operated by the Institute of Computer Science of the Czech Academy of Sciences.⁶

The output of the WRF model was compared to measurements from the four Prague stations (see Sect. 3.1.1). The overall agreement between the simulated values and the observations is reasonable and corresponds to long-term evaluations done earlier. For the period of 1–5 July (see Fig. S1), WRF shows a cold bias. The largest bias occurs in the urban Prague, Klementinum station (city centre), which is as expected given the urban parameterization not being enabled in the WRF model. On the other hand, the comparison with Prague, Kbely station (closest background station to the area of interest), shows only a small bias (see also the time series in Fig. S2). Also, the comparison with vertical profiles of temperature from Prague, Libuš station, shows good agreement (see Fig. S3). Despite the slight cold bias of the WRF simulation, we take the WRF-derived values as the best inputs available.

3.2.4 Surface and material parameters

Solving the USM energy balance equations requires a number of surface (albedo, emissivity, roughness length, thermal conductivity, and capacity of the skin layer) and volume (thermal capacity and volumetric thermal conductivity) material input parameters. When going to such a high resolution as in our test case (~ 2 m), the urban surfaces and wall materials become very heterogeneous. Any bulk parameter

⁶<http://medard-online.cz/>

setting would therefore be inadequate. Instead, we opted for a detailed setting of these parameters wherever possible. To obtain these data, a supplemental on-site data collection campaign was carried out and a detailed database of geospatial data was created. This includes information on wall, ground, and roof materials and colours which was used to estimate surface and material properties. Each surface is described by material category and albedo. Categories are assigned to parameters estimated based on surface and storage material composition and thickness. The parameters of all subsurface layers of the respective material were set to the same value. The parameters C_0 and Λ (see Eqs. 1 and 2) of the skin layer are inferred from the properties of the material near the surface, which may differ from the rest of the volume. Parameters associated with particular categories are given in Supplement Table S2. A tree is described by its position, diameter, and vertically stratified leaf area density. Building heights were available from the Prague 3-D model, maintained by the Prague Institute of Planning and Development.⁷ All descriptions of surfaces and materials and their properties were collected in GIS formats and then preprocessed into the USM input files corresponding to the particular domain set-up.

3.2.5 Anthropogenic heat

Anthropogenic heat sources for our particular case are dominated by heat from fuel combustion in cars (see also the discussion in Sect. 4). Based on Sailor and Lu (2004), we assume the average heat release to be 3975 J per vehicle per metre of travel. Traffic intensities and hourly traffic factors are based on the annual traffic census data. The traffic intensities vary for different arms of the crossroads and traffic directions. The total count of vehicles passing through the crossroads is 12 000 vehicles per day, and the intensity of the busiest road (western arm of the west–east street) is 6000 vehicles per day. The heat produced by the cars along their trajectories is released into the first model layer and spatially distributed into the model grid cells that correspond to the traffic lanes. Temporal distribution is done using prescribed hourly factors. The time factors are the same for all traffic lanes. Values of anthropogenic heat are 42 W m^{-2} on average (spatially and temporally), while the maximum value is 142 W m^{-2} (busiest road arm, peak hour). Those values refer to heat fluxes directly above the traffic lanes. The mean daily traffic heat flux averaged over the entire domain is 2 W m^{-2} . The daily course of the traffic heat release is plotted in Fig. 4. It has been shown before that for this particular case (with strong solar irradiance, high temperatures, and only moderate traffic) the inclusion of anthropogenic heat from transportation does not result in a noticeable change in temperatures and heat fluxes (Juruš et al., 2016).

⁷<http://www.geoportalpraha.cz>

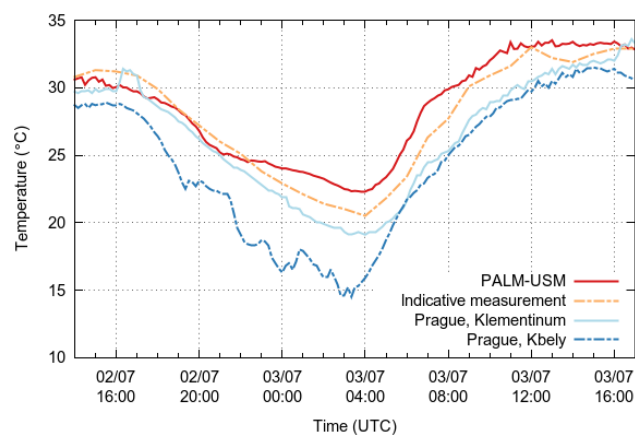


Figure 6. Air temperatures obtained from PALM-USM for location 1 in comparison to measured temperatures.

3.3 Evaluation of PALM-USM

First we compare the air temperatures from PALM-USM to the measurements taken during the observation campaign. Figure 6 shows the air temperature course calculated by the PALM-USM at observation location 1 at 2 m above ground. This temperature is compared to the indicative measurement taken at the same place and also to automatic weather stations Prague, Klementinum, and Prague, Kbely. The indicative measurement together with station Prague, Klementinum, represent the conditions inside the urban canopy, and as such, the results of PALM-USM should correspond to those values. Prague, Kbely station is plotted as a representative of the outskirts of the city. The UHI effect is clearly visible, especially at night, when the temperature outside of Prague drops down to 15°C , while on the street level, it drops to 20°C only. This effect is less pronounced during the day, when the temperature difference is only $2\text{--}3^\circ\text{C}$. This reflects the known fact that the UHI is basically a nighttime effect (Oke, 1982). The street-level air temperature as simulated by PALM-USM is in agreement with both measurements during the daytime of 2 July, but starting from 21:00 UTC, the decrease in the modelled temperature weakens, gradually leading to overestimations of up to 2°C in the morning of 3 July.

The vertical structure of the potential temperature from PALM-USM is shown together with radiosonde observations from station Prague, Libuš, in Fig. 7. As this is a suburban background station (10 km away), the profiles are not truly comparable, especially near the surface, where effects of the UHI are expected in the PALM-USM data. The Libuš profiles are considered here mainly as a representation of the general meteorological situation in the area of interest.

From Fig. 7 it is clearly visible that PALM-USM was able to reproduce the diurnal temperature cycle of the boundary layer reasonably well. During daytime, a convective boundary layer (CBL) develops that reaches depths of about 2 km, which is somewhat higher than the observed boundary layer,

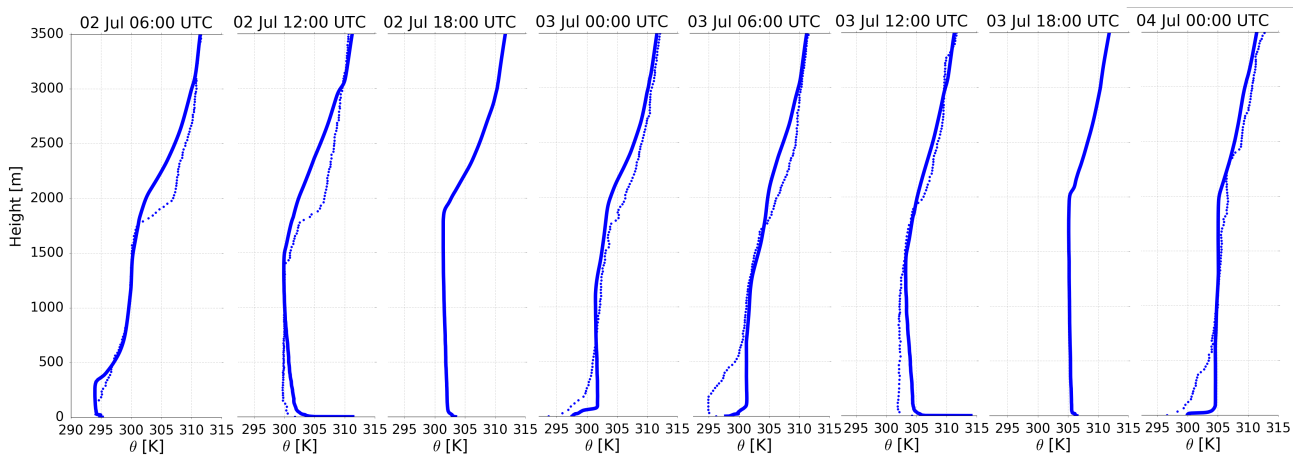


Figure 7. The vertical profiles of potential temperature modelled by PALM (solid line) and supplemented by radiosonde observations from station Prague, Libuš (except for hour 18; dotted line). Displayed are profiles from 2 July, 06:00 UTC to 4 July, 00:00 UTC with a 6 h time step.

particularly on 2 July (12:00 UTC). This can be attributed to the higher amount of heat released by the surfaces of densely built-up urban areas, as compared to the surfaces of suburban regions where the radiosonde was released. Moreover, it is visible that the potential temperature profile produced by PALM-USM displays an unstable stratification throughout the CBL on both days, while the observations show the expected nearly neutral profile. We will later see that this is an effect of the limited horizontal model domain that inhibits the free development of the largest eddies and thus is limiting the vertical turbulent mixing of warm air from the surface and relatively cold air from above. The result is an unstable layer with somewhat overly high near-surface temperatures.

During nighttime, a stable boundary layer developed in both LES and observations (due to nocturnal radiative cooling). As expected, this cooling is more rigorous in the (suburban) measurements, so that the stable layer was able to extend to heights of 500 m, whereas PALM-USM predicts a stable layer of not more than 100 m vertical extent (see 00:00 UTC on 3 and 4 July). This result is in agreement with what was already shown in Fig. 6 and is a known feature of the UHI (Oke, 1982).

Figure 8a–c shows the temporal development of the turbulence, which is here represented by the variance of vertical velocity. The diurnal turbulence cycle is very clearly visible, with maximum intensities of $1.4 \text{ m}^2 \text{ s}^{-2}$ around noon located in the well-mixed part of the boundary layer (Fig. 8c). Ideally, it would show a clear maximum in the middle of the boundary layer, but two processes avoid this. First, the urban canopy arranges the release of heat at different heights above the ground surface, and second, the limited horizontal model domain does not allow for a free development of turbulence. Figure 8a further shows that the turbulence immediately starts to decay after sunset, which is accompanied by the development of a stable boundary layer near the sur-

face (not shown here). During nighttime, the turbulence further decays and the maximum values of the variance reduce to $0.3 \text{ m}^2 \text{ s}^{-2}$. Due to the continuously heating urban surface layer, however, turbulence is kept alive until the next morning (see also Fig. 8a).

Next, in order to assess how well the model is able to model the energy transfer between material and atmosphere, we compare modelled values to on-site measurements of surface temperatures captured by the infrared camera. Here we present results from five selected locations, chosen to cover wall orientations to all cardinal directions and the ground: location 3 (south-facing wall) in Fig. 9, location 4 (west-facing wall) in Fig. 10, location 7 (north-facing wall) in Fig. 11, location 9 (east-facing wall) in Fig. 12, and location 8 (ground) in Fig. 13. Corresponding surface and material parameters for all evaluation points can be found in Tables S2 and S3 in the Supplement. Results for all nine locations are also displayed in the Supplement (Figs. S4–S12). In general, PALM-USM captures the observed daily temperature patterns very well. The temperature values during the daytime are captured reasonably well, while the model slightly overestimates nighttime temperatures.

Figure 9 shows a south-facing wall in the western arm of the west–east street measured from location 3. We evaluated the model performance in four points. All points are assigned the same material category (plastered brick wall; see Tables S2 and S3). Points 1, 2, and 3 are on a surface with the same colour, which is represented by an albedo of 0.2 in the model. Point 4 is placed on a surface of lighter colour (albedo of 0.7). The lighter surface colour in point 4 results in a significantly lower measured peak temperature of 6–9 °C less than in other points. The model correctly captures the lower temperature in point 4, although the modelled maximum in point 4 is a bit higher than the measured maximum. The effect of different albedos can be seen in Fig. 13

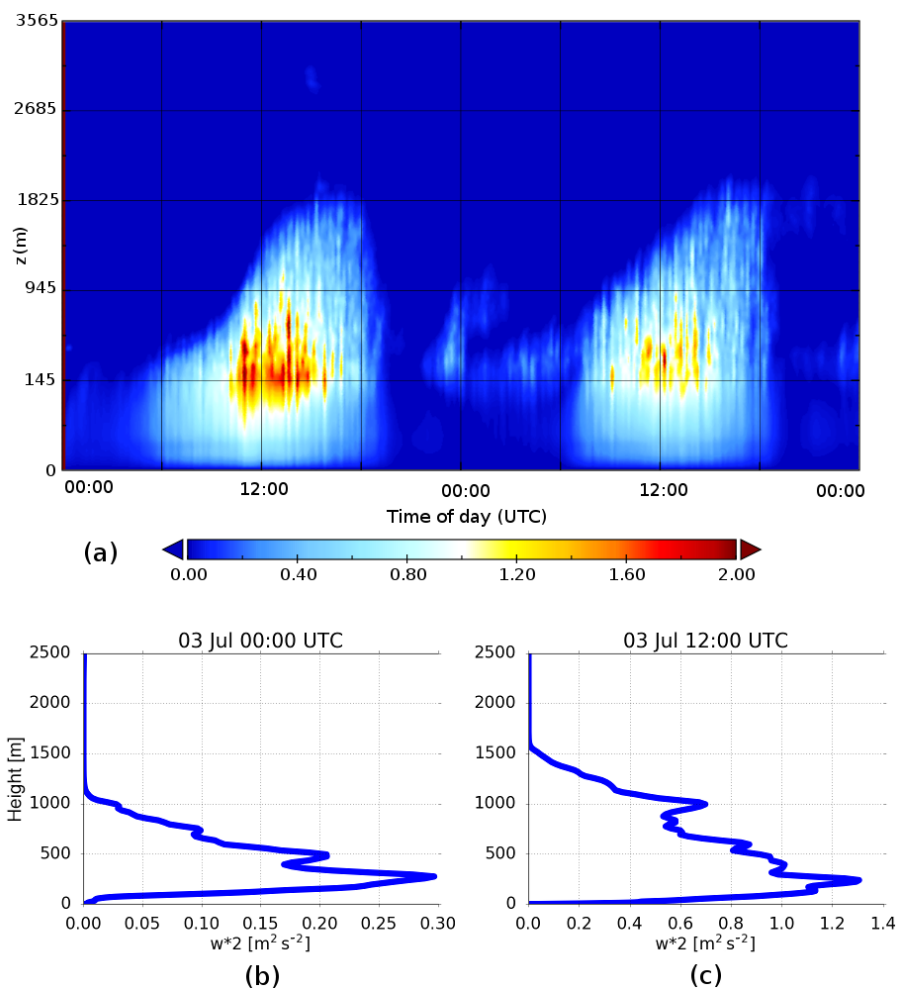


Figure 8. (a) Time–height cross section of the variance of the vertical velocity component (top), and vertical profiles of the same quantity at two selected times: (b) 3 July 00:00 UTC and (c) 3 July 12:00 UTC (bottom).

for points 2, 3, and 4, too. The observation that the model overestimates values at some evaluation points located in the lowest parts of the buildings can also be made at other observation locations (see location 4, Fig. 10, point 1, or location 5, Fig. S8, point 1).

In Fig. 9, daytime temperatures of points 1 and 2 are captured quite well, while the model overestimates the temperature in point 3. In reality, this point is shaded by an alcove until 08:10 UTC (see the IR picture in Fig. S13) and thus it is irradiated approximately 1 h later than point 1. As a consequence, the increase in its temperature is delayed and the reached maximum temperature is 4 °C lower than in point 1. This facade unevenness is not resolved by the topography model in PALM and it thus predicts the same values for points 1 and 3.

Figure 10 shows the same comparison for a west-facing wall in the southern arm of the north–south street measured from location 4. The temperature course in point 7 demonstrates the effect of surface shading by a tree that ob-

structs the solar radiation at this location between 13:10 and 14:50 UTC. This leads to a decrease in surface temperature between 13:00 and 15:00 UTC, whereas the surface temperature at the other points keeps increasing. This shading effect can also be seen in Fig. 12 for point 5, which is shaded by a tree between 06:15 and 08:15 UTC. Both cases are correctly represented by the model. Another illustration of tree shading is in Fig. S14.

The results for a north-facing wall in the eastern arm of the west–east street are shown in Fig. 11. In contrast to other walls, where daytime temperatures are captured quite well, we can see that for north-facing walls the model systematically overestimates the surface temperature (the same behaviour can be observed at another north-facing wall observed from location 2, Fig. S5). This effect emerges when the opposite walls are fully irradiated by the Sun (Fig. 11, 08:00–14:00 UTC). The same observation can be made for east-facing walls in the afternoon hours (Fig. S8, 12:00–

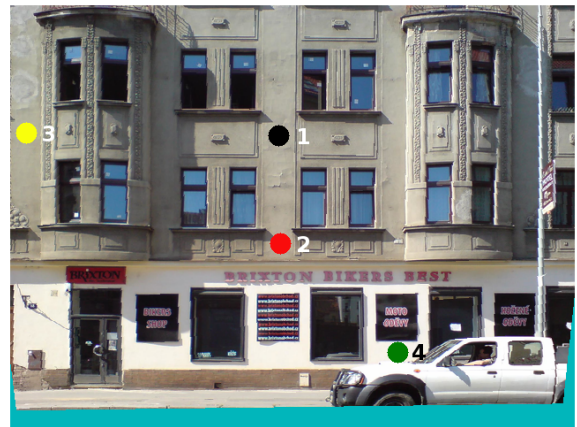
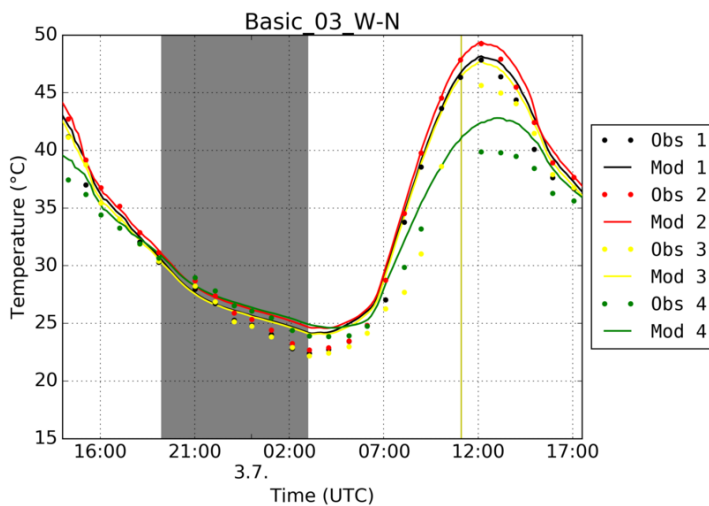


Figure 9. Comparison of modelled and observed surface temperatures from observation location 3 (50.10354° N, 14.45006° E) – view of the south-facing wall. The graph shows comparisons for selected evaluation points for the period of the observation campaign from 2 July 2015, 14:00 UTC to 3 July 2015, 17:00 UTC. The solid line represents modelled values, while the dots show the observed values. The shaded area depicts nighttime and the yellow vertical line depicts solar noon.

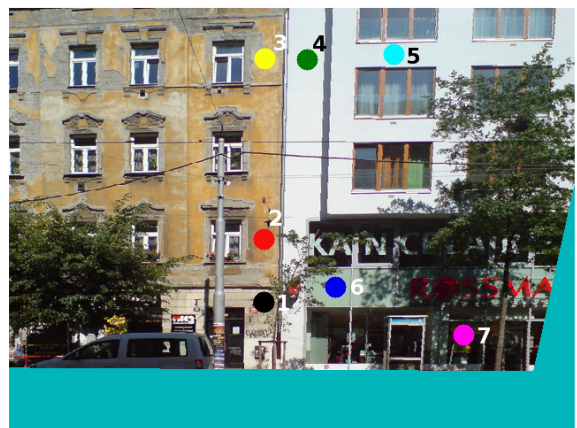
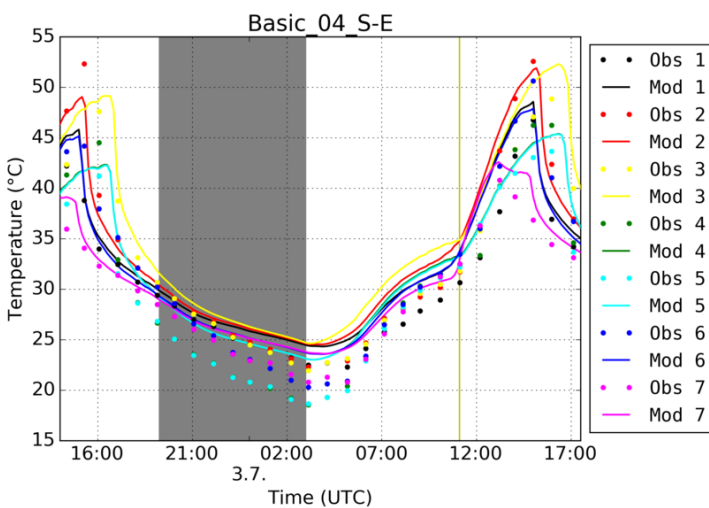


Figure 10. As for Fig. 9 for location 4 (50.10288° N, 14.44985° E) – view of the west-facing wall.

15:00 UTC). The possible reason for this overestimation is discussed later in Sect. 4.

Figure 12 shows the east-facing wall of the northern arm of the north–south street. We can observe the effect of shading by opposite buildings here. As the Sun rises and the shade cast by opposite buildings moves downward in the morning, the Sun gradually irradiates points 3 (from 04:45 UTC), 2 (from 05:40 UTC), and 1 (from 06:10 UTC). This is reflected in observations and also in model results, although the modelled temperature in point 3 starts to increase somewhat later than the observed temperature at the same point due to the discretized geometry of the buildings on the opposite side of the street. The effect of the shading of east-facing walls during the sunrise is further visible in Fig. 15.

Finally, Fig. 13 shows the measurement of the ground surface temperature. The model captures the maximum values well, which are higher for asphalt (points 2, 3, and 4) than for paving blocks (points 1, 5, 6, and 7). The lower temperature of the white crosswalk, represented in the model as a one-grid-width belt with higher albedo, is reflected in the model results as well. Also, the time when the temperature starts to increase in the morning is captured with some minor discrepancies, owing to the discretized representation of the surrounding buildings.

Figure 14 shows a view of the surface temperatures for the entire modelling domain on 3 July at 12:00 UTC, demonstrating different heating of facades due to different surface and material properties. As seen for all similarly irradiated

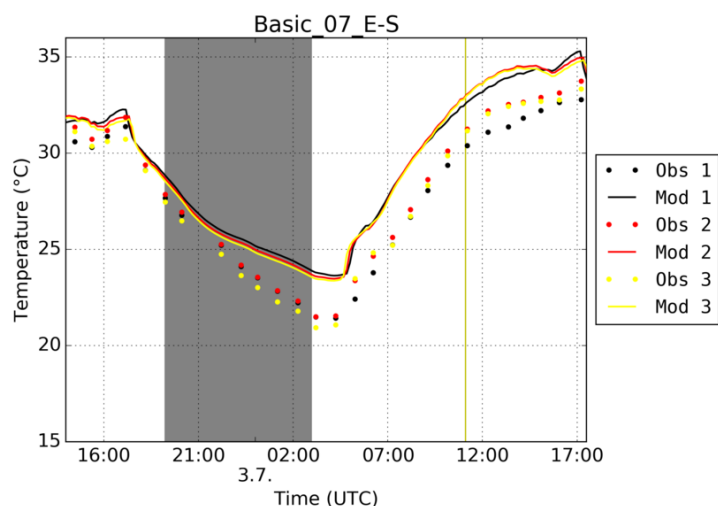


Figure 11. As for Fig. 9 for location 7 (50.10329° N, 14.45040° E) – view of the north-facing wall.

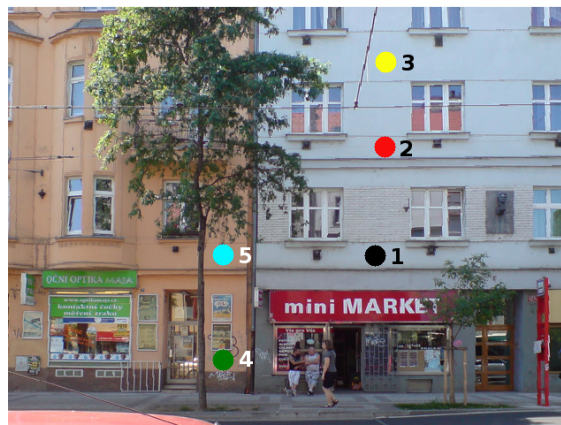
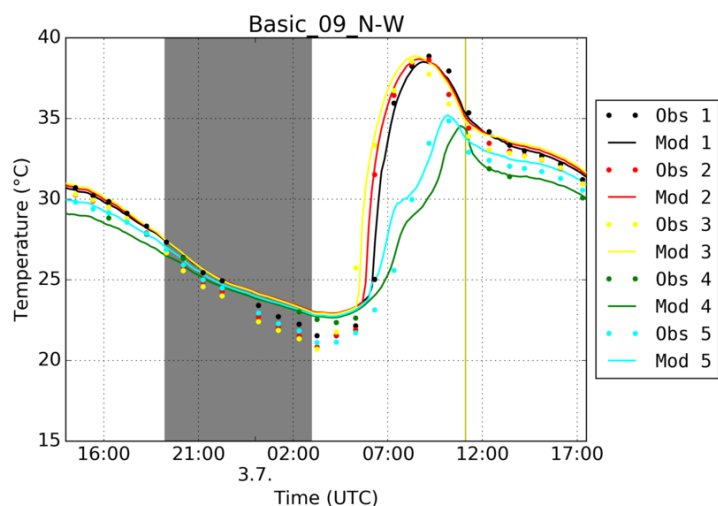


Figure 12. As for Fig. 9 for location 9 (50.10354° N, 14.45006° E) – view of the east-facing wall.

surfaces (e.g. all south-facing walls), the different wall properties lead to differently warmed surfaces. Further, cool spots resulting from shading by trees are clearly visible. This view also demonstrates the effect of transforming the real urban geometry into the regular modelling grid. The detailed view of east-facing walls in the north–south street in the morning of 3 July is shown in Fig. 15. This picture shows surface temperatures after the sunrise at 06:00 and 08:00 UTC. The view displays the effects of shading by buildings on the opposite side of the street as well as the thermal inertia of the material and the impact of different material properties.

3.4 Sensitivity tests

3.4.1 Sensitivity to the dynamics of surface heat fluxes

In order to show the effect of dynamically calculated surface heat fluxes that are derived by the USM depending on given material properties, we performed another simulation with disabled USM (PALM noUSM). In order to make both simulations comparable, they need to be based on the same energy input. This is achieved by prescribing a homogeneous surface heat flux to all surfaces (ground, roof, wall) in the noUSM set-up, with this heat-flux value derived from the original USM simulation as the average over all surfaces in the entire domain in the target time. Simulation parameters in the noUSM simulation were set to values of the original USM set-up from the selected period. The noUSM simula-

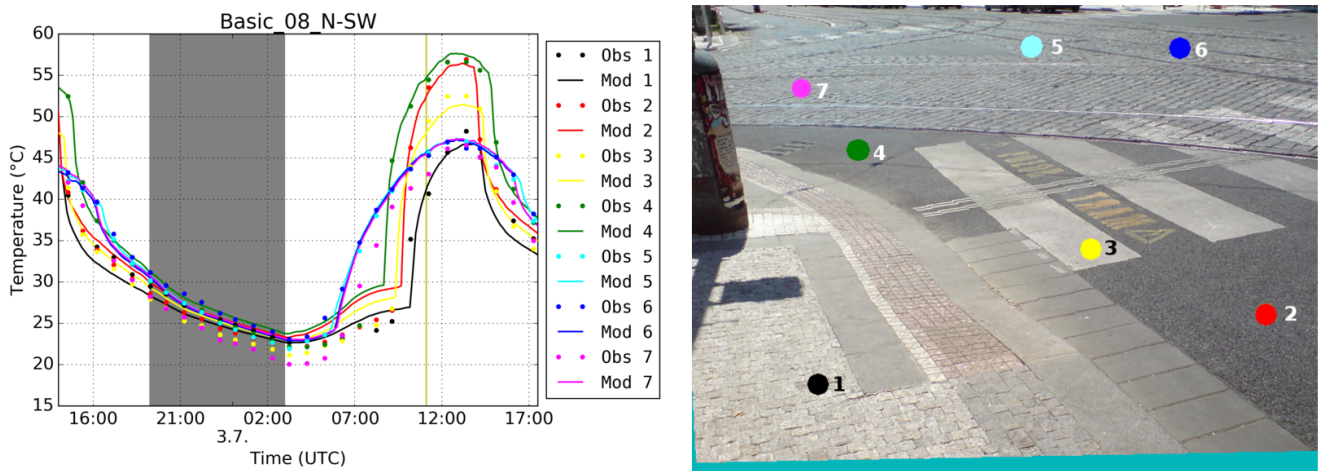


Figure 13. As for Fig. 9 for location 8 (50.10340° N, 14.45007° E) – view of the ground on the crossroads.

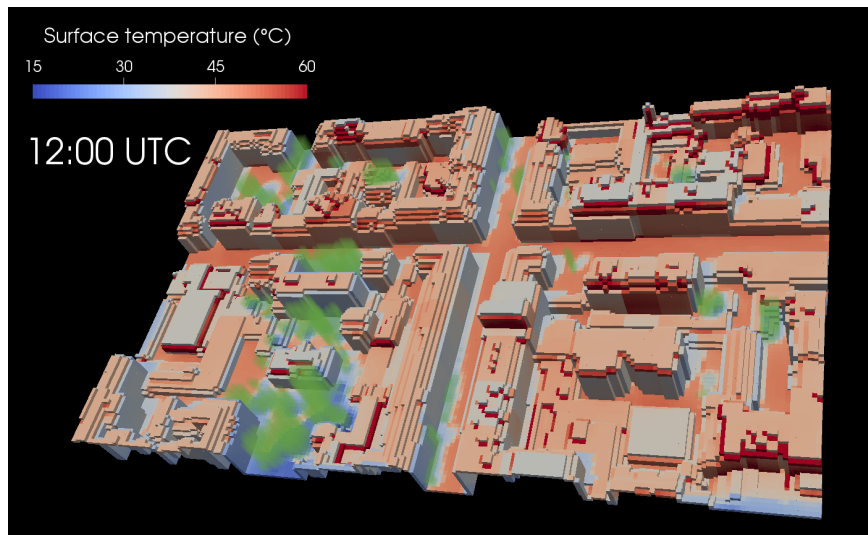


Figure 14. Modelled surface temperatures for the entire domain on 3 July at 12:00 UTC. Green areas represent vegetation (trees).

tion ran for 5 h to reach a quasi-steady state. Figure 16 shows the horizontal cross section of the time-averaged (1 h) vertical velocity at 10 m a.g.l. Figures correspond to simulation time 3 July at 14:00 UTC, when west- and south-facing walls were fully irradiated and heated up by the Sun. The wind above the roof top was north-west and its strength was about 2 m s^{-1} . In the PALM-noUSM case, a typical vortex perpendicular to the street axis in the west–east oriented street and in the southern part of the south–north oriented street was formed. In the reference case, however, the non-uniform heat flux was heating the air on the south- and west-facing walls, changing the strength of the street vortex. This effect is more intensely pronounced in the southern arm of the north–south oriented street where the strong vortex observed in case PALM-noUSM has significantly weakened. In Fig. 17 it becomes evident that the entire flow circulation pattern within

this street arm had changed, leading to a change in the vortex orientation.

The accurate prediction of the canyon flow is an essential prerequisite, among others, for the accurate prediction of pollutant concentrations at street level and their vertical mixing. Our results – in line with previous studies – show that an interactive surface scheme is a crucial part of the urban modelling system and alters the canyon flow significantly.

3.4.2 Sensitivity to material parameters

Gathering of properties of individual materials and surface types is a challenging task. For our case, materials were categorized, and representative parameters were assigned to each category. The only exception is the albedo which was set individually for each particular surface based on surface colour.

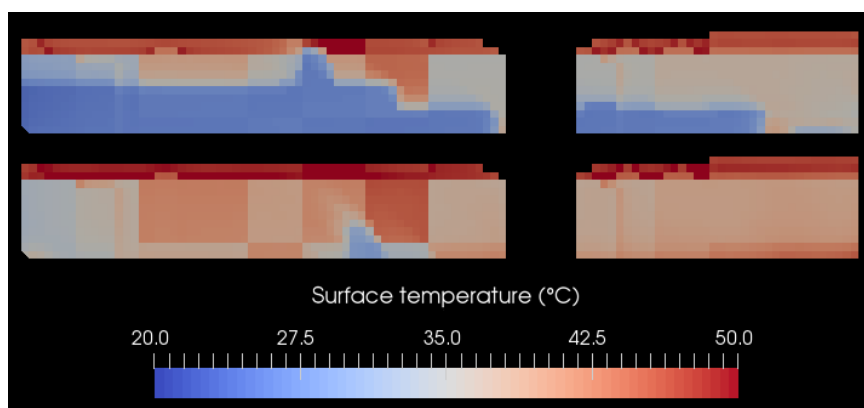


Figure 15. Modelled surface temperatures of the east-facing walls in the north–south street after the sunrise on 3 July at 06:00 UTC (top) and 08:00 (bottom) UTC.

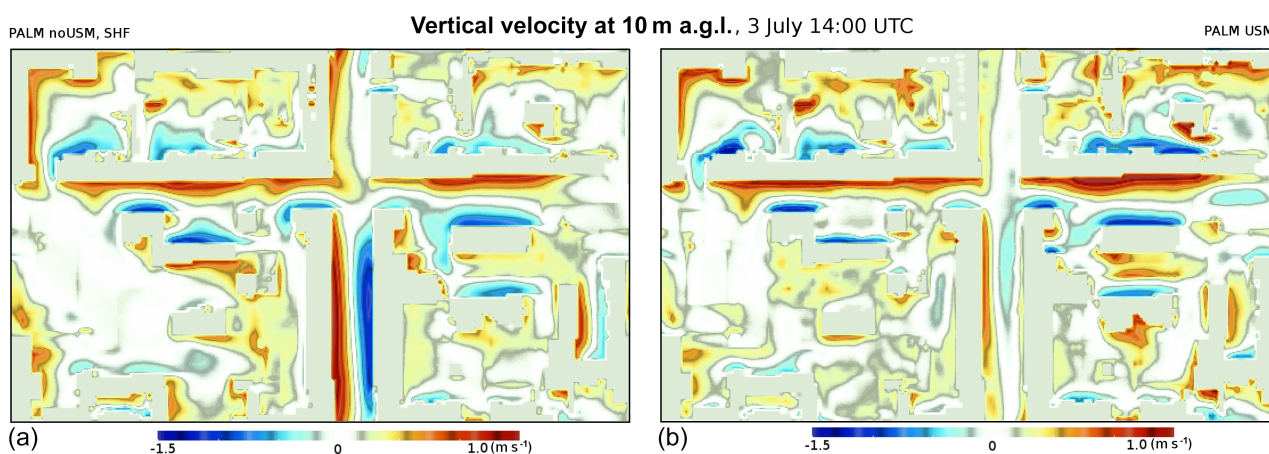


Figure 16. Horizontal view of modelled vertical velocity (1 h average) at 10 m a.g.l. on 3 July, 14:00 UTC. **(a)** presents a stationary simulation without USM with constant surface heat fluxes and **(b)** the reference simulation with USM enabled.

The uncertainty of the input parameters is high, though. In order to estimate related uncertainties of model results, a series of simulations was performed where one parameter was changed per simulation. The tests included the increase and decrease in albedo, the thermal conductivity of both the material and the skin layer, and the roughness length of the surface. The albedo was modified by ± 0.2 and all other parameters were adjusted by $\pm 30\%$ of their respective value. The sensitivities of the surface temperature at selected locations and evaluation points are presented in Fig. 18. The largest changes in model output are generally observed during daytime. The model behaves according to the physical meaning of the parameters: decreased roughness lowers turbulent exchange of heat between the surface and air, leading to the increase in surface temperature when the air is colder, which is usually the case in our simulation. A decrease in roughness to 70% leads to the increase in temperature by up to 4°C. A decrease in thermal conductivity leads to more intense heating of the surface when the net heat flux is positive

(usually during daytime) and to less intense cooling when it is negative (usually during night). The decrease in the albedo leads to higher absorption of SW radiation and an increase in the surface temperature during daytime. The sensitivity of the modelled surface temperature can reach up to 5°C.

This sensitivity analysis shows that even moderate changes in the wall material properties can lead to differences in the surface temperatures of a few degrees Celsius. As mentioned in Sect. 3.3, we observe an overestimation at some evaluation points located at the lower parts of the buildings (location 3, point 4; location 4, point 1; location 5, point 1). We hypothesize that a possible reason can be that walls at lower parts of buildings can be built from different material than the upper floors. In that case the thermal conductivity used in the model would be different than its true value. This can be the possible explanation for some discrepancies between model and observation. On the other hand, some discrepancies (e.g. overestimation of temperatures on north-facing walls) are systematic and they can probably be attributed to

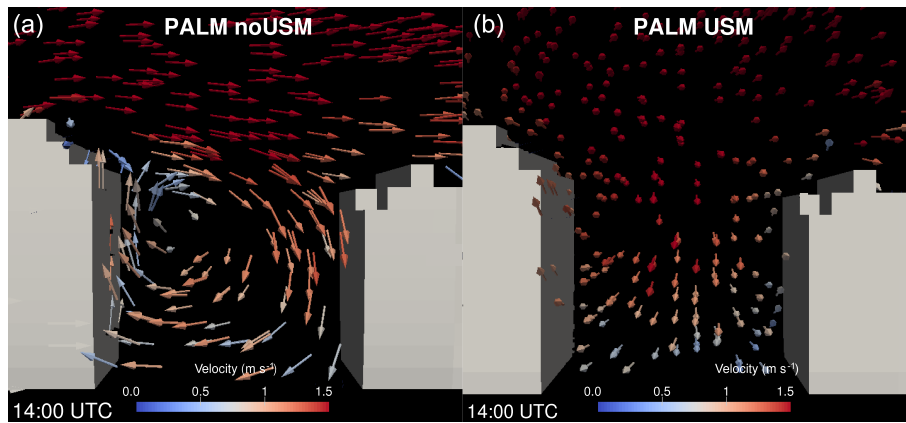


Figure 17. Wind field. Simulation without USM with prescribed surface heat fluxes (a) and with USM (b). View from the southern border of the domain towards the crossroads.

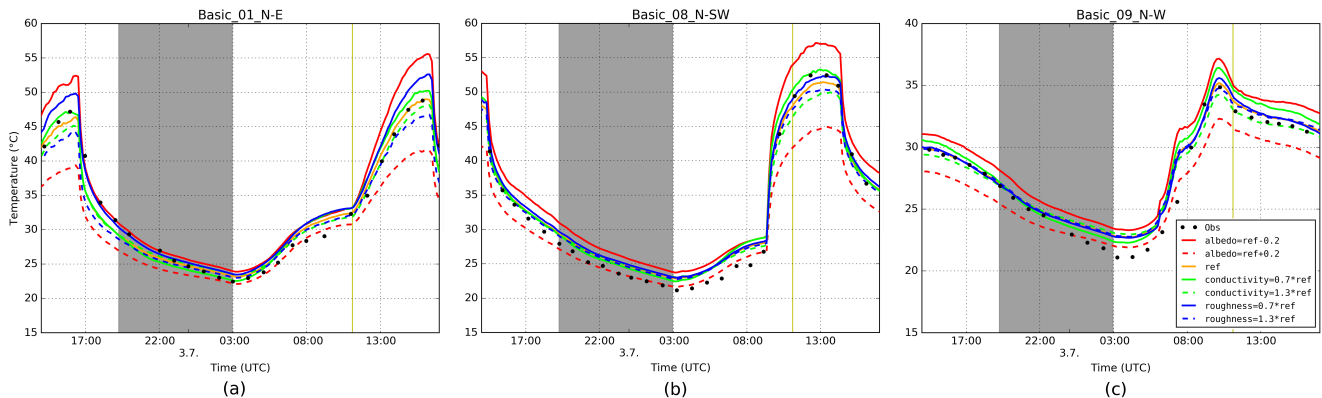


Figure 18. The sensitivity of PALM-USM to changes in surface and material parameters: (a) for the west-facing wall measured from location 1 for evaluation point 1, (b) for the ground measured from location 8 for evaluation point 3, and (c) for the east-facing wall measured from location 9 for evaluation point 5. ref is the reference run; other lines correspond to the increase (dashed line) and decrease (solid line) in the respective parameters with respect to the reference run: albedo was increased/decreased by 0.2, thermal conductivity of materials and skin surface layer (conductivity) was increased/decreased by 30 %, and so was the roughness length (roughness). Obs is the measurement in the evaluation point.

some limitation of the set-up, or the model itself. Some possible reasons are discussed in Sect. 4.

4 Discussion

The deficiencies in the model's description of reality and the discrepancies against observations may arise from limitations, simplifications, and omissions within the model itself and from limited exactness, representativity, and appropriateness of the model set-up.

4.1 Limitations of the model

The USM and its radiative transfer model (RTM) assume only a diffuse reflection and do not treat windows. In our configuration, specular reflection can play a role for glossy surfaces like flagstones and glass. Windows also transmit

part of the radiation into the building and only the rest is absorbed by the glass itself. Examples of IR camera observations of the south-facing wall taken from location 6 at 01:08, 10:08, and 13:17 UTC are shown in Fig. S15. The effective temperature of the window is usually lower by several K to a few tens of K compared to the surrounding wall. Since this is not captured by the model, the longwave radiative flux emitted from those walls can be overestimated. The approximate calculation for the area captured by these IR photos shows that average heat fluxes of the wall with windows are lower by 7 W m^{-2} (01:08 UTC), 27 W m^{-2} (10:08 UTC), and 25 W m^{-2} (13:17 UTC), as compared to the wall without windows. The difference in the average effective temperature of the wall is 1.5, 4, and 3.5 K, respectively. As mentioned in Sect. 3.3, the model overestimates the temperature of north-facing walls. Since the modelled net radiation on the north-facing walls ranges from -20 W m^{-2} during night up

to 70 W m^{-2} during the day, and since the opposite walls represent about one-third to half of the visible area, these differences are not negligible and may be responsible at least partly for the overestimation of the surface temperature of north-facing walls. This suggests that an extension of the USM by a proper window model is very desirable.

The RTM also simulates only a finite, configured number of reflections. After that, the remainder of reflected irradiance is considered fully absorbed by the respective surface. The amount of absorbed residual irradiance is available among model outputs and it can be used to find an optimum number of reflections until the residual irradiance is negligible. The optimum setting depends on the albedo and emissivity of the surfaces. In our set-up, the residual irradiance was below 1 % of the surface's total at most surfaces after three reflections, and it was negligible after five reflections.

The current version of the RTM model does not simulate absorption, emission, and scattering of radiation in the air within the urban canopy layer; thus, it is not suitable for modelling of situations with extremely low visibility like fog, dense rain, or heavy air pollution. However, under clear air conditions and in an urban set-up where typical distances of radiatively interacting surfaces are of the order of metres or tens of metres, these processes are negligible⁸. Most of the solar radiation's interaction with the atmosphere happens on the long paths from top of atmosphere to ground and during the interaction with clouds, i.e. above the urban layer, where the method of modelling of these processes depends on the selected solar radiation model in PALM.

The USM is currently coupled to PALM's simple clear-sky radiation model, which provides only limited information on sky longwave radiation, and it does not provide air heating and cooling rates. This limitation will be overcome in the near future when the USM will be coupled to the more advanced RRTMG model in PALM.

Shading by plant canopy is only modelled for shortwave radiation; in the longwave spectrum, the plant canopy is considered fully transparent. Typical daily maxima of SW radiative fluxes (mostly from direct solar radiation) are much higher than maxima of LW fluxes. Moreover, much of the LW heat exchange is compensated when surfaces are near radiative equilibrium. Therefore, for the LW shading by plant canopy to cause significant changes in the heat fluxes, two conditions must occur simultaneously: the plant canopy and the affected surface have to occupy a large portion of each other's field of view (e.g. a large and dense tree close to a wall); and the temperature of the plant canopy, the affected surface, and the background field of view have to differ significantly (e.g. the wall is under direct sunlight and the plant canopy is shaded or cooled by convection).

⁸Using MODTRAN (Berk et al., 2014) for a clean-air summer urban atmosphere, transmissivity for $10 \mu\text{m}$ radiation (i.e. peak wavelength of black-body radiance at 300 K) per 1 km of air is approximately 0.85, which equals 0.998 per 10 m.

To illustrate the amount of affected heat flux, let us propose a simple realistic scenario where these effects are very strong. Let us have two opposing walls, each occupying 50 % of the other's field of view (without regard for plant canopy), and let us add a row of trees directly between the walls, blocking 30 % of the mutual radiative exchange between the walls. Let the temperature of the ambient air, one of the walls, and the plant canopy be 300 K, and let the other wall heat to 320 K due to strong direct sunlight.

Under these conditions, the cool wall would be receiving 68 W m^{-2} of excess total radiative flux (absorption minus emission) due to the opposing wall being hotter. The hot wall would be losing the same excess total flux due to the opposing wall being cooler, both when not accounting for shading by plant canopy. With the plant canopy, the cool wall would only be receiving 41 W m^{-2} of excess total flux from the opposing wall and the remaining flux of 21 W m^{-2} would be absorbed by the plant canopy. The hotter wall would experience the same radiative cooling as without plant canopy.

With regard to our test scenario, we accepted the simplification, considering that the demonstrated omission would affect only a few spots in the modelled domain. Modelling of LW interaction with plant canopy is planned for the next version of the model.

Plant leaves are treated in the USM as having zero thermal capacity and a similar temperature to the surrounding air. Any radiation absorbed by leaves directly heats the surrounding modelled air mass. In reality, plant leaves are thin, they have a large surface area, and they readily exchange heat with air. This simplification is common among radiative transfer models (see e.g. Dai et al., 2003) and it is also in accordance with the current implementation of the non-urban plant canopy model in PALM.

Evapotranspiration of the plant canopy is not modelled and surfaces are considered impervious to water. Generally, these are important processes which will be accounted for in the upcoming versions of the model. The importance of evapotranspiration and latent heat grows with the modelled proportion of vegetation. The measurements in Grimmond and Oke (1999) – specifically in Table 2, p. 925 – show that in their case, latent heat flow vs. net radiation ratio ranged from 4 % in the downtown area (similar to the streets in our test case) up to 37 % in the suburban area with a high fraction of vegetation. In our case, however, street surfaces are covered by asphalt or granite paving blocks with gaps filled by asphalt. Only a part of the pavements in the north–south street that are paved with limestone blocks can be considered pervious to water to a larger extent. There are only a few trees in the streets, concentrated mostly in the north–south street, and their treetops are not very dense (Figs. 12 and 10). Moreover, the last precipitation before the observation campaign was recorded in Prague on 29 June (0.3 mm day^{-1}). Therefore, it can be expected that the neglect of these processes will not have large effects on the evaluation presented in this article.

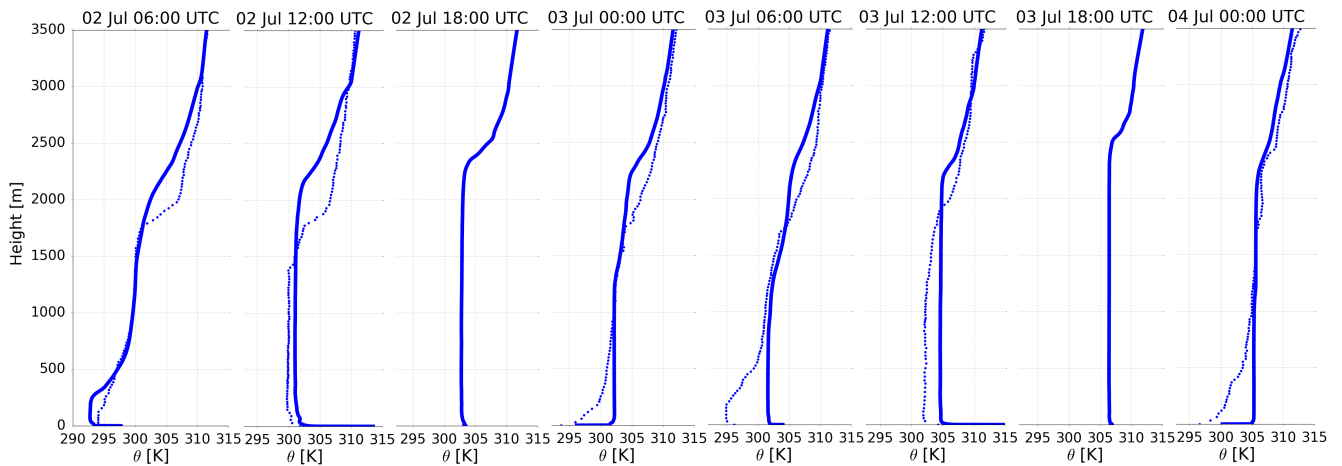


Figure 19. As for Fig. 7 for the idealized simulation with an enlarged domain (see Sect. 4).

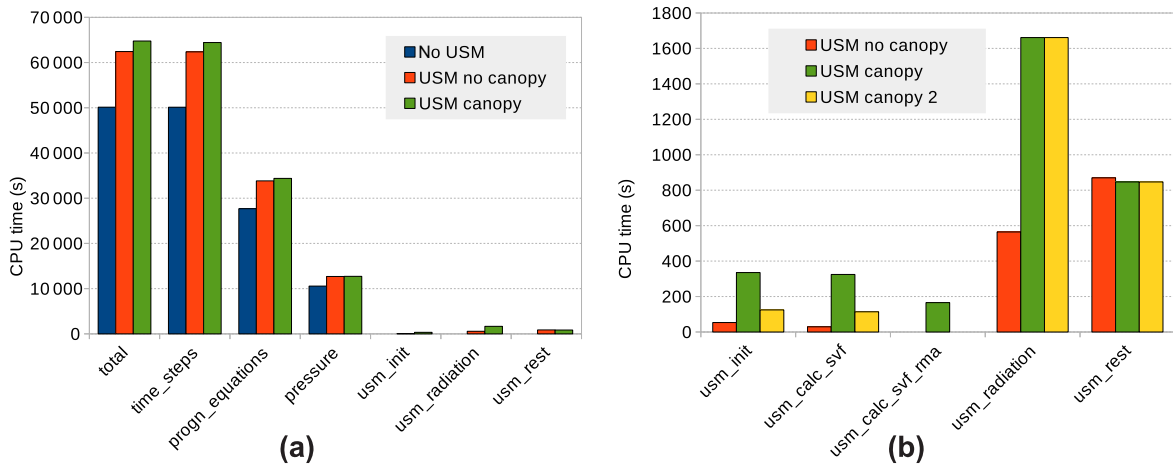


Figure 20. Comparison of the duration of the model run and the time spent in the chosen subprocesses of the model (a) and detailed comparison of parts of the USM model (b). Meaning of data series: “no USM” the run of PALM with USM switched off, “USM no canopy” the run with USM with no plant canopy, “USM canopy” run with USM and plant canopy, and “USM canopy 2” the same run with the model configuration option `usm_lad_rma` turned off. Meaning of items: *total* – total CPU time of the model run; *time_steps* – time spent in time stepping; *progn_equations* – evaluation of all prognostic equations; *pressure* – pressure calculation; *usm_init* – initialization routines of USM; *usm_radiation* – calculation of the USM radiation model; *usm_rest* – remaining USM processes (particularly energy balance and material thermal diffusion); *usm_calc_svf* – calculation of SVF and CSF; *usm_calc_svf_rma* – time spent with one-sided MPI communication. The set-up of the model corresponds to the set-up described in Sect. 3.2 with a reduced number of layers to 81.

4.2 Appropriateness of the presented set-up

One of the potential issues of the set-up is the model domain’s horizontal size. The CBL height reached values of up to 2000 m during daytime (see Fig. 7). It is well known that the largest structures in a CBL scale with the height of the boundary layer, and they typically form hexagonal cellular patterns. In this context, the chosen horizontal model domain is too small to resolve these structures. We must thus expect that the largest turbulent eddies were not able to freely develop during daytime. Nevertheless, the feedback of these eddies onto the surface–subsurface continuum can

be regarded as small. This is supported by our recent experiences using the PALM-LSM system for a dry bare-soil configuration (work in progress, not shown). Moreover, as we have seen in Sect. 3.3, the simulated skin temperatures compare well with observations and do not display significant fluctuations at turbulent timescales.

However, we have seen that the vertical profiles of potential temperature display an unusual unstably stratified shape during daytime. To estimate the possible influence of the domain extent on the mean vertical profiles, an idealized simulation was performed. The horizontal grid size was increased by a factor of 10 to 20.8 m, while all the rest of the set-up was

kept unchanged. This artificially increased the simulation domain to a horizontal extent of 3760 m × 2260 m, without having to increase the number of computational grid points. The topography of this domain is not fully comparable with the original domain as the street width is 10 times larger and the ratio of the sizes of individual grids also differs from the original set-up. Nevertheless, it can indicate the overall characteristics of the set-up with a large domain. Vertical profiles of potential temperature from this simulation are shown in Fig. 19. Compared to Fig. 7 we can see that the unstable stratification that was observed at 12:00 UTC and reached up to 1.5 km changed to near-neutral conditions in the large-domain simulation, corresponding to well-mixed boundary layer conditions. Based on this finding, we must be aware of the fact that the formation of the largest turbulent eddies was inhibited by the small model domain, but that they are essential for the efficient vertical transport of heat. While this is no problem for RANS-type models, where all turbulent eddies are parameterized, it imposes a limitation for the application of LES models in urban areas, as one has to ensure that the horizontal model domain is at least the size of the boundary-layer depth and thus will require enormous computational resources. However, one of the methods to overcome this problem is already under way. This is the two-way nesting system for urban applications that has already been implemented in PALM and allows for use of finer grid spacings in areas of special interest while having coarser grids in the surroundings.

Another limitation of the set-up is the fixed indoor temperature. The studied simulation spans only over 2 days with similar summer weather conditions. Considering the heat capacity of walls, the influence of changes in the indoor temperature can be regarded as small for the presented simulation. This issue could be more important for long-term simulations.

Gathering information about the detailed structure of the walls in the entire domain constitutes a significant challenge. For practical reasons, the material of every particular wall is considered homogeneous in our simulation. Thus, the thermal conductivity of the sandwich structure of insulated walls is not well represented, as well as the structure of pavements and streets. The conductivity of the entire wall structure can be substituted by the average conductivity with no effect to the long-term average heat flux going through the wall. However, layers of walls described by the same average parameters can actually have different thermal capacities and conductivities, resulting in different thermal dynamics. This can partially influence the shape of the surface temperatures in affected places.

Anthropogenic heat sources were limited to traffic in our test case. Other potentially significant anthropogenic sources can be heat emissions from buildings. Considering that the period of interest is in the summer, the relevant processes would be air conditioning, which however is not common in this part of the city.

When evaluating model results, the uncertainty of the measurements must also be taken into account. In our case, the measurements are affected by not using the emissivity correction option of the IR camera, and by possible reflections, mainly in the case of horizontal surfaces. For this reason, only those points where the influence of reflections was supposed to be negligible were considered for evaluation.

The presented evaluation of the model is limited to a specific city district and meteorological condition. However, since the model is based on general formulations, it should be applicable for arbitrary configurations of fully urbanized areas. Concerning the meteorological set-up, we suppose that the model with its current limitations is yet suitable for representing the urban surface–atmosphere interactions under meteorological conditions where the omitted processes do not play a significant role. Model limitations will be resolved in the future PALM-USM versions, which will be validated accordingly for a wider range of meteorological conditions and surface types. A key factor for a successful validation is good knowledge of these conditions and the properties of all urban surface elements.

5 Computational aspects

The correct functionality and computational efficiency of the implementation of USM was verified in various environments. The tested configurations varied in processor type (Intel⁹, AMD¹⁰), compiler (GNU¹¹, PGI¹², Intel¹³), implementation of MPI (MVAPICH2¹⁴, IMP¹⁵), and other aspects. The comparison presented in this chapter was performed on the Salomon supercomputer¹⁶ with Intel C and Fortran compilers and Intel MPI (2016 versions for all). The set-up of the model corresponds to the set-up described in Sect. 3.2 with a decreased number of vertical layers to 81 and 1-day simulation extent to get a reasonable computational time also for a smaller number of MPI processes.

Figure 20a shows the comparison of the total CPU time of the model run and the CPU time needed for particular chosen subroutines. Almost all of the total time is spent on time stepping. The direct expense of the USM can be split into three parts: the time spent in initialization routines of the USM at the start of the model run, the time needed for calculation of the urban radiation model, and finally the time of remaining USM processes, particularly the energy balance and the material thermal diffusion. The total increase in the calculation time with the USM switched on is about 25 %

⁹<https://ark.intel.com/>

¹⁰<http://www.amd.com/en-us/products/processors>

¹¹<https://gcc.gnu.org/>

¹²<http://www.pgroup.com/>

¹³<https://software.intel.com/en-us/intel-compilers>

¹⁴<http://mvapich.cse.ohio-state.edu/>

¹⁵<https://software.intel.com/en-us/intel-mpi-library>

¹⁶<https://docs.it4i.cz/salomon/introduction>

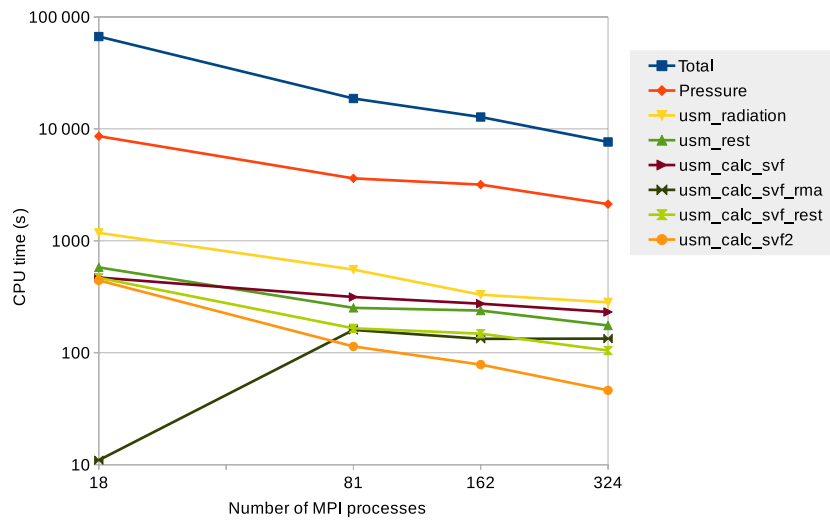


Figure 21. Comparison of the calculation time spent in model PALM-USM and in its chosen parts for various numbers of cores. Model configuration and the meaning of items is the same as in Fig. 20; additionally, *usm_calc_svf_rest* shows the difference *usm_calc_svf*–*usm_calc_svf_rma* and *usm_calc_svf2* depicts *usm_calc_svf* in the case of the run with option *usm_lad_rma* set to false.

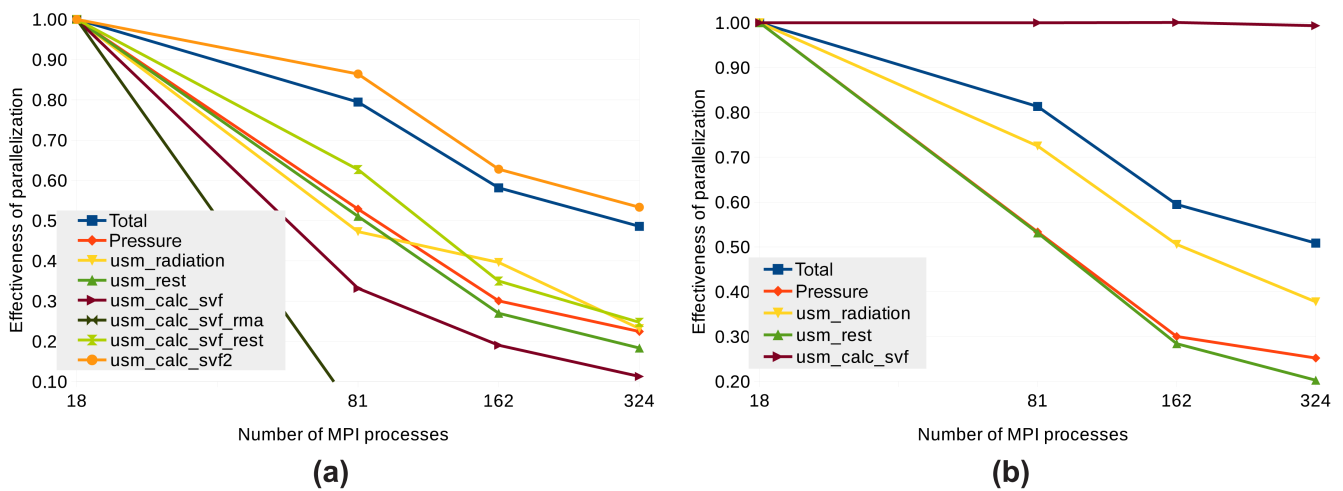


Figure 22. Effectiveness of the parallelization of the chosen subroutines: (a) simulation with plant canopy, (b) without plant canopy. The meaning of the items is the same as in Fig. 21.

(29 % with plant canopy). However, the direct USM calculation cost presents only about 2 % (4 % with plant canopy) of the total calculation time. The rest of the increase can be attributed to the raised turbulent flow which results in a decreased time step. Figure 20b shows the detailed comparison of USM processes. The initialization time of the USM is dominated by the calculation of SVF and CSF and about half of this calculation is spent with one-sided MPI communication in the case of the run with a plant canopy. The utilization of one-sided MPI routines can be avoided by distributing the global leaf area density (LAD) array into all MPI processes by setting the model configuration parameter *usm_lad_rma* to false, which reduces the time spent in the USM initialization process and markedly improves the scaling behaviour.

The effectiveness of the parallelization has been tested for a number of MPI processes in the range from 18 to 324 for simulation length 24 h and the results are shown in Figs. 21 and 22. Figure 21 compares the CPU time needed for calculation of the whole PALM-USM model and its chosen individual parts. Figure 22a and b show the effectiveness of the parallelization relative to a run with 18 processes for simulation with and without calculation of plant canopy, respectively. The graphs suggest that time-stepping routines *usm_radiation* and *usm_rest* scale similarly to calculation of the pressure, which is the most time-consuming individual process of the PALM model. The calculation of SVF during the initialization phase scales excellently in the tested range according to Fig. 22b. Scaling of the calculation of CSF is

on a par with the whole PALM model for configuration with the LAD array distributed into all processes (Fig. 22a, item *usm_calc_svf2*), while scaling of the *usm_calc_svf* is limited by latency of one-sided MPI operations implemented by an Infiniband RMA backend (Fig. 21, *usm_calc_svf_rma*). (Note that the run with 18 processes fits into one node of the computational cluster and all MPI communication is done through a shared memory backend in our set-up.) On the other hand, it also suggests that the computation of CSF can scale well when the computational domain is extended. However, the testing domain is relatively small and additional tests with larger domains are needed to extract deeper insight into the performance and scaling of PALM-USM. The first tests with the domain extent over 3 km suggest that the scalability of the present version of RTM is limited by growing memory requirements, particularly by the growth of the number of SVF and CSF. This issue will be solved in the next version of RTM.

6 Conclusions

The new model of energy processes in urban environments was developed and integrated into the PALM model as an optional module. The USM utilizes meteorological values calculated by PALM, and it provides sensible heat fluxes as boundary conditions for the atmospheric flow. In this paper, we described the technical details of the USM formulation. Moreover, a first evaluation against data from a measurement campaign in Prague, Czech Republic, was performed, as well as basic sensitivity tests to material parameters. The results are generally in good agreement with observations for our test case. In particular, the evaluation incorporated a detailed comparison of the simulated building wall and street surface temperatures with IR camera measurements. The results showed that the diurnal variation of the surface temperature was very well captured except for the north-facing walls, where the temperatures were overestimated by up to 3 °C. A similar overestimation was also found on some other walls during nighttime hours. These differences can be attributed to inaccurate description of the urban parameters such as heat capacity and conductivity of the wall material as well as to some limitations of the current version of the model and model set-up, e.g. no window model implementation.

Uncertainties due to the sensitivity to the setting of material parameters were estimated in a suite of simulations altering three basic parameters: albedo (± 0.2), thermal conductivity, and roughness length (both $\pm 30\%$). The results show that the tested albedo variation generally induces the largest changes in surface temperatures (up to ± 5 °C). The overall magnitude of changes confirms that the proper setting of material parameters is crucial for the application of the model in real-case simulations.

For tested configurations, the USM shows very moderate computational demand in the context of the other PALM components.

Addressing the current limitations of the USM is a subject of current and future development inside the PALM community. Major changes to the current USM version will involve the implementation of a tile approach to account for windows and green roofs/walls. An energy balance solver for trees will be added in order to explicitly predict the turbulent fluxes of sensible and latent heat from leaves. Also, the wall model will be coupled to an indoor climate and energy demand model, which predicts the indoor temperature, but also the energy demand of the buildings, including anthropogenic waste heat emissions from the buildings due to heating and air conditioning. Furthermore, the scalability of the urban radiative transfer model will be rigorously enhanced to allow for use of larger computational grids. The USM will be coupled to the RRTMG radiation model to improve the radiation input at the top of the urban layer. Finally, the USM will be coupled with the PALM-LSM, which allows one to represent processes related to latent heat (evaporation, transpiration) and urban areas that exhibit larger areas of parks and pervious surfaces compared to the present test case. Many of these actions are work in progress within the framework of the MOSAIK project.

Despite the current limitations, the PALM-USM model provides a new useful tool for climatology studies of urbanized areas, and has been successfully used to simulate urban development scenarios for the city of Prague.

Code availability. The USM code is freely available and it is distributed under GNU General Public License v3¹⁷. Its source code is a part of PALM and it has been available for download from the PALM web page¹⁸ via the SVN server¹⁹ since PALM revision 2008. The particular version used for computation of the simulations presented in this article is available in branch “resler”, revision 2325. This branch version also includes a simple air pollution model.

The Supplement related to this article is available online at <https://doi.org/10.5194/gmd-10-3635-2017-supplement>.

Competing interests. The authors declare that they have no conflict of interest.

Acknowledgements. The authors would like to thank three reviewers for the comments that helped to improve the manuscript

¹⁷<http://www.gnu.org/copyleft/gpl.html>

¹⁸<https://palm.muk.uni-hannover.de>

¹⁹<http://subversion.apache.org>

considerably. We acknowledge the following projects that supported this research. This work was done within the UrbanAdapt project (EHP-CZ02-OV-1-036-2015) supported by a grant from Iceland, Liechtenstein, and Norway.²⁰ This work was also supported by the long-term strategic development financing of the Institute of Computer Science of the Czech Academy of Sciences (RVO:67985807). Some of the simulations were done on supercomputer Salomon, which was supported by the Ministry of Education, Youth and Sports from the Large Infrastructures for Research, Experimental Development and Innovations project IT4Innovations National Supercomputing Center – LM2015070. Coauthors B. Maronga and F. Kanani-Sühring are funded by the German Federal Ministry of Education and Research (BMBF) under grant 01LP1601A (project MOSAIK²¹) within the framework of Research for Sustainable Development (FONA²²), which is greatly acknowledged. The authors would like to thank Linton Corbet for language revisions and useful comments. We would also like to thank to the coordinator of UrbanAdapt project Global Change Research Institute (CzechGlobe) for lending the IR camera and František Zemek for his help with the observation campaign. We thank UrbanAdapt project partner the Prague Institute of Planning and Development for providing geographical data and also the ATEM company for its help with the data processing.

Edited by: Jason Williams

Reviewed by: Reinder Ronda and two anonymous referees

References

- Arakawa, A. and Lamb, V. R.: Computational design of the basic dynamical processes of the UCLA general circulation model, in: *General Circulation Models of the Atmosphere*, edited by: Chang, J., vol. 17 of *Methods in Computational Physics: Advances in Research and Applications*, 173–265, Elsevier, 1977.
- Arnfield, A. J.: Two decades of urban climate research: a review of turbulence, exchanges of energy and water, and the urban heat island, *Int. J. Climatol.*, 23, 1–26, <https://doi.org/10.1002/joc.859>, 2003.
- Balsamo, G., Beljaars, A., Scipal, K., Viterbo, P., van den Hurk, B., Hirschi, M., and Betts, A. K.: A revised hydrology for the ECMWF model: verification from field site to terrestrial water storage and impact in the integrated forecast system, *J. Hydrometeorol.*, 10, 623–643, <https://doi.org/10.1175/2008JHM1068.1>, 2009.
- Berk, A., Conforti, P., Kennett, R., Perkins, T., Hawes, F., and van den Bosch, J.: MODTRAN6: a major upgrade of the MODTRAN radiative transfer code, in: *SPIE Defense+ Security, 90880H–90880H*, International Society for Optics and Photonics, 2014.
- Boland, J., Ridley, B., and Brown, B.: Models of diffuse solar radiation, *Renew. Energ.*, 33, 575–584, 2008.
- Clough, S., Shephard, M., Mlawer, E., Delamere, J., Iacono, M., Cady-Pereira, K., Boukabara, S., and Brown, P.: Atmospheric radiative transfer modeling: a summary of the AER codes, *J. Quant. Spectrosc. Ra.*, 91, 233–244, <https://doi.org/10.1016/j.jqsrt.2004.05.058>, 2005.
- Dai, Y., Zeng, X., Dickinson, R. E., Baker, I., Bonan, G. B., Bosilovich, M. G., Denning, A. S., Dirmeyer, P. A., Houser, P. R., Niu, G., Oleson, K. W., Schlosser, C. A., and Yang, Z.-L.: The Common Land Model, *B. Am. Meteorol. Soc.*, 84, 1013–1023, <https://doi.org/10.1175/BAMS-84-8-1013>, 2003.
- Deardorff, J. W.: Stratocumulus-capped mixed layers derived from a three-dimensional model, *Bound.-Lay. Meteorol.*, 18, 495–527, <https://doi.org/10.1007/BF00119502>, 1980.
- Ehrhard, J., Khatib, I. A., Winkler, C., Kunz, R., Moussiopoulos, N., and Ernst, G.: The microscale model MIMO: development and assessment, *J. Wind Eng. Ind. Aerod.*, 85, 163–176, 2000.
- ENVI-met: ENVI-met 3.1 Manual Contents, available at: <http://www.envi-met.info/documents/onlinehelpv3/helpindex.htm> (last access: September 2016), 2009.
- FLIR: FLIR SC660 R and D INFRARED CAMERA SYSTEM. Product leaflet, available at: <http://www.flir.com/assets/6e002ff6acaa46a599ce08197091e01a.pdf> (last access: September 2016), 2008.
- Grimmond, C. S. B. and Oke, T. R.: Heat storage in urban areas: local-scale observations and evaluation of a simple model, *J. Appl. Meteorol.*, 38, 922–940, [https://doi.org/10.1175/1520-0450\(1999\)038<0922:HSIUAL>2.0.CO;2](https://doi.org/10.1175/1520-0450(1999)038<0922:HSIUAL>2.0.CO;2), 1999.
- Heus, T., van Heerwaarden, C. C., Jonker, H. J. J., Pier Siebesma, A., Axelsen, S., van den Dries, K., Geoffroy, O., Moene, A. F., Pino, D., de Roode, S. R., and Vilà-Guerau de Arellano, J.: Formulation of the Dutch Atmospheric Large-Eddy Simulation (DALES) and overview of its applications, *Geosci. Model Dev.*, 3, 415–444, <https://doi.org/10.5194/gmd-3-415-2010>, 2010.
- Hong, S.-Y., Noh, Y., and Dudhia, J.: A new vertical diffusion package with an explicit treatment of entrainment processes, *Mon. Weather Rev.*, 134, 2318–2341, <https://doi.org/10.1175/MWR3199.1>, 2006.
- Howell, J. R., Menguc, M. P., and Siegel, R.: *Thermal Radiation Heat Transfer*, CRC Press, 2010.
- Järvi, L., Grimmond, C. S. B., and Christen, A.: The Surface Urban Energy and Water Balance Scheme (SUEWS): evaluation in Los Angeles and Vancouver, *J. Hydrol.*, 411, 219–237, <https://doi.org/10.1016/j.jhydrol.2011.10.001>, 2011.
- Juruš, P., Resler, J., Derbek, P., Krč, P., Belda, M., Benešová, N., Vlček, O., Srbová, D., Eben, K., and Hruběš, P.: High resolution modelling of anthropogenic heat from traffic in urban canopy: a sensitivity study, in: *2016 Smart Cities Symposium Prague (SCSP)*, 1–6, <https://doi.org/10.1109/SCSP.2016.7501031>, 2016.
- Kanda, M., Inagaki, A., Miyamoto, T., Gryschka, M., and Raasch, S.: A new aerodynamic parametrization for real urban surfaces, *Bound.-Lay. Meteorol.*, 148, 357–377, <https://doi.org/10.1007/s10546-013-9818-x>, 2013.
- Krayenhoff, E. S. and Voogt, J. A.: A microscale three-dimensional urban energy balance model for studying surface temperatures, *Bound.-Lay. Meteorol.*, 123, 433–461, <https://doi.org/10.1007/s10546-006-9153-6>, 2007.
- Kusaka, H., Kondo, H., Kikegawa, Y., and Kimura, F.: A simple single-layer urban canopy model for atmospheric models: comparison with multi-layer and slab models, *Bound.-Lay. Meteorol.*, 101, 329–358, <https://doi.org/10.1023/A:1019207923078>, 2001.

²⁰<http://urbanadapt.cz/en>

²¹<http://uc2-mosaik.org>

²²www.fona.de

- Letzel, M. O., Krane, M., and Raasch, S.: High resolution urban large-eddy simulation studies from street canyon to neighbourhood scale, *Atmos. Environ.*, 42, 8770–8784, <https://doi.org/10.1016/j.atmosenv.2008.08.001>, 2008.
- Letzel, M. O., Helmke, C., Ng, E., An, X., Lai, A., and Raasch, S.: LES case study on pedestrian level ventilation in two neighbourhoods in Hong Kong, *Meteorol. Z.*, 21, 575–589, <https://doi.org/10.1127/0941-2948/2012/0356>, 2012.
- Lindberg, F., Holmer, B., and Thorsson, S.: SOLWEIG 1.0 – modelling spatial variations of 3D radiant fluxes and mean radiant temperature in complex urban settings, *Int. J. Biometeorol.*, 52, 697–713, <https://doi.org/10.1007/s00484-008-0162-7>, 2008.
- Maronga, B. and Bosveld, F. C.: Key parameters for the life cycle of nocturnal radiation fog: a comprehensive large-eddy simulation study, *Q. J. Roy. Meteor. Soc.*, 143, 2463–2480, <https://doi.org/10.1002/qj.3100>, 2017.
- Maronga, B., Gryschka, M., Heinze, R., Hoffmann, F., Kanani-Sühring, F., Keck, M., Ketelsen, K., Letzel, M. O., Sühring, M., and Raasch, S.: The Parallelized Large-Eddy Simulation Model (PALM) version 4.0 for atmospheric and oceanic flows: model formulation, recent developments, and future perspectives, *Geosci. Model Dev.*, 8, 2515–2551, <https://doi.org/10.5194/gmd-8-2515-2015>, 2015.
- Martilli, A., Clappier, A., and Rotach, M. W.: An urban surface exchange parameterisation for mesoscale models, *Bound.-Lay. Meteorol.*, 104, 261–304, <https://doi.org/10.1023/A:1016099921195>, 2002.
- Masson, V.: A physically-based scheme for the urban energy budget in atmospheric models, *Bound.-Lay. Meteorol.*, 94, 357–397, <https://doi.org/10.1023/A:1002463829265>, 2000.
- Matzarakis, A., Rutz, F., and Mayer, H.: Modelling radiation fluxes in simple and complex environments: basics of the RayMan model, *Int. J. Biometeorol.*, 54, 131–139, <https://doi.org/10.1007/s00484-009-0261-0>, 2010.
- Mirzaei, P. A.: Recent challenges in modeling of urban heat island, *Sustain. Cities Soc.*, 19, 200–206, <https://doi.org/10.1016/j.scs.2015.04.001>, 2015.
- Mirzaei, P. A. and Haghighat, F.: Approaches to study Urban Heat Island – abilities and limitations, *Build. Environ.*, 45, 2192–2201, <https://doi.org/10.1016/j.buildenv.2010.04.001>, 2010.
- Moeng, C.-H. and Wyngaard, J. C.: Spectral analysis of Large-Eddy simulations of the convective boundary layer, *J. Atmos. Sci.*, 45, 3573–3587, [https://doi.org/10.1175/1520-0469\(1988\)045<3573:SAOLES>2.0.CO;2](https://doi.org/10.1175/1520-0469(1988)045<3573:SAOLES>2.0.CO;2), 1988.
- Moonen, P., Defraeye, T., Dorer, V., Blocken, B., and Carmeliet, J.: Urban physics: effect of the micro-climate on comfort, health and energy demand, *Frontiers of Architectural Research*, 1, 197–228, <https://doi.org/10.1016/j.foar.2012.05.002>, 2012.
- Musy, M., Malys, L., Morille, B., and Inard, C.: The use of SOLENE-microclimat model to assess adaptation strategies at the district scale, Part 2, *Urban Climate*, 14, 213–223, <https://doi.org/10.1016/j.uclim.2015.07.004>, 2015.
- Obukhov, A. M.: Turbulence in an atmosphere with a non-uniform temperature, *Bound.-Lay. Meteorol.*, 2, 7–29, <https://doi.org/10.1007/BF00718085>, 1971.
- Oke, T. R.: The energetic basis of the urban heat island, *Q. J. Roy. Meteor. Soc.*, 108, 1–24, <https://doi.org/10.1002/qj.49710845502>, 1982.
- Park, S.-B., and Baik, J.-J.: A Large-Eddy simulation study of thermal effects on turbulence coherent structures in and above a building array, *J. Appl. Meteorol. Clim.*, 52, 1348–1365, <https://doi.org/10.1175/JAMC-D-12-0162.1>, 2013.
- Saiki, E. M., Moeng, C.-H., and Sullivan, P. P.: Large-Eddy simulation of the stably stratified planetary boundary layer, *Bound.-Lay. Meteorol.*, 95, 1–30, <https://doi.org/10.1023/A:1002428223156>, 2000.
- Sailor, D. J. and Lu, L.: A top-down methodology for developing diurnal and seasonal anthropogenic heating profiles for urban areas, *Atmos. Environ.*, 38, 2737–2748, <https://doi.org/10.1016/j.atmosenv.2004.01.034>, 2004.
- Schlünzen, K. H., Hinneburg, D., Knoth, O., Lambrecht, M., Leidl, B., López, S., Lüpkes, C., Pankus, H., Renner, E., Schatzmann, M., Schoenemeyer, T., Trepte, S., and Wolke, R.: Flow and transport in the obstacle layer: first results of the micro-scale model MITRAS, *J. Atmos. Chem.*, 44, 113–130, <https://doi.org/10.1023/A:1022420130032>, 2003.
- Sievers, U.: Das kleinskalige Strömungsmodell MUKLIMO_3 Teil 1: Theoretische Grundlagen, PC-Basisversion und Validierung, *Berichte des Deutschen Wetterdienstes 240*, Offenbach am Main, Germany, 2012 (in German).
- Sievers, U.: Das kleinskalige Strömungsmodell MUKLIMO_3 Teil 2: Thermodynamische Erweiterungen, *Berichte des Deutschen Wetterdienstes Entwurf*, Offenbach am Main, Germany, 2014 (in German).
- Skamarock, W. C., Klemp, J. B., Dudhia, J., Gill, D. O., Barker, D., Duda, M. G., Huang, X.-Y., Wang, W., and Powers, J. G.: A Description of the Advanced Research WRF Version 3, NCAR Tech. Note NCAR/TN-475+STR, 113 pp., NCAR/UCAR, Boulder, 2008.
- Tewari, M., Chen, F., Wang, W., Dudhia, J., LeMone, M. A., Mitchell, K., Gayno, G., Ek, M., Wegiel, J., and Cuenca, R. H.: Implementation and verification of the unified NOAA land surface model in the WRF model, 11–15, *American Meteorological Society, 20th Conference on Weather Analysis and Forecasting/16th Conference on Numerical Weather Prediction*, Seattle, WA, US, presentation, 2004.
- United Nations 2014: World Urbanization Prospects: The 2014 Revision, United Nations, Department of Economic and Social Affairs, available at: <http://esa.un.org/unpd/wup/>, (last access: 12 December 2016), 2014.
- Wicker, L. J. and Skamarock, W. C.: Time-splitting methods for elastic models using forward time schemes, *Mon. Weather Rev.*, 130, 2088–2097, [https://doi.org/10.1175/1520-0493\(2002\)130<2088:TSMFEM>2.0.CO;2](https://doi.org/10.1175/1520-0493(2002)130<2088:TSMFEM>2.0.CO;2), 2002.
- Williamson, J. H.: Low-storage Runge–Kutta schemes, *J. Comput. Phys.*, 35, 48–56, [https://doi.org/10.1016/0021-9991\(80\)90033-9](https://doi.org/10.1016/0021-9991(80)90033-9), 1980.
- Yaghoobian, N. and Kleissl, J.: An indoor-outdoor building energy simulator to study urban modification effects on building energy use – model description and validation, *Energ. Buildings*, 54, 407–417, <https://doi.org/10.1016/j.enbuild.2012.07.019>, 2012.
- Yaghoobian, N., Kleissl, J., and Paw U, K. T.: An improved three-dimensional simulation of the diurnally varying street-canyon flow, *Bound.-Lay. Meteorol.*, 153, 251–276, <https://doi.org/10.1007/s10546-014-9940-4>, 2014.



Validation of the PALM model system 6.0 in a real urban environment: a case study in Dejvice, Prague, the Czech Republic

Jaroslav Resler¹, Kryštof Eben¹, Jan Geletič¹, Pavel Krč¹, Martin Rosecký¹, Matthias Sühling², Michal Belda³, Vladimír Fuka³, Tomáš Halenka³, Peter Huszár³, Jan Karlický³, Nina Benešová⁴, Jana Ďoubalová^{3,4}, Kateřina Honzáková⁴, Josef Keder⁴, Šárka Nápravníková⁴, and Ondřej Vlček⁴

¹Institute of Computer Science of the Czech Academy of Sciences, Prague, Czech Republic

²Institute of Meteorology and Climatology, Leibniz University Hannover, Hanover, Germany

³Department of Atmospheric Physics, Faculty of Mathematics and Physics, Charles University, Prague, Czech Republic

⁴Czech Hydrometeorological Institute, Prague, Czech Republic

Correspondence: Jaroslav Resler (resler@cs.cas.cz)

Received: 31 May 2020 – Discussion started: 14 August 2020

Revised: 3 May 2021 – Accepted: 25 June 2021 – Published: 3 August 2021

Abstract. In recent years, the PALM 6.0 modelling system has been rapidly developing its capability to simulate physical processes within urban environments. Some examples in this regard are energy-balance solvers for building and land surfaces, a radiative transfer model to account for multiple reflections and shading, a plant-canopy model to consider the effects of plants on flow (thermo)dynamics, and a chemistry transport model to enable simulation of air quality. This study provides a thorough evaluation of modelled meteorological, air chemistry, and ground and wall-surface quantities against dedicated in situ measurements taken in an urban environment in Dejvice, Prague, the Czech Republic. Measurements included monitoring of air quality and meteorology in street canyons, surface temperature scanning with infrared cameras, and monitoring of wall heat fluxes. Large-eddy simulations (LES) using the PALM model driven by boundary conditions obtained from a mesoscale model were performed for multiple days within two summer and three winter episodes characterized by different atmospheric conditions.

For the simulated episodes, the resulting temperature, wind speed, and chemical compound concentrations within street canyons show a realistic representation of the observed state, except that the LES did not adequately capture nighttime cooling near the surface for certain meteorological conditions. In some situations, insufficient turbulent mixing was

modelled, resulting in higher near-surface concentrations. At most of the evaluation points, the simulated surface temperature reproduces the observed surface temperature reasonably well for both absolute and daily amplitude values. However, especially for the winter episodes and for modern buildings with multilayer walls, the heat transfer through walls is not well captured in some cases, leading to discrepancies between the modelled and observed wall-surface temperature. Furthermore, the study corroborates model dependency on the accuracy of the input data. In particular, the temperatures of surfaces affected by nearby trees strongly depend on the spatial distribution of the leaf area density, land surface temperatures at grass surfaces strongly depend on the initial soil moisture, wall-surface temperatures depend on the correct setting of wall material parameters, and concentrations depend on detailed information on spatial distribution of emissions, all of which are often unavailable at sufficient accuracy. The study also points out some current model limitations, particularly the implications of representing topography and complex heterogeneous facades on a discrete Cartesian grid, and glass facades that are not fully represented in terms of radiative processes.

Our findings are able to validate the representation of physical processes in PALM while also pointing out specific shortcomings. This will help to build a baseline for future de-

velopments of the model and improvements of simulations of physical processes in an urban environment.

1 Introduction

A majority of the world's population live in large cities (55 % as of 2018), and this percentage is expected to grow (UN, 2019). At the same time, global climate change, especially global temperature increases, will influence nearly every natural ecosystem and human society, with potentially severe impacts worldwide. Thus, the high level of attention currently being paid to the impact of climate change on urban areas is amply justified and is supported by many important studies and reports of global standing (IPCC, 2014a, b). This intensifying urbanization has heightened the awareness that control of the microclimate in the urban environment, which can reduce heat stress and prompt other general environmental improvements, is crucial for the well-being of city inhabitants (Mutani and Fiermonte, 2017). The problem of increased heat stress in urban areas as a consequence of what has become known as the urban heat island (UHI) is, therefore, of direct concern to municipal authorities, who are well aware that the physical well-being of their inhabitants is vital to the well-being of the whole city. Moreover, the UHI effect is often followed by secondary processes, such as air quality issues. Researchers have responded to, or anticipated, such concern and the requirement for modelling of urban climate processes, and several small-grid-scale models and frameworks for numerical climate modelling have recently been developed (Geletić et al., 2018).

The health and well-being of the urban population is influenced by the conditions of the urban environment. The local microclimate, exposure to pollutants, and general human comfort depends strongly on the local conditions driven by the urban environment. The turbulent flow, exchange of latent and sensible heat, and radiative transfer processes play an important role in the urban microclimate and need to be considered in modelling approaches. The implementation of important microclimate processes (e.g. turbulence, heat fluxes and radiation) in street-level-scale models is typically partially or fully parameterized. The most exhaustive approach consists of a group of computational fluid dynamics (CFD) models. The explicit simulation of turbulent flow is computationally demanding; thus, various techniques have to be adapted to make calculations feasible, usually based on limiting the range of the length scales and timescales of the turbulent flow to be resolved.

This study uses the PALM model system 6.0 (Maronga et al., 2020), which is an atmospheric modelling system. The core of the system contains model dynamics based on the LES (large-eddy simulation) and RANS (Reynolds-averaged Navier–Stokes) techniques with additional modules for modelling of various atmospheric processes (e.g. interaction of

the atmosphere with the Earth's surface or cloud microphysics). This system core is complemented by a rich set of PALM-4U (PALM for urban applications) modules related to the modelling of physical phenomena relevant for urban climate, such as the interaction of solar radiation with urban surfaces and with urban vegetation, sensible and latent heat fluxes from the surfaces, storage of heat inside buildings and in pavements, or dispersion and chemical reaction of air pollutants (see Maronga et al., 2020). The first version of the PALM urban components represented the urban surface model (PALM-USM) which has been validated using data from a short experimental campaign in the centre of Prague (Resler et al., 2017). The new set of modules in PALM is more general and is divided according to the physical processes that they cover. The most relevant for urban climate are the land surface model (LSM), the building surface model (BSM), the radiative transfer model (RTM), the plant-canopy model (PCM), and the chemistry transport model (CHEM). The human biometeorology module (BIO) then allows the evaluation of the impact of simulated climate conditions on the human population.

Validation of the urban model requires a dataset of measurements of the urban meteorological and air quality conditions, the properties of the urban canopy elements, and the energy exchange among parts of the urban canopy. Several campaigns of comprehensive observations and measurements of the urban atmospheric boundary layer, covering more than one season, have been done in the past: the Basel UrBan Boundary Layer Experiment (BUBBLE) dataset containing observations from Basel is specifically targeted for validation of urban radiation models, urban energy-balance models, and urban canopy parameterizations (Rotach et al., 2005); MUSE (Montreal Urban Snow Experiment) is aimed at the thermoradiative exchanges and the effect of snow cover in the urban atmospheric boundary layer (Lemonsu et al., 2008); and the CAPITOU (Canopy and Aerosol Particles Interaction in TOulouse Urban Layer) project (Masson et al., 2008) is aimed at the role of aerosol particles in the urban layer.

Results of urban measurement campaigns have already been used for the validation of several micrometeorological models, models of radiative transfer, and microscale chemical transport models. Microscale model validation causes difficulties due to the high heterogeneity of the urban environment and the modelled variables, uncertainty in the detailed knowledge of urban canopy properties, and local irregularities caused by domain discretization. Important examples of such validation studies have been published by Qu et al. (2013), Maggiotto et al. (2014), and Toparlak et al. (2015). These validation studies most frequently analyse RANS-type micrometeorological models. Early examples of LES validation studies that include thermal conditions within cities were presented by Nozu et al. (2008) and Liu et al. (2012). Due to our previous experience with a limited validation of surface temperatures simulated by the PALM model (Resler et al.,

2017), the aim of this study was to design a comprehensive experiment for model validation, including air velocity, air pollution, and surface temperature analysis. The focus on the collection of detailed temporally and spatially localized observations in various urban canopy and meteorological conditions was dictated by the intention to use these observations to assess the performance of the newly developed or updated PALM modules: RTM, BSM, LSM, PCM, and CHEM. This focus of the study also complied with its additional purpose, which was assessment of the utility of the PALM model performance for detailed urban studies (Geletič et al., 2021).

These considerations influenced the selection of the study area. The Dejvice quarter is an urbanized area typical of others in Prague and similar central European cities with various types of urban environment. Further, the realization of the street-level observation campaign was technically and organizationally easier in this area than in areas such as the historical centre of Prague. Moreover, this area represents one of the pilot areas for urban adaptations studies carried out in cooperation with the Prague municipality and their organizations (e.g. Prague Institute of Urban Planning and Development). Their interest in the results of this study and their plans for subsequent modelling studies of urban heat island and air quality adaptation and mitigation strategies for this quarter also influenced our selection of this area.

Section 2 gives a detailed overview of the observation campaign, followed by a description and an evaluation of the numerical set-up in Sects. 3 and 4. In Sect. 5 results from the numerical experiment and the observation campaign are presented and compared. Finally, Sect. 6 closes with a summary, outlines the current limitations of the model, and gives ideas for future improvements.

2 Observation campaign

The observation campaign was designed with two main aims: (1) to evaluate PALM's capability, with its newly developed or improved thermal capability from the radiative transfer model (RTM), land and building surface modules (LSM and BSM respectively), and plant-canopy model (PCM), to reproduce surface temperatures; (2) to evaluate its capability to reproduce pollutant concentrations and meteorological quantities in different types of street canyons, with special focus on the impact of trees located in streets on both types of quantities. The campaign was carried out in a warm part of the year (10–23 July 2018 – further referred to as the summer campaign) and a cold part of the year (23 November–10 December 2018 – further referred to as the winter campaign). Measurement locations are shown in Fig. 1, and the measurements themselves are described in Sect. 2.3.1–2.3.5. More details on the campaign are available in ČHMÚ (2020).

2.1 Study area

The study area is located in the north-west centre of Prague, the capital city of the Czech Republic. The position and a map of this area are presented in Fig. S1 in the Supplement. This figure also marks the extent of the PALM modelling domains; for more information about model domain set-up, see Sect. 3.1. The study area includes complex terrain that is mainly located in the western part of the outer domain (further referred as the parent domain), with an altitude ranging from 175 to 346 m above sea level. The altitude variability in the inner domain (further referred as the child domain) is up to 30 m (see Fig. S2). The observations were located inside the child domain (blue square in Fig. S2). This is a densely built-up area with specific conditions created by the roundabout (Vítězné náměstí) in combination with west–east-oriented (Evropská–Čs. armády) and north–south-oriented (Jugoslávských partyzánů–Svatovítská) boulevards. The eastern and southern parts of the child domain represent a typical historical residential area in Dejvice, Prague, with a combination of old and new buildings and a variety of other urban components, such as gardens, parks, and parking places. The north-west quarter is home to the larger buildings of the Czech Technical University campus. The south-western and north-eastern parts of the domain are more sparsely built-up by family houses. Location-specific features include green intra-blocks with gardens and trees, usually with pervious ground surfaces; Prague historic centre usually has impervious intra-blocks. The building heights alongside the streets range from approximately 20 to 30 m, with the highest building in the domain being 60 m. Both boulevards are approximately 40 m wide and contain little green vegetation, except for Jugoslávských partyzánů Street which has some broadleaf trees that are about 20 m high. The majority of the trees are located in the intra-blocks and parks. The land cover map of the study area, based on the Urban Atlas 2012 geodatabase, is shown in Fig. S3.

2.2 Validation episodes and synoptic situation

2.2.1 Summer campaign

The summer observation campaign ran for 2 weeks from 10 to 23 July 2018 (see Table S2 in the Supplement), from which two shorter episodes were selected for model simulations: 14–16 July (e1) and 19–23 July (e2). Synoptically, for most of the summer campaign, the weather was influenced by a high-pressure ridge over central Europe between an Icelandic low and an eastern European low-pressure system. Daily maximum temperature as measured at the Praha-Karlov (WMO ID 11519) station was below 30 °C for the entire period, with the exception of 21 July when the maximum temperature reached 31.2 °C. The beginning of the period was partially cloudy, mostly with altostratus clouds which formed in the morning and early afternoon on 19 July.

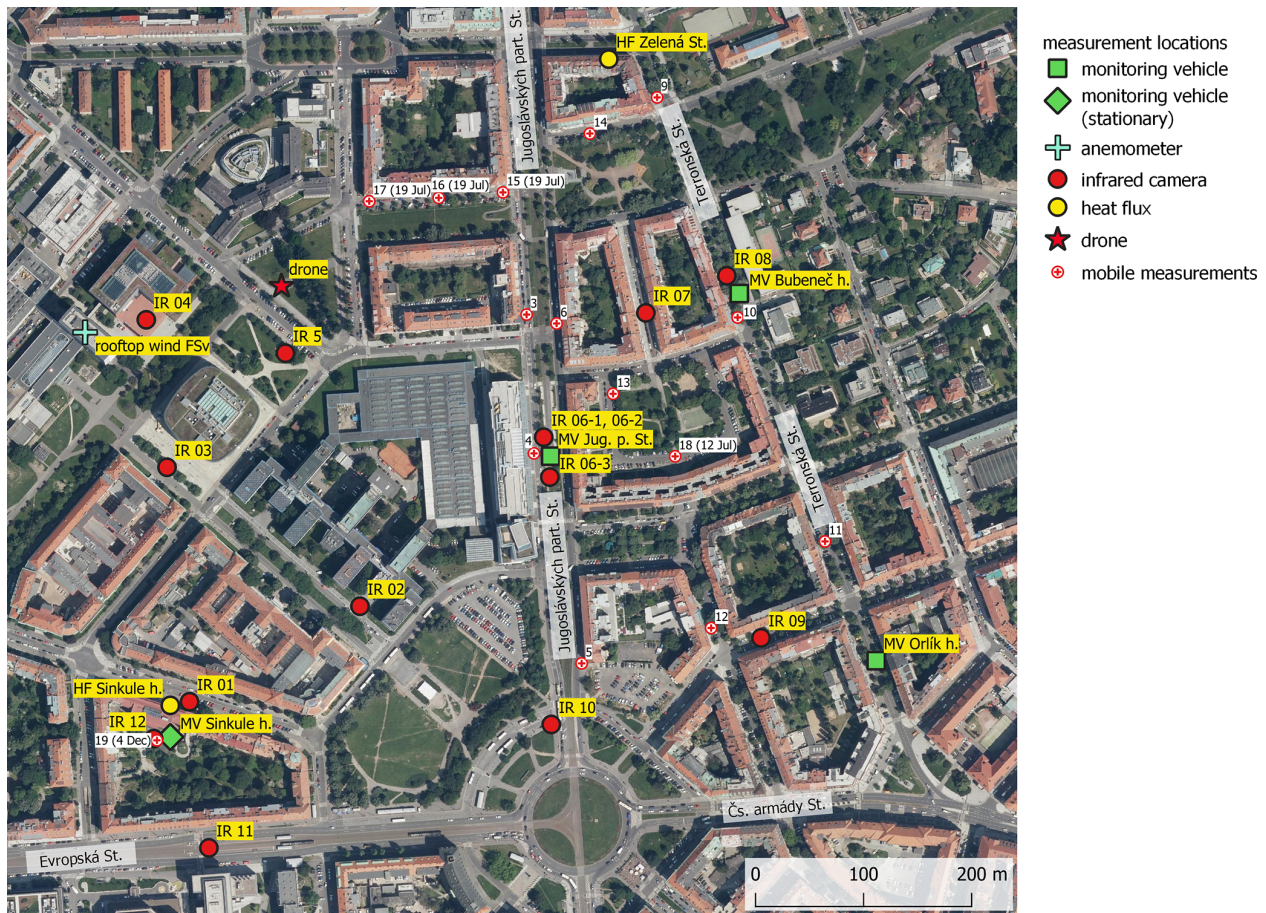


Figure 1. Map of measurement locations. Orthophoto was provided by the Web Map Service (WMS) of the Czech Office for Surveying, Mapping and Cadastre (ČÚZK, 2020). For more information about the point location (longitude, latitude etc.), see Table S1.

The period between the afternoon of 19 July and late afternoon on 21 July was mostly clear with cirrus clouds. The end of the campaign was cloudy, mostly with low-level cumulus. The mid-episode (19 July 2018) solar parameters were as follows: sunrise at 03:13 UTC, sunset at 19:02 UTC, and solar noon at 11:08 UTC.

2.2.2 Winter campaign

The winter part of the observation campaign lasted from 24 November to 10 December 2018 (see Table S3 in the Supplement), and for the purposes of model validation, three episodes were selected: 24–26 November (e1), 27–29 November (e2), and 4–6 December (e3). Weather was influenced by a typical late-autumn synoptical situation with westerly flow and low-pressure systems as well as a series of fronts separated by two anticyclonic events (27–29 November and 5 December). During the campaign, several occluded frontal passages were recorded in Prague: 24 and 30 November, and 2, 3, 4 and 6 December, with rainfall on 30 November (4.3 mm at Praha-Ruzyně station; WMO ID 11518) and 2 and 3 December (9.8 and 3.6 mm at Praha-Ruzyně sta-

tion). Average daily temperatures ranged from -4°C on 29 November to 9°C on 3 December. Average daily wind speed was around 3 m s^{-1} , except for 26 November when it reached 4.4 m s^{-1} and 4–6 December with daily values of 4.8, 6.0 and 5.7 m s^{-1} . The diurnal solar radiation parameters in Prague on 1 December 2018 were as follows: sunrise at 06:39 UTC, sunset at 15:02 UTC, solar noon at 10:51 UTC.

2.3 Observed quantities and equipment used

2.3.1 Infrared camera measurements

Surface temperature measurements by an infrared (IR) camera were carried out during 2 d (45 h total) of the summer and 3 d (50 h total) of the winter campaigns (see Tables S2 and S3). Measurements were taken at 12 locations shown in Fig. 1 approximately every 60–80 min. At each location, several directions were chosen, and usually two snapshots capturing horizontal (ground) and vertical (wall) surfaces were taken in each direction. We use the following nomenclature hereafter: <location_number>-<direction_number>_H/V. For example 02-1_H means im-

age of the ground taken from the second location in the first direction. In every image, a few evaluation points (EPs) labelled by numbers were chosen, and temperature time series were extracted. The particular point at which modelled and observed values are compared is then referred to, for example, as 02-1_H3. In total, the observation campaign gathered time series of surface temperature for 66 ground and 73 wall EPs, representing various surface types, in order to evaluate model performance under different surface parameter settings such as different surface materials and conditions.

Temperature was measured by the FLIR SC660 (FLIR, 2008) – the same camera used in Resler et al. (2017). As in this article, the camera's thermal sensor field of view is $24^\circ \times 18^\circ$ and the spatial resolution (given as an instantaneous field of view) is 0.65 mrad. The spectral range of the camera is 7.5 to 13.0 μm , and the declared thermal sensitivity at 30 $^\circ\text{C}$ is 45 mK. The measurement accuracy for an object with a temperature between 5 and 120 $^\circ\text{C}$ given an ambient air temperature between 9 and 35 $^\circ\text{C}$ is $\pm 1^\circ\text{C}$, or $\pm 1\%$ of the reading. The camera offers a built-in emissivity-correction option, which was not used for this study. Apart from the infrared pictures, the camera allowed us to simultaneously take pictures in the visible spectrum.

Where possible, pictures were processed semi-automatically as described in Resler et al. (2017). This processing requires the presence of four well-defined points in each picture, which are used to correct for changes in camera positioning between measurements as the camera was rotated around locations. Pictures that did not allow for semi-automatic processing (mostly ground images) were handled manually, and temperatures were extracted by the FLIR Tools v5.13.18031.2002 software (<https://www.flir.eu/products/flir-tools/>, last access: 28 June 2021). Examples of semi-automatic and manually processed images are shown in Fig. S4.

Surface temperature measured by the FLIR SC660 was compared with the data from heat flux measurements at Sinkule house captured by the heat flux measuring system TRSYS01 (see Sect. 2.3.2). The results are shown in Fig. S5. The IR camera generally gives higher values than the TRSYS01 system (instantaneous measurements are compared with 10 min averages): in summer, ground floor temperatures are on average 1 $^\circ\text{C}$ higher (difference range 0.0–2.8 $^\circ\text{C}$), and first floor temperatures are on average 0.1 $^\circ\text{C}$ higher (range of differences between -2.0 and $+1.3^\circ\text{C}$); in winter, the ground floor temperatures are on average 2.1 $^\circ\text{C}$ higher (difference range 0.5–3.5 $^\circ\text{C}$), and first floor temperatures are on average 1 $^\circ\text{C}$ higher (range of differences between -0.6 and $+2.0^\circ\text{C}$).

2.3.2 Wall heat flux measurements

Heat fluxes through the building facade and windows were measured by the high-accuracy building thermal resistance measuring system TRSYS01 equipped with two HFP01 heat

flux plates and two pairs of thermocouples (TCs). The operating temperature range of the HFP01 plates and TCs is -30 to $+70^\circ\text{C}$. The declared sensitivity of temperature difference measurements between the inner and outer sides of the wall is 0.02 $^\circ\text{C}$, and the heat flux measurement resolution is 0.02 W m^{-2} . The calibration uncertainty of HFP01 plates is $\pm 3\%$ (Hukseflux, 2020). Heat fluxes were measured through the north-east-facing wall of Sinkule house and through the north-facing wall and window of the building in Zelená Street (Fig. 2). The position of the sensors on both buildings is shown in Fig. S6. Silicone glue was used to attach the sensors to the outside wall on the first floor of Sinkule house during the winter campaign. Otherwise, sensors were mounted using two-sided carpet tape.

Sinkule house was built before World War II, and its walls are made of construction blocks. The ground floor wall is 34 cm thick without insulation, and the facade is made of ceramic tiles. The wall of the first floor is 41 cm thick, including 6 cm thick polystyrene insulation on the outer side. The facade surface is scratched plaster with scratches of 1–2 mm depth (see Fig. 2).

The house in Zelená Street is a typical representative of buildings in the area, with walls that are also made of construction blocks. The wall thickness at the measurement location was approx. 30 cm with 2.5 cm lime-cement plaster on the inner and outer sides of the wall. Heat flux measurement through the window was not used in PALM validation and, therefore, is not described here.

A quality check measurement was done at the beginning of the summer campaign – sensors were placed side-by-side on the first floor of Sinkule house between 19 July, 17:40 CEST, and 20 July, 12:00 CEST. The absolute difference of the facade surface temperature was 0.0–1.5 $^\circ\text{C}$ with a median value of 0.1 $^\circ\text{C}$. The absolute difference of measured heat fluxes was 0.0–2.1 W m^{-2} with a median value of 0.6 W m^{-2} .

2.3.3 Vehicle observations

Air quality and meteorological measurements in the street canyons were obtained by two monitoring vehicles, which were shuttled periodically among the three locations marked using green squares in Fig. 1. One location was in Jugoslávských partyzánů Street (Jug. p. Street), an approx. 42 m wide boulevard with sparse trees. The two remaining locations were in the 25 m wide Terronská Street, one next to Bubeneč house and the other next to Orlík house. Near Bubeneč house, there are full-grown broadleaf trees with crowns covering the whole street. Broadleaf trees near Orlík house are smaller and their crowns cover a maximum of two-thirds of the street canyon. Buildings at all locations are approx. 25 m high. Pictures of the measurement locations are shown in Fig. S7. The observations were organized so as to provide information about air quality and meteorological conditions at the three locations and also to compare the eastern and western sides of the street canyons. Each mon-

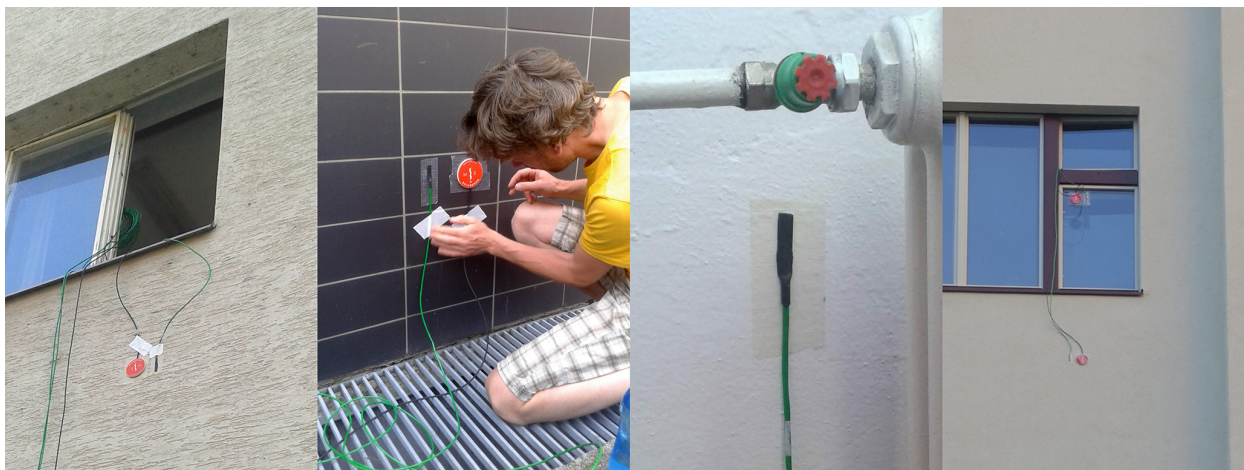


Figure 2. Details of heat flux sensor and thermocouple mounting. The left panel shows the first floor of Sinkule house, the centre-left panel shows the ground floor of Sinkule house, the centre-right panel shows the inner temperature sensor on the ground floor of Sinkule house, and the right panel shows Zelená Street. For the Sinkule house and Zelená Street locations, see Fig. 1.

itoring vehicle remained at a particular location for at least 2 whole days (see Tables S2 and S3). Based on our own traffic census from 4–6 December 2018, the total workday load on Terronská Street past Bubeneč house is 7700 vehicles, which is approximately 44 % of the traffic intensity in Jug. p. Street. The number of small trucks (60) in Terronská Street is only 20 % of that in Jug. p. Street, and the number of buses (20) is only 2 % of the number in Jug. p. Street. There was only one large truck per day noted in Terronská Street, compared with approx. 80 in Jug. p. Street. Apart from the street canyon measurements, one stationary monitoring vehicle was located in the courtyard of Sinkule house throughout the whole campaign to provide the urban background meteorological and air quality values.

The vehicles in the street canyons were equipped with analysers of NO_x , NO_2 , NO , O_3 , SO_2 , CO , PM_{10} , $\text{PM}_{2.5}$, and PM_1 measured at the top of the vehicle roof (approx. 4.6 m). Calibrations of all air quality analysers were performed during transfer between locations to eliminate loss of data during parallel measurements. Meteorological variables measured included wind speed and direction, as well as turbulent flow characteristics measured by the METEK 3D ultrasonic anemometer on a meteorological mast at a height of about 6.8 m above the ground (to fit under the tree crowns in Terronská Street next to Bubeneč house). In addition to the above-mentioned variables, air temperature, relative humidity, global radiation, and atmospheric pressure were measured at the top of the vehicle roof (approx. 4.6 m). Wind and turbulent flow characteristics measured by the METEK anemometer had a 10 min resolution, while the remaining variables were recorded at 1 min resolution. For further analysis and PALM evaluation, 10 min averages of measured variables were used. Both vehicles also had a video camera placed at the front windscreen. These recordings were then

used for detailed time disaggregation of traffic emissions at the measurement location and for calibration of an automatic counting system (see Sect. 3.4).

The vehicle in Sinkule house courtyard measured the same variables with the same time resolution except for the following differences: PM_1 , $\text{PM}_{2.5}$, and turbulence characteristics were not measured; wind speed and direction were measured by the GILL 2D WindSonic anemometer at the standard height of 10 m.

2.3.4 Mobile measurements

On selected days of the measurement campaigns, to get more detailed information on air quality in the child domain, mobile measurements using a dedicated monitoring vehicle were made (12, 18, 19 July, 26 November, and 4 December). This vehicle travelled between the locations shown in Fig. 1, stopping and measuring at each of them for 5 min. Two loops were made on every measurement day. On 19 July, only one loop among locations 3, 6, and 15–17 was made, with measurements taken over 15–20 min. The vehicle was equipped with NO_x , NO_2 , NO , O_3 , SO_2 , CO , PM_{10} , $\text{PM}_{2.5}$, and PM_1 analysers. Starting from the second measurement on 17 July, a GARNI 835 weather station was used for an indicative measurement of temperature, wind, and relative humidity. Some measurements were not available on particular days – details are given in Tables S2 and S3.

2.3.5 Higher-level observations

To get information about higher levels, the observation campaign used two other measurement platforms. The first was a stationary measurement of wind flow on the top of the highest building in the child domain (approx. 60 m high). A 2D anemometer was installed on the flat roof of the Faculty of

Civil Engineering of the Czech Technical University – (FSv; see Fig. 1). The anemometer was positioned approximately in the middle of the highest roof section, 2 m above the flat roof top. The location was the same in the summer and winter campaigns. Measurement frequency was 1 s, and 10 min averages were used for further evaluation. The second was a measurement of vertical profiles in the lowest part of the atmosphere by drone. Originally, two 1 d drone observation campaigns were scheduled. Due to administrative restrictions, the summer drone observations were not realized and the winter ones had to be moved from the centre of the child domain to the location marked in Fig. 1. Additionally, the maximum flight altitude had to be limited to 80 m above the ground. The drone was equipped with the GRIMM portable laser aerosol spectrometer and Dust Monitor Model 1.108 and a HC2A-S probe from ROTRONIC for temperature and relative humidity measurements (ROTRONIC, 2020). Unfortunately, the probe showed a longer than expected relaxation time which meant that the observation instruments were not able to stabilize quickly enough during the descent. Recalculation of particle counts to mass concentration was also burdened with large errors. The results obtained were not reliable enough to be used for PALM validation, but temperature and relative humidity profiles are provided in the Supplement (Figs. S8, S9).

2.3.6 Standard CHMI observations used for validation

Relevant standard CHMI¹ meteorological and air quality measurements were used for the evaluation of WRF (Weather Research and Forecasting) and CAMx (Comprehensive Air-quality Model with Extensions) simulations which provided initial and boundary conditions for PALM, as described in Sect. 3.3. This evaluation is presented in Sect. 4. WRF vertical profiles were evaluated against the upper air soundings from Praha-Libuš (WMO ID 11520) station located in a southern suburb of Prague, 11 km from the centre of the PALM child domain. A radiosonde is released every day at 00:00, 06:00, and 12:00 UTC. For the evaluation of global radiation, two meteorological stations were selected: (1) Praha-Libuš and (2) the Praha-Karlov (WMO ID 11519) station situated in a densely built-up area nearer the centre of Prague approximately 4 km from the PALM child domain. PM₁₀ and NO_x concentrations from the CAMx model were compared with measurements from automated air quality monitoring stations. Only the five background stations closest to the PALM child domain were used. Station locations are shown in Fig. S10. More detailed information about the stations is given in Tables S4 and S5.

Observations from the Praha-Ruzyně station (WMO ID 11518) situated at Prague airport approximately 9 km west of the centre of PALM domain were used to evaluate WRF

¹Czech Hydrometeorological Institute (<https://chmi.cz>, last access: 26 July 2021) is the official national meteorological service in the Czech Republic.

wind speed and, in conjunction with the campaign wind measurements on the FSv building roof, the modification of wind speed by the orography and buildings and how PALM captures this effect.

3 Model simulation set-up

3.1 PALM model and domains configuration

The PALM model system version 6.0 revision 4508 (Maronga et al., 2015, 2020) was utilized for this validation study. It consists of the PALM model core and components that have been specifically developed for modelling urban environments. The PALM model core solves the incompressible, filtered, Boussinesq-approximated Navier–Stokes equations for wind (u , v , w) and scalar quantities (potential temperature, water vapour mixing ratio, passive scalar) on a staggered Cartesian grid. The sub-grid-scale terms that arise from filtering are parameterized using a 1.5-order closure by Deardorff (1980) with modifications following Møeng and Wyngaard (1988) and Saiki et al. (2000). Buildings and orography are mapped onto the Cartesian grid using the mask method (Briscolini and Santangelo, 1989), where a grid cell is either 100% fluid or 100% obstacle. The advection terms are discretized by a fifth-order scheme after Wicker and Skamarock (2002). For temporal discretization, a third-order low-storage Runge–Kutta scheme (Williamson, 1980) is applied. The Poisson equation is solved by using a multi-grid scheme (Maronga et al., 2015).

The following are the urban-canopy-related PALM modules employed in this study. The land surface model (LSM, Gehrke et al., 2020) was utilized to solve the energy balance over pavements, natural surfaces, and water bodies. The building surface model (BSM, called USM in previous versions and in Resler et al., 2017) was used to solve the energy balance of building surfaces (walls and roofs). The BSM was configured to utilize an integrated support for modelling of fractional surfaces (Maronga et al., 2020). Dynamic and thermodynamic processes caused by resolved trees and shrubs were managed by the embedded plant-canopy model (PCM). Radiation interaction between resolved-scale vegetation, land surface, and building surfaces was modelled via the radiative transfer model (RTM; Krč et al., 2021). Downwelling shortwave (SW) and longwave (LW) radiation from the upper parts of the atmosphere, which were used as boundary conditions for the RTM, were explicitly prescribed from the stand-alone Weather Research and Forecasting model (WRF; see Sect. 3.3 for details) simulation output for the respective days, rather than being modelled by, for example, the Rapid Radiation Transfer Model for Global Models (RRTMG). This way, effects of mid- and high-altitude clouds on the radiation balance were considered in the simulations. It is important to note that by not using RRTMG some physical processes were missed, such as vertical diver-

gence of radiation fluxes leading to heating/cooling of the air column itself; these may become especially important at night-time. However, sensitivity tests with RRTMG applied revealed that the effect on night-time air temperature was negligible in our simulations. In addition to the meteorological quantities, the embedded online chemistry model (Khan et al., 2021) was applied to model concentrations of NO_x , PM_{10} , and $\text{PM}_{2.5}$. Chemical reactions were omitted in this case to simulate purely passive transport of the pollutants.

Both self-nesting and online nesting features of PALM were utilized. Self-nesting means that a domain with a finer resolution can be defined inside a larger domain, and this sub-domain (child domain) receives its boundary conditions from the coarse-resolution parent domain at every model time step. Here, a one-way nesting without any feedback from the child simulation on the parent simulation (Hellsten et al., 2021) was applied. The coarse-resolution parent simulation itself received its initial as well as lateral and top boundary conditions from the simulations of the WRF mesoscale model transformed to a PALM dynamic driver (see Sect. 3.3). This process is hereafter referred to as mesoscale nesting (Kadasch et al., 2020). The values of the velocity components, potential temperature, and values for the mixing ratio at the lateral and top boundary were updated at every model time step, while linear interpolation in time was used to interpolate between two WRF time steps. The WRF solution was mapped fully onto the boundaries starting at the first grid point above the surface; boundary grid points that lie below the surface were masked and were not considered further. As the mesoscale model does not resolve turbulence, turbulence was triggered at the model boundaries using an embedded synthetic turbulence generator (STG) according to Xie and Castro (2008), which imposed spatially and temporally correlated perturbations every time step onto the velocity components at the lateral boundaries. For additional details on PALM's mesoscale nesting approach, we refer to Kadasch et al., 2020.

The initial and boundary concentrations of modelled pollutants of the parent domain were taken from simulations of the CAMx model (Comprehensive Air-quality Model with Extensions; see Sect. 3.3). For more detailed information about the PALM model, embedded modules, and the PALM-4U components, see Maronga et al. (2020) and the associated papers in this special issue.

The locations of the parent and child modelling domains are shown in Fig. S1. The parent domain extends horizontally by $4\text{ km} \times 4\text{ km}$ in the x and y directions respectively, with an isotropic grid spacing of 10 m. The vertical z direction is covered by 162 layers for summer and 82 layers for winter simulations respectively. The vertical grid spacing is 10 m for the lower 250 m of the domain. Above 250 m, when the height was well above the building-affected layer, the vertical grid was successively stretched up to a maximum vertical grid spacing of 20 m in order to save computational resources. The domain top is at 2930 m for summer and 1330 m

for winter simulations respectively. This extent safely covers the convective layer with a sufficient buffer. We note that the 10 m resolution of the parent domain is sufficient to explicitly resolve the majority of the buildings and trees (see Figs. S11 and S12 in the Supplement); thus, no additional parameterization of the urban canopy is needed. The child domain extent is $1440 \times 1440 \times 242\text{ m}^3$ in the x , y , and z directions respectively, with an isotropic grid spacing of 2 m.

Parent and child domains were initialized by vertical profiles of u , v , w , potential temperature and mixing ratio, and soil moisture and soil temperature, transformed from WRF simulations (see Sect. 3.3). As the initial soil and wall temperatures from a mesoscale model are only a rough estimate due to its aggregated nature, the PALM spin-up mechanism was applied (Maronga et al., 2020). During a 2 d spin-up, the atmospheric code was switched off and only the LSM and BSM as well as the radiation and RTM model were executed. Using this method, the material temperatures were already close to their equilibrium value and significant changes in material temperatures at the beginning of the simulation were avoided.

3.2 Urban canopy properties

Data availability, their harmonization, and cost/efficiency trade-offs often need to be considered (Masson et al., 2020). For solving the energy-balance equations as well as for radiation interactions, BSM, LSM, and RTM require the use of detailed and precise input parameters describing the surface materials such as albedo, emissivity, roughness length, thermal conductivity, thermal capacity, and capacity and thermal conductivity of the skin layer. Also the plant canopy (trees and shrubs) is important, as it affects the flow dynamics, heating, and evapotranspiration as well as radiative transfer within the urban environment. Urban and land surfaces and subsurface materials become very heterogeneous in a real urban environment when going to very fine spatial resolution. Any bulk parameterization for the whole domain setting would, therefore, be inadequate. Instead, a detailed setting of these parameters was supplied wherever possible. To obtain the needed detailed data, a supplemental on-site data collection campaign was carried out and a detailed database of geospatial data was created. Land cover data are based on a combination of national (ZABAGED) and city of Prague (Prague OpenData) databases. ZABAGED geodatabase (ČÚZK, 2020) distinguishes 128 categories of well-targeted geographical objects and fields – for example, built-up areas, communications, hydrology, vegetation, and surface. The Prague OpenData geodatabase (Prague Geoportal, 2020) distinguishes many local, user-specified geographic information system (GIS) layers – for example, plans showing actual and future development, land cover for architects, and a photogrammetry-based digital elevation model (DEM). Building heights were available from the Prague 3D model, maintained by the Prague Institute of Planning and Devel-

opment. For the first tree canopy data mapping, lidar scanning was used in combination with a photogrammetric-based DEM. Derived heights were manually calibrated using data from the terrain mapping campaign and extended with additional parameters like crown height, width and shape, and trunk height and width. All descriptions of surfaces and materials and their properties were collected in GIS formats and then preprocessed into a PALM NetCDF input file corresponding to the PALM Input Data Standard (PIDS; Heldens et al., 2020). This file includes information on wall, ground, and roof materials as well as properties similar to those used to estimate surface and material properties in Resler et al. (2017) and Belda et al. (2021).

Each surface is described by material category, albedo, and emissivity. BSM surfaces additionally carry thickness and window fraction. Parameters such as thermal conductivity and capacity are assigned to categories and estimated based on surface and storage material composition. In the case of walls and roofs, which are limited to four layers in the current version of BSM, this means that the parameters of the two outer layers were assigned according to the properties of the covering material (e.g. plaster or insulation), while remaining layers were initialized by the properties of the wall material (e.g. bricks, construction blocks, concrete, insulation). Wall and roof properties are described in Table S6. For pavements and other LSM surfaces, all parameters except albedo and emissivity were assigned according to the PALM LSM categories.

Each tree in the child domain was detailed by its position, diameter, trunk parameters, and vertically stratified base leaf area density. The actual distribution of the leaf area density (LAD) within the treetop was then calculated according to the available light exposure of the particular grid box inside the treetop following the Beer–Lambert law, leading to lower LAD in the centres of large and/or dense treetops. At the moment, PALM does not consider the effect of trunks on the dynamic flow field and the thermodynamics; only LAD is considered. However, for the winter case, leafless deciduous trees were considered to be 10 % of their summer LAD to account for the effect of trunks and branches on the flow field.

3.3 Initial and boundary conditions

Initial and boundary meteorological conditions for the parent domain of the PALM simulations were obtained from the WRF model (Skamarock et al., 2008), version 4.0.3. The WRF model was run on three nested domains, with horizontal resolutions of 9, 3, and 1 km and 49 vertical levels. The child domain has 84×84 grid points in the horizontal. The choice of configuration started from the most usual settings for the given resolution and required latitude. Minor variations in parameterizations were then tested so as to provide the best possible boundary conditions to PALM for each simulation. Consequently the Noah land surface model (Chen and Dudhia, 2001) and RRTMG radiation (Iacono et

al., 2008) have been used in all simulations. Urban vs. non-urban parameterizations for PBL were tested and, as a result, the Yonsei University PBL scheme (Hong et al., 2006) was chosen for the summer episodes, whereas the Boulac urban PBL (Bougeault and Lacarrère, 1989) gave a better agreement with observations for the winter episodes. With this exception, no other urban parameterizations have been used in the WRF model. MODIS land use categories have not been altered. WRF was initialized from the Global Forecast System (GFS) operational analyses and forecasts, and output data from overlapping WRF 12 h runs was collected. The first 6 h of each run served as a spin-up. The boundary conditions for the mesoscale nesting were then generated from forecast horizons 7–12.

Air quality simulations that served as chemical initial and boundary conditions were made using the chemistry transport model (CTM) CAMx version 6.50 (ENVIRON, 2018). CAMx is an Eulerian photochemical CTM that contains multiple gas-phase chemistry options (CB5, CB6, SAPRC07TC). Here, the CB5 scheme (Yarwood et al., 2005) was invoked. Particle matter was treated using a static two-mode approach. Dry deposition was calculated following Zhang et al. (2003), and the Seinfeld and Pandis (1998) method was used for wet deposition. To calculate the composition and phase state of the ammonia–sulfate–nitrate–chloride–sodium–water inorganic aerosol system in equilibrium with gas-phase precursors, the ISORROPIA thermodynamic equilibrium model was used (Nenes et al., 1998). Finally, secondary organic aerosol (SOA) chemistry was solved using the secondary organic aerosol partitioning (SOAP) semi-volatile equilibrium scheme (Strader et al., 1999).

CAMx was coupled offline to WRF, meaning that CAMx ran on WRF meteorological outputs. WRF outputs were translated to CAMx input fields using the WRFCAMx pre-processor provided along with the CAMx source code (see <https://www.camx.com/download/support-software>, last access: 28 June 2021). For those CAMx input variables that were not available directly in WRF output, diagnostic methods were applied. One of the most important inputs for CAMx, which drives the vertical transport of pollutants, is the coefficient of vertical turbulent diffusion (Kv). Kv is a significant parameter that determines the city-scale air pollution, and it is substantially perturbed by the urban canopy effects (Huszar et al., 2018a, b, 2020a, b). Here, the “CMAQ” scheme (Byun, 1999) was applied for Kv calculations.

WRF and CAMx outputs were then post-processed into the PALM dynamic and chemistry driver. The data were transformed between coordinate systems and a horizontal and vertical interpolation was applied. As the coarse-resolution model terrain would not match the PALM model terrain exactly, the vertical interpolation method included terrain matching, and the atmospheric column above the terrain was gradually stretched following the WRF hybrid vertical levels as they were converted to the fixed vertical coordinates of the PALM model. The interpolated airflow was adjusted to

enforce mass conservation. A detailed technical description of the 3D data conversion procedure is given in the Supplement in Sect. S6. The Python code used for processing the WRF and CAMx data into the PALM dynamic driver file has been included in the official PALM distribution and published in the PALM SVN repository since revision 4766 in the directory trunk/UTIL/WRF_interface.

Emission data for Prague used in the CAMx model were as described in the following section. Other emission inputs are described in detail in Ďoubalová et al. (2020).

3.4 Emission data

Air pollution sources for our particular case are dominated by the local road traffic. Annual emissions totals were based on the traffic census 2016 conducted by the Technical Administration of Roads of the City of Prague – Department of Transportation Engineering (TSK-ÚDI). The emissions themselves were prepared by ATEM (Studio of ecological models; <http://www.atem.cz>, last access: 28 June 2021) using the road transport emission model MEFA 13. Jugoslávských partyzánů and Terronská streets, where air quality was measured during the campaigns, were both covered by this census. Emissions from streets not included in the census were available on a grid with a 500 m spatial resolution. These emissions were distributed between the streets not covered by the census according to their parameters. Particulate matter (PM) emissions included resuspension of dust from the road surface (Fig. 3). Time disaggregation was calculated using a Prague transportation yearbook (TSK-ÚDI, 2018), public bus timetables, and our own census conducted over a short time period (19–21 July and 4–6 December; days on which traffic intensities were derived from camera records). This time disaggregation was the same for the primary emissions (e.g. exhaust, brake wear) as well as for resuspended dust. Higher dust resuspension caused by sprinkle material during winter time was not considered.

Traffic data were supplemented by emissions from stationary sources from the Czech national inventory REZZO. Point sources correspond to the year 2017, the latest year available at the time of model input preparation. Residential heating was based on a 2017 inventory and rescaled to 2018 by multiplying by the ratio of degree days $DD(2018)/DD(2017)$; DD is the sum of the differences between the reference indoor temperature and the average daily outdoor temperature on heating days. Residential heating emissions were available on elemental dwelling units – urban areas with average area 0.5 km^2 – and were spatially distributed to building addresses, where local heating sources are registered, in proportion to the number of flats. Time disaggregation of point source emissions was based on monthly, day-of-week, and hour-of-day factors (Bultjes et al., 2003; available also in Denier van der Gon et al., 2011). Residential heating emissions were allocated to days according to the standardized load profile of natural gas supply for the households, which

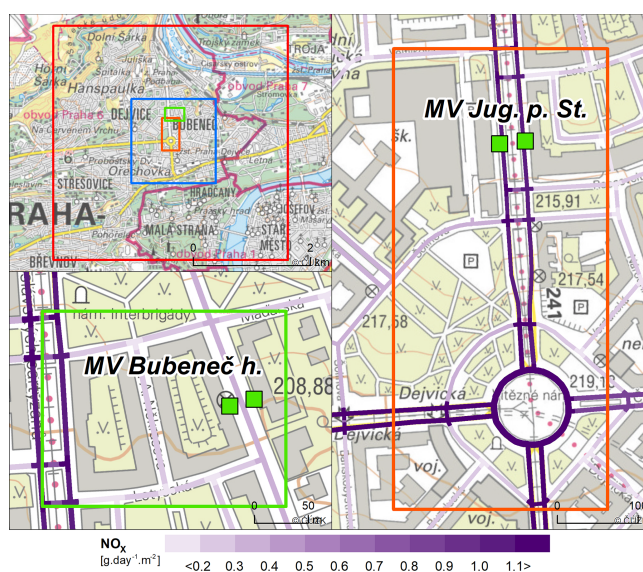


Figure 3. Nitrogen oxides (NO_x) emitted by cars along their trajectories in selected locations in Dejvice, Prague. Emissions were summarized in grams per day per square metre ($\text{g d}^{-1} \text{m}^{-2}$) and disaggregated to 1 h time steps. The red and blue squares in the top left map indicate the extent of the parent and child PALM domains respectively. The orange and green rectangles show the locations of the expanded views given in the right and lower left panels. The expanded views show the air quality measurement locations (MV) in Terronská Street – Bubeneč house (lower left) and Jugoslávských partyzánů Street (right) using green squares. The base map of the Czech Republic at 1 : 10 000 for the city of Prague was provided by the Czech Office for Surveying, Mapping and Cadastre (ČÚZK, 2020).

use it for heating only (Novák et al., 2019; OTE, 2020). Daily variation of residential heating emissions was taken from Bultjes et al. (2003).

All of these input emission data were processed into PALM input NetCDF files corresponding to the PALM Input Data Standard (PIDS).

3.5 Observation operator

To compare modelled and observed values, an observation operator that links model variables to observed quantities is needed. For vehicle measurements, the situation was straightforward: horizontally, we used atmospheric quantities and chemical compounds at the grid cell closest to the real placement of the sensors, whereas vertically, we performed linear interpolation to the real height of the sensor. This approach was sufficient given the fine 2 m resolution within the child domain. For surface observations at grid-aligned surfaces (wall sections without significant influence of step-like structures), the modelled values at the nearest grid face according to the actual placement of the sensor or EP were also taken. However, at non-grid-aligned walls (i.e. walls that are oriented in one of the south-west, south-east, north-west, and

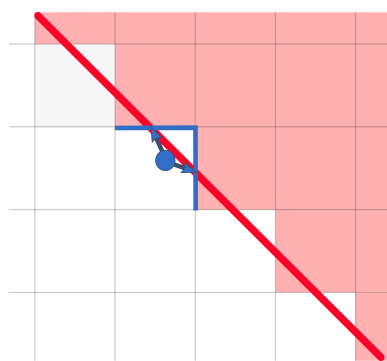


Figure 4. Sketch to illustrate the mapping of a wall surface observation point to a gridded step-wise approximation of the wall. The red line represents the real wall surface, light grey lines delineate the grid cells, the light red area shows the footprint of the gridded building, the blue circle shows the surface evaluation point, and the blue arrows represent the assignment of this point to the grid faces (blue lines) used for the calculation of the corresponding modelled values.

north-east directions), walls are approximated by step-like structures, and choosing the nearest grid face is no longer unique, as illustrated in Fig. 4. In these cases, the orientation of the real wall cannot be sufficiently represented by one grid face but is approximated by grid faces with perpendicular orientation. For this reason, we virtually sampled surface quantities at the two perpendicular surfaces and calculated the modelling counterpart of the observation as the average of these values. In the graphs of the surface temperature, the sampled values are plotted by thin dashed lines in addition to their average representing the modelled value which is shown by thick solid lines. Implications of this for the model evaluation as well as for the comparability of the model to the observations are discussed in Sect. 5.1.7, along with the grid discretization.

4 Evaluation of model simulation set-up

To ensure the correct model couple set-up and correspondence to general meteorological conditions, basic characteristics are evaluated in this section. This includes the evaluation of the driving synoptic-scale simulations of the WRF and CAMx models, the vertical representation of the boundary layer in PALM, and the spatial development of the turbulent flow characteristics from the boundaries of the PALM parent and child domains. Special focus is put on the summer e2 and winter e3 episodes, in which IR camera observations took place. A description of the statistical methods used is given in the Appendix A.

4.1 Meteorology

4.1.1 Evaluation of the driving synoptic-scale simulation

As the boundary conditions for the PALM simulations come from a model simulation as well, we need to check for potential misrepresentation of the real atmospheric conditions. First, we assess the overall performance of the WRF model simulation on the synoptic scale by comparing the results with the known state of the atmosphere, represented here by the ERA-Interim reanalysis and atmospheric soundings obtained by the CHMI radiosondes (downloaded from the University of Wyoming database; <http://weather.uwyo.edu/upperair/sounding.html>, last access: 28 June 2021). Figures S13 and S14 show maps of geopotential height at 500 and 850 hPa comparing the results of the WRF simulation (9 km domain) with the ERA-Interim reanalysis. Generally, the WRF simulations, driven by the Global Forecast System (GFS), correspond well to the ERA-Interim reanalysis in terms of the 500 hPa geopotential height field, with some shifts of the pressure field eastward on 19 July and northward on 21 July. Geopotential height at 850 hPa is also very well represented with some added detail, mainly during the day in the summer due to a better resolved topography in the higher-resolution regional model simulation.

Additionally, we compared the WRF results with atmospheric soundings for the station closest to our domain of interest, Praha-Libuš, which is about 11 km south-southeast of the modelled area. Figures 5 and 6 show observed and modelled profiles of the potential temperature and wind speed at the sounding location for 20–21 July (summer e2 episode) and 4–5 December (winter e3 episode) respectively. Graphs for other episodes are provided in the Supplement (Figs. S15, S16, and S17). The radiosonde measurements are taken three times per day at 00:00, 06:00, and 12:00 UTC. The modelled values are inferred from the 1 km resolution WRF model. In order to estimate spatial variability and, consequently, the utility of the sounding for validation of the WRF profiles within the PALM domain, WRF profiles for the centre of the PALM domain are also shown. Modelled profiles from the PALM parent domain simulation are also included in these graphs; these are discussed in Sect. 4.1.2 below.

WRF profiles of potential temperature generally correspond well with the observations with some notable exceptions near the surface, where WRF tends to underestimate night-time stability and shows less marked near-surface instability during daytime in the summer case. However, here we emphasize that the near-surface profiles might also be affected by the fact that the relevant WRF model surface is not necessarily representative of local detail. The WRF wind-speed profiles also mainly reflect the conditions as observed, with a well-modelled night-time low-level jet (e.g. 21 July at 00:00 UTC, 5 December at 06:00 UTC). However, compared with potential temperature, modelled wind speed exhibits

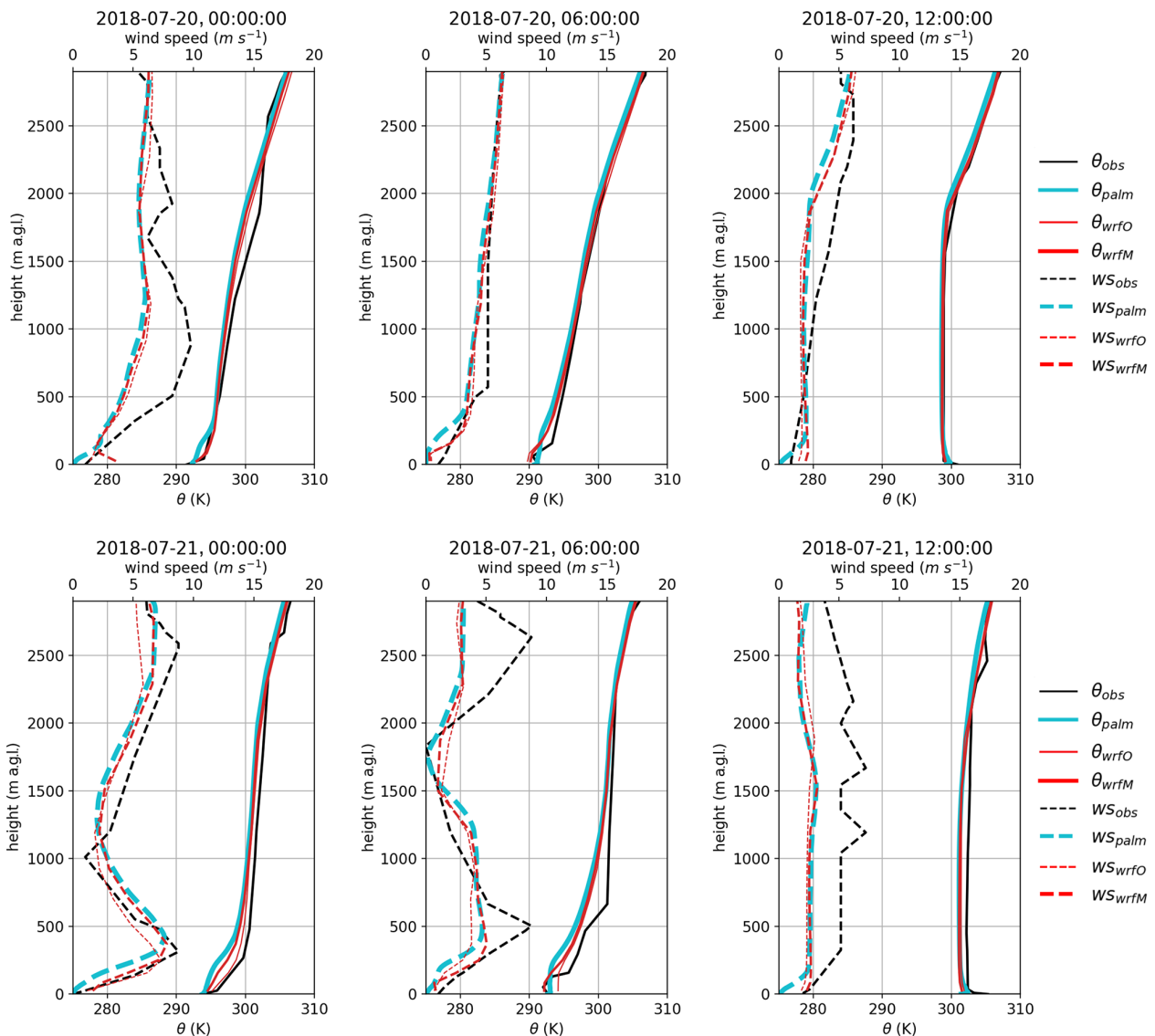


Figure 5. Vertical profiles of potential temperature and wind speed from the radiosonde observations at Praha-Libuš station for 20–21 July, with corresponding WRF (1 km horizontal resolution) and PALM (average from parent 10 m resolution domain) profiles. The potential temperature is represented by the solid lines, and the wind speed is denoted by the dashed lines. The black line is the sounding observation, the cyan line is the PALM model, and the red line is the WRF model. The thick red line is the WRF model in the centre of the PALM domain.

larger discrepancies to observations at various times (e.g. 20 July at 00:00 and 21 July at 12:00) and also tends to be higher, especially near the surface in the winter scenario. As discussed in the preceding paragraph, the radiosonde location is not within the PALM model domain. However, WRF profiles at the radiosonde location and the PALM domain centre show only marginal differences. Hence, we are confident that the modelled boundary layer profiles from WRF, which are used as boundary conditions for PALM, are a sufficiently good representation of reality for this study.

Another factor needing consideration is that the boundary layer depth during the daytime in the summer cases is

within the range of the 1 km horizontal grid resolution in the WRF simulations. Ching et al. (2014) and Zhou et al. (2014) showed that resolved-scale convection can develop in such situations, altering the boundary layer representation and leading to an overly large vertical energy transport. For an LES nested into a mesoscale WRF simulation, Mazzaro et al. (2017) showed that such under-resolved convection may propagate into the LES domain, biasing the location of the updraughts and downdraughts. In order not to bias our simulation results by under-resolved convection in WRF propagating into the LES, we checked the WRF simulation output

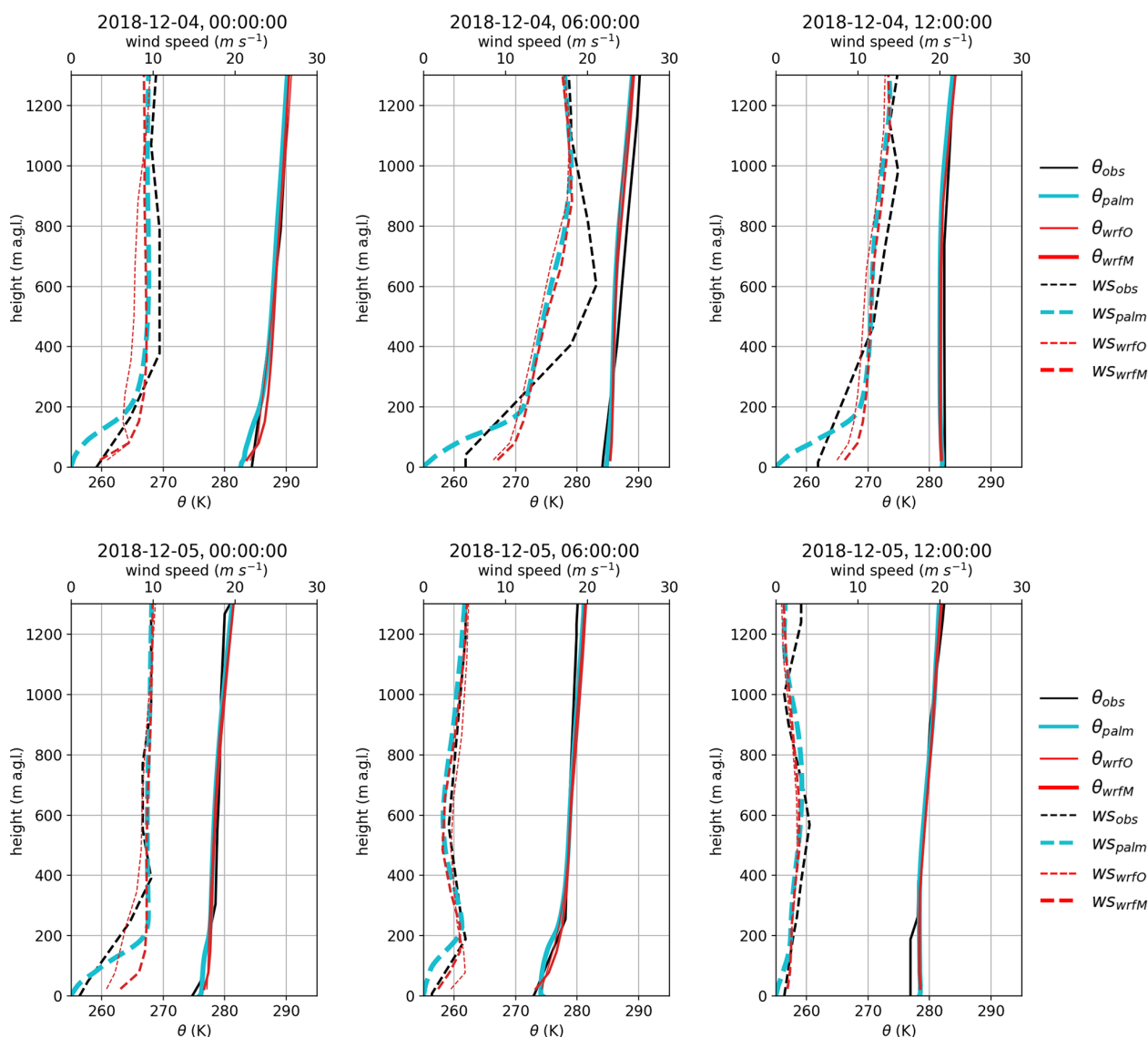


Figure 6. Vertical profile of potential temperature and wind speed from the radiosonde observations at Praha-Libuš station, with corresponding WRF (1 km horizontal resolution) and PALM (average from parent 10 m resolution domain) profiles for 4–5 December. The potential temperature is represented by the solid lines, and the wind speed is denoted by the dashed lines. The black line is the sounding observation, the cyan line is the PALM model, and the red line is the WRF model. The thin red line is the WRF model at the sounding location, and the thick red line is the WRF model in the centre of the PALM domain.

for the occurrence of under-resolved convection but did not find any (not shown).

In the PALM simulations, we prescribed the incoming LW and SW radiation obtained from the WRF simulations. To check for potential errors in incoming radiation, we compare downwelling SW radiation as simulated by WRF in the grid box covering the centre of the PALM child domain with observations at two CHMI stations in Prague with continuous downward SW radiation measurements: Praha-Karlov, approx. 4 km southeast from the modelled area, and Praha-Libuš, 11 km south-southeast (Fig. 7). WRF simulations show good agreement with observations in the sum-

mer campaign, with some overestimation of the SW radiation on 14 and 23 July at noon which we attribute to the underestimation of cloud cover in the WRF simulation. During the winter campaign, the downwelling SW radiation in WRF agrees with the observation on 26, 28, and 29 November, and on 5 December, whereas WRF significantly overestimates the SW radiation on other days due to underestimated cloud cover.

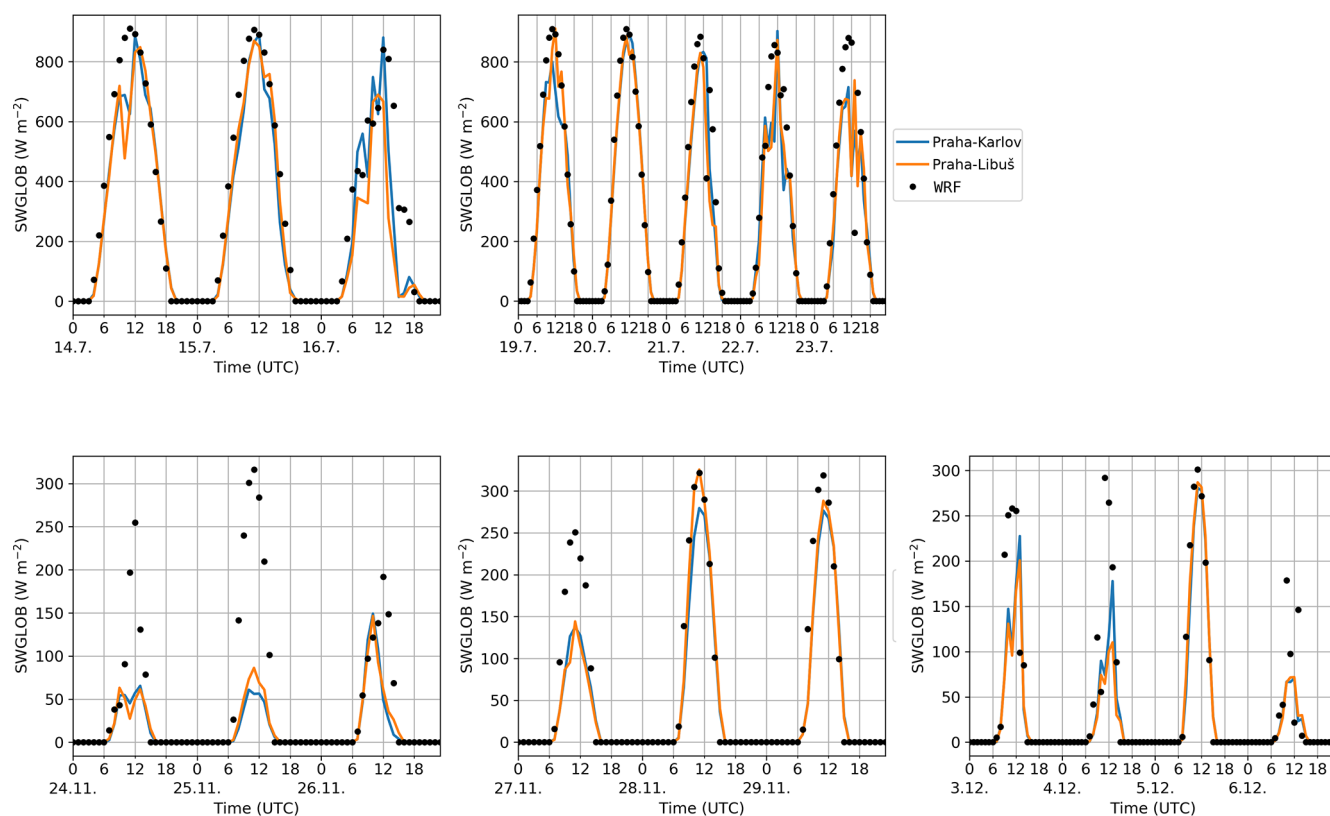


Figure 7. WRF modelled and observed downwelling SW radiation for the summer e1 and e2 (top row) and winter e1, e2, and e3 (bottom row) modelling episodes: CHMI station Praha-Karlov (blue line); CHMI station Praha-Libuš (orange line); WRF simulation (black dots).

4.1.2 Boundary layer representation in PALM

In order to check whether the observed boundary layer structure is represented realistically by the LES simulation, we compare domain-average model results from the parent domain against radio soundings from the Praha-Libuš station located roughly 11 km south-southeast of our area of interest. Praha-Libuš is in an area with slightly different topography and urban topology, located at the southern edge of the city, which means that comparison with the model simulation cannot be exact and, especially within the lower parts of the boundary layer, modelled and observed profiles cannot be expected to match. To estimate the spatial variability in the atmosphere between these two locations and, thus, assess whether the soundings can be reliably used for evaluation of the PALM profiles, the WRF modelled profiles for both locations, the sounding location and the PALM area, are provided.

Figure 5 shows vertical profiles of potential temperature and wind speed from PALM together with the soundings for the 20–21 July (summer e2 episode). Taking the limitations of this comparison into account, the model simulations show good agreement with observations with respect to temperature, capturing the overall shape of the profile with a slight tendency to underestimate actual values. However,

in the lower layers, the model tends to underestimate the diurnal variations, showing lower stability during the night and lower instability during the day. The wind speed generally follows the driving WRF profile except near the surface, where the wind speed tends to exhibit lower values due to increased surface friction from the explicit representation of microscale terrain features, buildings, and tall vegetation. During the first night (Fig. 5), the modelled and observed temperature profiles agree well. The modelled wind speed in the residual layer is generally lower than the radiosonde. On the following day, the modelled and observed potential temperature profiles agree very well, both indicating a vertically well-mixed boundary layer. During the second night, the modelled profile indicates a cooler boundary layer that is less stable near the surface. On 21 July at 00:00, the wind speed profile agrees well with the measurements. However, at 06:00, the low-level jet is still present in the observations but missing in the simulation. On the following day, the modelled and the observed temperature profiles again agree, although the modelled boundary layer tends to be about 1 K cooler. The wind weakens during the day and is lower than the observations throughout the entire depth of the model domain.

Figure 6 shows the modelled and observed profiles of potential temperature and wind speed for 4–5 December (win-

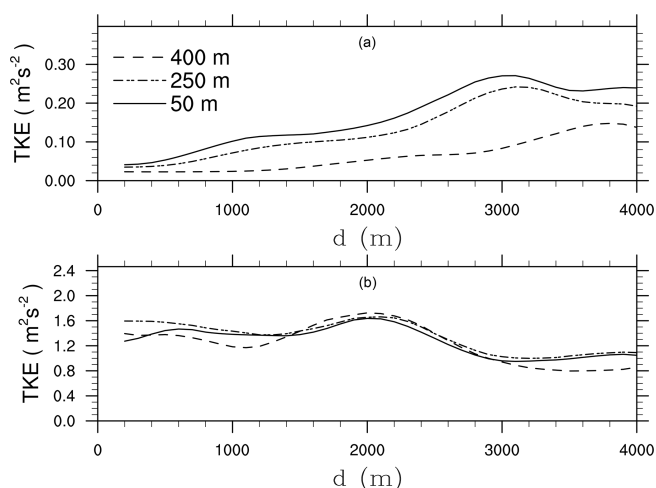


Figure 8. Horizontal profiles of 30 min time-averaged resolved-scale turbulent kinetic energy (TKE) in the parent domain plotted against distance from the inflow boundary (d) for (a) the winter case at 14:00 UTC on 5 December and (b) the summer case at 13:00 UTC on 20 July. The TKE is shown for heights at 50, 250, and 400 m above the terrain surface.

ter e3 episode). During the first night, the temperature profile suggests a more pronounced stable boundary layer. On the following day, the modelled temperature profile agrees fairly well with the observed profile. On the second night and during the second day, the temperature profiles agree reasonably well, even though the modelled profile indicates a slightly warmer near-surface layer of about 1 K. Considering the entire period, wind speed mostly matches the WRF-modelled profiles above 200 m but with some notable discrepancies compared with observations. Near the surface, PALM shows lower wind speeds compared with both the observations and WRF. At this point, however, we would like to emphasize again that a direct comparison between the PALM-modelled profiles and the observations should be made with care, especially within the near-surface layer where the profiles can be significantly affected by the different local surroundings.

4.1.3 Spatial development of the urban boundary layer

As described in Sect. 3.1, the parent domain receives boundary conditions from WRF where turbulent structures are not explicitly resolved. To trigger the spatial development of turbulence in the LES, synthetic turbulence is imposed at the lateral boundaries (Kadasch et al., 2020). However, even though this accelerates the development of turbulence in the LES, it still requires sufficiently large fetch distances for the turbulence to be spatially fully developed. Lee et al. (2018) pointed out that an insufficiently developed turbulent flow can bias results in urban boundary layer simulations. Hence, in order to assess how the turbulent flow develops within the model domain, Fig. 8 shows horizontal profiles of the turbulent kinetic energy (TKE) in the parent domain as the

distance from the inflow boundary increases. The TKE was computed as $\text{TKE} = 0.5 \cdot \sum \overline{u'_i u'_i}$, with $\overline{u'_i u'_i} = \overline{u_i u_i} - \overline{u_i} \overline{u_i}$; the overbar denotes a 30 min temporal average. For each grid point, we determined the distance to the inflow boundary for a given wind direction. In doing this, we calculated backward trajectories from the mean wind direction and determined the distance between the sampling location and the intersection point of the backward trajectory with the closest inflow boundary. Further, variances were averaged over similar distances to the inflow boundary; we then sorted similar distances into equally sized bins of 100 m to obtain a sufficiently large sample size for each discrete distance. Furthermore, we note that the TKE is evaluated at relative heights above the surface. In the winter case, which is characterized by neutrally stratified conditions at the given time point (see Fig. 6), the TKE increases with increasing distances from the inflow boundary at all illustrated heights and peaks at about $d = 3000$ m in the surface layer, while the peak position at larger heights is shifted towards larger distances. In the summer case, which is characterized by convective conditions at the given time point, the TKE is approximately constant up to 2 km from the inflow boundary and then slightly decreases with further increasing distances. However, the heterogeneous orography and nature of the buildings means that local effects will also play a role, so we would not expect to obtain a constant equilibrium TKE value. Considering that the child domain inflow boundary is placed at about 2 km from the parent inflow boundary in both cases, turbulence has already been developed at the child domain boundary, so we are confident that the error due to the overly short adjustment fetch length is minor, although we emphasize that – especially for the winter case – larger horizontal extents of the parent domain are also desirable in order to better represent mixing processes in the upper parts of the boundary layer. Moreover, the turbulent flow depends on the upstream surface conditions (e.g. terrain, buildings, and land use) which, in turn, depend on the wind direction. With insufficiently large model domains such effects might not be well represented. However, as our validation study mainly focuses on the building layer where turbulence is produced by building-induced shear, we believe that the error induced by not completely representative upstream conditions is small and does not significantly affect our validation results.

Beside the transition of the turbulent flow in the parent domain, the flow also undergoes a transition after entering the child domain with its finer grid resolution, as discussed in detail in Hellsten et al. (2021). In order to evaluate whether turbulence has been sufficiently adapted within the child domain at locations where simulation results are compared against observations, Fig. 9 shows frequency spectra of the TKE at different distances to the inflow boundary. We sampled time series of the velocity components at different positions over 1 h and calculated the spectra for each sampling location; afterwards, we averaged over all spectra with similar distance to the inflow boundary. In the winter case, the

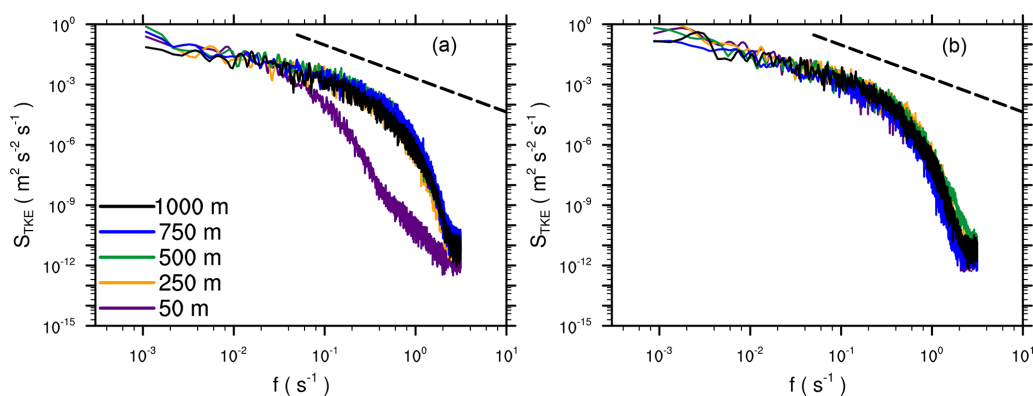


Figure 9. Frequency spectra of the TKE within the child domain at $z = 50$ m above the surface evaluated at locations with different distances downstream of the inflow boundary for (a) the winter case at 14:00 UTC on 5 December and (b) the summer case at 13:00 UTC on 20 July. The black dashed line indicates Kolmogorov's $-5/3$ scaling for reference.

spectra close to the inflow boundary show a significant drop-off of energy at smaller frequencies compared with spectra at distances ≥ 250 m, indicating that especially the smaller scales are still not sufficiently resolved on the numerical grid, whereas at larger distances, no dependence on the sampling location can be observed. In the summer case, the flow transition from the coarse into the fine grid is even faster; even spectra close to the inflow boundary indicate similar turbulence properties compared with the locations farther downstream. This is also in agreement with the findings presented in Hellsten et al. (2021) that the transition is small under convective conditions compared with neutrally stratified or stable conditions, as TKE is mainly produced locally by buoyancy rather than by shear.

4.2 Air quality

For the CAMx model evaluation, urban background air quality monitoring stations closest to the PALM parent domain were used (see Sect. 2.3.6). Validation was performed for hourly average concentrations of NO_x and PM_{10} . Evaluation was done for all PALM simulation episodes which were then grouped as summer and winter. Metrics according to Britter and Schatzmann (2007) and Chang and Hanna (2004) for both campaigns are summarized in Table 1. For graphs of diurnal variation plotted using the “openair” package (Carslaw and Ropkins, 2012), see Fig. S18.

For NO_x , the metrics show a significant underprediction of the measured concentrations (fractional bias, FB, of approx. -0.8) for the both summer and winter episodes. Nevertheless, the diurnal variation is captured quite well, although in winter modelled peaks in the evening are larger than in the morning, whereas the reverse is seen in the observed data.

Summer PM_{10} concentrations are less underestimated with an FB of approx. -0.5 , and morning and evening peaks are sharper and appear about 1 h earlier than in observations. Winter PM_{10} values are even slightly overestimated, but the

Table 1. Evaluation of CAMx 1 h concentrations against urban background stations for the summer and winter episodes.

	NO_x		PM_{10}	
	Summer	Winter	Summer	Winter
N	684	816	907	1078
mean obs. ($\mu\text{g m}^{-3}$)	22.6	59.5	22.1	30.4
mean mod. ($\mu\text{g m}^{-3}$)	10.1	24.4	13.4	33.3
FB	-0.76	-0.84	-0.49	0.09
NMSE	1.51	2.15	0.65	0.53
FAC2	0.38	0.31	0.50	0.69
R	0.54	0.28	0.34	0.13

N denotes ensemble size; mean obs. denotes the observed mean value; mean mod. denotes the modelled mean value; FB denotes the fractional bias; NMSE denotes the normalized mean square error; R denotes the Pearson correlation coefficient.

CAMx model is not able to represent their real diurnal variation. Modelled diurnal variation is very similar to that for NO_x , which indicates that it is dominated by diurnal variation of traffic, whereas in reality, different sources play a important role as well.

5 Results

5.1 Surface temperature

In the following section, we will discuss the model performance with respect to the surface temperature. First, we will show general surface temperature results and show an example of direct comparison against observed values. We will then draw a broader picture of model performance for different types of surfaces, supported by relevant statistical measures. Subsequently, particular cases at individual locations will be presented, and the related shortcomings of the model and the observations, as well as the implications of the shortcomings of the fine-scale input data, will be discussed.

5.1.1 Overall performance

Figure 10 shows an example of a 3D view of instantaneous surface temperature in the child domain at 13:00 UTC on 20 July. The heterogeneous distribution of surface temperature reflects the distribution of pavement and green areas, with higher temperatures over paved areas and at building walls and roofs. Below the trees, where most of the SW direct radiation is absorbed within tree crowns, surface temperatures of about 290 K are modelled (e.g. on the right side of the figure or within courtyards), while higher surface temperatures up to 330 K are modelled at intensively irradiated vertical building walls. Moreover, the effect of different wall and roof material parameters on surface temperature can be identified, with roofs showing lower surface temperatures where green fractions are present, while some other walls and roofs show values up to 320 K. In order to evaluate the modelled surface temperature more quantitatively, we compare the modelled surface temperature against observed values in the following parts of this section.

Figure 11 shows an example of the observed and modelled diurnal cycle of surface temperature profiles at one particular evaluation location, 11-1, along with a street view of the location area and the RGB and IR views of the location with the EPs labelled. Location 11-1 is situated on Evropská Street, a west–east-oriented boulevard between 40 and 50 m in width (building to building), with EPs placed on the concrete tramway belt, pavement, and on the nearly south-oriented wall of two traditional five-floor brick buildings, the left of which has an additional thermal insulation layer. For the summer scenario, the modelled surface temperature agrees fairly well at the horizontal and vertical locations with respect to the diurnal amplitude and temporal evolution. However, at the horizontal surfaces, the modelled night-time surface temperatures are underestimated by about 3–4 K. When the sun comes up the next day, the modelled surface temperature again matches the observed surface temperature; thus, the night-time bias in surface temperature does not propagate into the next day simulation. In the winter case, the modelled surface temperatures also agree with the observations, except for the nights where the modelled surface temperatures are about 1–2 K higher than the observed ones at both horizontal and vertical surfaces. Further, two sharp peaks in the modelled daytime surface temperatures during the morning hours as well as during the early afternoon hours are striking and are not present in the observations. Similar peaks can also be observed at some other locations, mainly during the winter episode. For a detailed discussion concerning these peaks, we refer to Sect. 5.1.5 where this effect and its causes are analysed.

A complete set of modelled and observed diurnal cycles of surface temperature for all EPs in all observation locations (see Fig. 1 in Sect. 2.1) for the summer e2 episode (19–21 July 2018) and for the winter e3 episode (4–6 December 2018) is given in the Supplement in Sect. S3. As sup-

porting information, the graphs of the modelled values of the surface sensible heat flux, ground heat flux, net radiation, and incoming and outgoing SW and LW radiation are also available in the Supplement in Sect. S4.

The observations cover a wide range of surface types. As we cannot show daily cycles for all observation points, we condensed the results to show the general performance of the ground and wall modelling capability of PALM. To distinguish model behaviour for different types of surfaces, the EPs were put into the following categories: pavements (paved areas without traffic), streets (paved areas with traffic), grass, wall of traditional building, wall of contemporary office building, wall of building with glass or glass-like surface, and plant-canopy-affected surface. The complete assignment of the EPs to the particular categories is given in table Table S7. Figure 12 shows scatter plots of the modelled and observed surface temperature for particular surface types during the summer e2 episode. The best agreement can be observed for street and pavement surfaces, and traditional building walls. At lower temperatures (which corresponds to night-time values), the scatter is generally lower compared with higher surfaces temperatures, where, especially at the buildings, a wide scatter can be observed. To support this qualitative impression from the scatter plots, Table 2 provides statistical error measures. Modelled surface temperatures at pavements and streets are slightly too cool, especially at night-time, as indicated by the negative bias. Further, the root mean square error (RMSE) indicates higher uncertainty at daytime and lower uncertainty at night-time, especially at building walls. The main reason for this behaviour is probably the typically lower thermal conductivity in comparison with ground surfaces, which causes more rapid reactions of the surface temperature to the changes in radiative forcing. This effect, in connection with binary changes in direct radiation during the course of the day due to shading effects, along with possible geometrical imperfections in the discretized terrain and building model, can cause temporally and spatially limited strong discrepancies between modelled and observed point values. This issue is analysed in more detail using location 11-1_V as an example (see Sect. 5.1.5). Mismatch of shading can also be caused by the imprecise description of the shapes of the tree crowns (see Sect. 5.1.6). Modelled surface temperatures at grass-like surfaces also show good agreement with the observations, with mostly low scatter both during the day and at night, but with slightly overestimated night-time values. A wider scatter, even at lower temperatures, can be observed for both glass-like surfaces and contemporary buildings walls, with the largest RMSE in the daytime. The reason for this higher spread is probably a more complex wall structure and the higher uncertainty in its identification (see Sect. 5.1.3). In the case of glass-like surfaces, these causes are accompanied by the fact that the IR camera photos of such locations contain a substantial amount of reflection from other surfaces (opposite buildings, sky) and, therefore, do not provide an

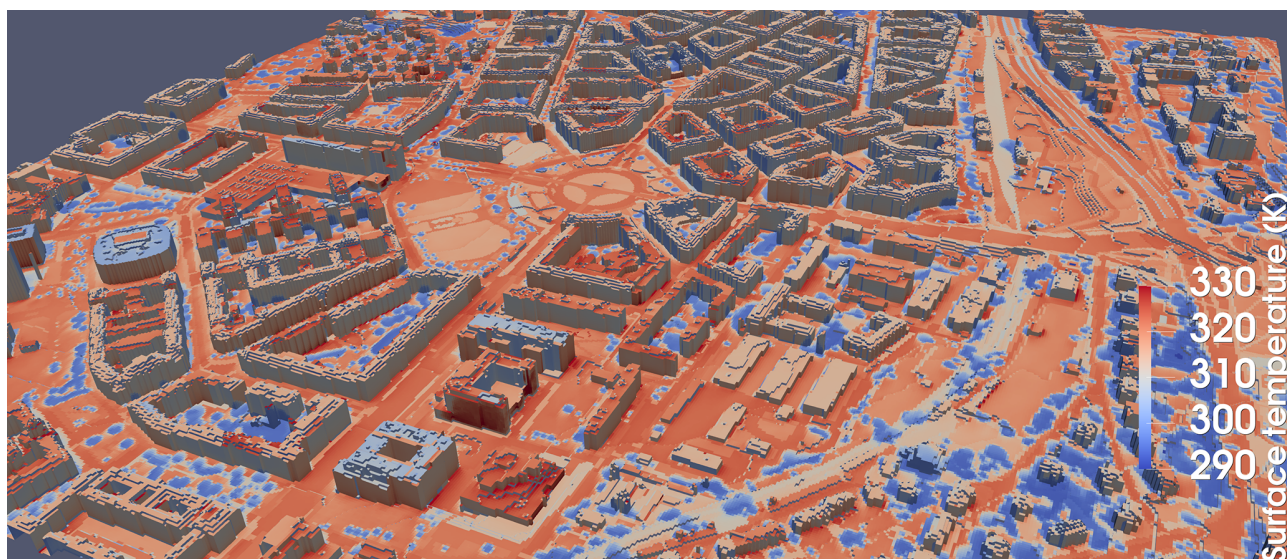


Figure 10. Example 3D view of the child modelling domain at 2 m resolution from the south-west direction on 20 July at 13:00 UTC (14:00 CET). The colour scale represents the modelled surface temperature.

adequate measure of the surface temperature. These effects are discussed in detail in Sect. 5.1.4.

Similarly, Fig. 13 shows scatter plots for the winter e3 episode. Again, the scatter is relatively low at streets, pavements, grass-like, and traditional wall surfaces, although it does not show a large difference between daytime and nighttime (see also RMSE in Table 2), in contrast to the summer case. In general, it is striking that modelled surface temperatures are slightly overestimated in the winter case, as indicated by the positive bias values. This is especially true for glass-like materials which show modelled surface temperatures that are far too high as well as a large scatter. However, the problems of surface temperature measurements of glass-like surfaces by IR cameras due to direct reflection from other surfaces, which is mentioned above and discussed in detail in Sect. 5.1.4, applies here. Grass surfaces' modelled temperatures are also overestimated. This overestimation can be seen in many individual locations (see Supplement Sect. S3). The reason for this overestimation of surface temperatures, which is more pronounced in wintertime (compare Fig. 12) than in summertime, however, remains unknown at this point. There is further discussion of modelling grass surfaces in summertime and the necessary prerequisites below (Sect. 5.1.2).

5.1.2 Grass surfaces

The energy balance of a grass-covered area may strongly depend on soil water content, assumed plant cover, leaf area index (LAI), and other factors (Gehrke et al., 2020), and these are mostly unknown in this study. Let us examine three grass-covered points, evaluation point 3 (EP 3) at location 05-1_H, EP 2 at location 06-3_H, and EP 1 at location 10-3_H dur-

ing the second day of the summer e2 episode, 20 July 2018 (see Fig. 14 and Sect. S3 of the Supplement for detailed information on these particular locations). These points are not significantly influenced by any adjacent tree or wall; thus, they are not affected by possible imperfection of the radiative transfer in the model. These points represent examples of three different grass-type surfaces. The first point is placed in a recently built park with an integrated irrigation system; the second one is located on a green tram line with a shallow soil layer and without irrigation; and the third point is located on quite a large lawn in an open square area with a deep soil layer without irrigation, thereby resembling natural grass conditions. To account for local differences in soil conditions for summer simulations, the grass areas within the model domain were split into three categories: natural-like grass, watered grass, and an urban grass type, and the original WRF soil moisture was roughly adjusted by factors of 1.0, 2.0, and 0.5 respectively. As we have no information about soil moisture at that level of detail, the chosen adjustment factors are a best guess based on a survey of the locations and personal experience. The soil moisture for winter simulations was not adjusted. The diurnal cycle of the modelled and observed surface temperature for the different grass surfaces agrees fairly well with maximum temperatures of 35, 52, and 45 °C respectively. Figure 14 also shows diurnal cycles of surface temperature at these points from a test simulation where the soil moisture of grass surfaces was uniformly prescribed from the WRF simulation. With non-adjusted soil moisture, the daytime surface temperature for urban grass (location 06-3, EP 2) and watered grass (location 05-1, EP 3) is under- and overestimated compared with observations respectively, although it agrees fairly well for the

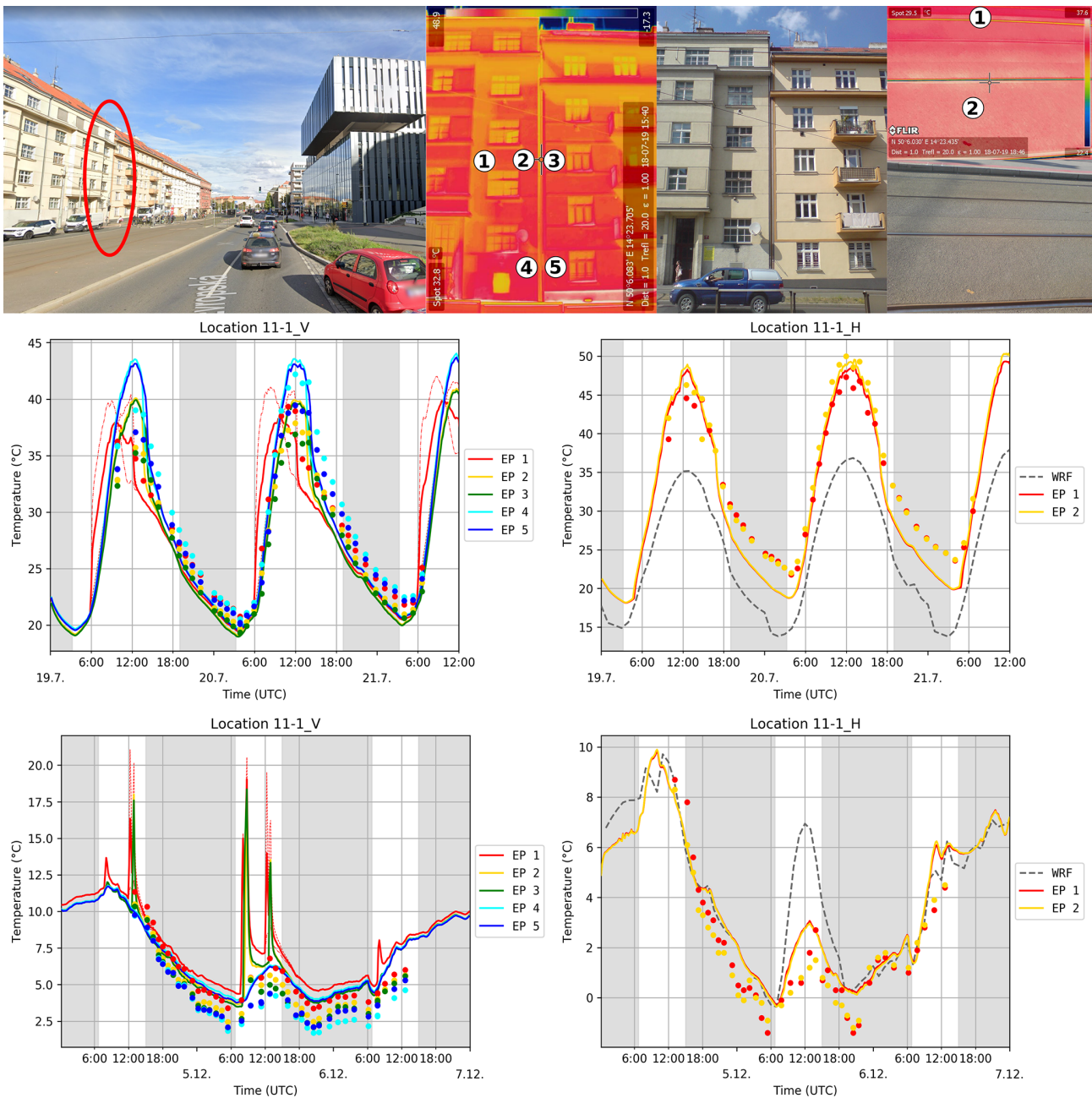


Figure 11. Observation location 11-1: the upper row shows the observation location and IR and RGB photos with placement of the evaluation points; the graphs show observed (dots) and modelled (lines) surface temperature for wall (left panels) and ground (right panels) for particular evaluation points (EP) for the summer e2 (middle panels) and winter e3 (bottom panels) episodes. The modelled values come from the child PALM domain, and the dotted and dashed lines represent the modelled temperature for the left and right grid faces (see Sect. 5.1.1). The grey dashed line shows the corresponding WRF skin layer temperature for horizontal surfaces. The grey areas denote night-time. The image in the left panel was sourced from © Google Maps 2020.

adjusted soil moisture case. This indicates that using correct soil moisture values is a necessary prerequisite to adequately model grass-like surfaces within an urban environment. For additional details concerning the sensitivity of surface temperatures modelled by PALM to the initial soil moisture in urban environments, we also refer to Belda et al. (2021). Apart

from soil moisture, sensitivity of grass surface temperatures to other parameters such as LAI, plant cover, and root distribution, might also be important. For details in this regard, we refer to Gehrke et al. (2020), who studied the sensitivity of the energy-balance components to different soil as well as land surface parameters.

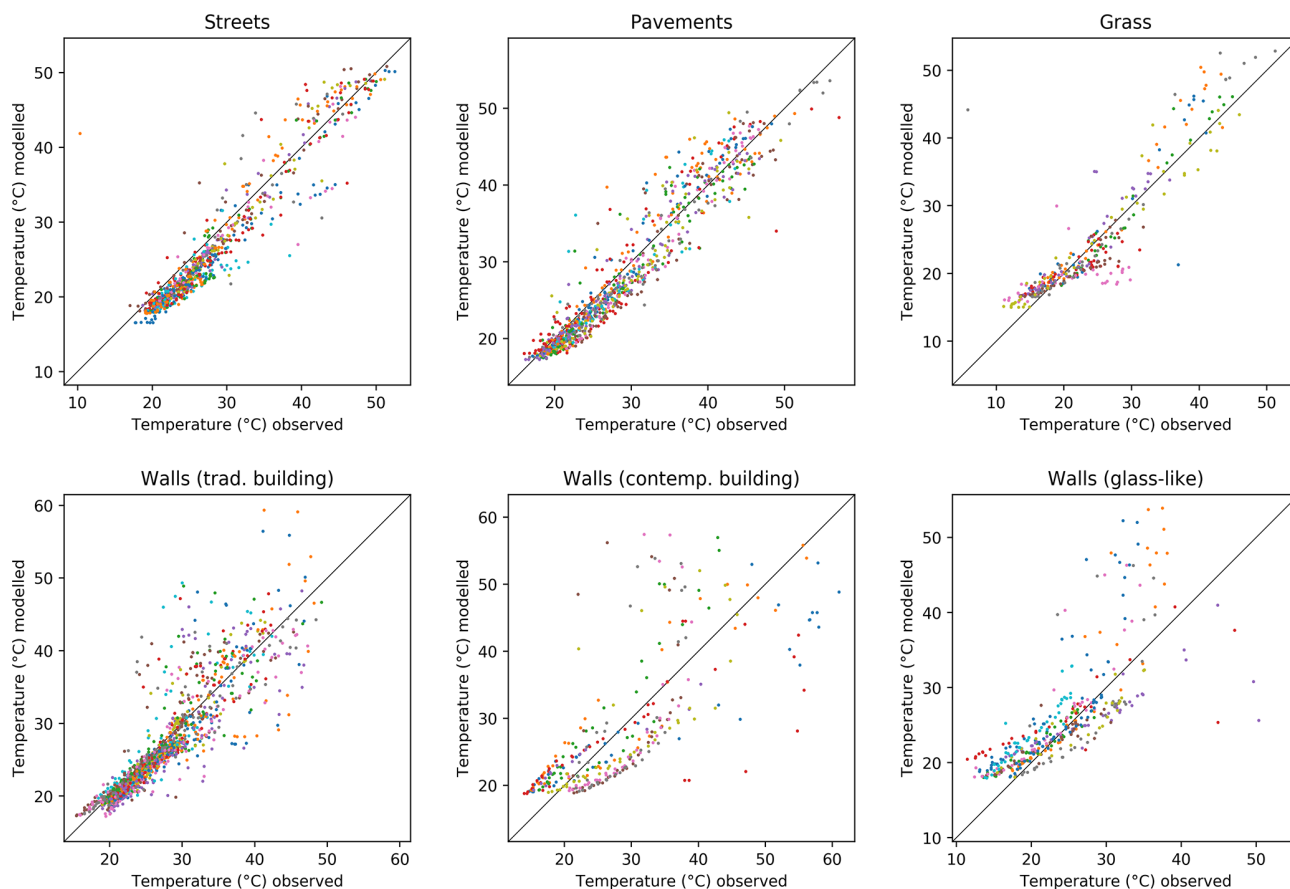


Figure 12. Scatter plots of the modelled and observed surface temperature for particular types of the surfaces in Table S7 during the summer e2 episode. Individual evaluation points are plotted using dots of different colours.

5.1.3 Complex structure of the walls

In the case of vertical surfaces (“walls”), the model behaves well for most cases of walls of traditional buildings, whereas walls of contemporary office buildings are modelled less accurately (see Figs. 12 and 13). We are convinced that the reason for this is the more complex structure of these walls which can not be fully described by the four layers allowed by the current version of the PALM input standard. Moreover, gathering precise information about this type of structure proved to be quite difficult. Let us show an example using EP 2 and 3 at location 02-3_V (see Fig. 15 and Sect. S3 of the Supplement for full information about the location).

While point 1 is captured by the model quite well except for slight overestimation during the night and morning hours, point 2 evinces an overestimation of around 15 °C during the afternoon hours. A closer direct inspection of this wall revealed that it consists of a thin outer layer followed by a 10 cm layer of air before the rest of the wall structure, whereas all of this is considered as a continuous wall in the model. Thus, the observed outermost layer was cooled from both sides, an effect which was not captured by the wall model.

5.1.4 Glass surfaces

Some buildings have walls covered with glass or similar types of reflective surfaces. These walls present a challenge for both observation and modelling. The main problem is the fact that the surfaces of these buildings are more or less specular, which means that a substantial part of the LW radiation entering the IR camera is a reflection of whatever is behind the camera. For example, location 11-2_V (see Fig. 16 and Sect. S3 of the Supplement for full information about the location) is a north-facing building, the lower part of which has a glass surface. The area of the building around EP 2 reflects the sky into the camera, while the area around EP 3, located just below, reflects the building opposite into the camera (the building opposite is around location 11-1_V). Consequently, the derived values of the surface temperature primarily represent the surface temperature of the reflected object (wall, ground, treetop, sky), not of the observed object itself. This can be well demonstrated by the different observed values at points EP 2 and EP 3. Thus, the modelling of this type of building cannot be validated by means of IR camera temperature measurements.

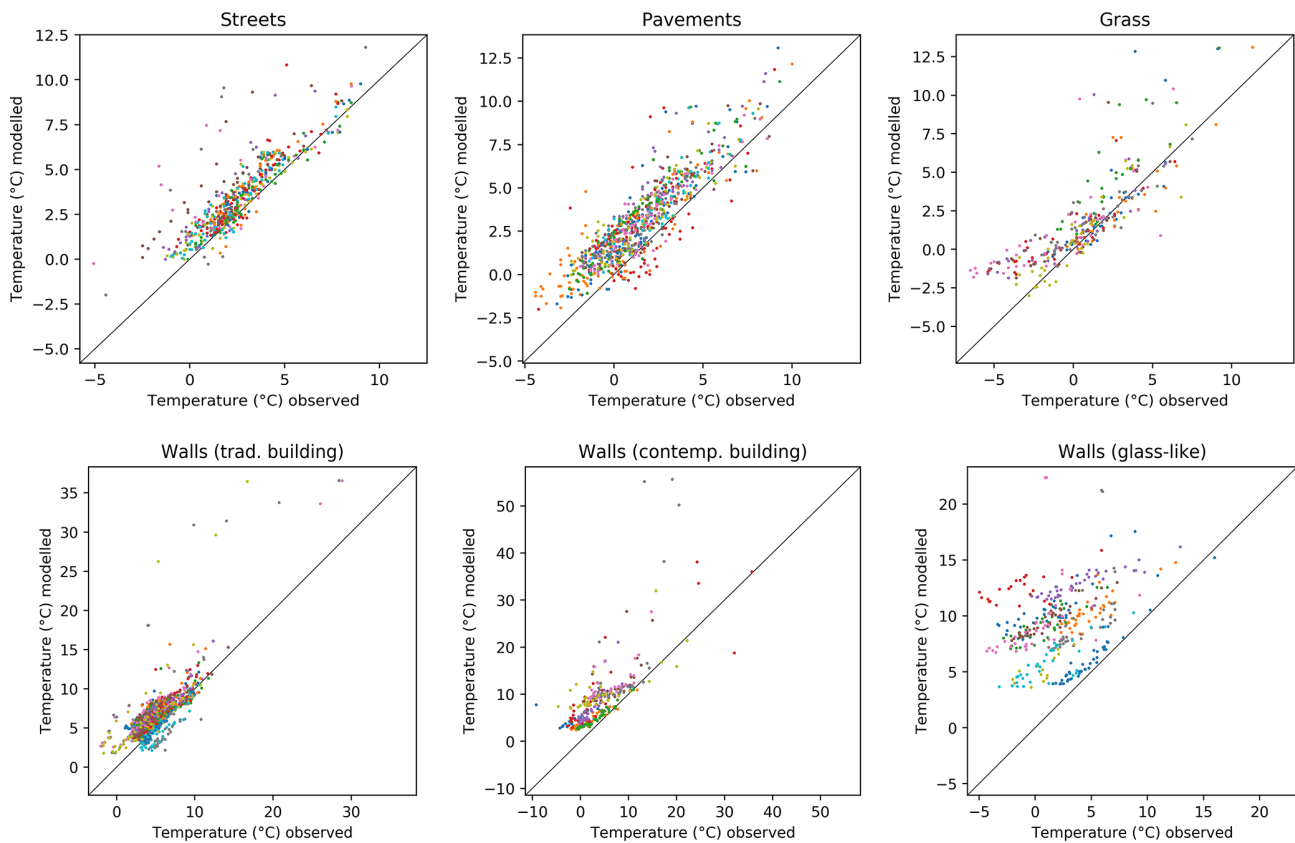


Figure 13. Scatter plots of the modelled and observed surface temperature for particular types of the surfaces in Table S7 during the winter e3 episode. Individual evaluation points are plotted using dots of different colours.

Table 2. Statistics of observed and modelled surface temperatures (K) for the simulated summer e2 and winter e3 episodes.

Surface type		All times			Daytime			Night-time		
		MB	MAB	RMSE	MB	MAB	RMSE	MB	MAB	RMSE
Pavements	S	-0.7	2.1	2.7	-0.2	2.3	3.0	-1.6	1.7	2.0
	W	1.5	1.7	1.9	1.9	2.0	2.4	1.4	1.5	1.7
Streets	S	-1.6	2.5	3.2	-1.4	2.7	3.6	-2.1	2.1	2.3
	W	0.9	1.0	1.4	1.3	1.4	2.0	0.7	0.8	1.0
Grass	S	0.6	2.7	4.1	0.3	3.2	4.9	1.1	1.7	2.0
	W	1.2	1.5	2.1	1.5	1.9	2.7	1.0	1.3	1.8
Walls (traditional building)	S	-0.5	2.0	3.3	-0.3	2.5	3.9	-0.9	1.1	1.4
	W	1.7	1.9	2.6	2.2	2.3	3.5	1.5	1.7	2.0
Walls (contemporary building)	S	-0.1	5.5	7.4	-0.4	6.4	8.8	0.2	4.2	4.5
	W	4.9	5.1	6.8	5.8	6.3	9.6	4.5	4.5	5.1
Walls (glass-like)	S	1.9	3.6	5.3	1.8	4.2	6.2	2.1	2.6	3.2
	W	7.1	7.1	7.9	6.8	6.8	7.8	7.2	7.2	8.0
Plant-canopy affected	S	-0.8	2.5	3.6	-0.7	2.8	4.1	-1.0	1.6	1.8
	W	1.0	1.5	1.9	1.3	1.7	2.1	0.9	1.4	1.7

S denotes the summer e2 episode; W denotes the winter e3 episode; MB denotes the mean bias; MAB denotes the mean absolute bias; RMSE denotes the root mean square error.

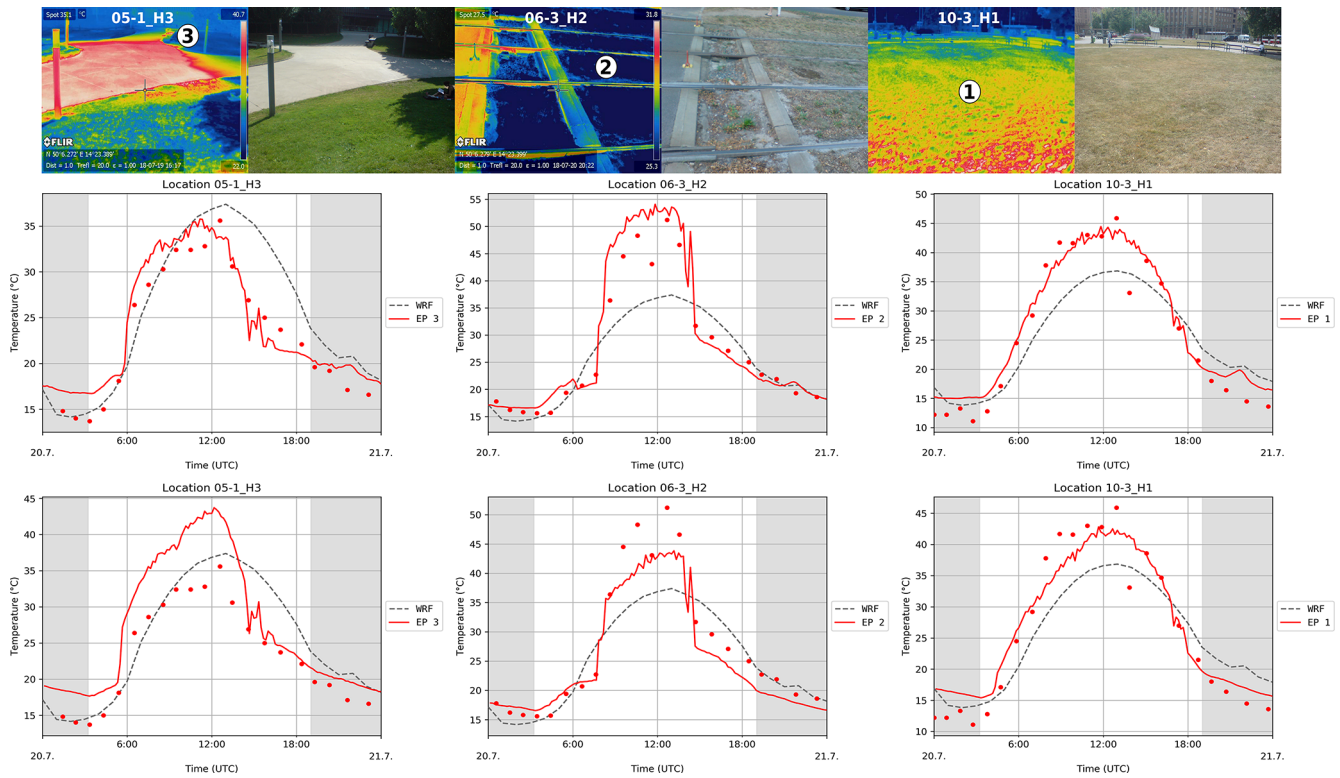


Figure 14. IR and RGB photos of locations 05-1_H, 06-3_H, and 10-3_H with placement of selected evaluation points (EP) (upper row) that represent three different grass-type surfaces found in the modelled urban area. The observed and modelled surface temperature at these locations for 20 July 2018 (second day of episode summer e2, middle row), and the same results from a test 1d simulation with all grass surfaces initialized with soil moisture uniformly prescribed from WRF output (bottom row). The grey dashed line shows the corresponding WRF skin layer temperature. The grey areas denote night-time. All results are from the child 2 m resolution domain.

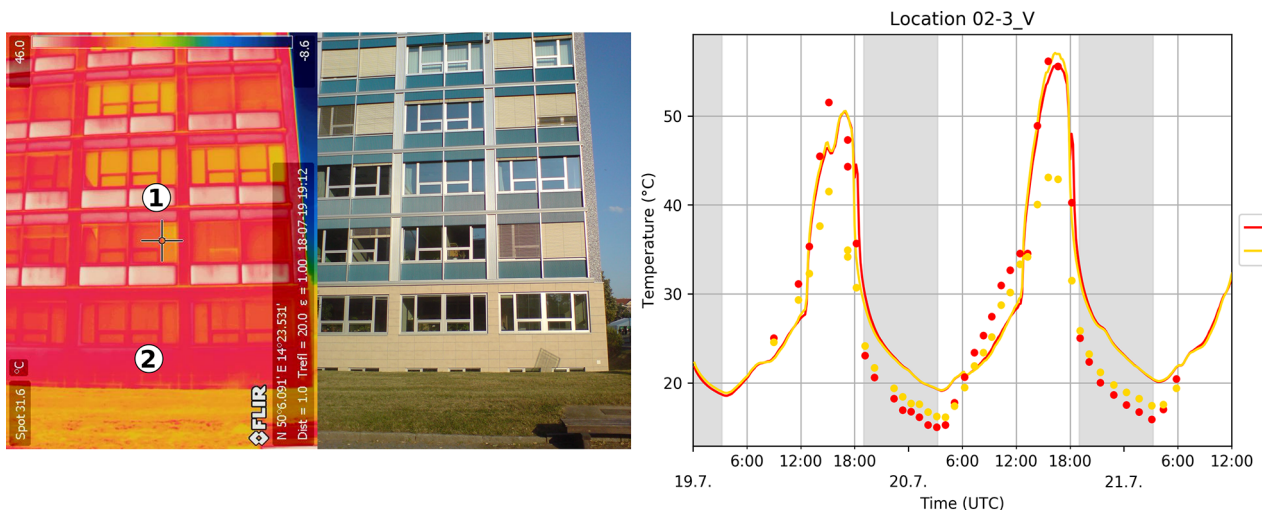


Figure 15. Observation location 2-3_V: the left panel shows IR and RGB photos of the building with placement of the evaluation points, and the right panel shows a graph of observed (dots) and modelled (lines) surface temperature for particular evaluation points (EP) for the summer e2 episode. The grey areas denote night-time.

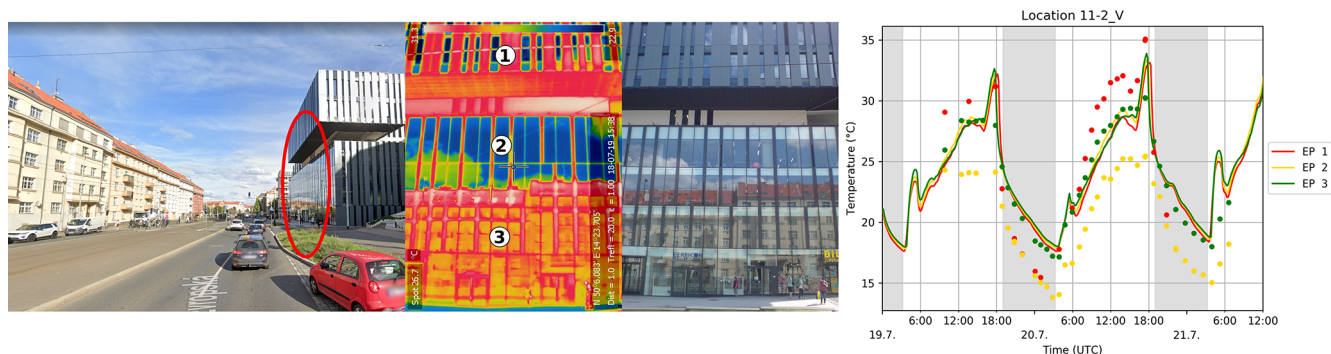


Figure 16. Observation location 11-2_V: the left panel shows the observation location; the centre panels show IR and RGB photos of the building and the placement of the evaluation points; the right panel displays a graph of observed (dots) and modelled (lines) surface temperature for particular evaluation points (EP) for the summer e2 episode. The grey areas denote night-time. The image in the left panel was sourced from © Google Maps 2020.

The modelling of the surroundings of these points can be partly influenced by the fact that the current version of RTM considers all surfaces as Lambertian (see Krč et al., 2021). This means that they reflect radiation in all directions in the model, whereas, in reality, part of the radiation undergoes specular reflection according to the law of reflection. This fact does not directly affect the reflective surface itself, but it can influence the distribution of reflected SW and LW radiation among nearby surfaces. As the amount of incoming direct radiation is significantly larger than the incoming reflected radiation (direct radiation can reach up to 900 W m^{-2} , whereas the reflected radiation is limited to 200 W m^{-2} for most common cases), this effect usually has little practical impact and is masked by the effect of the direct radiation. An example of this effect can be seen in location 06-1_H by comparing EP 2 with EP 3 (see Fig. 17 and, alternatively, Supplement Sect. S3 for full information about the location). These points are placed on similar asphalt concrete surfaces but with a different distance to the nearby glass facade. While the surface temperature at the more distant EP 3 is modelled well, EP 2 is overestimated by about 7°C on 20 July 2018 between 11:00 and 13:00 UTC. The observation at EP 2 at these times shows an atypical increase of about 7°C which is not observed at other points placed on the same surface type. We can attribute this increase to the effect of the specular reflection from the glass facade. As this effect is not considered by the model, the model gives similar results for both points EP 2 and EP 3. Results for EP 1 (limestone pavement) are less affected by the missing specular radiation in the model due to its much higher albedo.

5.1.5 Rapid changes in surface temperature

Some of the graphs of the surface temperature contain strong “peaks” in the diurnal cycle of the modelled wall temperature (see e.g. Fig. 11). This effect can be seen mainly during the winter episode (at locations such as 6-4_V, 7-1_V, 7-2_V, 8-2_V, 9-2_V6, 9-2_V7, and 11-1_V). Similar peaks can be

observed in the corresponding radiative, surface, and ground heat fluxes (see Sect. S4 in the Supplement). Some of these peaks can also be found in measurements (clearly visible for locations such as 6-4_V), although most observations contain no corresponding peaks. Let us analyse location 11-1_V in more detail (see Fig. 11), where this effect is very strong for EP 1, 2, and 3 on 5 December.

Figure 18 shows the observed IR and RGB camera photos at corresponding observation times along with their modelled counterparts at the closest saved model time step. For easier orientation, Fig. S19 in the Supplement shows an overview of the modelled surface temperatures in the given area at the same time steps. Figure 19 provides the complete timeline of 10 min model outputs of the wall surface temperature from 05:28 to 12:48 UTC. The time steps shown in the previous figure (Fig. 18) are highlighted using a red frame, and the red dots denote the position of EP 1, 2, and 3.

The first peak takes place between the first and second observation times (07:51 and 09:26 UTC); thus, it does not appear in the IR observations. The situation of the second peak is more complicated. This peak partly overlaps with the fourth observation at 12:48 UTC, which is only reflected in the observations by a very small increase in the surface temperature at EP 1. The reason for this can be seen in the comparison of the shading from direct radiation in the RGB photo and the corresponding figure for the modelled SW radiation (see Fig. 18). The shade created by the building on the opposite side of the street is approximately 3 m lower in the model than in reality at this time. These differences can be attributed to the geometrical imperfections of the digital building elevation model (BEM) used, as well as to the errors introduced by its discretization and by the PALM process of the placing of the buildings on the terrain. One of the sources of the imprecision in BEM can also be peripheral objects on the roof area (e.g. banisters, air-conditioning systems) which create shading but are not considered in BEM (see street view of shading buildings in Fig. S20 in the Supplement).

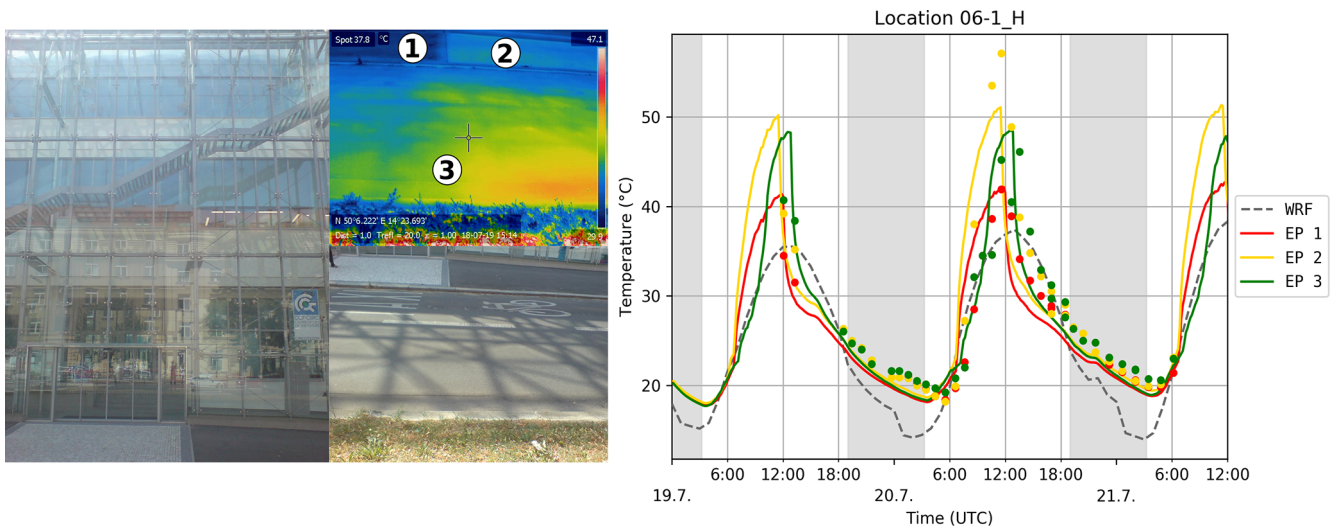


Figure 17. Location 06-1: the left panel shows IR and RGB photos of the observation location with placement of the evaluation points, and the right panel shows observed (dots) and modelled (lines) surface temperature for the summer e2 episode. The grey dashed line shows the corresponding WRF skin layer temperature. The grey areas denote night-time.

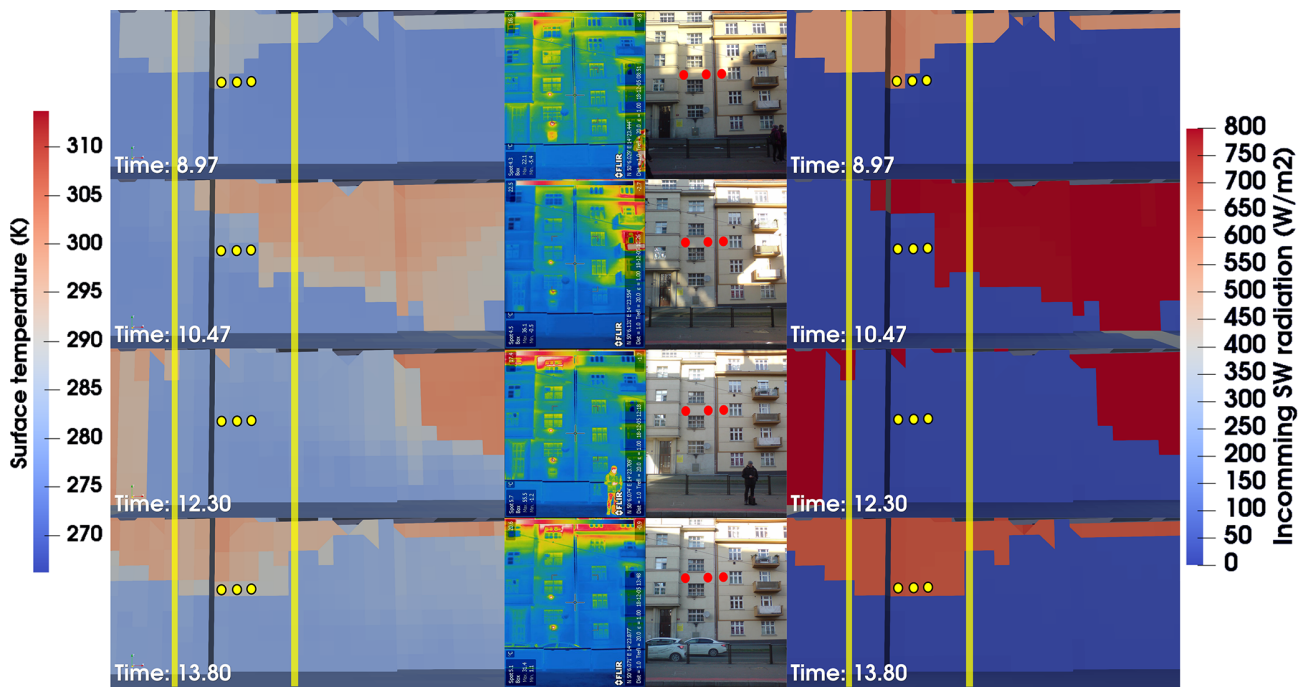


Figure 18. Observed camera photos (IR – centre left; RGB – centre right) on 5 December 2018 at observation times of 07:51, 09:26, 11:18, and 12:48 UTC, and the modelled counterparts for the closest saved model time step: surface temperature (left) and incoming SW radiation (right). The yellow dots denote positions of evaluation points 1, 2, and 3 (Fig. 11), and the yellow lines show the extent of the area shown on the IR and RGB photos. For technical reasons, the step times for the model views express minutes as decimal fractions of the hours.

Figure 20 shows a detailed graph of location 11-1_V for times from 07:00 to 14:00 UTC and provides additional information about the diurnal cycle of the surface temperature at this location. EP 1, 2, and 3 correspond to points from the graph in Fig. 11, whereas the new points, EP 4, 5, and 6, were added on the top layers of the wall. The graph shows that the

diurnal variability in the surface temperature at this location has similar magnitude in the model to that in the observations. This supports our conclusion that the model (namely the radiative transfer and surface energy balance) works reasonably well, and the differences in the values at particular EPs and times can be attributed mainly to the geomet-

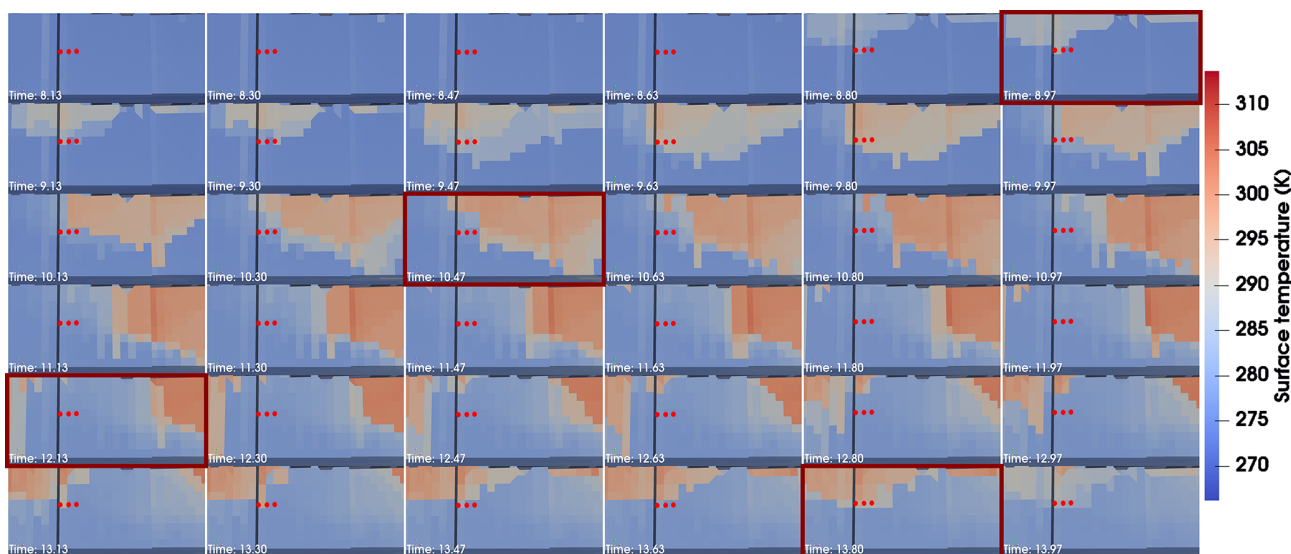


Figure 19. Timeline of 10 min model outputs of wall surface temperature on 5 December 2018 from 05:28 to 12:48 UTC. The time steps from the previous figure (Fig. 18) are highlighted using a red frame, and the positions of the evaluation points 1, 2, and 3 are marked by red dots. For technical reasons, the step times for the model views express minutes as decimal fractions of the hours.

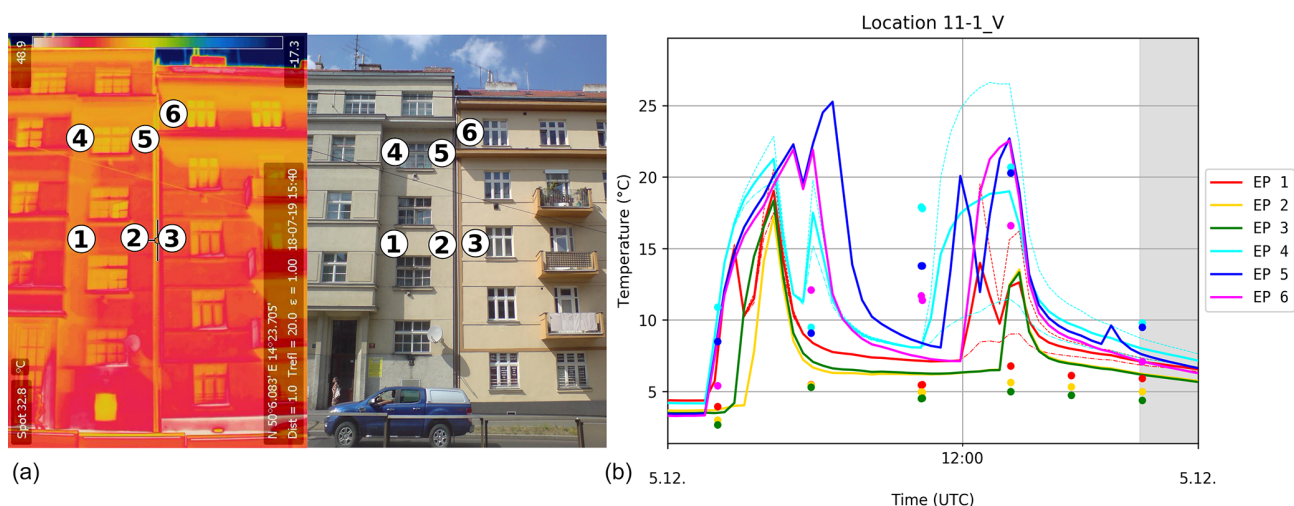


Figure 20. Comparison of IR observations and the model at location 11-1_V on 5 December 2018 from 07:00 to 16:00 UTC. The left photos show IR and RGB images of the location with the evaluation points marked, and the right image shows the graph of the modelled (line) and observed (dots) values of the surface temperature for these evaluation points. The grey area denotes night-time.

rical imperfections of the model which produce differences in the shading of the direct radiation. These changes in surface temperature also cause rapid changes in the temperature gradient in the wall which explains the peaks in the surface and ground heat flux visible in the corresponding graphs in Sect. S5 of the Supplement. The positive and negative peaks in the ground heat flux correspond to start and end times of irradiation of the given point by direct radiation. This analysis also outlines the complexity of a problem that is represented by spatially and temporally detailed modelling of radiation

energy processes and the surface energy balance in the complex heterogeneous urban environment.

5.1.6 Plant-canopy effects

Trees and shrubs are modelled in PALM as the resolved plant canopy (PC) which is described by a 3D structure of leaf area density (LAD). In addition to affecting the turbulent flow by adding LAD-dependent drag, resolved plant canopy also affects radiative transfer by partially intercepting SW and LW radiation as well as emitting LW radiation (see Krč et al., 2021). Further, the absorbed incoming radiation is trans-

formed into latent and sensible heating terms which are considered within prognostic equations of potential temperature and humidity. Many EPs are affected to different degrees by PC. A list of EPs where a significant impact of PC can be seen is given in Table S7 in the “Plant-canopy affected surface” row. In this section, we focus only on the summer scenarios, as deciduous trees (which constitute the majority of the trees in the domain) carry no leaves during the winter. The impact of branches during the winter episodes is roughly modelled as 10 % of the summer LAD.

Figure 21 shows two examples of locations affected by trees (12-1_H and 08-2_H; for full information about these locations, see Sect. S3 in the Supplement). Location 12-1_H is on the left, with two EPs placed on the same surface (asphalt concrete). The direct radiation at EP 2 is influenced by tree shading, but the tree shade does not reach EP 1 at this time of year. Shading from the treetop decreases the surface temperature after noon, which is well captured by the model. A similar situation is shown on the right for location 08-2_H. The EPs are similarly placed on an asphalt concrete surface in a street canyon surrounded by two alleys of trees with linked treetops forming an umbrella-like covering. The street surface temperature at location 08-2_H is underestimated by the model by up to 5 °C. Because a similar type of surface is modelled well at 12-1_H and other locations, the most probable explanation for this discrepancy is the tree shading. The reason could be a general overestimation of LAD in the input data and/or a discrepancy in its spatial distribution. The large tree crowns tend to arrange themselves into clusters with free space between them (see e.g. Mottus, 2006). Figure 21, with spots of direct SW radiation passing through the canopy, and location views in Sect. S3 of the Supplement suggest that this is the case at location 08-2_H. However, the method used for the calculation of the LAD distribution within the tree crown does not consider such clusters, leading to possible underestimation of total transmissivity of the whole tree crown. Moreover, PALM uses a constant extinction coefficient for calculation of the optical density from the LAD value, which can lead to overestimation of optical density if clusters are significant at the sub-grid scale. However, this can be mitigated by decreasing the LAD value. These examples confirm the importance of the precise estimate of the structure of the tree LAD in the inputs for the PALM simulations, although gathering of such information presents a complicated task.

5.1.7 Discretization issues

PALM discretizes the domain in a Cartesian grid, where all values in every grid box are represented by one value. This leads to standard discretization errors. Moreover, the current version of PALM uses the so-called mask method to represent obstacles (terrain, buildings), where a grid box is either 100 % fluid or 100 % obstacle; consequently, any surface is represented by orthogonal grid faces (see Fig. 4). Besides implications with respect to the near-surface flow dynamics,

which can be locally affected, this discretization increases effective roughness and enlarges surface area. The step-like surface representation also modifies the direction of the normal vector and the mutual visibility of the particular grid surfaces, which in turn also affects the surface net radiation and, thus, the surface energy balance. The observations of the surface temperature allow us to demonstrate a few selected implications for radiative transfer and surface energy balance.

The first observed consequence of the discretization is the fact that the sub-grid-sized surface features cannot be represented, whereas in reality, these objects can significantly influence the shading of parts of the surface. This effect can be observed in many of the studied locations (see Sect. S3 in the Supplement), and it needs to be carefully taken into account when making a point comparison of the related surface values.

The effects caused by the step-like surface representation include artificial shading and the alteration of the surface normal vector. Both of these effects can be observed and studied in the case of slope terrain as well as in the case of non-grid-aligned walls. As an example, let us show the wall around observation location 07-1 (see Fig. 22; for complete location information, see Sect. S3 in the Supplement). This wall is oriented to the east with a slight inclination to the north. The upper row of Fig. 22 shows the observed photo on 20 July 2018 at 09:37 UTC and the 3D view of the modelled incoming SW radiation on this wall at the corresponding modelling time step. The bottom row shows the same situation approximately 1 h later, at 10:38 UTC. In the first case, the entire wall is irradiated by direct solar radiation, whereas the model results indicate artificial shading of some grid faces caused by the step-like representation of the wall. The second case, 1 h later, shows the situation when the wall is shaded in reality but some of the corresponding model grid faces are irradiated by direct solar radiation due to their slight turn to the east in comparison with the real wall.

Two further consequences of the orthogonally gridded model surfaces are an altered distribution of the reflected radiation and artificial self-reflections owing to the step-like terrain and wall representation. The first effect is difficult to demonstrate in the observed data due to less direct attribution of the reflected radiation to the individual source surfaces and due to the partial masking of reflected radiation by the stronger direct radiation. The second effect can be demonstrated, for example, on the wall around location 07-2_V on 20 July at 11:37 CET (see Fig. 23). In reality, the wall is not irradiated by direct solar radiation at this moment, as can be seen from the RGB photo. The south-facing grids of the model wall (“steps”) are illuminated by direct radiation, and the radiation reflected from them then irradiates adjacent grid faces turned to the west (oriented close to the original wall direction) – an effect which has no counterpart in reality.

These potential sources of problems especially need to be considered, due to their local nature, when making point-

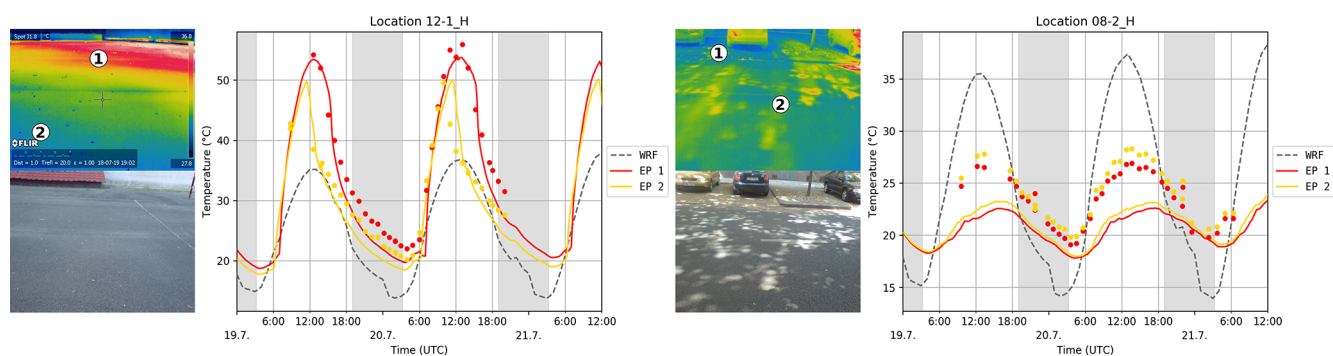


Figure 21. IR and RGB photos showing the locations of evaluation points, and the graph of the observed (dots) and modelled (lines) surface temperature for these evaluation points during the summer e2 episode (19–21 July 2018). The left half of the figure shows location 12-1_H (the asphalt playground in the courtyard of Sinkule house), and the right half of the figure shows location 08-2_H (asphalt concrete surface in Terronská Street). The grey dashed line shows the corresponding WRF skin layer temperature. The grey areas denote night-time.

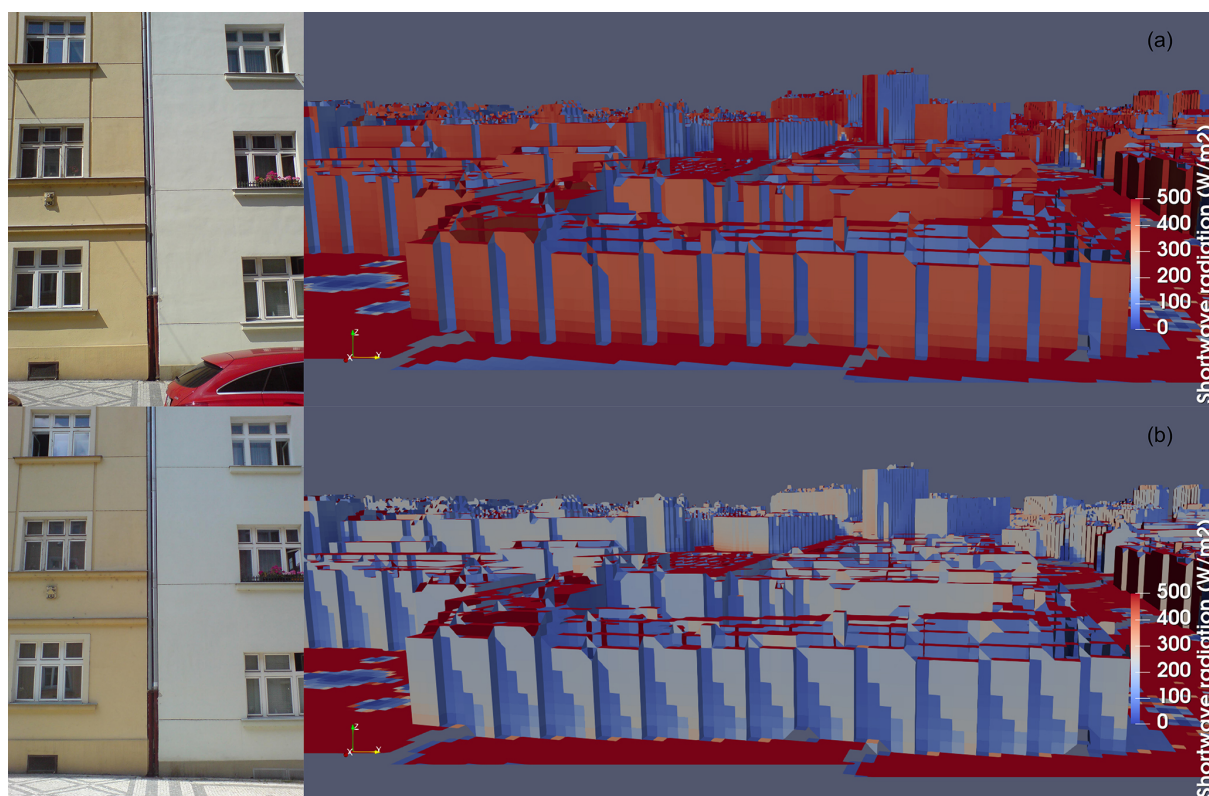


Figure 22. East-facing wall in N. A. Někrasova Street around location 07-1_V (see Fig. 1 and the detailed location information in Supplement Sect. S3). The top row shows the observed photo on 20 July 2018 at 09:37 UTC and the 3D view of the modelled incoming SW radiation on this wall at the corresponding time step, and the bottom row shows the same situation at 10:38 UTC.

to-point comparisons of modelled and observed quantities. However, when averaging over larger areas, one may expect that these artificial effects partially mutually compensate for one another due to the unchanged amount of incoming global radiation. However, the differences in reflections can still lead to significant changes in the global energy balance of the surface.

To estimate the impact of the discretization on the averaged simulation results of the wall, we ran two idealized simulations of a street canyon. The simulation domain had 2 m grid resolution and it contained one west–east-oriented 30 m wide street canyon that had a height of 20 m. The simulated day was 19 July 2018 (the first day of the summer e2 episode). The radiation was simulated by the coupled RRTMG model and the meteorological conditions were set

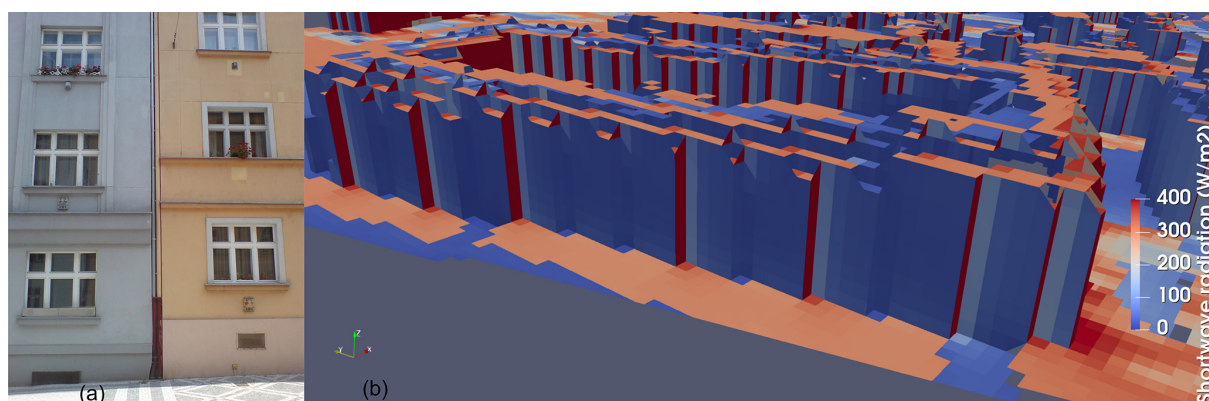


Figure 23. West-facing wall in N. A. Někrasova Street around location 07-2_V (see Fig. 1 and the detailed location information in Supplement Sect. S3). The figure shows the observed photo on 20 July 2018 at 10:37 UTC (left) and the 3D view of the modelled incoming SW radiation on this wall at the corresponding modelling time step (right).

as constant (west wind 1 m s^{-1} , potential temperature at surface 295 K). The simulation started at 03:00 am with a preceding 24 h spin-up run and covered the 16 sunny hours of the day. The first simulation employed the standard grid with no rotation, whereas the second simulation had the grid rotated by 45° , utilizing PALM's ability to set grid rotation. This means that the walls of the street canyon were precisely aligned with the grid in the first case, whereas they were represented by steps-like structures in the second case due to the 45° angle that they form with the grid. The averaged results of the surface temperature, SW irradiation and net radiation over the south-facing wall are presented in Figs. S22 and S23 in the Supplement. The results show that the differences can reach about 3°C for surface temperature, over 100 W m^{-2} for SW irradiance, and about 80 W m^{-2} in the case of net radiation. These effects cannot simply be neglected, and more focused research is needed. Some potential ways to amend the model are discussed in Sect. 6.2.

5.2 Wall heat flux

Observations of the wall heat flux (HF) in two locations (see Sect. 2.3.2) allow a direct comparison with the wall heat flux simulated by the model. Moreover, the observations of the surface temperature from the sensor allow both validation of the PALM model and the observations obtained by the IR camera (see Sect. 2.3.2).

During the summer campaign, HF observations took place in Sinkule house from 19 July to 3 August and at the Zelená location from 3 to 7 August. This period only partly overlaps with the summer e2 modelling episode. The graphs of heat flux and surface temperature are shown in Fig. 24. The sharp rise in observed HF and temperature before 06:00 UTC is caused by the direct irradiation of the sensors by the sun; therefore, the data between around 06:00 and 08:00 UTC cannot be taken as valid measurements. (Similar peaks are visible in the PALM outputs before sunset.) The sharp drop

in HF on 20 July after 06:00 UTC was caused by the sensor becoming unglued, which was fixed at about 08:00 UTC. The modelled and observed wall heat flux on the ground floor shows a similar diurnal cycle with similar amplitude, although the model slightly overestimates the observed values by about 5 to 10 W m^{-2} , whereas the corresponding modelled surface temperature agrees fairly well with the observations. The modelled wall heat flux on the first floor shows a pronounced diurnal cycle, whereas the observed wall heat flux shows only a weak diurnal cycle with a significantly smaller amplitude. The modelled surface temperature, however, shows a smaller amplitude with higher night-time but lower daytime temperatures compared with the observations, which is in agreement with the respective wall heat fluxes where the model increasingly partitions the available energy into the wall heat flux.

The winter HF observations at Sinkule house cover the e3 episode from 4 to 6 December, and the observations at the Zelená location fit with the e2 episode for 27–28 November (see Fig. 25). Even though the modelled surface temperature at Sinkule house for the ground floor observation is overestimated by around 2°C with respect to the observed value during daytime, the modelled and observed wall heat fluxes agree fairly well during the period shown, especially for the first and second day. In contrast, on the first floor, the modelled wall heat flux (absolute value) and surface temperature are strongly overestimated, especially during the nights. The minimum of the modelled wall heat flux goes down to -50 W m^{-2} during the night from 5 to 6 December while observations suggest values between -10 and -15 W m^{-2} . The situation at the Zelená location is similar: the observed HF fluctuates around -40 W m^{-2} during the nights while the modelled counterpart goes down to -80 W m^{-2} . This behaviour suggests that the thermal wall resistance of higher floors of the Sinkule and Zelená buildings are underestimated. Sinkule house is an older building that was insulated in the past except for the ground floor. The real thermal re-

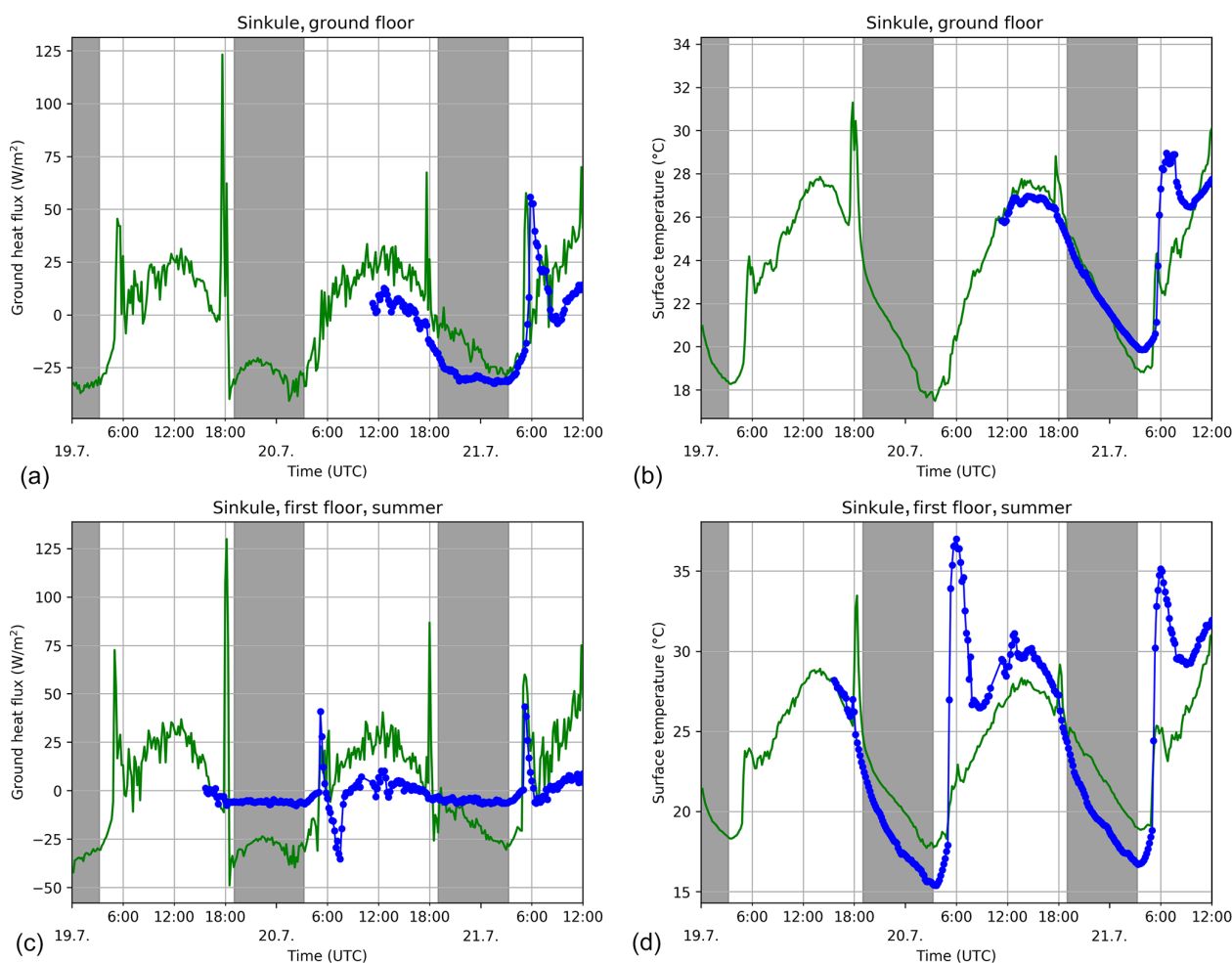


Figure 24. Modelled (green) and observed (blue) wall heat flux (a, c) and surface temperature (b, d) for 19–21 July 2018 for the ground floor wall (a, b) and for the first floor wall (c, d) at the Sinkule house location. The grey areas denote night-time

sistance of this additional insulation layer, which is set in the input data to approximately 6 cm of polystyrene, is probably underestimated, and the real insulation is more efficient. The details regarding the wall material used in the Zelená building were not available, and some type of construction block was assumed; however, its thermal conductivity in the model is probably overestimated.

5.3 Street canyon meteorological quantities

Data collected by the mobile meteorological stations and vehicles allow us to compare modelled atmospheric quantities against observations within several street canyons. This section presents graphs and statistics of modelled and observed temperature and wind speed. Graphs are presented for summer e1, summer e2, and winter e3 episodes here; the complete results for all episodes are available in Sect. S5 in the Supplement, which also contains corresponding graphs of vertical sensible heat flux and relative humidity. The com-

parison graphs contain values from the WRF simulation to allow assessment of the benefits of the microscale model.

5.3.1 Air temperature

Figure 26 shows time series of modelled and observed air temperature within different street canyons for the summer e1, summer e2, and winter e3 episodes. In the summer scenarios, the daily cycle of air temperature is generally captured by PALM. The modelled maximum air temperature generally agrees well with the observed maximum but is somewhat underestimated, especially at the Sinkule location. The modelled night-time minimum values tend to be too warm compared with the observation, which is in accordance with the less stable modelled conditions as indicated by Fig. 5. The spatial variability in the model air temperature shown, indicated by the red shaded area, is rather low, suggesting that the comparison of modelled and observed air temperature does not suffer from any location biases. In addition, Fig. 26 also shows 1-hourly averaged 2 m air tem-

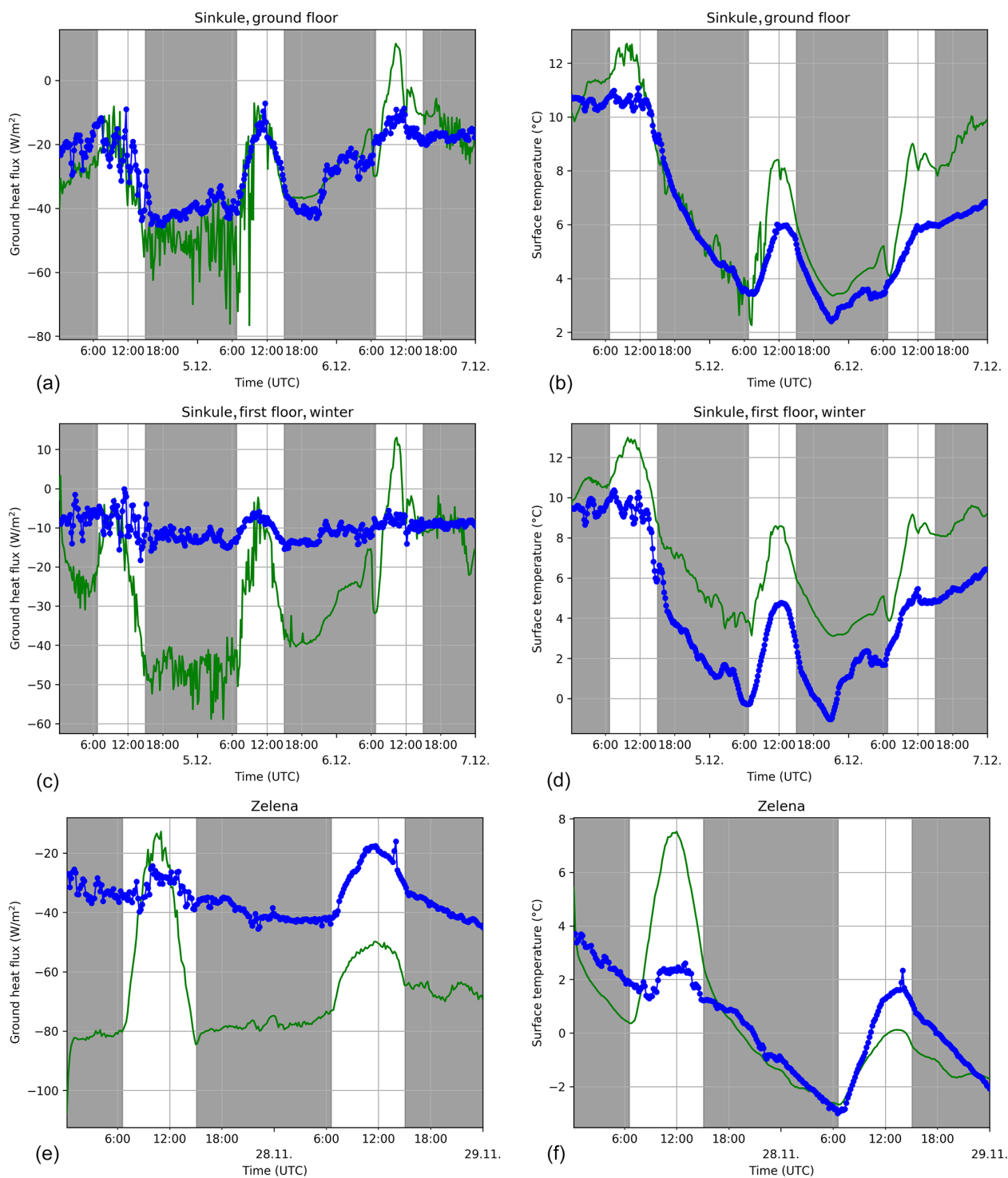


Figure 25. Modelled (green) and observed (blue) wall heat flux (a, c, e) and surface temperature (b, d, f) for 5–6 December for the ground floor (a, b) and the first floor (c, d) at the Sinkule house location, and at the Zelená location on 27–28 November (e, f). The grey areas denote night-time.

perature as modelled by WRF and inferred from the WRF grid point closest to the observations. As WRF was set up without urban parameterization and buildings were not explicitly considered, a direct comparison of PALM and WRF results for street canyon locations is not appropriate, but it can provide useful insight into whether deviations of PALM-modelled values arise from the driving mesoscale model or from a different source. Similar to the temperature simulated in PALM, the WRF-modelled 2 m air temperature also shows lower daytime maximum temperatures compared with the observations, while even lower minimum temperatures are modelled at night-time, which is in contrast to PALM. This, in turn, suggests that the overly warm night-time temperatures within the street canyon do not arise from the driving mesoscale simulation but from a different source.

In the winter case, the modelled air temperature reflects the evolution of the observed air temperature, although the air temperature during the first day and the minimum temperature during the first night are overestimated in all street canyons, while WRF-modelled temperatures agree well with the observations. Starting from the second night until the end of the simulation, it is striking that the modelled air temperature is significantly overestimated by about 2 to 5 K. This can be attributed to the driving mesoscale WRF simulation which indicates a similar overestimation of air temperature when WRF was not able to capture night-time cooling. This nicely shows that the performance of the building-resolving LES strongly depends on the driving mesoscale simulation. If the results on the mesoscale are biased, this error will also propagate into the LES.

Statistical metrics for the model performance over all locations and scenarios considered are given in Table 3. For the summer scenarios, the street canyon air temperature is slightly underestimated during daytime, whereas it is overestimated during night-time due to insufficient cooling near the surface. For the winter scenarios PALM overestimates the day- and night-time temperatures by about 1.5 K, which can be partly explained by the driving synoptic conditions. The scatter between observations and model results is about 2 K without any significant difference between day- and night-time or between summer- and wintertime. It is striking that the correlation between modelled and observed air temperature is higher during the daytime where the daily cycle is usually well captured, whereas the correlation is lower at night-time where the night-time air temperature is often overestimated.

5.3.2 Wind speed

The simulated and observed wind speed in the respective street canyons for the summer e1, summer e2, and winter e3 episodes is summarized in Table 4 and plotted in Fig. 27; the complete graphs for all episodes are shown in the Supplement in Sect. S5. The graphs also show values simulated by the WRF model to illustrate the added value of the high-

resolution LES simulations. Summary metrics for both models and all episodes (Table 4) show similar model performance in summer and winter with only slightly better statistics in summer. Both campaigns exhibit a significant overestimation. However, all measures show that PALM is partially able to correct biases imposed by its driving boundary conditions.

The wind speed in the summer campaign generally shows good agreement except at the Orlík location, where significantly higher wind speeds are simulated by the model. We hypothesize that this is attributable to the nearby tree crowns in the street, which have a radius of 2 m in the model, but a radius of about 5 m in reality (see corresponding photo in Fig. S7 in the Supplement). The uncertainty of the results at this location is also increased by large spatial gradients of the wind speed near the buildings which makes precise fitting of the modelled and observed values sensitive to any spatial inaccuracy.

The daily cycle of the modelled wind speed in the winter scenario is roughly captured at the Sinkule location, except at night-time when the PALM-modelled wind speed is generally overestimated (as also indicated in Fig. 6). This overestimation of the modelled wind speed, which is also accompanied by increased temporal variability, is also visible at the other stations; this might be linked to the insufficient representation of the stable boundary layer. Moreover, the daytime values are mostly overestimated, but this overestimation is much lower than that during nights. This overestimation could also be generally linked to the inaccuracies in the boundary conditions from WRF (which overestimates near-surface wind speed), which is expected when not using an urban parameterization (see e.g. Halenka et al., 2019), while the wind speed is partly overestimated also at higher levels (see Fig. 6).

5.3.3 Wind speed on the roof

To assess model behaviour in the urban canopy outside the street canyon, a comparison of the wind speed measured on the roof of the highest building in the child LES domain (FSv – Faculty of Civil Engineering CTU) with PALM is presented. In order to illustrate the added value of the high-resolution LES simulations, outputs of the WRF are provided along with measurements from the nearest synoptic station Praha-Ruzyně for reference (reliable wind direction measurements were only available from the synoptic station). The graphs for the summer e2 and winter e3 episodes are shown in Fig. 28. The time series for the summer e1 episode and the winter e1 and e2 episodes are presented in Fig. S21 in the Supplement. Summary metrics for all episodes are given in Table 5. The wind speed is generally overestimated, with smaller errors in the summer simulations – a difference already present in the driving WRF simulation. In a comparison of the two models, PALM shows better agreement with observations with the exception of the correlation coefficient,

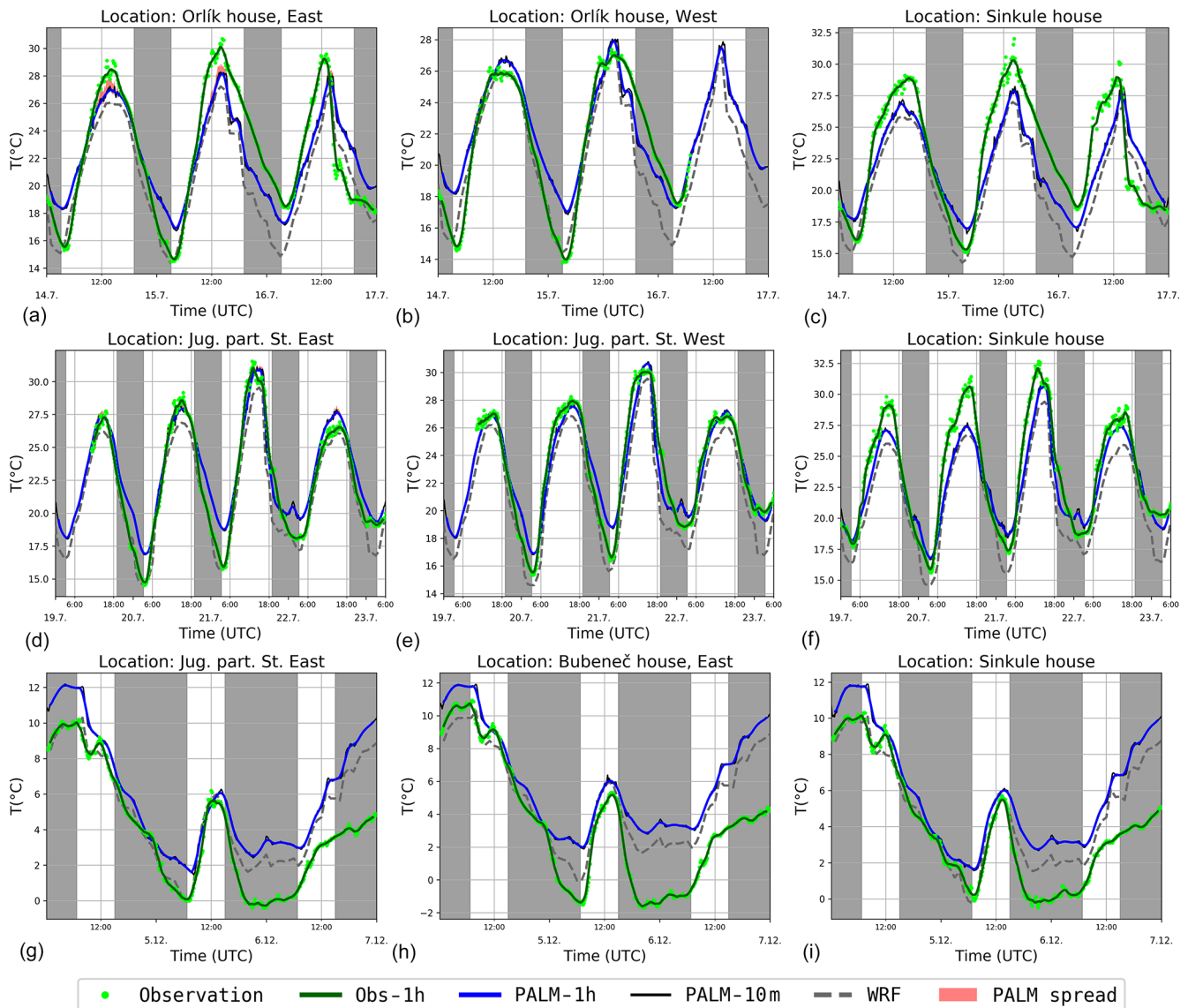


Figure 26. Street canyon temperature at 3.9 m (Sinkule house) and 4.6 m (other) for the summer e1 (a, b, c), summer e2 (d, e, f), and winter e3 (g, h, i) episodes. Observations are shown as 10 min averages (green dots) and moving 1 h averages (green line). PALM simulations are shown as moving 1 h averages (blue line), 10 min averages (solid black line), and the interval between the smallest and the largest 10 min average among the neighbouring grid points (red band). The grey dashed line denotes the 1 h averages of temperature at 2 m at the closest WRF grid point. The grey shaded areas indicate night-time. Please note that the black curve indicating the 10 min average is mostly hidden by the blue curve indicating the 1 h average. The spatial variations in temperature are usually very small, especially in the winter case, meaning that the red curve is hidden most of the time.

which is similar in summer and even higher for WRF results in winter. For most of the episode, the PALM-simulated wind speed is closer to the FSv observations than the WRF results as well as the background Praha-Ruzyně observations. During the winter e3 episode, the differences are considerable. In particular, there is a large peak in the evening of 6 December, which confirms the disagreement of the wind profiles in Fig. 6.

5.4 Street canyon air quality

This section presents a comparison of modelled and observed concentrations of NO_x and PM_{10} . The simulated and measured concentrations of NO_x in the summer e1, summer e2, and winter e3 episodes are shown in Fig. 29. The complete graphs for NO_x , PM_{10} , and $\text{PM}_{2.5}$ for all episodes can be found in Sect. S5 in the Supplement. Summary statistics for NO_x 1 h average concentrations for aggregated summer and winter episodes are presented in Tables 6 and 7. Statistics

Table 3. Statistical metrics of modelled 1 h averaged air temperature within different street canyons. The statistics are evaluated over all locations and episodes considered, and they are partitioned into summer and winter as well as day- and night-time. The statistical metrics for the modelled 2 m air temperature in WRF are also given for completeness.

	Summer episodes				Winter episodes			
	Day		Night		Day		Night	
	PALM	WRF	PALM	WRF	PALM	WRF	PALM	WRF
<i>N</i>	233	233	122	122	210	210	370	363
mean obs. (°C)	24.1	24.1	19.3	19.3	3.5	3.5	2.4	2.4
mean mod. (°C)	23.5	22.4	20.0	17.7	5.1	4.2	4.0	2.7
MB (°C)	−0.6	−1.7	0.7	−1.6	1.6	0.7	1.6	0.3
RMSE (°C)	2.0	2.4	1.8	2.3	2.1	1.7	2.5	2.2
<i>R</i>	0.91	0.93	0.73	0.78	0.91	0.89	0.85	0.81

N denotes ensemble size; mean obs. denotes the observed mean value; mean mod. denotes the modelled mean value; MB denotes the mean bias; RMSE denotes the root mean square error; *R* denotes the Pearson correlation coefficient.

Table 4. Statistical metrics of modelled 1 h averaged wind velocities within different street canyons. The statistics are evaluated over all locations and episodes considered. Summer and winter episodes are distinguished. The statistical metrics for the modelled 10 m wind speed in WRF are also given for completeness.

	Summer episodes		Winter episodes		All episodes	
	PALM	WRF	PALM	WRF	PALM	WRF
<i>N</i>	354	354	580	573	934	927
mean obs. (m s ^{−1})	0.5	0.5	0.6	0.6	0.5	0.5
mean mod. (m s ^{−1})	0.9	2.0	1.1	3.5	1.0	2.9
FB	0.5	1.2	0.6	1.4	0.6	1.4
NMSE	1.0	3.4	1.3	6.6	1.2	5.9
<i>R</i>	0.50	0.38	0.55	0.45	0.53	0.42

N denotes ensemble size; mean obs. denotes the observed mean value; mean mod. denotes the modelled mean value; FB denotes the fractional bias; NMSE denotes the normalized mean square error; *R* denotes the Pearson correlation coefficient.

were calculated separately for street canyon locations influenced directly by the traffic and for the courtyard of Sinkule house, which, with respect to traffic, represents an urban background. Similar summary statistics for PM₁₀ are presented in the Supplement (Tables S8, S9).

PALM coupled with a driving mesoscale model has a potential to represent both the magnitude and the temporal evolution of street-level NO_x concentrations and, thus, eliminate the underprediction of the mesoscale model. This is especially true for different types of street canyons, but it is also important to mention that the differences between urban background and street canyon locations are captured well. Variability in PALM 1 h average NO_x concentrations expressed as a standard deviation is about 50 % larger than that of observed data in summer episodes for both street canyon and background locations. In winter episodes, the situation is the opposite. When we check the large PALM overpredictions (e.g. 15 July after sunset, 21 July in the morning, or 25 November after sunrise), these all happen, almost exclusively, when the driving CAMx model gives values within the range of the observations or even largely overestimates

the observations. Similarly, situations when PALM underpredicts the NO_x concentrations happen when the increase in the observed values is not reflected by the driving model, as is the case for the second half of the winter e2 episode. As can be seen from Fig. S17, a strong surface temperature inversion on 28 November at 00:00 UTC and especially at 06:00 UTC is not captured by WRF which, in turn, impacts PALM meteorology (which at least partially reflects the observed inversion) and boundary concentrations.

It is also evident that the simulated NO_x concentrations are closer to the measurements in the summer episodes, especially in the street canyon locations. However, high-resolution modelling of concentrations in winter is more challenging due to local heating and the associated uncertainties of the emissions. The strong simulated peak in the morning of 25 November, which is also present in the CAMx results, does not appear to be present in the measurements at all. A detailed examination of the concentration fields revealed the strong effect of local heating sources as well as an impact from the boundary conditions.

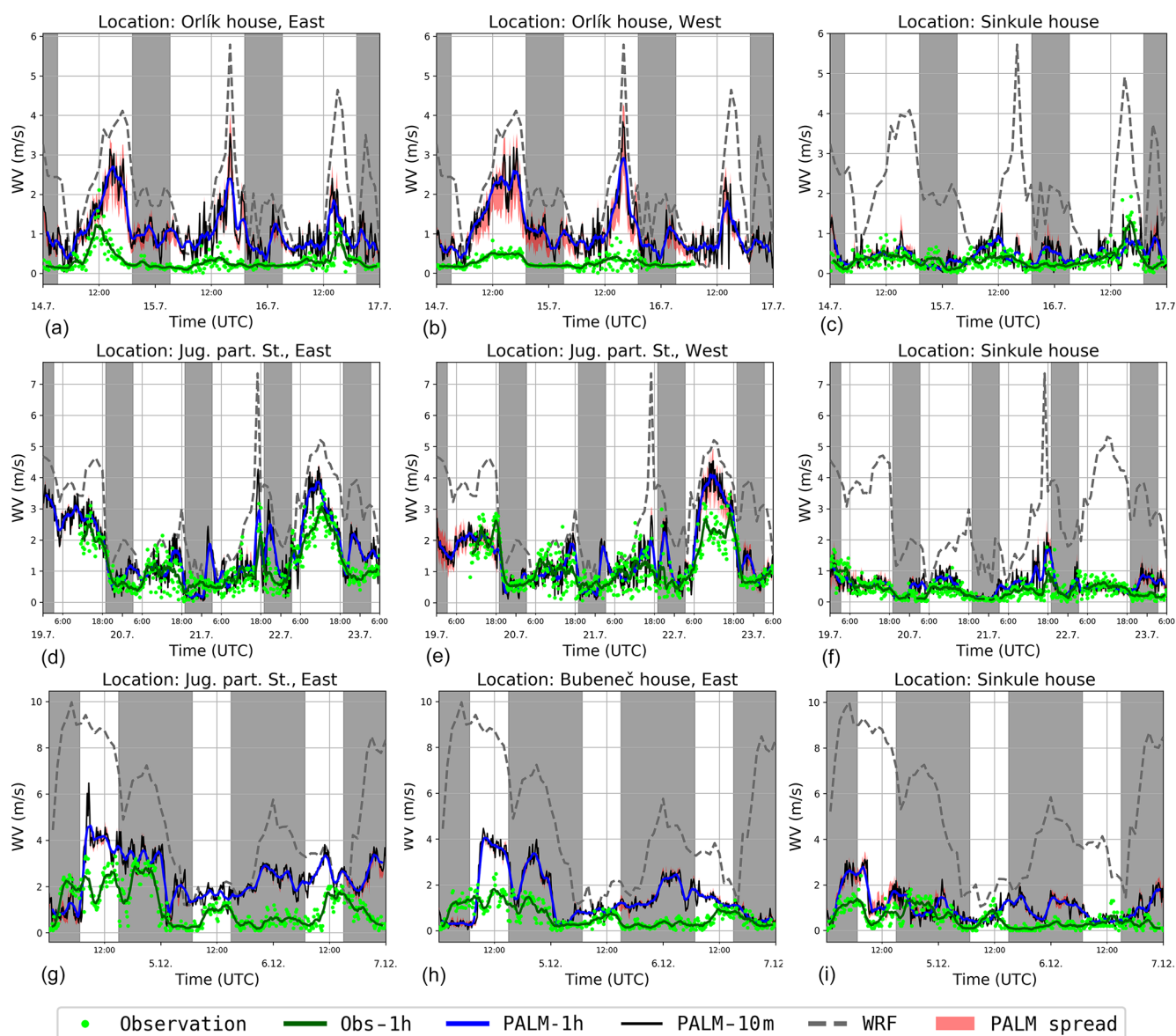


Figure 27. Street canyon wind speed at 10 m (Sinkule house) and 6.8 m (other) for the summer e1 (a, b, c), summer e2 (d, e, f), and winter e3 (g, h, i) episodes. Observations are shown as 10 min averages (green dots) and moving 1 h averages (green line). PALM simulations are shown as moving 1 h averages (blue line), 10 min averages (solid black line), and the interval between the smallest and the largest 10 min average among neighbouring grid points (red band). The grey dashed line denotes 1 h averages at 10 m at the closest WRF grid point. The grey shaded areas indicate night-time.

For PM_{10} , PALM overpredicts observations during winter episodes, and the variability in its outputs is also approx. 50 % larger than in observed data; this is the complete opposite of the case for NO_x .

The PALM metrics for NO_x and PM_{10} computed from all available 1 h concentration averages at all points where measurements were available (not shown) fulfil the criteria for dispersion models as suggested by Chang and Hanna (2004). Although these criteria were developed for simpler models, they are applied to a more complex problem here and are

good indicators of fitness for purpose. More specifically, the absolute value of the fractional bias is less than 0.3, the fraction of predictions within a factor of 2 of the observations is more than 50 %, and the random scatter expressed as geometric variance (VG; not shown in tables) is within a factor of 2 of the mean (i.e. $\text{VG} < 1.6$). These criteria are also fulfilled for data split into summer/winter episodes and street canyon/background locations with the following exceptions: VG is 1.8 for winter background NO_x and no criteria are fulfilled for summer background PM_{10} .

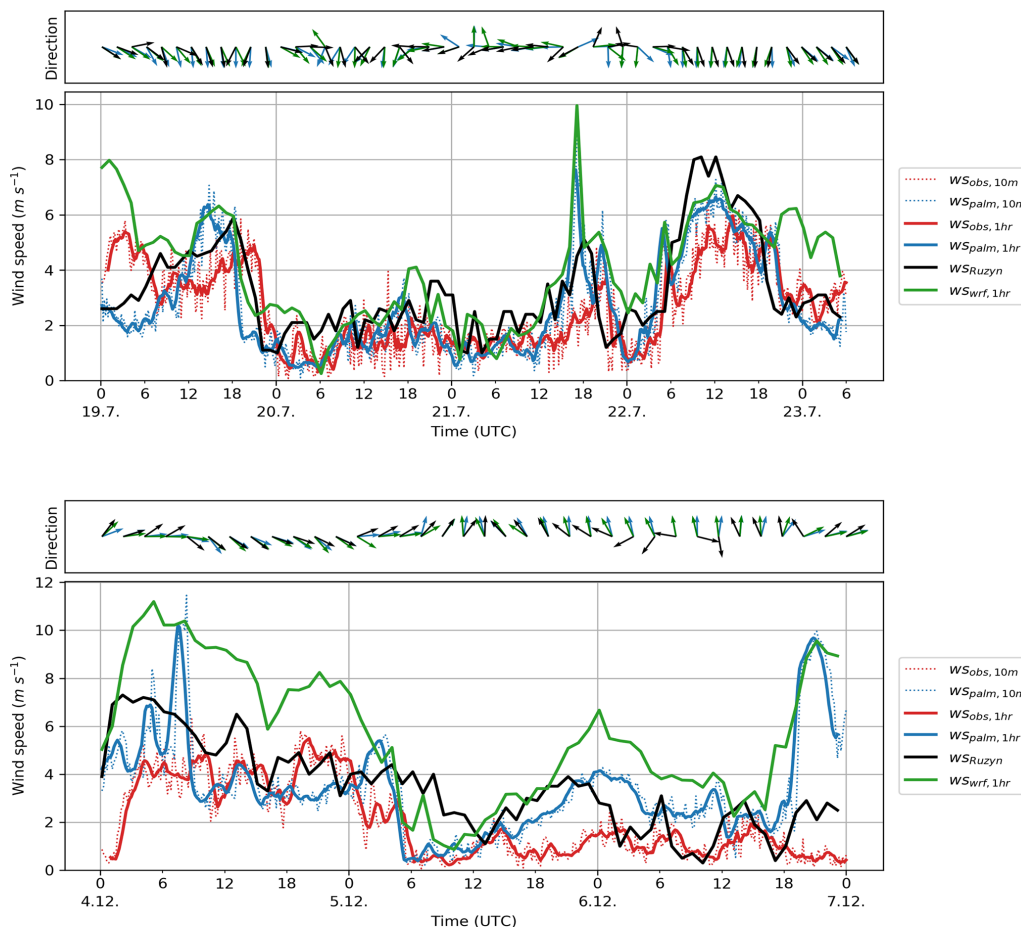


Figure 28. Time series of wind speed and wind direction on the roof of the tallest building of the Faculty of Civil Engineering of the Czech Technical University for the summer e2 (top) and winter e3 (bottom) episodes. The graphs show wind speed, and the boxes of arrows show wind direction. The red colour represents the observations, the blue colour represents the PALM modelled values, the green colour represents values from the WRF model, and the black line represents the values from the nearest synoptic station at Praha-Ruzyně. Thin dotted lines represent 10 min averages, and the thick solid lines are 1 h moving averages of wind speed. The arrows represent 2 h averages of wind direction. PALM model results are taken from the child domain with a 2 m horizontal resolution.

Table 5. Comparison of 1 h average wind speed measured on the rooftop of FSv with WRF and PALM results for the same location.

	Summer episodes		Winter episodes		All episodes	
	PALM	WRF	PALM	WRF	PALM	WRF
<i>N</i>	176	172	219	213	395	385
mean obs. (m s ⁻¹)	2.3	2.3	1.7	1.7	2.0	2.0
mean mod. (m s ⁻¹)	2.5	3.5	2.6	4.1	2.5	3.8
FB	0.07	0.41	0.43	0.85	0.26	0.65
NMSE	0.34	0.47	0.75	1.47	0.54	0.97
<i>R</i>	0.61	0.60	0.43	0.59	0.49	0.52

N denotes ensemble size; mean obs. denotes the observed mean value; mean mod. denotes the modelled mean value; FB denotes the fractional bias; NMSE denotes the normalized mean square error; *R* denotes the Pearson correlation coefficient.

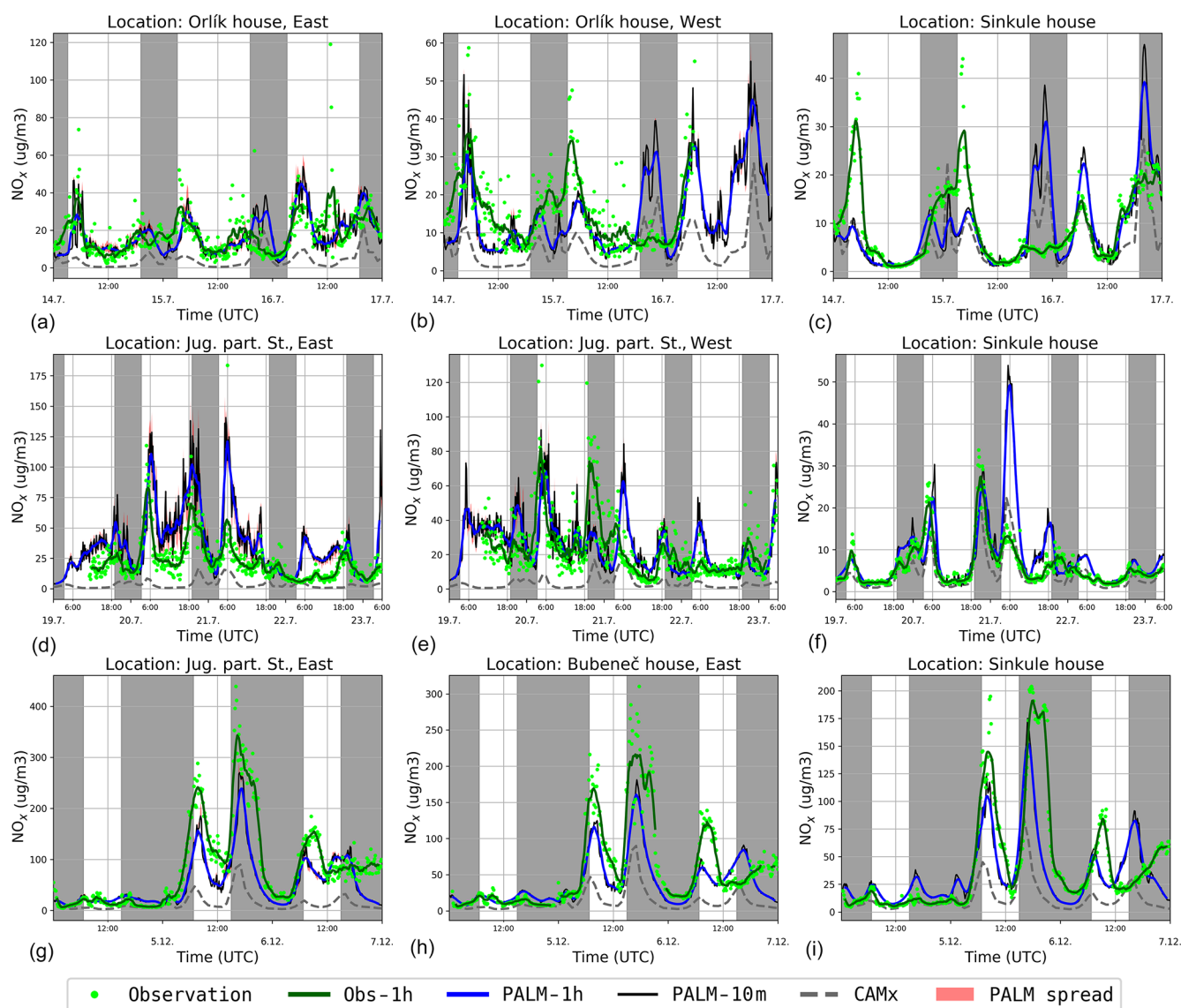


Figure 29. Street canyon NO_x concentrations at 3.9 m (Sinkule house) and 4.6 m (other locations) for the summer e1 (a, b, c), summer e2 (d, e, f), and winter e3 (g, h, i) episodes. Observations are shown as 10 min averages (green dots) and moving 1 h averages (green line). PALM simulations are shown as moving 1 h averages (blue line), 10 min averages (black line), and the interval between the smallest and the largest 10 min average among the neighbouring grid points (red band). The grey dashed line denotes the CAMx 1 h concentration for the lowest level (lowest 50 m above ground) at the closest CAMx grid point. The grey shaded areas indicate night-time.

In addition to the stationary measurements, mobile observations of the air quality indicators were performed (see Sect. 2.3.4 for measurement details and Fig. 1 for placement of the measurement locations). Figure 30 shows graphs comparing observed values of NO_x with modelled values in grid boxes corresponding to the position of the mobile instruments. For the comparison of PM_{10} , see Sect. S5 in the Supplement. The observed NO_x values show quite high variability within the short time frame of the measurements at many locations (variability between 20 and $160 \mu\text{g m}^{-3}$). On the other hand, the oscillations are very small during some other measurements (e.g. location 6–17 on 19 July and partly

location 13 on 4 December). This high variability in some measured values suggests the impact of a very close local emission source (e.g. buses at bus stations or local heating), but this cannot be verified with the data available. Moreover, these oscillations are not present in the PM_{10} observations, which supports the hypothesis of local NO_x sources in contrast to dynamical causes.

During the winter episode, NO_x observations show much higher variability than during the summer episode. During the morning series, modelled values correspond quite well to observations for the most part with the exception of location 11 where the model is 2–5 times lower. The afternoon

Table 6. Comparison of 1 h average NO_x concentrations measured in the street canyons with CAMx and PALM results for the same location.

	Summer episodes		Winter episodes		All episodes	
	PALM	CAMx	PALM	CAMx	PALM	CAMx
<i>N</i>	224	224	363	360	587	584
mean obs. (μg m ⁻³)	22.6	22.6	54.5	54.7	42.3	42.4
mean mod. (μg m ⁻³)	26.2	4.6	42.1	13.9	36.0	10.4
standard deviation obs (μg m ⁻³)	14.9	14.9	56.1	56.3	47.7	47.8
standard deviation mod (μg m ⁻³)	21.8	4.5	33.4	13.8	30.5	12.1
FB	0.1	-1.3	-0.3	-1.2	-0.2	-1.2
NMSE	0.5	5.0	0.8	5.5	0.8	6.4
FAC2	0.70	0.09	0.67	0.20	0.68	0.16
<i>R</i>	0.62	0.29	0.70	0.52	0.70	0.57

N denotes ensemble size; obs. denotes the observed concentration; mod. denotes the modelled value; FB denotes the fractional bias; NMSE denotes the normalized mean square error; FAC2 denotes the fraction of predictions within a factor of 2 of the observations; *R* denotes the Pearson correlation coefficient.

Table 7. Comparison of 1 h average NO_x concentrations measured in the Sinkule yard with CAMx and PALM results for the same location.

	Summer episodes		Winter episodes		All episodes	
	PALM	CAMx	PALM	CAMx	PALM	CAMx
<i>N</i>	130	130	200	197	330	327
mean obs. (μg m ⁻³)	8.6	8.6	33.9	34.2	23.9	24.0
mean mod. (μg m ⁻³)	9.6	5.7	35.5	13.6	25.3	10.5
standard deviation obs. (μg m ⁻³)	7.1	7.1	39.1	39.3	33.1	33.2
standard deviation mod. (μg m ⁻³)	9.5	5.5	29.5	12.7	26.9	11.1
FB	0.1	-0.4	0.0	-0.9	0.1	-0.8
NMSE	0.9	0.8	1.0	3.7	1.2	4.2
FAC2	0.78	0.60	0.66	0.49	0.71	0.53
<i>R</i>	0.50	0.62	0.54	0.39	0.61	0.47

N denotes ensemble size; obs. denotes the observed concentration; mod. denotes the modelled value; FB denotes the fractional bias; NMSE denotes the normalized mean square error; FAC2 denotes the fraction of predictions within a factor of 2 of the observations; *R* denotes the Pearson correlation coefficient.

series shows good agreement at locations 2, 3, 4, 13, and 14. At locations 10 and 11, the model results are again consistently lower than observations.

6 Summary and conclusions

6.1 Summary of the results

In this study, PALM LES simulations driven by mesoscale WRF and CAMx simulations were performed for a real urban environment in Dejvice, Prague, the Czech Republic. Modelled meteorological, air quality, and surface quantities were compared against in situ measurements taken during a specially designed observation campaign.

The PALM model properly adjusts to the temporally evolving WRF and CAMx conditions and simulates the temporal evolution and daily amplitude of street canyon quantities in most cases, with some noticeable exceptions such as insufficient night-time cooling under some conditions. How-

ever, correct results depend on proper driving conditions as well as on the correct setting of the urban canopy properties in the model and the spatial and temporal distribution of emissions. The importance of the urban canopy properties was demonstrated in many particular cases. It was also shown that the driving WRF model does not perfectly reproduce the observations, resulting in discrepancies in the wind speed and potential temperature propagating into the PALM solution via the boundary conditions given by WRF.

Concentrations of NO_x were modelled well in some situations and PALM properly adds a local air pollution increment to the urban background values provided by the CAMx simulation, although the model overestimates the concentrations of NO_x for some places and times (mainly around sunset or sunrise). This is probably related to atmospheric stability and uncertainties in modelling stably stratified turbulent flow. The opposite situation (i.e. the underestimation of NO_x) occurs less often. These discrepancies could be partially attributed to uncertainties of the emissions and imperfection in boundary conditions provided by WRF and CAMx, al-

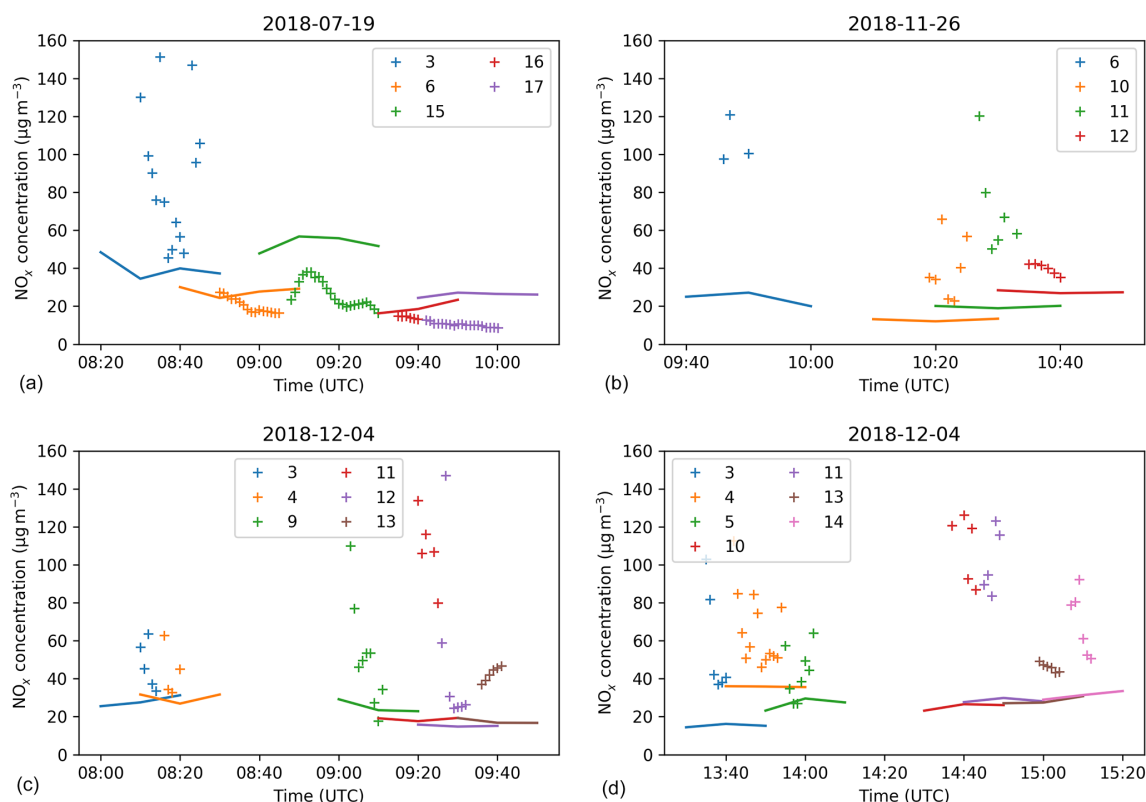


Figure 30. Mobile NO_x measurements (+ markers) and modelled concentrations (solid lines) for the morning of 19 July (a), the morning of 26 November (b), the morning of 4 December (c), and the afternoon of 4 December (d). Numbers refer to mobile measurement locations according to Fig. 1.

though another probable cause is PALM misrepresenting the turbulent flow under some meteorological conditions. This issue needs further investigation. PM_{10} concentrations were modelled less accurately than NO_x , which can be mainly attributed to the driving model and overestimated emissions of resuspended dust.

The modelled surface temperature agrees reasonably well with the observed one at most of the surface EPs. However, it is striking that the agreement is usually better for the summer episodes when strong radiative forcing exists than for the winter episodes when the model results are more prone to uncertain specification of material properties as well as inaccuracies in atmospheric conditions from the driving mesoscale model. The surface temperature of pavement surfaces and of wall surfaces belonging to traditional buildings based on bricks or building blocks is usually modelled well, whereas the surface temperature of modern buildings with multilayer prefabricated walls is captured less accurately. At low-vegetated ground surfaces, the modelled surface temperature also agrees well with the observation, even though we note that the model results strongly depend on a proper description of initial soil moisture and probably on other soil parameters. In addition to an accurate prescription of surface-material parameters, an accurate representation of

the LAD is also essential for accurate modelling of the local atmosphere–surface exchange. Even though this study contains some indicative sensitivity investigations for the studied domain and episodes, we note that a systematic sensitivity study on the model input parameters is outside the scope of this paper; thus, the reader is referred to Belda et al. (2021).

6.2 Lessons learnt and outlook for future improvements

This study also points towards particular aspects in the model, its configuration, the input data preparation, and the observation strategy that deserve particular focus in the future.

The current version of the PALM input standard (PIDS) and implementation of BSM allows discretization of the walls into four layers, independent of the thickness and the structure of the real wall, meaning that the grid resolution of the wall layers may differ among different wall surfaces. Further, wall material properties for complex walls with multiple layers are sometimes not well captured by only four wall layers, leading to under- or overestimation of the thickness of the insulating layer, among other discrepancies. A variable number of wall layers would allow more realistic representation of wall material properties. Moreover, prespecified typ-

ical structures of complex wall compositions in BSM would simplify proper initialization of these walls.

The current method of discretization of terrain and buildings in PALM is bound to the Cartesian model grid, which means that the entire volume of each grid cell contains either atmosphere or obstacle. If the modelled domain contains uneven terrain, sloped roofs, or walls that are not parallel to the grid axes, the discretization creates artificial steps which affect radiative fluxes as well as the airflow. Such step-like surfaces on facades create both artificially shaded and artificially sunlit surfaces which also affect the energy balance of the facade. Even though these effects are strongest locally, they can also bias the aggregated values for larger surface areas. A major change of discretization is planned for future versions of the PALM model in which the representation of arbitrarily oriented surfaces will be allowed for all PALM surface-related processes, thereby avoiding the creation of artificial steps.

In the current version of the radiative transfer model (RTM), all surfaces are considered as Lambertian reflectors, meaning that directional reflection at windows or polished materials cannot be considered, even though such reflection can be found at almost every facade. This, in turn, adds uncertainty to the surface net radiation and, thus, to the energy balance at the surrounding surfaces. Implementation of specular reflection is planned to better simulate the radiative transfer at glass and polished surfaces.

The analysis of air and surface temperatures revealed insufficient nocturnal air cooling under certain meteorological conditions where the stratification is not captured properly by the model. In this study, the incoming radiation is explicitly prescribed, while radiative cooling of the air volume itself is not considered. Hence, in order to check how sensitive the model results are to this, test simulations where we applied the RRTMG radiation scheme and where radiative cooling of the air volume is considered were run; however, we observed a similar insufficient cooling in this case. This insufficient nocturnal cooling requires further future investigation.

Another implication arises from the mesoscale nesting approach. The analysis of the wind speeds at higher levels and the analysis of temperatures revealed that PALM partly reflects the conditions simulated by the mesoscale model (WRF), especially during wintertime. Thus, the error made on the mesoscale is propagated into the LES, biasing its simulation results. To minimize this mesoscale forcing bias on the LES results, the driving mesoscale conditions might be further combined with additional nudging terms inferred from observations, continuously nudging the imposed boundary conditions for the LES towards the observations.

The study suggests strong sensitivity of the results to the accuracy of input data, such as the wall-material properties and the structure of tree crowns. The sensitivity of PALM to material parameters is more systematically investigated in Belda et al. (2021). Bulk parameters prescribed for certain building categories might strongly deviate from the actual

conditions at the building. Hence, the usage of bulk input parameters might significantly modify the simulation results locally. Other detailed observations are needed to improve properties of the wall, roof, and pavement material categories. The study also stresses the need for correct setting of the initial soil moisture for low-vegetation surfaces.

The experimental campaign also serves as a source of useful experience for future studies of similar type. Modern buildings with high amounts of glass and other reflective exterior surfaces proved to be challenging for surface temperature measurements using an IR camera. The reflections often obscure the emitted thermal radiation from the surface; thus, the IR camera does not provide a reliable way to observe surface temperature for such surfaces.

Data from mobile measurement vehicles proved to be difficult to interpret and difficult to draw statistically relevant conclusions from due to the influence of the strong local temporally and spatially evolving emissions, which are difficult to simulate in the emission model. In future, either a significantly higher number of measurements would be required or the effort should be concentrated elsewhere. One direction for consideration is a combination of traditionally comprehensive vehicle-observation stations with a wider network of more limited sensors.

Although drones, at first sight, offer another promising direction, drone measurements in a city are unfortunately limited by various restrictions imposed by the air traffic control and land owners. The entire city of Prague is located in controlled airspace starting at ground level and including our area of interest. Other requirements for useful drone observations are matching height and speed changes to instrumentation characteristics, such as relaxation time. Preparatory test flights in consultation with the drone operator may be necessary. Regular balloon soundings from the Praha-Libuš station proved to be indispensable. In future, increasing the frequency of measurements during a measurement campaign would be very useful, and the possibility of dedicated soundings in the area of interest should be considered. However, this is also limited by restrictions similar to those on drone observations.

In summary, the ability of PALM to represent reality to a reasonable degree depends not just on the representation of physical processes in the model itself, but on input-data quality and the accuracy of the mesoscale forcing. Thus, for future studies, it is valid to question where the focus should lie: should it be on further improving the model to better reflect physical processes in the urban boundary layer, or should it be on obtaining as accurate and detailed input data as possible. In the authors' opinion, however, these options are not mutually exclusive but have to be balanced against each other. Focusing mainly on the input data will sooner or later result in a situation where the model performance is constrained by an insufficient representation of the physics, and a model with perfect physical processes will still need very good and detailed input data to produce practically rel-

evant output. The task of attributing the relative importance of these sources of uncertainty has been extensively tested in the field of numerical weather prediction and climate modelling in a number of coordinated projects producing large ensembles of simulations, including the currently ongoing CMIP6 (Eyring et al., 2016) and CORDEX (Giorgi et al., 2009; Gutowski et al., 2016) projects. In our case, a similar approach of employing different models and model setups as well as testing their respective sensitivity to input data would allow assessment of the sources of uncertainty. However, due to the enormous computational resources required for these kinds of simulations, such an endeavour is not feasible for one modelling team and it would benefit from the kind of framework of coordinated experiments that are a norm in the climate modelling community.

Appendix A: Statistical measures used in the paper

Apart from the means and standard deviations of observed and modelled values, the following normalized statistics are used to summarize model performance. Please note that we adopted the convention that bias is positive when the model overestimates observations.

The factor of 2 (FAC2) refers to the fraction of predictions within a factor of 2 of the observations.

The fractional bias is calculated as follows:

$$FB_X = 2 \cdot \frac{\overline{X_{\text{model}} - X_{\text{obs}}}}{\overline{X_{\text{model}} + X_{\text{obs}}}}$$

The normalized mean square error is calculated as follows:

$$NMSE_X = \frac{\overline{(X_{\text{model}} - X_{\text{obs}})^2}}{\overline{X_{\text{model}} \cdot X_{\text{obs}}}}$$

For temperature (in °C) the following non-normalized statistics were used:

the mean bias, calculated as

$$MB = \overline{T_{\text{model}} - T_{\text{obs}}};$$

the mean absolute bias, calculated as

$$MAB = \overline{|T_{\text{model}} - T_{\text{obs}}|};$$

and the root mean square error, calculated as

$$RMSE = \sqrt{\overline{(T_{\text{model}} - T_{\text{obs}})^2}}.$$

Code and data availability. The PALM model system is freely available from <http://palm-model.org> (PALM, 2021) and is distributed under the GNU General Public Licence v3 (<http://www.gnu.org/copyleft/gpl.html>, last access: 28 June 2021). The model source code version 6.0 in revision r4508 used in this article is also available from <https://doi.org/10.25835/0073713> (Resler et al., 2020a). The configurations and inputs of the model for all simulated episodes are available from <http://hdl.handle.net/11104/0315416> (Resler et al., 2020b).

Supplement. The supplement related to this article is available online at: <https://doi.org/10.5194/gmd-14-4797-2021-supplement>.

Author contributions. JR coordinated the study, led the UrbiPragensi KK4 concept, and leads the TURBAN project. OV coordinated the observation campaign. JKe, OV, JR, and MB designed the observation campaign. OV, JR, JG, KE, PK, MB, VF, PH, JKa, JD, TH, KH, and JKe realized the observation campaign. OV, KH, SN, JR, JG, PK, MR, MB, and VF carried out the observation post-processing. JG, JR, PK, OV, and NB carried out the urban input data collection and processing. KE, PH, MB, JK, JR, PK, OV, NB, and JD undertook the WRF and CAMx simulations and their processing. JR, MS, PK, and VF carried out the PALM model development and testing. JR, MS, and PK were responsible for the PALM simulations' configuration and model runs. JR, JG, MR, PK, MB, VF, and OV post-processed the results and were responsible for visualization of the results. MS, MB, VF, OV, PH, and JKe provided their meteorology and air quality expertise. All co-authors contributed to the text and to revisions of the paper.

Competing interests. The authors declare that they have no conflict of interest.

Disclaimer. Publisher's note: Copernicus Publications remains neutral with regard to jurisdictional claims in published maps and institutional affiliations.

Acknowledgements. Financial support was provided by the Operational Program Prague – Growth Pole of the Czech Republic project “Urbanization of weather forecast, air-quality prediction and climate scenarios for Prague” (Urbi Pragensi; grant no. CZ.07.1.02/0.0/0.0/16_040/0000383, <http://www.urbipragensi.cz>, last access: 27 July 2021), which is co-financed by the EU. Matthias Sühling was supported by the Federal German Ministry of Education and Research (BMBF; grant no. 01LP1601) within the framework of “Research for Sustainable Development” (FONA; <https://www.fona.de>, last access: 28 June 2021). Financial support was also provided by the Norway Grants and Technology Agency of the Czech Republic “Turbulent-resolving urban modelling of air quality and thermal comfort” project (TURBAN, project no. TO01000219, <https://www.project-turban.eu>, last access: 27 July 2021).

The terrain mapping campaign of building properties was co-financed by the Strategy AV21 project “Energy interactions of

buildings and the outdoor urban environment”, which is financed by the Czech Academy of Sciences. We would like to thank Jiří Cajthaml and students of the Faculty of Civil Engineering of the Czech Technical University in Prague for their help with the terrain mapping campaign.

We would also like to thank the Global Change Research Institute (CzechGlobe) for providing the IR camera, Ivana Hájíčková for enabling the HF measurements in Zelená Street, and the Czech Technical University (Lenka Bedrníková and Josef Šteffel) for enabling us to perform the heat flux measurement at Sinkule house and the wind measurements on the rooftop of the Faculty of Civil Engineering of CTU.

We would like to acknowledge our colleagues who organized and carried out the measurements during the observation campaign but are not authors of this article: Zdeněk Běčák, Petr Goll, Jan Kufel, and Luboš Vrána (monitoring vehicles); Petra Bauerová, Jan Hadinger, Zdeněk Proškovec, and Hana Škáčková (mobile and rooftop wind measurement); Jana Řadová and Michal Žák (IR measurements); and Jiří Gajdoš (technician). We are also grateful to our colleague Martin Glew for language revision of the text.

The PALM simulations and pre- and post-processing were performed on the HPC infrastructure of the Institute of Computer Science of the Czech Academy of Sciences (ICS) supported by the long-term strategic development financing of the ICS (RVO:67985807). Part of the simulations was performed on the supercomputer of the Czech supercomputing centre IT4I, which was supported by the Ministry of Education, Youth and Sports from the Large Infrastructures for Research, Experimental Development and Innovations project “IT4Innovations National Supercomputing Center – LM2015070”, and on the supercomputers of the North German Supercomputing Alliance (HLRN). The WRF and CAMx simulations were carried out on the HPC infrastructure of the Department of Atmospheric Physics of the Faculty of Mathematics and Physics of the Charles University in Prague, which was supported by the Operational Program Prague – Growth Pole of the Czech Republic project “Urbanization of weather forecast, air-quality prediction and climate scenarios for Prague” (grant no. CZ.07.1.02/0.0/0.0/16_040/0000383), which is co-financed by the EU.

Financial support. This research has been supported by the European Structural and Investment Funds (grant no. CZ.07.1.02/0.0/0.0/16_040/0000383), the Federal German Ministry of Education and Research (grant no. 01LP1601A), and the Norway Grants and Technology Agency of the Czech Republic (grant no. TO01000219).

Review statement. This paper was edited by Ignacio Pizzo and reviewed by two anonymous referees.

References

- Belda, M., Resler, J., Geletič, J., Krč, P., Maronga, B., Sühling, M., Kurppa, M., Kanani-Sühling, F., Fuka, V., Eben, K., Benešová, N., and Auvinen, M.: Sensitivity analysis of the PALM model

- system 6.0 in the urban environment, *Geosci. Model Dev.*, 14, 4443–4464, <https://doi.org/10.5194/gmd-14-4443-2021>, 2021.
- Bougeault, P. and Lacarrère, P.: Parameterization of Orography-Induced Turbulence in a Mesobeta-Scale Model, *Mon. Weather Rev.*, 117, 1872–1890, [https://doi.org/10.1175/1520-0493\(1989\)117<1872:POOITI>2.0.CO;2](https://doi.org/10.1175/1520-0493(1989)117<1872:POOITI>2.0.CO;2), 1989.
- Briscolini, M., and Santangelo, P.: Development of the mask method for incompressible unsteady flows, *J. Comp. Phys.*, 84, 57–75, [https://doi.org/10.1016/0021-9991\(89\)90181-2](https://doi.org/10.1016/0021-9991(89)90181-2), 1989.
- Britter, R. and Schatzmann, M.: Model Evaluation Guidance and Protocol Document, COST Office Brussels, Brussels/Belgium, 28 pp., ISBN 3-00-018312-4, 2007.
- Brugger, P., Banerjee, T., De Roo, F., Kröniger, K., Qubaja, R., Rohatyn, S., Rotenberg, E., Tatarinov, F., Yakir, D., Yang, F., and Mauder, M.: Effect of Surface Heterogeneity on the Boundary-Layer Height: A Case Study at a Semi-Arid Forest, *Bound.-Lay. Meteorol.*, 169, 233–250, <https://doi.org/10.1007/s10546-018-0371-5>, 2018.
- Builtjes, P. J. H., van Loon, M., Schaap, M., Teeuwse, S., Visschedijk, A. J. H., and Bloos, J. P.: Project on the modelling and verification of ozone reduction strategies: contribution of TNO-MEP. TNO-report, MEP-R2003/166, Apeldoorn, Netherlands, 2003.
- Byun, D. W.: Dynamically Consistent Formulations in Meteorological and Air Quality Models for Multiscale Atmospheric Studies. Part II: Mass Conservation Issues, *J. Atmos. Sci.*, 56, 3808–3820, [https://doi.org/10.1175/1520-0469\(1999\)056<3808:DCFIMA>2.0.CO;2](https://doi.org/10.1175/1520-0469(1999)056<3808:DCFIMA>2.0.CO;2), 1999.
- Carslaw, D. C. and Ropkins, K.: openair – an R package for air quality data analysis, *Environ. Modell. Softw.*, 27–28, 52–61, <https://doi.org/10.1016/j.envsoft.2011.09.008>, 2012.
- Chang, J. and Hanna, S.: Air quality model performance evaluation, *Meteorol. Atmos. Phys.*, 87, 167–196, <https://doi.org/10.1007/s00703-003-0070-7>, 2004.
- Chen, F. and Dudhia, J.: Coupling an advanced land-surface/hydrology model with the Penn State/ NCAR MM5 modeling system. Part I: Model description and implementation, *Mon. Weather Rev.*, 129, 569–585, [https://doi.org/10.1175/1520-0493\(2001\)129<0569:CAALSH>2.0.CO;2](https://doi.org/10.1175/1520-0493(2001)129<0569:CAALSH>2.0.CO;2), 2001.
- Ching, J., Rotunno, R., LeMone, M., Martilli, A., Kosovic, B., Jimenez, P. A., and Dudhia, J.: Convectively Induced Secondary Circulations in Fine-Grid Mesoscale Numerical Weather Prediction Models, *Mon. Weather Rev.*, 142, 3284–3302, <https://doi.org/10.1175/MWR-D-13-00318.1>, 2014.
- ČHMÚ (Czech Hydrometeorological Institute): Measurements of air quality and micrometeorology in street canyons in Prague 6 – Dejvice, 2018. Campaign within the Urbi Pragensis project financed from the Operational Programme Prague – Growth Pole of the Czech Republic, project No. CZ.07.1.02/0.0/0.0/16_040/0000383, ČHMÚ’s Technical document No. TD 000129, Prague, Czech Rep., 2020.
- ČÚZK (Czech Office for Surveying, Mapping and Cadastre): GeoPortal Datasets (ZABAGED and orthophoto), available at: [https://geoportal.cuzk.cz/\(S\(hwwp4jhepqmkrmonodglvjwu\)\)/Default.aspx?lng=EN&head_tab=sekce-02-gp&mode=TextMeta&text=dSady_uvod&menu=20](https://geoportal.cuzk.cz/(S(hwwp4jhepqmkrmonodglvjwu))/Default.aspx?lng=EN&head_tab=sekce-02-gp&mode=TextMeta&text=dSady_uvod&menu=20) (last access: 28 June 2021), 2020.
- Deardorff, J. W.: Stratocumulus-capped mixed layers derived from a three-dimensional model, *Bound.-Lay. Meteorol.*, 18, 495–527, <https://doi.org/10.1007/BF00119502>, 1980.
- Denier van der Gon, H., Hendriks, C., Kuenen, J., Segers, A., and Visschedijk, A.: Description of current temporal emission patterns and sensitivity of predicted AQ for temporal emission patterns. EU FP7 MACC deliverable report D_D-EMIS_1.3, available at: https://atmosphere.copernicus.eu/sites/default/files/2019-07/MACC_TNO_del_1_3_v2.pdf (last access: 28 June 2021), 2011.
- Ďoubalová, J., Huszár, P., Eben, K., Benešová, N., Belda, M., Vlček, O., Karlický, J., Geletič, J., and Halenka, T.: High Resolution Air Quality Forecasting Over Prague within the URBI PRAGENSI Project: Model Performance During the Winter Period and the Effect of Urban Parameterization on PM, *Atmosphere*, 11, 625, <https://doi.org/10.3390/atmos11060625>, 2020.
- ENVIRON, CAMx User’s Guide, Comprehensive Air Quality model with Extensions, version 6.50, Novato, California, available at: <https://www.camx.com>, (last access: 28 June 2021), 2018.
- Eyring, V., Bony, S., Meehl, G. A., Senior, C. A., Stevens, B., Stouffer, R. J., and Taylor, K. E.: Overview of the Coupled Model Intercomparison Project Phase 6 (CMIP6) experimental design and organization, *Geosci. Model Dev.*, 9, 1937–1958, <https://doi.org/10.5194/gmd-9-1937-2016>, 2016.
- FLIR: FLIR SC660 R and D INFRARED CAMERA SYSTEM, Product leaflet, available at: <https://www.flir.eu/support/products/t660> (last access: 28 June 2021), 2008.
- Gehrke, K. F., Sühling, M., and Maronga, B.: Modeling of land-surface interactions in the PALM model system 6.0: Land surface model description, first evaluation, and sensitivity to model parameters, *Geosci. Model Dev. Discuss.* [preprint], <https://doi.org/10.5194/gmd-2020-197>, in review, 2020.
- Geletič, J., Lehnert, M., Savić, S., and Milošević, D.: Modelled spatiotemporal variability of outdoor thermal comfort in local climate zones of the city of Brno, Czech Republic, *Sci. Total Environ.*, 624, 385–395, <https://doi.org/10.1016/j.scitotenv.2017.12.076>, 2018.
- Geletič, J., Lehnert, M., Krč, P., Resler, J., and Krayenhoff, E. S.: High-Resolution Modelling of Thermal Exposure during a Hot Spell: A Case Study Using PALM-4U in Prague, Czech Republic, *Atmosphere*, 12, 175, <https://doi.org/10.3390/atmos12020175>, 2021.
- Giorgi, F., Jones, C., and Asrar, G.: Addressing climate information needs at the regional level: the CORDEX framework, *WMO Bulletin*, 58, 175–183, 2009.
- Gutowski Jr., W. J., Giorgi, F., Timbal, B., Frigon, A., Jacob, D., Kang, H.-S., Raghavan, K., Lee, B., Lennard, C., Nikulin, G., O’Rourke, E., Rixen, M., Solman, S., Stephenson, T., and Tangang, F.: WCRP COordinated Regional Downscaling EXperiment (CORDEX): a diagnostic MIP for CMIP6, *Geosci. Model Dev.*, 9, 4087–4095, <https://doi.org/10.5194/gmd-9-4087-2016>, 2016.
- Halenka, T., Belda, M., Huszar, P., Karlicky, J., Novakova, T., and Zak, M.: On the comparison of urban canopy effects parameterisation, *Int. J. Environ. Pollut.*, 65, 1–3, <https://doi.org/10.1504/IJEP.2019.101840>, 2019.
- Heldens, W., Burmeister, C., Kanani-Sühling, F., Maronga, B., Pavlik, D., Sühling, M., Zeidler, J., and Esch, T.: Geospatial input

- data for the PALM model system 6.0: model requirements, data sources and processing, *Geosci. Model Dev.*, 13, 5833–5873, <https://doi.org/10.5194/gmd-13-5833-2020>, 2020.
- Hellsten, A., Ketelsen, K., Sühling, M., Auvinen, M., Maronga, B., Knigge, C., Barmpas, F., Tsegas, G., Moussiopoulos, N., and Raasch, S.: A nested multi-scale system implemented in the large-eddy simulation model PALM model system 6.0, *Geosci. Model Dev.*, 14, 3185–3214, <https://doi.org/10.5194/gmd-14-3185-2021>, 2021.
- Hong, S.-Y., Noh, Y., and Dudhia, J.: A new vertical diffusion package with an explicit treatment of entrainment processes, *Mon. Weather Rev.*, 134, 2318–2341, <https://doi.org/10.1175/MWR3199.1>, 2006.
- Hukseflux: TRSYS01 heat flux measuring system, available at: <https://www.hukseflux.com/products/heat-flux-sensors/heat-flux-measuring-systems/trsys01-heat-flux-measuring-system> (last access: 28 June 2021), 2020.
- Huszár, P., Karlický, J., Belda, M., Halenka, T., and Pišoft, P.: The impact of urban canopy meteorological forcing on summer photochemistry, *Atmos. Environ.*, 176, 209–228, <https://doi.org/10.1016/j.atmosenv.2017.12.037>, 2018a.
- Huszár, P., Belda, M., Karlický, J., Bardachova, T., Halenka, T., and Pišoft, P.: Impact of urban canopy meteorological forcing on aerosol concentrations, *Atmos. Chem. Phys.*, 18, 14059–14078, <https://doi.org/10.5194/acp-18-14059-2018>, 2018b.
- Huszár, P., Karlický, J., Ďoubalová, J., Šindelářová, K., Nováková, T., Belda, M., Halenka, T., Žák, M., and Pišoft, P.: Urban canopy meteorological forcing and its impact on ozone and PM_{2.5}: role of vertical turbulent transport, *Atmos. Chem. Phys.*, 20, 1977–2016, <https://doi.org/10.5194/acp-20-1977-2020>, 2020a.
- Huszár, P., Karlický, J., Ďoubalová, J., Nováková, T., Šindelářová, K., Švábik, F., Belda, M., Halenka, T., and Žák, M.: The impact of urban land-surface on extreme air pollution over central Europe, *Atmos. Chem. Phys.*, 20, 11655–11681, <https://doi.org/10.5194/acp-20-11655-2020>, 2020b.
- Iacono, M. J., Delamere, J. S., Mlawer, E. J., Shephard, M. W., Clough, S. A., and Collins, W. D.: Radiative forcing by long-lived greenhouse gases: Calculations with the AER radiative transfer models, *J. Geophys. Res.*, 113, D13103, <https://doi.org/10.1029/2008JD009944>, 2008.
- IPCC: Climate Change 2014: Impacts, Adaptation, and Vulnerability. Part A: Global and Sectoral Aspects. Contribution of Working Group II to the Fifth Assessment Report of the Intergovernmental Panel on Climate Change, edited by: Field, C. B., Barros, V. R., Dokken, D. J., Mach, K. J., Mastrandrea, M. D., Bilir, T. E., Chatterjee, M., Ebi, K. L., Estrada, Y. O., Genova, R. C., Girma, B., Kissel, E. S., Levy, A. N., MacCracken, S., Mastrandrea, P. R., and White, L. L., Cambridge University Press, Cambridge, United Kingdom and New York, NY, USA, 1132 pp., <https://doi.org/10.1017/CBO9781107415379>, 2014a.
- IPCC: Climate Change 2014: Mitigation of Climate Change. Contribution of Working Group III to the Fifth Assessment Report of the Intergovernmental Panel on Climate Change, edited by: Edenhofer, O., Pichs-Madruga, R., Sokona, Y., Farahani, E., Kadner, S., Seyboth, K., Adler, A., Baum, I., Brunner, S., Eickmeier, P., Kriemann, B., Savolainen, J., Schlömer, S., von Stechow, C., Zwickel, T., and Minx, J. C., Cambridge University Press, Cambridge, United Kingdom and New York, NY, USA, <https://doi.org/10.1017/CBO9781107415416>, 2014b.
- Kadasch, E., Sühling, M., Gronemeier, T., and Raasch, S.: Mesoscale nesting interface of the PALM model system 6.0, *Geosci. Model Dev. Discuss.* [preprint], <https://doi.org/10.5194/gmd-2020-285>, in review, 2020.
- Khan, B., Banzhaf, S., Chan, E. C., Forkel, R., Kanani-Sühling, F., Ketelsen, K., Kurppa, M., Maronga, B., Mauder, M., Raasch, S., Russo, E., Schaap, M., and Sühling, M.: Development of an atmospheric chemistry model coupled to the PALM model system 6.0: implementation and first applications, *Geosci. Model Dev.*, 14, 1171–1193, <https://doi.org/10.5194/gmd-14-1171-2021>, 2021.
- Krč, P., Resler, J., Sühling, M., Schubert, S., Salim, M. H., and Fuka, V.: Radiative Transfer Model 3.0 integrated into the PALM model system 6.0, *Geosci. Model Dev.*, 14, 3095–3120, <https://doi.org/10.5194/gmd-14-3095-2021>, 2021.
- Lee, G.-J., Muñoz-Esparza, D., Yi, Ch., and Choe, H. J.: Application of the Cell Perturbation Method to Large-Eddy Simulations of a Real Urban Area, *J. Appl. Meteorol. Clim.*, 58, 1125–1139, <https://doi.org/10.1175/JAMC-D-18-0185.1>, 2018.
- Lemonsu, A., Bélair, S., Mailhot, J., Benjamin, M., Morneau, G., Harvey, B., Chagnon, F., Jean, M., and Voogt, J.: Overview and First Results of the Montreal Urban Snow Experiment 2005, *J. Appl. Meteorol. Clim.*, 47, 59–75, <https://doi.org/10.1175/2007JAMC1639.1>, 2008.
- Liu, Y. S., Miao, S. G., Zhang, C. L., Cui, G. X., and Zhang, Z. S.: Study on micro-atmospheric environment by coupling large eddy simulation with mesoscale model, *J. Wind Eng. Ind. Aerod.*, 107–108, 106–117, <https://doi.org/10.1016/j.jweia.2012.03.033>, 2012.
- Maggiotto, G., Buccolieri, R., Santo, M. A., Leo, L. S., and Di Sabatino, S.: Validation of temperature-perturbation and CFD-based modelling for the prediction of the thermal urban environment, *Environ. Modell. Softw.*, 60, 69–83, <https://doi.org/10.1016/j.envsoft.2014.06.001>, 2014.
- Maronga, B., Gryscha, M., Heinze, R., Hoffmann, F., Kanani-Sühling, F., Keck, M., Ketelsen, K., Letzel, M. O., Sühling, M., and Raasch, S.: The Parallelized Large-Eddy Simulation Model (PALM) version 4.0 for atmospheric and oceanic flows: model formulation, recent developments, and future perspectives, *Geosci. Model Dev.*, 8, 2515–2551, <https://doi.org/10.5194/gmd-8-2515-2015>, 2015.
- Maronga, B., Banzhaf, S., Burmeister, C., Esch, T., Forkel, R., Fröhlich, D., Fuka, V., Gehrke, K. F., Geletič, J., Giersch, S., Gronemeier, T., Groß, G., Heldens, W., Hellsten, A., Hoffmann, F., Inagaki, A., Kadasch, E., Kanani-Sühling, F., Ketelsen, K., Khan, B. A., Knigge, C., Knoop, H., Krč, P., Kurppa, M., Maamari, H., Matzarakis, A., Mauder, M., Pallasch, M., Pavlik, D., Pfäfferott, J., Resler, J., Rissmann, S., Russo, E., Salim, M., Schrempf, M., Schwenkel, J., Seckmeyer, G., Schubert, S., Sühling, M., von Tils, R., Vollmer, L., Ward, S., Witha, B., Wurps, H., Zeidler, J., and Raasch, S.: Overview of the PALM model system 6.0, *Geosci. Model Dev.*, 13, 1335–1372, <https://doi.org/10.5194/gmd-13-1335-2020>, 2020.
- Masson, V., Gomes, L., Pigeon, G., Lioussé, C., Pont, V., Lagouarde, J.-P., Voogt, J., Salmond, J., Oke, T. R., Hidalgo, J., Legain, D., Garrouste, O., Lac, C., Connan, O., Briottet X., and Lachéradé, S.: The Canopy and Aerosol Particles Interactions in

- Toulouse Urban Layer (CAPITOU) experiment, *Meteorol. Atmos. Phys.*, 102, 3–4, 135–157, <https://doi.org/10.1007/s00703-008-0289-4>, 2008.
- Masson, V., Heldens, W., Bocher, E., Bonhomme, M., Bucher, B., Burmeister, C., deMunck, C., Esch, T., Hidalgo, J., Kanani-Sühring, F., and Kwok, Y. T.: City-descriptive input data for urban climate models: model requirements, data sources and challenges, *Urban Clim.*, 31, 100536, <https://doi.org/10.1016/j.uclim.2019.100536>, 2020.
- Mazzaro, L. J., Muñoz-Esparza, D., Lundquist, J. K., and Linn, R. R.: Nested mesoscale-to-LES modeling of the atmospheric boundary layer in the presence of under-resolved convective structures, *J. Adv. Model. Earth Sy.*, 9, 1795–1810, <https://doi.org/10.1002/2017MS000912>, 2017.
- Moeng, C.-H. and Wyngaard, J. C.: Spectral analysis of large-eddy simulations of the convective boundary layer, *J. Atmos. Sci.*, 45, 3573–3587, [https://doi.org/10.1175/1520-0469\(1988\)045<3573:SAOLES>2.0.CO;2](https://doi.org/10.1175/1520-0469(1988)045<3573:SAOLES>2.0.CO;2), 1988.
- Möhtus, M., Sulev, M., Lang, M., and Wyngaard, J. C.: Estimation of crown volume for a geometric radiation model from detailed measurements of tree structure, *Ecol. Model.*, 198, 506–514, <https://doi.org/10.1016/j.ecolmodel.2006.05.033>, 2006.
- Muñoz-Esparza, D., Lundquist, J. K., Sauer, J. A., Kosović, B., and Linn, R. R.: Coupled mesoscale-LES modeling of a diurnal cycle during the CWEX -13 field campaign: From weather to boundary-layer eddies, *J. Adv. Model. Earth Sy.*, 9, 1572–1594, <https://doi.org/10.1002/2017MS000960>, 2017.
- Mutani, G. and Fiermonte, F.: Microclimate models for a sustainable and liveable urban planning, in: *Topics and Methods for Urban and Landscape Design*, edited by: Ingaramo, R. and Voghera, A., Springer International Publishing, 183–209, <https://doi.org/10.1007/978-3-319-51535-9>, 2017.
- Nenes, A., Pandis, S. N., and Pilinis, C.: ISORROPIA: a new thermodynamic equilibrium model for multiphase multicomponent inorganic aerosols, *Aquat. Geochem.*, 4, 123–152, <https://doi.org/10.1023/A:1009604003981>, 1998.
- Novák, J., Jiřina, M., and Benešová, M.: Projekt TDD–ČR, Popis modelu TDD verze 3.9, Výzkumná zpráva č. V-1261, Ústav Informatiky AV ČR, v.v.i., Prague, Czech Republic, available at: https://www.ote-cr.cz/en/documentation/gas-documentation/tdd-documentation?set_language=en (last access: 28 June 2021), 2019.
- Nozu, T., Tamura, T., Okuda, Y., and Sanada, S.: LES of the flow and building wall pressures in the center of Tokyo, *J. Wind Eng. Ind. Aerod.*, 96, 1762–1773, <https://doi.org/10.1016/j.jweia.2008.02.028>, 2008.
- OTE: Normalizované typové diagramy dodávek plynu, available at: <https://www.ote-cr.cz/cs/statistika/typove-diagramy-dodavek-plynu/normalizovane-tdd> (last access: 28 June 2021), 2020.
- PALM: The PALM model system web pages, available at: <http://palm-model.org>, last access: July 2021.
- Prague Geoportal: Prague geographic data in one place, available at: <https://www.geoportalpraha.cz/en> (last access: 28 June 2021), 2020.
- Qu, Y., Milliez, M., Musson-Genon, L., and Carissimo, B.: 3D Radiative and Convective Modeling of Urban Environment: An Example for the City Center of Toulouse, in: *Air Pollution Modeling and its Application XXII*, edited by: Steyn, D., Builtjes, P., and Timmermans, R., NATO Science for Peace and Security Series C: Environmental Security, Springer, Dordrecht, 727–731, https://doi.org/10.1007/978-94-007-5577-2_123, 2013.
- Resler, J., Krč, P., Belda, M., Juruš, P., Benešová, N., Lopata, J., Vlček, O., Damašková, D., Eben, K., Derbek, P., Maronga, B., and Kanani-Sühring, F.: PALM-USM v1.0: A new urban surface model integrated into the PALM large-eddy simulation model, *Geosci. Model Dev.*, 10, 3635–3659, <https://doi.org/10.5194/gmd-10-3635-2017>, 2017.
- Resler, J., Eben, K., Geletič, J., Krč, P., Rosecký, M., Sühring, M., Belda, M., Fuka, V., Halenka, T., Huszár, P., Karlický, J., Benešová, N., Ďoubalová, J., Honzák, K., Keder, J., Nápravníková, Š., and Vlček, O.: Dataset: PALM 6.0 revision 4508, Research Data Repository of the Leibniz University of Hannover [code], <https://doi.org/10.25835/0073713>, 2020a.
- Resler, J., Eben, K., Geletič, J., Krč, P., Rosecký, M., Sühring, M., Belda, M., Fuka, V., Halenka, T., Huszár, P., Karlický, J., Benešová, N., Ďoubalová, J., Honzák, K., Keder, J., Nápravníková, Š., and Vlček, O.: Dataset: Validation of the PALM model system 6.0 in real urban environment; case study of Prague-Dejvice, Czech Republic. ASEP [data set], <http://hdl.handle.net/11104/0315416>, 2020b.
- Rotach, M. W., Vogt, R., Bernhofer, C., Batchvarova, E., Christen, A., Clappier, A., Feddersen, B., Gryning, S.-E., Martucci, G., Mayer, H., Mitev, V., Oke, T. R., Parlow, E., Richner, H., Roth, M., Roulet, Y.-A., Ruffieux, D., Salmond, J. A., Schatzmann, M., and Voogt, J. A.: BUBBLE – an urban boundary layer meteorology project. *Theor. Appl. Climatol.*, 81, 231–261, <https://doi.org/10.1007/s00704-004-0117-9>, 2005.
- ROTRONIC: HC2A-S – Humidity Probe, available at: <https://www.rotrotron.com/en/hc2a-s.html> (last access: 28 June 2021), 2020.
- Saiki, E. M., Moeng, C.-H., and Sullivan, P. P.: Large-eddy simulation of the stably stratified planetary boundary layer, *Bound.-Lay. Meteorol.*, 95, 1–30, <https://doi.org/10.1023/A:1002428223156>, 2000.
- Seinfeld, J. H. and Pandis, S. N.: *Atmospheric Chemistry and Physics: From Air Pollution to Climate Change*, J. Wiley, New York, 1152 pp., ISBN: 978-1-118-94740-1, 1998.
- Shaded Relief geoportal: Terrain, maps, and more, available at: <http://www.shadedrelief.com> (last access: 28 June 2021), 2020.
- Skamarock, W. C., Klemp, J. B., Dudhia, J., Gill, D. O., Barker, D., Duda, M. G., Huang, X.-Y., Wang, W., and Powers, J. G.: A Description of the Advanced Research WRF Version 3 (No. NCAR/TN-475+STR), University Corporation for Atmospheric Research, <https://doi.org/10.5065/D68S4MVH>, 2008.
- Stewart, I. D., and Oke, T. R.: Local climate zones for urban temperature studies, *B. Am. Meteorol. Soc.*, 93, 1879–1900, <https://doi.org/10.1175/BAMS-D-11-00019.1>, 2012.
- Strader, R. L., Lurmann, F., and Pandis, S. N.: Evaluation of secondary organic aerosol formation in winter, *Atmos. Environ.*, 33, 4849–4863, [https://doi.org/10.1016/S1352-2310\(99\)00310-6](https://doi.org/10.1016/S1352-2310(99)00310-6), 1999.
- Toparlar, Y., Blocken, B., Vos, P., van Heijst, G. J. F., Janssen, W. D., van Hooff, T., Montazeri, H., and Timmermans, H. J. P.: CFD simulation and validation of urban microclimate: a case study for Bergpolder Zuid, Rotterdam, *Build Environ.*, 83, 79–90, <https://doi.org/10.1016/j.buildenv.2014.08.004>, 2015.
- TSK-ÚDI: Prague Transportation Yearbook 2017, available at: <http://www.tsk-praha.cz/static/udi-rocenka-2017-en.pdf> (last access: 28 June 2021), 2018.

- United Nations, Department of Economic and Social Affairs, Population Division: World Urbanization Prospects: The 2018 Revision, New York, 126 pp., ISBN 978-92-1-148319-2, 2019.
- Wicker, L. J. and Skamarock, W. C.: Time-Splitting Methods for Elastic Models Using Forward Time Schemes, *Mon. Weather Rev.*, 130, 2088–2097, [https://doi.org/10.1175/1520-0493\(2002\)130<2088:TSMFEM>2.0.CO;2](https://doi.org/10.1175/1520-0493(2002)130<2088:TSMFEM>2.0.CO;2), 2002.
- Williamson, J. H.: Low-storage Runge-Kutta schemes, *J. Comput. Phys.*, 35, 48–56, [https://doi.org/10.1016/0021-9991\(80\)90033-9](https://doi.org/10.1016/0021-9991(80)90033-9), 1980.
- Xie, Z.-T. and Castro, I. P.: Efficient Generation of Inflow Conditions for Large Eddy Simulation of Street-Scale Flows, *Flow Turbul. Combust.*, 81, 449–470, <https://doi.org/10.1007/s10494-008-9151-5>, 2008.
- Yarwood, G., Rao, S., Yocke, M., and Whitten, G. Z.: Updates to the Carbon Bond chemical mechanism: CB05, Final Report prepared for US EPA, Novato, NC, USA, available at: https://www.camx.com/Files/CB05_Final_Report_120805.pdf (last access: 28 June 2021), 2005.
- Zhang, L., Brook, J. R., and Vet, R.: A revised parameterization for gaseous dry deposition in air-quality models, *Atmos. Chem. Phys.*, 3, 2067–2082, <https://doi.org/10.5194/acp-3-2067-2003>, 2003.
- Zhou, B., Simon, J. S., and Chow, F. K.: The Convective Boundary Layer in the Terra Incognita, *J. Atmos. Sci.*, 71, 2545–2563, <https://doi.org/10.1175/JAS-D-13-0356.1>, 2014.



Sensitivity analysis of the PALM model system 6.0 in the urban environment

Michal Belda¹, Jaroslav Resler², Jan Geletič², Pavel Krč², Björn Maronga³, Matthias Sühling³, Mona Kurppa⁶, Farah Kanani-Sühling^{3,4}, Vladimír Fuka¹, Kryštof Eben², Nina Benešová⁵, and Mikko Auvinen⁶

¹Department of Atmospheric Physics, Faculty of Mathematics and Physics, Charles University, Prague, Czech Republic

²Institute of Computer Science of the Czech Academy of Sciences, Prague, Czech Republic

³Institute of Meteorology and Climatology, Leibniz University Hannover, Hanover, Germany

⁴Harz Energie GmbH & Co. KG, Goslar, Germany

⁵Czech Hydrometeorological Institute, Prague, Czech Republic

⁶Atmospheric Composition Research, Finnish Meteorological Institute, Helsinki, Finland

Correspondence: Michal Belda (michal.belda@mff.cuni.cz)

Received: 14 May 2020 – Discussion started: 4 August 2020

Revised: 17 June 2021 – Accepted: 18 June 2021 – Published: 20 July 2021

Abstract. Sensitivity of the PALM model 6.0 with respect to land-surface and building properties is tested in a real urban environment in the vicinity of a typical crossroads in a densely built-up residential area in Prague, Czech Republic. The turbulence-resolving PALM is able to simulate the urban boundary layer flow for realistic setups. Besides an accurate representation of the relevant physical processes, the model performance also depends on the input data describing the urban setup, namely the building and land-surface properties. Two types of scenario are employed. The first one is the synthetic scenarios altering mainly surface and material parameters such as albedo, emissivity or wall conductivity, testing sensitivity of the model simulations to potentially erroneous input data. Second, urbanistic-type scenarios are analysed, in which commonly considered urban heat island mitigation measures such as greening of the streets or changing surface materials are applied in order to assess the limits of the effects of a particular type of scenario. For the synthetic scenarios, surface parameters used in radiation balance equations are found to be the most sensitive overall followed by the volumetric heat capacity and thermal conductivity of walls. Other parameters show a limited average effect; however, some can still be significant during some parts of the day, such as surface roughness in the morning hours. The second type, the urbanistic scenarios, shows urban vegetation to be the most effective measure, especially when considering both physical and biophysical temperature indica-

tors. The influence of both types of scenario was also tested for air quality, specifically PM_{2.5} dispersion, which generally shows opposite behaviour to that of thermal indicators; i.e. improved thermal comfort brings deterioration of PM_{2.5} concentrations.

1 Introduction

Investigation of the urban climate and especially that of the urban heat island (UHI) phenomenon still faces new challenges, despite decades of intensive research (Oke, 1982; Arnfield, 2003; Souch and Grimmond, 2006; Mills, 2014). Even with increasing computing capabilities and geographic information systems (GISs), there is a need for standardized research methods. Furthermore, research output should be applicable in practice (Stewart, 2011; Mills, 2014). Microscale meteorological and climate models have been increasingly used for simulations of real urban city environments, especially the impacts of changes in the city structure on the environmental conditions that affect the inhabitants. For a long time, cities have been known to strongly modify the surface energy balance and atmospheric conditions by trapping energy in the city, causing the UHI (Oke, 1982). In addition to that, global changes in climate, especially global temperature increase, are expected to have a worldwide in-

fluence on human society and other natural ecosystems with potentially severe impacts (IPCC, 2014a).

The increase in heat load in urban areas has been reported to have a substantially harmful effect on public health (Patz et al., 2005; Haines et al., 2006; Ebi, 2011) with an increase in mortality rates (Kovats and Hajat, 2008; Zanobetti et al., 2012). On the other hand, when appropriate adaptation measures are applied, these negative consequences can be mitigated (Gill et al., 2007; Hunt and Watkiss, 2011; Müller et al., 2013; IPCC, 2014b). In this context, various UHI mitigation measures are being considered, with greening of the environment as a typical example. Application of these measures, however, needs some prior information about their potential effectiveness. For that, it is important to know how sensitive the environment is to the city layout (e.g. building height or street width) and the material-specific parameters used to describe urban surfaces (e.g. reflectivity or roughness).

As the public and the administrative authorities are becoming aware of the problem, the demand for scientifically based urban climate studies grows, particularly model-based studies that can provide reliable projections on the city- or street-level scale. Besides an accurate representation of the relevant physical processes in urban climate models, their performance also depends on the accuracy of the input data that define the urban environment, for example, the building heights and building physical properties; the location of trees, their shape and leaf area density; or land-surface parameters. However, many model or physical parameters describing the city environment are only known approximately or are not available at all. Therefore, it is important to know the sensitivity of the model results to the uncertainties in the input data in order to assess the spread of potential deviations in model simulations or, in planning stages, which parameters are to be gathered with higher priority in data collection campaigns.

In practice, different model types are being used for urban studies, ranging from radiation models (SOLWEIG – Lindberg et al., 2008, 2018; RayMan – Matzarakis et al., 2010) to atmospheric kilometre-scale numerical weather prediction (NWP) and climate models with integrated urban parameterizations to detailed street-scale models. Considering their respective approaches and resolutions, different model groups can give quite different answers to the potential users. Regional climate models, for example, typically use idealized street canyon schemes (e.g. single-layer urban canopy model, SLUCM – Kusaka et al., 2001; building effect parameterization, BEP – Martilli et al., 2002; building energy model, BEM – Salamanca et al., 2010) which can be useful for simulations of city quarters or entire cities, but given their relatively low resolution, they can perform simulations on long timescales and for large regions or even continents. On the other side of the spectrum are very high resolution metre-scale models that can give quite a detailed picture of individual streets and buildings, but due to computational requirements they are usually limited in their spatial and temporal

coverage. Our study uses the latter approach, so we limit the following summary of the state of the art to the street-scale models.

Parameter sensitivity studies for urban flow models based on computational fluid dynamics (CFD) are rare and typically deal with parameters such as grid size and/or resolution or the type of turbulence model included (e.g. Ai and Mak, 2014; Ramponi and Blocken, 2012; Crank et al., 2018). More common are studies that consider the effect of potential changes in urban development, such as tree planting, green roofs or changes in certain surface materials, typically increasing reflectivity. For example, Ashie and Kono (2010) evaluate the impact of a redevelopment plan in two districts of Tokyo using a RANS-based (Reynolds-averaged Navier–Stokes) CFD model and Gross (2012) considers the effects of various green design elements, such as green facades, green roofs, lawns and trees, also using a RANS-based CFD code. Many previous studies have also applied the RANS code called ENVI-met, though the focus has been on a small number of specific changes instead of a systematic model sensitivity study (e.g. Su et al., 2014; Emmanuel and Loconsole, 2015; Lobaccaro and Acero, 2015). For an extensive review of available studies with a description of the ENVI-met model, we refer to Gál and Kantor (2020); for a comprehensive metastudy comparing methodologies and results of microscale and mesoscale models, please see Krayenhoff et al. (2021).

Large-eddy simulation (LES) is a branch of CFD in which the large turbulent eddies are explicitly resolved and simulated, unlike RANS where all turbulent eddies are parameterized. The LES method has been shown to perform better in resolving instantaneous turbulence structures in a complex urban environment (e.g. García-Sánchez et al., 2018; Salim et al., 2011; Gousseau et al., 2011; Tominaga and Stathopoulos, 2011). However, to the best of our knowledge, comprehensive sensitivity studies on how LES results for urban environments depend on the input data accuracy are non-existent to date.

This paper presents a systematic sensitivity analysis of the LES-based PALM model system 6.0 (Maronga et al., 2015, 2020) during a heatwave period. The selected area of interest is based in a real urban district in Prague, Czech Republic. Our interest concentrates on the sensitivity of the air temperature, surface temperature and $PM_{2.5}$ (particulate matter less than $2.5\ \mu\text{m}$ in aerodynamic diameter) concentration to the parameters describing the properties of the urban surfaces. The purpose of this study is twofold: first, to evaluate potential errors in model simulations introduced by erroneous setting of material parameters in the model (e.g. if the parameters are not measured correctly or with enough detail or are only roughly estimated) and, second, to show the potential and limits of various idealized measures typically considered for urban heat island mitigation.

The paper is organized as follows: Sect. 2 describes the LES model and the numerical setup and gives an overview

of the sensitivity simulations. The results of the sensitivity analysis and mitigation measures are presented in Sect. 3. A summary and discussion of the results is given in Sect. 4.

2 Experiment setup

2.1 Model description

The PALM model system 6.0 (revision 4093) (Maronga et al., 2015, 2020) consists of the PALM model core, several embedded modules and PALM-4U (short for PALM for urban applications) components which have been specifically developed for modelling the urban environment. The PALM model core resolves the non-hydrostatic, filtered, incompressible Navier–Stokes equations for wind (u, v, w) and scalar quantities (potential temperature, water vapour mixing ratio, passive scalar) on a staggered Cartesian grid in Boussinesq-approximated form. The sub-grid-scale terms that arise from filtering are parameterized using a 1.5-order closure by Deardorff (1980), with modifications after Moeng and Wyngaard (1988) and Saiki et al. (2000). One of the assets of PALM is its excellent scalability for massively parallel computer architectures (up to 50 000 processor cores; see Maronga et al., 2015).

This study applies several modules embedded in PALM, namely the land surface model (LSM; Gehrke et al., 2020), plant canopy model (PCM) and radiation model. The radiation model applies the Rapid Radiation Transfer Model for GCMs (RRTMG), which has been used as an external library. Furthermore, the following PALM-4U components are applied: the Cartesian topography, building surface model (BSM, formerly USM; see Resler et al., 2017), model of radiation interaction with surfaces and plant canopy – the so-called radiative transfer model (RTM; see Krč et al., 2021), and human biometeorology (BIO; see Frölich and Matzarakis, 2020 and Krč et al., 2021) and online chemistry (CHEM; see Khan et al., 2021) modules.

Additionally, both self-nesting and offline nesting features of PALM-4U are utilized. In self-nesting a domain with a finer resolution can be defined inside a larger domain, and this subdomain (child domain) receives its boundary conditions from the coarse-resolution parent domain at every model time step (Hellsten et al., 2021). In offline nesting, the initial and boundary conditions for the mean flow of the parent domain are provided from, for example, a mesoscale model using a dynamic driver, while the child domain receives all information from its parent (Kadasch et al., 2020). As offline nesting is usually used for coupling to a large-scale or mesoscale model that does not resolve turbulence, it is triggered at the model boundaries using a synthetic turbulence generator (STG), which imposes spatially and temporally correlated perturbations at every time step onto the velocity components at the lateral boundaries.

Two modelling domains were connected with the one-way online nesting feature of PALM (see Sect. 2.3 for more details). The initial and boundary conditions of the parent domain were taken from a WRF model simulation using the offline nesting feature of PALM-4U; the boundary conditions were updated at every model time step (Sect. 2.2.2). The WRF data were processed by the PALM supplementary WRF_interface; for a description see Resler et al. (2020).

For an overview of the PALM model, embedded modules and the PALM-4U components, see Maronga et al. (2020), and for details see the other papers in this special issue.

2.2 PALM model setup

2.2.1 General model configuration

The dynamic core of the PALM model was configured with the Wicker and Skamarock fifth-order advection scheme (Wicker and Skamarock, 2002) and the multigrid pressure solver (Hackbusch, 1985; Maronga et al., 2015). The radiative fluxes were simulated by RRTMG, and their interactions with the urban canopy layer were modelled by RTM (Krč et al., 2021). The surface energy balance for the individual surfaces (vegetation, pavement, buildings, water) was calculated by the LSM and BSM components (Maronga et al., 2020). The dynamic and energy processes caused by resolved trees and shrubs were modelled by PCM. The chemistry module was configured for NO_x , PM_{10} and $\text{PM}_{2.5}$ species without chemical reactions, and boundary conditions were set to zero to simulate purely the passive transport of the emitted pollutants and consequently to simplify attribution of the sensitivity tests to local features.

To initialize temperatures of walls, grounds and roofs, a 48 h spin-up simulation for the BSM and LSM was conducted. During this spin-up run, the model solves only simplified energy processes while the effects of the airflow on the energy balance were held constant (see Maronga et al., 2020). The simplifications also include a simple radiation model instead of RRTMG and switching off the window treatment in BSM. The spin-up allows us to establish reasonable initial temperatures inside the ground, wall and roof material layers while keeping the computational demands within an acceptable range.

2.2.2 WRF model configuration

Initial and boundary conditions for the parent domain of the PALM-4U simulations were obtained from a WRF model simulation initialized from the Global Forecast System (GFS) operational analyses and forecasts. WRF (version 3.8.1) was run on two nested domains with horizontal resolutions of 9 and 3 km and 49 vertical levels. The dimensions of the inner domain were 187×121 grid points. The configuration was standard: Noah LSM, RRTMG radiation and Yonsei University scheme for the planetary boundary layer (PBL).

According to preliminary tests no urban parameterization has been used in the WRF model and the settings arising from the MODIS land use categories have not been altered. We used four runs of GFS daily, starting at synoptic times, namely 18:00 UTC on the previous day and 00:00, 06:00 and 12:00 UTC on the day of the simulation. From each of these GFS runs, the first 12 h was taken and downscaled by WRF. The forecast horizons 0–6 h served as a spin-up and were discarded. The remaining horizons 7–12 from each run were assembled into 24 hourly outputs per day. Thus a surrogate for local analysis has arisen, aiming at elimination of a possible drift of WRF model fields from reality while adding local effects not simulated by the global GFS.

WRF outputs from the 3 km domain were postprocessed into the PALM dynamic driver. The data were transformed between coordinate systems, and a horizontal and vertical interpolation was applied including terrain-matching procedures. The interpolated airflow was adjusted to enforce mass conservation. The tool for processing the WRF data into the PALM dynamic driver file has been a part of the official PALM distribution as WRF_interface since revision 4766; the description of this process is given in Resler et al. (2020).

2.2.3 Surface and material parameters

For solving the energy balance equations, BSM and LSM require using detailed and precise input parameters describing the surface materials (e.g. albedo, emissivity, roughness length, thermal conductivity, capacity of the skin layer, thermal capacity and volumetric thermal conductivity). Urban and land surfaces and materials become very heterogeneous in a real urban environment when going to a very fine spatial resolution. Any bulk parameterization for the whole domain would be inadequate. For our study, a very detailed setting of the parameters was supplied everywhere possible. In order to obtain the data, an extensive on-site campaign was performed which provided a detailed database of geospatial data including information on wall, ground, and roof materials and colours for estimating the surface and material properties (Resler et al., 2017). The original geodatabase was extended with information about neighbouring streets and updated with new modifications (see Sect. 2.3 for detailed description).

Surfaces are described by their respective material category and albedo. Parameters other than albedo are estimated and assigned to each category based on surface and subsurface material composition and thickness. The parameters of all subsurface layers of the respective material were set to the same value. The skin layer heat capacity C_0 and heat conductivity between the skin layer and the first material layer Λ (see Eqs. 1 and 2 in Resler et al., 2017) were inferred from the properties of the near-surface material, which may be different in the rest of the volume. Parameter settings of the categories used in this study are given in the Supplement as Table S01. Trees in the analysed domain were described

by their respective position, diameter, trunk parameters and vertically stratified leaf area density. The Prague 3D model available from the Prague Institute of Planning and Development was used to obtain the building height database. The Prague 3D model is based on photogrammetric (aerial) mapping and is freely available on the Prague Opendata portal (<https://www.geoport Praha.cz/cs/data/otevrena-data/44EE8B0A-641A-45E8-8DC9-CF209ED00897>, last access: 13 July 2021 – only available in Czech). Data are provided in CAD (DWG or DGN) or Esri (polygon or multipatch) format. The original product accuracy in 2012 was 0.5 m, but the model is updated yearly and current accuracy is around 0.2 m. Description and properties of surfaces and materials were assembled into standard GIS formats and subsequently transformed into the PALM input NetCDF files corresponding to the PALM Input Data Standard (PIDS – Heldens et al., 2020).

2.3 Study domain description

The study domain in Holešovice, Prague, was adapted from Resler et al. (2017), covering the vicinity of a crossroads of the streets Dělnická and Komunardů in a densely built-up area in Prague, Czech Republic (50°06.195' N, 14°27.000' E). The area is well suited for this type of study as it represents a typical Prague residential area in a rather topographically flat (terrain elevation ~ 180 m a.s.l.) part of the city with a variety of urban components, including old and new residential buildings, backyards, and parking spaces. The two streets run north to south (Komunardů) and west to east (Dělnická) and have the width of roughly 25 and 17 m, respectively. The buildings in the area range approximately from 10 to 35 m in height. There is not much vegetation in the area, and the majority of the trees are located in the courtyards. The surrounding neighbourhood is very similar to the study area (Fig. 1, right).

A few minor modifications were made to the study domain from the previous analysis of Resler et al. (2017). Firstly, the horizontal extent of the domain was extended from the original $376 \text{ m} \times 226 \text{ m}$ to $400 \text{ m} \times 256 \text{ m}$. This was important for the domain multiplication in a synthetic domain setup (see Sect. 2.4); the new domain ends in the middle of streets in all directions. Secondly, the central part of the intersection, where a small asphalt polygon ($\sim 11 \text{ m}^2$) in the real street was partially replaced by cobblestones ($\sim 7 \text{ m}^2$ of cobblestones and $\sim 4 \text{ m}^2$ of asphalt), was modified in the input data accordingly. A last minor change from the previous analysis is the height of the highest building which was physically rebuilt and is now 35 m high. The domain covers an area of $102\,400 \text{ m}^2$, of which $48\,451 \text{ m}^2$ is the total building footprint, $48\,356 \text{ m}^2$ ($\sim 22.9\%$ of total domain surface area) is impervious surfaces and 5593 m^2 ($\sim 2.7\%$) is pervious surfaces (e.g. grass). Each building has three levels – lower, often markets and shops; upper, typically residential; and roof. The lower level is covered by 9933 m^2 ($\sim 4.7\%$) of

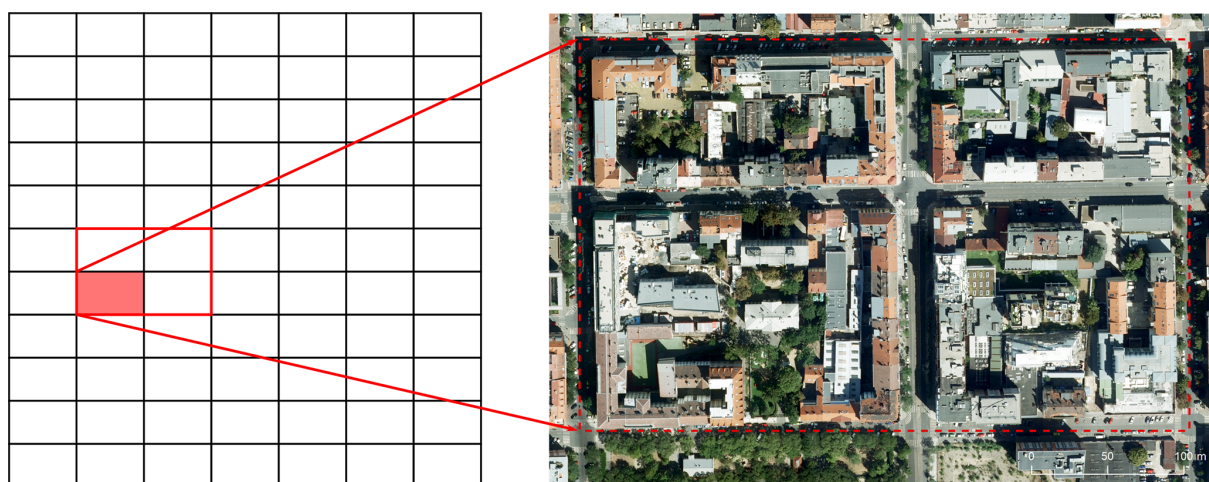


Figure 1. Design of model domains; black-bordered rectangles represent the parent domain; red-bordered rectangle represents the child domain. Solid red rectangle represents one unique domain with the real environment before multiplication. Projection: WGS 84 / UTM zone 33N; orthophoto source: Prague Institute of Planning and Development.

windows and $20\,837\text{ m}^2$ ($\sim 9.9\%$) of walls; the upper level is covered by $22\,861\text{ m}^2$ ($\sim 10.8\%$) of windows and $52\,169\text{ m}^2$ ($\sim 24.7\%$) of walls. The roof area is $51\,044\text{ m}^2$ ($\sim 24.2\%$). The total area of all surfaces in the domain is $210\,793\text{ m}^2$. At the time of this study, 158 trees were in the area of which 4 were coniferous and 154 were broadleaved.

2.4 Synthetic modelling domains

The study domain described above is too small for realistic large-eddy simulations because the largest turbulent eddies are of the size of the boundary layer height, which in Europe can reach up to 2.5 km in summertime (e.g. Seidel et al., 2012, or Zhang et al., 2013). In order to resolve the turbulent transport of these eddies, the horizontal model domain size must be at least 2–3 times the boundary layer height and thus be on the order of several square kilometres, which is much larger than the model domain employed in the present study (Resler et al., 2017). Moreover, to allow simulations of real meteorological conditions, non-cyclic boundary conditions with offline nesting were considered, using the meteorological model WRF and a synthetic turbulence generator. This setting, however, requires a sufficient horizontal extent of the domain to allow development of the correct turbulent flow. For this purpose, a nested two-domain setup with one-way online nesting was utilized as described in Sect. 2.1, and synthetic domains were generated by horizontal multiplication of the original domain.

The parent domain had a horizontal grid spacing of 8 m and was created by 7 repetitions of the original domain in the west–east direction and 11 repetitions in the south–north direction. Moreover, an additional flat buffer zone was added on all sides of the domain. The width of this buffer was 25 grid cells at the west and east boundaries and

24 grid cells at the south and north boundaries. Thus, the extent of the complete parent domain is 400×400 grid cells ($3200\text{ m} \times 3200\text{ m}$) in both directions. The domain was configured with 120 vertical layers using the layer-stretching approach so that the vertical grid spacing of 8 m was stretched above 120 m by a factor of 1.08 until a grid spacing of 24 m was reached. The resulting domain top was at 2.5 km.

The nested fine-resolution domain (hereafter child domain) was configured with a refinement ratio of 4, having a 2 m grid resolution in all directions, and it consisted of four original domains: two in the west–east direction and two in the south–north direction. The extent of the domain was $400 \times 256 \times 40$ grid cells ($800\text{ m} \times 512\text{ m} \times 80\text{ m}$). The child domain was located asymmetrically in the left part of the parent domain, and the evaluation was carried out on the southwest part of it (see Fig. 1). This configuration was selected due to an easterly wind flow during the modelled episode.

2.5 The modelled heatwave episode

This study focuses on modelling the thermal comfort, and therefore a heatwave episode on 2–3 July 2015 was chosen for these simulations. One advantage of this choice is that the previous version of the model was also validated on this period (see Resler et al., 2017). A detailed description of the weather during the modelled period is also provided in Resler et al. (2017). The weather was characterized by a high-pressure system centred above the Baltic Sea with mostly clear skies and the daily maximum temperature exceeding $30\text{ }^\circ\text{C}$ while the minimum did not fall below $20\text{ }^\circ\text{C}$ (tropical night). Relative humidity values ranged from 30 % during the day to 65 % at night. Easterly winds were observed with values mostly below 2.5 m s^{-1} above the roof level. A maximum wind speed of $3\text{--}4\text{ m s}^{-1}$ at a 10 m height

was observed at the Karlov station (WMO 11519, around 4 km south of the modelled domain) on the afternoon of 2 July 2015, during the spin-up, and at the end of 3 July 2015. According to the atmospheric sounding, a low-level jet from the south and south-east was observed during the night, with a maximum wind speed of 10 m s^{-1} at 640 m a.s.l. (950 hPa). At night, a south to south-east low-level jet was observed in the atmospheric soundings, with a 10 m s^{-1} maximum wind speed at 640 m a.s.l. (950 hPa). The time of the sunset was 19:15 UTC on 2 July 2015; sunrise was at 02:58 UTC and solar noon at 11:06 UTC on 3 July 2015.

2.6 Air pollution and emissions

Air pollution sources in the modelling domain are dominated by the local road traffic. Based on the Czech national emission database, the mobile sources represent approximately 60 % of total emissions for Prague for particulate matter and 75 % for NO_x (CHMI, 2018). Considering those ratios and the fact that there is no major point source in the area, we decided to include only the traffic sources in the analysis. The emission fluxes are estimated based on the daily traffic intensities, which are available from annual traffic census data, for all streets in both directions. Emission factors, taken from a local Czech database (MEFA 13, 2013), give the pollutant release per vehicle per metre of travel, based on vehicle and fuel type. For our study area, the assumption was that all vehicles were passenger cars, which is reasonable for this residential neighbourhood. The traffic-related emissions are spatially uniformly distributed into traffic lanes and temporally distributed using prescribed hourly factors also derived from available annual traffic census data (see Fig. S10 for daily spatial distribution). Magnitudes of emission fluxes range from 0.03 to $0.34 \text{ g d}^{-1} \text{ m}^{-2}$ for NO_x , from 6 to $58 \times 10^{-3} \text{ g d}^{-1} \text{ m}^{-2}$ for PM_{10} and from 3 to $32 \times 10^{-3} \text{ g d}^{-1} \text{ m}^{-2}$ for $\text{PM}_{2.5}$. We chose the $\text{PM}_{2.5}$ to be the pollutant of interest; however, considering the emission creation methodology and the fact that all chemical reactions are omitted in our simulations, the conclusions (in a qualitative sense) would be the same for other pollutants. We opted not to include interactive chemistry and only consider the dispersion of $\text{PM}_{2.5}$ due to the time frame of the secondary aerosol formation being considerably longer than the lifetime of air in the domain and thus not significantly influencing the sensitivity experiments (see Sect. 4.2 for discussion of this limitation).

2.7 Sensitivity tests

For evaluating the influence of the parameter changes, a *baseline* simulation was performed in which the parameters tested were set to “real” values, that is, values measured or estimated based on materials used in the actual buildings and other surfaces in the domain. The scenario simulations, divided into two groups, synthetic and urbanistic, then changed

one or more of these parameters as described in the following two sections.

2.7.1 Synthetic scenarios – sensitivity to the setting of material parameters

For the first group of sensitivity tests, a suite of synthetic scenarios was selected based on the most important variables in the urban environment. These scenarios target potential biases in the model outputs connected to the imprecise setting of relevant city environment parameters which have a major influence on the energy balance and dynamics of the model such as albedo or roughness. These parameters are notoriously difficult to obtain with a sufficient resolution and are thus usually set in a very general way and sometimes even tuned to the model results. As model errors can stem from many different sources, such as model deficiencies, chaotic behaviour or imperfect input data, we aim to quantify which part of the error can be attributed to the setting of these parameters.

Since the analysis by Resler et al. (2017), the PALM modelling system has been extended with new features. According to the new functionalities, window and wall fractions were mapped for each building in BSM and more detailed plant canopy parameters were included in PCM. In total 21 scenarios (hereafter SA scenarios) were prepared that each change one specific parameter of the surfaces (and/or plant canopy) from the baseline simulation. Table 1 summarizes the parameter changes for the SA scenarios, the surfaces affected by the change and the fraction of the total surface area affected in the respective scenario.

2.7.2 Urbanistic scenarios – sensitivity to urban heat island mitigation measures

The second group of scenarios was designed more from the urban planners’ point of view, i.e. assessing the influence of (in)appropriate urban planning actions on improving thermal comfort and air quality. These scenarios present several measures typically taken into account when dealing with the UHI effect, such as greening or changes in the surface materials, simplified to distinguish individual influence (e.g. when changing roads to grass, the emissions are not changed). Although not necessarily realistic, these scenarios provide the urban planners with an assessment of the maximum potential influence of certain common types of urban development (e.g. removal of all trees versus planting trees everywhere). The design of the scenarios stemmed from discussion with various authorities of the City of Prague in the framework of the Urbi Pragensi project (<http://www.urbipragensi.cz>, last access: 13 July 2021). A detailed description of this group of scenarios (hereafter denoted by SB) is included in Table 2.

Table 1. Scenarios testing model sensitivity to changes in material parameters with fraction of affected domain surface area (column Surf. fraction). A detailed description of surfaces is in Sect. 2.3.

Scenario	Description	Surfaces	Surf. fraction (%)
SA01	Albedo increase +20 %	Walls, roofs, surfaces	100.0
SA02	Albedo decrease –20 %	Walls, roofs, surfaces	100.0
SA03	Emissivity set to the average for each group of surfaces	Land cover: 0.8922; lower walls: 0.9263; upper walls: 0.9278; Roofs: 0.7233	100.0
SA04	Average SA03 emissivity +20 %	Average is SA03, max 1.0	100.0
SA05	Average SA03 emissivity –20 %	Average is SA03	100.0
SA06	Roughness increase +20 %	Walls, roofs, surfaces	100.0
SA07	Roughness decrease –20 %	Walls, roofs, surfaces	100.0
SA08	Thickness increase +20 %	Walls, roofs, surfaces	100.0
SA09	Thickness decrease –20 %	Walls, roofs, surfaces	100.0
SA10	Transmissivity of windows increase +20 %	Walls (windows only)	15.6
SA11	Transmissivity of windows decrease –20 %	Walls (windows only)	15.6
SA12	Thermal conductivity inside wall increase +20 %	Walls	34.6
SA13	Thermal conductivity inside wall decrease –20 %	Walls	34.6
SA14	Volumetric heat capacity increase +20 %	Walls, roofs, surfaces	100.0
SA15	Volumetric heat capacity decrease –20 %	Walls, roofs, surfaces	100.0
SA16	Window fraction increase +20 %	Walls	18.7
SA17	Window fraction decrease –20 %	Walls	12.5
SA18	Leaf area density increase +20 %	Trees	
SA19	Leaf area density decrease –20 %	Trees	
SA20	Soil moisture increase +20 %	Pervious surfaces only	2.7
SA21	Soil moisture decrease –20 %	Pervious surfaces only	2.7

3 Results

Due to the different nature of the two sets of scenarios, the analysis of the model results will be performed separately for the synthetic SA scenarios and urbanistic SB scenarios. However, some aspects of the analysis are common to both. The chaotic nature of the turbulent flow in the domain requires an application of time averaging which needs to be sufficiently long to smooth out turbulent fluctuations yet short enough to capture the diurnal variability. In the time series plots, we opted to show 10 min averaged values together with hourly moving averages. Summary tables (Table S02 in the Supplement), on the other hand, show 3 h averages along with daily averages, minima and maxima. One important aspect of the modelling setup which must be kept in mind when analysing the results is that the model spin-up period uses a constant dynamic and simplified energy model (see

Sect. 2.2.1), and thus the initial thermal conditions (ground, wall and roof temperatures) are not in total agreement with temperatures that would have been obtained by a full model run. This can impose differences on the simulation behaviour in the first hours from standard behaviour in the following hours when this initial effect vanishes, which may limit the applicability of the results in the first few hours of the simulation after the spin-up. However, as most of the differences between respective simulations begin to appear after sunrise, this influence can be neglected.

Spatial variability is analysed by averaging over the whole domain as well as separately over several selected domain parts. A particular focus is on the two crossing streets and courtyards. For maps with point positions and area selections, see the Supplement (Figs. S01–S09). The most important variables for the end users were chosen as primary indicators. They include surface temperature, air temperature,

Table 2. Scenarios testing sensitivity of the model results to UHI mitigation measures.

Scenario	Description	Note
SB01	Building height increase +20 %	Street canyon ratio
SB02	Building height decrease –20 %	Street canyon ratio
SB03	All surfaces (pavement) changed to asphalt	Land cover
SB04	All surfaces (pavement) changed to concrete	Land cover
SB05	All surfaces (pavement) changed to cobblestones	Land cover
SB06	All surfaces (pavement) changed to white cobblestones	Land cover
SB07	Tram green line	Land cover
SB08*	All surfaces insulated*	Walls only*
SB09	Water channel instead of tram line, roads changed to grass	Land cover, no changes in emissions
SB10	Green areas changed to asphalt, trees deleted	Grey city 1
SB11	Asphalt except main roads and pavements changed to grass, all trees deleted	Grey city 2
SB12	Trees planted at each possible place, placed 128 <i>Acer platanoides</i>	Green city
SB13	New tree alley: Dělnická, centre-line position	<i>Acer platanoides</i>
SB14	New tree alley: Dělnická, both-side position	<i>Acer platanoides</i>
SB15	New tree alley: both streets, both-side position	<i>Acer platanoides</i>
SB16	All trees coniferous	More dense crown
SB17	Include anthropogenic heat flux	A/Cs, heating, etc.

* Scenario SB08 was removed from further analysis because results were significantly affected by numerical instability solved in PALM revision 4240.

PM_{2.5} concentrations and two biophysical temperature characteristics – mean radiant temperature (MRT) and physiological equivalent temperature (PET) – all at the height of the human body represented by the first 2 m high layer (for definitions and information about the implementation of MRT and PET in PALM, see Frölich and Matzarakis, 2020, and Krč et al., 2021).

All scenario simulations are analysed with respect to the baseline simulation (a model run with the original parameter values). Figure 2 shows the spatial distribution of basic variables in the domain for the baseline simulation.

3.1 Sensitivity to material parameters

In the first part of the assessment, we analyse the model sensitivity to the setting of building and material parameters such as albedo or roughness (SA scenarios). Figure 3 shows the sensitivity as differences between respective scenarios and the baseline simulation for air temperature (other variables are included in the Supplement as Figs. S11–S14) in 24 h averages. Table S02 in the Supplement summarizes all five analysed variables showing absolute values and differences (plus the relative difference) of each SA scenario from the baseline. Results are averaged for several areas: domain, east–west street (Dělnická), south–north street (Komunardů), both streets (Streets) and courtyards. In general, the following four parameters show the highest sensitivity for temperature: albedo (SA01, SA02), emissivity (SA03–05), thermal conductivity of walls (SA12, SA13) and volumetric heat capacity (SA14, SA15) with a median response of up to ± 0.1 K (Fig. 3) and a maximum response reaching up to ± 0.18 K in 3 h averages and up to ± 0.4 K in 10 min aver-

ages for some parameters during the day (Table S02). Overall, the albedo setting (SA01, SA02) shows the highest sensitivity of all parameters in this group. The lowest sensitivity is observed for wall thickness (SA08, SA09), transmissivity of windows (SA10, SA11) and soil moisture (SA20, SA21). However, the reason for the low sensitivity to the changes in the soil moisture lies mainly in a low percentage of the green areas in the domain.

The daily cycle of air temperature also has an imprint on the relative importance of respective parameters throughout the day. Parameters used in incoming radiation routines (namely albedo; SA01, SA02) are the most sensitive ones in the middle of the day, when the radiative balance is governed mostly by incoming short-wave radiation. During the night, emissivity (SA03–05) and the heat capacity of walls (SA14, SA15) play a major role (see Table S02); thus sensitivity to these parameters is higher then. Some parameters show quite high sensitivity only for short periods during the day. For example the window fraction shows low sensitivity in the morning hours, after which it increases at around 09:00–12:00 UTC (11:00–14:00 local time) and peaks in the early evening at around 18:00–21:00 UTC (see SA16–17 in Table S02). In this particular case, given that the response to a lower window fraction is an increase in temperatures and vice versa, the most likely explanation is the difference in heat storage between windows (very low) and walls (higher), which has a prevalent influence in low-sun periods of the day.

Air temperature, though fundamental for physical evaluation, is not necessarily the best quantity for evaluating biophysical properties, namely thermal comfort. For this purpose, MRT and PET variables combining other relevant physical variables (radiation, humidity, airflow, etc.) are

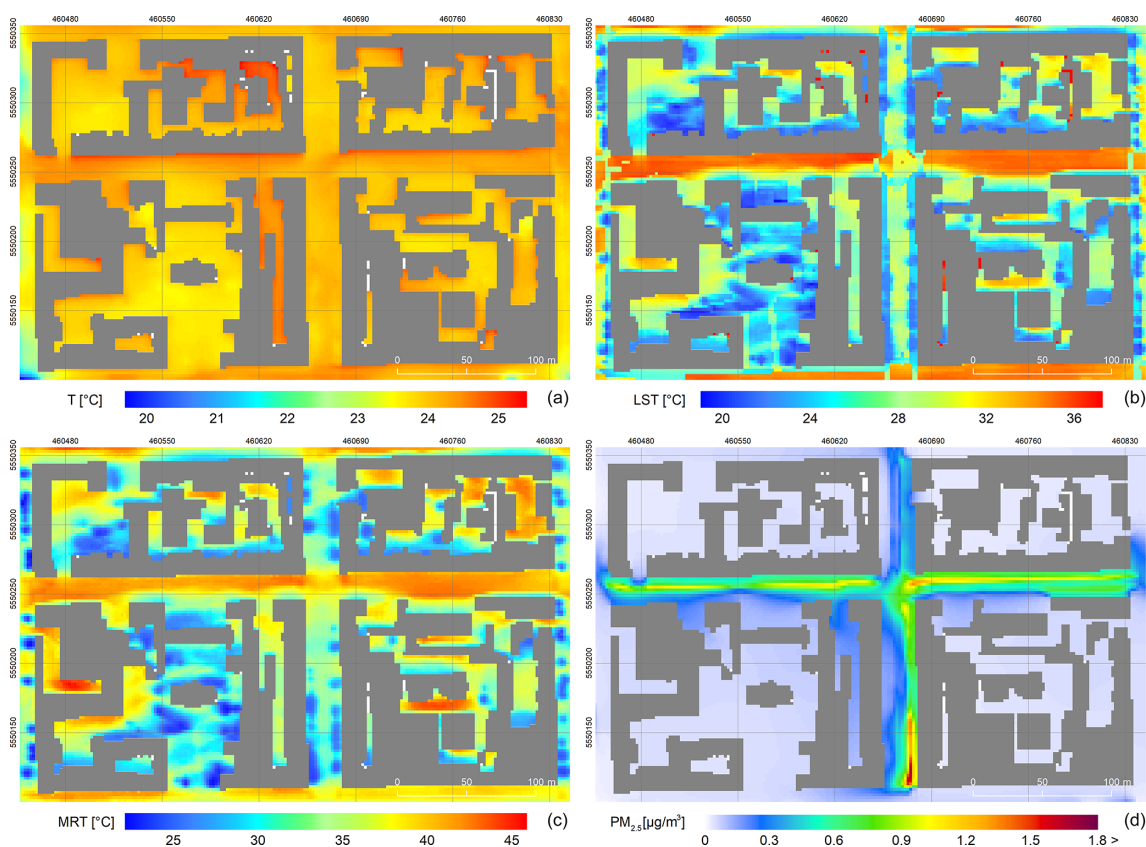


Figure 2. Daily average spatial variability in (a) air temperature, (b) surface temperature, (c) mean radiant temperature – MRT – and (d) $\text{PM}_{2.5}$ concentrations for the baseline simulation. Projection: WGS 84 / UTM zone 33N; layer with roofs is own data source.

used. Given the combination of various influences, MRT and PET often show sensitivity higher than but inverse to that of the air temperature. As a demonstration we show this for the two most prominent scenarios, SA01 and SA02. In SA01, the albedo is increased by 20 %, which results in a decrease in daily surface temperatures by 0.5 K and a decrease of around 0.1 K for air temperature. On the other hand, by increasing reflection at the surfaces, this change increases both MRT and PET by 0.6 and 0.3 K, respectively. In daily maxima, the increase in both biometeorological variables is even more prominent and reaches up to 1.7 and 1.6 K, respectively. Decreasing albedo by 20 % in SA02 has a similar effect in terms of absolute numbers but with the opposite sign.

Influence on air quality, represented here by changes in $\text{PM}_{2.5}$ concentrations at the first model layer, originating from emissions from local transportation, is generally much less pronounced in all scenarios. For the dominant parameters, such as albedo or emissivity, we still observe a similar general tendency to increase (decrease) $\text{PM}_{2.5}$ values with increased (decreased) albedo (emissivity). This is opposite behaviour to that of the surface and air temperatures, and it is likely primarily caused by connected changes in the flow regime as illustrated in Figs. 4 and 5 by a decrease (increase) in wind speed with increased (decreased) albedo (also dis-

cussed in e.g. Žák et al., 2016). It should be noted here that, due to non-linearity, the response to the symmetrically constructed scenarios (e.g. SA01 and SA02) need not be symmetric in the spatial distribution as also illustrated in Figs. 4 and 5. For example, the changes in wind speed are more pronounced in the western part of the west–east-oriented street and at the crossroads when decreasing the albedo. Furthermore, the sensitivity in some places, e.g. the northern part of the north–south-oriented street or some courtyards, is such that decreasing or increasing albedo both result in increasing wind speed.

Long-term average changes in $\text{PM}_{2.5}$ concentrations are generally small and with the exception of singular peaks (Fig. 6) lie within $\pm 5\%$ in most of the domain. The temporal evolution of the response, however, may also differ depending on the geometric configuration as is also evident from Fig. 6 which shows spatially averaged values for the two main streets in the albedo-changing SA01 and SA02 scenarios. The difference between the two scenarios is more pronounced in the north–south-oriented Komunardů street in the afternoon hours, while in the morning hours, the difference is larger in the west–east-oriented Dělnická street.

The parameters we analyse influence the results mainly by changing the energy balance of the horizontal and vertical

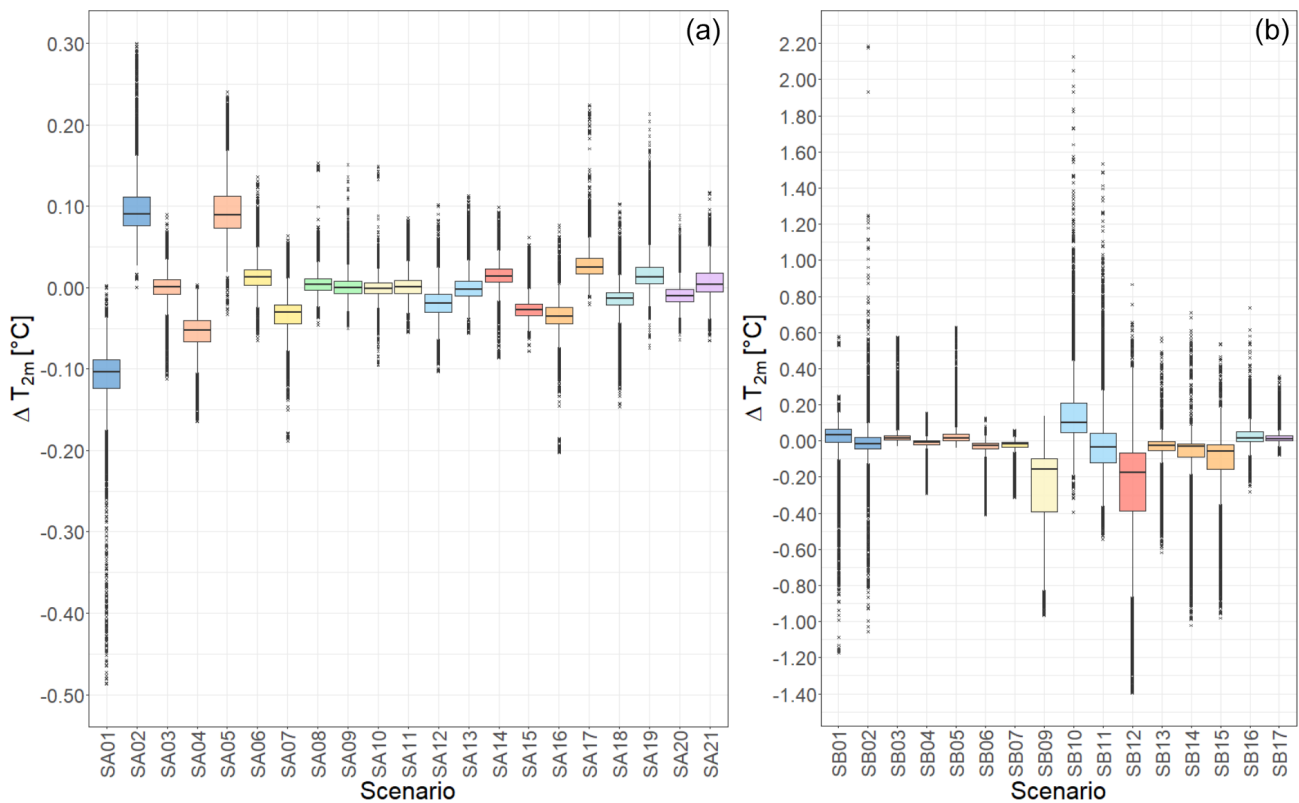


Figure 3. Sensitivity of air temperature in SA (a) and SB (b) scenarios. Values represent grid box differences (scenario – baseline) of 24 h averages in the first 2 m high layer. Box colours indicate related scenarios (e.g. blue for changing albedo, orange for changing emissivity). Whiskers: values within $1.5\times$ the interquartile range; crosses: outliers.

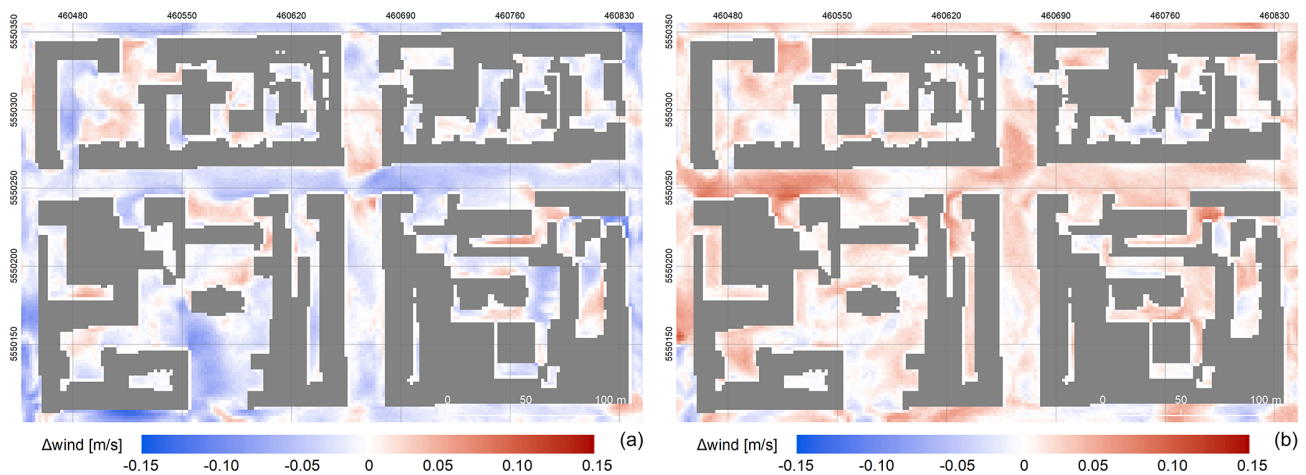


Figure 4. Daily average sensitivity of horizontal wind speed (1 m) expressed as the difference between scenario and baseline. (a) Scenario SA01 (albedo increased by 20 %); (b) scenario SA02 (albedo decreased by 20 %). Projection: WGS 84 / UTM zone 33N; layer with roofs is own data source.

surfaces in the model domain. Air temperature changes are then mainly driven by the transfer of heat between these surfaces and air. In this context, we will now focus on the effect on surface temperatures. The highest sensitivity of surface temperature is observed in the same scenarios as for

air temperature: albedo SA01 and SA02 (Fig. 7), emissivity SA03–05, thermal conductivity SA12 and SA13, and volumetric heat capacity SA14 and SA15. The average response reaches up to ± 0.5 K and the 3 h maxima reach up to ± 0.9 K

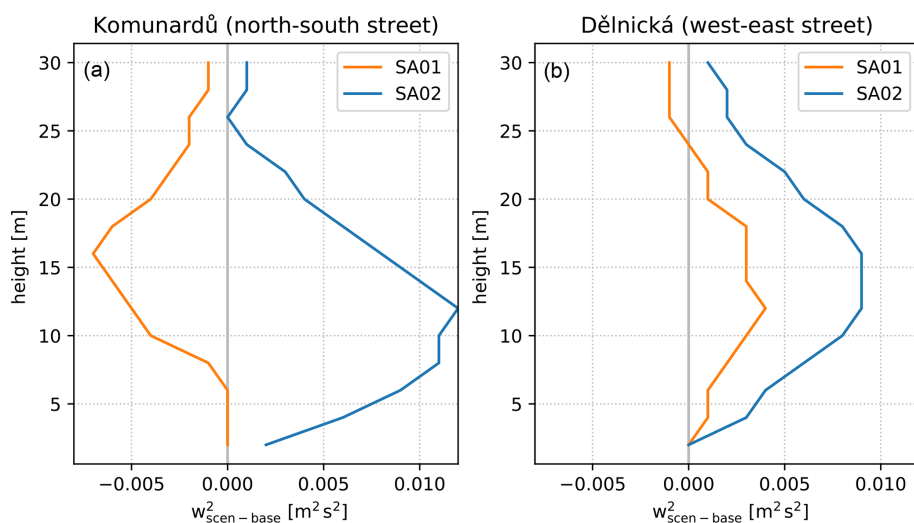


Figure 5. Daily average profiles of w^2 (plotted as the difference: scenario – base case) averaged over the two main streets: the north–south-oriented Komunardů (a) and the west–east-oriented Dělnická (b).

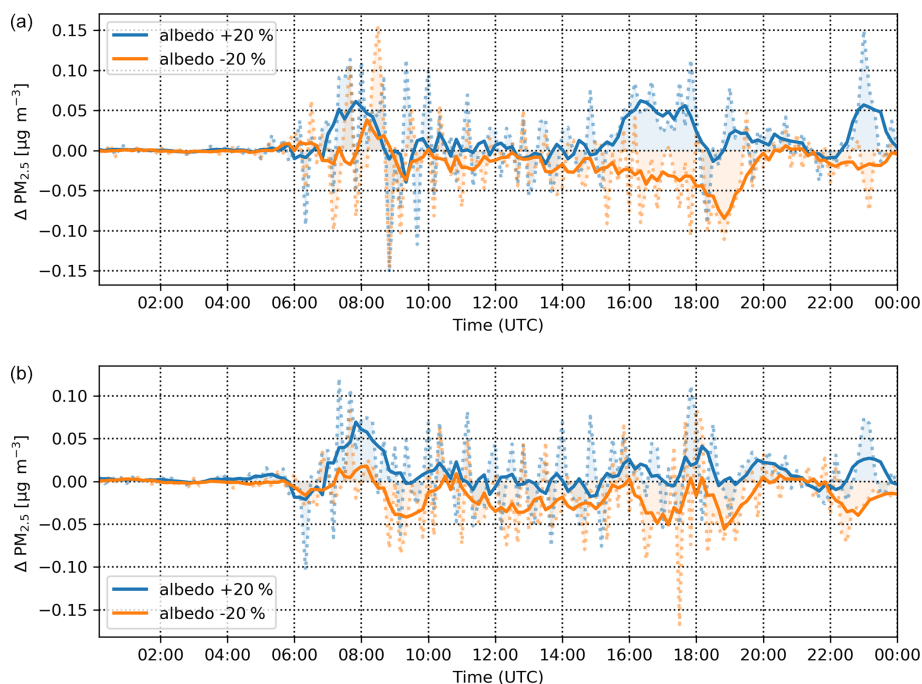


Figure 6. Changes in $\text{PM}_{2.5}$ for the north–south-oriented Komunardů street (a) and the west–east-oriented Dělnická street (b) in scenarios SA01 (albedo +20 %, blue) and SA02 (albedo –20 %, orange). Dotted lines: 10 min values; solid lines: 1 h moving average.

with albedo changes (SA01, SA02) and decreased emissivity (SA05).

The model response to the surface parameters is also dependent on the location. This stems mainly from the differences in the radiation budget during the day caused by positioning of urban elements (buildings and trees). At individual points, the differences in surface temperature with respect to the base case reach up to ± 4 K in shorter periods in the

albedo change scenarios SA01 and SA02 (e.g. points C02 and C05 in the upper two panels of Fig. 7).

Air temperature showed a rather small sensitivity to changes in soil moisture, which we attribute to a rather low percentage of green areas in the domain. However, small areas covered with or in the direct vicinity of vegetation are influenced significantly as shown in Fig. 8 for point F03. For this and other similar points (e.g. F02, F04, H02), changes in soil moisture show much higher sensitivity in surface tem-

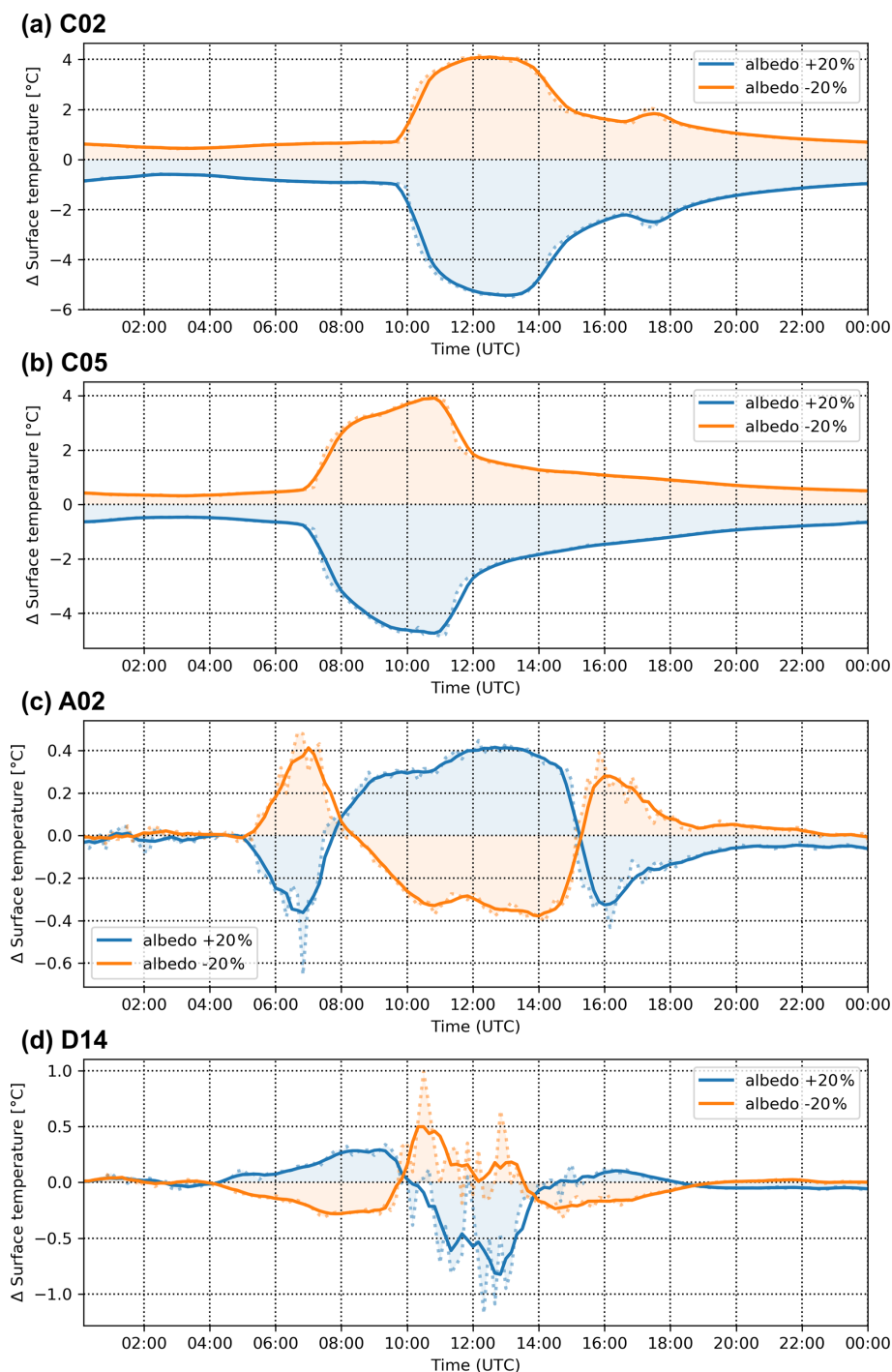


Figure 7. Differences in surface temperature in evaluation points C02 (a), C05 (b), A02 (c) and D14 (d) for albedo-changing scenarios SA01 (blue) and SA02 (orange). Dotted lines: 10 min values; solid lines: 1 h moving average.

perature and biometeorological indicators (in the additional outputs; see “Code and data availability” section for URL) around noon with differences reaching up to 6 K. For other examples of the influence of soil moisture on surface temperature in a validation study of a real city environment, see also Resler et al. (2020).

In some parts of the domain, the typical daily cycle of the differences is even reversed in certain periods of the day. A typical example of this behaviour is the sensitivity of surface temperature to albedo changes (Fig. 7). While most surfaces show an expected increase (decrease) in temperature with the decrease (increase) in albedo (typical examples are points

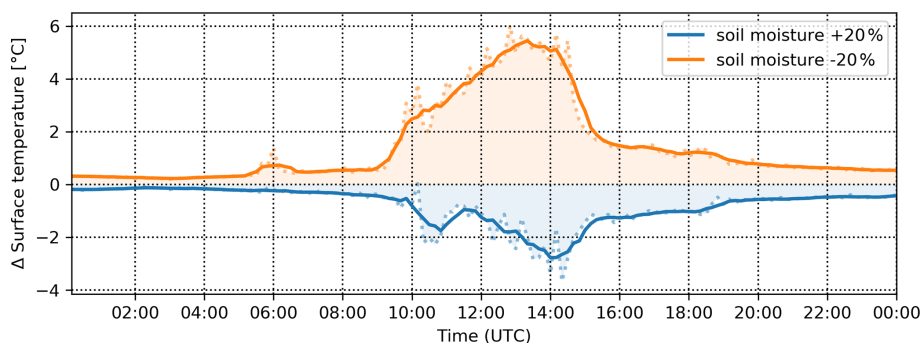


Figure 8. Soil moisture sensitivity of surface temperature difference for scenario SA20 (blue line) and SA21 (orange line) at point F03. Dotted lines: 10 min values; solid lines: 1 h moving average.

C02 and C05 in Fig. 7), some analysis points (e.g. A02, A04, B04, B06, D13, D14) show a reverse influence. Two examples of the inverse behaviour are illustrated in Fig. 7 for points A02 and D14 (lower two panels), clearly showing higher (lower) albedo resulting in higher (lower) surface temperatures during some parts of the day, when presumably increased (decreased) reflection from other surfaces brings more (less) SW radiation at these points compared to for the base case. The difference in the incoming SW radiation for points A01 and A02 is demonstrated in Fig. S15 comparing the S01 (blue) and S02 (orange) scenarios with the baseline (black): the A01 point (solid lines) receives less incoming radiation with increased albedo, while for the A02 point (dashed line) the incoming radiation is increased with increased albedo due to reflection from opposite surfaces in the corresponding time.

High spatial variability is also evident from other scenarios and shows the importance of using very high resolution models for local studies. As can be seen from, for example, figures for the emissivity changing scenarios SA03–SA05 (in the additional outputs; see “Code and data availability” section for URL), while the spatially averaged response shows mostly a simple daily cycle with a maximum change around noon, some individual points (e.g. A02, A04) show maxima in the morning and afternoon hours, while around noon the effect diminishes. Depending on the individual surface radiation budget given by the incoming solar radiation and reflections from other surfaces, some points experience a delayed peak in the afternoon hours with an inverse response; i.e. increased emissivity leads to an increase in temperatures (C04, D02).

3.2 Sensitivity to urban heat island mitigation measures

The second part of the sensitivity analysis focuses on the urbanistic scenarios. These scenarios include UHI mitigation measures, which planners and decision makers might apply to improve the bioclimatic situation in the city during high-temperature conditions, especially heatwaves. Typically con-

sidered measures include planting trees or changing surface materials (Table S02). As a contrast to SA scenarios, SB scenarios usually require changing more than one parameter at once. For instance, replacing concrete with grass results in changes in albedo, emissivity and roughness as well as in other parameters.

Sensitivity of the model response to SB scenarios is also summarized in Table S02. The most significant changes in surface temperature are observed in scenarios SB09 (land cover changes), SB10 (grey city 1) and SB11 (grey city 2), while for air temperature (Fig. 3), SB09–11, SB12 (green city with many planted trees), SB14 (new tree alley with both-side position on the Dělnická street) and SB15 (new tree alley with both-side position on both streets) show the strongest sensitivity. Scenario SB09, in which grass replaces roads and a tram line is replaced with a water channel, shows a decrease in surface temperatures by up to 3.0 K and in air temperature by up to 0.3 K. Grey-city scenarios SB10 and SB11 (Fig. 9), on the other hand, tend to increase temperatures significantly with 3 h maximum differences exceeding 2 K on the horizontal surfaces, whereas for air temperatures an increase by 0.3 and 0.1 K, respectively, is found. However, this difference between the two scenarios is dependent on the area of interest. For example, in the north–south street (Komunardů), the change in air temperatures is much more consistent between the scenarios, with maxima reaching +0.5 K in the late afternoon (Table S02 in the Supplement).

Scenario SB12 (green city with many planted trees) appears the most effective in decreasing temperature during the day with surface temperature cooler by up to 4.0 K and air temperature cooler by almost 0.5 K (Fig. 9). The effect is smaller during the nighttime, when the decrease in temperature is 0.8 and 0.12 K, respectively. Instead, scenario SB09 and even SB11 (removing trees but increasing grass-covered area) show decreases of more than 1.0 and 0.15 K in the surface and air temperatures.

In terms of thermal comfort, the two analysed characteristics (MRT and PET) show behaviour qualitatively similar to the physical temperatures. Again, the SB12 scenario (green

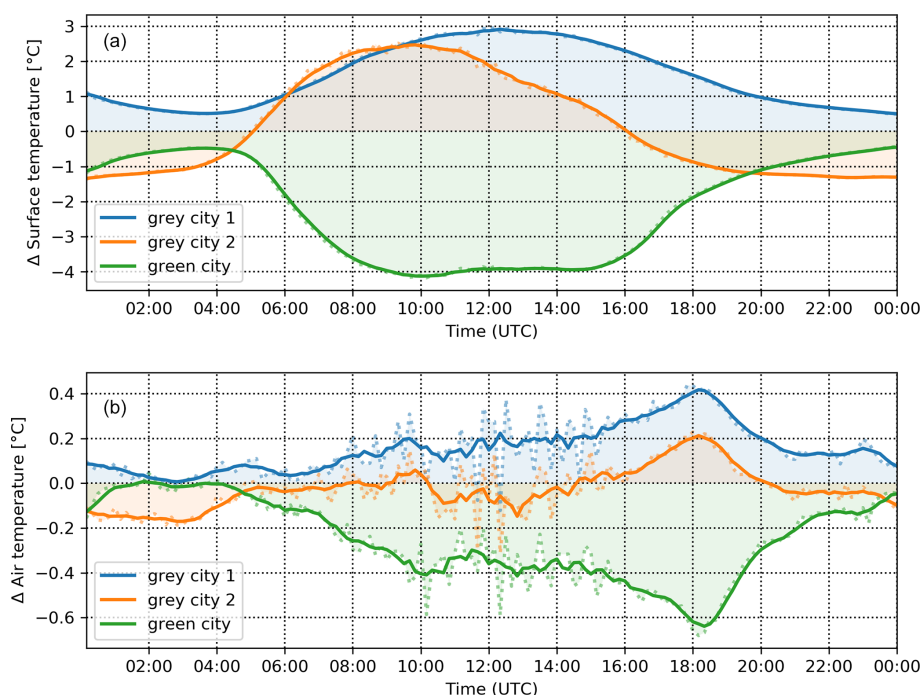


Figure 9. Domain-averaged differences in the surface temperature (a) and air temperature (b) for grey-city scenarios SB10 (blue) and SB11 (orange) and green-city scenario SB12 (green). Dotted lines: 10 min values; solid lines: 1 h moving average.

city with many planted trees) shows the most effective reduction with a maximum decrease of around 9 K in MRT and 4 K in PET in the entire domain. However, the effect varies considerably in space. The strongest change is observed in the west–east-oriented Dělnická street, while the north–south-oriented Komunardů street shows a much smaller decrease of 0.0–1.2 K (Fig. 10). This difference can be partly attributed to the geometric orientation of the streets and consequent differences in insolation during the day but also to the actual number of trees added with respect to the base case, in which more trees already grow in the Komunardů street. Similar behaviour is shown in the SB13–SB15 scenarios (new-tree-alley scenarios) with decreases of up to 4.0 K in MRT and 1.6 K in PET on average.

On the other hand, SB10 and SB11 scenarios (grey city 1 and 2) show a significant increase in both biophysical properties. The MRT is increased by 8 K (5 K) and PET is increased by 3 K (1.6 K; see Fig. 11) at around noon in the entire domain in SB10 (SB11). Similarly to the previous comparison, there is a marked spatial difference throughout the domain. However, the effect is strongest in the Komunardů street, with an increase of over 12 (MRT) and 3 K (PET), and courtyards (over 9 K and 4 K), while in the Dělnická street, the increase is only around 3 K in MRT and 1 K in PET.

Unlike for the SA sensitivity cases, $PM_{2.5}$ shows a significant dependence on the measures applied. However, the influence is almost universally inverse to the one for temperature. Generally, decreasing surface/air temperature increases

$PM_{2.5}$ concentrations by suppressing ventilation and turbulent mixing. On average the strongest effect is observed in the SB12 (green city with many planted trees) and SB15 (planting the highest number of trees) scenarios (Fig. 12), which show an increase of 24 % and 21 % in $PM_{2.5}$ with maxima over 30 % in the late afternoon hours. Scenarios that simulate planting trees only in the Dělnická street, SB13, one tree alley in the centre) and SB14 (tree alleys on both sides of the street), show similar responses in terms of the shape of the daily cycle but with a lower overall increase (Fig. 12); on average, these scenarios show an increase of 5 %–14 % in $PM_{2.5}$ concentrations, with maxima reaching almost 20 % for SB14 and 10 % for SB13 scenario (Fig. 12).

Interestingly, over the perpendicular Komunardů street with no new trees planted, the concentrations tend to decrease throughout most of the day, although this decrease is mostly concentrated at the crossroads; for the street sections north and south further away from the crossroads, no significant changes are modelled. The effect is connected to spatial changes and intensification of the street canyon eddy induced by the tree-obstructed Dělnická street which acts effectively as a part of the street canyon (not shown). The grey-city scenarios SB10 and SB11 conversely show decreased $PM_{2.5}$ concentrations of around 20 % in the afternoon and evening. Considering the spatial differences, the highest decrease is observed in the Komunardů street (over 50 %; see Fig. 13).

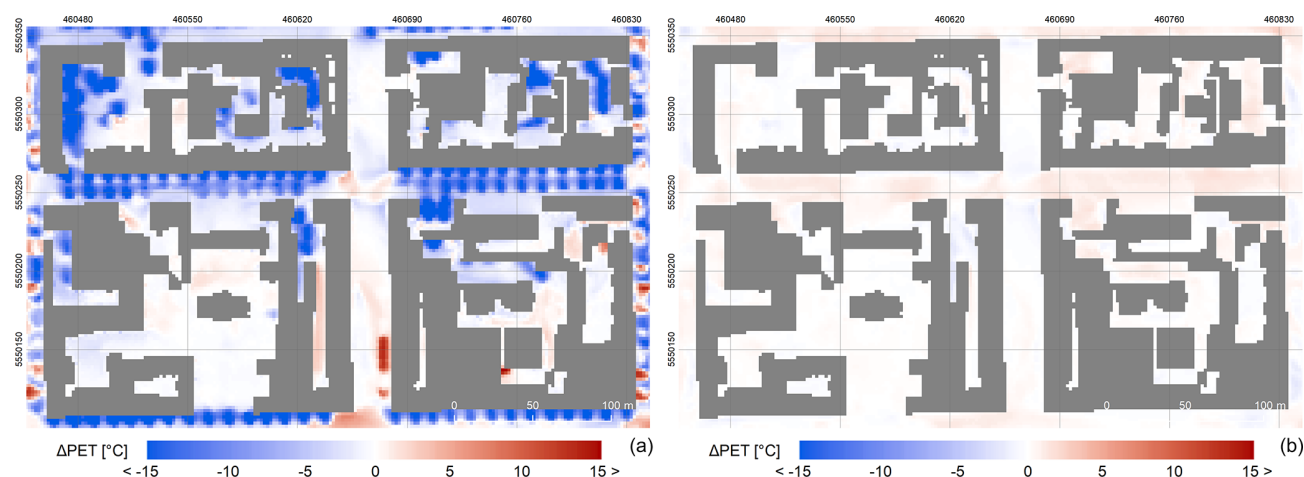


Figure 10. Example of spatio-temporal variability of 3 h PET differences for green-city scenario SB12 at 09:00–12:00 UTC (a) and 21:00–24:00 UTC (b). Projection: WGS 84 / UTM zone 33N; layer with roofs is own data source.

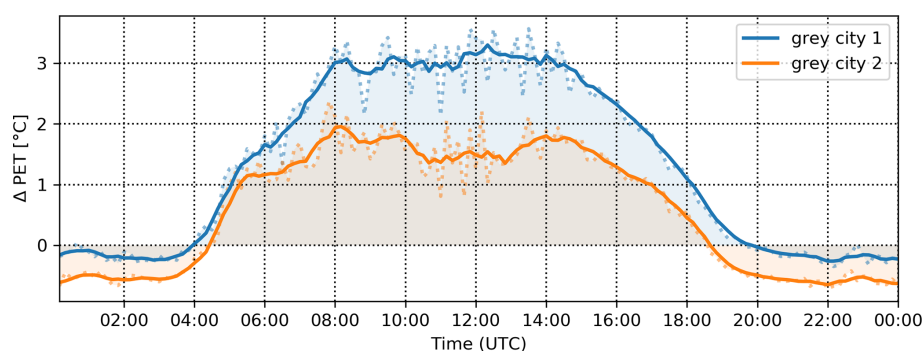


Figure 11. Domain-averaged differences in PET for grey-city scenarios SB10 (blue) and SB11 (orange). Dotted lines: 10 min values; solid lines: 1 h moving average.

4 Discussion and conclusions

4.1 Discussion

In this work, we assessed the sensitivity of air and surface temperature, MRT, PET, and $\text{PM}_{2.5}$ within the PALM model system 6.0 as a response to the modification of basic surface material parameters as well as to common UHI mitigation strategies. For this we performed a set of semi-idealized model simulations for a diurnal cycle in a city quarter in Prague.

The first set of scenarios, designed to examine the sensitivity to the parameter settings, shows the importance of the correct setting of the radiation parameters of albedo and emissivity. This can be expected as the solar radiation is the main source of energy in the surface energy budget. Additionally, unlike some other parameters, radiation parameters are changed for all surfaces.

In addition to albedo and emissivity, thermal conductivity of walls and volumetric heat capacity of the materials play an important role. Other parameters show a limited av-

erage effect on the diurnal timescale, which, however, can be quite significant during some parts of the day, such as surface roughness in the morning hours and the window fraction in the evening. Changing soil moisture by 20 % is shown to be negligible overall in the context of the chosen domain, with only a small percentage of the surface covered by vegetation (see Table 1), except for surface temperature during the high-sun part of the day. Individual parts of the domain with larger coverage of vegetation show greater influence. Note that we investigated only the short-term response of the urban canopy on the outlined modifications. The trends might be more prominent if long-term storage of energy in the materials were considered, i.e. when simulating a full heatwave.

The second part of the sensitivity analysis focused on the UHI mitigation measures. One of the commonly considered measures is to paint surfaces white to increase surface albedo. However, our results indicate that this is only effective for lowering the surface and air temperature. In contrast, the biophysical indicators MRT and PET tend to be negatively affected; i.e. thermal comfort in the street deteriorates due to increasing the amount of reflected radiation (note that

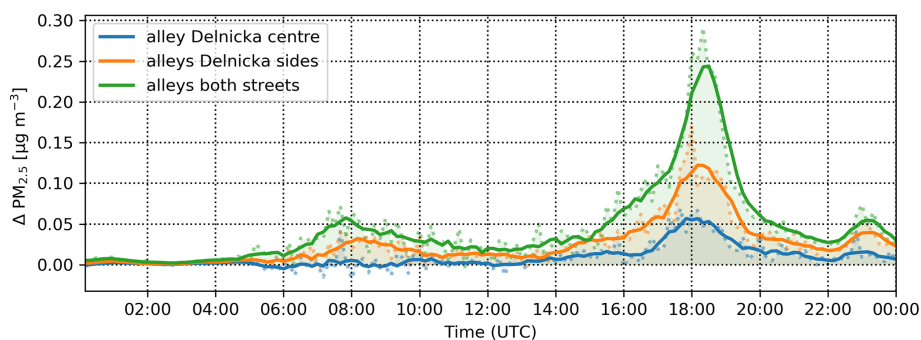


Figure 12. Domain-averaged differences in $\text{PM}_{2.5}$ for new-tree-alley scenarios SB13 (blue), SB14 (orange) and SB15 (green). Dotted lines: 10 min values; solid lines: 1 h moving average.

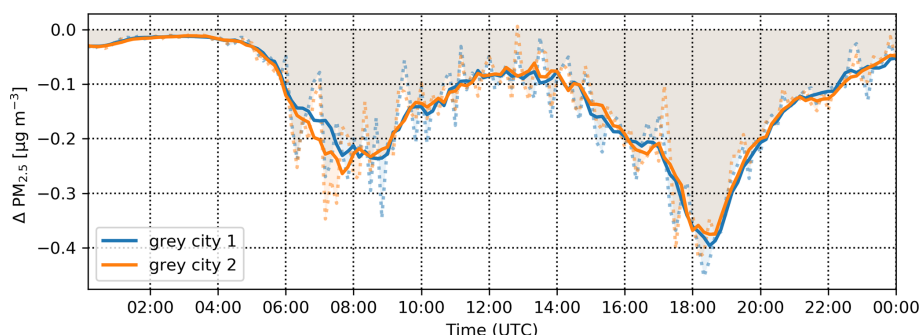


Figure 13. Differences in $\text{PM}_{2.5}$ in the Komunardů street for a grey-city scenarios SB10 (blue) and SB11 (orange). Dotted lines: 10 min values; solid lines: 1 h moving average.

the effect can be different on purely horizontal surfaces such as roofs). Improving both physical and biophysical temperature indicators requires the application of other measures, such as urban greening at the same time. Similar findings have also been reported in, for example, a meta-analysis of 52 ENVI-met simulations by Tsoka et al. (2018) and Yang et al. (2015), who stress the need for precaution when adopting high-reflectivity surfaces, or Aflaki et al. (2017), who found low-albedo vegetation effective in reducing mean radiant temperature.

Urban vegetation is found to be the most effective measure when considering reduction in both physical and biophysical temperature indicators. Conversely, grey-city scenarios that reduce the amount of urban vegetation show significant worsening of the thermal comfort. Urban greenery is very often found to be an effective mitigation tool for the UHI phenomenon; for example a recent study by McRae et al. (2020) reports vegetation-induced cooling of more than 3°C in an ENVI-met simulation. However, some studies (e.g. Wang et al., 2016; Tsoka et al., 2018; or Makido et al., 2019) show that for the best effect it is necessary to combine several measures and also to consider that different parts of the city may need different measures.

One of the most important results of our analysis is that it confirms opposite behaviour of thermal comfort and air

quality indicators (see example in Fig. 14). Observed in both types of scenarios, the $\text{PM}_{2.5}$ concentrations typically increase with decreasing temperatures and vice versa. The main reason for this behaviour is decreased ventilation in the street canyon due to airflow blocking. The decreased vertical turbulent transport due to reduced urban canopy temperatures and thus buoyancy can play a role too, as shown by Huszár et al. (2018b, 2020), who found significant PM decreases due to urban-canopy-induced vertical eddy diffusion. However, in these simulations, only aerosol passive transfer was taken into account, and thus the results may be different for other air quality indicators, e.g. when considering the influence of changing reaction coefficients and a decrease in solar radiation for ozone chemistry (Huszár et al., 2018a).

The $\text{PM}_{2.5}$ concentrations in Fig. 14 also show the important added value of the high-resolution CFD models for urban modelling compared to parameterized urban schemes in NWP and climate models or radiation models. In this case it is the spatial variability within the streets. As can be seen, the combined radiative and dynamical effects manifest in quite a heterogeneous response where (in this particular case) the increase in concentrations is most prominent in the northern half of the Dělnická street, while in some parts on the southern side the model shows a decrease in concentrations. In the Komunardů street, the response shows very small changes in

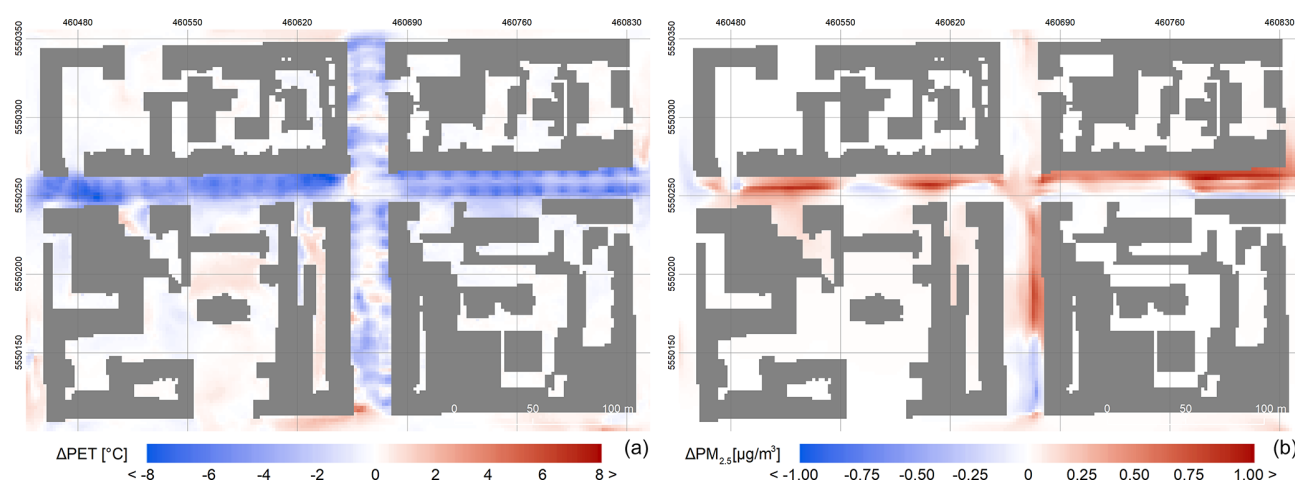


Figure 14. Example of opposite behaviour of thermal comfort and air quality indicators represented by average daily difference in PET and $PM_{2.5}$ for new-alley scenario SB15.

the upper section of the street while in the lower section the model shows almost a see-saw response with increased concentrations in the upper half and a decrease in the lower half of the section.

4.2 Study limitations

This study applied the PALM model revision 4093. The model itself and the configuration applied for this study have some limitations, with the following being the most important ones in our case:

- The model is configured without the PALM-4U building energy model (BEM), and the building inner temperature is considered constant (300 K) during the simulation. The impacts of the absence of a more complex indoor model differ in the summer and winter seasons. In winter, assuming that the rooms are heated to the exact prescribed temperature by either direct local heat sources or long-distance heating with the heating plant being outside the modelled domain, the model adds correct heat fluxes to the insides of the buildings, albeit not providing the amount of heating energy consumed among its outputs. In summer, the constant indoor temperature can be seen as a simplification for buildings without air conditioning where the wall insulation and wall heat capacity dampen most of the daily temperature difference, as long as the inner temperature is realistic and the daily total net heat flux is near zero. Buildings with air conditioning need a more complex indoor model with correctly placed heat exchangers (windows for individual A/C units and roofs for central A/C systems). For the simulated domain, there was no information available about the number and placement of A/C systems, with the majority of the buildings being old apartment houses with presumably no cen-

tral A/C systems and no visible individual A/C units at windows. For long-term simulations, missing waste heat which could be provided by PALM's indoor model will be important although, given the short timescale of the present study simulations, the indoor model should not affect the outcome. The outer wall layers react very fast to changes in the surface energy balance, but the inner wall layers have large inertia, so nothing is likely to change if the indoor temperature changes in time.

- The model sensitivities are tested only during meteorological conditions of heatwave episodes as the main focus is on simulation of the UHI mitigation measures. Only the short-term response of the urban canopy was investigated. The behaviour, including the long-term response, during other seasons and weather conditions can and probably will differ from presented results.
- The simulations do not consider any chemical reactions or aerosol dynamic processes of air pollutants; only the dispersion of traffic-related $PM_{2.5}$ is considered. Moreover, the boundary conditions of the chemical species on the parent domain were set to zero. This experiment design was selected as the focus of the study is on the sensitivity of the concentrations to the local conditions. The time needed for secondary organic aerosol (SOA) formation is much longer than the typical time the chemical species spent in the studied domain (e.g. Du et al., 2018, or Tang et al., 2018). The consequence is that the SOA concentration field is almost constant over the studied domain. It means that even though the SOAs constitute an important part of the $PM_{2.5}$, their omission does not change the differences in $PM_{2.5}$ between particular scenarios.
- This version initiates the building wall properties through the `building_2d` property in the model

static driver; i.e. the wall properties are set to the roof grid cell over the wall (i.e. border grid cells of the roof). This leads to the following two simplifications.

- The properties of the wall can be set only in two height zones, and the corner grid cells set the properties of two surface grid cells corresponding to different walls.
- The roof properties in the border grid cells are initialized to the wall properties. This limitation leads to artefacts in roof and wall surface temperature and heat fluxes. This drawback was removed in later versions (model revision 4240 and later) by implementation of reading separate properties for individual surface cells from the new static driver variable `building_surface_pars`.
- The ventilation of very tight areas surrounded by high buildings is underestimated by the model, and the temperatures and concentrations of pollutants become unrealistically high in some circumstances. It is known that higher concentrations can be expected in enclosed spaces due to low turbulence (Gronemeier and Sühling, 2019). This problem was addressed in the model revision 4110. For the purpose of this analysis, these small areas were excluded from the evaluation.

Taking these limitations into account, we consider the simulation to produce plausible results both in actual values and in their spatial and temporal distribution in the baseline simulation. This was confirmed by comparing the general agreement of the results to the previously validated simulations (Resler et al., 2017) in the preparatory stage of this experiment (not shown). Obviously, extensive validation of the model against observations is beyond the scope of this paper. For systematic validation of the current model version, we refer the readers to the accompanying paper by Resler et al. (2020).

The LES is quite demanding in terms of computational power, especially when compared with its RANS-based counterpart. Since we did not perform evaluation of the model results against observations in this study, it cannot be shown whether the additional computer resources used bring about an improvement in the model performance. However, numerous studies have been published showing the added value of LES for street canyon simulations especially where air quality is concerned. For example Gousseau et al. (2011), Salim et al. (2011), and Tominaga and Stathopoulos (2011) evaluated LES and RANS simulations against wind-tunnel measurements in street canyon experiments, and all conclude that LES shows better performance. More recently, Antoniou et al. (2017) studied outdoor ventilation in a real urban area of Nicosia, Cyprus, again evaluating RANS simulations and LES against wind-tunnel measurements. They conclude that LES shows smaller deviations from the measurements than

RANS simulations for mean wind speed and turbulence intensity.

4.3 Conclusions

In conclusion, this analysis shows that the proper setting of urban surface parameters is crucial for high-resolution LES models of the urban environment and that collecting this large number of data is an essential part of the modelling technique. High temporal and spatial variability also shows the importance of using truly local information for each area of interest. This fact also poses certain limits on the applicability of the findings of this study for other locations. On the one hand, the above comparisons with other studies showed qualitatively similar results in average behaviour, and in this sense we can expect similar average results in other densely built urban areas in similar climatic conditions (e.g. many European cities). However, quantitative assessment is largely dependent on the location studied, namely the physical configuration of buildings and other urban components, and thus the actual sensitivity values may differ between locations. This is evident, for example, from the albedo scenarios, for which the response in some locations was reversed depending on the geometrical configuration or soil moisture scenarios, when the small amount of existing vegetation limits the potential response of the system to changing soil moisture in larger areas. When assessing the very local influences, e.g. pedestrian-level thermal comfort, the local settings play a major role and thus need to be considered for proper evaluation.

Altogether, the LES method proves to be an asset thanks to its capability to fully resolve the flow and to consider heterogeneity in the modelling domain. Hence, LES modelling results can be really applied to support urban planning when aiming to mitigate the UHI phenomenon in urban neighbourhoods.

Code and data availability. The PALM model system is freely available from <http://palm-model.org> (last access: 30 March 2020) and distributed under the GNU General Public License v3 (<http://www.gnu.org/copyleft/gpl.html>, last access: 30 March 2020). The model source code of version 6.0 in revision r4093 used in this article is also available via <https://doi.org/10.25835/0068421> (Geletic et al., 2020).

Model configuration files; input data needed for running the simulations; and model output postprocessing code, i.e. extraction and visualization scripts, together with necessary data extracted from the raw model outputs and additional outputs, are available for download at <http://hdl.handle.net/11104/0309669> (Library of Czech Academy of Sciences, 2020).

Supplement. The supplement related to this article is available online at: <https://doi.org/10.5194/gmd-14-4443-2021-supplement>.

Author contributions. MB was the main coordinator of manuscript proceedings and responsible for the general topic of the paper and the analysis of results. All co-authors contributed to the manuscript text. KE configured and processed WRF simulations used for preparation of boundary conditions; JG was involved in geodata preprocessing, result postprocessing and data mining. JR and PK were strongly involved in the PALM model setup and processed the PALM simulations; JR also participated in the experiment design. VF, FKS, MS and BM participated in the general topic, discussion and text preparation. NB, MA and MK are specialists in air quality modelling and participated in this field of study.

Competing interests. The authors declare that they have no conflict of interest.

Disclaimer. Publisher's note: Copernicus Publications remains neutral with regard to jurisdictional claims in published maps and institutional affiliations.

Acknowledgements. The simulations were performed on the HPC infrastructure of the Institute of Computer Science (ICS) of the Czech Academy of Sciences supported by the long-term strategic development financing of the ICS (RVO 67985807) and partly in the supercomputing centre IT4I which was supported by the Ministry of Education, Youth and Sports through the Large Infrastructures for Research, Experimental Development and Innovations project IT4Innovations National Supercomputing Center – LM2015070.

Financial support was provided by the Operational Program Prague – Growth Pole of the Czech Republic project Urbanization of weather forecast, air-quality prediction and climate scenarios for Prague (CZ.07.1.02/0.0/0.0/16_040/0000383), which is co-financed by the EU. The co-authors Björn Maronga, Farah Kanani-Sühring and Matthias Sühring were supported by the German Federal Ministry of Education and Research (BMBF) under grant 01LP1601 within the framework of Research for Sustainable Development (FONA; <https://www.fona.de/de/>, last access: 27 May 2021). Financial support was also provided by the Norway Grants and Technology Agency of the Czech Republic project TO01000219: Turbulent-resolving urban modeling of air quality and thermal comfort.

Financial support. This research has been supported by the European structural and investment funds (grant no. CZ.07.1.02/0.0/0.0/16_040/0000383), the German Federal Ministry of Education and Research (grant no. 01LP1601A), and the Norway Grants and Technology Agency of the Czech Republic (Turbulent-resolving urban modeling of air quality and thermal comfort (grant no. TO01000219)).

Review statement. This paper was edited by Simon Unterstrasser and reviewed by two anonymous referees.

References

- Aflaki, A., Mirnezhad, M., Ghaffarianhoseini, A., Ghaffarianhoseini, A., Omrany, H., Wang, Z., and Akbari, H.: Urban heat island mitigation strategies: A state-of-the-art review on Kuala Lumpur, Singapore and Hong Kong, *Cities*, 62, 131–145, <https://doi.org/10.1016/j.cities.2016.09.003>, 2017.
- Ai, Z. T. and Mak, C. M.: Modeling of coupled urban wind flow and indoor air flow on a high-density near-wall mesh: Sensitivity analyses and case study for single-sided ventilation. *Environ. Modell. Softw.*, 60, 57–68, <https://doi.org/10.1016/j.envsoft.2014.06.010>, 2014.
- Antoniou, N., Montazeri, H., Wigo, H., Neophytou, M. K. A., Blocken, B., and Sandberg, M.: CFD and wind-tunnel analysis of outdoor ventilation in a real compact heterogeneous urban area: Evaluation using “air delay”, *Build. and Environ.*, 126, 355–372, <https://doi.org/10.1016/j.buildenv.2017.10.013>, ISSN 0360-1323, 2017.
- Arnfield, A. J.: Two decades of urban climate research: a review of turbulence, exchanges of energy and water, and the urban heat island. *Int. J. Climatol.*, 23, 1–26, <https://doi.org/10.1002/joc.859>, 2003.
- Ashie, Y. and Kono, T.: Urban-scale CFD analysis in support of a climate-sensitive design for the Tokyo Bay area. *Int. J. Climatol.*, 31, 174–188, <https://doi.org/10.1002/joc.2226>, 2010.
- CHMI: Emission balance of the Czech Republic, Table, available at: <http://pr-asu.chmi.cz:8080/EmisBalanceView/faces/viewBalance.xhtml>, last access: 25 January 2021.
- Crank, P. J., Sailor, D. J., Ban-Weiss, G., and Taleghani, M.: Evaluating the ENVI-met microscale model for suitability in analysis of targeted urban heat mitigation strategies, *Urban Climate*, 26, 188–197, <https://doi.org/10.1016/j.uclim.2018.09.002>, 2018.
- Deardorff, J. W.: Stratocumulus-capped mixed layers derived from a three-dimensional model, *Bound.-Lay. Meteorol.*, 18, 495–527, 1980.
- Du, Z., Hu, M., Peng, J., Zhang, W., Zheng, J., Gu, F., Qin, Y., Yang, Y., Li, M., Wu, Y., Shao, M., and Shuai, S.: Comparison of primary aerosol emission and secondary aerosol formation from gasoline direct injection and port fuel injection vehicles, *Atmos. Chem. Phys.*, 18, 9011–9023, <https://doi.org/10.5194/acp-18-9011-2018>, 2018.
- Ebi, K.: Climate change and health risks: assessing and responding to them through “adaptive management”, *Health Affair.*, 30, 5, 924–930, <https://doi.org/10.1377/hlthaff.2011.0071>, 2011.
- Emmanuel, R. and Loconsole, A.: Green infrastructure as an adaptation approach to tackling urban overheating in the Glasgow Clyde Valley Region, UK, *Landscape Urban Plan.*, 138, 71–86, <https://doi.org/10.1016/j.landurbplan.2015.02.012>, 2015.
- Fröhlich, D. and Matzarakis, A.: Calculating human thermal comfort and thermal stress in the PALM model system 6.0, *Geosci. Model Dev.*, 13, 3055–3065, <https://doi.org/10.5194/gmd-13-3055-2020>, 2020.
- Gál, C.V. and Kántor, N.: Modeling mean radiant temperature in outdoor spaces, A comparative numerical simulation and validation study, *Urban Climate*, 32, 100571, <https://doi.org/10.1016/j.uclim.2019.100571>, 2020.
- García-Sánchez, C., van Beeck, J., and Gorlé, C.: Predictive large eddy simulations for urban flows: Challenges and opportunities, *Build. Environ.*, 139, 146–156, <https://doi.org/10.1016/j.buildenv.2018.05.007>, 2018.

- Gehrke, K. F., Sühling, M., and Maronga, B.: Modeling of land-surface interactions in the PALM model system 6.0: Land surface model description, first evaluation, and sensitivity to model parameters, *Geosci. Model Dev. Discuss.* [preprint], <https://doi.org/10.5194/gmd-2020-197>, in review, 2020.
- Geletić, J., Resler, J., Krč, P., Maronga, B., Sühling, M., and Fuka, V.: Dataset: PALM 6.0 r4093, <https://doi.org/10.25835/0068421>, 2020.
- Gill, S., Handley, J., Ennos, A., and Pauleit, S.: Adapting cities for climate change: the role of the green infrastructure. *Built Environment*, 33, 1, 115–133, <https://doi.org/10.2148/benv.33.1.115>, 2007.
- Gousseau, P., Blocken, B., Stathopoulos, T., and van Heijst, G. J. F.: CFD simulation of near-field pollutant dispersion on a high-resolution grid: A case study by LES and RANS for a building group in downtown Montreal, *Atmos. Environ.*, 45, 428–438, <https://doi.org/10.1016/j.atmosenv.2010.09.065>, ISSN 1352-2310, 2011.
- Gronemeier, T. and Sühling, M.: On the Effects of Lateral Openings on Courtyard Ventilation and Pollution – A Large-Eddy Simulation Study, *Atmosphere*, 10, 63, <https://doi.org/10.3390/atmos10020063>, 2019.
- Gross, G.: Effects of different vegetation on temperature in an urban building environment. Micro-scale numerical experiments, *Meteorol. Z.*, 21, 399–412, <https://doi.org/10.1127/0941-2948/2012/0363>, 2012.
- Hackbusch, W.: *Multi-Grid Methods and Applications*, Springer, Berlin, Heidelberg, 2nd printing, <https://doi.org/10.1007/978-3-662-02427-0>, 1985.
- Haines, A., Kovats, R. S., Campbell-Lendrum, D., and Corvalan, C.: Climate change and human health: impacts, vulnerability and public health, *Public Health*, 120, 585–596, <https://doi.org/10.1016/j.puhe.2006.01.002>, 2006.
- Heldens, W., Burmeister, C., Kanani-Sühling, F., Maronga, B., Pavlik, D., Sühling, M., Zeidler, J., and Esch, T.: Geospatial input data for the PALM model system 6.0: model requirements, data sources and processing, *Geosci. Model Dev.*, 13, 5833–5873, <https://doi.org/10.5194/gmd-13-5833-2020>, 2020.
- Hellsten, A., Ketelsen, K., Sühling, M., Auvinen, M., Maronga, B., Knigge, C., Barmpas, F., Tsegas, G., Moussiopoulos, N., and Raasch, S.: A nested multi-scale system implemented in the large-eddy simulation model PALM model system 6.0, *Geosci. Model Dev.*, 14, 3185–3214, <https://doi.org/10.5194/gmd-14-3185-2021>, 2021.
- Hunt, A. and Watkiss, P.: Climate change impacts and adaptation in cities: a review of the literature, *Clim. Change*, 104, 13–49, <https://doi.org/10.1007/s10584-010-9975-6>, 2011.
- Huszár, P., Karlický, J., Belda, M., Halenka, T., and Pišoft, P.: The impact of urban canopy meteorological forcing on summer photochemistry, *Atmos. Environ.*, 176, 209–228, <https://doi.org/10.1016/j.atmosenv.2017.12.037>, 2018a.
- Huszár, P., Belda, M., Karlický, J., Bardachova, T., Halenka, T., and Pišoft, P.: Impact of urban canopy meteorological forcing on aerosol concentrations, *Atmos. Chem. Phys.*, 18, 14059–14078, <https://doi.org/10.5194/acp-18-14059-2018>, 2018b.
- Huszár, P., Karlický, J., Ďoubalová, J., Šindelářová, K., Nováková, T., Belda, M., Halenka, T., Žák, M., and Pišoft, P.: Urban canopy meteorological forcing and its impact on ozone and PM_{2.5}: role of vertical turbulent transport, *Atmos. Chem. Phys.*, 20, 1977–2016, <https://doi.org/10.5194/acp-20-1977-2020>, 2020.
- IPCC: Climate Change 2014: Impacts, Adaptation, and Vulnerability. Part A: Global and Sectoral Aspects, in: Contribution of Working Group II to the Fifth Assessment Report of the Intergovernmental Panel on Climate Change, edited by: Field, C. B., Barros, V. R., Dokken, D. J., Mach, K. J., Mastrandrea, M. D., Bilir, T. E., Chatterjee, M., Ebi, K. L., Estrada, Y. O., Genova, R. C., Girma, B., Kissel, E. S., Levy, A. N., MacCracken, S., Mastrandrea, P. R., and White, L. L., Cambridge University Press, Cambridge, United Kingdom and New York, NY, USA, 1132 pp., <https://doi.org/10.1017/CBO9781107415379>, 2014a.
- IPCC: Climate Change 2014: Mitigation of Climate Change, in: Contribution of Working Group III to the Fifth Assessment Report of the Intergovernmental Panel on Climate Change, edited by: Edenhofer, O., Pichs-Madruga, R., Sokona, Y., Farahani, E., Kadner, S., Seyboth, K., Adler, A., Baum, I., Brunner, S., Eickemeier, P., Kriemann, B., Savolainen, J., Schlömer, S., von Stechow, C., Zwickel, T., and Minx, J. C., Cambridge University Press, Cambridge, United Kingdom and New York, NY, USA, <https://doi.org/10.1017/CBO9781107415416>, 2014b.
- Kadasch, E., Sühling, M., Gronemeier, T., and Raasch, S.: Mesoscale nesting interface of the PALM model system 6.0, *Geosci. Model Dev. Discuss.* [preprint], <https://doi.org/10.5194/gmd-2020-285>, in review, 2020.
- Khan, B., Banzhaf, S., Chan, E. C., Forkel, R., Kanani-Sühling, F., Ketelsen, K., Kurppa, M., Maronga, B., Mauder, M., Raasch, S., Russo, E., Schaap, M., and Sühling, M.: Development of an atmospheric chemistry model coupled to the PALM model system 6.0: implementation and first applications, *Geosci. Model Dev.*, 14, 1171–1193, <https://doi.org/10.5194/gmd-14-1171-2021>, 2021.
- Kovats, R. S. and Hajat, S.: Heat stress and public health: a critical review, *Annu. Rev. Publ. Health*, 29, 41–55, <https://doi.org/10.1146/annurev.publhealth.29.020907.090843>, 2008.
- Krayenhoff, E. S., Broadbent, A. M., Zhao, L., Georgescu, M., Middel, A., Voogt, J. A., Martilli, A., Sailor, D. J., and Erell, E.: Cooling hot cities: A systematic and critical review of the numerical modelling literature, *Environ. Res. Lett.*, 16, 053007, <https://doi.org/10.1088/1748-9326/abdcf1>, 2021.
- Krč, P., Resler, J., Sühling, M., Schubert, S., Salim, M. H., and Fuka, V.: Radiative Transfer Model 3.0 integrated into the PALM model system 6.0, *Geosci. Model Dev.*, 14, 3095–3120, <https://doi.org/10.5194/gmd-14-3095-2021>, 2021.
- Kusaka, H., Kondo, H., Kikegawa, Y., and Kimura, F.: A Simple Single-Layer Urban Canopy Model For Atmospheric Models: Comparison With Multi-Layer And Slab Models, *Bound.-Lay. Meteorol.*, 101, 329–358, <https://doi.org/10.1023/A:1019207923078>, 2001.
- Library of Czech Academy of Sciences: Sensitivity Analysis of the PALM Model System 6.0 in the Urban Environment, available at: <http://hdl.handle.net/11104/0309669> (last access: 13 July 2021), 2020.
- Lindberg, F., Holmer, B., and Thorsson, S.: SOLWEIG 1.0 – modelling spatial variations of 3d radiant fluxes and mean radiant temperature in complex urban settings, *Int. J. Biometeorol.*, 52, 697–713, 2008.

- Lindberg, F., Grimmond, C. S. B., Gabey, A., Huang, B., Kent, C. W., Sun, T., Theeuwes, N. E., Järvi, L., Ward, H. C., and Capel-Timms, I.: Urban multi-scale environmental predictor (umep): an integrated tool for city-based climate services, *Environ. Modell. Softw.*, 99, 70–87, 2018.
- Lobaccaro, G. and Acero, J. A.: Comparative analysis of green actions to improve outdoor thermal comfort inside typical urban street canyons, *Urban Climate*, 14, 251–267, <https://doi.org/10.1016/j.uclim.2015.10.002>, 2015.
- Makido, Y., Hellman, D., and Shandas, V.: Nature-Based Designs to Mitigate Urban Heat: The Efficacy of Green Infrastructure Treatments in Portland, Oregon, *Atmosphere*, 10, 282, <https://doi.org/10.3390/atmos10050282>, 2019.
- Maronga, B., Gryschka, M., Heinze, R., Hoffmann, F., Kanani-Sühring, F., Keck, M., Ketelsen, K., Letzel, M. O., Sühring, M., and Raasch, S.: The Parallelized Large-Eddy Simulation Model (PALM) version 4.0 for atmospheric and oceanic flows: model formulation, recent developments, and future perspectives, *Geosci. Model Dev.*, 8, 2515–2551, <https://doi.org/10.5194/gmd-8-2515-2015>, 2015.
- Maronga, B., Banzhaf, S., Burmeister, C., Esch, T., Forkel, R., Fröhlich, D., Fuka, V., Gehrke, K. F., Geletič, J., Giersch, S., Gronemeier, T., Groß, G., Heldens, W., Hellsten, A., Hoffmann, F., Inagaki, A., Kadasch, E., Kanani-Sühring, F., Ketelsen, K., Khan, B. A., Knigge, C., Knoop, H., Krč, P., Kurppa, M., Maamari, H., Matzarakis, A., Mauder, M., Pallasch, M., Pavlik, D., Pfafferoth, J., Resler, J., Rissmann, S., Russo, E., Salim, M., Schrempf, M., Schwenkel, J., Seckmeyer, G., Schubert, S., Sühring, M., von Tils, R., Vollmer, L., Ward, S., Witha, B., Wurps, H., Zeidler, J., and Raasch, S.: Overview of the PALM model system 6.0, *Geosci. Model Dev.*, 13, 1335–1372, <https://doi.org/10.5194/gmd-13-1335-2020>, 2020.
- Martilli, A., Clappier, A., and Rotach, M. W.: An Urban Surface Exchange Parameterisation for Mesoscale Models, *Bound.-Lay. Meteorol.*, 104, 261–304, <https://doi.org/10.1023/A:101609921195>, 2002.
- Matzarakis, A., Rutz, F., and Mayer, H.: Modelling Radiation fluxes in simple and complex environments – Basics of the RayMan model, *Int. J. Biometeorol.*, 54, 131–139, 2010.
- McRae, I., Freedman, F., Rivera, A., Li, X., Dou, J., Cruz, I., Ren, C., Dronova, I., Fraker, H., and Bornstein, R.: Integration of the WUDAPT, WRF, and ENVI-met models to simulate extreme daytime temperature mitigation strategies in San Jose, California, *Build. Environ.*, 184, 107180, <https://doi.org/10.1016/j.buildenv.2020.107180>, 2020.
- Ateliér ekologických modelů, s.r.o (ATEM): MEFA 13: User guide, Prague, May 2013, available at: http://www.atem.cz/ke_stazeni.php, last access: 21 March 2020 (software and user guide documentation in Czech language only).
- Mills, G.: Urban climatology: History, status and prospects, *Urban Climate*, 10, 479–489, <https://doi.org/10.1016/j.uclim.2014.06.004>, 2014.
- Moeng, C.-H. and Wyngaard, J. C.: Spectral analysis of large-eddy simulations of the convective boundary layer, *J. Atmos. Sci.*, 45, 3573–3587, [https://doi.org/10.1175/1520-0469\(1988\)045<3573:SAOLES>2.0.CO;2](https://doi.org/10.1175/1520-0469(1988)045<3573:SAOLES>2.0.CO;2), 1988.
- Müller, N., Kuttler, W., and Barlag, A. B.: Counteracting urban climate change: adaptation measures and their effect on thermal comfort, *Theor. Appl. Climatol.*, 115, 243–257, <https://doi.org/10.1007/s00704-013-0890-4>, 2013.
- Oke, T. R.: The energetic basis of the urban heat island, *Q. J. Roy. Meteor. Soc.*, 108, 1–24, <https://doi.org/10.1002/qj.49710845502>, 1982.
- Patz, J. A., Campbell-Lendrum, D., Holloway, T., and Foley, J. A.: Impact of regional climate change on human health, *Nature*, 438, 310–317, <https://doi.org/10.1038/nature04188>, 2005.
- Ramponi, R. and Blocken, B.: CFD simulation of cross-ventilation for a generic isolated building: Impact of computational parameters, *Build. Environ.*, 53, 34–48, <https://doi.org/10.1016/j.buildenv.2012.01.004>, 2012.
- Resler, J., Krč, P., Belda, M., Juruš, P., Benešová, N., Lopata, J., Vlček, O., Damašková, D., Eben, K., Derbek, P., Maronga, B., and Kanani-Sühring, F.: PALM-USM v1.0: A new urban surface model integrated into the PALM large-eddy simulation model, *Geosci. Model Dev.*, 10, 3635–3659, <https://doi.org/10.5194/gmd-10-3635-2017>, 2017.
- Resler, J., Eben, K., Geletič, J., Krč, P., Rosecký, M., Sühring, M., Belda, M., Fuka, V., Halenka, T., Huszár, P., Karlický, J., Benešová, N., Ďoubalová, J., Honzák, K., Keder, J., Nápravníková, Š., and Vlček, O.: Validation of the PALM model system 6.0 in real urban environment; case study of Prague-Dejvice, Czech Republic, *Geosci. Model Dev. Discuss.* [preprint], <https://doi.org/10.5194/gmd-2020-175>, in review, 2020.
- Saiki, E. M., Moeng, C.-H., and Sullivan, P. P.: Large-eddy simulation of the stably stratified planetary boundary layer, *Bound. Lay.-Meteorol.*, 95, 1–30, <https://doi.org/10.1023/A:1002428223156>, 2000.
- Salamanca, F., Krpo, A., Martilli, A., and Clappier, A.: A new building energy model coupled with an urban canopy parameterization for urban climate simulations—part I. formulation, verification, and sensitivity analysis of the model, *Theor. Appl. Climatol.*, 99, 331, <https://doi.org/10.1007/s00704-009-0142-9>, 2010.
- Salim M. S., Buccolieri, R., Chan, A., and Di Sabatino, S.: Numerical simulation of atmospheric pollutant dispersion in an urban street canyon: Comparison between RANS and LES, *J. Wind Eng. Ind. Aerod.*, 99, 103–113, <https://doi.org/10.1016/j.jweia.2010.12.002>, 2011.
- Seidel, D. J., Zhang, Y., Beljaars, A., Golaz, J., Jacobson, A. R., and Medeiros, B.: Climatology of the planetary boundary layer over the continental United States and Europe, *J. Geophys. Res.*, 117, D17106, <https://doi.org/10.1029/2012JD018143>, 2012.
- Souch, C. and Grimmond, S.: Applied climatology: urban climate, *Prog. Phys. Geog.*, 30, 270–279, <https://doi.org/10.1191/0309133306pp484pr>, 2006.
- Stewart, I. D.: A systematic review and scientific critique of methodology in modern urban heat island literature, *Int. J. Climatol.*, 31, 200–217, <https://doi.org/10.1002/joc.2141>, 2011.
- Su, W., Zhang, Y., Yang, Y., and Ye, G.: Examining the Impact of Greenspace Patterns on Land Surface Temperature by Coupling LiDAR Data with a CFD Model, *Sustainability*, 6, 6799–6814, <https://doi.org/10.3390/su6106799>, 2014.
- Tang, R., Wu, Z., Li, X., Wang, Y., Shang, D., Xiao, Y., Li, M., Zeng, L., Wu, Z., Hallquist, M., Hu, M., and Guo, S.: Primary and secondary organic aerosols in summer 2016 in Beijing, *Atmos. Chem. Phys.*, 18, 4055–4068, <https://doi.org/10.5194/acp-18-4055-2018>, 2018.

- Tominaga, Y. and Stathopoulos, T.: CFD modeling of pollution dispersion in a street canyon: Comparison between LES and RANS, *J. Wind Eng. Ind. Aerod.*, 99, 340–348, <https://doi.org/10.1016/j.jweia.2010.12.005>, ISSN 0167-6105, 2011.
- Tsoka, S., Tsikaloudaki, A., and Theodosiou, T.: Analyzing the ENVI-met microclimate model's performance and assessing cool materials and urban vegetation applications – A review, *Sustain. Cities Soc.*, 43, 55–76, <https://doi.org/10.1016/j.scs.2018.08.009>, 2018.
- Wang, Y., Berardi, U., and Akbari, H.: Comparing the effects of urban heat island mitigation strategies for Toronto, Canada, *Energ. Buildings*, 114, 2–19, <https://doi.org/10.1016/j.enbuild.2015.06.046>, 2016.
- Wicker, L. J. and Skamarock, W. C.: Time-Splitting Methods for Elastic Models Using Forward Time Schemes, *Mon. Weather Rev.*, 130, 2088–2097, [https://doi.org/10.1175/1520-0493\(2002\)130<2088:TSMFEM>2.0.CO;2](https://doi.org/10.1175/1520-0493(2002)130<2088:TSMFEM>2.0.CO;2), 2002.
- Yang, J., Wang, Z., and Kaloush, K. E.: Environmental impacts of reflective materials: Is high albedo a “silver bullet” for mitigating urban heat island?, *Renewable and Sustainable Energy Reviews*, 47, 830–843, <https://doi.org/10.1016/j.rser.2015.03.092>, 2015.
- Žák, M., Zahradníček, P., Skalák, P., Halenka, T., Aleš, D., Fuka, V., Kazmuková, M., Zemánek, O., Flegl, J., Kiesel, K., Jareš, R., Resler, J., and Huszár, P.: Pilot Actions in European Cities – Prague, in: Counteracting Urban Heat Island Effects in a Global Climate Change Scenario, edited by: Musco, F., Springer, Cham, 373–400, https://doi.org/10.1007/978-3-319-10425-6_14, 2016.
- Zanobetti, A., O'Neill, M. S., Gronlund, C. J., and Schwartz, J. D.: Summer temperature variability and long-term survival among elderly people with chronic disease, *P. Natl. Acad. Sci. USA*, 109, 6608–6613, <https://doi.org/10.1073/pnas.1113070109>, 2012.
- Zhang, Y., Seidel, D. J., and Zhang, S.: Trends in Planetary Boundary Layer Height over Europe, *J. Climate*, 26, 10071–10076, <https://doi.org/10.1175/JCLI-D-13-00108.1>, 2013.